ISBN 978-82-326-4306-6 (printed version)
ISBN 978-82-326-4307-3 (electronic version)
ISSN 1503-8181

Doctoral theses at NTNU, 2019:355

Jon Vegard Venås

Acoustic Scattering in an Isogeometric Framework

NTNU
Norwegian University of
Science and Technology
Faculty of Information Technology
and Electrical Engineering
Department of Mathematical Sciences

NTNU
Norwegian University of
Science and Technology

Doctoral theses at NTNU, 2019:355

NTNU

NTNU
Norwegian University of
Science and Technology

Jon Vegard Venås

Acoustic Scattering in an Isogeometric Framework

Thesis for the degree of Philosophiae Doctor

Trondheim, December 2019

Norwegian University of Science and Technology
Faculty of Information Technology
and Electrical Engineering
Department of Mathematical Sciences

NTNU
Norwegian University of
Science and Technology

NTNU
Norwegian University of Science and Technology

Thesis for the degree of Philosophiae Doctor

Faculty of Information Technology
and Electrical Engineering
Department of Mathematical Sciences

ISBN 978-82-326-4306-6 (printed version)
ISBN 978-82-326-4307-3 (electronic version)
ISSN 1503-8181

Doctoral theses at NTNU, 2019:355

Printed by Skipnes Kommunikasjon as

To my family.

Preface

The phrase "A picture is worth a thousand words" is an adage that resonate throughout this thesis and my academic work. Creating properly made figures to explain scientific work is both crucial and time consuming, but nevertheless very satisfactory in the end. Several opinions exist for how to write good articles, especially when it comes to the length. In the spirit of Thomas Hughes quote "Don't tell me; show me", this work contains a lot of figures. Moreover, much of the work is self-contained, resulting in an even longer thesis. Not only does it ease the workflow for the reader, but it also makes the work more accessible to a greater audience.

I was introduced to isogeometric analysis (IGA) by my main supervisor Trond Kvamsdal in the first year of my master's degree, right after an introductory course in the finite element method. My co-supervisor Trond Jenserud proposed to combine IGA with acoustic scattering in my master's thesis entitled "Isogeometric Analysis of Acoustic Scattering". This work set the stage for my continued work on the topic for this PhD thesis.

Countless hours have been used programming in MATLAB resulting in a comprehensive toolbox I have named ASIGA (Acoustic Scattering using IsoGeometric Analysis). I'm an advocate for open research, and for this reason the ASIGA toolbox is open source. The toolbox is far from complete, but it will most likely be improved in future projects.

I would like to thank Trond Kvamsdal for guiding me through every stage of my career as a research scientist. I am not only grateful for Kvamsdal's scientific supervision, but also for giving me so many great life experiences abroad. I would also like to thank Trond Jenserud for his supervision and feedback on my work. I have very much enjoyed my stay at IMF[1], both as a student and as a PhD-candidate. Moreover, I would like to thank FFI[2] for the support and the opportunity to work on the topic of acoustics in two summer jobs, the second of which (supervised by Jenserud) gave me a head start for my PhD. Thanks to Karl Thomas Hjelmervik not only for supervising my first summer job at FFI and his

[1] Department of Mathematical Sciences.
[2] Norwegian Defence Research Establishment.

interest for my work, but also for including me into the research community with countless hours of board games. Thanks also to Kjetil André Johannessen for his scientific supervision and inspiration throughout the last 6 years. I would also like to thank Torbjørn Ringholm, Sølve Eidnes, Hallvard Norheim Bø, Morten Andreas Nome, Charles Curry, Winston Heap, Petter Kjeverud Nyland, Tale Bakken Ulfsby, Håvard Bakke Bjerkevik, Fredrik Arbo Høeg, Ingeborg Gullikstad Hem, Fredrik Hildrum, Kristoffer Varholm, Torstein Fjeldstad, Thea Roksvåg, Sondre Tesdal Galtung, Nicky Cordua Mattsson, Vanje Rebni Kjer, Maria Lie Selle, Mathias Nikolai Arnesen, Erik Rybakken, Alexander Sigurdsson, Ola Isaac Høgåsen Mæhlen, and many others for their support and entertainment making my PhD-study truly enjoyable. Finally, I would like to thank my family for their support and patience throughout this work.

Contents

Abbreviations

ABC	Absorbing boundary condition
AMR	Adaptive mesh refinement
ANSYS	Analysis Systems
ASCII	American standard code for information interchange
ASI	Acoustic structure interaction
ASIGA	Acoustic scattering using isogeometric analysis (toolbox)
BA	Best approximation
BEM	Boundary element method
BeTSSi	Benchmark target strength simulation
BGC	Bubnov–Galerkin conjugated
BGU	Bubnov–Galerkin unconjugated
BiCGstab	Biconjugate gradient stabilized method
BIE	Boundary integral equation
(C/G)CBIE	(Collocation/Galerkin) Conventional BIE
(C/G)HBIE	(Collocation/Galerkin) Hypersingular BIE
(C/G)BM	(Collocation/Galerkin) Burton–Miller
CAD	Computer aided design
CPU	Central processing unit
CHIEF	Combined Helmholtz integral formulation
DRDC	Defence Research and Development Canada
ESBC	Elastic sphere boundary condition
FDM	Finite difference method
FEA	Finite element analysis
FEM	Finite element method
FFT	Fast Fourier Transform
FWG	Die Forschungsanstalt der Bundeswehr für Wasserschall und Geophysik
GF	Gauss–Freud (quadrature)
GGL	Generalized Gauss–Laguerre (quadrature)
GL	Gauss-Legendre (quadrature)
GLL	Gauss-Lobatto-Legendre (nodes)

GMRES	Generalized minimal residual method
IE(M)	Infinite element (method)
IENSG	Infinite element for non-separable geometries
IGA	Isogeometric analysis
KDT	Kirchhoff diffraction theory
LR B-splines	Locally refined B-splines
LR	Lloyd's Register
MATLAB	MATrix LABoratory
MFS	Method of fundamental solutions
NACA	National Advisory Committee for Aeronautics
NNBC	Neumann-Neumann boundary condition
NURBS	Non-uniform rational B-splines
NSD	Numerical steepest descent
ODE	Ordinary differential equation
PDE	Partial differential equation
PGC	Petrov–Galerkin conjugated
PGU	Petrov–Galerkin unconjugated
PML	Perfectly matched layer
RAFAEL	Rafael advanced defense systems
RAM	Random-access memory
RDDC	Recherche et développement pour la défense Canada
SEM	Spectral element method
SHBC	Sound-hard boundary condition
SSBC	Sound-soft boundary condition
TKMS	ThyssenKrupp Marine Systems
TNO	The Netherlands Organisation for applied scientific research
TS	Target strength
WTD 71	Wehrtechnische Dienststelle für Schiffe und Marinewaffen
XIBEM	Extended isogeometric boundary element method

Notation

This thesis follows the following general notation conventions (inspired by the ISO-80000-2 standard).

- The usage of bars always indicates complex conjugation. For example, $\bar{p}$.
- Indices are denoted by i, j, l, m, n.
- The usage of breve indicates the time-dependent equivalent function of the corresponding function in the frequency domain. For example, $\breve{p}(\boldsymbol{x}, t)$, $p(\boldsymbol{x}, \omega)$.
- The usage of marks always indicates derivative. For example, $f'(\xi) = \frac{\mathrm{d}f}{\mathrm{d}\xi}$.
- The usage of tildes indicates an alternative variable. For example, σ_{ij}, $\tilde{\sigma}_{ij}$.
- The usage of hats over vectors indicates normalized vectors. For example, $\hat{\boldsymbol{x}} = \boldsymbol{x}/|\boldsymbol{x}|$.
- Bold notation is used for vectors, matrices and tensors. For example, $\boldsymbol{x}$, $\boldsymbol{C}$ and $\boldsymbol{\sigma}$. The components should not be written in bold notation, i.e. x_i, C_{ij}, σ_{ij}.
- Units, fundamental constants and fundamental functions should be in upright mode (Euler's number e, kilograms kg, meter m, spherical Bessel function j_n, spherical Hankel function h_n, etc.).
- Descriptive text is written in right mode i.e. p_{inc} (the incident pressure field).

General notation

$\boldsymbol{A}$	Global matrix of linear equations
$B_\epsilon(\boldsymbol{x})$	Ball of radius ϵ centered at $\boldsymbol{x}$
$B(p, q)$	Bilinear form

$B_{i,\check{p},\boldsymbol{t}}$	The i^{th} B-spline basis function of degree $\check{p}$ and with knot vector $\boldsymbol{t}$
B_n	Radial integral in infinite elements
C^n	Space of continuous functions that have continuous first n derivatives
C_n	Coefficients for manufactured solution
$\mathbb{C}$	Space of complex numbers
c_f	Sound speed in fluid
d	Differential
$\boldsymbol{d}_\mathrm{inc}$	Unit vector pointing in the direction of the incident plane wave
d	Spatial dimension
$D_{m\tilde{m}}$	Coefficients for radial basis functions in the solution space of the infinite elements
$\tilde{D}_{n\tilde{n}}$	Coefficients for radial basis functions in the test space of the infinite elements
$\boldsymbol{e}$	Unit basis vector
$\boldsymbol{e}_i$	Standard Cartesian basis vector
$\boldsymbol{e}_\mathrm{r}$, $\boldsymbol{e}_\vartheta$, $\boldsymbol{e}_\varphi$	Basis vectors for the spherical coordinate system
e	Euler's number $\mathrm{e} = 2.718\,281\,828\,459\,045\ldots$
E	Young's modulus
E_n	Exponential integral
f	Frequency
$\mathcal{F}$	Fourier transform
g	Neumann data
G	Shear modulus
G^n	Geometric continuity of order n (G^0 being a geometry with kinks)
h, h_max	Maximal element size
$\boldsymbol{H}_n$	Global matrix for the linear system of equations for the n^{th} mode
$\mathrm{h}_n^{(i)}$	The n^{th} spherical Hankel function of i^{th} kind
i	Imaginary unit $\mathrm{i} = \sqrt{-1}$
$\boldsymbol{J}$	Jacobian matrix
J	Jacobian determinant
j_n	The n^{th} spherical Bessel function of first kind
J_n	The n^{th} Bessel function of first kind
k (k_m)	Angular wave number (in the m^{th} fluid layer)
$\check{k}$	Continuity
K	Bulk modulus
$\boldsymbol{K}$	Stiffness matrix
$L(p)$	Linear form
$\boldsymbol{M}$	Mass matrix
$\mathcal{M}^{\mathrm{IGA}}_{m,\check{p},\check{k}}$	IGA mesh number m with polynomial order $\check{p}$ and continuity $\check{k}$
$\mathcal{M}^{\mathrm{FEM}}_{m,\check{p},\mathrm{i}}$	Isoparametric FEM mesh number m with polynomial order $\check{p}$
$\mathcal{M}^{\mathrm{FEM}}_{m,\check{p},\mathrm{s}}$	Subparametric FEM mesh number m with polynomial order $\check{p}$

$\mathbb{N}$	Space of non-negative integers
$\mathbb{N}^*$	Space of positive integers
N	Number of basis functions in the radial direction for infinite elements
n_ξ	Number of basis functions in the ξ-direction
n_η	Number of basis functions in the η-direction
n_ζ	Number of basis functions in the ζ-direction
n_{dof}	Number of degrees of freedom
$\boldsymbol{n}$	Outward pointing (unit) normal vector
P_n	Legendre polynomial
P_n^m	Associated Legendre functions
p_0	Far field pattern
p, $\breve{p}$	Scattered pressure field
p_{inc}	The incident wave
P_{inc}	Amplitude of incident wave
p_{tot}	Total pressure field $p_{\text{tot}} = p + p_{\text{inc}}$
$\breve{p}$	Polynomial degree (or degree of NURBS functions)
$\breve{p}_\xi$	Degree of basis functions in the ξ-direction
$\breve{p}_\eta$	Degree of basis functions in the η-direction
$\breve{p}_\zeta$	Degree of basis functions in the ζ-direction
r	Radius in the spherical (or prolate spheroidal) coordinate system
r_{a}	Radius at artificial boundary in the spherical (or prolate spheroidal) coordinate system
$\mathbb{R}$	Space of real numbers
R	Distance between the arguments of Φ_k, $R = \lvert\boldsymbol{x} - \boldsymbol{y}\rvert$
R_i	NURBS basis function (with global index i)
$R_{i,j,l}$	NURBS basis function (with local indices i, j and l)
$\mathcal{S}$	Solution space
$\mathcal{S}_h$	Finite dimensional solution space
t	Time variable
$\boldsymbol{t}_\xi$	Knot vector in the ξ-direction
$\boldsymbol{t}_\eta$	Knot vector in the η-direction
$\boldsymbol{t}_\zeta$	Knot vector in the ζ-direction
T	Period
$\boldsymbol{T}$	Exterior traction vector
TS	Target strength
$\boldsymbol{x}$	Spatial variable in Cartesian coordinates
$\boldsymbol{X}$	Geometric parameterization
$\boldsymbol{u}$, $\breve{\boldsymbol{u}}$	Displacement in the solid domain
$\mathcal{V}$	Test space
$\mathcal{V}_h$	Finite dimensional test space
y_n	The n^{th} spherical Bessel function of second kind
Y_n	The n^{th} Bessel function of second kind

$\boldsymbol{y}_n$	Source points for manufactured solution
$\mathbb{Z}$	Space of integers
α (α_s)	Aspect angle (for the source point)
$\mathit{\Gamma}$	Boundary of scatterer
$\mathit{\Gamma}_{\check{p}}$	Outer boundary of BeTSSi submarine ($\check{p} \geqslant 2$)
γ	Euler-Mascheroni constant $\gamma = 0.577\,215\,664\,901\,532\,861\ldots$
δ_{ij}	Kronecker delta
$\mathit{\Delta}$	Triangle constructor $\mathit{\Delta}(\boldsymbol{x}_1, \boldsymbol{x}_2, \boldsymbol{x}_3) \subset \mathbb{R}^d$
Δ	Difference operator
ε	Machine epsilon precision
ε_{ij}	Strain field in Cartesian coordinates
η	Second parameter of the parameter space
ζ	Third parametric NURBS parameter
ϑ (ϑ_s)	Polar angle in the spherical coordinate system (at the source point)
$\boldsymbol{\kappa}$	Set of indices (for NURBS functions in solution/test space)
λ	Wavelength
ν	Poisson's ratio
ξ	First parameter of the parameter space
ξ_1, ξ_2, ξ_3	Area coordinates (barycentric coordinates) of a triangle
π	Archimedes' constant (pi) $\pi = 3.141\,592\,653\,589\,793\ldots$
ρ	Substitution variable $\varrho = r/r_\mathrm{a}$
ϱ_1	Simplifying notation variable $\varrho_1 = \Upsilon/r_\mathrm{a}$
ϱ_2	Simplifying notation variable $\varrho_2 = kr_\mathrm{a}$
ϱ_3	Simplifying notation variable $\varrho_3 = k\Upsilon$
ρ_f	Mass density of fluid
ρ_s	Mass density of solid
σ_{ij}	Stress field in Cartesian coordinates
τ	Minimal number of degrees of freedom per wavelength
Υ	Focus in the elliptic/prolate spheroidal coordinate system
φ (φ_s)	Azimuth angle in the spherical coordinate system (at the source point)
$\mathit{\Phi}_k$	Fundamental solution of Helmholtz equation
ω	Angular frequency
$\mathit{\Omega}_\mathrm{s}$	Solid domain
$\mathit{\Omega}^+$	Unbounded exterior fluid domain
$\mathit{\Omega}^-$	Interior fluid domain
∂	Partial derivatives

Notation for paper I

a (a_m)	Longitudinal angular wave number (in the m^{th} shell)

$A_n^{(i)}$	Coefficients of potential function ϕ in the solid domain
b (b_m)	Transverse angular wave number (in the m^{th} shell)
$B_n^{(i)}$	Coefficients of potential function ψ_φ in the solid domain
B	Bandwidth
$\boldsymbol{B}_{m,n}$	Local vector of unknown coefficients in the linear system of equations for the n^{th} mode
$c_{\text{s},1}$	The longitudinal wave velocity in a solid
$c_{\text{s},2}$	The transverse wave velocity in a solid
C_ε	Upper bound for scaled frequency, regarding round-off error with precision ε
$\boldsymbol{C}$	Linear elasticity matrix
$\boldsymbol{C}_n$	Vector of unknown coefficients in the system of equation for the n^{th} mode
$\boldsymbol{C}_{m,n}$	Local vector of unknown coefficients in the system of equations for the n^{th} mode
$C_n^{(i)}$	Coefficients of the scattered pressure p
$\boldsymbol{D}$	Stress coordinate transformation matrix
$\boldsymbol{D}_n$	Right hand side vector for the linear system of equation for the n^{th} mode
f_{c}	Center frequency in wavelet
$F_n^{(i)}$	Coefficients of the incident wave expanded in Legendre functions at the outer surface
$G_{p,q}^{m,n}$	Meijer G-function
h_{r}, h_ϑ, h_φ	Scale factors for the spherical (or prolate spheroidal) coordinate system
$\boldsymbol{H}_{m,n}^{(i,j)}$	Submatrices of $\boldsymbol{H}_n$
M	Number of spherical shells
N	Number of terms in Fourier sum
N_ε	Infinite series truncation number
$Q_n^{(i)}$	Derivatives of Legendre polynomials with cosine argument
$R_{0,m}$	Outer surface radius of m^{th} spherical shell
$R_{1,m}$	Outer surface radius of m^{th} spherical shell
$S_{j,n}^{(i)}$	Simplifying notation. Superposition of Bessel functions with argument $\xi = ar$
$T_{j,n}^{(i)}$	Simplifying notation. Superposition of Bessel functions with argument $\eta = br$
$Z_n^{(i)}$	Spherical Bessel functions
α_{ij}	Cosine between two basis vectors in a coordinate transformation
ζ	Simplifying notation $\zeta = kr$
η	Simplifying notation $\eta = br$

ξ	Simplifying notation $\xi = ar$
Υ_ε	Simplifying parameter for the upper bound C_ε
υ	Order of Bessel function
ϕ	First potential function in solid
$\boldsymbol{\psi}$	Second potential function in solid
Ψ, $\boldsymbol{\Psi}$	General scalar or vector function
ω_c	Center angular frequency in wavelet
φ	Azimuth angle in the spherical coordinate system
φ_s	Azimuth (or aspect) angle for the source point

Notation for paper II

d_1, d_2	Distances from foci in prolate coordinate system
R_0	Outer surface radius of spherical shell
R_1	Inner surface radius of spherical shell
w	Weights for weighted Sobolev spaces in Ω^+ for the trial space
w^*	Weights for weighted Sobolev spaces in Ω^+ for the test space
p_1	Scattered pressure in exterior domain Ω^+
p_2	Scattered pressure in interior domain Ω^-
Q_m	Polynomial function of the radial shape functions ϕ
$\tilde{Q}_n$	Polynomial function of the radial shape functions ψ
Γ_a	Artificial boundary
Γ_0	Outer boundary of scatterer
Γ_1	Inner boundary of scatterer
ϕ_n	Basis function in radial direction in infinite elements for the trial space
ψ_n	Basis function in radial direction in infinite elements for the test space
Ω_a	Fluid domain inside artificial boundary Γ_a
Ω_a^+	Fluid domain outside the artificial boundary Γ_a

Notation for paper III

$C^\pm$	Jump-term in the exterior (+) or interior (−) problem
f_t	NACA profile function of foil with width t
l	Distance from the center of an element to a source point
$n_{\mathrm{eqp},1}$	Number of extra quadrature points in BEM formulation (in addition to the standard $\check{p}+1$ points) in elements not containing singularity
$n_{\mathrm{eqp},2}$	Number of extra quadrature points in BEM formulation (in addition to the standard $\check{p}+1$ points) in elements containing singularity

N	Number of terms in manufactured solution
s_1	Parameter controlling adaptivity of quadrature integration
γ^+	Trace operator in Ω^+
γ^-	Trace operator in Ω^-
α	Coupling parameter in BM formulation
Ψ	Jump-term in the exterior (+) or interior (-) problem

Notation for paper IV

$f(\cdot)$	Amplitude function in oscillatory integrals
$F(\cdot)$	Non-oscillatory exponentially integral
$g(\cdot)$	Oscillator function in oscillatory integrals
h_ξ	Path in the complex plane at which the oscillatory integral is not oscillatory
α	Exponent of weight factor in GGL quadrature

Notation for addendum

$f(\cdot)$	Right hand side function for the Poisson equation
$l_{i,\boldsymbol{t}}$	The i^{th} Lagrange basis function defined over the interpolation points in $\boldsymbol{t}$
Φ_n	Generating polynomial

Notation for appendices

a	Longitudinal angular wave number for the first potential function (in the solid)
b	Transverse angular wave number for the second potential function (in the solid)
E_j	Energy of beam B_j
h	Solid layer thickness
N	Number of rays/beams
R	Reflection coefficient
s	Parameter for parameterizing rays
T	Transmission coefficient
θ_1	Angle of incidence
θ_2	Angle of refraction
θ_3	Angle of transmission
τ	Phase function in ray series

ϕ	First potential function in solid
ψ	Second potential function in solid

Introduction

Introduction

Wave phenomena occur throughout nature in many forms. As Nikola Tesla puts it: "If you want to find the secrets of the universe, think in terms of energy, frequency and vibration". Examples include:

- Electromagnetic waves [1] with application into dental radiography (X-rays), microwave ovens, television, radios, just to name a few.
- Seismic waves with application including predicting tsunamis [2] and volcano eruptions [3].
- Structural vibrations with applications into noise prediction and control, architectural and musical acoustics.
- Acoustic waves with applications in ocean acoustics and acoustical oceanography [4, 5].

In this thesis the focus is mainly on acoustic waves, but also in combination with structural vibration, namely how sound and structures interact [6]. The study of acoustic-structure interaction (ASI) is the topic of the first two papers while the latter two are restricted to the fluid part. Acoustic waves are used to detect and localize objects [7], for underwater communication, and for remote sensing of the ocean: to remotely classify distributions of biological organisms such as fish [8] and plankton [9], for the purpose of fish supply management and ecological studies [10]; to characterize the seafloor micro relief, with application in sound propagation, geological studies and mining; to remotely measure physical properties of the ocean such as temperature, flow and turbulence, with applications in climate monitoring [11] and the study of bottom boundary layer dynamics and hydrocarbon seeps.

Common for all applications above is the possibility to linearize the governing equations such that the problems may be modeled by the much simpler wave equation

$$\nabla^2 \breve{p} = \frac{1}{c_{\mathrm{f}}^2} \frac{\partial^2 \breve{p}}{\partial t^2} \tag{1}$$

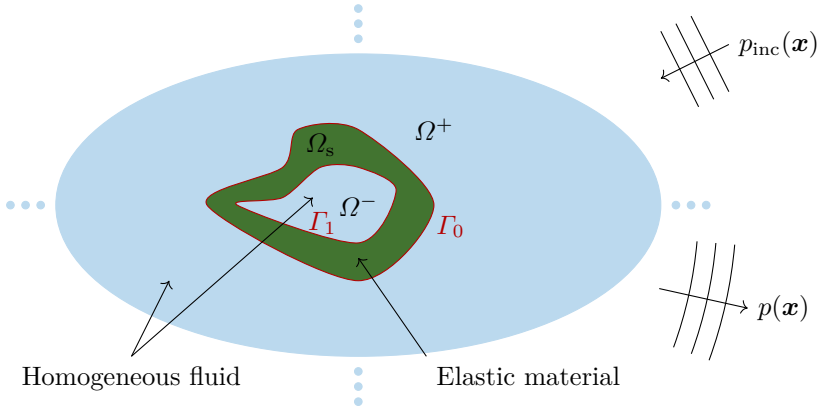

Figure 1: Illustration of the physical problem. A plane incident wave, $p_{\text{inc}}(\boldsymbol{x})$, is scattered by the scatterer, Ω_{s}, in an unbounded domain, Ω^+, resulting in the scattered wave, $p(\boldsymbol{x})$. The scatterer, which is bounded by the boundaries Γ_0 and Γ_1, envelops a fluid domain, Ω^-.

with wave speed c_{f}. Looking for solutions of the form $\breve{p}(\boldsymbol{x}, t) = \mathrm{e}^{-\mathrm{i}\omega t} p(\boldsymbol{x})$ (with angular frequency ω) the wave equation may be analyzed in the frequency domain as the Helmholtz equation

$$\nabla^2 p + k^2 p = 0 \tag{2}$$

with the wave number $k = \omega / c_{\text{f}}$.

Figure 1 illustrates the general problem setup considered in this thesis. For subsurface acoustics, the unbounded domain Ω^+ is modeled as water whereas internal fluid domains may either be water or air (i.e. pressure hulls in submarines). Sound signals is the only practical way of transmitting sound in water [12], and so an understanding of the physical properties of such signals are important, not only for sonar (sound navigation ranging) technologies, but also the study of marine life. The precise behavior of subsurface sound waves is dependent on a vast set of parameters including the temperature, the salinity and the depth. In this work, however, linearized equations like the wave equation in Eq. (1) will be used with constant sound speed, c_{f}. That is, the fluid domains are assumed to be homogeneous.

Solution of the time dependent wave equation in Eq. (1) may be found by transforming solutions of the Helmholtz equation for a range of frequencies $f = \omega/(2\pi)$ using an inverse Fourier transformation [12]. This approach is advantageous for several reasons. First, the dimension of the problem is reduced by one, enabling trivial parallelization over the frequencies. Second, the Fourier transformations step may be computed by a fast Fourier transform with a reduced complexity from $\mathcal{O}(N^2)$ to $\mathcal{O}(N \log N)$ with N being the data size. Third, working with elliptic equations is often easier than hyperbolic equations, especially for exterior

Helmholtz problems. Finally, many acoustic applications are of narrow-band nature [12] leading to a reduction of the spectrum of frequencies in which solutions of the Helmholtz equation are needed.

In three dimensions the scattering problem in Figure 1 only admits analytic solutions on closed form for very simple geometries. The scarcity of such solutions makes the existing solution very valuable and is the subject of the first paper.

For slightly more complex geometries, however, numerical methods are required. To this end, a vast set of methods are available. Finite element analysis is the subject of the second paper, the boundary element method is the subject of the third paper and Kirchhoff approximation is the subject of the fourth paper. Additionally, the ray/beam tracing method is investigated in the appendices. Most of these methods fit very well in the isogeometric framework which will be introduced more thoroughly in the introduction part. Finally, the finite difference method (FDM) should be mentioned as an alternative [13]. The FDM is not very suited for the present 3D problem setup (in the frequency domain) due to tedious handling of general geometries. However, it is commonly used for discretizing the time dimension when solving the time-dependent wave equation in Eq. (1) (where the spatial dimensions are discretized with finite elements).

The main application studied in this thesis is acoustic scattering on submarines. In this regards the quantity of interest is the *target strength* defined by

$$\mathrm{TS} = 20\log_{10}\left(\frac{|p_0(\hat{\boldsymbol{x}})|}{|P_{\mathrm{inc}}|}\right) \tag{3}$$

where P_{inc} is the amplitude of the incident wave at the geometric center of the scatterer (i.e. the origin) and the far field pattern of the scattered pressure, p, is given by

$$p_0(\hat{\boldsymbol{x}}) = \lim_{r\to\infty} r\mathrm{e}^{-\mathrm{i}kr}p(r\hat{\boldsymbol{x}}), \tag{4}$$

with $r = |\boldsymbol{x}|$ and $\hat{\boldsymbol{x}} = \boldsymbol{x}/|\boldsymbol{x}|$ being the far field observation point. The observation point can be represented in terms of the aspect angle α and elevation angle β (see Figure 2)

$$\hat{\boldsymbol{x}} = \begin{bmatrix} \cos\beta\cos\alpha \\ \cos\beta\sin\alpha \\ \sin\beta \end{bmatrix}.$$

TS models are also used to discriminate man-made objects, such as mines, toxic waste containers, from natural objects such as rocks. The method known as acoustic resonance scattering utilizes the differences of target strength at low frequencies of natural irregular objects and man-made regular elastic objects [14, 15].

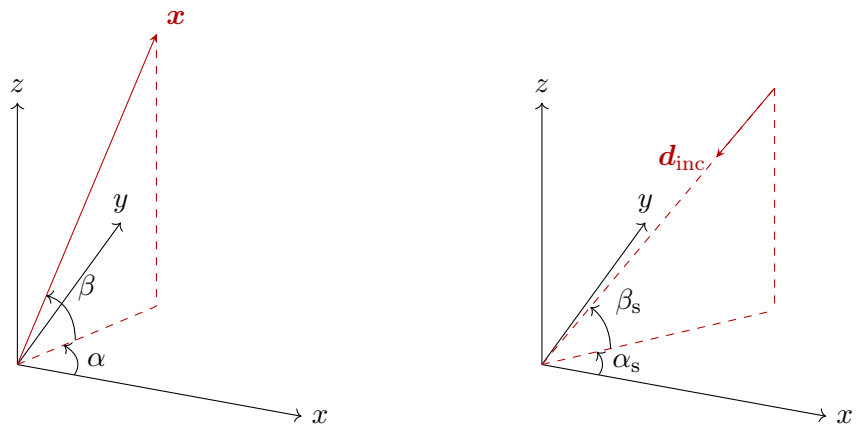

Figure 2: Illustration of the aspect angle α and the elevation angle β describing an observation point $\boldsymbol{x}$. The direction of the incident wave can be represented in terms of the aspect angle α_s and the elevation angle β_s.

1. Background

The target strength of a submarine is considered highly classified and is typically kept within each nation. The desire to simulate scattering on classified submarines has led to the need of benchmarks not subject to military classification that can be shared such that results could be compared between institutes.

The BeTSSi[1] community gives a solid basis for the benchmarking exercise which is very important for code development. The first BeTSSi workshop was initiated by FWG[2] in 2001 where several models (some of which are illustrated in Figure 3) were presented as benchmark problems to be analyzed. The first and second workshop were held in Kiel in 2002 and 2012, respectively. The third was held in the Hague in 2016.

The objective is to compute the target strength of submarine structures. More specifically the analysis of the scattered pressure from a plane wave

$$p_\mathrm{inc}(\boldsymbol{x}) = P_\mathrm{inc}\mathrm{e}^{\mathrm{i}k\boldsymbol{d}_\mathrm{inc}\cdot\boldsymbol{x}} \tag{5}$$

incident on the models. Here, $\boldsymbol{d}_\mathrm{inc}$ is the traveling directing of the plane wave which can be represented in terms of the aspect angle α_s and elevation angle β_s

[1] Benchmark Target Strength Simulation.

[2] Die Forschungsanstalt der Bundeswehr für Wasserschall und Geophysik. Integrated with WTD 71 (Wehrtechnische Dienststelle für Schiffe und Marinewaffen, Maritime Technologie und Forschung) in 2009.

(see Figure 2)

$$\boldsymbol{d}_{\text{inc}} = -\begin{bmatrix} \cos\beta_{\text{s}}\cos\alpha_{\text{s}} \\ \cos\beta_{\text{s}}\sin\alpha_{\text{s}} \\ \sin\beta_{\text{s}} \end{bmatrix}.$$

Results from the BeTSSi workshops appears in several publications e.g. [16–20]. An example of a test case that was presented on the workshop in the Hague was a monostatic[3] sweep over the elevation angles $\beta \in [-30°, 60°]$ at $\alpha = 90°$ of the full BeTSSi submarine (illustrated in Figure 4) at given frequencies, $f \in [1, 3, 10, 30]$ kHz. The institutes that contributed to this benchmark were the DRDC (Defence Research and Development Canada), LR (Lloyd's Register), RAFAEL (Rafael Advanced Defense Systems, Israeli defense technology company), Tel Aviv University, Thales Group, TKMS (ThyssenKrupp Marine Systems), TNO (the Netherlands Organisation for applied scientific research) and WTD 71.

The results are illustrated in Figure 5. Clearly such a complex benchmark requires advanced software to obtain accurate solutions which are arguably lacking in this benchmark test case. The state-of-the-art is not satisfactory, which is a motivation for the research in the BeTSSi community. To first obtain accurate solutions for simpler benchmark examples is crucial in order to advance to this level of complexity. It is recommended by the community that the participants first obtain good results on spherical shells which admits analytic solutions [23], before advancing to the BeTSSi models which do not have exact reference solutions available. A benchmark that will be used throughout this thesis is a plane wave incident in the positive z-axis

$$p_{\text{inc}}(\boldsymbol{x}) = P_{\text{inc}}\mathrm{e}^{\mathrm{i}kx_3}$$

scattering by a rigid unit sphere ($R_0 = 1\,\text{m}$). The analytic solution is given by[4] (expressed in spherical coordinates)

$$p(r,\theta) = -P_{\text{inc}}\sum_{n=0}^{\infty}\mathrm{i}^n(2n+1)\frac{\mathrm{j}_n'(kR_0)}{\mathrm{h}_n'(kR_0)}\mathrm{P}_n(\cos\theta)\mathrm{h}_n(kr) \tag{6}$$

Due to axis symmetry, this solution can be generalized for arbitrary incident wave direction (Eq. (5)) with a simple orthogonal transformation. The advantage of having several models with different complexity is to have a gradual increase in complexity to be able to run simulations on the full BeTSSi submarine. In particular, the BeTSSi model 1 represents a convex model, model 4 represents a triple reflector (which can be found in the more advance BeTSSi model 2) and

[3]For *monostatic* scattering we have $\alpha_{\text{s}} = \alpha$ and $\beta_{\text{s}} = \beta$ as opposed to *bistatic* scattering where both the aspect angle and elevation angle in general do not coincide.

[4]Where $\mathrm{j}_n(x)$ is the n^{th} spherical Bessel function of the first kind and $\mathrm{h}_n(x)$ is the n^{th} spherical Hankel function of the first kind.

(a) The BeTSSi model 1 - air filled

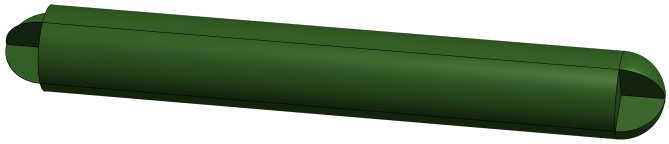

(b) The BeTSSi model 2 - air filled

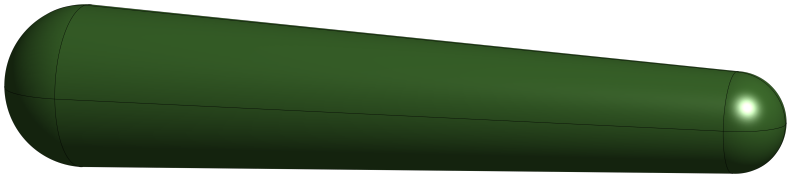

(c) The BeTSSi model 3 - water filled

(d) The BeTSSi model 4

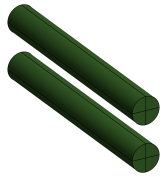

(e) The BeTSSi model 5A

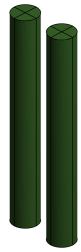

(f) The BeTSSi model 5B

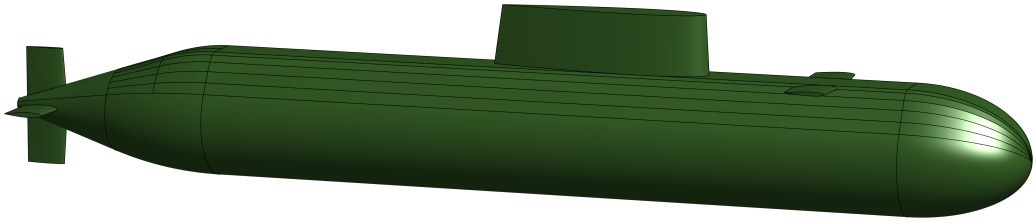

(g) The outer hull of the BeTSSi submarine

Figure 3: **BeTSSi models**: The BeTSSi model 3 is described and analyzed in [21] and the BeTSSi submarine is described and analyzed in [22].

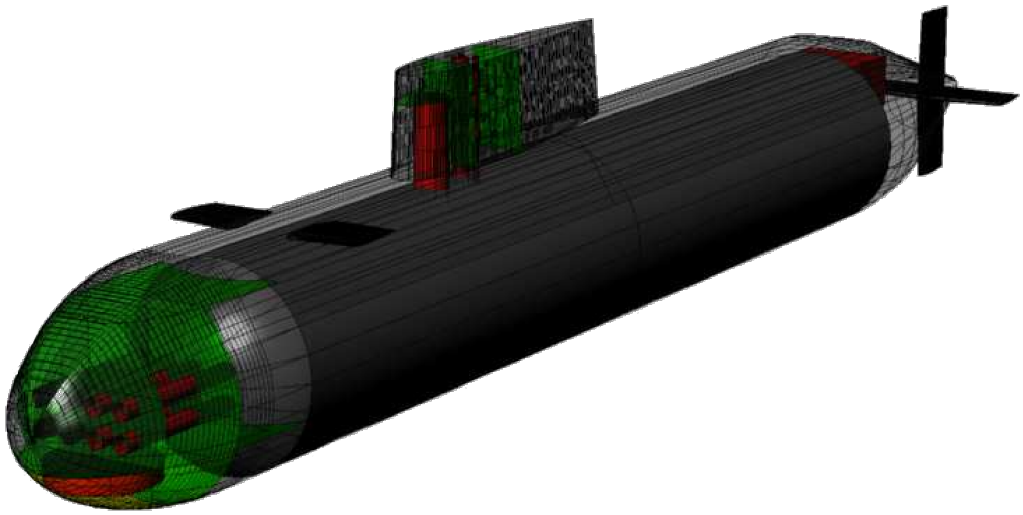

Figure 4: The full BeTSSi submarine has internal structures including 8 torpedo tubes, cylindrical hydrophone array, and bulkheads.

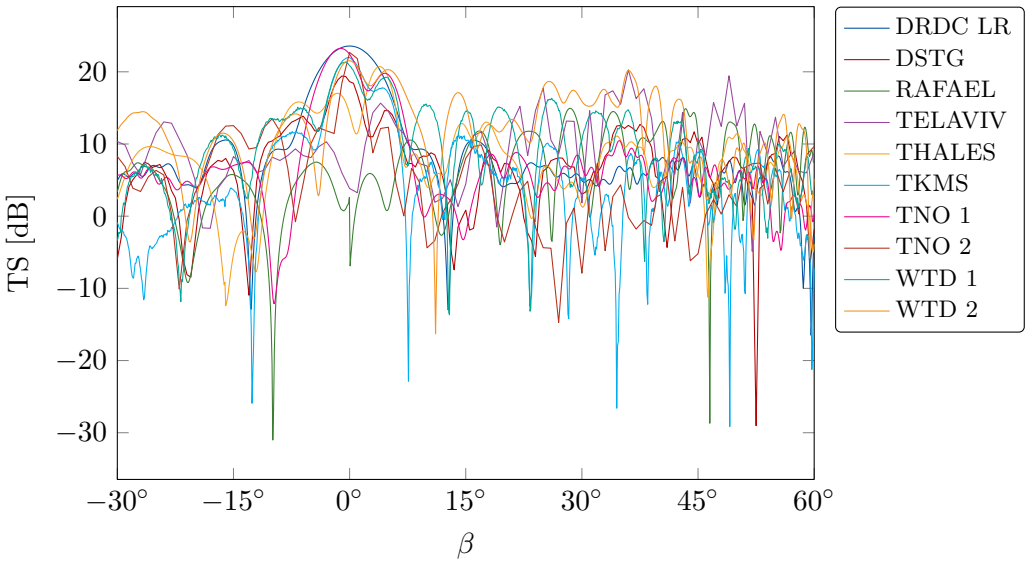

Figure 5: Monostatic scattering of the full BeTSSi submarine at $f = 1\,\mathrm{kHz}$ sweeping through the elevation angle β at $\alpha = 90°$.

model 5 represent disjoint geometries. The natural start would be to consider rigid scattering (with hard walled boundary condition) such that only fluid domains need to be modeled. Next, more realistic boundary conditions can be considered which incorporates interaction with elastic shells. The BeTSSi model 1 or 2 may then be embedded in BeTSSi model 3 to check the ability to simulate internal structures. This approach sets the stage for simulating on the full BeTSSi submarine.

2. Isogeometric analysis

IGA is basically an extension of the FEM using either B-splines or non-uniform rational B-splines (NURBS) as basis functions not only representing the geometry, but also the solution space. Being introduced in 2005 by Hughes et al. [24], followed by the book [25] in 2009, IGA tries to bridge the gap between finite element analysis and computer aided design (CAD) tools. The important feature of IGA is that it uses the same basis as CAD software for describing the given geometry, and thus exact representation of the model is possible. It is therefore natural to include a section considering this basis in the beginning before we set up the IGA for the problem at hand.

The isogeometric framework is illustrated in Figure 6, where a wine glass is used as an example. Products are often designed in CAD software which enables rendering (or image synthesis) functionality for a photorealistic view of the product. Before producing a visually satisfactory product it is often of interest to do some analysis to check whether or not the product serves its purpose. For decades the finite element method (FEM) has been a crucial framework where this analysis has been obtained. FEM requires an analysis suitable discretization of the model before analysis can be performed. The isogeometric analysis (IGA) framework tries to avoid this discretization step as it uses the parametrization directly from the CAD model. A significant amount of time has traditionally been needed in this step ($\sim$80%), and so the potential of the isogeometric framework is for this reason alone very intriguing. In the realm of local refinement, it should be mentioned that creating an analysis suitable model is a hot research topic also in the IGA community [26–32]. The IGA framework may also be used in the post processing step where the visualization is computed using the same NURBS basis from analysis [33]. Finally, it turns out that the spline basis functions are particularly suited to solve elliptical problems [34, 35]. This effect is arguably the main motivator for using IGA in this work as numerical dispersion and dissipation errors are reduced in wave propagation problems [36–39]. One can then conclude that IGA is particularly well suited to solve acoustic scattering problems.

The classical $\check{p}$-refinement and h-refinement are often obtained for more accurate solutions in FEA. IGA comes with an additional refinement feature called the $\check{k}$-refinement with not only an increase in polynomial order, but also the continuity.

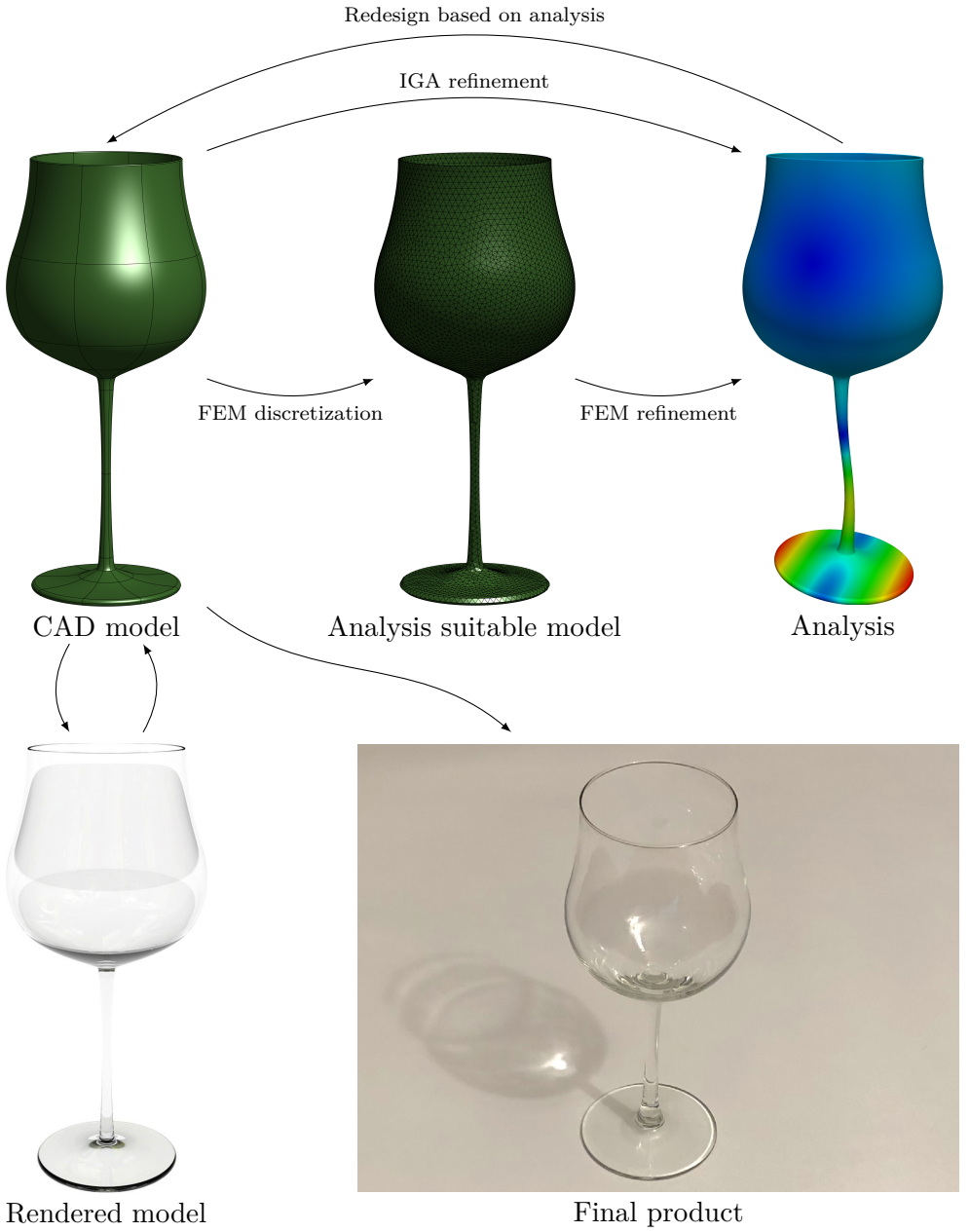

Figure 6: **The isogeometric framework**: Isogeometric analysis (IGA) avoids the creation of an analysis suitable discretization step of the finite element method (FEM) as it uses the discretization given by the computer aided design (CAD) system.

This is the beauty of IGA as it allows control of the continuity in the discretization spaces. The mathematical potential of the $\check{k}$-refinement is presented in [34], and the application of this technique will be illustrated in paper II and paper III.

Since IGAs conception in 2005, it has obtained an impressive growth in terms of published articles, citations and active researchers in the field. IGA has excelled in a number of applications including continuum damage models [40], blood flow [41–43], free surface flow [44], wind energy [45, 46], fracture mechanics [47–49], topology optimization [50], shape optimization [51, 52], shell theory [53], contact problems [54, 55], structural vibrations [56], immersed boundary methods [57], sliding interfaces [58], and phase-field modeling [59]. The academic interest of IGA has so far been a huge success, and it remains to see when the industry fully incorporates this progress into modeling software. Classical finite element technologies are deeply rooted into comprehensive software, but we can already see several major software companies showing interest (i.e. Abaqus [60]).

2.1. B-splines

The NURBS basis is constructed using B-splines. Therefore, an understanding of B-splines is crucial to understanding NURBS. Let $\check{p}$ be the polynomial order[5], let n be the number of basis functions and define a *knot vector* $\boldsymbol{t} = \{\xi_1, \xi_2, \ldots, \xi_{n+\check{p}+1}\}$ to be an ordered vector with non-decreasing elements, called *knots*. Then, the n B-splines, $\{B_{i,\check{p},\boldsymbol{t}}\}_{i\in[1,n]}$, are recursively defined by

$$B_{i,\check{p},\boldsymbol{t}}(\xi) = \frac{\xi - \xi_i}{\xi_{i+\check{p}} - \xi_i} B_{i,\check{p}-1,\boldsymbol{t}}(\xi) + \frac{\xi_{i+\check{p}+1} - \xi}{\xi_{i+\check{p}+1} - \xi_{i+1}} B_{i+1,\check{p}-1,\boldsymbol{t}}(\xi)$$

starting with

$$B_{i,0,\boldsymbol{t}}(\xi) = \begin{cases} 1 & \text{if } \xi_i \leqslant \xi < \xi_{i+1} \\ 0 & \text{otherwise.} \end{cases} \tag{7}$$

This formula is referred to as Cox-de Boor formula, and the derivative of a B-spline may be computed by

$$\frac{\mathrm{d}}{\mathrm{d}\xi} B_{i,\check{p},\boldsymbol{t}}(\xi) = \frac{\check{p}}{\xi_{i+\check{p}} - \xi_i} B_{i,\check{p}-1,\boldsymbol{t}}(\xi) - \frac{\check{p}}{\xi_{i+\check{p}+1} - \xi_{i+1}} B_{i+1,\check{p}-1,\boldsymbol{t}}(\xi). \tag{8}$$

Throughout this work, we shall use *open knot vectors* (in order to easily handle boundary conditions). That is, the first and last element in the vector are repeated $\check{p}+1$ times. Moreover, a knot is said to have *multiplicity* m if it is repeated m times in $\boldsymbol{t}$.

Some important properties of B-splines are given by the following (for proof, cf. [61]).

[5]The usage of a check sign above the polynomial order p is to avoid ambiguity between the polynomial order and the scattered pressure.

1. $B_{i,\check{p},\boldsymbol{t}}$ are piecewise polynomials.
2. $B_{i,\check{p},\boldsymbol{t}}$ depends only on the knots $\xi_i, \xi_{i+1}, \ldots, \xi_{i+\check{p}+1}$.
3. In general $B_{i,\check{p},\boldsymbol{t}}(\xi) \geqslant 0$, and if $\xi \notin [\xi_i, \xi_{i+\check{p}+1})$ then $B_{i,\check{p},\boldsymbol{t}}(\xi) = 0$.
4. If $\xi \in [\xi_j, \xi_{j+1})$ then $B_{i,\check{p},\boldsymbol{t}}(\xi) = 0$ if $i < j - \check{p}$ or $i > j$.
5. If $\xi \in (\xi_i, \xi_{i+\check{p}+1})$ then $B_{i,\check{p},\boldsymbol{t}}(\xi) > 0$.
6. If $\tilde{\xi} = \xi_{j+1} = \cdots = \xi_{j+\check{p}} < \xi_{j+\check{p}+1}$ then $B_{i,\check{p},\boldsymbol{t}}\left(\tilde{\xi}\right) = \delta_{ij}$.
7. If a knot $\tilde{\xi} \in \{\xi_i, \ldots, \xi_{i+\check{p}+1}\}$ has multiplicity m then $B_{i,\check{p},\boldsymbol{t}}$ is $\check{p} - m$ differentiable at $\tilde{\xi}$.
8. B-splines satisfies the partition of unity property. That is,

$$\sum_{i=1}^{n} B_{i,\check{p},\boldsymbol{t}}(\xi) = 1 \qquad \forall \xi, \check{p}.$$

9. B-splines forms a *stable* basis for piecewise polynomials.

To ease the understanding of B-splines we shall construct an illustrative example. Consider quadratic B-splines ($\check{p} = 2$) with the knot vector $\boldsymbol{t} = \{0, 0, 0, 1, 2, 2, 3, 3, 3\}$. Note that the use of a non-normalized knot vector is only for convenience and carries no importance; the B-splines would have had the same characteristics if we divided all knots by 3. Since $|\boldsymbol{t}| = 10$, the number of basis functions is given by $n = |\boldsymbol{t}| - \check{p} - 1 = 6$. In Figure 7, Figure 8 and Figure 9, we have plotted not only the 6 basis functions of second order, but also the functions of order zero and one needed to evaluate these basis functions. By property 7 in the previous list, we see that $B_{1,2}$ and $B_{6,2}$ are discontinuous at $\xi = 0$ and $\xi = 3$, respectively ($\check{p} = 2$ and $m = 3$ yields C^{-1} continuity in the endpoints). This is characteristic for all open knot vectors. Also note that the repeated knot at $\xi = 2$ forces the function to have the Kronecker delta property; that is, $B_{i,\check{p}}(\xi_j) = \delta_{ij}$ if ξ_j has multiplicity $m = \check{p}$.

We may now define a *spline curve* by

$$\boldsymbol{P}(\xi) = \sum_{i=1}^{n} B_{i,\check{p}}(\xi) \boldsymbol{P}_i$$

where $\{\boldsymbol{P}_i\}_{i\in[1,n]}$ are the *control points* of the curve. To continue the example, consider the control points $\boldsymbol{P}_1 = (5, 2)$, $\boldsymbol{P}_2 = (3, 2)$, $\boldsymbol{P}_3 = (1, 6)$, $\boldsymbol{P}_4 = (4, 3)$, $\boldsymbol{P}_5 = (7, 6)$ and $\boldsymbol{P}_6 = (7, 1)$. Using the same basis functions $\{B_{i,2}\}_{i\in[1,6]}$ as in the previous example, we get the curve depicted in Figure 10. In addition to the curve,

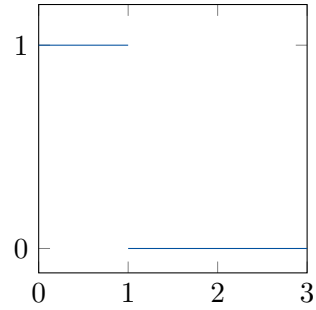

(a) Plot of $B_{3,0}$.

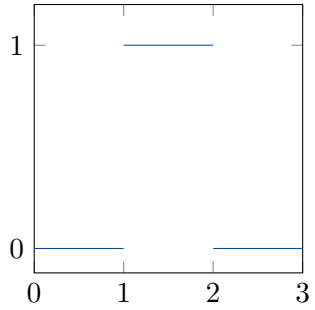

(b) Plot of $B_{4,0}$.

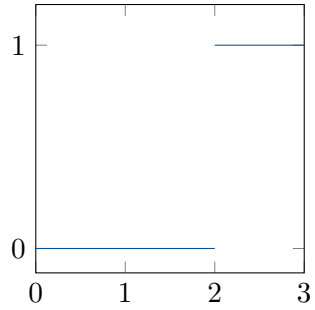

(c) Plot of $B_{6,0}$.

Figure 7: Plot of the non-zero B-splines of order zero, where the knot vector is given by $\boldsymbol{t} = \{0, 0, 0, 1, 2, 2, 3, 3, 3\}$. Note that $B_{j,0} \equiv 0$ for $j \in \{1, 2, 5, 6, 7, 8\}$.

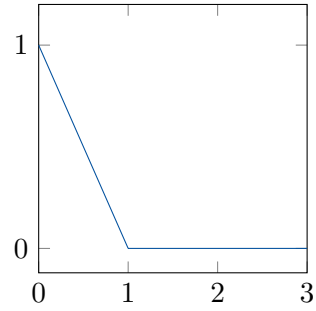

(a) Plot of $B_{2,1}$.

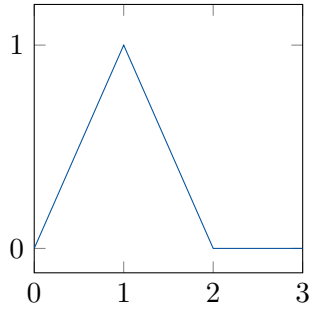

(b) Plot of $B_{3,1}$.

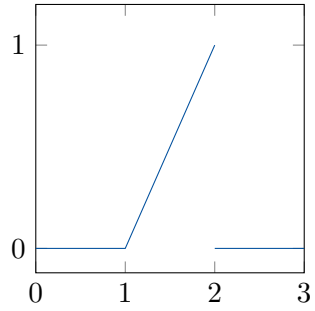

(c) Plot of $B_{4,1}$.

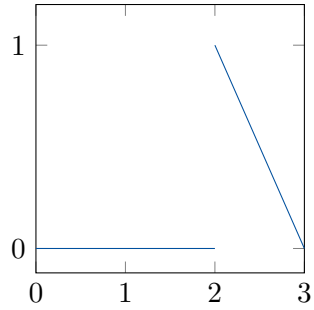

(d) Plot of $B_{5,1}$.

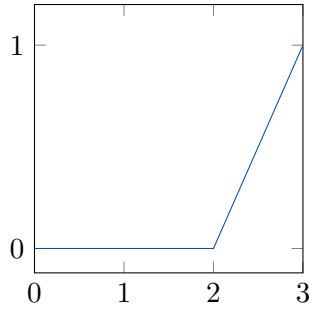

(e) Plot of $B_{6,1}$.

Figure 8: Plot of the non-zero B-spline basis functions (of first degree), where the knot vector is given by $\boldsymbol{t} = \{0, 0, 0, 1, 2, 2, 3, 3, 3\}$. Note that $B_{j,1} \equiv 0$ for $j \in \{1, 7\}$.

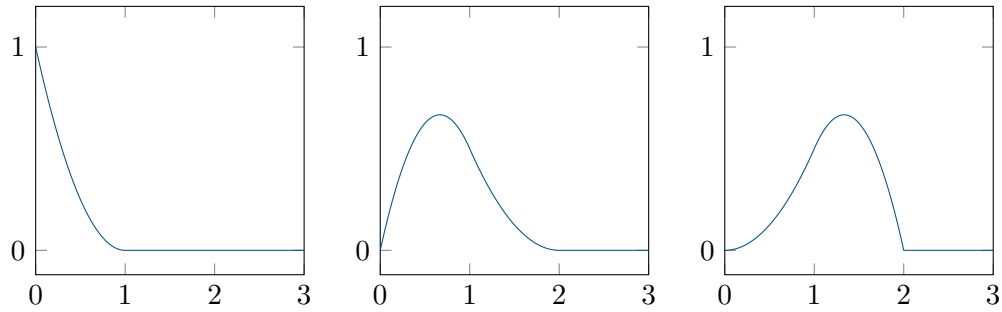

(a) Plot of $B_{1,2}$. (b) Plot of $B_{2,2}$. (c) Plot of $B_{3,2}$.

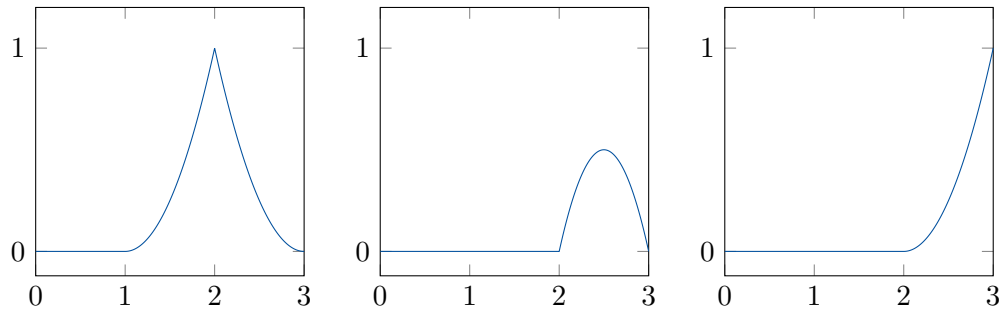

(d) Plot of $B_{4,2}$. (e) Plot of $B_{5,2}$. (f) Plot of $B_{6,2}$.

Figure 9: Plot of the 6 different B-spline basis functions (of second degree), where the knot vector is given by $\boldsymbol{t} = \{0, 0, 0, 1, 2, 2, 3, 3, 3\}$.

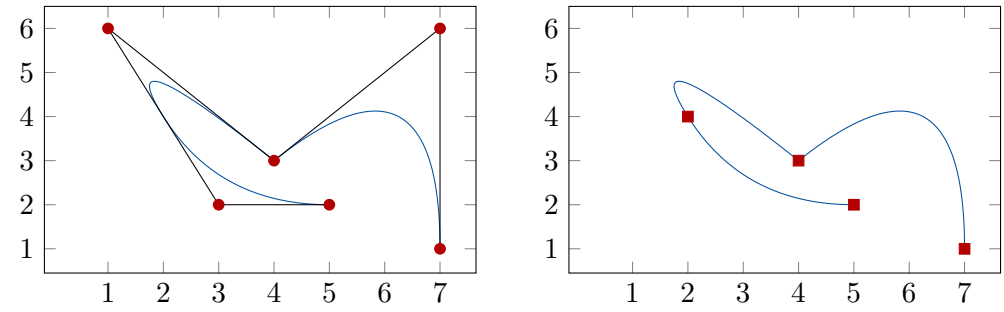

(a) Curve and control polygon. (b) Curve and location of knots.

Figure 10: Plot of a spline curve. Since $\boldsymbol{P}_1 = (5, 2)$, this is the point where the curve starts ($\xi = 0$).

the *control polygon* is drawn, which is simply the piece wise linear curve between the ordered control points. Note that the smoothness of the curve degrades at the point $(4, 3)$. This is the result of the repeated knot $\xi = 2$ which yields an interpolation effect, such that the control point lies on the curve (which is also the case at the end points).

2.2. B-spline knot insertion

Knot insertion is a process for which knots are inserted into the knot vector, which would create more basis function without changing the geometry. This is a very important concept as it allows us to enrich the basis and corresponds for this reason to the classical h-refinement procedure in FEM (refining the mesh). This is because the knot vector defines the mesh; such that when more knots are inserted, we get a more refined mesh.

The goal is to insert more knots into $\boldsymbol{t}$ without changing the shape of the curve. We shall do this by *Böhm's method* (cf. [61]) which does knot insertion by inserting one knot at a time. Let $\tilde{\boldsymbol{t}}$ be the new knot vector after a knot have been inserted into $\boldsymbol{t}$. Let $\{B_{i,\check{p},\boldsymbol{t}}\}_{i\in[1,n]}$ be the old basis (corresponding to $\boldsymbol{t}$) and $\{B_{i,\check{p},\tilde{\boldsymbol{t}}}\}_{i\in[1,n+1]}$ the new basis after a knot has been inserted (note that since $\tilde{\boldsymbol{t}}$ is known, the basis is completely determined). We then want to find the new set of control points $\left\{\tilde{\boldsymbol{P}}_i\right\}_{i\in[1,n+1]}$ (here $\tilde{\boldsymbol{P}}_i \in \mathbb{R}^d$ where d is the dimension of the space for which the spline curve belongs) such that

$$\boldsymbol{P}(\xi) = \sum_{i=1}^{n} B_{i,\check{p},\boldsymbol{t}}(\xi)\boldsymbol{P}_i \overset{!}{=} \sum_{i=1}^{n+1} B_{i,\check{p},\tilde{\boldsymbol{t}}}(\xi)\tilde{\boldsymbol{P}}_i.$$

This results in a linear system of equations which could be solved by brute force. However, Böhm method exploits the support property of B-splines to improve efficiency. Assume that the new knot $\tilde{\xi}$ is inserted in the interval $[\xi_j, \xi_{j+1}]$. Then

$$\tilde{\boldsymbol{P}}_i = \begin{cases} \boldsymbol{P}_i, & \text{if } 1 \leqslant i \leqslant j - \check{p} \\ \frac{\tilde{\xi}-\xi_i}{\xi_{i+\check{p}}-\xi_i}\boldsymbol{P}_i + \frac{\xi_{i+\check{p}}-\tilde{\xi}}{\xi_{i+\check{p}}-\xi_i}\boldsymbol{P}_{i-1}, & \text{if } j - \check{p} + 1 \leqslant i \leqslant j \\ \boldsymbol{P}_{i-1}, & \text{if } j + 1 \leqslant i \leqslant n + 1. \end{cases}$$

Let's continue our example by inserting the knots $\xi = 0.5$ and $\xi = 1.5$ into our knot vector. We then simply use Böhms method twice to calculate the new control points. The curve with the mesh before and after the knot insertion is depicted in Figure 11. In Figure 12 we see that the control polygon has changed. Indeed, it has moved towards the curve where the refinement has occurred, which is another nice property of knot insertion.

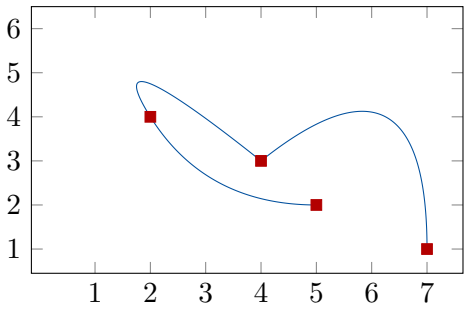

(a) Curve with mesh before refinement.

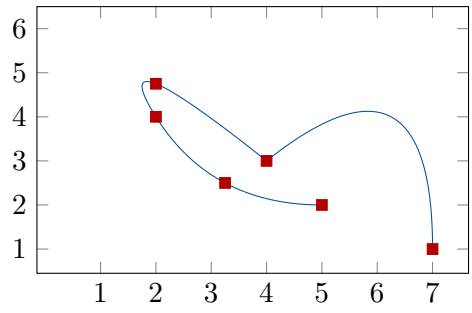

(b) Curve with mesh after refinement.

Figure 11: Mesh comparison for knot refinement.

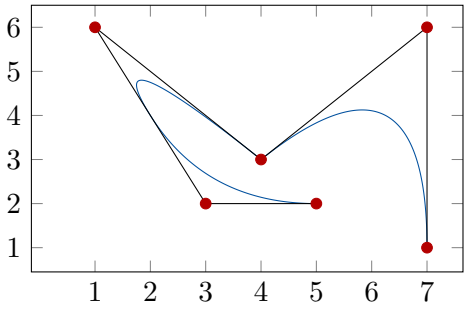

(a) Control polygon before refinement.

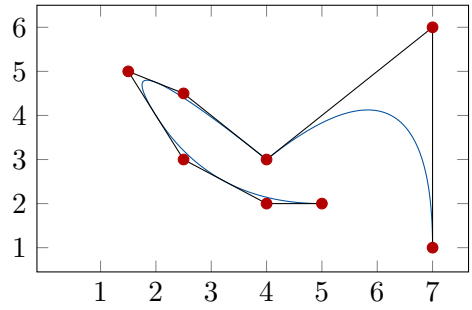

(b) Control polygon after refinement.

Figure 12: Control polygon comparison for knot insertion.

2.3. B-spline degree elevation

Having a basis of a higher order creates more accurate solution in FEM/IGA. Thus, we want to have an algorithm which increases the order from $\check{p}$ to $\check{p}+m$ without changing the geometry and the parametric space. Since the continuity at each knot must be preserved, it follows from property 7 on page 12 that we must increase the multiplicity of each knot by m. We also need to find the new set of control points. As for knot insertion, we must find the new set of control points $\{\boldsymbol{Q}_i\}_{i\in[1,\tilde{n}]}$ such that

$$\boldsymbol{P}(\xi)=\sum_{i=1}^{n}B_{i,\check{p},\boldsymbol{t}}(\xi)\boldsymbol{P}_i\overset{!}{=}\sum_{i=1}^{\tilde{n}}B_{i,\check{p}+m,\tilde{\boldsymbol{t}}}(\xi)\boldsymbol{Q}_i=:\boldsymbol{Q}(\xi).$$

Let S be an integer such that $S+1$ is the number of unique knots in $\boldsymbol{t}$. Since $\boldsymbol{t}$ is open ($\xi_1=\cdots=\xi_{\check{p}+1}$ and $\xi_{n+1}=\cdots=\xi_{n+\check{p}+1}$), it may be written on the form

$$\begin{aligned}\boldsymbol{t}&=\{\underbrace{\xi_1,\ldots,\xi_{\check{p}+1}}_{p+1},\xi_{\check{p}+2},\ldots,\xi_n,\underbrace{\xi_{n+1},\ldots,\xi_{n+\check{p}+1}}_{\check{p}+1}\}\\&=\{\underbrace{u_0,\ldots,u_0}_{\check{p}+1},\underbrace{u_1,\ldots,u_1}_{z_1},\ldots,\underbrace{u_{S-1},\ldots,u_{S-1}}_{z_{S-1}},\underbrace{u_S,\ldots,u_S}_{\check{p}+1}\}\end{aligned}$$

where z_i denotes the multiplicity of the knot with value u_i for $i=1,\ldots,S-1$. If we now want to elevate the degree m times (from $\check{p}$ to $\check{p}+m$), we get the new knot vector

$$\begin{aligned}\tilde{\boldsymbol{t}}&=\{\underbrace{\tilde{\xi}_1,\ldots,\tilde{\xi}_{\check{p}+1+m}}_{\check{p}+1+m},\tilde{\xi}_{\check{p}+2},\ldots,\tilde{\xi}_{\tilde{n}},\underbrace{\tilde{\xi}_{\tilde{n}+1},\ldots,\tilde{\xi}_{\tilde{n}+\check{p}+1+m}}_{\check{p}+1+m}\}\\&=\{\underbrace{u_0,\ldots,u_0}_{\check{p}+1+m},\underbrace{u_1,\ldots,u_1}_{z_1+m},\ldots,\underbrace{u_{S-1},\ldots,u_{S-1}}_{z_{S-1}+m},\underbrace{u_S,\ldots,u_S}_{\check{p}+1+m}\}.\end{aligned}$$

It is also easy to observe that the new number of basis functions is given by $\tilde{n}=n+S\cdot m$. What remains to be found is the new set of control points $\{\boldsymbol{Q}_i\}_{i\in[1,\tilde{n}]}$. Several efficient algorithms exist for this purpose, but we shall follow the idea presented by Huang et al. in [62]. Since the notation of the article does not correspond to the notation presented here, a complete derivation of the algorithm will be presented here. Denote by $\boldsymbol{P}^{(l)}$ the l'th derivative of the spline curve of degree $\check{p}$ (which will have degree $\check{p}-l$) such that (using an inductive argument and Eq. (8))

$$\boldsymbol{P}^{(j)}(\xi)=\sum_{i=1}^{n-j}B_{i+l,\check{p}-j,\boldsymbol{t}}(\xi)\boldsymbol{P}_i^j\quad\text{and}\quad\boldsymbol{Q}^{(j)}(\xi)=\sum_{i=1}^{\tilde{n}-j}B_{i+j,\check{p}+m-j,\tilde{\boldsymbol{t}}}(\xi)\boldsymbol{Q}_i^j$$

where the coefficients $\boldsymbol{P}_i^j$ are defined recursively by

$$\boldsymbol{P}_i^j = \begin{cases} \frac{\check{p}+1-j}{\xi_{i+\check{p}+1}-\xi_{i+j}}\left(\boldsymbol{P}_{i+1}^{j-1} - \boldsymbol{P}_i^{j-1}\right) & \text{if } \xi_{i+\check{p}+1} > \xi_{i+j} \\ \boldsymbol{0} & \text{if } \xi_{i+\check{p}+1} = \xi_{i+j} \end{cases} \tag{9}$$

for $j > 0$, starting with $\boldsymbol{P}_i^0 = \boldsymbol{P}_i$ for $j = 0$. Correspondingly we have,

$$\boldsymbol{Q}_i^j = \begin{cases} \frac{\check{p}+m+1-j}{\tilde{\xi}_{i+\check{p}+m+1}-\tilde{\xi}_{i+j}}\left(\boldsymbol{Q}_{i+1}^{j-1} - \boldsymbol{Q}_i^{j-1}\right) & \text{if } \tilde{\xi}_{i+\check{p}+m+1} > \tilde{\xi}_{i+j} \\ \boldsymbol{0} & \text{if } \tilde{\xi}_{i+\check{p}+m+1} = \tilde{\xi}_{i+j}. \end{cases} \tag{10}$$

Note that this implies the following useful formula we shall use later

$$\boldsymbol{Q}_{i+1}^{j-1} = \boldsymbol{Q}_i^{j-1} + \frac{\tilde{\xi}_{i+1+\check{p}+m} - \tilde{\xi}_{i+j}}{\check{p}+m+1-j}\boldsymbol{Q}_i^j \qquad \text{if } \tilde{\xi}_{i+\check{p}+m+1} > \tilde{\xi}_{i+j}. \tag{11}$$

Since $u_0 = \xi_{j+1} = \xi_{j+1+1} = \cdots = \xi_{j+1+\check{p}-j} < \xi_{\check{p}+2}$ for $0 \leqslant j \leqslant p$, property 6 on page 12 implies that

$$B_{i+j,\check{p}-j,\boldsymbol{t}}(u_0) = \delta_{i+j,j+1}.$$

Hence,

$$\boldsymbol{P}^{(j)}(u_0) = \sum_{i=1}^{n-j} B_{i+j,\check{p}-j,\boldsymbol{t}}(u_0)\boldsymbol{P}_i^j = \sum_{i=1}^{n-j} \delta_{i+j,j+1}\boldsymbol{P}_i^j = \boldsymbol{P}_1^j.$$

We have a corresponding result for $\boldsymbol{Q}^{(j)}$ such that

$$\boldsymbol{P}^{(j)}(u_0) = \boldsymbol{P}_1^j \quad \text{and} \quad \boldsymbol{Q}^{(j)}(u_0) = \boldsymbol{Q}_1^j.$$

Moreover, $\boldsymbol{P}(\xi)$ and $\boldsymbol{Q}(\xi)$ have the same geometry and parameterization (that is, $\boldsymbol{P}^{(j)}(\xi) = \boldsymbol{Q}^{(j)}(\xi)$), and we must therefore have

$$\boldsymbol{Q}_1^j = \boldsymbol{P}_1^j \tag{12}$$

for $0 \leqslant j \leqslant p$.

Define

$$\beta_i = \sum_{l=1}^{i} z_l,$$

such that we have $u_i = \xi_{\beta_i+\check{p}+1}$ (the last of the repeated knot). Let $\check{p}+1-z_i \leqslant j \leqslant \check{p}$ and $1 \leqslant i \leqslant S-1$, such that we only consider the case when the degree of $\boldsymbol{P}^{(j)}$ satisfy $p - j \leqslant z_i - 1$. Since the knot u_i is repeated z_i times, property 6 on page 12 now implies that

$$B_{\tilde{i},\check{p}-j,\boldsymbol{t}}(u_i) = \delta_{\tilde{i},\beta_i+1+j},$$

such that

$$\begin{aligned}\boldsymbol{P}^{(j)}(u_i) &= \sum_{\tilde{i}=1}^{n-j} B_{\tilde{i}+j,\check{p}-j,\boldsymbol{t}}(u_i)\boldsymbol{P}_{\tilde{i}}^{j} = \sum_{\tilde{i}=1}^{n-j} \delta_{\tilde{i}+j,\beta_i+1+j}\boldsymbol{P}_{\tilde{i}}^{j} \\ &= \boldsymbol{P}_{\beta_i+1}^{j}\end{aligned}$$

for $\check{p}+1-z_i \leqslant j \leqslant p$ and $1 \leqslant i \leqslant S-1$.

We note that $u_i = \tilde{\xi}_{\beta_i+\check{p}+1+m+im}$ and that this knot has multiplicity z_i+m in $\tilde{\boldsymbol{t}}$. Again, we consider the indices i and j to satisfy $\check{p}+1-z_i \leqslant j \leqslant \check{p}$ and $1 \leqslant i \leqslant S-1$, such that we only consider the case when the degree of $\boldsymbol{Q}^{(j)}$ satisfy $\check{p}+m-j \leqslant z_i+m-1$. Using once again property 6 on page 12 we have

$$B_{\tilde{i},\check{p}+m-j,\tilde{\boldsymbol{t}}}(u_i) = \delta_{\tilde{i},\beta_i+1+j},$$

such that

$$\begin{aligned}\boldsymbol{Q}^{(j)}(u_i) &= \sum_{\tilde{i}=1}^{\tilde{n}-j} B_{\tilde{i}+j,\check{p}+m-j,\tilde{\boldsymbol{t}}}(u_i)\boldsymbol{Q}_{\tilde{i}}^{j} = \sum_{\tilde{i}=1}^{\tilde{n}-j} \delta_{\tilde{i}+j,\beta_i+1+j}\boldsymbol{Q}_{\tilde{i}}^{j} \\ &= \boldsymbol{Q}_{\beta_i+1}^{j}\end{aligned}$$

for $\check{p}+1-z_i \leqslant j \leqslant \check{p}$ and $1 \leqslant i \leqslant S-1$. Using the fact that $\boldsymbol{P}^{(j)}(\xi) = \boldsymbol{Q}^{(j)}(\xi)$, we have obtained the formula

$$\boldsymbol{Q}_{\beta_i+1+im}^{j} = \boldsymbol{P}_{\beta_i+1}^{j}, \qquad \check{p}+1-z_i \leqslant j \leqslant \check{p}, \quad 1 \leqslant i \leqslant S-1. \tag{13}$$

Since $\boldsymbol{P}(\xi)$ has degree $\check{p}$, its $(\check{p}+1)$'th derivative must be zero, and thus also the $(\check{p}+1)$'th derivative of $\boldsymbol{Q}(\xi)$. Using property 4 on page 12 and letting $\xi \in [u_i, u_{i+1}) = [\tilde{\xi}_{\beta_i+p+1+m+im}, \tilde{\xi}_{\beta_i+\check{p}+1+m+im+1})$, we have

$$\begin{aligned}\boldsymbol{0} = \boldsymbol{P}^{(\check{p}+1)}(\xi) = \boldsymbol{Q}^{(\check{p}+1)}(\xi) &= \sum_{\tilde{i}=1}^{\tilde{n}-(\check{p}+1)} B_{\tilde{i}+\check{p}+1,m-1,\tilde{\boldsymbol{t}}}(\xi)\boldsymbol{Q}_{\tilde{i}}^{\check{p}+1} \\ = \sum_{\tilde{i}=\beta_i+1+im}^{\beta_i+m+im} B_{\tilde{i}+\check{p}+1,m-1,\tilde{\boldsymbol{t}}}(\xi)\boldsymbol{Q}_{\tilde{i}}^{\check{p}+1},\end{aligned}$$

which implies, that

$$\boldsymbol{Q}_{\tilde{i}}^{\check{p}+1} = \boldsymbol{0}, \qquad \beta_i+1+im \leqslant \tilde{i} \leqslant \beta_i+m+im,$$

for $0 \leqslant i \leqslant S-1$. Using Eq. (11) with $j = \check{p}+1$, we therefore have

$$\boldsymbol{Q}_{\tilde{i}+1}^{\check{p}} = \boldsymbol{Q}_{\tilde{i}}^{\check{p}}, \qquad \beta_i+1+im \leqslant \tilde{i} \leqslant \beta_i+m+im, \quad 0 \leqslant i \leqslant S-1,$$

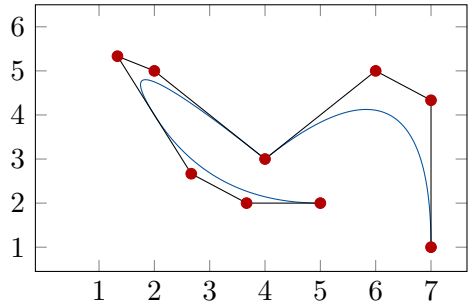

(a) Curve and control polygon after degree elevation.

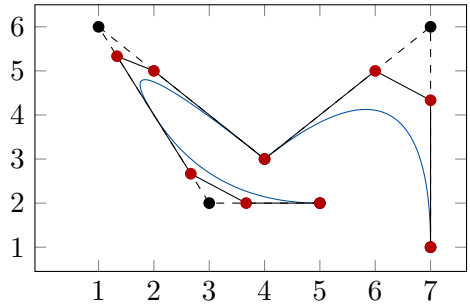

(b) Control polygon comparison showing the corner cutting effect.

Figure 13: Control polygon comparison for degree elevation of a spline curve.

or equivalently

$$\boldsymbol{Q}^{\check{p}}_{\beta_i+1+im+l} = \boldsymbol{Q}^{\check{p}}_{\beta_i+1+im}, \qquad 1 \leqslant l \leqslant m, \quad 0 \leqslant i \leqslant S-1. \tag{14}$$

In addition, we see from Eq. (10) that $\boldsymbol{Q}^{\check{p}}_{\tilde{i}} = \boldsymbol{0}$ whenever $\tilde{\xi}_{\tilde{i}+\check{p}+m+1} = \tilde{\xi}_{\tilde{i}+\check{p}}$. Since the knots u_{i+1} are repeated $z_{i+1}+m$ times in $\tilde{\boldsymbol{t}}$ (starting at $\tilde{\xi}_{\beta_i+1+\check{p}+im+m+1}$) we have

$$\boldsymbol{Q}^{\check{p}}_{\beta_i+1+im+l} = \boldsymbol{0}, \qquad m+1 \leqslant l \leqslant m-1+z_{i+1}, \quad 0 \leqslant i \leqslant S-1.$$

It turns out that these points are not needed.

So, in summary, the algorithm does the following steps

1. Set $\boldsymbol{P}^0_i = \boldsymbol{P}_i$ for $1 \leqslant i \leqslant n$.
2. Compute $\boldsymbol{P}^j_1$ for $0 \leqslant j \leqslant \check{p}$ and $\boldsymbol{P}^j_{\beta_i+1}$ for $\check{p}+1-z_i \leqslant j \leqslant p$ and $1 \leqslant i \leqslant S-1$ using Eq. (9).
3. Compute $\boldsymbol{Q}^j_1$ for $0 \leqslant j \leqslant \check{p}$ using Eq. (12)
4. Compute $\boldsymbol{Q}^j_{\beta_i+1+im}$ for $p+1-z_i \leqslant j \leqslant \check{p}$ and $1 \leqslant i \leqslant S-1$ using Eq. (13).
5. Compute $\boldsymbol{Q}^{\check{p}}_{\beta_i+1+im+k}$ for $1 \leqslant k \leqslant m$ and $0 \leqslant i \leqslant S-1$ using Eq. (14).
6. Compute the new control points $\boldsymbol{Q}_i = \boldsymbol{Q}^0_i$ backwards from Eq. (11).

This algorithm may be optimized as discussed in [62] but will not be presented here as the efficiency of this algorithm is not of great importance for this thesis.

Continuing our example, let's elevate the degree of the original spline curve by one (from 2 to 3). As we can see in Figure 13a, the geometry of the curve has

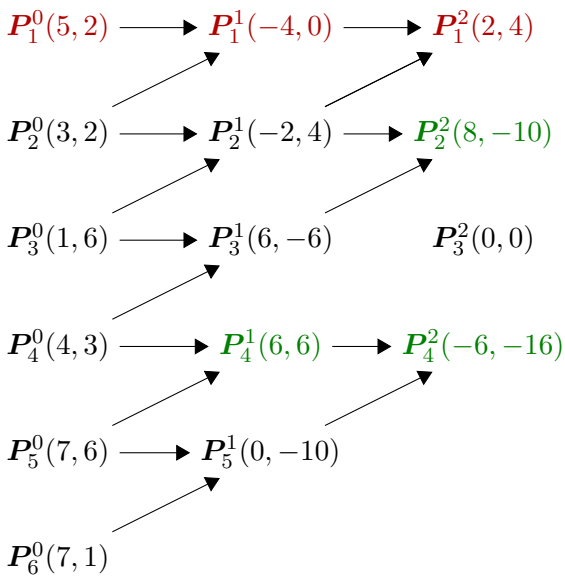

Figure 14: Graph of differential coefficients of $\boldsymbol{P}(\xi)$ in the example.

not changed but the control polygon has changed. As we can see in Figure 13b only non-interpolating control points in the control polygon have changed. Two new control points replaces each of these control points such that we get a corner cutting effect in the control polygon. Therefore, degree elevation of spline curves is called corner cutting.

In Figure 14 we have a graph which illustrates this process. The points which are colored are used directly to compute coefficients in the set $\{\boldsymbol{Q}_i^j\}_{i,j}$ (which have corresponding colors in the graph in Figure 15). Except for $\boldsymbol{P}_3^2(0,0)$ (which is set to zero because $\xi_6 = \xi_5$) all points are thus needed.

In Figure 15 we illustrate how the differential coefficients of $\boldsymbol{Q}(\xi)$ are computed. The coefficients in red are first computed (step 3), the coefficients in green are then computed (step 4) such that the coefficients in yellow may be computed (step 5). The rest of the coefficients are computed by Eq. (11). Note that $\boldsymbol{Q}_5^2$ is not really needed.

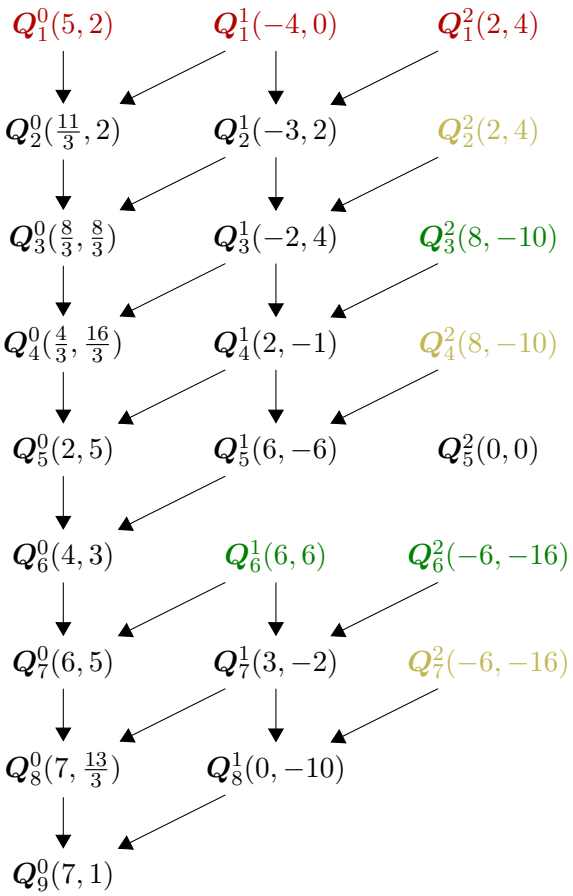

Figure 15: Differential coefficients of $\boldsymbol{Q}(\xi)$ in the example.

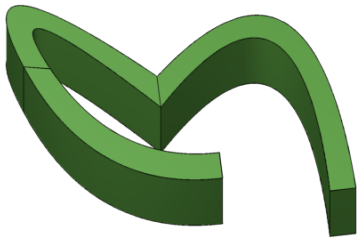

(a) Spline volume.

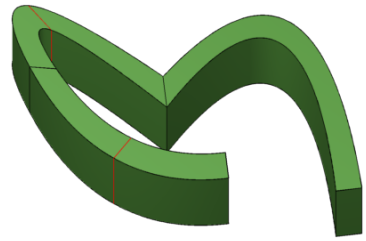

(b) Knots inserted in the ξ-direction.

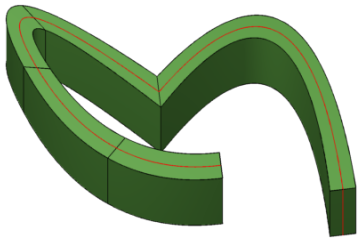

(c) Knots inserted in the η-direction.

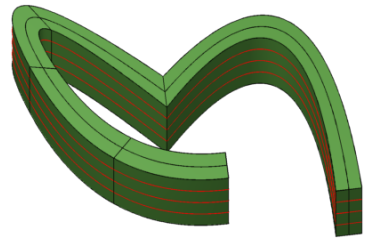

(d) Knots inserted in the ζ-direction.

Figure 16: Spline volume and its knot insertions. We here choose to first insert knots in the ξ-direction followed by the η- and ζ-direction, respectively.

2.4. Spline volumes

The extension to bivariate spline surfaces and trivariate spline volumes is straight forward (we shall only here consider volumes). Let $\left\{B_{i,\check{p}_\xi}\right\}_{i\in[1,n_\xi]}$, $\left\{B_{j,\check{p}_\eta}\right\}_{j\in[1,n_\eta]}$ and $\left\{B_{l,\check{p}_\zeta}\right\}_{l\in[1,n_\zeta]}$ be the set of B-spline basis functions in ξ-, η- and ζ-direction, respectively. These sets have their own degree ($\check{p}_\xi$, $\check{p}_\eta$ and $\check{p}_\zeta$, respectively) and knot vectors ($\boldsymbol{t}_\xi$, $\boldsymbol{t}_\eta$ and $\boldsymbol{t}_\zeta$, respectively). A spline volume is then defined by

$$\boldsymbol{X}(\xi,\eta,\zeta) = \sum_{i=1}^{n_\xi}\sum_{j=1}^{n_\eta}\sum_{l=1}^{n_\zeta} B_{i,\check{p}_\xi}(\xi)B_{j,\check{p}_\eta}(\eta)B_{l,\check{p}_\zeta}(\zeta)\boldsymbol{P}_{i,j,l}.$$

We may extend our spline curve example into a volume by adding the knot vectors $\boldsymbol{t}_\eta = \{0,0,1,1\}$ and $\boldsymbol{t}_\zeta = \{0,0,1,1\}$. By adding appropriate control points, we get the spline volume in Figure 16. We have here in addition to the volume drawn the mesh on top showing three elements.

Once again, we want to be able to refine this mesh into more elements without changing the geometry. For spline volumes, this is done by refining the mesh in each parameter direction (in the ξ-, η- and ζ-direction). This refining process thus involves refining in each direction separately. For each knot vector, we do knot insertion by Böhms method once again. Here, we have to order the structure of

the control points $\{\boldsymbol{P}_{i,j,l}\}$ in a specific way. As an example, say we want to insert s knots in the $\boldsymbol{t}_\xi$ direction for a spline object living in a d-dimensional space using Böhms method. We then want to find the new set of control points $\left\{\tilde{\boldsymbol{P}}_{i,j,l}\right\}$ such that

$$\begin{aligned}\boldsymbol{X}(\xi,\eta,\zeta) &= \sum_{i=1}^{n_\xi}\sum_{j=1}^{n_\eta}\sum_{l=1}^{n_\zeta} B_{i,\check{p}_\xi,\boldsymbol{t}_\xi}(\xi)B_{j,\check{p}_\eta,\boldsymbol{t}_\eta}(\eta)B_{l,\check{p}_\zeta,\boldsymbol{t}_\zeta}(\zeta)\boldsymbol{P}_{i,j,l} \\ &\overset{!}{=} \sum_{i=1}^{n_\xi+s}\sum_{j=1}^{n_\eta}\sum_{l=1}^{n_\zeta} B_{i,p,\tilde{\boldsymbol{t}_\xi}}(\xi)B_{j,\check{p}_\eta,\boldsymbol{t}_\eta}(\eta)B_{l,\check{p}_\zeta,\boldsymbol{t}_\zeta}(\zeta)\tilde{\boldsymbol{P}}_{i,j,l}.\end{aligned}$$

We shall use the ordering $\boldsymbol{Q}_i = \{\boldsymbol{P}_{i,1,1}, \boldsymbol{P}_{i,2,1}, \ldots, \boldsymbol{P}_{i,n_\eta,1}, \boldsymbol{P}_{i,1,2}, \ldots, \boldsymbol{P}_{i,n_\eta,n_\zeta}\}$. We create a new fictitious spline curve given by

$$\boldsymbol{Q}(\xi) = \sum_{i=1}^{n_\xi} B_{i,\check{p}_\xi,\boldsymbol{t}_\xi}(\xi)\boldsymbol{Q}_i \overset{!}{=} \sum_{i=1}^{n_\xi+s} B_{i,\check{p}_\xi,\tilde{\boldsymbol{t}_\xi}}(\xi)\tilde{\boldsymbol{Q}}_i$$

where $\tilde{\boldsymbol{Q}}_i$ is to be determined using Böhms method s times. Note that this spline curve is in a $(d \cdot n_\eta \cdot n_\zeta)$-dimensional space. Reordering $\{\tilde{\boldsymbol{Q}}_i\}$ back to the old structure, we obtain the resulting $\{\tilde{\boldsymbol{P}}_{i,j,l}\}$. A similar procedure is done if knots are inserted in η- and ζ-direction.

Let's say we want to insert the knots $\{0.5, 1.5\}$ in the ξ-direction (as we did for the spline curve) and the knots $\{0.5\}$ and $\{0.25, 0.5, 0.75\}$ for the η- and ζ-direction, respectively. The result (in Figure 16) is a refined mesh from 3 elements to 40 elements.

A corresponding procedure is done for degree elevation in spline volumes.

2.5. NURBS

With the B-splines in our arsenal, we are ready to present Non-Uniform Rational B-Splines (NURBS). Although B-splines may represent many complex curves, there are a class of curves that may not be represented exactly by B-splines, namely, conic sections like circles. Such shapes are often used in engineering, and thus, an extension, which enables this, would be valuable. NURBS enables us to tackle such geometries as well.

Let $\{w_i\}_{i\in[1,n]}$ be a set of *weights*, and define the *weighting function* by

$$W(\xi) = \sum_{\tilde{i}=1}^{n} B_{\tilde{i},\check{p},\boldsymbol{t}}(\xi)w_{\tilde{i}}.$$

The one-dimensional NURBS basis functions can now be defined by

$$R_i^{\check{p}}(\xi) = \frac{B_{i,\check{p},\boldsymbol{t}}(\xi)w_i}{W(\xi)},$$

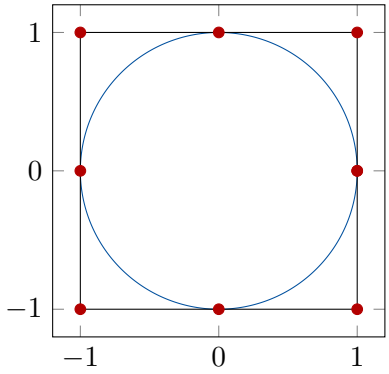

Figure 17: NURBS representation of a unit circle with the corresponding control polygon. The curve goes counterclockwise around the unit circle (which is a result of the corresponding ordering in the control points), starts at $(1, 0)$ and ends at $(1, 0)$.

such that a NURBS curve may be expressed by

$$\boldsymbol{P}(\xi) = \sum_{i=1}^{n} R_i^{\check{p}}(\xi)\boldsymbol{P}_i$$

where $\boldsymbol{P}_i$ are the control points of the curve.

There are several ways to construct a circle using NURBS (but we need $\check{p} \geqslant 2$). For example, consider the knot vector $\boldsymbol{t} = \{0, 0, 0, \frac{1}{4}, \frac{1}{4}, \frac{1}{2}, \frac{1}{2}, \frac{3}{4}, \frac{3}{4}, 1, 1, 1\}$, the degree $\check{p} = 2$, the weights given by $\{w_i\}_{i\in[1,9]}$ where

$$w_i = \begin{cases} \frac{1}{\sqrt{2}} & \text{for } i \text{ even} \\ 1 & \text{otherwise} \end{cases}$$

and the control points $\boldsymbol{P}_1 = (0, 0)$, $\boldsymbol{P}_2 = (1, 1)$, $\boldsymbol{P}_3 = (0, 1)$, $\boldsymbol{P}_4 = (-1, 1)$, $\boldsymbol{P}_5 = (-1, 0)$, $\boldsymbol{P}_6 = (-1, -1)$, $\boldsymbol{P}_7 = (0, -1)$, $\boldsymbol{P}_8 = (1, -1)$ and $\boldsymbol{P}_9 = (1, 0)$. This will produce the unit circle, which is depicted in Figure 17. Note that there are no non-repeated knots in the knot vector, so we will have interpolation between the location of the knots and the control polygon (since $\check{p} = 2$).

2.6. NURBS knot insertion

A d-dimensional NURBS curve is a projection of a $(d + 1)$-dimensional B-spline curve (cf. [25]). We may exploit this property to insert new knots into a NURBS.

Let's say we want to insert s new knots into a NURBS curve defined by the knot vector $\boldsymbol{t}$, the control points $\{\boldsymbol{P}_i\}_{i\in[1,n]} = \{(x_i, y_i)\}_{i\in[1,n]}$, and the weights

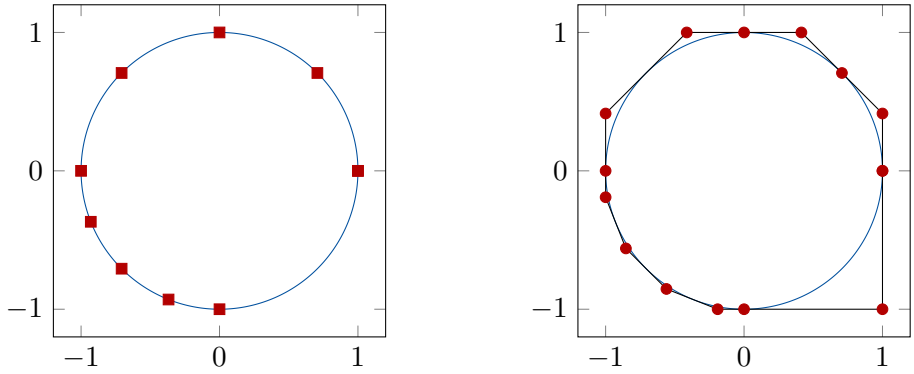

(a) Knot locations after refinement.

(b) Control polygon after refinement.

Figure 18: Knot insertion for a NURBS circle.

$\{w_i\}_{i\in[1,n]}$. We then construct a 3D B-spline curve with control points given by

$$\{\boldsymbol{Q}_i\}_{i\in[1,n]} = \{(w_i x_i, w_i y_i, w_i)\}_{i\in[1,n]}.$$

We now have a B-spline curve in 3D defined by $\boldsymbol{t}$ (the same knot vector) and the control points $\{\boldsymbol{Q}_i\}_{i\in[1,n]}$. We may now insert knots using Böhms method as before, which yields the extended knot vector $\tilde{\boldsymbol{t}}$ and the new control points $\left\{\tilde{\boldsymbol{Q}}_i\right\}_{i\in[1,n+s]} = \{(\tilde{x}_i, \tilde{y}_i, \tilde{w}_i)\}_{i\in[1,n+s]}$. Projecting this B-spline curve back to a 2D NURBS with control points given by

$$\left\{\tilde{\boldsymbol{P}}_i\right\}_{i\in[1,n+s]} = \left\{\left(\frac{\tilde{x}_i}{\tilde{w}_i}, \frac{\tilde{y}_i}{\tilde{w}_i}\right)\right\}_{i\in[1,n+s]}$$

and weights given by $\{\tilde{w}_i\}_{i\in[1,n+s]}$, we get the refined NURBS. To insert knots in a 3D NURBS curve, we apply an analogous procedure to the control points $\{\boldsymbol{P}_i\}_{i\in[1,n]} = \{(x_i, y_i, z_i)\}_{i\in[1,n]}$.

In Figure 18 we have inserted the knots $\{0.5, 0.5, 1.5, 2.25, 2.5, 2.75\}$ into the NURBS circle in Figure 17. Note that many of the same properties of B-spline curves are preserved for the NURBS curve. Also note that the mesh is not changed by adding an extra knot at $\xi = 0.5$, but we still have added a new basis function. A reduction of continuity in the basis functions will here occur, but the geometric continuity of the curve remains the same.

The extensions to bivariate NURBS surfaces and trivariate NURBS volumes are straightforward. For NURBS volumes, let $\left\{B_{i,\check{p}_\xi,\boldsymbol{t}_\xi}\right\}_{i\in[1,n_\xi]}$, $\left\{B_{j,\check{p}_\eta,\boldsymbol{t}_\eta}\right\}_{j\in[1,n_\eta]}$ and $\left\{B_{l,\check{p}_\zeta,\boldsymbol{t}_\zeta}\right\}_{k\in[1,n_\zeta]}$ be the sets of B-spline basis functions in ξ-, η- and ζ-direction, respectively. These sets have their own order ($\check{p}_\xi$, $\check{p}_\eta$ and $\check{p}_\zeta$, respectively) and

knot vectors ($\boldsymbol{t}_\xi$, $\boldsymbol{t}_\eta$ and $\boldsymbol{t}_\zeta$, respectively). The trivariate NURBS basis functions are then defined by

$$R_{i,j,l}(\xi,\eta,\zeta) = \frac{B_{i,\check{p}_\xi,\boldsymbol{t}_\xi}(\xi)B_{j,\check{p}_\eta,\boldsymbol{t}_\eta}(\eta)B_{l,\check{p}_\zeta,\boldsymbol{t}_\zeta}(\zeta)w_{i,j,l}}{W(\xi,\eta,\zeta)} \tag{15}$$

where the weighting function is now given by

$$W(\xi,\eta,\zeta) = \sum_{\tilde{i}=1}^{n_\xi}\sum_{\tilde{j}=1}^{n_\eta}\sum_{\tilde{l}=1}^{n_\zeta} B_{\tilde{i},\check{p}_\xi,\boldsymbol{t}_\xi}(\xi)B_{\tilde{j},\check{p}_\eta,\boldsymbol{t}_\eta}(\eta)B_{\tilde{l},\check{p}_\zeta,\boldsymbol{t}_\zeta}(\zeta)w_{\tilde{i},\tilde{j},\tilde{l}}.$$

In the next section, the single index notation (global indexing system) is used $R_I = R_{i,j,l}$, where for a single patch (with no collapsed control points) we have $I = i + n_\xi(j-1) + n_\xi n_\eta(l-1)$.

The partial derivatives of these functions are then given by the quotient rule. For example, we have

$$\frac{\partial R_{i,j,l}}{\partial\xi} = \frac{W(\xi,\eta,\zeta)B'_{i,\check{p}_\xi,\boldsymbol{t}_\xi}(\xi) - W_\xi(\xi,\eta,\zeta)B_{i,\check{p}_\xi,\boldsymbol{t}_\xi}(\xi)}{(W(\xi,\eta,\zeta))^2} B_{j,\check{p}_\eta,\boldsymbol{t}_\eta}(\eta)B_{l,\check{p}_\zeta,\boldsymbol{t}_\zeta}(\zeta)w_{i,j,l} \tag{16}$$

where

$$W_\xi(\xi,\eta,\zeta) = \sum_{\tilde{i}=1}^{n_\xi}\sum_{\tilde{j}=1}^{n_\eta}\sum_{\tilde{l}=1}^{n_\zeta} B'_{\tilde{i},\check{p}_\xi,\boldsymbol{t}_\xi}(\xi)B_{\tilde{j},\check{p}_\eta,\boldsymbol{t}_\eta}(\eta)B_{\tilde{l},\check{p}_\zeta,\boldsymbol{t}_\zeta}(\zeta)w_{\tilde{i},\tilde{j},\tilde{l}}$$

and

$$B'_{i,\check{p}_\xi,\boldsymbol{t}_\xi}(\xi) = \frac{\mathrm{d}B_{i,\check{p}_\xi,\boldsymbol{t}_\xi}(\xi)}{\mathrm{d}\xi}.$$

Analogous expressions may be found for the partial derivatives with respect to η and ζ.

A 3D NURBS volume is now defined by

$$\boldsymbol{X}(\xi,\eta,\zeta) = \sum_{i=1}^{n_\xi}\sum_{j=1}^{n_\eta}\sum_{l=1}^{n_\zeta} R_{i,j,l}(\xi,\eta,\zeta)\boldsymbol{P}_{i,j,l}$$

Knot insertion into such an object is once again done by inserting knots into a 4D B-splines volume with control points

$$\boldsymbol{Q}_{i,j,l} = (w_{i,j,l}x_{i,j,l}, w_{i,j,l}y_{i,j,l}, w_{i,j,l}z_{i,j,l}, w_{i,j,l})$$

for $i \in [1, n_\xi]$, $j \in [1, n_\eta]$ and $l \in [1, n_\zeta]$. Using the same procedure as in Subsection 2.4 we obtain the new set of control points $\tilde{\boldsymbol{Q}}_{i,j,l} = (\tilde{x}_{i,j,l}, \tilde{y}_{i,j,l}, \tilde{z}_{i,j,l}, w_{i,j,l})$ which after the projection yields our new set of control points for the NURBS volume given by

$$\left\{\tilde{\boldsymbol{P}}_{i,j,l}\right\}_{i,j,l} = \left\{\left(\frac{\tilde{x}_{i,j,l}}{\tilde{w}_{i,j,l}}, \frac{\tilde{y}_{i,j,l}}{\tilde{w}_{i,j,l}}, \frac{\tilde{z}_{i,j,l}}{\tilde{w}_{i,j,l}}\right)\right\}_{i,j,l}$$

and a set of weights given by $\{\tilde{w}_{i,j,l}\}_{i,j,l}$.

A corresponding procedure is done for degree elevation in NURBS volumes.

2.7. The weak form and Galerkin's method

The foundation for finite element technologies is the Galerkin's method. Most partial differential equations may not be solved by analytic expressions in closed forms, and one must then resort to numerical methods implemented on some computational resource. As computational resources are limited, the infinitely dimensional function space (in which the solution lies) must be reduced to a finite dimensional function space (where the approximate solution is to be found). Galerkin's method yields the framework for this transition.

For illustrative purposes, consider the interior Helmholtz equation (in strong form)

$$\nabla^2 p + k^2 p = 0 \quad \text{in} \quad \Omega \subset \mathbb{R}^d, \tag{17}$$

$$\partial_n p = g \quad \text{on} \quad \Gamma = \partial\Omega, \tag{18}$$

where ∂_n denotes the partial derivative in the normal direction, $\boldsymbol{n}$, on the surface Γ pointing out from the interior domain Ω. Note that this problem is not well posed for certain wave numbers k (corresponding to the eigenfrequencies of the problem).

The *weak form* of the problem is derived from the strong form. Typically, one defines two classes of functions: $\mathcal{S}$ denotes the *solution space* and $\mathcal{V}$ denotes the *test space*. Here, $\mathcal{S}$ is a subspace of the Sobolev space $H^1(\Omega)$ defined by

$$H^1(\Omega) = \left\{ p \in L^2(\Omega) \,:\, \frac{\partial p}{\partial x_i} \in L^2(\Omega),\, \forall i = 1, \ldots, d \right\}$$

where $L^2(\Omega)$ is the set of square integrable functions. The test space is usually defined to be the same as the solution space, $\mathcal{S} = \mathcal{V}$, which is the Bubnov–Galerkin formulation. When these spaces differ, we have the Petrov–Galerkin formulation which will be investigated in depth in the context of the infinite element method in the second paper.

The Helmholtz equation is first written in weak form. Multiply (17) by a test functions $q \in \mathcal{V}$

$$q\nabla^2 p + k^2 q p = 0$$

and integrate over Ω

$$\int_\Omega \left[q\nabla^2 p + k^2 q p \right] \mathrm{d}\Omega = 0.$$

Using Greens first identity this can be written as

$$-\int_\Omega \nabla q \cdot \nabla p \,\mathrm{d}\Omega + \int_{\partial\Omega} q \nabla p \cdot \boldsymbol{n} \,\mathrm{d}\Gamma + k^2 \int_\Omega q p \,\mathrm{d}\Omega = 0.$$

Thus,

$$\int_\Omega \nabla q \cdot \nabla p \,\mathrm{d}\Omega - k^2 \int_\Omega qp \,\mathrm{d}\Omega = \int_{\partial\Omega} qg \,\mathrm{d}\Gamma. \tag{19}$$

The weak formulation then becomes:

$$\text{Find} \quad p \in \mathcal{S} \quad \text{such that} \quad B(q,p) = L(q), \qquad \forall q \in \mathcal{V}, \tag{20}$$

where the bilinear form is given by

$$B(q,p) = \int_\Omega \Big[\nabla q \cdot \nabla p - k^2 qp\Big] \,\mathrm{d}\Omega \tag{21}$$

and the corresponding linear form is given by

$$L(q) = \int_\Gamma qg \,\mathrm{d}\Gamma.$$

We now want to transform this weak statement into a system of algebraic equations. We here apply Galerkin's method and turn to a finite-dimensional subspace $\mathcal{S}_h \subset \mathcal{S}$ (and $\mathcal{V}_h \subset \mathcal{V}$ for the test space). In the IGA context the basis for this subspace is represented by the same splines that parameterizes the domain Ω. The Galerkin approximation of the weak form is now given by:

$$\text{Find} \quad p_h \in \mathcal{S}_h \quad \text{such that} \quad B(q_h,p_h) = L(q_h), \qquad \forall q_h \in \mathcal{V}_h. \tag{22}$$

To find the system of algebraic equations we need to write p_h and q_h as a linear combination of the basis functions (here, the NURBS basis functions, R_i)

$$q_h = \sum_i R_i c_i \quad \text{and} \quad p_h = \sum_j R_j d_j,$$

respectively. Insertion of these function representations in Eq. (22) yields

$$B\left(\sum_i R_i c_i, \sum_j R_j d_j\right) - L\left(\sum_i R_i c_i\right) = 0$$

which using the bilinearity of B and the linearity of L may be written as

$$\sum_i c_i \left(\sum_j B(R_i,R_j) d_i - L(R_i)\right) = 0.$$

Since the coefficients c_i are arbitrary (the relation should hold for all $q_h \in \mathcal{V}_h$, and in particular $q_h = R_i$ for all i) the term in the parentheses must vanish. That is,

$$\sum_j B(R_i,R_j) d_j = L(R_i), \quad \forall i.$$

The resulting system of equation may then be written as

$$\boldsymbol{A}\boldsymbol{d} = \boldsymbol{F}$$

with components

$$\begin{aligned} A_{ij} &= B(R_i, R_j), \\ F_i &= L(R_i). \end{aligned}$$

The matrix $\boldsymbol{A}$ is usually written as a combination of the *stiffness matrix*, $\boldsymbol{K}$ and the *mass matrix*, $\boldsymbol{M}$, as $\boldsymbol{A} = \boldsymbol{K} - k^2\boldsymbol{M}$.

2.8. Assembly

One typically does not loop through the basis functions. Rather, one loops through the elements constructing local stiffness/mass matrices and successfully place their contribution in the global stiffness/mass matrix. The next step is thus to build the global matrices from the local element matrices, often referred to as assembly.

Let Ω^e be the domain of a given element, where the index e loops over all elements. The support of the spline basis functions is highly localized. To reduce computations, we should only integrate over functions which have support in Ω^e. Denote by n_{en} the number of *local shape functions*, R_a^e, with support in Ω^e, and let a and b iterate over these functions, we may calculate the entries in the local stiffness matrix as

$$k_{ab}^e = \int_{\Omega^e} \nabla R_a^e \cdot \nabla R_b^e \,\mathrm{d}\Omega.$$

Similarly, for the local mass matrix and the local force vector we have

$$m_{ab}^e = \int_{\Omega^e} R_a^e R_b^e \,\mathrm{d}\Omega \quad \text{and} \quad f_a^e = \int_{\Gamma^e} R_a^e g \,\mathrm{d}\Gamma, \tag{23}$$

respectively. The integration is done by quadrature formulas. One first maps to the parametric domain, and then maps this domain to a parent domain. The element in the parametric domain (corresponding to Ω^e) is given (in 3D) by

$$\hat{\Omega}^e = [\xi_i, \xi_{i+1}] \times [\eta_j, \eta_{j+1}] \times [\zeta_l, \zeta_{l+1}].$$

We want to linearly map this domain into the parent domain $\tilde{\Omega}^e = [-1, 1]^d$. So given $(\tilde{\xi}, \tilde{\eta}, \tilde{\zeta}) \in \tilde{\Omega}^e$, we calculate $(\xi, \eta, \zeta) \in \hat{\Omega}^e$ by

$$\begin{aligned} \xi &= \xi_i + (\tilde{\xi} + 1)\frac{\xi_{i+1} - \xi_i}{2}, \\ \eta &= \eta_j + (\tilde{\eta} + 1)\frac{\eta_{j+1} - \eta_j}{2}, \\ \zeta &= \zeta_k + (\tilde{\zeta} + 1)\frac{\zeta_{k+1} - \zeta_k}{2}. \end{aligned}$$

The Jacobian determinant for the parent to parametric mapping is thus given by

$$J_2 = \begin{vmatrix} \frac{\partial \xi}{\partial \tilde{\xi}} & \frac{\partial \xi}{\partial \tilde{\eta}} & \frac{\partial \xi}{\partial \tilde{\zeta}} \\ \frac{\partial \eta}{\partial \tilde{\xi}} & \frac{\partial \eta}{\partial \tilde{\eta}} & \frac{\partial \eta}{\partial \tilde{\zeta}} \\ \frac{\partial \zeta}{\partial \tilde{\xi}} & \frac{\partial \zeta}{\partial \tilde{\eta}} & \frac{\partial \zeta}{\partial \tilde{\zeta}} \end{vmatrix} = \frac{1}{8}(\xi_{i+1} - \xi_i)(\eta_{j+1} - \eta_j)(\zeta_{k+1} - \zeta_k).$$

Similarly, we need the Jacobian for the mapping from the parametric domain into the physical domain. Given $(\xi, \eta, \zeta) \in \hat{\Omega}^e$, we calculate $\boldsymbol{X} \in \Omega^e$ by

$$\boldsymbol{X} = \begin{bmatrix} x_1 \\ x_2 \\ x_3 \end{bmatrix} = \sum_{i=1}^{n_\xi} \sum_{j=1}^{n_\eta} \sum_{l=1}^{n_\zeta} R_{i,j,l}(\xi, \eta, \zeta) \boldsymbol{P}_{i,j,l} = \sum_{a=1}^{n_{\text{en}}} R_a^e(\xi, \eta, \zeta) \boldsymbol{P}_a$$

where $\boldsymbol{P}_{i,j,k}$ are the control points and $R_{i,j,l}^{\check{p}_\xi, \check{p}_\eta, \check{p}_\zeta}$ are the NURBS basis functions which are computed by Eq. (15). We shall denote this mapping by $\boldsymbol{X} : \hat{\Omega} \to \Omega$. Note that the last equality again comes from the highly localized support of the NURBS basis. The Jacobian matrix is then given by

$$\boldsymbol{J} = \begin{bmatrix} \frac{\partial x_1}{\partial \xi} & \frac{\partial x_1}{\partial \eta} & \frac{\partial x_1}{\partial \zeta} \\ \frac{\partial x_2}{\partial \xi} & \frac{\partial x_2}{\partial \eta} & \frac{\partial x_2}{\partial \zeta} \\ \frac{\partial x_3}{\partial \xi} & \frac{\partial x_3}{\partial \eta} & \frac{\partial x_3}{\partial \zeta} \end{bmatrix} = \begin{bmatrix} \boldsymbol{P}_1, & \boldsymbol{P}_2, & \cdots, & \boldsymbol{P}_{n_{\text{en}}} \end{bmatrix} \begin{bmatrix} \frac{\partial R_1}{\partial \xi} & \frac{\partial R_1}{\partial \eta} & \frac{\partial R_1}{\partial \zeta} \\ \frac{\partial R_2}{\partial \xi} & \frac{\partial R_2}{\partial \eta} & \frac{\partial R_2}{\partial \zeta} \\ \vdots & \vdots & \vdots \\ \frac{\partial R_{n_{\text{en}}}}{\partial \xi} & \frac{\partial R_{n_{\text{en}}}}{\partial \eta} & \frac{\partial R_{n_{\text{en}}}}{\partial \zeta} \end{bmatrix} \tag{24}$$

such that the Jacobian determinant of this mapping is given by

$$J_1 = \det(\boldsymbol{J})$$

where the derivatives of the NURBS basis functions are computed by Eq. (16). The local stiffness matrix contains derivatives of the NURBS functions w.r.t. physical coordinates, and so we need to find expressions for $\frac{\partial R_i}{\partial x_j}$. By the chain rule we have

$$\begin{aligned} \frac{\partial R_i}{\partial \xi} &= \frac{\partial R_i}{\partial x_1}\frac{\partial x_1}{\partial \xi} + \frac{\partial R_i}{\partial x_2}\frac{\partial x_2}{\partial \xi} + \frac{\partial R_i}{\partial x_3}\frac{\partial x_3}{\partial \xi} \\ \frac{\partial R_i}{\partial \eta} &= \frac{\partial R_i}{\partial x_1}\frac{\partial x_1}{\partial \eta} + \frac{\partial R_i}{\partial x_2}\frac{\partial x_2}{\partial \eta} + \frac{\partial R_i}{\partial x_3}\frac{\partial x_3}{\partial \eta} \\ \frac{\partial R_i}{\partial \zeta} &= \frac{\partial R_i}{\partial x_1}\frac{\partial x_1}{\partial \zeta} + \frac{\partial R_i}{\partial x_2}\frac{\partial x_2}{\partial \zeta} + \frac{\partial R_i}{\partial x_3}\frac{\partial x_3}{\partial \zeta}. \end{aligned}$$

And thus, we may write

$$\begin{bmatrix} \frac{\partial R_i}{\partial x_1}, & \frac{\partial R_i}{\partial x_2}, & \frac{\partial R_i}{\partial x_3} \end{bmatrix} \boldsymbol{J} = \begin{bmatrix} \frac{\partial R_i}{\partial \xi}, & \frac{\partial R_i}{\partial \eta}, & \frac{\partial R_i}{\partial \zeta} \end{bmatrix}. \tag{25}$$

Multiplying with the inverse of the Jacobian, $\boldsymbol{J}^{-1}$, from the right, and taking the transpose on each side of the equation finally yields

$$\begin{bmatrix} \frac{\partial R_i}{\partial x_1} \\ \frac{\partial R_i}{\partial x_2} \\ \frac{\partial R_i}{\partial x_3} \end{bmatrix} = \boldsymbol{J}^{-\top} \begin{bmatrix} \frac{\partial R_i}{\partial \xi} \\ \frac{\partial R_i}{\partial \eta} \\ \frac{\partial R_i}{\partial \zeta} \end{bmatrix}. \tag{26}$$

With these expressions in mind the local mass matrix can be computed in the parent domain as

$$m_{ab}^e = \int_{\tilde{\Omega}^e} R_a^e R_b^e J_1 J_2 \, \mathrm{d}\tilde{\Omega}.$$

Collecting the basis functions R_a^e being non zero on the element, Ω^e, into a vector $\boldsymbol{R}^e = [R_1^e, R_2^e, \ldots, R_{n_{\mathrm{en}}}^e]^\top$ enables us to write the full local element mass matrix in terms of an outer product

$$\boldsymbol{m}^e = \int_{\tilde{\Omega}^e} \boldsymbol{R}^e [\boldsymbol{R}^e]^\top J_1 J_2 \, \mathrm{d}\tilde{\Omega},$$

with corresponding expressions for the local stiffness matrix and the local force vector.

The integrals are approximated with quadrature rules. If we want to approximate the integral

$$\int_{\tilde{\Omega}} g(\tilde{\xi}, \tilde{\eta}, \tilde{\zeta}) \, \mathrm{d}\tilde{\Omega},$$

the approximation by Gaussian quadrature is given by

$$\int_{\tilde{\Omega}} g(\tilde{\xi}, \tilde{\eta}, \tilde{\zeta}) \, \mathrm{d}\tilde{\Omega} \approx \sum_{i=1}^{n_{\mathrm{q}}} \rho_i g(\tilde{\xi}_i, \tilde{\eta}_i, \tilde{\zeta}_i),$$

where n_{q} are the number of quadrature points, and $(\tilde{\xi}_i, \tilde{\eta}_i, \tilde{\zeta}_i)$ and ρ_i are given quadrature points and weights, respectively.

2.9. Error analysis

In developing the ASIGA[6] toolbox (developed in MATLAB) for this PhD the error analysis has been a crucial debugging and researching approach. It is not only crucial to obtain numerical evidence for the correctness of the implemented code, but it can be used in research to compare methods. It is typically done by finding an analytic solution and analyze the convergence of the numerical solution towards this analytic solution in some suitable norm. What norm to compute the error in is not obvious and is very much problem dependent. For V-elliptic problems like

[6]The ASIGA (Acoustic Scattering using IsoGeometric Analysis) toolbox is available at the Zetison/ASIGA GitHub repository.

the Poisson problem it is natural to use the energy norm defined by the H^1-semi norm

$$|||u|||_\Omega = \sqrt{B(u,u)} = |u|_{H^1}, \quad \text{with} \quad B(v,u) = \int_\Omega \nabla v \cdot \nabla u \, \mathrm{d}\Omega$$

as Galerkin's method minimizes the error in this norm. In [63] we find the following result: Let $\check{p}$ be the highest degree of a complete polynomial in the FE basis and denote by $\|u\|_{H^{\check{p}+1}}$ the Sobolev norm of order $\check{p}+1$. For problems where the solution is not sufficiently smooth, $u \notin H^{\check{p}+1}$ we have the error bound

$$|||u - u_h|||_\Omega \leqslant Ch^\alpha \|u\|_{H^{\alpha+1}}$$

where the constant C is among other things dependent of the transformation from the parametric space to the physical space. It is not however depending on the maximal element size[7], h. So, as h become smaller, we expect the convergence to be of order α which is defined by

$$\alpha = \min\{\check{p}, \lambda\}$$

where λ is the strength of the singularity. Such that $\lambda < \check{p}$ limits the rate of convergence to the strength of singularity, rather than the polynomial order. This problem may be resolved by using adaptive mesh refinement to obtain $\alpha = \check{p}$. That is, one can obtain the same convergence as for sufficiently smooth solutions u. Adaptive mesh refinement (AMR) using T-splines was investigated in [26, 28]. Moreover, the recent LR B-splines was introduced in [64] followed by AMR analysis in [65–68]. Other AMR techniques include THB-splines [69, 70] and U-splines [31]. As suggested in [71], the need for AMR applies to solving Helmholtz problems as well.

The Helmholtz equation (with B defined in Eq. (21)) is not, however, V-elliptic [72, p. 46]. In fact, B does not even induce a semi-norm. Moreover, for comparison with the boundary element method using volumetric norms is not only unfeasible, but these methods obtain super convergence in appropriate negative fractional Sobolev norms [73]. Each method may have a preferred norm in which it excels and a priori error estimates often exist in such cases and it certainly makes sense to use these norms for code development. For research purposes it is not clear in which norm the comparison should be made. In the context of acoustic scattering with the target strength being the quantity of interest, it is natural to consider a norm over the boundary of the scatterer, Γ, since the far field is computed based on the Helmholtz integral (Eq. (33)) over the same domain. The $L^2(\Gamma)$-norm then represent an arguably good compromise in this context and has been used frequently in this thesis.

[7] The element size is defined as the smallest ball in which the element can be inscribed.

3. Helmholtz problems

Recall that the Helmholtz problem is given by

$$\nabla^2 p + k^2 p = 0 \quad \text{in} \quad \Omega, \tag{27}$$

$$\partial_n p = g \quad \text{on} \quad \Gamma, \tag{28}$$

where ∂_n denotes the partial derivative in the normal direction, $\boldsymbol{n}$, on the surface Γ. For the exterior problem we must impose the Sommerfeld radiation condition [74]

$$\frac{\partial p}{\partial r} - \mathrm{i}kp = o\Big(r^{-1}\Big) \quad \text{with} \quad r = |\boldsymbol{x}| \tag{29}$$

in order to restrict the field in the limit $r \to \infty$ uniformly in $\hat{\boldsymbol{x}} = \frac{\boldsymbol{x}}{r}$, such that no waves originate from infinity (to obtain uniqueness of the solution p).

A common approach for solving unbounded scattering problems with the FEM is to introduce an artificial boundary that encloses the scatterer. On the artificial boundary some sort of absorbing boundary condition (ABC) is prescribed. The problem is then reduced to a finite domain problem, and the bounded domain between the scatterer and the artificial boundary can be discretized with finite elements. Several methods exist for handling the exterior Helmholtz problem (on unbounded domain), including

- the infinite element method (IEM) [75, 76]
- local differential ABC operators [77–80]
- the perfectly matched layer (PML) [81, 82]
- the boundary element method (BEM) [83–86]
- Dirichlet to Neumann-operators (DtN-operators) [87].

The initial formulation of the IEM assumed the artificial boundary to be a sphere. This restriction results in unnecessary large computational domains for elongated scatterers and is somewhat relaxed in the ellipsoidal formulation after Burnett [88, 89], in which the infinite elements are attached on an ellipsoid as in Figure 19. These formulations are the ones used in the second paper of this thesis. A further generalization of the artificial boundary was attempted in the work of Shirron and Dey [90] where the artificial boundary may be any convex surface. For convex scatterer this enables the infinite elements to be attached directly onto the scatterer as in Figure 20. It is stated that this infinite element formulation preserves "the accuracy (and convergence characteristics)" of the IEM. A statement which can arguably be disputed as illustrated in the appendices as it very much so relies on the geometry of the artificial boundary. However, the reduced computational

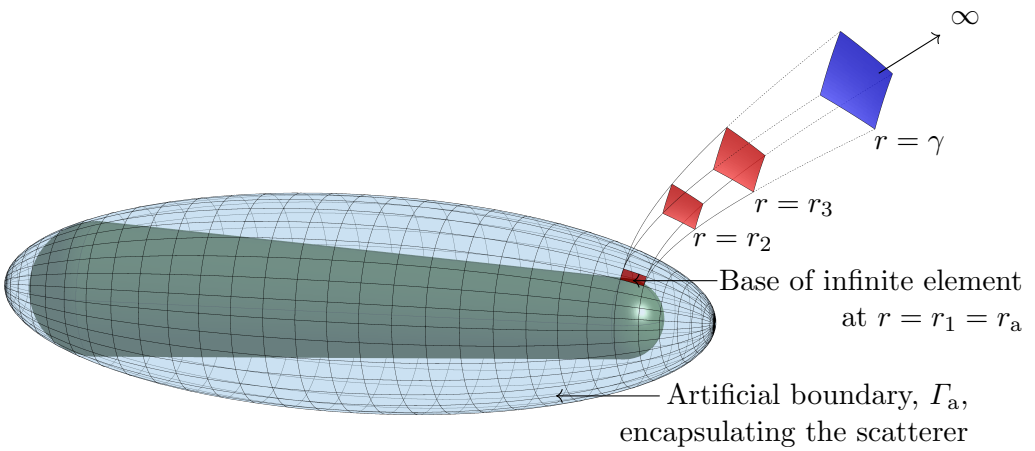

Figure 19: An infinite element in a prolate spheroidal coordinate system.

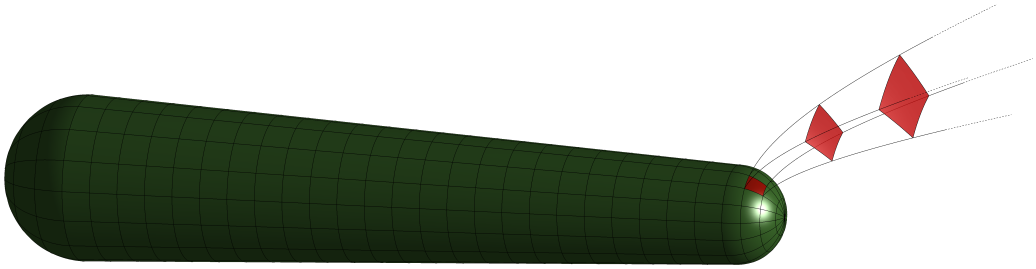

Figure 20: An infinite element attached directly onto the scatterer (which is here the BeTSSi model 3).

domain and simpler construction of the artificial boundary may be a sufficient compromise for the accuracy loss.

The approach based on ABC operators has developed in much the same way as for the infinite elements with for example an artificial boundary of cigar shape presented in [80]. Engineering precision (∼1%) may be obtained by simple second order operators, but for higher accuracy the formulations becomes arguably more tedious to implement compared to the IEM as higher order derivatives are required. On the other hand, the conditioning of the system matrices for this approach is better than that of the infinite element method. Several attempts have been presented for the IEM to resolve the conditioning problem including [91–93]. In [93] Safjan and Newman present basis functions with compact support (in the radial direction) also outside of the artificial boundary. Combining this approach with that of Shirron and Dey would be an approach to solve the conditioning problem while at the same time having lots of freedom to construct the artificial boundary.

The problems outlined above are not present for the BEM approach. Additionally, BEM comes with several advantages including reduction of problem dimension (3D volume to 3D surface), no need to do surface-to-volume parametrization (thus, especially suited for IGA), and automatic incorporation of the Sommerfeld radiation condition. However, a host of new challenges arises. This includes fictitious eigenfrequencies, singular integrals and fully dense system matrices. All of which are presented in the third paper.

3.1. Far field pattern

The target strength (the quantity of interest) is defined in the far field and we are only solving for the near field. The Helmholtz integral equation gives us a convenient way to link these two fields.

If the field at the scatterer is known (i.e. after obtaining the solution numerically), one can compute the solution in the exterior domain, Ω^+, using the following integral equation (cf. [86, Theorem 2.21])

$$p(\boldsymbol{x}) = \int_\Gamma \left[p(\boldsymbol{y}) \frac{\partial \Phi_k(\boldsymbol{x},\boldsymbol{y})}{\partial n(\boldsymbol{y})} - \Phi_k(\boldsymbol{x},\boldsymbol{y}) \frac{\partial p(\boldsymbol{y})}{\partial n(\boldsymbol{y})} \right] \mathrm{d}\Gamma(\boldsymbol{y}), \quad \boldsymbol{x} \in \Omega^+ \tag{30}$$

where $\boldsymbol{y}$ is a point on the surface Γ, $\boldsymbol{n}$ lies on Γ pointing "into" Ω^+ at $\boldsymbol{y}$, and Φ_k is the free space Green's function for the Helmholtz equation in Eq. (27) given (in 3D) by

$$\Phi_k(\boldsymbol{x},\boldsymbol{y}) = \frac{\mathrm{e}^{\mathrm{i}kR}}{4\pi R}, \quad \text{where} \quad R = |\boldsymbol{x}-\boldsymbol{y}| \tag{31}$$

with

$$\frac{\partial \Phi_k(\boldsymbol{x},\boldsymbol{y})}{\partial n(\boldsymbol{y})} = \frac{\Phi_k(\boldsymbol{x},\boldsymbol{y})}{R}(\mathrm{i}kR - 1)\frac{\partial R}{\partial n(\boldsymbol{y})}.$$

Using the limits (with $\boldsymbol{x} = \hat{\boldsymbol{x}}/r$ and $r = |\boldsymbol{x}|$)

$$\begin{aligned} \lim_{r\to\infty} r\mathrm{e}^{-\mathrm{i}kr}\Phi_k(r\hat{\boldsymbol{x}}, \boldsymbol{y}) &= \frac{1}{4\pi}\mathrm{e}^{-\mathrm{i}k\hat{\boldsymbol{x}}\cdot\boldsymbol{y}} \\ \lim_{r\to\infty} r\mathrm{e}^{-\mathrm{i}kr}\frac{\partial\Phi_k(r\hat{\boldsymbol{x}}, \boldsymbol{y})}{\partial n(\boldsymbol{y})} &= -\frac{\mathrm{i}k}{4\pi}\mathrm{e}^{-\mathrm{i}k\hat{\boldsymbol{x}}\cdot\boldsymbol{y}}\hat{\boldsymbol{x}}\cdot\boldsymbol{n}(\boldsymbol{y}) \end{aligned} \tag{32}$$

the formula in Eq. (30) simplifies in the far field to (cf. [72, p. 32])

$$p_0(\hat{\boldsymbol{x}}) = -\frac{1}{4\pi}\int_\Gamma \left[\mathrm{i}kp(\boldsymbol{y})\hat{\boldsymbol{x}}\cdot\boldsymbol{n}(\boldsymbol{y}) + \frac{\partial p(\boldsymbol{y})}{\partial n(\boldsymbol{y})}\right]\mathrm{e}^{-\mathrm{i}k\hat{\boldsymbol{x}}\cdot\boldsymbol{y}}\,\mathrm{d}\Gamma(\boldsymbol{y}). \tag{33}$$

from which the target strength in Eq. (3) may be computed.

4. Spectral methods

One of the cornerstones for IGA is the ability to control the continuity, and it has been proven to significantly increase the accuracy per degree of freedom (compared to classical C^0 FEM). The natural follow up question is then if it makes sense to increase the continuity even further. This results in spectral methods and are investigated in the following.

The main characteristics of the spectral methods considered in this section is the spectral convergence properties. That is, instead of an error decreasing algebraically as a function of the number of degrees of freedom (classical FEM result), spectral convergence is exponential. However, this is strongly contingent on the smoothness of the analytic solution. For this reason, spectral methods would excel in the solution on scattering from a sphere compared to finite element methods. The method of fundamental solution (MFS) involves basis functions that are in $C^\infty(\Omega^+)$ and will perform poorly on geometries with G^0 continuities (with kinks). The spectral element method is a hybrid version in the sense that it may incorporate C^0 continuities on the G^0 lines of the geometry while maintaining the C^∞ continuity within each patch.

4.1. Spectral element method

The spectral element method [94] is investigated in more detail in the addendum of this thesis where a comparison is made with IGA.

4.2. Method of fundamental solutions

Writing the solution as a sum of fundamental solutions of the Helmholtz equation (given by Eq. (31)) with singular points at a set of unique points $\boldsymbol{y}_j$ for $j = 1, \ldots, n_{\mathrm{sp}}$ we have

$$p(\boldsymbol{x}) = \sum_{j=1}^{n_{\mathrm{sp}}} C_j\Phi_k(\boldsymbol{x}, \boldsymbol{y}_j) \tag{34}$$

where the source points $\boldsymbol{y}_j$ will have to be located inside the scatterer. Note that p will solve the Helmholtz equation in Ω^+ and the Sommerfeld equation by construction. Collocating the equation

$$\frac{\partial p}{\partial n} = -\frac{\partial p_{\text{inc}}}{\partial n}$$

at n_{sp} collocation points $\boldsymbol{x}_i$, $i = 1, \ldots, n$, we arrive at a system of equations

$$\frac{\partial p}{\partial n(\boldsymbol{x}_i)}\bigg|_{\boldsymbol{x}=\boldsymbol{x}_i} = \sum_{j=1}^{n_{\text{cp}}} C_j \frac{\partial \Phi_k}{\partial n(\boldsymbol{x}_i)}(\boldsymbol{x}_i, \boldsymbol{y}_j) = -\frac{\partial p_{\text{inc}}}{\partial n(\boldsymbol{x}_i)}(\boldsymbol{x}_i) \tag{35}$$

namely $\boldsymbol{AC} = \boldsymbol{B}$ where the entries of $\boldsymbol{A}$ and $\boldsymbol{B}$ are given by

$$A_{ij} = \frac{\partial \Phi_k}{\partial n(\boldsymbol{x})}(\boldsymbol{x}_i, \boldsymbol{y}_j) \quad \text{and} \quad B_i = -\frac{\partial p_{\text{inc}}}{\partial n}(\boldsymbol{x}_i).$$

Note that a convenient formula for the far field pattern is obtained for the pressure in Eq. (34), namely (using the limits in Eq. (32))

$$p_0(\hat{\boldsymbol{x}}) = \frac{1}{4\pi} \sum_{j=1}^{n_{\text{cp}}} C_j \mathrm{e}^{-\mathrm{i}k\hat{\boldsymbol{x}}\cdot\boldsymbol{y}_j}.$$

That is, for the MFS there is no need to evaluate the far field through the Helmholtz integral in Eq. (30).

The MFS is reviewed in [95]. The main advantages of MFS is the ease of implementation as it requires no meshing and no handling of singular integrals. As for the boundary element method, there is no need for introducing any artificial boundary using the MFS. One of the main challenges with the MFS is the placement of the source points $\boldsymbol{y}_j$ which has impact on the conditioning of the system matrix and the accuracy of the numerical solution. For smooth domains the accuracy is increased by moving the source points away from the boundary with the cost of increasing the condition number (as the source points will then need to be clustered closer together). For well-behaved boundaries like the sphere, the location of the source points can be placed uniformly along the boundary at some given distance. For non-smooth boundaries these points would need to be adapted to the behavior of the boundary. The location of the source points could be found by solving Eq. (35) as a non-linear system of equation with unknowns $\boldsymbol{y}_j$ and C_j. Although the non-linearity of this approach is a weakness it can be handled by existing software (for example MINPACK-1 [96]).

In Figure 21 the spectral convergence is illustrated and compared to the algebraic convergence of finite elements. The finite element solution is here represented as the best approximation (BA) solution where the analytic solution is projected onto the solution space (here with polynomial order $\check{p} = 4$). The method

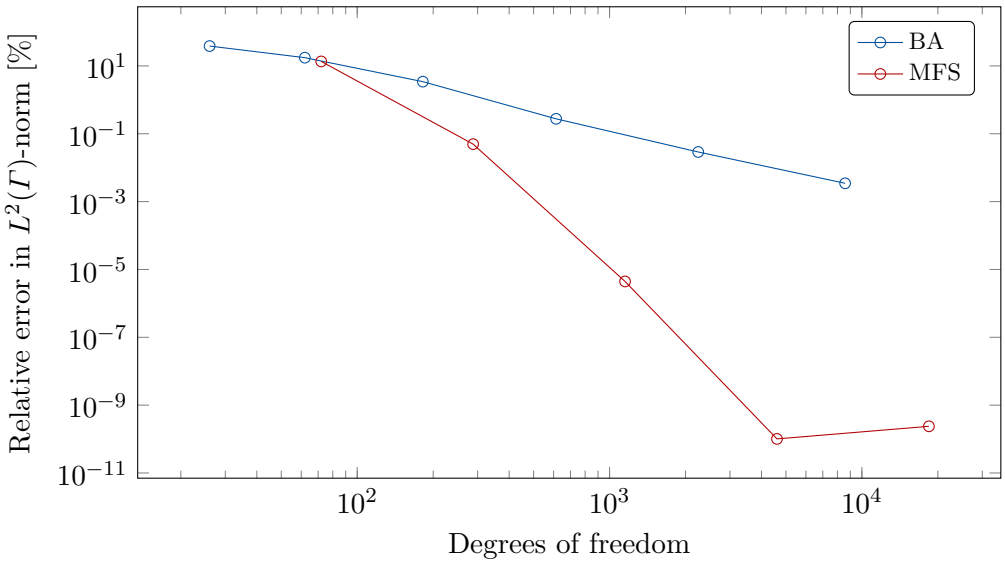

Figure 21: **Rigid scattering on a unit sphere:** A comparison between a spectral method solution (method of fundamental solution) and a finite element solution (best approximation).

of fundamental solution excels in such smooth problems but falls behind for more complex non-smooth geometries like the BeTSSi submarine. Optimal accuracy is obtained when the continuity of the solution space mirrors that of the physical problem. The cost of such an approach is however less sparse global matrices (in the case of MFS the global matrices are fully dense).

5. Summary of Papers

5.1. Paper I: Exact 3D scattering solutions for spherical symmetric scatterers

The first paper sets the stage for proper code development for acoustic scattering problems as it presents a very general exact solution for spherical symmetric scatterers. These scatterers can consist of an arbitrary number of (concentric) elastic shells, each shell with its own material parameters (outer and inner radii, mass density, Youngs modulus and Poisson ratio). Correspondingly, the intermediate fluid layers also have its own material parameters (mass density and speed of sound). Moreover, in addition to the full acoustic structure interaction boundary condition three other boundary conditions (BC) are implemented including sound hard BC (rigid scattering), sound soft BC and a boundary condition modeling an elastic sphere. All in all, the implemented program (in MATLAB) enables a vast range of benchmark tests for acoustic structure interaction problems.

Several numerical examples are presented including verification to existing benchmark examples. Numerical experiments of the residual error of the exact solution are also performed showing that the error only originates from round-off errors. Finally, two acoustic structure interaction problems in the time domain are presented using a Fourier transform.

5.2. Paper II: Isogeometric Analysis of Acoustic Scattering using Infinite Elements

The second paper investigates the contribution of isogeometric analysis (IGA) to acoustic structure interaction problems with the infinite element method. Four infinite element formulations are investigated including the conjugate and unconjugated versions of both the Petrov–Galerkin formulation and the Bubnov–Galerkin formulation.

Several numerical experiments on a spherical shell are performed and compared to the exact solution presented in the first paper. In this test setting, the power of the k-refinement strategy, unique to IGA, is clearly demonstrated. For resolved meshes k-refinement leads to significantly higher accuracy with only a small increase in the number of degrees of freedom.

A comparison between C^0 finite element method (FEM) and IGA is also performed. The exact geometry is of less importance in comparison with higher order FEM, as the increase of inter-element continuity plays a much more significant role in the accuracy improvement as a function of the number of degrees of freedom.

Finally, the performance of IGA with the infinite element using a prolate ellipsoidal coordinate system is investigated on a stripped BeTSSi submarine model.

5.3. Paper III: Isogeometric boundary element method

The third paper continues the active research on isogeometric boundary element method (IGABEM), where the focus is to analyze the approximability of IGABEM and application to complex geometries.

The usage of the infinite element method for handling the unbounded domain in the second paper is by no means an obvious choice in acoustic scattering problems. Indeed, many good candidates exist, and the boundary element method (BEM) is such an option. The BEM is in particular intriguing in combination with IGA as the bridging of CAD and analysis is improved; there is no need to mesh the geometry between the scatterer and an artificial boundary since BEM only require surface representation.

The approach in the numerical experiments taken in the second paper is also used in this paper, as it establishes convincing results where analytic solutions exist before moving onto more complex cases. Since BEM only require surface representation, it is much easier to investigate complex geometries. And the outer

hull of the BeTSSi submarine is in this regard investigated in depth and compared to independent reference solutions.

The main conclusions from the usage of IGA in combination with the infinite element method in the second paper also holds true for IGABEM. Moreover, proper numerical integration of weakly singular integrals is investigated and shown to be crucial for obtaining results close to the best approximation. Both the collocation and Galerkin approach are used in combination with several boundary integral equations (BIEs) including the conventional BIE (CBIE) and the Burton-Miller formulation. The application of the latter formulation removes fictitious eigenfrequencies with the cost of somewhat reduced accuracy compared to the CBIE formulation. The application of IGABEM to the BeTSSi submarine posed some problems for non-Lipschitz areas in the model but results with engineering precision ($< 1\%$ error) are still obtained.

5.4. Paper IV: Isogeometric Kirchhoff approximation using numerical steepest descent

The oscillatory nature of acoustic scattering problems is an intrinsic problem for classical finite element technologies. The usual rule of thumb is a requirement of 10-12 degrees of freedom per wavelength. For high frequencies this requirement becomes too restrictive, especially for 3D scattering problems. This problem is also present for IGA even though it uses slightly less degrees of freedom per wavelength. As a reference, requiring engineering precision at 30 kHz for the BeTSSi submarine would require an estimate of $27 \cdot 10^9$ dofs of 3D IGA elements. Which is more than a factor one thousand of the computational limit of the clusters available to the author both in terms of memory and computational time. Clearly another approach is needed.

The idea of enriching the basis functions with the same oscillatory nature as the given problem has shown promising results [86, 97–99]. A big challenge remaining on this front is the numerical integration (for 3D problems) as classical quadrature also becomes too computationally expensive. As a step in the direction of solving this problem, the fourth paper considers the simpler[8] problem of using the numerical steepest descent to evaluate the integrals of the Kirchhoff approximation method.

The Kirchhoff approximation method is a high frequency approximation where the solution at the boundary is approximated using a physical optics approximation. The classical way of using this method is to tessellate the model into triangles which enables exact integration. However, the number of required triangles is not independent of the frequency, and results in high memory consumption at high frequencies. This problem is avoided entirely with the proposed isogeometric

[8] Although it should be mentioned that the problem of integrating around the shadow boundary with the numerical steepest descent is not present for the boundary element method.

Kirchhoff approach where the boundary data are calculated on the exact CAD model.

References

[1] R. Dobbs, *Electromagnetic Waves*, Springer Netherlands, 1985.

[2] E. Bernard, A. Robinson, *Tsunamis*, Sea, ideas and observations on progress in the study of the seas, Harvard University Press, 2009.

[3] F. Brenguier, N. M. Shapiro, M. Campillo, V. Ferrazzini, Z. Duputel, O. Coutant, A. Nercessian, Towards forecasting volcanic eruptions using seismic noise, *Nature Geoscience*, 1:126–130 (2008).

[4] W. Munk, P. Worcester, C. Wunsch, *Ocean Acoustic Tomography*, Cambridge Monographs on Mechanics, Cambridge University Press, 2009.

[5] D. D. Iorio, Thirty years of scintillating acoustic data in diverse ocean environments, thanks to david farmer, *The Journal of the Acoustical Society of America*, 141:3547–3547 (2017).

[6] M. C. Junger, D. Feit, *Sound, structures, and their interaction*, vol. 225, MIT press Cambridge, MA, 1986.

[7] X. Lurton, *An Introduction to Underwater Acoustics: Principles and Applications*, Geophysical Sciences Series, Springer, 2002.

[8] D. N. MacLennan, Acoustical measurement of fish abundance, *The Journal of the Acoustical Society of America*, 87:1–15 (1990).

[9] T. Stanton, Review and recommendations for the modelling of acoustic scattering by fluid-like elongated zooplankton: euphausiids and copepods, *ICES Journal of Marine Science*, 57:793–807 (2000).

[10] H. Peña, K. G. Foote, Modelling the target strength of trachurus symmetricus murphyi based on high-resolution swimbladder morphometry using an MRI scanner, *ICES Journal of Marine Science*, 65:1751–1761 (2008).

[11] T. A. Consortium, Ocean climate change: Comparison of acoustic tomography, satellite altimetry, and modeling, *Science*, 281:1327–1332 (1998).

[12] F. B. Jensen, W. A. Kuperman, M. B. Porter, H. Schmidt, *Computational Ocean Acoustics*, 2nd edition, Springer New York, 2011.

[13] S. Wang, Finite-difference time-domain approach to underwater acoustic scattering problems, *The Journal of the Acoustical Society of America*, 99:1924–1931 (1996).

[14] M. Zampolli, A. Tesei, F. B. Jensen, Benchmark solutions for low-frequency structural acoustic target scattering, *The Journal of the Acoustical Society of America*, 122:3068 (2007).

[15] M. Zampolli, A. L. Espana, K. L. Williams, S. G. Kargl, E. I. Thorsos, J. L. lopes, J. L. Kennedy, P. L. Marston, Low- to mid-frequency scattering from elastic objects on a sand sea floor: Simulation of frequency and aspect dependent structural echoes, *Journal of Computational Acoustics*, 20 (2012).

[16] H. G. Schneider, R. Berg, L. Gilroy, I. Karasalo, I. MacGillivray, M. Morshuizen, A. Volker, Acoustic scattering by a submarine: Results from a benchmark target strength simulation workshop, *ICSV10*, pp. 2475–2482 (2003).

[17] B. Nolte, J. Ehrlich, H.-G. Hofmann, I. Schäfer, A. Schäfke, A. Stoltenberg, R. Burgschweiger, Numerical methods in underwater acoustics-sound propagation and backscattering, Tech. rep. (2015).

[18] R. Burgschweiger, I. Schafer, M. Ochmann, B. Nolte, Results of the ray-tracing based solver BEAM for the approximate determination of acoustic backscattering from thin-walled objects, in *INTER-NOISE and NOISE-CON Congress and Conference Proceedings*, vol. 249, Institute of Noise Control Engineering, 2014, pp. 1218–1227.

[19] L. Fillinger, M. Nijhof, C. de Jong, An efficient numerical target strength prediction model: Validation against analysis solutions, in *Papadakis, JS Bjorno, L., Proceedings 2nd International Conference and Exhibition on Underwater Acoustics, UA2014, 22-27 June, Rhodes, Greece, 487–493*, 2014.

[20] M. Nijhof, L. Fillinger, L. Gilroy, J. Ehrlich, I. Schäfer, BeTSSi IIb: Submarine target strength modeling workshop, in *International conference and exhibition on Underwater Acoustics*, 2017.

[21] J. V. Venås, Isogeometric analysis of acoustic scattering, Master's thesis, Norwegian University of Science and Technology, Trondheim, Norway (2015).

[22] J. V. Venås, T. Kvamsdal, Isogeometric boundary element method for acoustic scattering by a submarine, *Computer Methods in Applied Mechanics and Engineering* (2019).

[23] J. V. Venås, T. Jenserud, Exact 3D scattering solutions for spherical symmetric scatterers, *Journal of Sound and Vibration*, 440:439–479 (2019).

[24] T. Hughes, J. Cottrell, Y. Bazilevs, Isogeometric analysis: CAD, finite elements, NURBS, exact geometry and mesh refinement, *Computer Methods in Applied Mechanics and Engineering*, 194:4135–4195 (2005).

[25] J. Cottrell, T. Hughes, Y. Bazilevs, *Isogeometric Analysis: Toward Integration of CAD and FEA*, Wiley, 2009.

[26] Y. Bazilevs, V. Calo, J. Cottrell, J. Evans, T. Hughes, S. Lipton, M. Scott, T. Sederberg, Isogeometric analysis using T-splines, *Computer Methods in Applied Mechanics and Engineering*, 199:229–263 (2010), Computational Geometry and Analysis.

[27] M. A. Scott, T-splines as a design-through-analysis technology, Ph.D. thesis, The University of Texas at Austin (2011).

[28] M. Scott, X. Li, T. Sederberg, T. Hughes, Local refinement of analysis-suitable T-splines, *Computer Methods in Applied Mechanics and Engineering*, 213-216:206–222 (2012).

[29] M. Scott, R. Simpson, J. Evans, S. Lipton, S. Bordas, T. Hughes, T. Sederberg, Isogeometric boundary element analysis using unstructured T-splines, *Computer Methods in Applied Mechanics and Engineering*, 254:197–221 (2013).

[30] E. Evans, M. Scott, X. Li, D. Thomas, Hierarchical T-splines: Analysis-suitability, Bézier extraction, and application as an adaptive basis for isogeometric analysis, *Computer Methods in Applied Mechanics and Engineering*, 284:1–20 (2015), Isogeometric Analysis Special Issue.

[31] G. Sangalli, T. Takacs, R. Vázquez, Unstructured spline spaces for isogeometric analysis based on spline manifolds, *Computer Aided Geometric Design*, 47:61–82 (2016), SI: New Developments Geometry.

[32] D. Toshniwal, H. Speleers, T. J. Hughes, Smooth cubic spline spaces on unstructured quadrilateral meshes with particular emphasis on extraordinary points: Geometric design and isogeometric analysis considerations, *Computer Methods in Applied Mechanics and Engineering*, 327:411–458 (2017), Advances in Computational Mechanics and Scientific Computation – the Cutting Edge.

[33] A. Stahl, T. Kvamsdal, C. Schellewald, Post-processing and visualization techniques for isogeometric analysis results, *Computer Methods in Applied Mechanics and Engineering*, 316:880–943 (2017), Special Issue on Isogeometric Analysis: Progress and Challenges.

[34] L. Beirão da Veiga, A. Buffa, J. Rivas, G. Sangalli, Some estimates for h–p–k-refinement in isogeometric analysis, *Numerische Mathematik*, 118:271–305 (2011).

[35] L. Beirão da Veiga, A. Buffa, G. Sangalli, R. Vázquez, Mathematical analysis of variational isogeometric methods, *Acta Numerica*, 23:157–287 (2014).

[36] J. Cottrell, T. Hughes, A. Reali, Studies of refinement and continuity in isogeometric structural analysis, *Computer Methods in Applied Mechanics and Engineering*, 196:4160–4183 (2007).

[37] L. Dedè, C. Jäggli, A. Quarteroni, Isogeometric numerical dispersion analysis for two-dimensional elastic wave propagation, *Computer Methods in Applied Mechanics and Engineering*, 284:320–348 (2015), Isogeometric Analysis Special Issue.

[38] W. Wen, S. Duan, K. Wei, Y. Ma, D. Fang, A quadratic B-spline based isogeometric analysis of transient wave propagation problems with implicit time integration method, *Applied Mathematical Modelling*, 59:115–131 (2018).

[39] L. Pegolotti, L. Dedè, A. Quarteroni, Isogeometric Analysis of the electrophysiology in the human heart: Numerical simulation of the bidomain equations on the atria, *Computer Methods in Applied Mechanics and Engineering*, 343:52–73 (2019).

[40] C. V. Verhoosel, M. A. Scott, T. J. R. Hughes, R. de Borst, An isogeometric analysis approach to gradient damage models, *International Journal for Numerical Methods in Engineering*, 86:115–134 (2011).

[41] Y. Bazilevs, V. M. Calo, Y. Zhang, T. J. R. Hughes, Isogeometric fluid–structure interaction analysis with applications to arterial blood flow, *Computational Mechanics*, 38:310–322 (2006).

[42] Y. Zhang, Y. Bazilevs, S. Goswami, C. L. Bajaj, T. J. Hughes, Patient-specific vascular NURBS modeling for isogeometric analysis of blood flow, *Computer Methods in Applied Mechanics and Engineering*, 196:2943–2959 (2007).

[43] S. Morganti, F. Auricchio, D. Benson, F. Gambarin, S. Hartmann, T. Hughes, A. Reali, Patient-specific isogeometric structural analysis of aortic valve closure, *Computer Methods in Applied Mechanics and Engineering*, 284:508–520 (2015), Isogeometric Analysis Special Issue.

[44] I. Akkerman, Y. Bazilevs, C. Kees, M. Farthing, Isogeometric analysis of free-surface flow, *Journal of Computational Physics*, 230:4137–4152 (2011), Special issue High Order Methods for CFD Problems.

[45] M.-C. Hsu, I. Akkerman, Y. Bazilevs, High-performance computing of wind turbine aerodynamics using isogeometric analysis, *Computers & Fluids*, 49:93–100 (2011).

[46] Y. Bazilevs, M.-C. Hsu, M. Scott, Isogeometric fluid–structure interaction analysis with emphasis on non-matching discretizations, and with application

to wind turbines, *Computer Methods in Applied Mechanics and Engineering*, 249-252:28–41 (2012), Higher Order Finite Element and Isogeometric Methods.

[47] M. J. Borden, C. V. Verhoosel, M. A. Scott, T. J. Hughes, C. M. Landis, A phase-field description of dynamic brittle fracture, *Computer Methods in Applied Mechanics and Engineering*, 217-220:77–95 (2012).

[48] M. J. Borden, T. J. Hughes, C. M. Landis, C. V. Verhoosel, A higher-order phase-field model for brittle fracture: Formulation and analysis within the isogeometric analysis framework, *Computer Methods in Applied Mechanics and Engineering*, 273:100–118 (2014).

[49] G. Moutsanidis, D. Kamensky, J. Chen, Y. Bazilevs, Hyperbolic phase field modeling of brittle fracture: Part II—immersed IGA–RKPM coupling for air-blast–structure interaction, *Journal of the Mechanics and Physics of Solids*, 121:114–132 (2018).

[50] L. Dedè, M. J. Borden, T. J. R. Hughes, Isogeometric analysis for topology optimization with a phase field model, *Archives of Computational Methods in Engineering*, 19:427–465 (2012).

[51] N. D. Manh, A. Evgrafov, A. R. Gersborg, J. Gravesen, Isogeometric shape optimization of vibrating membranes, *Computer Methods in Applied Mechanics and Engineering*, 200:1343–1353 (2011).

[52] J. Kiendl, R. Schmidt, R. Wüchner, K.-U. Bletzinger, Isogeometric shape optimization of shells using semi-analytical sensitivity analysis and sensitivity weighting, *Computer Methods in Applied Mechanics and Engineering*, 274:148–167 (2014).

[53] D. Benson, Y. Bazilevs, M. Hsu, T. Hughes, Isogeometric shell analysis: The Reissner–Mindlin shell, *Computer Methods in Applied Mechanics and Engineering*, 199:276–289 (2010), Computational Geometry and Analysis.

[54] M. Dittmann, M. Franke, İ. Temizer, C. Hesch, Isogeometric analysis and thermomechanical mortar contact problems, *Computer Methods in Applied Mechanics and Engineering*, 274:192–212 (2014).

[55] İ. Temizer, P. Wriggers, T. Hughes, Contact treatment in isogeometric analysis with NURBS, *Computer Methods in Applied Mechanics and Engineering*, 200:1100–1112 (2011).

[56] J. Cottrell, A. Reali, Y. Bazilevs, T. Hughes, Isogeometric analysis of structural vibrations, *Computer Methods in Applied Mechanics and Engineering*, 195:5257–5296 (2006).

[57] D. Schillinger, L. Dedè, M. A. Scott, J. A. Evans, M. J. Borden, E. Rank, T. J. Hughes, An isogeometric design-through-analysis methodology based on adaptive hierarchical refinement of NURBS, immersed boundary methods, and T-spline CAD surfaces, *Computer Methods in Applied Mechanics and Engineering*, 249-252:116–150 (2012), Higher Order Finite Element and Isogeometric Methods.

[58] Y. Bazilevs, T. J. R. Hughes, NURBS-based isogeometric analysis for the computation of flows about rotating components, *Computational Mechanics*, 43:143–150 (2008).

[59] H. Gómez, V. M. Calo, Y. Bazilevs, T. J. Hughes, Isogeometric analysis of the Cahn–Hilliard phase-field model, *Computer Methods in Applied Mechanics and Engineering*, 197:4333–4352 (2008).

[60] Y. Lai, Y. J. Zhang, L. Liu, X. Wei, E. Fang, J. Lua, Integrating CAD with Abaqus: A practical isogeometric analysis software platform for industrial applications, *Computers & Mathematics with Applications*, 74:1648–1660 (2017), High-Order Finite Element and Isogeometric Methods 2016.

[61] T. Lyche, K. Mørken, *Spline methods draft*, Department of Informatics, Center of Mathematics for Applications, University of Oslo, Oslo, 2008.

[62] Q.-X. Huang, S.-M. Hu, R. R. Martin, Efficient degree elevation and knot insertion for B-spline curves using derivatives, *Computer-Aided Design and Applications*, 1:719–725 (2004).

[63] K. A. Johannessen, T. Kvamsdal, T. Dokken, Isogeometric analysis using LR B-splines, *Computer Methods in Applied Mechanics and Engineering*, 269:471–514 (2014).

[64] T. Dokken, T. Lyche, K. F. Pettersen, Polynomial splines over locally refined box-partitions, *Computer Aided Geometric Design*, 30:331–356 (2013).

[65] K. A. Johannessen, M. Kumar, T. Kvamsdal, Divergence-conforming discretization for Stokes problem on locally refined meshes using LR B-splines, *Computer Methods in Applied Mechanics and Engineering*, 293:38–70 (2015).

[66] K. A. Johannessen, F. Remonato, T. Kvamsdal, On the similarities and differences between classical hierarchical, truncated hierarchical and LR B-splines, *Computer Methods in Applied Mechanics and Engineering*, 291:64–101 (2015).

[67] M. Kumar, T. Kvamsdal, K. A. Johannessen, Simple a posteriori error estimators in adaptive isogeometric analysis, *Computers & Mathematics with Applications*, 70:1555–1582 (2015).

[68] M. Kumar, T. Kvamsdal, K. A. Johannessen, Superconvergent patch recovery and a posteriori error estimation technique in adaptive isogeometric analysis, *Computer Methods in Applied Mechanics and Engineering*, 316:1086–1156 (2017).

[69] C. Giannelli, B. Jüttler, H. Speleers, THB-splines: The truncated basis for hierarchical splines, *Computer Aided Geometric Design*, 29:485–498 (2012), Geometric Modeling and Processing 2012.

[70] X. Wei, Y. Zhang, T. J. Hughes, M. A. Scott, Truncated hierarchical Catmull–Clark subdivision with local refinement, *Computer Methods in Applied Mechanics and Engineering*, 291:1–20 (2015).

[71] K. Gerdes, L. Demkowicz, Solution of 3D-Laplace and Helmholtz equations in exterior domains using *hp*-infinite elements, *Computer Methods in Applied Mechanics and Engineering*, 137:239–273 (1996).

[72] F. Ihlenburg, *Finite Element Analysis of Acoustic Scattering*, vol. 132 of *Applied Mathematical Sciences*, Springer, New York, USA, 1998.

[73] J. Dölz, H. Harbrecht, M. Peters, An interpolation-based fast multipole method for higher-order boundary elements on parametric surfaces, *International Journal for Numerical Methods in Engineering*, 108:1705–1728 (2016).

[74] A. Sommerfeld, *Partial differential equations in physics*, vol. 1, Academic press, 1949.

[75] P. Bettess, Infinite elements, *International Journal for Numerical Methods in Engineering*, 11:53–64 (1977).

[76] P. Bettess, O. C. Zienkiewicz, Diffraction and refraction of surface waves using finite and infinite elements, *International Journal for Numerical Methods in Engineering*, 11:1271–1290 (1977).

[77] J. J. Shirron, Solution of exterior Helmholtz problems using finite and infinite elements, Ph.D. thesis, University of Maryland College Park (1995).

[78] A. Bayliss, M. Gunzburger, E. Turkel, Boundary conditions for the numerical solution of elliptic equations in exterior regions, *SIAM Journal on Applied Mathematics*, 42:430–451 (1982).

[79] T. Hagstrom, S. Hariharan, A formulation of asymptotic and exact boundary conditions using local operators, *Applied Numerical Mathematics*, 27:403–416 (1998), Special Issue on Absorbing Boundary Conditions.

[80] R. Tezaur, A. Macedo, C. Farhat, R. Djellouli, Three-dimensional finite element calculations in acoustic scattering using arbitrarily shaped convex artificial boundaries, *International Journal for Numerical Methods in Engineering*, 53:1461–1476 (2001).

[81] J.-P. Berenger, A perfectly matched layer for the absorption of electromagnetic waves, *Journal of Computational Physics*, 114:185–200 (1994).

[82] J.-P. Berenger, Perfectly matched layer for the FDTD solution of wave-structure interaction problems, *IEEE Transactions on Antennas and Propagation*, 44:110–117 (1996).

[83] S. A. Sauter, C. Schwab, *Boundary Element Methods*, Springer Berlin Heidelberg, Berlin, Heidelberg, 2011, pp. 183–287.

[84] M. Schanz, O. Steinbach, *Boundary Element Analysis: Mathematical Aspects and Applications*, Lecture Notes in Applied and Computational Mechanics, Springer Berlin Heidelberg, 2007.

[85] S. Marburg, B. Nolte, *Computational Acoustics of Noise Propagation in Fluids-Finite and Boundary Element Methods*, vol. 578, Springer, 2008.

[86] S. N. Chandler-Wilde, I. G. Graham, S. Langdon, E. A. Spence, Numerical-asymptotic boundary integral methods in high-frequency acoustic scattering, *Acta Numerica*, 21:89–305 (2012).

[87] D. Givoli, *Numerical methods for problems in infinite domains*, vol. 33, Elsevier, 2013.

[88] D. S. Burnett, A three-dimensional acoustic infinite element based on a prolate spheroidal multipole expansion, *The Journal of the Acoustical Society of America*, 96:2798–2816 (1994).

[89] D. S. Burnett, R. L. Holford, An ellipsoidal acoustic infinite element, *Computer Methods in Applied Mechanics and Engineering*, 164:49–76 (1998).

[90] J. J. Shirron, S. Dey, Acoustic infinite elements for non-separable geometries, *Computer Methods in Applied Mechanics and Engineering*, 191:4123–4139 (2002).

[91] D. Dreyer, O. von Estorff, Improved conditioning of infinite elements for exterior acoustics, *International Journal for Numerical Methods in Engineering*, 58:933–953 (2003).

[92] A. Safjan, M. Newman, The ill-conditioning of infinite element stiffness matrices, *Computers & Mathematics with Applications*, 41:1263–1291 (2001).

[93] A. Safjan, M. Newman, Three-dimensional infinite elements utilizing basis functions with compact support, *Computers & Mathematics with Applications*, 43:981–1002 (2002).

[94] A. T. Patera, A spectral element method for fluid dynamics: Laminar flow in a channel expansion, *Journal of Computational Physics*, 54:468–488 (1984).

[95] G. Fairweather, A. Karageorghis, P. Martin, The method of fundamental solutions for scattering and radiation problems, *Engineering Analysis with Boundary Elements*, 27:759–769 (2003), Special issue on Acoustics.

[96] J. J. Moré, B. S. Garbow, K. E. Hillstrom, User guide for MINPACK-1, Tech. rep., CM-P00068642 (1980).

[97] M. Peake, J. Trevelyan, G. Coates, Extended isogeometric boundary element method (XIBEM) for two-dimensional Helmholtz problems, *Computer Methods in Applied Mechanics and Engineering*, 259:93–102 (2013).

[98] M. Peake, Enriched and isogeometric boundary element methods for acoustic wave scattering, Ph.D. thesis, Durham University (2014).

[99] M. Peake, J. Trevelyan, G. Coates, Extended isogeometric boundary element method (XIBEM) for three-dimensional medium-wave acoustic scattering problems, *Computer Methods in Applied Mechanics and Engineering*, 284:762–780 (2015), Isogeometric Analysis Special Issue.

Paper I

Exact 3D Scattering Solutions for Spherical Symmetric Scatterers

Jon Vegard Venås and Trond Jenserud

Published in *Journal of Sound and Vibration* (2019) **440**:439–479

Exact 3D scattering solutions for spherical symmetric scatterers

Jon Vegard Venås[a,*], Trond Jenserud[b]

[a] *Department of Mathematical Sciences, Norwegian University of Science and Technology, Alfred Getz' vei 1, 7034 Trondheim, Norway*
[b] *Department of Marine Systems, Norwegian Defence Research Establishment, Postboks 115, 3191 Horten, Norway*

Abstract

In this paper, exact solutions to the problem of acoustic scattering by elastic spherical symmetric scatterers are developed. The scatterer may consist of an arbitrary number of fluid and solid layers and scattering with single Neumann conditions (replacing Neumann-to-Neumann conditions) is added. The solution is obtained by separation of variables, resulting in an infinite series which must be truncated for numerical evaluation. The implemented numerical solution is exact in the sense that numerical error is solely due to round-off errors, which will be shown using the symbolic toolbox in MATLAB. A system of benchmark problems is proposed for future reference. Numerical examples are presented, including comparisons with reference solutions, far-field patterns and near-field plots of the benchmark problems, and time-dependent solutions obtained by Fourier transformation.

1. Introduction

Acoustic scattering by elastic objects is a continuing area of study. Most phenomena in the scattering process can be adequately described by linear elasticity theory, and by further restricting the analysis to homogeneous, isotropic bodies of simple geometries, the mathematical formalism becomes simple enough to be handled by conventional analytic methods.

The problems fall into mainly three categories: scattering of acoustic waves from elastic objects, scattering of elastic waves from fluid-filled cavities and solid inclusions, and inverse scattering, i.e., obtaining properties of a scattering object from the remotely sensed field. In the first category, the classical problems include scattering by spheres and infinite cylinders: fluid spheres [1], solid spheres and

*Corresponding author.
Email addresses: Jon.Venas@ntnu.no (J.V. Venås), Trond.Jenserud@ffi.no (T. Jenserud).

cylinders [2–7], and spherical and cylindrical shells with various combinations of material properties [8–15]. Much of the work in this field up to around 1980, is summarized in Flax et al. [16].

The surrounding medium is usually considered to be a lossless fluid, but viscous fluids [17] and viscoelastic media and materials [18] are also considered.

The acoustic illumination is often taken to be a plane wave which is relevant for far-field sources, otherwise point sources are applied in the near-field. For the infinite cylinder, the incident field is in most cases applied normal to the cylinder, but obliquely incident fields are also considered [19, 20]. More recently, the problem of scattering of beams has received much attention [21, 22].

Solutions to some non-symmetric problems are also given; e.g. partially fluid filled spheres [23], spheres with eccentric cavities [18], and open spheres with internal point sources [24].

The studies mentioned above consider a single object in the free field. It is also of interest to study interactions between objects, and between an object and a boundary. The problem of multiple scattering is studied in e.g. [25] for two elastic spheres, and in [26] for many fluid spheres, while the scattering by objects close to boundaries, and by partially buried objects is addressed in [27].

Applications of the theory are numerous, and include scattering from marine life [1, 28, 29], various aspects of sonar, nondestructive testing, seismology, detection of buried objects [30], medical imaging [31], determination of material properties by inverse scattering [32], and acoustic cloaking. Acoustic cloaking, i.e., making an object acoustically 'invisible', requires acoustic metamaterials and is difficult to realize in practice, but reducing the backscattering strength of an object is an important issue, and can be realized either passively by coating or actively as suggested in e.g. [33]. A recent area of research is noise control in aerospace- and automotive engineering, where sound transmission through cylindrical shells constructed from new composite materials [34] and functionally graded materials [20] are studied in order to reduce noise level inside the cabin. The latter problem requires a full 3D solution.

The method referred to as classical scattering theory starts with the linearized elasto-dynamic equation of motion (also called Naviers equation). For the intended applications, nonlinear effects are negligible, which justifies the use of the linear approximation. For a certain class of coordinate systems, the field can be expressed in terms of three scalar potentials, which satisfy scalar Helmholtz equations, and admit solutions in the form of infinite series, termed normal modes or partial waves. The formal series expansions contain all the physical features of the solution, i.e., the reflected, transmitted and circumferential (or creeping) waves. The most general problems on finite scatterers in free space are scattering by the spherical shells which requires all three potentials and give solutions in terms of double sums. However, assuming axisymmetric illumination there is no loss of generality in aligning the coordinate axis of the sphere with the axis of the incident field,

resulting in an axisymmetric problem. This results in a single infinite series which is much more computational efficient than the general case. This is the approach taken here.

As the solution is in the form of an infinite series, it needs to be truncated at some point. The summation is terminated when the relative magnitude of the last term is less than some prescribed tolerance, such that no computational parameters are introduced if this tolerance is chosen to be the precision used in the calculations (typically double precision). It is shown, by using symbolic precision in MATLAB, that the computational errors in the implementation are due to round-off errors. This is a natural definition of a computational exact solution.

The work reviewed above solves a host of different problems, and several reference solutions are available, with complexity up to three layers. What the present work provides is the explicit solution for a fully general multilayered sphere, and with corresponding analysis of the computational residual errors. This allows easy design and modeling of reference solutions for the purpose of validating numerical methods. More specific, the model solves the problem of scattering by an incident plane wave, or wave from a point source, by spherical objects consisting of an arbitrary number of layers. Any combinations of fluid and solid layers can be handled, and the special cases of replacing the Neumann-to-Neumann condition by a single Neumann condition is also included.

An early work on scattering from multilayered spheres and infinite cylinders is Jenserud and Tollefsen [35]. The method employed here is referred to as the global matrix method [36] and is a systematic way of assembling local solutions for the individual layers into a global matrix for the total problem. The present work uses the same approach and builds mainly upon the work of Chang and Demkowicz [13], which is generalized to multilayered spherical objects.

2. Governing equations

In this section the governing equations for the problem at hand will be presented. In [37, pp. 13-14] Ihlenburg briefly derives the governing equations for the acoustic-structure interaction problem. As the physical problem of interest is a time dependent problem, it is natural to first present the governing equations in the time-domain before presenting the corresponding equations in the frequency domain (obtained by Fourier transformation). It is noted right away that the fields described in this paper (both in the time-domain and frequency-domain) are all perturbation fields.

2.1. Governing equations in the time domain

Einstein's summation convention will be used throughout this work, such that repeated indices in products imply summation. For example, any vector $\boldsymbol{x} \in \mathbb{R}^3$

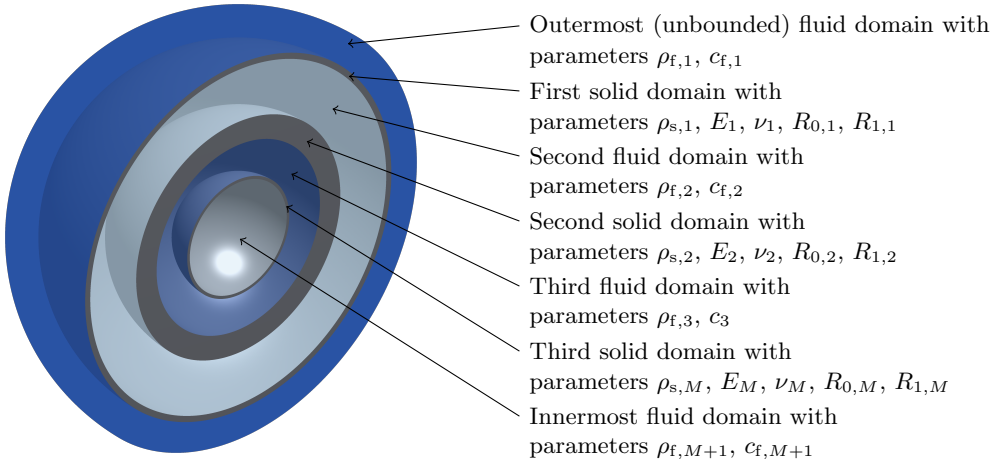

Figure 1: A model with $M = 3$ steel shells with different thicknesses (clip view), illustrating the distribution of the physical parameters over the different domains.

can be expressed as

$$\boldsymbol{x} = \begin{bmatrix} x_1 \\ x_2 \\ x_3 \end{bmatrix} = \sum_{i=1}^{3} x_i \boldsymbol{e}_i = x_i \boldsymbol{e}_i, \tag{1}$$

where $\boldsymbol{e}_i \in \mathbb{R}^3$ is the standard basis vectors in a three-dimensional Euclidean space.

Let $\breve{\boldsymbol{u}} = \breve{u}_i \boldsymbol{e}_i$ be the time-dependent displacement field in a given solid domain, and $\breve{\boldsymbol{\sigma}}$ the corresponding stress tensor (see Appendix B for details). Each of the components depend on the spatial variable $\boldsymbol{x}$ and the time variable t, such that $\breve{\boldsymbol{u}} = \breve{\boldsymbol{u}}(\boldsymbol{x}, t)$. The solid domain is then governed by Navier's equation of motion [15] (derived from Newton's second law)

$$G\nabla^2 \breve{\boldsymbol{u}} + \left(K + \frac{G}{3}\right) \nabla(\nabla \cdot \breve{\boldsymbol{u}}) = \rho_{\mathrm{s}} \frac{\partial^2 \breve{\boldsymbol{u}}}{\partial t^2}, \tag{2}$$

which is equivalent to [38, p. 223]

$$\frac{\partial \breve{\sigma}_{ij}}{\partial x_j} = \rho_{\mathrm{s}} \frac{\partial^2 \breve{u}_i}{\partial t^2}, \quad i = 1, 2, 3. \tag{3}$$

The *bulk modulus*, K, and the *shear modulus*, G, can be defined by the Young's modulus, E, and Poisson's ratio, ν, as

$$K = \frac{E}{3(1-2\nu)} \quad \text{and} \quad G = \frac{E}{2(1+\nu)}. \tag{4}$$

Correspondingly, denote by $\breve{p}$ the time-dependent scattered pressure field in a given fluid domain, which is governed by the wave equation

$$\nabla^2 \breve{p} = \frac{1}{c_\mathrm{f}^2} \frac{\partial^2 \breve{p}}{\partial t^2}. \tag{5}$$

2.2. Governing equations in the frequency domain

The dimension of the governing equations may be reduced by one using a time–frequency Fourier[1] pair [40, p. 71]

$$\Psi(\boldsymbol{x}, \omega) = \Big(\mathcal{F}\, \breve{\Psi}(\boldsymbol{x}, \cdot)\Big)(\omega) = \int_{-\infty}^{\infty} \breve{\Psi}(\boldsymbol{x}, t) \mathrm{e}^{\mathrm{i}\omega t}\, \mathrm{d}t \tag{6}$$

$$\breve{\Psi}(\boldsymbol{x}, t) = \Big(\mathcal{F}^{-1}\, \Psi(\boldsymbol{x}, \cdot)\Big)(t) = \frac{1}{2\pi} \int_{-\infty}^{\infty} \Psi(\boldsymbol{x}, \omega) \mathrm{e}^{-\mathrm{i}\omega t}\, \mathrm{d}\omega \tag{7}$$

where Ψ represents the scattered pressure field p or the displacement field $\boldsymbol{u}$. The frequency f and the angular frequency ω is related by $\omega = 2\pi f$, and the angular wave number is given by $k = \omega / c_\mathrm{f}$.

Consider first the scattered pressure. By differentiating Eq. (7) twice with respect to time, such that

$$\frac{\partial^2}{\partial t^2} \breve{p}(\boldsymbol{x}, t) = -\omega^2 \breve{p}(\boldsymbol{x}, t), \tag{8}$$

the following is obtained (using Eq. (5))

$$\begin{aligned} \nabla^2 p(\boldsymbol{x}, \omega) + k^2 p(\boldsymbol{x}, \omega) &= \int_{-\infty}^{\infty} \nabla^2 \breve{p}(\boldsymbol{x}, t) \mathrm{e}^{\mathrm{i}\omega t}\, \mathrm{d}t + \int_{-\infty}^{\infty} k^2 \breve{p}(\boldsymbol{x}, t) \mathrm{e}^{\mathrm{i}\omega t}\, \mathrm{d}t \\ &= \int_{-\infty}^{\infty} \left[\nabla^2 \breve{p}(\boldsymbol{x}, t) - \frac{1}{c_\mathrm{f}^2} \frac{\partial^2}{\partial t^2} \breve{p}(\boldsymbol{x}, t) \right] \mathrm{e}^{\mathrm{i}\omega t}\, \mathrm{d}t = 0. \end{aligned}$$

That is, $p(\boldsymbol{x}, \omega)$ satisfies the Helmholtz equation

$$\nabla^2 p + k^2 p = 0. \tag{9}$$

A corresponding argument shows that the displacement field $\boldsymbol{u}(\boldsymbol{x}, \omega)$ satisfies

$$G \nabla^2 \boldsymbol{u} + \left(K + \frac{G}{3} \right) \nabla (\nabla \cdot \boldsymbol{u}) + \rho_\mathrm{s} \omega^2 \boldsymbol{u} = \boldsymbol{0}. \tag{10}$$

The scattered pressure, p, must in addition to the Helmholtz equation satisfy the Sommerfeld radiation condition for the outermost fluid layer [42]

$$\frac{\partial p(\boldsymbol{x}, \omega)}{\partial r} - \mathrm{i}k p(\boldsymbol{x}, \omega) = o\Big(r^{-1}\Big) \quad r = |\boldsymbol{x}| \tag{11}$$

[1] The sign convention in the Fourier transform differs from the classical Fourier transform [39], but agrees with most literature on the subject, for example [15, 37, 40, 41].

as $r \to \infty$ uniformly in $\hat{\boldsymbol{x}} = \frac{\boldsymbol{x}}{r}$.

The coupling conditions (Neumann-to-Neumann) between the solid and the fluid boundaries are given by [37, pp. 13-14]

$$\rho_{\mathrm{f}}\omega^2 u_i n_i - \frac{\partial p_{\mathrm{tot}}}{\partial n} = 0 \tag{12}$$

$$\sigma_{ij} n_i n_j + p_{\mathrm{tot}} = 0 \tag{13}$$

where $\boldsymbol{n}$ is the normal vector at the surface, and p_{tot} is the total pressure[2] (scattered pressure with the incident pressure field added for the outermost fluid). In addition, since the fluid is assumed to be ideal, there is no tangential traction at the surfaces. For spherical symmetric objects $\boldsymbol{n} = \boldsymbol{e}_{\mathrm{r}}$, such that the coupling equations reduces to

$$\rho_{\mathrm{f}}\omega^2 u_{\mathrm{r}} - \frac{\partial p_{\mathrm{tot}}}{\partial r} = 0 \tag{14}$$

$$\sigma_{\mathrm{rr}} + p_{\mathrm{tot}} = 0 \tag{15}$$

in the spherical coordinate system (see Appendix A). The tangential traction free boundary conditions become [13, p. 15]

$$\sigma_{\mathrm{r}\vartheta} = 0 \tag{16}$$

$$\sigma_{\mathrm{r}\varphi} = 0. \tag{17}$$

3. General solution in the solid domain

It turns out that Navier's equation can be reduced to a set of Helmholtz equations. Since the fluid domain also is governed by the Helmholtz equation, both solid and fluid domains share the same fundamental solutions, and it thus suffices to present the general solution in the solid domain.

3.1. Lamé solution

Fender [15] shows that the solution of Eq. (10) can be written in terms of a scalar potential ϕ and a vector potential $\boldsymbol{\psi}$ as follows

$$\boldsymbol{u} = \nabla\phi + \nabla \times \boldsymbol{\psi}. \tag{18}$$

Such a solution of Navier's equation is called a Lamé solution. The potentials ϕ and $\boldsymbol{\psi}$ satisfy the scalar and vector Helmholtz equation, respectively. That is,

$$\nabla^2\phi + a^2\phi = 0 \tag{19}$$

$$\nabla^2\boldsymbol{\psi} + b^2\boldsymbol{\psi} = \boldsymbol{0} \tag{20}$$

[2]Since only perturbation fields are considered, p_{tot} does not include the static background pressure (and does therefore not represent the physical total pressure field).

where

$$a = \frac{\omega}{c_{\mathrm{s},1}}, \quad b = \frac{\omega}{c_{\mathrm{s},2}}, \quad c_{\mathrm{s},1} = \sqrt{\frac{3K+4G}{3\rho_{\mathrm{s}}}}, \quad c_{\mathrm{s},2} = \sqrt{\frac{G}{\rho_{\mathrm{s}}}}. \tag{21}$$

Here, the parameters $c_{\mathrm{s},1}$ and $c_{\mathrm{s},2}$ are the longitudinal and transverse (elastic) wave velocities, respectively, and a and b are the corresponding angular wave numbers in the solid.

Throughout this work, axisymmetry around the x_3-axis is assumed. Assuming symmetry around this particular axis causes no loss of generality, as both the incident wave and the spherical shell share this symmetry property (a simple orthogonal transformation restores the generality of axisymmetry about an arbitrary axis). In the spherical coordinate system, the pressure p and the displacement $\boldsymbol{u}$ are then independent of the azimuth angle φ in the fluid and solid domains, respectively. Moreover, the solid component in the azimuth angle direction is zero, $u_\varphi = 0$. This is a result of the axisymmetry of the problem.

3.2. Series representation using separation of variables

Using these assumptions Fender [15] shows that $\boldsymbol{\psi} = \psi_\varphi \boldsymbol{e}_\varphi$, such that when Eqs. (19) and (20) are expanded in terms of spherical coordinates, the following is obtained (using Eqs. (A.22) and (A.24))

$$\frac{\partial}{\partial r}\left(r^2 \frac{\partial \phi}{\partial r}\right) + \frac{1}{\sin\vartheta}\frac{\partial}{\partial \vartheta}\left(\sin\vartheta \frac{\partial \phi}{\partial \vartheta}\right) + (ar)^2 \phi = 0 \tag{22}$$

$$\frac{\partial}{\partial r}\left(r^2 \frac{\partial \psi_\varphi}{\partial r}\right) + \frac{1}{\sin\vartheta}\frac{\partial}{\partial \vartheta}\left(\sin\vartheta \frac{\partial \psi_\varphi}{\partial \vartheta}\right) + \left[(br)^2 - \frac{1}{\sin^2\vartheta}\right]\psi_\varphi = 0. \tag{23}$$

Using separation of variables, each of these equations can be reduced to a couple of spherical Bessel and Legendre equations, with the associate Legendre polynomials of zero and first order (described in Subsection C.1) and spherical Bessel functions (described in Subsection C.2) as solutions. More explicitly,

$$\phi(r,\vartheta) = \sum_{n=0}^{\infty} \mathrm{P}_n(\cos\vartheta)\Big[A_n^{(1)}\mathrm{j}_n(ar) + A_n^{(2)}\mathrm{y}_n(ar)\Big] \tag{24}$$

$$\psi_\varphi(r,\vartheta) = \sum_{n=0}^{\infty} \mathrm{P}_n^1(\cos\vartheta)\Big[B_n^{(1)}\mathrm{j}_n(br) + B_n^{(2)}\mathrm{y}_n(br)\Big] \tag{25}$$

where the coefficients $A_n^{(i)}, B_n^{(i)} \in \mathbb{C}$, $i = 1, 2$, are chosen such that the boundary conditions are satisfied.

By using Eq. (C.6) these functions and their partial derivatives will have their ϑ-dependency contained in functions of the form (the ones relevant for this work are listed in Eq. (C.8))

$$Q_n^{(j)}(\vartheta) = \frac{\mathrm{d}^j}{\mathrm{d}\vartheta^j}\mathrm{P}_n(\cos\vartheta). \tag{26}$$

That is, there is no need for the associated Legendre polynomials.

For ease of notation, the function $Z_n^{(i)}(\zeta)$, $i = 1, 2$, is introduced (as in [13, 14]), where

$$Z_n^{(1)}(\zeta) = \mathrm{j}_n(\zeta), \quad Z_n^{(2)}(\zeta) = \mathrm{y}_n(\zeta). \tag{27}$$

Moreover, the notation $\xi = \xi(r) = ar$ and $\eta = \eta(r) = br$ is used for convenience. Using the Einstein summation convention, Eqs. (24) and (25) may now be rewritten as

$$\phi(r, \vartheta) = \sum_{n=0}^{\infty} Q_n^{(0)}(\vartheta) A_n^{(i)} Z_n^{(i)}(\xi) \tag{28}$$

$$\psi_\varphi(r, \vartheta) = \sum_{n=0}^{\infty} Q_n^{(1)}(\vartheta) B_n^{(i)} Z_n^{(i)}(\eta). \tag{29}$$

3.3. Expressions for the displacement and stress field

By expanding Eq. (18) in spherical coordinates (using Eqs. (A.21) and (A.25)) yields

$$\boldsymbol{u} = \nabla\phi + \nabla \times \boldsymbol{\psi} = \frac{\partial\phi}{\partial r}\boldsymbol{e}_\mathrm{r} + \frac{1}{r}\frac{\partial\phi}{\partial\vartheta}\boldsymbol{e}_\vartheta + \frac{1}{r\sin\vartheta}\frac{\partial}{\partial\vartheta}(\psi_\varphi \sin\vartheta)\boldsymbol{e}_\mathrm{r} - \frac{1}{r}\frac{\partial}{\partial r}(r\psi_\varphi)\boldsymbol{e}_\vartheta \tag{30}$$

such that

$$u_\mathrm{r} = \frac{\partial\phi}{\partial r} + \frac{1}{r}\frac{\partial\psi_\varphi}{\partial\vartheta} + \frac{1}{r}\psi_\varphi \cot\vartheta \tag{31}$$

and

$$u_\vartheta = \frac{1}{r}\frac{\partial\phi}{\partial\vartheta} - \frac{\partial\psi_\varphi}{\partial r} - \frac{1}{r}\psi_\varphi. \tag{32}$$

Insertion of Eqs. (28) and (29) (using Eqs. (C.4), (C.6) and (C.27)) yields

$$u_\mathrm{r} = \frac{1}{r}\sum_{n=0}^{\infty} Q_n^{(0)}(\vartheta)\Big[A_n^{(i)} S_{1,n}^{(i)}(\xi) + B_n^{(i)} T_{1,n}^{(i)}(\eta)\Big] \tag{33}$$

and

$$u_\vartheta = \frac{1}{r}\sum_{n=0}^{\infty} Q_n^{(1)}(\vartheta)\Big[A_n^{(i)} S_{2,n}^{(i)}(\xi) + B_n^{(i)} T_{2,n}^{(i)}(\eta)\Big] \tag{34}$$

where

$$\begin{aligned}
S_{1,n}^{(i)}(\xi) &= \xi\frac{\mathrm{d}}{\mathrm{d}\xi}Z_n^{(i)}(\xi) = nZ_n^{(i)}(\xi) - \xi Z_{n+1}^{(i)}(\xi) \\
T_{1,n}^{(i)}(\eta) &= -n(n+1)Z_n^{(i)}(\eta) \\
S_{2,n}^{(i)}(\xi) &= Z_n^{(i)}(\xi) \\
T_{2,n}^{(i)}(\eta) &= -Z_n^{(i)}(\eta) - \eta\frac{\mathrm{d}}{\mathrm{d}\eta}Z_n^{(i)}(\eta) = -(n+1)Z_n^{(i)}(\eta) + \eta Z_{n+1}^{(i)}(\eta).
\end{aligned}$$

To compute the stresses defined in Appendix A, the partial derivatives of the displacement field in the spherical coordinate system are needed. These derivatives are found to be (using Eqs. (C.14), (C.26) and (C.27))

$$\frac{\partial u_{\mathrm{r}}}{\partial r} = \frac{1}{r^2}\sum_{n=0}^{\infty} Q_n^{(0)}(\vartheta)\Big[A_n^{(i)} S_{3,n}^{(i)}(\xi) + B_n^{(i)} T_{3,n}^{(i)}(\eta)\Big] \tag{35}$$

$$\frac{\partial u_{\vartheta}}{\partial r} = \frac{1}{r^2}\sum_{n=0}^{\infty} Q_n^{(1)}(\vartheta)\Big[A_n^{(i)} S_{4,n}^{(i)}(\xi) + B_n^{(i)} T_{4,n}^{(i)}(\eta)\Big] \tag{36}$$

$$\frac{\partial u_{\mathrm{r}}}{\partial \vartheta} = \frac{1}{r}\sum_{n=0}^{\infty} Q_n^{(1)}(\vartheta)\Big[A_n^{(i)} S_{1,n}^{(i)}(\xi) + B_n^{(i)} T_{1,n}^{(i)}(\eta)\Big] \tag{37}$$

$$\frac{\partial u_{\vartheta}}{\partial \vartheta} = \frac{1}{r}\sum_{n=0}^{\infty} Q_n^{(2)}(\vartheta)\Big[A_n^{(i)} S_{2,n}^{(i)}(\xi) + B_n^{(i)} T_{2,n}^{(i)}(\eta)\Big] \tag{38}$$

where

$$S_{3,n}^{(i)}(\xi) = \xi\frac{\mathrm{d}}{\mathrm{d}\xi}S_{1,n}^{(i)}(\xi) - S_{1,n}^{(i)}(\xi) = (n^2 - \xi^2 - n)Z_n^{(i)}(\xi) + 2\xi Z_{n+1}^{(i)}(\xi)$$

$$T_{3,n}^{(i)}(\eta) = \eta\frac{\mathrm{d}}{\mathrm{d}\eta}T_{1,n}^{(i)}(\eta) - T_{1,n}^{(i)}(\eta) = -n(n+1)\Big[(n-1)Z_n^{(i)}(\eta) - \eta Z_{n+1}^{(i)}(\eta)\Big]$$

$$S_{4,n}^{(i)}(\xi) = \xi\frac{\mathrm{d}}{\mathrm{d}\xi}Z_n^{(i)}(\xi) - Z_n^{(i)}(\xi) = (n-1)Z_n^{(i)}(\xi) - \xi Z_{n+1}^{(i)}(\xi)$$

$$T_{4,n}^{(i)}(\eta) = \eta\frac{\mathrm{d}}{\mathrm{d}\eta}T_{2,n}^{(i)}(\eta) - T_{2,n}^{(i)}(\eta) = (\eta^2 - n^2 + 1)Z_n^{(i)}(\eta) - \eta Z_{n+1}^{(i)}(\eta).$$

Using Eqs. (B.8) and (B.9), and the relation[3]

$$\frac{1}{2}\left(\frac{b}{a}\right)^2 = \frac{2}{3} + \frac{K}{2G} \tag{39}$$

the following formulas for the stress field components are obtained[4]

$$\sigma_{\mathrm{rr}} = \frac{2G}{r^2}\sum_{n=0}^{\infty} Q_n^{(0)}(\vartheta)\Big[A_n^{(i)} S_{5,n}^{(i)}(\xi) + B_n^{(i)} T_{5,n}^{(i)}(\eta)\Big] \tag{40}$$

$$\sigma_{\vartheta\varphi} = 0 \tag{41}$$

$$\sigma_{\mathrm{r}\varphi} = 0 \tag{42}$$

[3]This relation is obtained by inserting the definition of the angular wave numbers a and b (Eq. (21)) into the left-hand side.

[4]One can save some work by observing the similarities between $\sigma_{\vartheta\vartheta}$ and $\sigma_{\varphi\varphi}$

$$\sigma_{\vartheta\vartheta} = \frac{2}{r}\Big(K + \frac{G}{3}\Big)u_{\mathrm{r}} + \Big(K - \frac{2G}{3}\Big)\frac{\partial u_{\mathrm{r}}}{\partial r} + \frac{3K - 2G}{3r}\Big(u_{\vartheta}\cot\vartheta + \frac{\partial u_{\vartheta}}{\partial\vartheta}\Big) + \frac{2G}{r}\frac{\partial u_{\vartheta}}{\partial\vartheta}$$

$$\sigma_{\varphi\varphi} = \frac{2}{r}\Big(K + \frac{G}{3}\Big)u_{\mathrm{r}} + \Big(K - \frac{2G}{3}\Big)\frac{\partial u_{\mathrm{r}}}{\partial r} + \frac{3K - 2G}{3r}\Big(u_{\vartheta}\cot\vartheta + \frac{\partial u_{\vartheta}}{\partial\vartheta}\Big) + \frac{2G}{r}u_{\vartheta}\cot\vartheta.$$

$$\sigma_{\vartheta\vartheta} = \frac{2G}{r^2}\sum_{n=0}^{\infty}\Big\{Q_n^{(0)}(\vartheta)\Big[A_n^{(i)}S_{6,n}^{(i)}(\xi)+B_n^{(i)}T_{6,n}^{(i)}(\eta)\Big] +Q_n^{(2)}(\vartheta)\Big[A_n^{(i)}S_{2,n}^{(i)}(\xi)+B_n^{(i)}T_{2,n}^{(i)}(\eta)\Big]\Big\} \tag{43}$$

$$\sigma_{\varphi\varphi} = \frac{2G}{r^2}\sum_{n=0}^{\infty}\Big\{Q_n^{(0)}(\vartheta)\Big[A_n^{(i)}S_{6,n}^{(i)}(\xi)+B_n^{(i)}T_{6,n}^{(i)}(\eta)\Big] +Q_n^{(1)}(\vartheta)\cot(\vartheta)\Big[A_n^{(i)}S_{2,n}^{(i)}(\xi)+B_n^{(i)}T_{2,n}^{(i)}(\eta)\Big]\Big\} \tag{44}$$

$$\sigma_{\mathrm{r}\vartheta} = \frac{2G}{r^2}\sum_{n=0}^{\infty}Q_n^{(1)}(\vartheta)\Big[A_n^{(i)}S_{7,n}^{(i)}(\xi)+B_n^{(i)}T_{7,n}^{(i)}(\eta)\Big] \tag{45}$$

where

$$\begin{aligned}
S_{5,n}^{(i)}(\xi) &= \frac{1}{2G}\Big[\Big(K+\frac{4G}{3}\Big)S_{3,n}^{(i)}(\xi)-\Big(K-\frac{2G}{3}\Big)n(n+1)Z_n^{(i)}(\xi) \\
&\qquad +2\Big(K-\frac{2G}{3}\Big)S_{1,n}^{(i)}(\xi)\Big] \\
&= \Big[n^2-n-\frac{1}{2}\Big(\frac{b}{a}\Big)^2\xi^2\Big]Z_n^{(i)}(\xi)+2\xi Z_{n+1}^{(i)}(\xi) \\
T_{5,n}^{(i)}(\eta) &= \frac{1}{2G}\Big[\Big(K+\frac{4G}{3}\Big)T_{3,n}^{(i)}(\eta)-\Big(K-\frac{2G}{3}\Big)n(n+1)T_{2,n}^{(i)}(\eta) \\
&\qquad +2\Big(K-\frac{2G}{3}\Big)T_{1,n}^{(i)}(\eta)\Big] \\
&= -n(n+1)\Big[(n-1)Z_n^{(i)}(\eta)-\eta Z_{n+1}^{(i)}(\eta)\Big] \\
S_{6,n}^{(i)}(\xi) &= -\Big(\frac{K}{2G}-\frac{1}{3}\Big)n(n+1)S_{2,n}^{(i)}(\xi)+\Big(\frac{1}{3}+\frac{K}{G}\Big)S_{1,n}^{(i)}(\xi)+\Big(\frac{K}{2G}-\frac{1}{3}\Big)S_{3,n}^{(i)}(\xi) \\
&= \Big[n-\frac{1}{2}\Big(\frac{b}{a}\Big)^2\xi^2+\xi^2\Big]Z_n^{(i)}(\xi)-\xi Z_{n+1}^{(i)}(\xi) \\
T_{6,n}^{(i)}(\eta) &= -\Big(\frac{K}{2G}-\frac{1}{3}\Big)n(n+1)T_{2,n}^{(i)}(\eta)+\Big(\frac{1}{3}+\frac{K}{G}\Big)T_{1,n}^{(i)}(\eta)+\Big(\frac{K}{2G}-\frac{1}{3}\Big)T_{3,n}^{(i)}(\eta) \\
&= -n(n+1)Z_n^{(i)}(\eta) \\
S_{7,n}^{(i)}(\xi) &= \frac{1}{2}\Big[S_{1,n}^{(i)}(\xi)+S_{4,n}^{(i)}(\xi)-S_{2,n}^{(i)}(\xi)\Big] \\
&= (n-1)Z_n^{(i)}(\xi)-\xi Z_{n+1}^{(i)}(\xi) \\
T_{7,n}^{(i)}(\eta) &= \frac{1}{2}\Big[T_{1,n}^{(i)}(\eta)+T_{4,n}^{(i)}(\eta)-T_{2,n}^{(i)}(\eta)\Big] \\
&= -\Big(n^2-1-\frac{1}{2}\eta^2\Big)Z_n^{(i)}(\eta)-\eta Z_{n+1}^{(i)}(\xi).
\end{aligned} \tag{46}$$

3.4. Validation of the displacement and stress formulas

The correctness of the formulas may be controlled by considering Navier's equation (Eq. (10)) in spherical coordinates. The three components of Navier's equation in spherical coordinates are given in Eqs. (B.10) to (B.12), the last of which is automatically satisfied due to the symmetry assumptions. The first two equations simplify to

$$\frac{\partial \sigma_{\mathrm{rr}}}{\partial r} + \frac{1}{r}\frac{\partial \sigma_{\mathrm{r}\vartheta}}{\partial \vartheta} + \frac{1}{r}(2\sigma_{\mathrm{rr}} - \sigma_{\vartheta\vartheta} - \sigma_{\varphi\varphi} + \sigma_{\mathrm{r}\vartheta}\cot\vartheta) + \omega^2\rho_{\mathrm{s}}u_{\mathrm{r}} = 0 \tag{47}$$

and

$$\frac{\partial \sigma_{\mathrm{r}\vartheta}}{\partial r} + \frac{1}{r}\frac{\partial \sigma_{\vartheta\vartheta}}{\partial \vartheta} + \frac{1}{r}[(\sigma_{\vartheta\vartheta} - \sigma_{\varphi\varphi})\cot\vartheta + 3\sigma_{\mathrm{r}\vartheta}] + \omega^2\rho_{\mathrm{s}}u_{\vartheta} = 0. \tag{48}$$

Differentiation of the stress field components yields

$$\begin{aligned}
\frac{\partial \sigma_{\mathrm{rr}}}{\partial r} &= \frac{2G}{r^3}\sum_{n=0}^{\infty} Q_n^{(0)}(\vartheta)\Big[A_n^{(i)}S_{8,n}^{(i)}(\xi) + B_n^{(i)}T_{8,n}^{(i)}(\eta)\Big] \\
\frac{\partial \sigma_{\vartheta\vartheta}}{\partial \vartheta} &= \frac{2G}{r^2}\sum_{n=0}^{\infty}\Big\{Q_n^{(1)}(\vartheta)\Big[A_n^{(i)}S_{6,n}^{(i)}(\xi) + B_n^{(i)}T_{6,n}^{(i)}(\eta)\Big] \\
&\qquad + Q_n^{(3)}(\vartheta)\Big[A_n^{(i)}S_{2,n}^{(i)}(\xi) + B_n^{(i)}T_{2,n}^{(i)}(\eta)\Big]\Big\} \\
\frac{\partial \sigma_{\mathrm{r}\vartheta}}{\partial r} &= \frac{2G}{r^3}\sum_{n=0}^{\infty} Q_n^{(1)}(\vartheta)\Big[A_n^{(i)}S_{9,n}^{(i)}(\xi) + B_n^{(i)}T_{9,n}^{(i)}(\eta)\Big] \\
\frac{\partial \sigma_{\mathrm{r}\vartheta}}{\partial \vartheta} &= \frac{2G}{r^2}\sum_{n=0}^{\infty} Q_n^{(2)}(\vartheta)\Big[A_n^{(i)}S_{7,n}^{(i)}(\xi) + B_n^{(i)}T_{7,n}^{(i)}(\eta)\Big]
\end{aligned}$$

where

$$\begin{aligned}
S_{8,n}^{(i)}(\xi) &= -2S_{5,n}^{(i)}(\xi) + \xi\frac{\mathrm{d}}{\mathrm{d}\xi}S_{5,n}^{(i)}(\xi) \\
&= \left[n^3 - 3n^2 + 2n - \frac{n}{2}\left(\frac{b}{a}\right)^2\xi^2 + 2\xi^2\right]Z_n^{(i)}(\xi) \\
&\quad + \left[-n^2 - n - 6 + \frac{1}{2}\left(\frac{b}{a}\right)^2\xi^2\right]\xi Z_{n+1}^{(i)}(\xi) \\
T_{8,n}^{(i)}(\eta) &= -2T_{5,n}^{(i)}(\eta) + \eta\frac{\mathrm{d}}{\mathrm{d}\eta}T_{5,n}^{(i)}(\eta) \\
&= n(n+1)\Big[\Big(-n^2 + 3n - 2 + \eta^2\Big)Z_n^{(i)}(\eta) - 4\eta Z_{n+1}^{(i)}(\eta)\Big] \\
S_{9,n}^{(i)}(\xi) &= -2S_{7,n}^{(i)}(\xi) + \xi\frac{\mathrm{d}}{\mathrm{d}\xi}S_{7,n}^{(i)}(\xi) \\
&= \Big[n^2 - 3n + 2 - \xi^2\Big]Z_n^{(i)}(\xi) + 4\xi Z_{n+1}^{(i)}(\xi)
\end{aligned}$$

$$
\begin{aligned}
T_{9,n}^{(i)}(\eta) &= -2T_{7,n}^{(i)}(\eta) + \eta\frac{\mathrm{d}}{\mathrm{d}\eta}T_{7,n}^{(i)}(\eta) \\
&= \left(-n^3 + 2n^2 + n - 2 + \frac{n}{2}\eta^2 - \eta^2\right) Z_n^{(i)}(\eta) \\
&\quad + \left(n^2 + n + 2 - \frac{1}{2}\eta^2\right)\eta Z_{n+1}^{(i)}(\eta).
\end{aligned}
$$

Inserting these expressions (alongside the stress components in Eqs. (40) to (45)) into Eqs. (47) and (48) and using Eqs. (C.14) and (C.15), and observing that

$$
\begin{aligned}
\frac{\partial\sigma_{\vartheta\vartheta}}{\partial\vartheta} + (\sigma_{\vartheta\vartheta} - \sigma_{\varphi\varphi})\cot\vartheta = \frac{2G}{r^2}\sum_{n=0}^{\infty} Q_n^{(1)}(\vartheta)\Big\{ & A_n^{(i)} S_{6,n}^{(i)}(\xi) + B_n^{(i)} T_{6,n}^{(i)}(\eta) \\
& + \left(-n^2 - n + 1\right)\Big[A_n^{(i)} S_{2,n}^{(i)}(\xi) + B_n^{(i)} T_{2,n}^{(i)}(\eta)\Big]\Big\},
\end{aligned}
$$

the left-hand side of Eq. (47) and Eq. (48) are indeed equal to zero.

4. Establishing constraints from boundary conditions

As the solution is represented as an infinite sum, the coefficients $A_{m,n}^{(i)}$, $B_{m,n}^{(i)}$ and $C_{m,n}^{(i)}$ (coefficients from the fluid domains described below) must be computed for each n (see Figure 2). By enforcing the boundary conditions in Eqs. (14) and (15) at each surface, constraints are developed to establish expressions for these coefficients.

4.1. Notation for the solution in layered domains

For the m^{th} solid shell the displacement field from Eqs. (33) and (34) is written as

$$
\boldsymbol{u}_m = u_{\mathrm{r},m}\boldsymbol{e}_{\mathrm{r}} + u_{\vartheta,m}\boldsymbol{e}_{\vartheta} \tag{49}
$$

where

$$
u_{\mathrm{r},m}(r,\vartheta) = \sum_{n=0}^{\infty} Q_n^{(0)}(\vartheta) u_{\mathrm{r},m,n}(r) \tag{50}
$$

$$
u_{\vartheta,m}(r,\vartheta) = \sum_{n=0}^{\infty} Q_n^{(1)}(\vartheta) u_{\vartheta,m,n}(r) \tag{51}
$$

and

$$
u_{\mathrm{r},m,n}(r) = \frac{1}{r}\Big[A_{m,n}^{(i)} S_{1,n}^{(i)}(a_m r) + B_{m,n}^{(i)} T_{1,n}^{(i)}(b_m r)\Big] \tag{52}
$$

$$
u_{\vartheta,m,n}(r) = \frac{1}{r}\Big[A_{m,n}^{(i)} S_{2,n}^{(i)}(a_m r) + B_{m,n}^{(i)} T_{2,n}^{(i)}(b_m r)\Big]. \tag{53}
$$

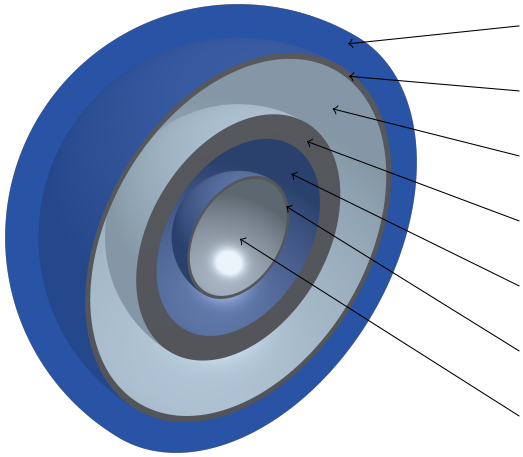

Figure 2: A model with $M = 3$ steel shells with different thicknesses (clip view), illustrating the distribution of the coefficients $A_{m,n}^{(i)}$, $B_{m,n}^{(i)}$ and $C_{m,n}^{(i)}$ over the different domains.

Corresponding expressions for the stress field in Eq. (46) are obtained as

$$\sigma_{\mathrm{rr},m}(r,\vartheta) = \sum_{n=0}^{\infty} Q_n^{(0)}(\vartheta)\sigma_{\mathrm{rr},m,n}(r) \tag{54}$$

$$\sigma_{\vartheta\vartheta,m}(r,\vartheta) = \sum_{n=0}^{\infty} Q_n^{(0)}(\vartheta)\sigma_{\vartheta\vartheta,m,n}^{(1)}(r) + Q_n^{(2)}(\vartheta)\sigma_{\vartheta\vartheta,m,n}^{(2)}(r) \tag{55}$$

$$\sigma_{\varphi\varphi,m}(r,\vartheta) = \sum_{n=0}^{\infty} Q_n^{(0)}(\vartheta)\sigma_{\varphi\varphi,m,n}^{(1)}(r) + Q_n^{(1)}(\vartheta)\cot(\vartheta)\sigma_{\varphi\varphi,m,n}^{(2)}(r) \tag{56}$$

$$\sigma_{\mathrm{r}\varphi,m}(r,\vartheta) = 0 \tag{57}$$

$$\sigma_{\vartheta\varphi,m}(r,\vartheta) = 0 \tag{58}$$

$$\sigma_{\mathrm{r}\vartheta,m}(r,\vartheta) = \sum_{n=0}^{\infty} Q_n^{(1)}(\vartheta)\sigma_{\mathrm{r}\vartheta,m,n}(r) \tag{59}$$

where

$$\sigma_{\mathrm{rr},m,n}(r) = \frac{2G_m}{r^2}\left[A_{m,n}^{(i)}S_{5,n}^{(i)}(a_m r) + B_{m,n}^{(i)}T_{5,n}^{(i)}(b_m r)\right]$$

$$\sigma_{\vartheta\vartheta,m,n}^{(1)}(r) = \frac{2G_m}{r^2}\left[A_{m,n}^{(i)}S_{6,n}^{(i)}(a_m r) + B_{m,n}^{(i)}T_{6,n}^{(i)}(b_m r)\right]$$

$$\sigma_{\vartheta\vartheta,m,n}^{(2)}(r) = \frac{2G_m}{r^2}\left[A_{m,n}^{(i)}S_{2,n}^{(i)}(a_m r) + B_{m,n}^{(i)}T_{2,n}^{(i)}(b_m r)\right]$$

$$\sigma^{(1)}_{\varphi\varphi,m,n}(r) = \frac{2G_m}{r^2}\Big[A^{(i)}_{m,n}S^{(i)}_{6,n}(a_m r) + B^{(i)}_{m,n}T^{(i)}_{6,n}(b_m r)\Big]$$
$$\sigma^{(2)}_{\varphi\varphi,m,n}(r) = \frac{2G_m}{r^2}\Big[A^{(i)}_{m,n}S^{(i)}_{2,n}(a_m r) + B^{(i)}_{m,n}T^{(i)}_{2,n}(b_m r)\Big]$$
$$\sigma_{\mathrm{r}\vartheta,m,n}(r) = \frac{2G_m}{r^2}\Big[A^{(i)}_{m,n}S^{(i)}_{7,n}(a_m r) + B^{(i)}_{m,n}T^{(i)}_{7,n}(b_m r)\Big].$$

The solution to the Helmholtz equation in the m^{th} fluid domain (for $2 \leqslant m \leqslant M$) has the same general form as ϕ in Eq. (28)

$$p_m(r,\vartheta) = \sum_{n=0}^{\infty} Q^{(0)}_n(\vartheta) C^{(i)}_{m,n} Z^{(i)}_n(k_m r) \tag{60}$$

where the coefficients $C^{(i)}_{m,n} \in \mathbb{C}$ are chosen such that the boundary conditions are satisfied. As the spherical Hankel functions of first and second kind (described in Subsection C.2) are linear combinations of the spherical Bessel functions of first and second kind, the general solution can be written in terms of these functions. For the outer (unbounded) fluid the Hankel function of the second kind is eliminated due to the Sommerfeld radiation condition in Eq. (11) [37, p. 26]. Thus, for the outermost fluid, the scattered pressure field is given by

$$p_1(r,\vartheta) = \sum_{n=0}^{\infty} Q^{(0)}_n(\vartheta) C^{(1)}_{1,n} \mathrm{h}^{(1)}_n(k_1 r). \tag{61}$$

Moreover, it is required that the pressure in the innermost fluid domain is bounded [15, p. 10]. Hence, the coefficients $C^{(2)}_{M+1,n}$ must be set to zero as the spherical Bessel function of second kind is unbounded at the origin. The pressure in the innermost fluid is therefore given by (cf. [15, p. 10])

$$p_{M+1}(r,\vartheta) = \sum_{n=0}^{\infty} Q^{(0)}_n(\vartheta) C^{(1)}_{M+1,n} \mathrm{j}_n(k_{M+1} r). \tag{62}$$

The total pressure in the m^{th} fluid domain shall be denoted by

$$p_{\mathrm{tot},m} = \begin{cases} p_1 + p_{\mathrm{inc}} & m = 1 \\ p_m & \text{otherwise} \end{cases} \tag{63}$$

where p_{inc} is the incident wave.

If the coefficients $A^{(i)}_{m,n}$, $B^{(i)}_{m,n}$ and $C^{(i)}_{m,n}$ can be determined, the solution is fully determined in all domains. Hence, a system of equations will be developed to find these coefficients. Indeed, at the boundaries (at a fixed radius) the series can all be written in terms of the Legendre functions $\mathrm{P}_n(\cos\vartheta)$, such that the resulting coefficients can be compared for each n. A term in the solution is often referred to

as a *mode*, such that the resulting constraints from the boundary conditions form a set of *modal equations*. The terminology comes from the vibration analysis [13], where each of these modes represent vibration modes. For example, $u_{\mathrm{r},m,n}$ is referred to be the radial displacement in the m^{th} solid domain in the n^{th} mode.

4.2. Tangential traction conditions

Eq. (17) is automatically fulfilled due to the axisymmetric assumption. For the m^{th} shell, evaluating Eq. (16) at both the inner and outer radius, yields two equations

$$\sigma_{\mathrm{r}\vartheta,m,n}(R_{j,m},\vartheta)=0,\quad j=0,1. \tag{64}$$

As $Q_0^{(1)}(\vartheta)=0$, these equations are automatically satisfied for $n=0$. In addition, since $T_{1,0}^{(i)}(\eta)=0$ and $T_{6,0}^{(i)}(\eta)=0$, the coefficients $B_{m,0}^{(i)}$ are redundant (which is convenient, as two constraints are lost in this case).

Denote by $\boldsymbol{H}_{m,n}^{(1)}$, $m=1,\ldots,M$, the eigenfrequency matrix[5] [13, p. 17] of the m^{th} shell

$$\boldsymbol{H}_{m,n}^{(1)}=\begin{bmatrix} S_{5,n}^{(1)}(a_mR_{0,m}) & S_{5,n}^{(2)}(a_mR_{0,m}) & T_{5,n}^{(1)}(b_mR_{0,m}) & T_{5,n}^{(2)}(b_mR_{0,m})\\ S_{7,n}^{(1)}(a_mR_{0,m}) & S_{7,n}^{(2)}(a_mR_{0,m}) & T_{7,n}^{(1)}(b_mR_{0,m}) & T_{7,n}^{(2)}(b_mR_{0,m})\\ S_{7,n}^{(1)}(a_mR_{1,m}) & S_{7,n}^{(2)}(a_mR_{1,m}) & T_{7,n}^{(1)}(b_mR_{1,m}) & T_{7,n}^{(2)}(b_mR_{1,m})\\ S_{5,n}^{(1)}(a_mR_{1,m}) & S_{5,n}^{(2)}(a_mR_{1,m}) & T_{5,n}^{(1)}(b_mR_{1,m}) & T_{5,n}^{(2)}(b_mR_{1,m}) \end{bmatrix}, \tag{65}$$

for $n>0$, and

$$\boldsymbol{H}_{m,0}^{(1)}=\begin{bmatrix} S_{5,0}^{(1)}(a_mR_{0,m}) & S_{5,0}^{(2)}(a_mR_{0,m})\\ S_{5,0}^{(1)}(a_mR_{1,m}) & S_{5,0}^{(2)}(a_mR_{1,m}) \end{bmatrix}, \tag{66}$$

for $n=0$. From Eqs. (54) and (59) one observes that the first and the last row of $\boldsymbol{H}_{m,n}^{(1)}$ correspond to $\sigma_{\mathrm{rr},m,n}(r)$ at $r=R_{0,m}$ and $r=R_{1,m}$, respectively, and the second and third row (for $n>0$) correspond to $\sigma_{\mathrm{r}\vartheta,m,n}(r)$ at $r=R_{0,m}$ and $r=R_{1,m}$, respectively. The notation $H_{ij,m,n}^{(1)}$, will be used for the elements of the matrices $\boldsymbol{H}_{m,n}^{(1)}$.

For $n>0$, the two conditions in Eq. (64) may be written as

$$H_{21,m,n}^{(1)}A_{m,n}^{(1)}+H_{22,m,n}^{(1)}A_{m,n}^{(2)}+H_{23,m,n}^{(1)}B_{m,n}^{(1)}+H_{24,n}^{(1)}B_{m,n}^{(2)}=0 \tag{67}$$

$$H_{31,m,n}^{(1)}A_{m,n}^{(1)}+H_{32,m,n}^{(1)}A_{m,n}^{(2)}+H_{33,m,n}^{(1)}B_{m,n}^{(1)}+H_{34,m,n}^{(1)}B_{m,n}^{(2)}=0. \tag{68}$$

This gives (for each n) $2M$ equations in terms of the $6M$ unknown coefficients $A_{m,n}^{(i)}$, $B_{m,n}^{(i)}$ and $C_{m,n}^{(i)}$, $i=1,2$. Thus, an additional $4M$ equations are needed to

[5] As illustrated in [13], the matrix $\boldsymbol{H}_{m,n}^{(1)}$ represent the modal characteristic equations of the m^{th} shell. That is, the eigenfrequencies of each shell can be found by solving $\det\boldsymbol{H}_{m,n}^{(1)}=0$ in terms of the frequency.

determine these coefficients. These equations come from the coupling conditions in Eqs. (14) and (15) (displacement condition and pressure condition, respectively) which are applied at the outer and inner radius of each shell. The outermost and innermost fluid domains will have to be considered separately.

4.3. Displacement and pressure condition in intermediate fluid layers

Consider the m^{th} fluid domain, with $2 \leqslant m \leqslant M$, where the pressure field is given by Eq. (60). Inserting Eqs. (50) and (60) into the displacement condition in Eq. (14) at $r = R_{1,m-1}, R_{0,m}$, yields

$$\frac{\rho_{\mathrm{f},m}\omega^2}{R_{j,m-j}}\Big[A^{(i)}_{m-j,n}S^{(i)}_{1,n}(a_{m-j}R_{j,m-j}) + B^{(i)}_{m-j,n}T^{(i)}_{1,n}(b_{m-j}R_{j,m-j})\Big] - k_m\Big[C^{(1)}_{m,n}\mathrm{j}'_n(k_mR_{j,m-j}) + C^{(2)}_{m,n}y'_n(k_mR_{j,m-j})\Big] = 0$$

which yield the relation

$$H^{(4,j)}_{1,m-j,n}A^{(1)}_{m-j,n} + H^{(4,j)}_{2,m-j,n}A^{(2)}_{m-j,n} + H^{(4,j)}_{3,m-j,n}B^{(1)}_{m-1,n} + H^{(4,j)}_{4,m-j,n}B^{(2)}_{m-1,n} + H^{(3,j)}_{i,m,n}C^{(i)}_{m,n} = 0, \quad (69)$$

for $j = 0, 1$, where

$$\begin{aligned} H^{(4,j)}_{1,m,n} &= S^{(1)}_{1,n}(a_mR_{j,m}), \quad H^{(4,j)}_{2,m,n} = S^{(2)}_{1,n}(a_mR_{j,m}),\\ H^{(4,j)}_{3,m,n} &= T^{(1)}_{1,n}(b_mR_{j,m}), \quad H^{(4,j)}_{4,m,n} = T^{(2)}_{1,n}(b_mR_{j,m}), \end{aligned} \quad (70)$$

and (using Eq. (C.27) to rewrite the derivative of the Bessel functions)

$$H^{(3,j)}_{i,m,n} = -\frac{1}{\rho_{\mathrm{f},m}\omega^2}\Big[nZ^{(i)}_n(\zeta) - \zeta Z^{(i)}_{n+1}(\zeta)\Big]\Big|_{\zeta=k_mR_{j,m-j}}. \quad (71)$$

Correspondingly, inserting Eqs. (54) and (62) into Eq. (15) at $r = R_{1,m-1}, R_{0,m}$ yields

$$\frac{2G_{m-j}}{R^2_{j,m-j}}\Big[A^{(i)}_{m-j,n}S^{(i)}_{5,n}(a_{m-j}R_{j,m-j}) + B^{(i)}_{m-j,n}T^{(i)}_{5,n}(b_{m-j}R_{j,m-j})\Big] + C^{(i)}_{m,n}Z^{(i)}_n(k_mR_{j,m-j}) = 0$$

which can be rewritten as

$$H^{(1)}_{11,m-j,n}A^{(1)}_{m-j,n} + H^{(1)}_{12,m-j,n}A^{(2)}_{m-j,n} + H^{(1)}_{13,m-j,n}B^{(1)}_{m-j,n} + H^{(1)}_{14,m-j,n}B^{(2)}_{m-j,n} + H^{(2,j)}_{i,m,n}C^{(i)}_{m,n} = 0 \quad (72)$$

where

$$H^{(2,j)}_{i,m,n} = \frac{R^2_{j,m-j}}{2G_{m-j}}Z^{(i)}_n(k_mR_{j,m-j}). \quad (73)$$

4.4. Displacement and pressure condition in the outermost fluid

It is assumed that the incident wave, $p_{\mathrm{inc}}(\boldsymbol{x},\omega)$, and its normal derivative at the outermost solid surface can be written on the form

$$\begin{aligned} p_{\mathrm{inc}}\Big|_{r=R_{0,1}} &= \sum_{n=0}^{\infty} F_n^{(1)} \mathrm{P}_n(\cos\vartheta), \\ \frac{\partial p_{\mathrm{inc}}}{\partial r}\Big|_{r=R_{0,1}} &= \sum_{n=0}^{\infty} F_n^{(2)} \mathrm{P}_n(\cos\vartheta), \end{aligned} \tag{74}$$

respectively. The coefficients $F_n^{(1)}$ and $F_n^{(2)}$ are discussed in Appendix D.

Inserting Eqs. (50) and (61) into the displacement condition in Eq. (14) yields

$$\frac{\rho_{\mathrm{f},1}\omega^2}{R_{0,1}}\Big[A_{n,1}^{(i)} S_{1,n}^{(i)}(a_1 R_{0,1}) + B_{n,1}^{(i)} T_{1,n}^{(i)}(b_1 R_{0,1})\Big] - k_1 C_{1,n}^{(1)} \frac{\mathrm{d}\mathrm{h}_n^{(1)}}{\mathrm{d}\zeta}\Big|_{\zeta=k_1 R_{0,1}} = F_n^{(2)},$$

which yields the relation

$$H_{1,1,n}^{(4,0)} C_{1,n}^{(1)} + H_{2,1,n}^{(4,0)} C_{1,n}^{(2)} + H_{3,1,n}^{(4,0)} C_{1,n}^{(3)} + H_{4,1,n}^{(4,0)} C_{1,n}^{(4)} + H_{1,1,n}^{(3,0)} C_{1,n}^{(1)} = D_{1,n}, \tag{75}$$

where $H_{i,1,n}^{(4,0)}$ for $i = 1,2,3,4$, are given by Eq. (70) and (using Eq. (C.34))

$$H_{1,1,n}^{(3,0)} = -\frac{1}{\rho_{\mathrm{f},1}\omega^2}\Big[n\mathrm{h}_n^{(1)}(\zeta) - \zeta \mathrm{h}_{n+1}^{(2)}(\zeta)\Big]\Big|_{\zeta=k_1 R_{0,1}} \tag{76}$$

and

$$D_{1,n} = \frac{R_{0,1}}{\rho_{\mathrm{f},1}\omega^2} F_n^{(2)}. \tag{77}$$

Correspondingly, by inserting Eqs. (54) and (61) into Eq. (15) one obtains

$$\begin{aligned} \frac{2G_1}{R_{0,1}^2}\Big[C_{n,1}^{(1)} S_{5,n}^{(1)}(a_1 R_{0,1}) + C_{n,1}^{(2)} T_{5,n}^{(1)}(b_1 R_{0,1}) + C_{n,1}^{(3)} S_{5,n}^{(2)}(a_1 R_{0,1}) + C_{n,1}^{(4)} T_{5,n}^{(2)}(b_1 R_{0,1})\Big] \\ + C_{1,n}^{(1)} \mathrm{h}_n^{(1)}(k_1 R_{0,1}) = -F_n^{(1)}, \end{aligned}$$

which yields the relation

$$H_{1,1,n}^{(1)} C_{1,n}^{(1)} + H_{2,1,n}^{(1)} C_{1,n}^{(2)} + H_{3,1,n}^{(1)} C_{1,n}^{(3)} + H_{4,1,n}^{(1)} C_{1,n}^{(4)} + H_{1,1,n}^{(2,0)} C_{1,n}^{(1)} = D_{2,n}, \tag{78}$$

where

$$H_{1,1,n}^{(2,0)} = \frac{R_{0,1}^2}{2G_1} \mathrm{h}_n^{(1)}(k_1 R_{0,1}) \tag{79}$$

and

$$D_{2,n} = -\frac{R_{0,1}^2}{2G_1} F_n^{(1)}. \tag{80}$$

4.5. Displacement and pressure condition in the innermost fluid

For the innermost fluid the pressure field is given by Eq. (62). Inserting Eqs. (50) and (62) into the displacement condition in Eq. (14) at $r = R_{1,M}$ yields

$$\frac{\rho_{\mathrm{f},M+1}\omega^2}{R_{1,M}}\left[A_{M,n}^{(i)}S_{1,n}^{(i)}(a_M R_{1,M}) + B_{M,n}^{(i)}T_{1,n}^{(i)}(b_M R_{1,M})\right] - k_{M+1}C_{M+1,n}^{(1)}\mathrm{j}_n'(k_{M+1}R_{1,M}) = 0,$$

which yields the relation

$$H_{1,M,n}^{(4,1)}A_{M,n}^{(1)} + H_{2,M,n}^{(4,1)}A_{M,n}^{(2)} + H_{3,M,n}^{(4,1)}B_{M,n}^{(1)} + H_{4,M,n}^{(4,1)}B_{M,n}^{(2)} + H_{1,M+1,n}^{(3,1)}C_{M+1,n}^{(1)} = 0, \tag{81}$$

where $H_{i,M,n}^{(4,1)}$ for $i = 1, 2, 3, 4$, are defined in Eq. (70), and

$$H_{1,M+1,n}^{(3,1)} = -\frac{1}{\rho_{\mathrm{f},M+1}\omega^2}[n\mathrm{j}_n(\zeta) - \zeta\mathrm{j}_{n+1}(\zeta)]\Big|_{\zeta=k_{M+1}R_{1,M}}. \tag{82}$$

Correspondingly, by inserting Eqs. (54) and (62) into Eq. (15) at $r = R_{1,M}$ the following is obtained

$$\frac{2G_M}{R_{1,M}^2}\left[A_{M,n}^{(i)}S_{5,n}^{(i)}(a_M R_{1,M}) + B_{M,n}^{(i)}T_{5,n}^{(i)}(b_M R_{1,M})\right] + C_{M+1,n}^{(1)}\mathrm{j}_n(k_{M+1}R_{1,M}) = 0,$$

which yields the relation

$$H_{11,M,n}^{(1)}A_{M,n}^{(1)} + H_{12,M,n}^{(1)}A_{M,n}^{(2)} + H_{13,M,n}^{(1)}B_{M,n}^{(1)} + H_{14,M,n}^{(1)}B_{M,n}^{(2)} + H_{1,M+1,n}^{(2,1)}C_{M+1,n}^{(1)} = 0, \tag{83}$$

where

$$H_{1,M+1,n}^{(2,1)} = \frac{R_{1,M}^2}{2G_M}\mathrm{j}_n(k_{M+1}R_{1,M}). \tag{84}$$

5. Assembling the linear system of equations

In the previous section, $6M$ equations for the $6M$ unknowns $A_{m,n}^{(i)}$, $B_{m,n}^{(i)}$ and $C_{m,n}^{(i)}$ for all $n > 0$ and $4M$ equations for the $4M$ unknowns for $n = 0$ was established. So far, the solution has been presented for M elastic spherical shells with standard displacement and pressure conditions; *the default case with Neumann-to-Neumann conditions*. By some matrix manipulations of the global matrix, one can implement other cases as well, including solid spheres, and single Neumann conditions replacing the Neumann-to-Neumann conditions on the innermost domain.

5.1. The default case with Neumann-to-Neumann conditions

For the default case all equations can be collected into one single linear system of equations

$$\boldsymbol{H}_n \boldsymbol{C}_n = \boldsymbol{D}_n \tag{85}$$

where[6]

$$\boldsymbol{H}_n = \begin{bmatrix}
H_{1,1,n}^{(3,0)} & \boldsymbol{H}_{1,n}^{(4,0)} & & & & & \\
H_{1,1,n}^{(2,0)} & & & & & & \\
 & \boldsymbol{H}_{1,n}^{(1)} & & & & & \\
 & & \boldsymbol{H}_{2,n}^{(2,1)} & & & & \\
 & \boldsymbol{H}_{1,n}^{(4,1)} & \boldsymbol{H}_{2,n}^{(3,1)} & & & & \\
 & & \boldsymbol{H}_{2,n}^{(3,0)} & \boldsymbol{H}_{2,n}^{(4,0)} & & & \\
 & & \boldsymbol{H}_{2,n}^{(2,0)} & & & & \\
 & & & \ddots & & & \\
 & & & & \boldsymbol{H}_{M,n}^{(2,1)} & & \\
 & & & \boldsymbol{H}_{M-1,n}^{(4,1)} & \boldsymbol{H}_{M,n}^{(3,1)} & & \\
 & & & & \boldsymbol{H}_{M,n}^{(3,0)} & \boldsymbol{H}_{M,n}^{(4,0)} & \\
 & & & & \boldsymbol{H}_{M,n}^{(2,0)} & & \\
 & & & & & \boldsymbol{H}_{M,n}^{(1)} & \\
 & & & & & & H_{1,M+1,n}^{(2,1)} \\
 & & & & & \boldsymbol{H}_{M,n}^{(4,1)} & H_{1,M+1,n}^{(3,1)}
\end{bmatrix}$$

with submatrices $\boldsymbol{H}_{m,n}^{(1)}$ has entries given in Eq. (65) and Eq. (66). The submatrices

$$\boldsymbol{H}_{m,n}^{(2,j)} = \begin{bmatrix} H_{1,m,n}^{(2,j)} & H_{2,m,n}^{(2,j)} \end{bmatrix}$$

has entries given in Eq. (73). The submatrices

$$\boldsymbol{H}_{m,n}^{(3,j)} = \begin{bmatrix} H_{1,m,n}^{(3,j)} & H_{2,m,n}^{(3,j)} \end{bmatrix}$$

has entries given in Eq. (71). The submatrices

$$\boldsymbol{H}_{m,n}^{(4,j)} = \begin{bmatrix} H_{1,m,n}^{(4,j)} & H_{2,m,n}^{(4,j)} & H_{3,m,n}^{(4,j)} & H_{4,m,n}^{(4,j)} \end{bmatrix}$$

[6]Note that the matrix pattern is scaled for the case $n > 0$, as $\boldsymbol{H}_{m,n}^{(1)} \in \mathbb{R}^{4\times 4}$ and $\boldsymbol{H}_{m,n}^{(4,j)} \in \mathbb{R}^{1\times 4}$ for $n > 0$, as opposed to $\boldsymbol{H}_{m,n}^{(1)} \in \mathbb{R}^{2\times 2}$ and $\boldsymbol{H}_{m,n}^{(4,j)} \in \mathbb{R}^{1\times 2}$ when $n = 0$ (for $j = 1, 2$).

for $n > 0$, and

$$\boldsymbol{H}_{m,n}^{(4,j)} = \begin{bmatrix} H_{1,m,n}^{(4,j)} & H_{2,m,n}^{(4,j)} \end{bmatrix}$$

for $n = 0$, has entries given in Eq. (70). The entries $H_{1,1,n}^{(3,0)}$, $H_{1,1,n}^{(2,0)}$, $H_{1,M+1,n}^{(3,1)}$ and $H_{1,M+1,n}^{(2,1)}$, are given in Eqs. (76), (79), (82) and (84), respectively.

Finally, the column vectors in Eq. (85) are given by

$$\boldsymbol{C}_n = \begin{bmatrix} C_{1,n}^{(1)} \\ \boldsymbol{A}_{1,n} \\ \boldsymbol{B}_{1,n} \\ \boldsymbol{C}_{2,n} \\ \vdots \\ \boldsymbol{A}_{M-1,n} \\ \boldsymbol{B}_{M-1,n} \\ \boldsymbol{C}_{M,n} \\ \boldsymbol{A}_{M,n} \\ \boldsymbol{B}_{M,n} \\ C_{M+1,n}^{(1)} \end{bmatrix} \quad \boldsymbol{A}_{m,n} = \begin{bmatrix} A_{m,n}^{(1)} \\ A_{m,n}^{(2)} \end{bmatrix} \quad \boldsymbol{B}_{m,n} = \begin{bmatrix} B_{m,n}^{(1)} \\ B_{m,n}^{(2)} \end{bmatrix} \quad \boldsymbol{C}_{m,n} = \begin{bmatrix} C_{m,n}^{(1)} \\ C_{m,n}^{(2)} \end{bmatrix} \quad \boldsymbol{D}_n = \begin{bmatrix} D_{1,n} \\ D_{2,n} \\ 0 \\ 0 \\ \vdots \\ 0 \end{bmatrix}.$$

where the entries $D_{1,n}$ and $D_{2,n}$, are given in Eqs. (77) and (80), respectively.

5.2. Alternative boundary conditions

By removing the last five (three) rows and columns of $\boldsymbol{H}_n$ for $n > 0$ ($n = 0$), the Neumann-to-Neumann boundary condition (NNBC) is replaced by a single Neumann condition[7]

$$\frac{\partial p_{\mathrm{tot},M}}{\partial r} = 0 \tag{86}$$

at the innermost solid domain. This Neumann boundary condition may be replaced by other boundary conditions, for example the Robin boundary condition (impedance boundary condition) by corresponding manipulation of the matrix $\boldsymbol{H}_n$. By removing the last row and column of the matrix $\boldsymbol{H}_n$ a Neumann condition ($\sigma_{\mathrm{rr}} = 0$) is obtained on the inside of the innermost shell[8]. Moreover, one can model scattering on solid spheres[9] (such that the innermost domain is no longer fluid, but solid) by removing the three last rows (corresponding to the boundary conditions at $R_{1,M}$) and three columns (corresponding to the coefficients $A_{M,n}^{(2)}$, $B_{M,n}^{(2)}$ and $C_{M+1,n}^{(1)}$) of the matrix $\boldsymbol{H}_n$ (and corresponding entries of $\boldsymbol{C}_n$ and $\boldsymbol{D}_n$). The reason for not using the coefficients $A_{M,n}^{(2)}$ and $B_{M,n}^{(2)}$ is that the corresponding

[7] That is, the normal velocity component of the fluid at the surface is zero, such that $u_{\mathrm{r}} = 0$ in Eq. (14). This is often referred to as a sound-hard boundary condition, SHBC.

[8] This is often referred to as a sound-soft boundary condition, SSBC.

[9] This type of boundary conditions is named elastic sphere boundary conditions, ESBC.

spherical Bessel functions of second kind are unbounded at the origin, such that these coefficients must be set to zero. The displacement of the inner solid sphere is then given by

$$\boldsymbol{u}_M = u_{\mathrm{r},M}\boldsymbol{e}_{\mathrm{r}} + u_{\vartheta,M}\boldsymbol{e}_{\vartheta} \tag{87}$$

where

$$u_{\mathrm{r},M}(r,\vartheta) = \frac{1}{r}\sum_{n=0}^{\infty} Q_n^{(0)}(\vartheta)\Big[A_{M,n}^{(1)} S_{1,n}^{(1)}(a_M r) + B_{M,n}^{(1)} T_{1,n}^{(1)}(b_M r)\Big] \tag{88}$$

$$u_{\vartheta,M}(r,\vartheta) = \frac{1}{r}\sum_{n=0}^{\infty} Q_n^{(1)}(\vartheta)\Big[A_{M,n}^{(1)} S_{2,n}^{(1)}(a_M r) + B_{M,n}^{(1)} T_{2,n}^{(1)}(b_M r)\Big]. \tag{89}$$

It should be noted that the solution is well defined also at the origin due to the formulas in Eqs. (C.24) and (C.25). In fact, on can show that (using Eq. (A.19))

$$\lim_{r\to 0}\boldsymbol{u}_M(r,\vartheta) = \frac{1}{3}\Big[a_M A_{M,1}^{(1)} - 2b_M B_{M,1}^{(1)}\Big]\boldsymbol{e}_3,$$

and (using Eq. (A.20))

$$\begin{aligned}
\lim_{r\to 0}\frac{\partial u_{1,M}}{\partial x_1}(r,\vartheta) &= \frac{G_M}{9K_M}\Big(4a_M^2 - 3b_M^2\Big)A_{M,0}^{(1)} - \frac{1}{15}\Big(a_M^2 A_{M,2}^{(1)} - 3b_M^2 B_{M,2}^{(1)}\Big)\\
\lim_{r\to 0}\frac{\partial u_{2,M}}{\partial x_2}(r,\vartheta) &= \frac{G_M}{9K_M}\Big(4a_M^2 - 3b_M^2\Big)A_{M,0}^{(1)} - \frac{1}{15}\Big(a_M^2 A_{M,2}^{(1)} - 3b_M^2 B_{M,2}^{(1)}\Big)\\
\lim_{r\to 0}\frac{\partial u_{3,M}}{\partial x_3}(r,\vartheta) &= \frac{G_M}{9K_M}\Big(4a_M^2 - 3b_M^2\Big)A_{M,0}^{(1)} + \frac{2}{15}\Big(a_M^2 A_{M,2}^{(1)} - 3b_M^2 B_{M,2}^{(1)}\Big)\\
\lim_{r\to 0}\frac{\partial u_{i,M}}{\partial x_j}(r,\vartheta) &= 0 \quad \text{for} \quad i \neq j
\end{aligned}$$

where $u_{i,M}$ is the i^{th} Cartesian component of $\boldsymbol{u}$. The stress field can then be computed in the origin as (using Eq. (B.7))

$$\begin{aligned}
\lim_{r\to 0}\sigma_{11,M}(r,\vartheta) &= \frac{G_M}{15}\Big[5\Big(4a_M^2 - 3b_M^2\Big)A_{M,0}^{(1)} - 2a_M^2 A_{M,2}^{(1)} + 6b_M^2 B_{M,2}^{(1)}\Big]\\
\lim_{r\to 0}\sigma_{22,M}(r,\vartheta) &= \frac{G_M}{15}\Big[5\Big(4a_M^2 - 3b_M^2\Big)A_{M,0}^{(1)} - 2a_M^2 A_{M,2}^{(1)} + 6b_M^2 B_{M,2}^{(1)}\Big]\\
\lim_{r\to 0}\sigma_{33,M}(r,\vartheta) &= \frac{G_M}{15}\Big[5\Big(4a_M^2 - 3b_M^2\Big)A_{M,0}^{(1)} + 4a_M^2 A_{M,2}^{(1)} - 12b_M^2 B_{M,2}^{(1)}\Big]\\
\lim_{r\to 0}\sigma_{23,M}(r,\vartheta) &= 0\\
\lim_{r\to 0}\sigma_{13,M}(r,\vartheta) &= 0\\
\lim_{r\to 0}\sigma_{12,M}(r,\vartheta) &= 0
\end{aligned}$$

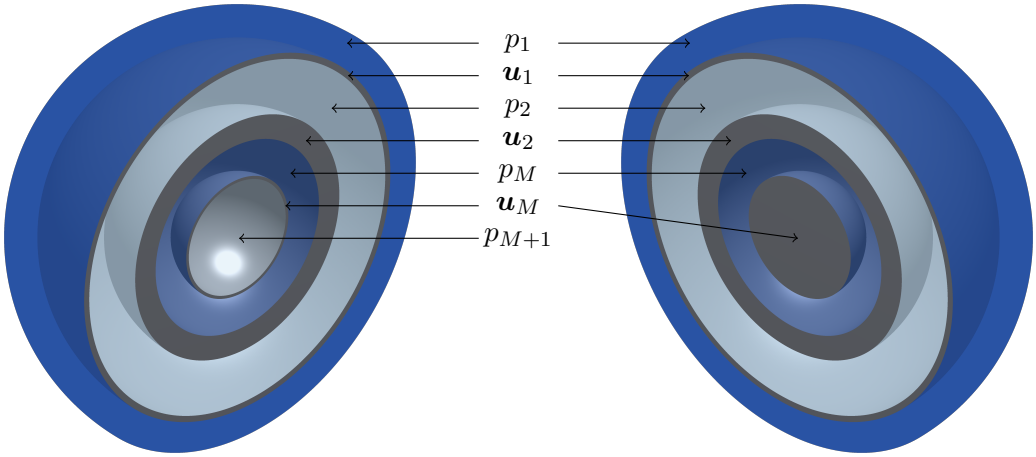

Figure 3: Illustration (clip view) of a model (to the left) with 3 steel shells and a model (to the right) with 2 steel shells surrounding a solid steel sphere, illustrating the distribution of functions (in the case $M = 3$). The model to the left models a fluid as the innermost domain, while the model to the right models a solid domain as the innermost domain (note that the expression $\boldsymbol{u}_M$ is slightly altered in this case).

where $\sigma_{ij,M}$ is the stress field in the solid sphere in Cartesian coordinates. If the innermost domain is a fluid, then

$$\lim_{r\to 0} p_{M+1}(r,\vartheta) = C^{(1)}_{M+1,0}$$
$$\lim_{r\to 0} \nabla p_{M+1}(r,\vartheta) = \frac{k_{M+1}}{3} C^{(1)}_{M+1,1}\boldsymbol{e}_3$$
$$\lim_{r\to 0} \nabla^2 p_{M+1}(r,\vartheta) = -k^2_{M+1} C^{(1)}_{M+1,0}.$$

Finally, note that one can model connected fluid or solid layers by manipulating the the matrix $\boldsymbol{H}_n$ to match the pressure and displacement condition between these domains. An example of such an application is air bubbles in water [15].

5.3. Summary of solution formulas

In this sub section, the final expressions have been summarized (see Figure 3). Recall that $\mathrm{h}^{(i)}_n$, $Z^{(i)}_{j,n}$, $S^{(i)}_{j,n}$ and $T^{(i)}_{j,n}$ are all derived from spherical Bessel functions (j_n and y_n), while $Q^{(i)}_n$ are derived from Legendre functions. All coefficients ($A^{(i)}_{m,n}$, $B^{(i)}_{m,n}$ and $C^{(i)}_{m,n}$) are found by solving the linear system of equations in Eq. (85). The scattered pressure field in the outermost (unbounded) fluid domain, the m^{th} fluid layer (for $2 \leqslant m \leqslant M$), and the innermost fluid domain (if present), are given

by

$$p_1(r,\vartheta) = \sum_{n=0}^{\infty} Q_n^{(0)}(\vartheta) C_{1,n}^{(1)} \mathrm{h}_n^{(1)}(k_1 r) \tag{90}$$

$$p_m(r,\vartheta) = \sum_{n=0}^{\infty} Q_n^{(0)}(\vartheta) C_{m,n}^{(i)} Z_n^{(i)}(k_m r) \tag{91}$$

$$p_{M+1}(r,\vartheta) = \sum_{n=0}^{\infty} Q_n^{(0)}(\vartheta) C_{M+1,n}^{(1)} \mathrm{j}_n(k_{M+1} r), \tag{92}$$

respectively. The displacement field in the m^{th} solid domain is given by

$$\boldsymbol{u}_m = u_{\mathrm{r},m} \boldsymbol{e}_{\mathrm{r}} + u_{\vartheta,m} \boldsymbol{e}_{\vartheta} \tag{93}$$

where

$$u_{\mathrm{r},m}(r,\vartheta) = \frac{1}{r} \sum_{n=0}^{\infty} Q_n^{(0)}(\vartheta) \Big[A_{m,n}^{(i)} S_{1,n}^{(i)}(a_m r) + B_{m,n}^{(i)} T_{1,n}^{(i)}(b_m r) \Big] \tag{94}$$

$$u_{\vartheta,m}(r,\vartheta) = \frac{1}{r} \sum_{n=0}^{\infty} Q_n^{(1)}(\vartheta) \Big[A_{m,n}^{(i)} S_{2,n}^{(i)}(a_m r) + B_{m,n}^{(i)} T_{2,n}^{(i)}(b_m r) \Big]. \tag{95}$$

If the inner domain is a solid domain, the terms involving $S_{1,n}^{(2)}$ and $T_{1,n}^{(2)}$ in $\boldsymbol{u}_M$, are not present.

6. Computational aspects

Several computational issues arise when implementing the exact solution (which has been implemented in MATLAB). The source code can be downloaded from GitHub at https://github.com/Zetison/e3Dss. In this section, a discussion of some of these issues will be presented.

6.1. Matrix manipulations

Note that the only complex valued matrix entries of $\boldsymbol{H}_n$ are the first two entries in the first column. So instead of using a complex matrix solution routine to solve the system, one can exploit this fact to solving a real valued linear system of equations with two right hand sides. Refer to Fender [15, pp. 18-20] for details. Moreover, Fender shows that some further matrix manipulation may reduce the overall computational time by 30% (when doing a frequency sweep). By using the same ideas, the size of $\boldsymbol{H}_n$ can be reduced from $6M$ to $4M$.

Note that for $n > 0$, column number $2l$, $l = 1, 2, \ldots, 3M$, of $\boldsymbol{H}_n$ contains entries which are linear combinations of j_n and j_{n+1} (and no spherical Bessel functions

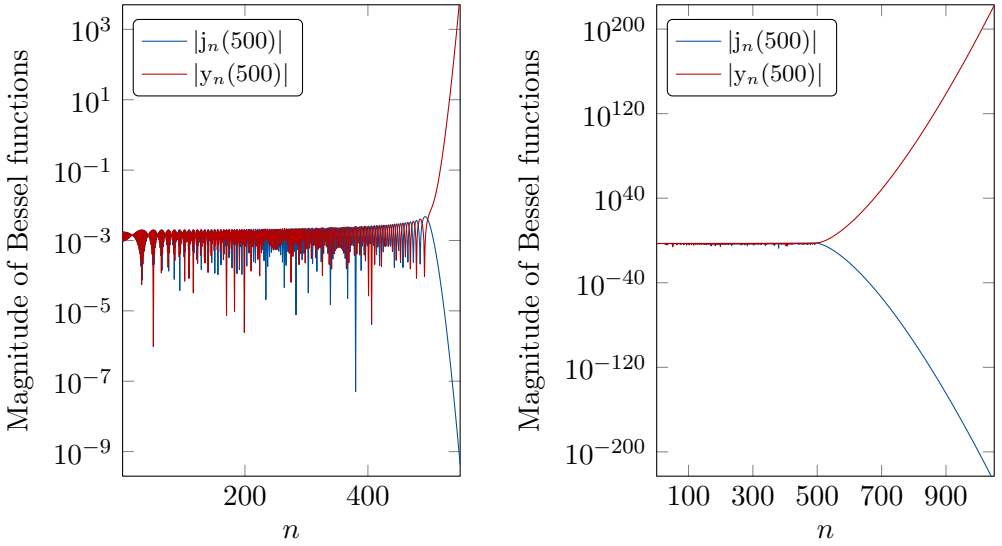

(a) Magnitude of Bessel functions plotted for $n \in [0, 550]$.

(b) Magnitude of Bessel functions plotted for $n \in [0, 1050]$.

Figure 4: Illustration of the asymptotic behavior, of the spherical Bessel functions of first ($\mathrm{j}_n(x)$) and second ($\mathrm{y}_n(x)$) kind, as a function of n, for a fixed argument $x = 500$.

of second kind), while column number $2l - 1$, $l = 1, 2, \ldots, 3M$, of $\boldsymbol{H}_n$ contains entries which are linear combinations of y_n and y_{n+1}. So since

$$\lim_{n\to\infty} |\mathrm{j}_n(\zeta)| = 0 \quad \text{and} \quad \lim_{n\to\infty} |\mathrm{y}_n(\zeta)| = \infty, \tag{96}$$

(which is illustrated in Figure 4) the matrix $\boldsymbol{H}_n$ becomes poorly scaled for large n. This issue can be solved by scaling the matrix with a (diagonal) preconditioning matrix $\boldsymbol{P}_n$ where the diagonal entries are given by the maximal modulus of the corresponding column vectors of $\boldsymbol{H}_n$. Defining the vector $\tilde{\boldsymbol{C}}_n = \boldsymbol{P}_n \boldsymbol{C}_n$ and solving the system $\tilde{\boldsymbol{H}}_n \tilde{\boldsymbol{C}}_n = \boldsymbol{D}_n$ with $\tilde{\boldsymbol{H}}_n = \boldsymbol{H}_n \boldsymbol{P}_n^{-1}$, the solution is obtained by $\boldsymbol{C}_n = \boldsymbol{P}_n^{-1} \tilde{\boldsymbol{C}}_n$. In Figures 5a and 5b the magnitude of the entries in $\boldsymbol{H}_n$ is visualized before and after preconditioning, respectively. This example is the matrix $\boldsymbol{H}_{300}$ of the S135 benchmark problem (described in Subsection 7.4) at $f = 30\,\mathrm{kHz}$. The condition number was improved from $\mathrm{cond}(\boldsymbol{H}_{300}) \approx 7.4 \cdot 10^{278}$ to $\mathrm{cond}(\tilde{\boldsymbol{H}}_{300}) \approx 9.4 \cdot 10^{4}$.

6.2. Series evaluation

As the series involves summation over infinitely many terms, the series needs to be truncated at some number $n = N_\varepsilon$. Denote by $p_1^{(N)}$, the truncated sum for the

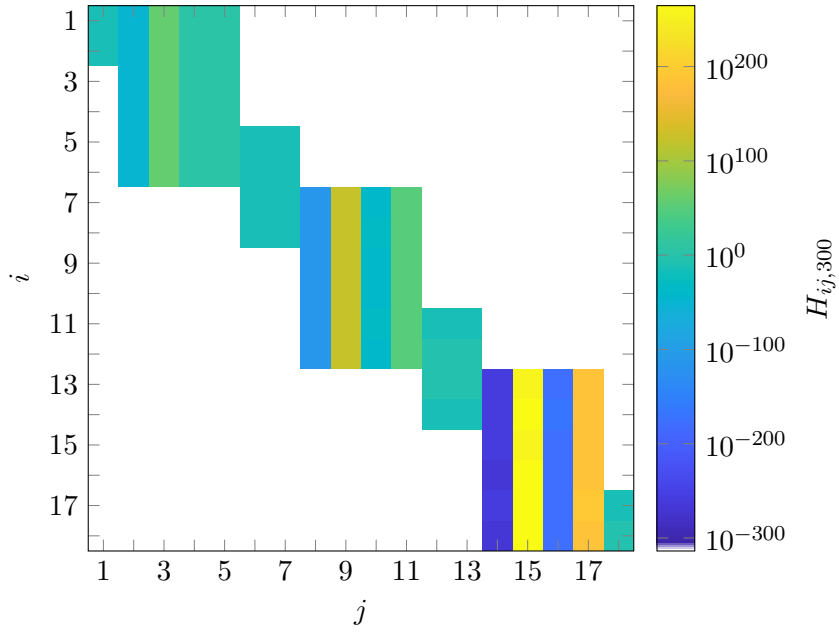

(a) Before preconditioning.

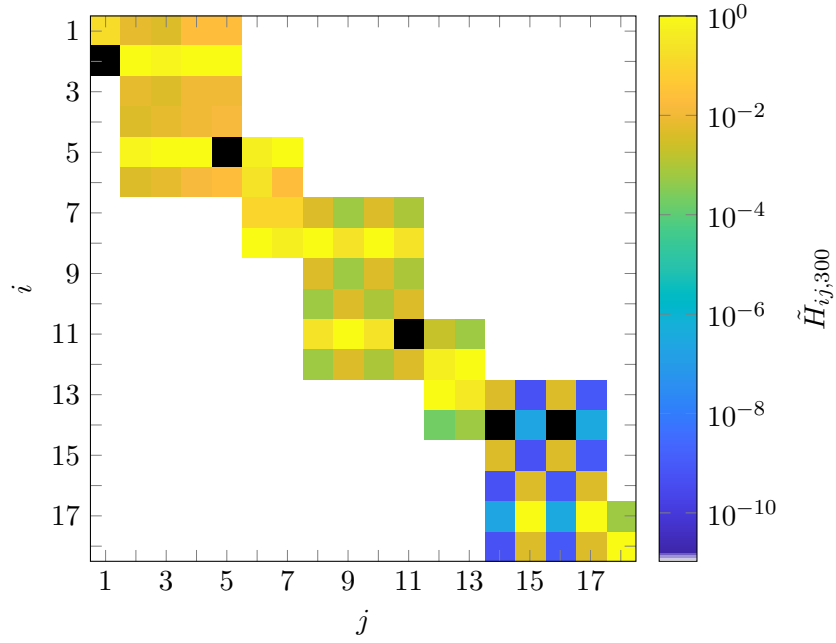

(b) After preconditioning.

Figure 5: **Matrix manipulations**: Plot of the magnitude of the matrix entries of $\boldsymbol{H}_{300}$ and $\tilde{\boldsymbol{H}}_{300}$.

scattered pressure in the outer domain (Eq. (91)),

$$p_1^{(N)}(r,\vartheta) = \sum_{n=0}^{N} Q_n^{(0)}(\vartheta) C_{1,n}^{(1)} \mathrm{h}_n^{(1)}(k_1 r), \tag{97}$$

and correspondingly for the other fields in Eqs. (91) to (93). In [37, pp. 32-35], Ihlenburg discusses such a value based on the decay of Bessel functions, in which he suggests using $N \approx 2kr$. In this work, however, the summation is terminated whenever the magnitude of term $n = N_\varepsilon$ divided by the magnitude of the partial sum (based on the first $N_\varepsilon + 1$ terms) is less than some prescribed tolerance ε. Typically machine epsilon is used for this number, i.e. $\varepsilon \approx 2.220446 \cdot 10^{-16}$. As with the suggestion of Ihlenburg, the number of terms, N_ε, grows linearly with the frequency. The computational complexity of the problem is thus $\mathcal{O}(\omega)$.

The solution is often needed at several points, or frequencies (or a combination of both). In this case, one should compute the solutions at all points at once, such that the calls to the implemented Bessel functions are minimized.

6.3. Round-off errors

Although the products $A_{m,n}^{(2)} S_{j,n}^{(2)}(\zeta)$, $B_{m,n}^{(2)} T_{j,n}^{(2)}(\zeta)$ and $C_{m,n}^{(2)} Z_n^{(2)}(\eta)$ all goes to zero as $n \to \infty$, the functions $S_{j,n}^{(2)}(a_m r)$, $T_{j,n}^{(2)}(\zeta)$ and $Z_n^{(2)}(\eta)$ does not. In fact, these functions become unbounded when $n \to \infty$ because they are all superposition of Bessel functions of second kind with this property. So, since the floating point number has an upper bound[10], there is a limit to the number of terms that can be used.

A naive solution to this problem is to try higher precision, which can easily be done with MATLAB symbolic class. This, however, increases the computational time drastically.

In Figure 6 several round-off phenomena which typically arises are illustrated. The specific example used here is the S135 benchmark problem with SSBC (described in Subsection 7.4). The incident wave, p_{inc}, is a plane wave traveling in the direction given by $\vartheta = 60°$ and $\varphi = 240°$ (see Section 7). An uniform (relative to the spherical coordinate system) set of sample points are distributed in all domains[11] where the residual error in the Helmholtz equation (Eq. (9)), the 1st and 2nd component of Navier's equation in spherical coordinates (Eqs. (47) and (48), respectively), the displacement condition (Eq. (14)) and the pressure condition (Eq. (15)), is measured. By using the infinity norm, $\|\cdot\|_\infty$, for each residual, and dividing by the magnitude of the terms involved, the relative residual error is

[10] For double precision this is typically $V_{\max} \approx 1.797693134862316 \cdot 10^{308}$.

[11] It is placed 32 points in each domain except for the inner domain with 25 points. The distribution of point in the radial direction in the exterior domain is limited to the interval $[R_{0,1}, 2R_{0,1}]$.

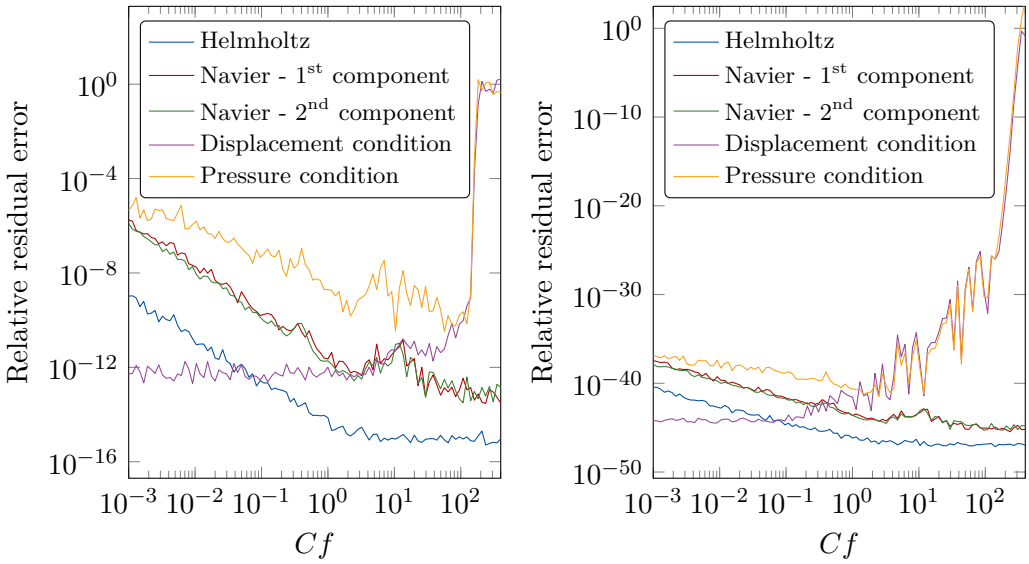

(a) Double precision, $\varepsilon \approx 10^{-16}$

(b) Symbolic precision $\varepsilon \approx 10^{-40}$

Figure 6: **Round-off errors**: Residual errors for the governing equations and boundary conditions. The use of symbolic precision in MATLAB illustrate that the errors are due to round-off errors. The relative residual formulas for the Helmholtz equation, the first and second components of the Navier equation, the displacement condition and the pressure conditions are given by Eqs. (98) to (102), respectively.

obtained. The maximal relative residual in all domains can then be calculated. In particular, these relative residual errors are given by

$$\max_{1\leqslant m\leqslant M+1} \frac{\left\|(\nabla^2 + k_m^2)p_m\right\|_\infty}{\left\|k_m^2 p_m\right\|_\infty} \tag{98}$$

$$\max_{1\leqslant m\leqslant M} \frac{\left\|\frac{\partial \sigma_{\mathrm{rr},m}}{\partial r} + \frac{1}{r}\frac{\partial \sigma_{\mathrm{r}\vartheta,m}}{\partial \vartheta} + \frac{1}{r}(2\sigma_{\mathrm{rr},m} - \sigma_{\vartheta\vartheta,m} - \sigma_{\varphi\varphi,m} + \sigma_{\mathrm{r}\vartheta,m}\cot\vartheta) + \omega^2\rho_{\mathrm{s},m}u_{\mathrm{r},m}\right\|_\infty}{\left\|\omega^2\rho_{\mathrm{s},m}u_{\mathrm{r},m}\right\|_\infty} \tag{99}$$

$$\max_{1\leqslant m\leqslant M} \frac{\left\|\frac{\partial \sigma_{\mathrm{r}\vartheta,m}}{\partial r} + \frac{1}{r}\frac{\partial \sigma_{\vartheta\vartheta,m}}{\partial \vartheta} + \frac{1}{r}[(\sigma_{\vartheta\vartheta,m} - \sigma_{\varphi\varphi,m})\cot\vartheta + 3\sigma_{\mathrm{r}\vartheta,m}] + \omega^2\rho_{\mathrm{s},m}u_{\vartheta,m}\right\|_\infty}{\left\|\omega^2\rho_{\mathrm{s},m}u_{\vartheta,m}\right\|_\infty} \tag{100}$$

$$\max_{1\leqslant m\leqslant M} \frac{\left\|\rho_{\mathrm{f}}\omega^2 u_{\mathrm{r}} - \frac{\partial p_{\mathrm{tot}}}{\partial r}\right\|_\infty}{\left\|\frac{\partial p_{\mathrm{tot}}}{\partial r}\right\|_\infty} \tag{101}$$

$$\max_{1\leqslant m\leqslant M} \frac{\left\|\sigma_{\mathrm{rr}} + p_{\mathrm{tot}}\right\|_\infty}{\left\|p_{\mathrm{tot}}\right\|_\infty}. \tag{102}$$

By comparing these error results for both double precision and symbolic precision in MATLAB, one can conclude that the errors indeed originate from round-off errors. When using double precision, the summation is ended whenever $|\mathrm{y}_n(\eta)| > 10^{290}$, such that invalid solutions is obtained for sufficiently large n. Since one needs to have enough terms for the solution to converge, and at the same time have to avoid computing $\mathrm{y}_n(\eta)$ for low η (and large n), the following bound on the frequency based on experimental data is suggested

$$f \lesssim \frac{100}{C}, \qquad C = \left(\frac{R_{0,1}}{c_{\mathrm{f},1}}\right)^{\frac{3}{2}} \frac{1}{\sqrt{\Upsilon}} \tag{103}$$

with

$$\Upsilon = \min\left\{\min_{1\leqslant m\leqslant M} \frac{R_{1,m}}{\max\{c_{\mathrm{s},1,m}, c_{\mathrm{s},2,m}\}}, \min_{1\leqslant m\leqslant M} \frac{R_{0,m}}{c_{\mathrm{f},m}}\right\}$$

where $c_{\mathrm{s},1,M}$ and $c_{\mathrm{s},2,M}$ is the transverse and longitudinal wave velocity for the M^{th} spherical shell, respectively. The constant Υ corresponds to the lowest argument η used for the Bessel functions of second kind. An addendum will be given to yield more numerical evidence for this bound. In particular, plots similar to the ones in Figure 6 will be presented for all benchmarks and corresponding boundary conditions in Subsection 7.4. However, it would certainly be possible to construct models in which this bound is not valid.

One can also observe significant round-off errors for very low frequencies which is again due to the evaluation of the spherical Bessel functions of the second kind with the property

$$\lim_{\zeta\to 0} |\mathrm{y}_n(\zeta)| = \infty. \tag{104}$$

Finally, observe that problems for higher frequencies also occur when using the symbolic class in MATLAB (even though the summation is not terminated prematurely), which calls for a more mathematically sound way of solving this issue. To avoid evaluating the Bessel functions directly, one could include a scaling such that one need to evaluate products of the form $\mathrm{j}_n(\xi)\mathrm{y}_n(\eta)$, $\mathrm{j}_{n+1}(\xi)\mathrm{y}_n(\eta)$, $\mathrm{j}_n(\xi)\mathrm{y}_{n+1}(\eta)$ and $\mathrm{j}_{n+1}(\xi)\mathrm{y}_{n+1}(\eta)$ (which will be $0\cdot\infty$ type products). One would then probably need to use relations like [43, 03.21.26.0047.01 and 03.21.26.0049.01]

$$\mathrm{j}_n(\sqrt{z})\mathrm{y}_n(\sqrt{z}) = -\frac{\sqrt{\pi}}{2}G^{2,0}_{1,3}\left(z\middle|\begin{matrix}0\\ -\frac{1}{2}, n, -n-1\end{matrix}\right) \tag{105}$$

$$\mathrm{j}_{n+1}(\sqrt{z})\mathrm{y}_n(\sqrt{z}) = \frac{\sqrt{\pi}}{2}G^{2,1}_{2,4}\left(z\middle|\begin{matrix}0, -\frac{1}{2}\\ 0, n+\frac{1}{2}, -1, -n-\frac{3}{2}\end{matrix}\right) \tag{106}$$

where G is the Meijer G-function. This investigation is left as future work.

7. Numerical examples

To give further evidence for the correctness of the implemented code, comparison to existing benchmark solutions by Chang [14], Ihlenburg [37] and Fender [15], will be presented. A final benchmark problem in the time-domain will be added.

It is customary to present results in the *far-field*. For the scattered pressure p_1, it is defined by

$$p_0(\hat{\boldsymbol{x}},\omega) = r\mathrm{e}^{-\mathrm{i}k_1 r}p_1(\boldsymbol{x},\omega), \quad r = |\boldsymbol{x}| \to \infty, \tag{107}$$

with $\hat{\boldsymbol{x}} = \boldsymbol{x}/|\boldsymbol{x}|$. As a side note, using Eq. (C.31), the far-field pattern of the scattered pressure in Eq. (61), is given by (in the axisymmetric case)

$$p_0 = \frac{1}{k_1}\sum_{n=0}^{\infty}\mathrm{i}^{-n-1}Q_n^{(0)}(\vartheta)C_{1,n}^{(1)} \tag{108}$$

which yields a very efficient way of computing the far-field pattern.

From the far-field pattern, the *target strength*, TS, can be computed. It is defined by

$$\mathrm{TS} = 20\log_{10}\left(\frac{|p_0(\hat{\boldsymbol{x}},\omega)|}{|P_{\mathrm{inc}}(\omega)|}\right) \tag{109}$$

where P_{inc} is the amplitude of the incident wave at the geometric center of the scatterer (i.e. the origin). Note that TS is independent of P_{inc}.

The directional vector, $\boldsymbol{d}_{\mathrm{s}}$, in spherical coordinates, is given by

$$\boldsymbol{d}_{\mathrm{s}} = -\begin{bmatrix}\sin\vartheta_{\mathrm{s}}\cos\varphi_{\mathrm{s}}\\ \sin\vartheta_{\mathrm{s}}\sin\varphi_{\mathrm{s}}\\ \cos\vartheta_{\mathrm{s}}\end{bmatrix}. \tag{110}$$

Table 1: **Chang parameters:** Parameters for the examples in figure 16 and figure 17 in [14].

Parameter	Description
$E = 2.0 \cdot 10^{11}\,\mathrm{Pa}$	Young's modulus
$\nu = 0.3$	Poisson's ratio
$\rho_\mathrm{s} = 7800\,\mathrm{kg\,m^{-3}}$	Density of solid
$\rho_\mathrm{f} = 1000\,\mathrm{kg\,m^{-3}}$	Density of water
$c_{\mathrm{f},1} = 1460\,\mathrm{m\,s^{-1}}$	Speed of sound in fluid
$R_{0,1} = 1.005\,\mathrm{m}$	Outer radius of spherical shell
$R_{1,1} = 0.995\,\mathrm{m}$	Inner radius of spherical shell

If the source of the incident wave is located at

$$\boldsymbol{x}_\mathrm{s} = -r_\mathrm{s}\boldsymbol{d}_\mathrm{s}, \tag{111}$$

the far-field pattern of an incident wave from the point source

$$p_\mathrm{inc}(\boldsymbol{x},\omega) = P_\mathrm{inc}(\omega)\frac{\mathrm{e}^{\mathrm{i}k_1|\boldsymbol{x}_\mathrm{s}-\boldsymbol{x}|}}{|\boldsymbol{x}_\mathrm{s}-\boldsymbol{x}|}, \tag{112}$$

is actually a plane wave

$$\lim_{r_\mathrm{s}\to\infty} r_\mathrm{s}\mathrm{e}^{-\mathrm{i}k_1 r_\mathrm{s}} p_\mathrm{inc}(\boldsymbol{x},\omega) = P_\mathrm{inc}(\omega)\mathrm{e}^{\mathrm{i}k_1\boldsymbol{d}_\mathrm{s}\cdot\boldsymbol{x}}. \tag{113}$$

Unless stated otherwise, plane waves will be used for the incident wave. Note that the direction of plane waves and location of far-field points is often expressed in the *aspect angle*, $\alpha = \varphi$, and the *elevation angle*, $\beta = 90^\circ - \vartheta$.

7.1. Chang benchmark problem

Chang [14] considers a single spherical shell, with a single homogeneous Neumann condition (sound-soft boundary conditions, SSBC) on the inside of the shell, scattering an incident plane wave (with amplitude $P_\mathrm{inc} = 1\,\mathrm{Pa}$). Chang sends the incident plane wave along the positive x_3-axis, and uses the parameters in Table 1. Moreover, the total pressure (Eq. (63)) is measured at the surface. In Figures 7a and 7b the results are found with $k = 15\,\mathrm{m^{-1}}$ and $k = 20\,\mathrm{m^{-1}}$, respectively[12]. In both cases, the shadow region of the scatterer, $\vartheta \in [0, 90^\circ]$, is clearly visible (with total pressure significantly lower than P_inc).

A simple convergence analysis is shown in Figure 8 where the error in the truncated series in Eq. (97) is plotted. As discussed in Subsection 6.2 the convergence

[12]The discrepancies probably comes from the fact that the data set is collected by the software WebPlotDigitizer where a digital scan of figure 16 and figure 17 [14, pp. 32-33] has been made.

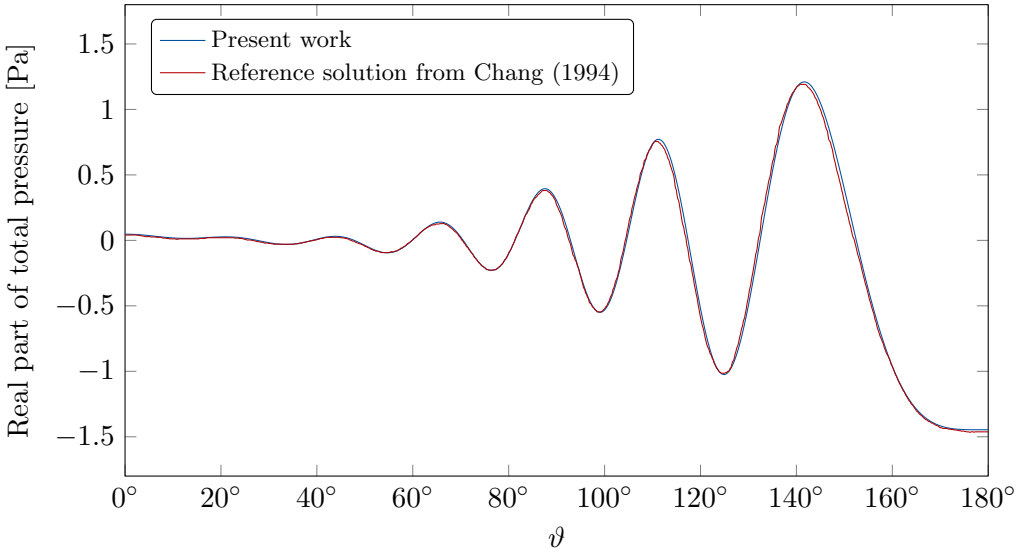

(a) Wave number $k_1 = 15\,\mathrm{m}^{-1}$ and series truncation at $N_\varepsilon = 46$.

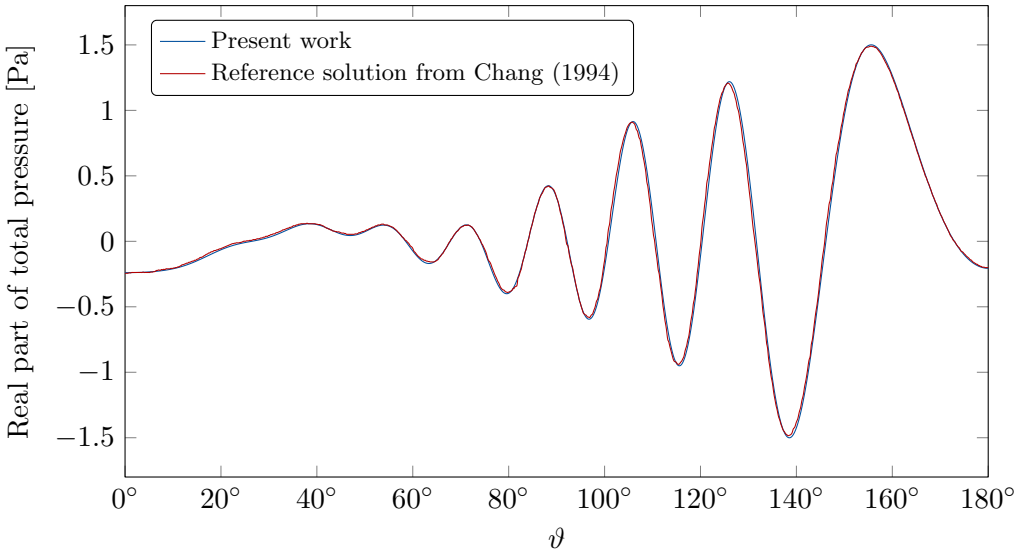

(b) Wave number $k_1 = 20\,\mathrm{m}^{-1}$ and series truncation at $N_\varepsilon = 54$.

Figure 7: **Chang benchmark problem**: Predicted total pressure as a function of the polar angle ϑ.

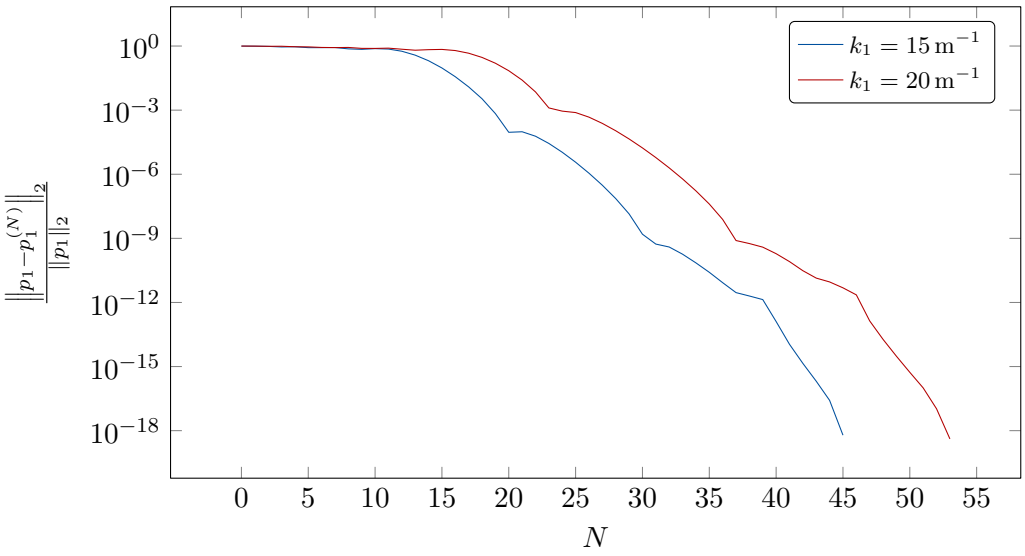

Figure 8: **Chang benchmark problem**: Relative error (with 2000 sample points uniformly placed in the ϑ-direction) of the truncated series in Eq. (97) as a function of N.

is delayed by the increased frequency from $k_1 = 15\,\mathrm{m}^{-1}$ to $k_1 = 20\,\mathrm{m}^{-1}$. To obtain machine epsilon precision (double precision) $N_\varepsilon = 45$ and $N_\varepsilon = 53$ is needed for these frequencies, respectively.

7.2. Ihlenburg benchmark problem

Ihlenburg [37] considers a single spherical shell with a single homogeneous Neumann condition (sound-soft boundary conditions, SSBC) on the inside of the shell, scattering an incident plane wave.

Building upon this example, the corresponding rigid scattering (sound-hard boundary conditions, SHBC) case and scattering with fluid fill will be presented (Neumann-Neumann boundary conditions, NNBC). The parameters in Table 2 are here used.

Frequency sweeps of the target strength (in Eq. (109)) are plotted in Figures 13a and 13b at the polar angles $\vartheta = 180°$ and $\vartheta = 0°$, respectively.

Convergence plots for the three different cases are plotted in Figures 10 to 12, respectively. The linear computational complexity discussed in Subsection 6.2 is revealed. Moreover, by comparing the SHBC case in Figure 10 to the SSBC and NNBC cases in Figures 11 and 12, it is clear that the eigenmodes requires more terms (larger N) in order to achieve better than 1% error precision (this is in particular the case for eigenmodes at higher frequencies).

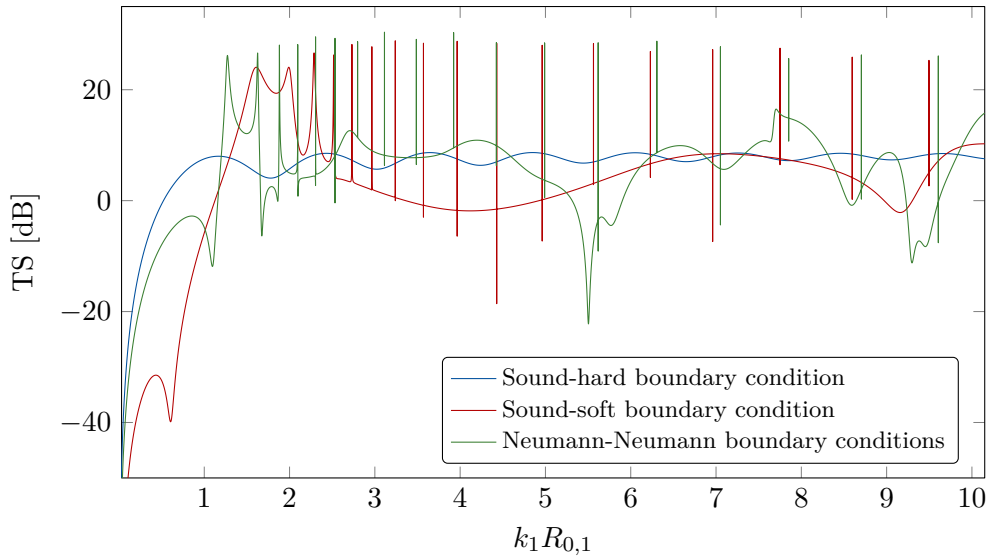

(a) Measured at $\vartheta = 180°$.

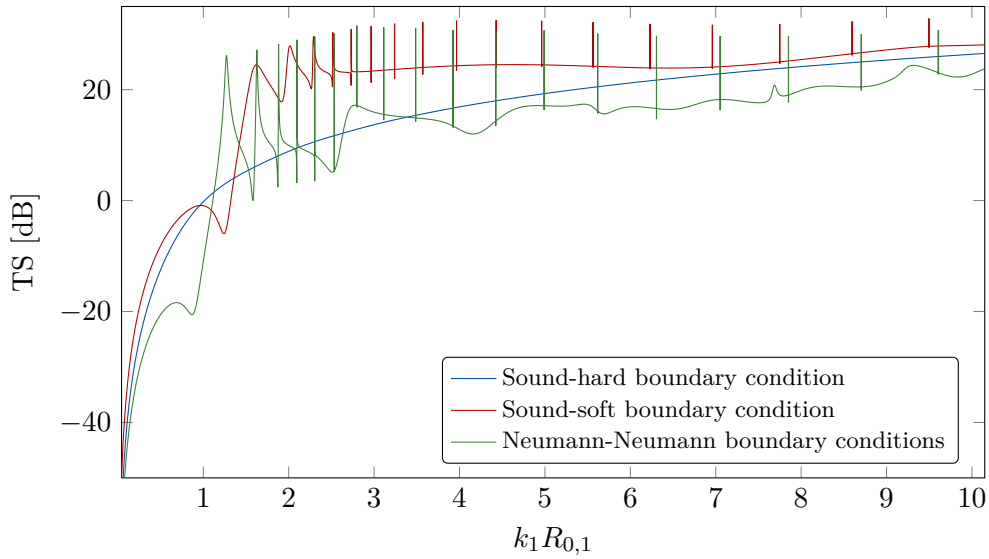

(b) Measured at $\vartheta = 0°$.

Figure 9: **Ihlenburg benchmark problem**: Plots of the target strength, TS. The backscattered pressure will correspond to $\vartheta = 180°$, which is also the specific case considered by Ihlenburg [37, p. 192] (note that Ihlenburg plots the far field instead of the target strength).

Table 2: **Ihlenburg parameters:** Parameters for the Ihlenburg benchmark problem.

Parameter	Description
$E = 2.07 \cdot 10^{11}\,\mathrm{Pa}$	Young's modulus
$\nu = 0.3$	Poisson's ratio
$\rho_\mathrm{s} = 7669\,\mathrm{kg\,m^{-3}}$	Density of solid
$\rho_\mathrm{f} = 1000\,\mathrm{kg\,m^{-3}}$	Density of water
$c_\mathrm{f} = 1524\,\mathrm{m\,s^{-1}}$	Speed of sound in fluid
$R_{0,1} = 5.075\,\mathrm{m}$	Outer radius
$R_{1,1} = 4.925\,\mathrm{m}$	Inner radius

Table 3: **Fender parameters:** Parameters for the examples in figure 2 and figure 3 in [15].

Parameter	Description
$c_{\mathrm{s},1} = 6412\,\mathrm{m\,s^{-1}}$	Longitudinal wave velocity
$c_{\mathrm{s},2} = 3043\,\mathrm{m\,s^{-1}}$	Transverse wave velocity
$\rho_{\mathrm{s},1} = 2700\,\mathrm{kg\,m^{-3}}$	Density of solid
$\rho_{\mathrm{f},1} = 1026\,\mathrm{kg\,m^{-3}}$	Density of outer fluid (water)
$\rho_{\mathrm{f},2} = 1.21\,\mathrm{kg\,m^{-3}}$	Density of inner fluid (air)
$c_{\mathrm{f},1} = 1500\,\mathrm{m\,s^{-1}}$	Speed of sound in water
$c_{\mathrm{f},2} = 343\,\mathrm{m\,s^{-1}}$	Speed of sound in air
$R_{0,1} = 1\,\mathrm{m}$	Outer radius of spherical shell
$R_{1,1} = 0.95\,\mathrm{m}$	Inner radius of spherical shell

However, the eigenmodes has no need of more terms in order to reach machine epsilon precision. So in the case of elastic scattering, the series termination strategy described in Subsection 6.2 is more rigorous than termination of the series at a given N linearly depending on the frequency.

7.3. Fender benchmark problem

Fender [15] consider a single air-filled spherical shell scattering an incident plane wave (with amplitude $P_\mathrm{inc} = 1\,\mathrm{Pa}$). The parameters in Table 3 are here used, where the following conversion formulas is of convenience

$$E = \rho_s c_{\mathrm{s},2}^2 \frac{3c_{\mathrm{s},1}^2 - 4c_{\mathrm{s},2}^2}{c_{\mathrm{s},1}^2 - c_{\mathrm{s},2}^2} \quad \text{and} \quad \nu = \frac{1}{2}\frac{c_{\mathrm{s},1}^2 - 2c_{\mathrm{s},2}^2}{c_{\mathrm{s},1}^2 - c_{\mathrm{s},2}^2}. \tag{114}$$

Fender also sends the incident plane wave along the x_3-axis, but in negative direction. The frequency sweep results of the total pressure (in Eq. (63)) are

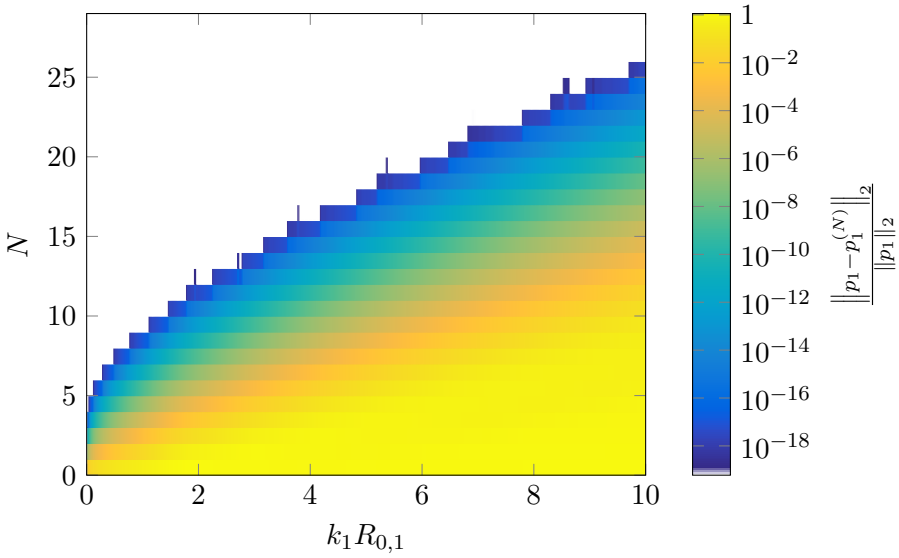

Figure 10: **Ihlenburg benchmark problem - the sound-hard case**: Relative error in the l_2-norm (with two sample points at $\vartheta = 0°$ and $\vartheta = 180°$) of the truncated series in Eq. (97) as a function of N. The "exact" solution, p_1, is obtained as described in Subsection 6.2.

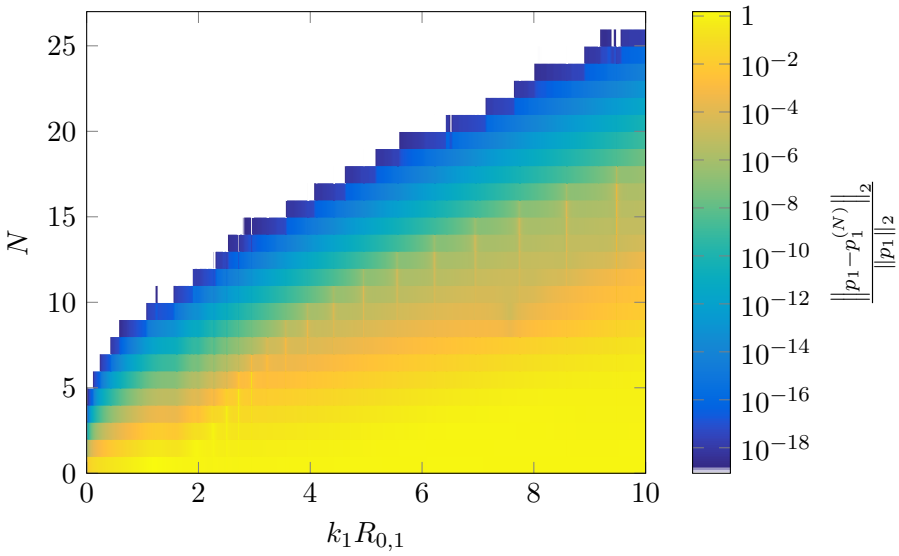

Figure 11: **Ihlenburg benchmark problem - the sound-soft case**: Relative error in the l_2-norm (with two sample points at $\vartheta = 0°$ and $\vartheta = 180°$) of the truncated series in Eq. (97) as a function of N. The "exact" solution, p_1, is obtained as described in Subsection 6.2.

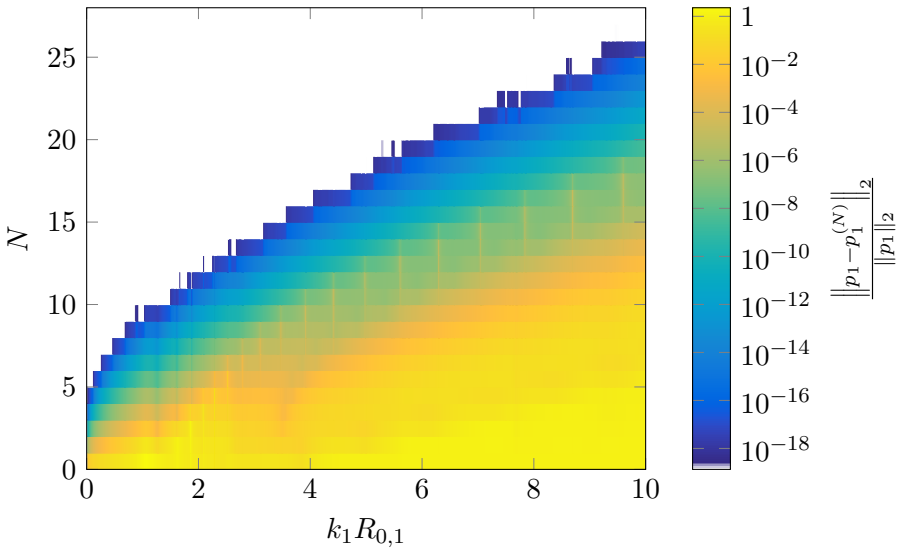

Figure 12: **Ihlenburg benchmark problem - the Neumann-Neumann case**: Relative error in the l_2-norm (with two sample points at $\vartheta = 0°$ and $\vartheta = 180°$) of the truncated series in Eq. (97) as a function of N. The "exact" solution, p_1, is obtained as described in Subsection 6.2.

measured at the surface. In Figures 13a and 13b the results are found at polar angles $\vartheta = 0°$ and $\vartheta = 180°$, respectively[13].

In Figure 14, another convergence study is illustrated. The Fender benchmark problem was run with increasing frequency until a Bessel function was evaluated to be above 10^{290} (the termination criterion as described in Subsection 6.3). Due to the linear behavior of N as a function of ω needed for convergence (computational complexity) and the concave behavior of the smallest number N such that $|\mathrm{y}_N(\omega\Upsilon)| > 10^{290}$ (where Υ is given by Eq. (103)), prematurely termination of the series is inevitable for large enough frequencies.

7.4. Benchmark problems

Let S1, S3 and S5 be benchmark models of spherical shells characterized by the outer radius $R_{0,1}$ and the inner radius $R_{1,1}$ of the shell. The shells are filled with the given fluid (Table 4) and embedded in water. The remaining parameters are given in Table 5. These models can be combined into a new set of benchmark

[13]The discrepancies again probably comes from the fact that the data set is collected by the software WebPlotDigitizer where a digital scan of Figure 2 and Figure 3 [15, pp. 30-31] has been made. Moreover, the spectrum has been sampled rather closely, revealing small (less significant) eigenmodes not shown by Fender.

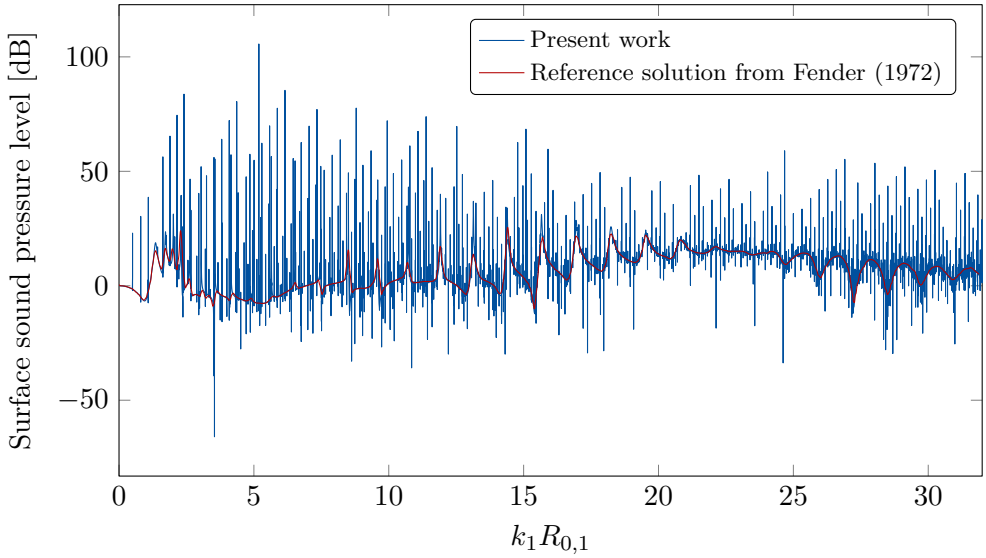

(a) Measured at $\vartheta = 0°$.

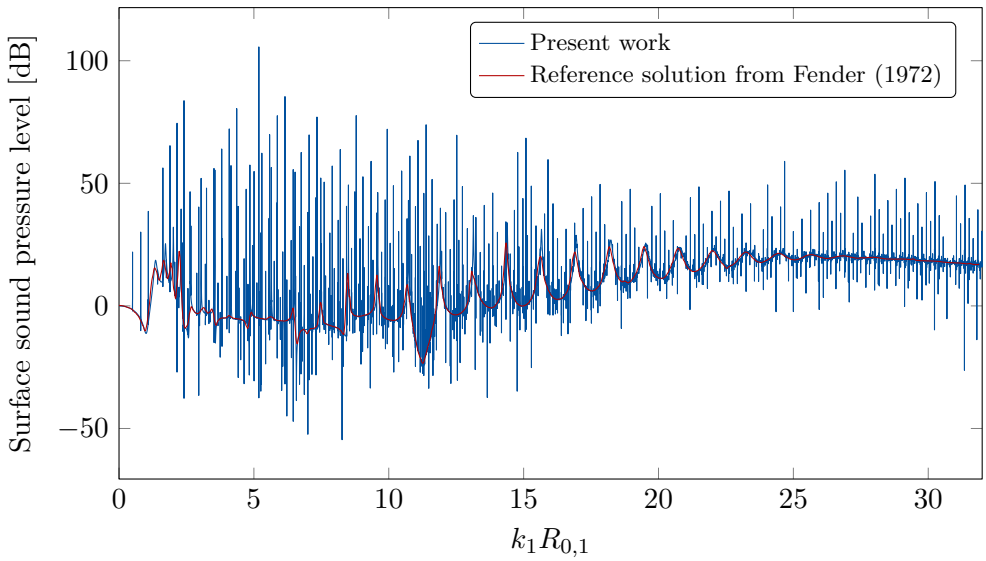

(b) Measured at $\vartheta = 180°$.

Figure 13: **Fender benchmark problem**: Predicted total pressure as a function of $k_1 R_{0,1}$ at the surface of the shell.

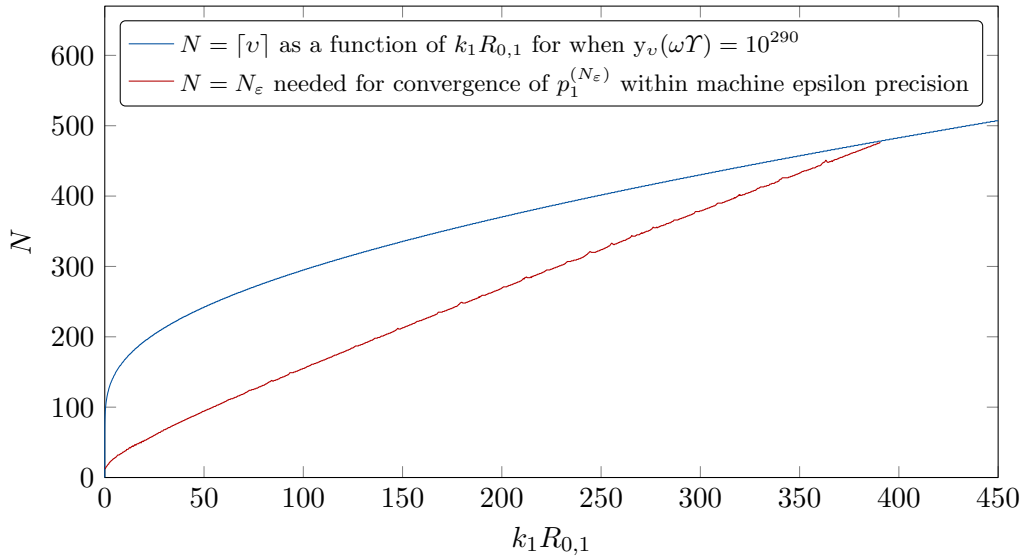

Figure 14: **Fender benchmark problem**: The intersection of these to graphs marks the largest frequency for which the algorithms presented in this work will give satisfactory results. Here, Υ is given by Eq. (103) and the truncated series $p_1^{(N_\varepsilon)}$ is given by Eq. (97).

Table 4: **Benchmark problems:** Parameters for S1, S3 and S5.

	S1	S3	S5
Outer radius, $R_{0,1}$	1 m	3 m	5 m
Inner radius, $R_{1,1}$	0.95 m	2.98 m	4.992 m
Fluid fill	air	air	water

Table 5: **Benchmark problems:** Common parameters for the benchmark problems.

Parameter	Description
$E = 2.10 \cdot 10^{11}\,\mathrm{Pa}$	Young's modulus
$\nu = 0.3$	Poisson's ratio
$\rho_\mathrm{s} = 7850\,\mathrm{kg\,m^{-3}}$	Density of solid
$\rho_\mathrm{f,water} = 1000\,\mathrm{kg\,m^{-3}}$	Density of water
$\rho_\mathrm{f,air} = 1.2\,\mathrm{kg\,m^{-3}}$	Density of air
$c_\mathrm{f,water} = 1500\,\mathrm{m\,s^{-1}}$	Speed of sound in water
$c_\mathrm{f,air} = 340\,\mathrm{m\,s^{-1}}$	Speed of sound in air

problems: S13 (S1 inside S3 with air in between), S15 (S1 inside S5 with water in between), S35 (S3 inside S5 with water in between) and S135 (S1 inside S3 inside S5 with air in between S1 and S3 and water in between S3 and S5). These benchmark problems are illustrated in Figure 15.

By default, all benchmarks have acoustic structure interaction (ASI) on all of the interfaces between fluid and solid domains (with Neumann-to-Neumann boundary conditions, NNBC, in Eqs. (14) and (15)). As described in Subsection 5.2, the boundary conditions on the innermost shell may be replaced by other boundary conditions like the sound-soft (SSBC) and sound-hard boundary condition (SHBC). The elastic sphere boundary condition (ESBC) results from filling the innermost shell with the given elastic material.

In Figure 16, the near field is plotted for some of these benchmarks. In Figure 16b the classical interference pattern emerging behind the rigid scatterer S5 (with SHBC) can be observed. In contrast, the corresponding case with NNBC in Figures 16c and 16d gives a different picture entirely because most of the energy simply passes straight through the thin spherical shell. The example is expanded further in Figures 16e to 16h. For the latter case, the energy transmitted is greatly reduced due to air-filled fluid inside the second shell. The S135 benchmark was visually identical to this benchmark due to this fact (that is, it is hard to reveal objects inside air-filled domains). However, it is clear that sound-hard boundary conditions are not a good approximation of NNBC in this case. The more natural approximation would be to use SSBC. Indeed, the SSBC approximate the innermost fluid with $p_{M+1} = 0$, which is clearly a good approximation in this case.

7.5. Benchmark problems in the time domain

Finally, the application of the work in the time domain will be presented. In particular, consider scattering by a single wavelet given by (from [40, p. 633])

$$\breve{P}_{\text{inc}}(t) = \begin{cases} \frac{4}{3\sqrt{3}}\Big[\sin(\omega_{\text{c}} t) - \frac{1}{2}\sin(2\omega_{\text{c}} t)\Big] & 0 < t < \frac{1}{f_{\text{c}}} \\ 0 & \text{otherwise,} \end{cases} \tag{115}$$

with $\omega_{\text{c}} = 2\pi f_{\text{c}}$ and $k_{\text{c}} = \omega_{\text{c}}/c_{\text{f},1}$, and where f_{c} is the center frequency (Figure 17a). The corresponding frequency spectrum (using the definition of the Fourier transform in Eq. (6)), is given by (Figure 17b)

$$P_{\text{inc}}(\omega) = \Big(\mathcal{F}\,\breve{P}_{\text{inc}}\Big)(\omega) = \begin{cases} \frac{4}{3\sqrt{3}}\frac{\mathrm{i}\pi}{\omega}\mathrm{e}^{\mathrm{i}\pi\omega/\omega_{\text{c}}} & \omega \in \{\pm\omega_{\text{c}}, \pm 2\omega_{\text{c}}\} \\ \frac{4}{\sqrt{3}}\frac{\omega_{\text{c}}^3}{(\omega^2-\omega_{\text{c}}^2)(\omega^2-4\omega_{\text{c}}^2)}\Big(1-\mathrm{e}^{-2\pi\mathrm{i}\omega/\omega_{\text{c}}}\Big) & \text{otherwise.} \end{cases} \tag{116}$$

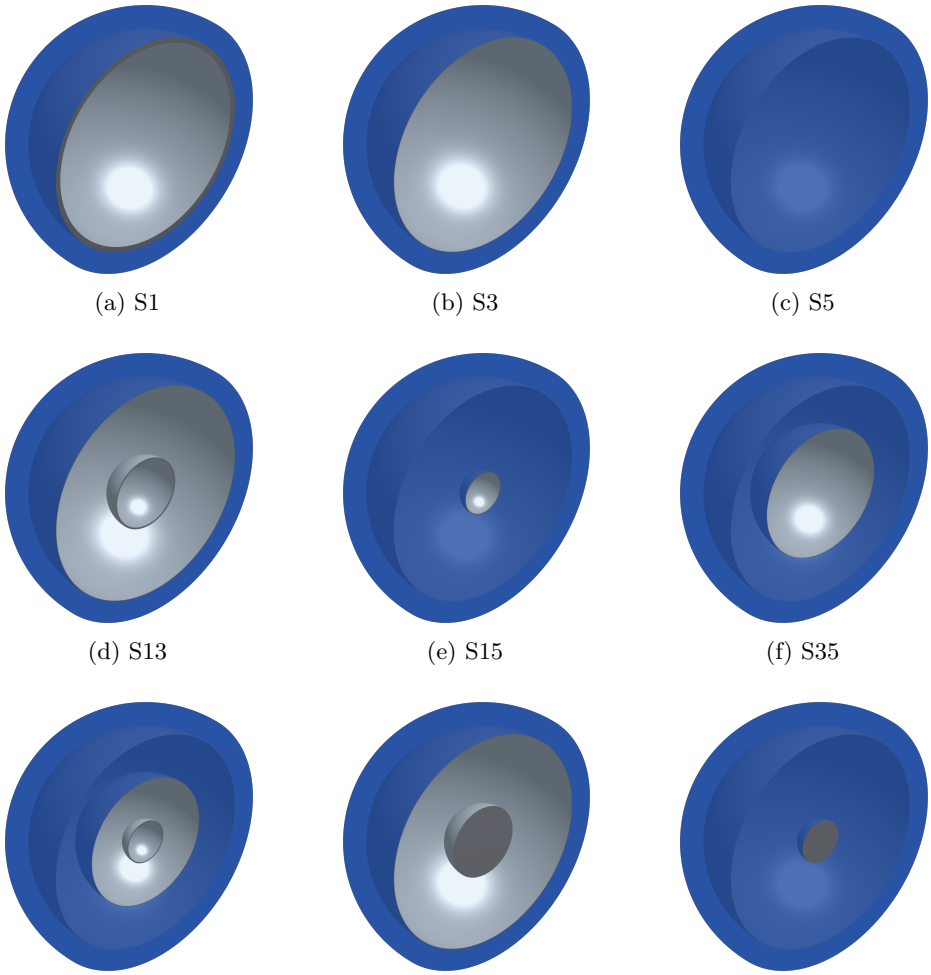

(a) S1 (b) S3 (c) S5

(d) S13 (e) S15 (f) S35

(g) S135 (h) S13 with ESBC (i) S15 with ESBC

Figure 15: **Benchmark problems**: The first row (S1, S2, S3) represent the default set of benchmarks from which the others are built (clip view). The model S5 and S3 is, respectively, 5 and 3 times the size of S1 (the figures are thus not to scale). S13 is a combination of S1 and S2, S13 is a combination of S1 and S3, and S23 is a combination of S2 and S3. S123 is a combination of S1, S2 and S3. The final two figures are derived models with a solid sphere as the innermost domain.

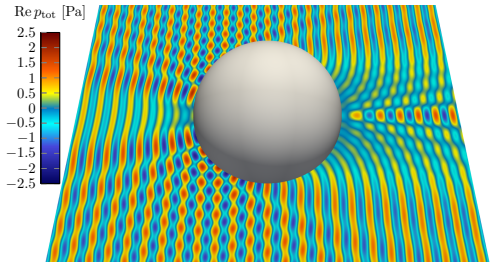

(a) **S5 with SHBC**: Plot of $\operatorname{Re} p_{\text{tot}}$.

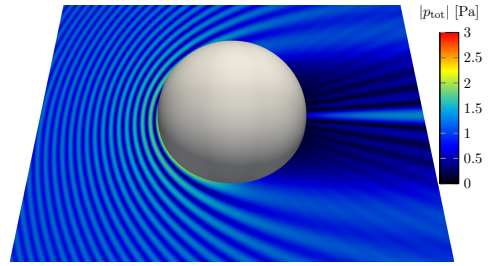

(b) **S5 with SHBC**: Plot of $|p_{\text{tot}}|$.

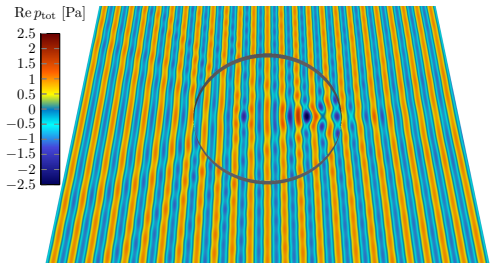

(c) **S5 with NNBC**: Plot of $\operatorname{Re} p_{\text{tot}}$.

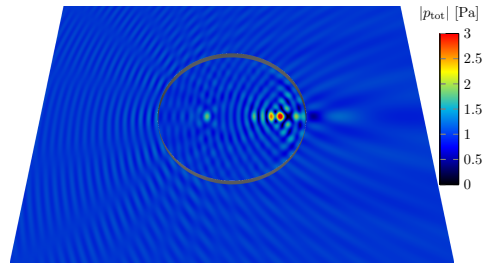

(d) **S5 with NNBC**: Plot of $|p_{\text{tot}}|$.

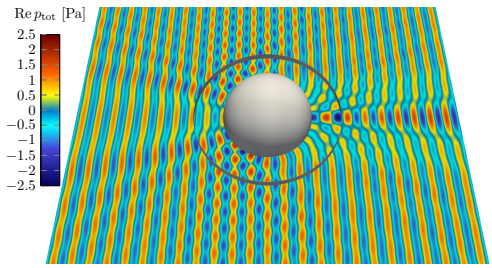

(e) **S35 with SHBC**: Plot of $\operatorname{Re} p_{\text{tot}}$.

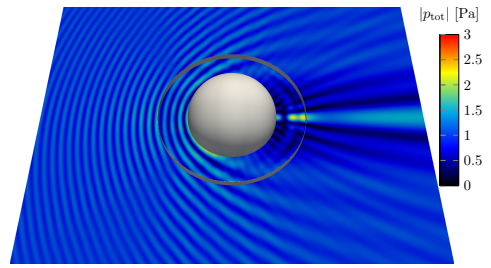

(f) **S35 with SHBC**: Plot of $|p_{\text{tot}}|$.

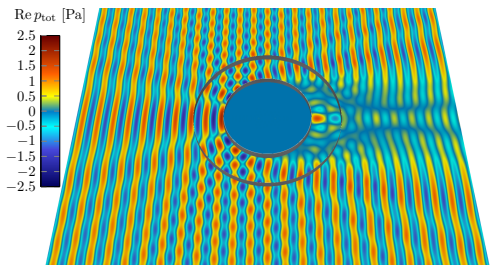

(g) **S135 with NNBC**: Plot of $\operatorname{Re} p_{\text{tot}}$.

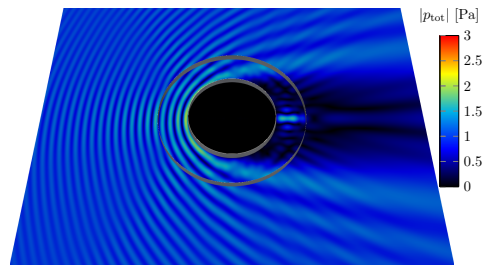

(h) **S135 with NNBC**: Plot of $|p_{\text{tot}}|$.

Figure 16: **Benchmark problems**: Plots of the near field of some benchmark problems. The shells are cut open whenever a domain inside the shell is present. The visualization was done in Paraview.

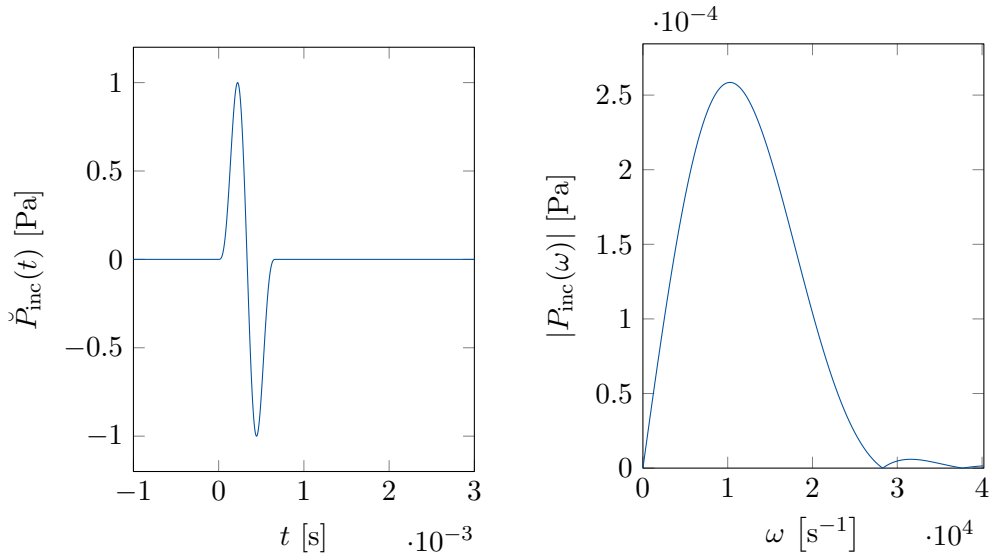

(a) Wavelet in time domain.

(b) Wavelet in frequency domain.

Figure 17: **Benchmark problems in the time domain**: Wavelet $\breve{P}_{\text{inc}}(t)$ and corresponding frequency spectrum $|P_{\text{inc}}(\omega)|$. The wavelet has compact support on the interval $[0, 1/f_{\text{c}}]$, where $f_{\text{c}} = 1.5 \cdot 10^3\,\text{Hz}$. The frequency spectrum is plotted for positive frequencies to the end of the bandwidth, $f = B/2 = 6.4 \cdot 10^3\,\text{Hz}$ (with $B = \breve{N}/T$).

A plane wave with this wavelet in the time-domain then takes the form

$$\breve{p}_{\mathrm{inc}}(\boldsymbol{x},t)=\breve{P}_{\mathrm{inc}}\left(t-\frac{x_3}{c_{\mathrm{f},1}}\right), \tag{117}$$

with corresponding field in the frequency domain given by

$$p_{\mathrm{inc}}(\boldsymbol{x},\omega)=(\mathcal{F}\,\breve{p}_{\mathrm{inc}}(\boldsymbol{x},\cdot))(\omega)=P_{\mathrm{inc}}(\omega)\mathrm{e}^{\mathrm{i}k_1x_3}. \tag{118}$$

An alternative to plane waves, is waves due to point sources. Using the wavelet in Eq. (115), these waves are given by

$$\breve{p}_{\mathrm{inc}}(\boldsymbol{x},t)=\breve{P}_{\mathrm{inc}}\left(t-\frac{|\boldsymbol{x}_{\mathrm{s}}-\boldsymbol{x}|}{c_{\mathrm{f},1}}\right)\frac{r_{\mathrm{s}}}{|\boldsymbol{x}_{\mathrm{s}}-\boldsymbol{x}|} \tag{119}$$

and

$$p_{\mathrm{inc}}(\boldsymbol{x},\omega)=P_{\mathrm{inc}}(\omega)\frac{r_{\mathrm{s}}}{|\boldsymbol{x}_{\mathrm{s}}-\boldsymbol{x}|}\mathrm{e}^{\mathrm{i}k_1|\boldsymbol{x}_{\mathrm{s}}-\boldsymbol{x}|}$$

where $\boldsymbol{x}_{\mathrm{s}}$ is location of the point source given in Eq. (111) (at a finite distance $r_{\mathrm{s}}=|\boldsymbol{x}_{\mathrm{s}}|$).

As $\Psi(\boldsymbol{x},\omega)$ cannot be computed for infinitely many frequencies, an approximation of the time dependent fields in Eq. (7) by [40, p. 614] can be used

$$\breve{\Psi}(\boldsymbol{x},t_m)\approx\frac{2}{T}\,\mathrm{Re}\left\{\sum_{n=1}^{\breve{N}/2-1}\Psi(\boldsymbol{x},\omega_n)\mathrm{e}^{-2\pi\mathrm{i}nm/\breve{N}}\right\} \tag{120}$$

where

$$t_m=m\Delta t,\quad \Delta t=\frac{T}{\breve{N}},\quad \omega_n=n\Delta\omega,\quad \Delta\omega=\frac{2\pi}{T}. \tag{121}$$

Note that the contribution from the static case ($n=0$) has not been included as the incident wave, $p_{\mathrm{inc}}(\boldsymbol{x},0)=0$, results in the trivial solution $\Psi(\boldsymbol{x},0)=0$. The Fourier series approximation results in periodic time-dependent fields, with period T, sampled in the interval $[0,T]$ with $\breve{N}$ time steps. The parameter $\breve{N}$ also quantifies the number of terms in the Fourier series approximation, such that it also controls the error (aliasing). By choosing $\breve{N}$ to be powers of two, the approximation can be very efficiently evaluated by the fast Fourier transformation.

In Figure 18 an example based on the S5 benchmark problem with ESBC is illustrated; An elastic sphere (with parameters given in Table 5) is impinged by the incident wave in Eq. (117). In this example, the following parameters has been used: $f_{\mathrm{c}}=1.5\,\mathrm{kHz}$, $\breve{N}=2^{10}=1024$ and $T=120/f_{\mathrm{c}}$. In Figure 18, the total pressure is plotted in the fluid, and the von Mises stress given by

$$\sigma_{\mathrm{v}}=\sqrt{\frac{(\sigma_{11}-\sigma_{22})^2+(\sigma_{22}-\sigma_{33})^2+(\sigma_{11}-\sigma_{33})^2+6(\sigma_{23}^2+\sigma_{13}^2+\sigma_{12}^2)}{2}} \tag{122}$$

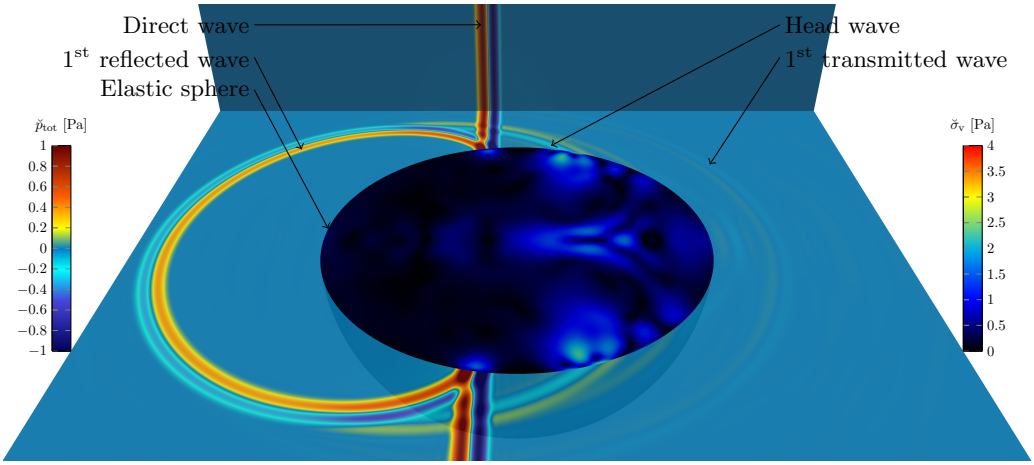

Figure 18: **Benchmark problems in the time domain**: Visualization of a wavelet (from a far-field point) in the time domain which transmits (the 1st transmitted wave) and reflects (the 1st reflected wave) an elastic sphere (which is cut open for visualization purposes). The 2nd transmitted wave through the elastic sphere takes a lead of the direct wave as the wave speed in the elastic material is larger than that of the fluid. Aliasing is also visible. Two transparent planes have been inserted to visualize the total pressure field. The von Mises stress, $\breve{\sigma}_{\mathrm{v}}$, is visualized in the solid. The visualization was done in Paraview.

is plotted in the solid domain.

For the benchmark problems, the longitudinal speed and transverse speed in the solid is $c_{\mathrm{s},1} \approx 6001\,\mathrm{ms}^{-1}$ and $c_{\mathrm{s},2} \approx 3208\,\mathrm{ms}^{-1}$, respectively. So since, $c_{\mathrm{s},1} \approx 4c_{\mathrm{f}}$ and $c_{\mathrm{s},2} \approx 2c_{\mathrm{f}}$, the waves traveling through the elastic sphere with the longitudinal wave speed will transmit through the solid 4 times as fast as the waves in the surrounding fluid (this wave corresponds to the 1st transmitted wave in Figure 18). Correspondingly for the waves traveling with the transverse wave speed. This can indeed be observed as well, but the amplitude of the transverse wave traveling at the speed $c_{\mathrm{s},1}$ is only about 2% of the amplitude of the incident wave P_{inc} and is therefore barely visible. Much more energy is transmitted through the wave with the transverse wave speed (the amplitude is approximately 14% of P_{inc}).

Consider finally the S15 benchmark problem with ESBC; A thin shell surrounding a solid sphere is impinged by the incident wave in Eq. (119) (that is, the incident wave originates from a point source in the near field). The point source is located at a radius of $r_{\mathrm{s}} = 10\,\mathrm{m}$ away from the center of the scatterer (the origin). All other parameters remain the same as in the previous example.

In Figure 19 the effects from previous example can again be observed. In addition, waves traveling in the thin shell are reflected backwards through a head wave in the intermediate fluid. In addition, the corresponding waves are

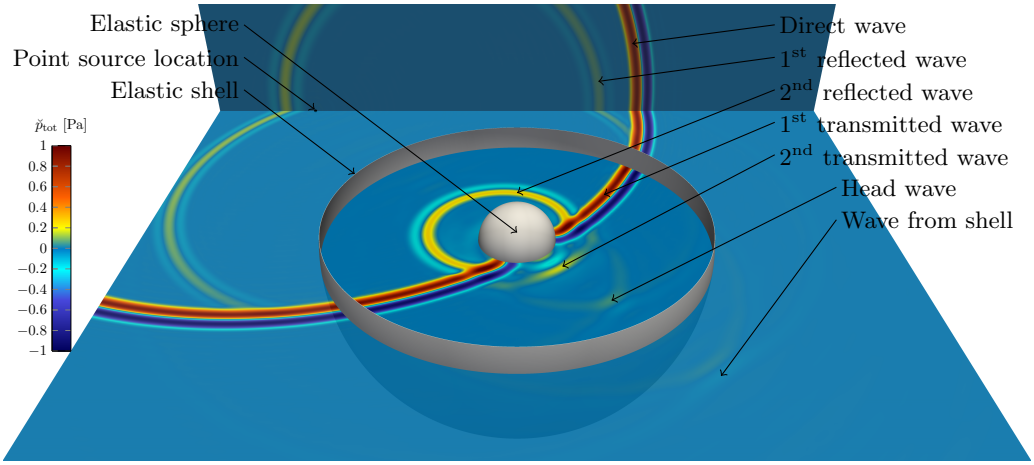

Figure 19: **Benchmark problems in the time domain**: Visualization of a wavelet (from a point source) in the time domain which transmits (the 1st transmitted wave) and reflects (the 1st reflected wave) the outermost thin shell (which is cut open for visualization purposes), and is then scattered (the 2nd reflected wave) by the innermost solid sphere. The 2nd transmitted wave through the elastic sphere takes a lead of the direct wave as the wave speed in the elastic material is larger than that of the fluid. Aliasing is also visible. Two transparent planes have been inserted to visualize the total pressure field. The displacement field is here not visualized. The visualization was done in Paraview.

transmitted through the shell denoted as “Wave from shell”.

It should be pointed out that aliasing (pollution of the solution from the previous incident waves due to periodicity) is present, although not visible in these plots. The aliasing can be decreased further by increasing the period T. To preserve the size of the *bandwidth* $B = \check{N}/T$, $\check{N}$ must be correspondingly increased.

8. Conclusions

An exact solution to 3D scattering problems on spherical symmetric scatterers has been presented. From a computational point of view, the solution is exact in the sense that round-off errors are the only source of errors. However, these round-off errors play a crucial role for higher frequencies (and also for very low frequencies) when implementing the solution naively. In any case, the computational complexity of the solution is $\mathcal{O}(\omega)$.

A set of benchmark problems have been presented for future references. Results have been presented for some of these benchmarks in both the far-field (frequency domain) and the time domain (near-field). The exact solution presents a vast set of parameters for large ranges, which makes it a good reference solution, as many numerical phenomena can occur for different combinations of these parameters.

Acknowledgements

This work was supported by the Department of Mathematical Sciences at the Norwegian University of Science and Technology and by the Norwegian Defence Research Establishment.

The authors wish to thank Trond Kvamsdal who assisted in the proof-reading of the manuscript. The authors would also like to thank the reviewers for detailed response and many constructive comments.

A. The spherical coordinate system

The spherical coordinate system is defined by the transformation $\boldsymbol{x}(r, \vartheta, \varphi) = x_i(r, \vartheta, \varphi)\boldsymbol{e}_i$, where $\boldsymbol{e}_i$ are the standard basis vectors in the Cartesian coordinate system and (see Figure A20)

$$x_1 = r \sin\vartheta \cos\varphi \tag{A.1}$$
$$x_2 = r \sin\vartheta \sin\varphi \tag{A.2}$$
$$x_3 = r \cos\vartheta. \tag{A.3}$$

The inverse relation is then found to be

$$r = |\boldsymbol{x}|, \quad \text{with} \quad |\boldsymbol{x}| = \sqrt{x_1^2 + x_2^2 + x_3^2} \tag{A.4}$$
$$\vartheta = \arccos\left(\frac{x_3}{|\boldsymbol{x}|}\right) \tag{A.5}$$
$$\varphi = \operatorname{atan2}(x_2, x_1), \tag{A.6}$$

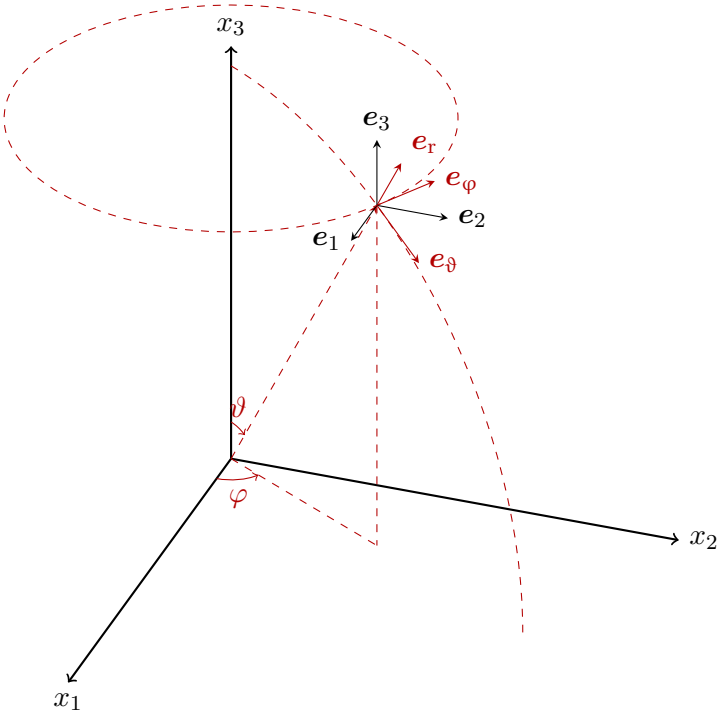

Figure A20: The spherical and Cartesian coordinate system.

where

$$\operatorname{atan2}(x_2, x_1) = \begin{cases} \arctan(\frac{x_2}{x_1}) & \text{if } x_1 > 0 \\ \arctan(\frac{x_2}{x_1}) + \pi & \text{if } x_1 < 0 \text{ and } x_2 \geq 0 \\ \arctan(\frac{x_2}{x_1}) - \pi & \text{if } x_1 < 0 \text{ and } x_2 < 0 \\ \frac{\pi}{2} & \text{if } x_1 = 0 \text{ and } x_2 > 0 \\ -\frac{\pi}{2} & \text{if } x_1 = 0 \text{ and } x_2 < 0 \\ \text{undefined} & \text{if } x_1 = 0 \text{ and } x_2 = 0. \end{cases} \tag{A.7}$$

Hence, the Jacobian matrix of the spherical transformation is given by

$$\boldsymbol{J}_{\mathrm{s}} = \begin{bmatrix} \frac{\partial x_1}{\partial r} & \frac{\partial x_1}{\partial \vartheta} & \frac{\partial x_1}{\partial \varphi} \\ \frac{\partial x_2}{\partial r} & \frac{\partial x_2}{\partial \vartheta} & \frac{\partial x_2}{\partial \varphi} \\ \frac{\partial x_3}{\partial r} & \frac{\partial x_3}{\partial \vartheta} & \frac{\partial x_3}{\partial \varphi} \end{bmatrix} = \begin{bmatrix} \sin\vartheta\cos\varphi & r\cos\vartheta\cos\varphi & -r\sin\vartheta\sin\varphi \\ \sin\vartheta\sin\varphi & r\cos\vartheta\sin\varphi & r\sin\vartheta\cos\varphi \\ \cos\vartheta & -r\sin\vartheta & 0 \end{bmatrix} \tag{A.8}$$

with inverse given by

$$\boldsymbol{J}_{\mathrm{s}}^{-1} = \begin{bmatrix} \frac{\partial r}{\partial x_1} & \frac{\partial r}{\partial x_2} & \frac{\partial r}{\partial x_3} \\ \frac{\partial \vartheta}{\partial x_1} & \frac{\partial \vartheta}{\partial x_2} & \frac{\partial \vartheta}{\partial x_3} \\ \frac{\partial \varphi}{\partial x_1} & \frac{\partial \varphi}{\partial x_2} & \frac{\partial \varphi}{\partial x_3} \end{bmatrix} = \begin{bmatrix} \sin\vartheta\cos\varphi & \sin\vartheta\sin\varphi & \cos\vartheta \\ \frac{1}{r}\cos\vartheta\cos\varphi & \frac{1}{r}\cos\vartheta\sin\varphi & -\frac{1}{r}\sin\vartheta \\ -\frac{1}{r}\frac{\sin\varphi}{\sin\vartheta} & \frac{1}{r}\frac{\cos\varphi}{\sin\vartheta} & 0 \end{bmatrix}. \tag{A.9}$$

So, for a scalar valued function Ψ the following is obtained (using the chain rule)

$$\begin{bmatrix} \frac{\partial \Psi}{\partial r} \\ \frac{\partial \Psi}{\partial \vartheta} \\ \frac{\partial \Psi}{\partial \varphi} \end{bmatrix} = \boldsymbol{J}_{\mathrm{s}}^{\top} \begin{bmatrix} \frac{\partial \Psi}{\partial x_1} \\ \frac{\partial \Psi}{\partial x_2} \\ \frac{\partial \Psi}{\partial x_3} \end{bmatrix}. \tag{A.10}$$

The scale factors in the spherical coordinate system are given by

$$h_{\mathrm{r}} = \left|\frac{\partial \boldsymbol{x}}{\partial r}\right| = 1, \quad h_{\vartheta} = \left|\frac{\partial \boldsymbol{x}}{\partial \vartheta}\right| = r, \quad h_{\varphi} = \left|\frac{\partial \boldsymbol{x}}{\partial \varphi}\right| = r\sin\theta, \tag{A.11}$$

from which the following basis vectors are derived (see Figure A20)

$$\boldsymbol{e}_{\mathrm{r}} = \frac{1}{h_{\mathrm{r}}}\frac{\partial \boldsymbol{x}}{\partial r} = \boldsymbol{e}_1\sin\vartheta\cos\varphi + \boldsymbol{e}_2\sin\vartheta\sin\varphi + \boldsymbol{e}_3\cos\vartheta \tag{A.12}$$

$$\boldsymbol{e}_{\vartheta} = \frac{1}{h_{\vartheta}}\frac{\partial \boldsymbol{x}}{\partial \vartheta} = \boldsymbol{e}_1\cos\vartheta\cos\varphi + \boldsymbol{e}_2\cos\vartheta\sin\varphi - \boldsymbol{e}_3\sin\vartheta \tag{A.13}$$

$$\boldsymbol{e}_{\varphi} = \frac{1}{h_{\varphi}}\frac{\partial \boldsymbol{x}}{\partial \varphi} = -\boldsymbol{e}_1\sin\varphi + \boldsymbol{e}_2\cos\varphi. \tag{A.14}$$

This can be written in the following matrix form

$$\begin{bmatrix} \boldsymbol{e}_{\mathrm{r}} & \boldsymbol{e}_{\vartheta} & \boldsymbol{e}_{\varphi} \end{bmatrix} = \boldsymbol{J}_{\mathrm{e}}^{\top} \begin{bmatrix} \boldsymbol{e}_1 & \boldsymbol{e}_2 & \boldsymbol{e}_3 \end{bmatrix} = \boldsymbol{J}_{\mathrm{e}}^{\top} \tag{A.15}$$

where

$$\boldsymbol{J}_{\mathrm{e}} = \begin{bmatrix} \sin\vartheta\cos\varphi & \sin\vartheta\sin\varphi & \cos\vartheta \\ \cos\vartheta\cos\varphi & \cos\vartheta\sin\varphi & -\sin\vartheta \\ -\sin\varphi & \cos\varphi & 0 \end{bmatrix} \tag{A.16}$$

and inverse given by

$$\boldsymbol{J}_{\mathrm{e}}^{-1} = \begin{bmatrix} \sin\vartheta\cos\varphi & \cos\vartheta\cos\varphi & -\sin\varphi \\ \sin\vartheta\sin\varphi & \cos\vartheta\sin\varphi & \cos\varphi \\ \cos\vartheta & -\sin\vartheta & 0 \end{bmatrix}. \tag{A.17}$$

So, for any vector field

$$\boldsymbol{\Psi} = \Psi_1\boldsymbol{e}_1 + \Psi_2\boldsymbol{e}_2 + \Psi_3\boldsymbol{e}_3 = \Psi_{\mathrm{r}}\boldsymbol{e}_{\mathrm{r}} + \Psi_{\vartheta}\boldsymbol{e}_{\vartheta} + \Psi_{\varphi}\boldsymbol{e}_{\varphi} \tag{A.18}$$

the following relation is found (by comparing each component)

$$\begin{bmatrix} \Psi_1 \\ \Psi_2 \\ \Psi_3 \end{bmatrix} = \boldsymbol{J}_{\mathrm{e}}^{\top} \begin{bmatrix} \Psi_{\mathrm{r}} \\ \Psi_{\vartheta} \\ \Psi_{\varphi} \end{bmatrix}, \tag{A.19}$$

and the Jacobian of $\boldsymbol{\Psi}$ is given by (using the chain rule)

$$\begin{aligned} \begin{bmatrix} \frac{\partial\Psi_1}{\partial x_1} & \frac{\partial\Psi_1}{\partial x_2} & \frac{\partial\Psi_1}{\partial x_3} \\ \frac{\partial\Psi_2}{\partial x_1} & \frac{\partial\Psi_2}{\partial x_2} & \frac{\partial\Psi_2}{\partial x_3} \\ \frac{\partial\Psi_3}{\partial x_1} & \frac{\partial\Psi_3}{\partial x_2} & \frac{\partial\Psi_3}{\partial x_3} \end{bmatrix} &= \begin{bmatrix} \frac{\partial\Psi_1}{\partial r} & \frac{\partial\Psi_1}{\partial\vartheta} & \frac{\partial\Psi_1}{\partial\varphi} \\ \frac{\partial\Psi_2}{\partial r} & \frac{\partial\Psi_2}{\partial\vartheta} & \frac{\partial\Psi_2}{\partial\varphi} \\ \frac{\partial\Psi_3}{\partial r} & \frac{\partial\Psi_3}{\partial\vartheta} & \frac{\partial\Psi_3}{\partial\varphi} \end{bmatrix} \boldsymbol{J}_{\mathrm{s}}^{-1} \\ &= \left(\boldsymbol{J}_1\Psi_{\mathrm{r}} + \boldsymbol{J}_2\Psi_{\vartheta} + \boldsymbol{J}_3\Psi_{\varphi} + \boldsymbol{J}_{\mathrm{e}}^{\top} \begin{bmatrix} \frac{\partial\Psi_{\mathrm{r}}}{\partial r} & \frac{\partial\Psi_{\mathrm{r}}}{\partial\vartheta} & \frac{\partial\Psi_{\mathrm{r}}}{\partial\varphi} \\ \frac{\partial\Psi_{\vartheta}}{\partial r} & \frac{\partial\Psi_{\vartheta}}{\partial\vartheta} & \frac{\partial\Psi_{\vartheta}}{\partial\varphi} \\ \frac{\partial\Psi_{\varphi}}{\partial r} & \frac{\partial\Psi_{\varphi}}{\partial\vartheta} & \frac{\partial\Psi_{\varphi}}{\partial\varphi} \end{bmatrix} \right) \boldsymbol{J}_{\mathrm{s}}^{-1} \end{aligned} \tag{A.20}$$

where

$$\boldsymbol{J}_1 = \begin{bmatrix} 0 & \cos\vartheta\cos\varphi & -\sin\vartheta\sin\varphi \\ 0 & \cos\vartheta\sin\varphi & \sin\vartheta\cos\varphi \\ 0 & -\sin\vartheta & 0 \end{bmatrix}, \quad \boldsymbol{J}_2 = \begin{bmatrix} 0 & -\sin\vartheta\cos\varphi & -\cos\vartheta\sin\varphi \\ 0 & -\sin\vartheta\sin\varphi & \cos\vartheta\cos\varphi \\ 0 & -\cos\vartheta & 0 \end{bmatrix},$$

$$\boldsymbol{J}_3 = \begin{bmatrix} 0 & 0 & -\cos\varphi \\ 0 & 0 & -\sin\varphi \\ 0 & 0 & 0 \end{bmatrix}.$$

Using Eqs. (A.10), (A.15) and (A.19), the following formulas are obtained

$$\nabla\Psi = \frac{\partial\Psi}{\partial r}\boldsymbol{e}_{\mathrm{r}} + \frac{1}{r}\frac{\partial\Psi}{\partial\vartheta}\boldsymbol{e}_{\vartheta} + \frac{1}{r\sin\vartheta}\frac{\partial\Psi}{\partial\varphi}\boldsymbol{e}_{\varphi} \tag{A.21}$$

$$\nabla^2\Psi = \frac{1}{r^2}\frac{\partial}{\partial r}\left(r^2\frac{\partial\Psi}{\partial r}\right) + \frac{1}{r^2\sin\vartheta}\frac{\partial}{\partial\vartheta}\left(\sin\vartheta\frac{\partial\Psi}{\partial\vartheta}\right) + \frac{1}{r^2\sin^2\vartheta}\frac{\partial^2\Psi}{\partial\varphi^2} \tag{A.22}$$

$$\nabla\cdot\boldsymbol{\Psi} = \frac{1}{r^2}\frac{\partial(r^2\Psi_{\mathrm{r}})}{\partial r} + \frac{1}{r\sin\vartheta}\frac{\partial(\Psi_{\vartheta}\sin\vartheta)}{\partial\vartheta} + \frac{1}{r\sin\vartheta}\frac{\partial\Psi_{\varphi}}{\partial\varphi} \tag{A.23}$$

$$\begin{aligned}\nabla^2\boldsymbol{\Psi} = {} & \left(\nabla^2\Psi_{\mathrm{r}} - \frac{2}{r^2}\Psi_{\mathrm{r}} - \frac{2}{r^2\sin\vartheta}\frac{\partial(\Psi_{\vartheta}\sin\vartheta)}{\partial\vartheta} - \frac{2}{r^2\sin\vartheta}\frac{\partial\Psi_{\varphi}}{\partial\varphi}\right)\boldsymbol{e}_{\mathrm{r}} \\ & + \left(\nabla^2\Psi_{\vartheta} - \frac{1}{r^2\sin^2\vartheta}\Psi_{\vartheta} + \frac{2}{r^2}\frac{\partial\Psi_{\mathrm{r}}}{\partial\vartheta} - \frac{2\cos\vartheta}{r^2\sin^2\vartheta}\frac{\partial\Psi_{\varphi}}{\partial\varphi}\right)\boldsymbol{e}_{\vartheta} \\ & + \left(\nabla^2\Psi_{\varphi} - \frac{1}{r^2\sin^2\vartheta}\Psi_{\varphi} + \frac{2}{r^2\sin\vartheta}\frac{\partial\Psi_{\mathrm{r}}}{\partial\varphi} + \frac{2\cos\vartheta}{r^2\sin^2\vartheta}\frac{\partial\Psi_{\vartheta}}{\partial\varphi}\right)\boldsymbol{e}_{\varphi}\end{aligned} \tag{A.24}$$

$$\begin{aligned}\nabla\times\boldsymbol{\Psi} = {} & \frac{1}{r\sin\vartheta}\left(\frac{\partial}{\partial\vartheta}(\Psi_{\varphi}\sin\vartheta) - \frac{\partial\Psi_{\vartheta}}{\partial\varphi}\right)\boldsymbol{e}_{\mathrm{r}} + \frac{1}{r}\left(\frac{1}{\sin\vartheta}\frac{\partial\Psi_{\mathrm{r}}}{\partial\varphi} - \frac{\partial}{\partial r}(r\Psi_{\varphi})\right)\boldsymbol{e}_{\vartheta} \\ & + \frac{1}{r}\left(\frac{\partial}{\partial r}(r\Psi_{\vartheta}) - \frac{\partial\Psi_{\mathrm{r}}}{\partial\vartheta}\right)\boldsymbol{e}_{\varphi}.\end{aligned} \tag{A.25}$$

B. Linear elasticity

In this section the needed formulas from linear elasticity used in this paper are listed. A more comprehensive introduction to linear elasticity may be found in [44]. From the displacement field $\boldsymbol{u} = u_i\boldsymbol{e}_i$ the strain field, ε_{ij}, is defined by

$$\varepsilon_{ij} = \frac{1}{2}\left(\frac{\partial u_i}{\partial x_j} + \frac{\partial u_j}{\partial x_i}\right) \tag{B.1}$$

from which the stress field, σ_{ij}, can be obtained through the constitutive relation[14] (derived from the generalized Hooke's law)

$$\begin{bmatrix}\sigma_{11}\\ \sigma_{22}\\ \sigma_{33}\\ \sigma_{23}\\ \sigma_{13}\\ \sigma_{12}\end{bmatrix} = \boldsymbol{C}\begin{bmatrix}\varepsilon_{11}\\ \varepsilon_{22}\\ \varepsilon_{33}\\ 2\varepsilon_{23}\\ 2\varepsilon_{13}\\ 2\varepsilon_{12}\end{bmatrix} \quad \text{with} \quad \boldsymbol{C} = \begin{bmatrix}K+\frac{4G}{3} & K-\frac{2G}{3} & K-\frac{2G}{3} & 0 & 0 & 0\\ K-\frac{2G}{3} & K+\frac{4G}{3} & K-\frac{2G}{3} & 0 & 0 & 0\\ K-\frac{2G}{3} & K-\frac{2G}{3} & K+\frac{4G}{3} & 0 & 0 & 0\\ 0 & 0 & 0 & G & 0 & 0\\ 0 & 0 & 0 & 0 & G & 0\\ 0 & 0 & 0 & 0 & 0 & G\end{bmatrix} \tag{B.2}$$

[14] This representation is often referred to as the Voight notation.

where it has been assumed that the elastic material is isotropic. Note that

$$\boldsymbol{C}^{-1} = \frac{1}{E}\begin{bmatrix} 1 & -\nu & -\nu & 0 & 0 & 0 \\ -\nu & 1 & -\nu & 0 & 0 & 0 \\ -\nu & -\nu & 1 & 0 & 0 & 0 \\ 0 & 0 & 0 & 2(1+\nu) & 0 & 0 \\ 0 & 0 & 0 & 0 & 2(1+\nu) & 0 \\ 0 & 0 & 0 & 0 & 0 & 2(1+\nu) \end{bmatrix}. \tag{B.3}$$

In [44, p. 19] the transformation formula for the stress tensor from an arbitrary coordinate system to another can be found. If $\boldsymbol{e}_i$ and $\tilde{\boldsymbol{e}}_i$ represents the basis vectors of these two coordinate systems and the stress field is known in the first coordinate system, then the stress field in terms of the second coordinate system is found by

$$\tilde{\sigma}_{ij} = \alpha_{ik}\alpha_{\mathrm{s}l}\sigma_{kl}, \tag{B.4}$$

where

$$\alpha_{ij} = \cos(\tilde{\boldsymbol{e}}_i, \boldsymbol{e}_j) = \tilde{\boldsymbol{e}}_i \cdot \boldsymbol{e}_j \tag{B.5}$$

represents the cosine of the angle between the axes corresponding to the vectors $\tilde{\boldsymbol{e}}_i$ and $\boldsymbol{e}_i$. Letting $\tilde{\boldsymbol{e}}_1 = \boldsymbol{e}_{\mathrm{r}}$, $\tilde{\boldsymbol{e}}_2 = \boldsymbol{e}_\vartheta$ and $\tilde{\boldsymbol{e}}_3 = \boldsymbol{e}_\varphi$ (the basis vectors in the spherical coordinate system), and $\{\boldsymbol{e}_1, \boldsymbol{e}_2, \boldsymbol{e}_3\}$ the standard basis vectors in Cartesian coordinates, one gets (using Eq. (A.15))

$$[\alpha_{ij}] = \begin{bmatrix} \sin\vartheta\cos\varphi & \sin\vartheta\sin\varphi & \cos\vartheta \\ \cos\vartheta\cos\varphi & \cos\vartheta\sin\varphi & -\sin\vartheta \\ -\sin\varphi & \cos\varphi & 0 \end{bmatrix} = \boldsymbol{J}_{\mathrm{e}}. \tag{B.6}$$

This yields the relation

$$\begin{bmatrix} \sigma_{\mathrm{rr}} \\ \sigma_{\vartheta\vartheta} \\ \sigma_{\varphi\varphi} \\ \sigma_{\vartheta\varphi} \\ \sigma_{\mathrm{r}\varphi} \\ \sigma_{\mathrm{r}\vartheta} \end{bmatrix} = \boldsymbol{D}\begin{bmatrix} \sigma_{11} \\ \sigma_{22} \\ \sigma_{33} \\ \sigma_{23} \\ \sigma_{13} \\ \sigma_{12} \end{bmatrix} \tag{B.7}$$

where

$$\boldsymbol{D} = \begin{bmatrix} \sin^2\vartheta\cos^2\varphi & \sin^2\vartheta\sin^2\varphi & \cos^2\vartheta & \sin 2\vartheta\sin\varphi & \sin 2\vartheta\cos\varphi & \sin^2\vartheta\sin 2\varphi \\ \cos^2\vartheta\cos^2\varphi & \cos^2\vartheta\sin^2\varphi & \sin^2\vartheta & -\sin 2\vartheta\sin\varphi & -\sin 2\vartheta\cos\varphi & \cos^2\vartheta\sin 2\varphi \\ \sin^2\varphi & \cos^2\varphi & 0 & 0 & 0 & -\sin 2\varphi \\ -\frac{1}{2}\cos\vartheta\sin 2\varphi & \frac{1}{2}\cos\vartheta\sin 2\varphi & 0 & -\sin\vartheta\cos\varphi & \sin\vartheta\sin\varphi & \cos\vartheta\cos 2\varphi \\ -\frac{1}{2}\sin\vartheta\sin 2\varphi & \frac{1}{2}\sin\vartheta\sin 2\varphi & 0 & \cos\vartheta\cos\varphi & -\cos\vartheta\sin\varphi & \sin\vartheta\cos 2\varphi \\ \frac{1}{2}\sin 2\vartheta\cos^2\varphi & \frac{1}{2}\sin 2\vartheta\sin^2\varphi & -\frac{1}{2}\sin 2\vartheta & \cos 2\vartheta\sin\varphi & \cos 2\vartheta\cos\varphi & \frac{1}{2}\sin 2\vartheta\sin 2\varphi \end{bmatrix}.$$

The inverse relation is found by inverting the matrix $\boldsymbol{D}$, which takes the form

$$\boldsymbol{D}^{-1} = \begin{bmatrix} \sin^2\vartheta\cos^2\varphi & \cos^2\vartheta\cos^2\varphi & \sin^2\varphi & -\cos\vartheta\sin 2\varphi & -\sin\vartheta\sin 2\varphi & \sin 2\vartheta\cos^2\varphi \\ \sin^2\vartheta\sin^2\varphi & \cos^2\vartheta\sin^2\varphi & \cos^2\varphi & \cos\vartheta\sin 2\varphi & \sin\vartheta\sin 2\varphi & \sin 2\vartheta\sin^2\varphi \\ \cos^2\vartheta & \sin^2\vartheta & 0 & 0 & 0 & -\sin 2\vartheta \\ \frac{1}{2}\sin 2\vartheta\sin\varphi & -\frac{1}{2}\sin 2\vartheta\sin\varphi & 0 & -\sin\vartheta\cos\varphi & \cos\vartheta\cos\varphi & \sin\varphi\cos 2\vartheta \\ \frac{1}{2}\sin\vartheta\sin 2\varphi & -\frac{1}{2}\sin 2\vartheta\cos\varphi & 0 & \sin\vartheta\sin\varphi & -\cos\vartheta\sin\varphi & \cos 2\vartheta\cos\varphi \\ \frac{1}{2}\sin^2\vartheta\sin 2\varphi & \frac{1}{2}\cos^2\vartheta\sin 2\varphi & -\frac{1}{2}\sin 2\varphi & \cos\vartheta\cos 2\varphi & \cos 2\varphi\sin\vartheta & \frac{1}{2}\sin 2\vartheta\sin 2\varphi \end{bmatrix}.$$

Moreover,

$$\begin{bmatrix} \sigma_{\mathrm{rr}} \\ \sigma_{\vartheta\vartheta} \\ \sigma_{\varphi\varphi} \\ \sigma_{\vartheta\varphi} \\ \sigma_{\mathrm{r}\varphi} \\ \sigma_{\mathrm{r}\vartheta} \end{bmatrix} = \boldsymbol{C} \begin{bmatrix} \varepsilon_{\mathrm{rr}} \\ \varepsilon_{\vartheta\vartheta} \\ \varepsilon_{\varphi\varphi} \\ 2\varepsilon_{\vartheta\varphi} \\ 2\varepsilon_{r\varphi} \\ 2\varepsilon_{\mathrm{r}\vartheta} \end{bmatrix}, \tag{B.8}$$

where (cf [38, p. 150])

$$\begin{aligned} \varepsilon_{\mathrm{rr}} &= \frac{\partial u_{\mathrm{r}}}{\partial r} \\ \varepsilon_{\vartheta\vartheta} &= \frac{1}{r}\left(\frac{\partial u_\vartheta}{\partial\vartheta} + u_{\mathrm{r}}\right) \\ \varepsilon_{\varphi\varphi} &= \frac{1}{r\sin\vartheta}\left(\frac{\partial u_\varphi}{\partial\varphi} + u_{\mathrm{r}}\sin\vartheta + u_\vartheta\cos\vartheta\right) \\ \varepsilon_{\vartheta\varphi} &= \frac{1}{2r}\left(\frac{1}{\sin\vartheta}\frac{\partial u_\vartheta}{\partial\varphi} + \frac{\partial u_\varphi}{\partial\vartheta} - u_\varphi\cot\vartheta\right) \\ \varepsilon_{\mathrm{r}\varphi} &= \frac{1}{2}\left(\frac{1}{r\sin\vartheta}\frac{\partial u_{\mathrm{r}}}{\partial\varphi} + \frac{\partial u_\varphi}{\partial r} - \frac{u_\varphi}{r}\right) \\ \varepsilon_{\mathrm{r}\vartheta} &= \frac{1}{2}\left(\frac{1}{r}\frac{\partial u_{\mathrm{r}}}{\partial\vartheta} + \frac{\partial u_\vartheta}{\partial r} - \frac{u_\vartheta}{r}\right). \end{aligned} \tag{B.9}$$

Finally, note that Navier's equation of motion (Eq. (10)) in spherical coordinates are given by (cf. [38, p. 189])

$$\begin{aligned} &\frac{\partial\sigma_{\mathrm{rr}}}{\partial r} + \frac{1}{r}\frac{\partial\sigma_{\mathrm{r}\vartheta}}{\partial\vartheta} + \frac{1}{r\sin\vartheta}\frac{\partial\sigma_{\mathrm{r}\varphi}}{\partial\varphi} \\ &\qquad + \frac{1}{r}(2\sigma_{\mathrm{rr}} - \sigma_{\vartheta\vartheta} - \sigma_{\varphi\varphi} + \sigma_{\mathrm{r}\vartheta}\cot\vartheta) + \omega^2\rho_{\mathrm{s}}u_{\mathrm{r}} = 0 \end{aligned} \tag{B.10}$$

$$\frac{\partial\sigma_{\mathrm{r}\vartheta}}{\partial r} + \frac{1}{r}\frac{\partial\sigma_{\vartheta\vartheta}}{\partial\vartheta} + \frac{1}{r\sin\vartheta}\frac{\partial\sigma_{\vartheta\varphi}}{\partial\varphi} + \frac{1}{r}[(\sigma_{\vartheta\vartheta} - \sigma_{\varphi\varphi})\cot\vartheta + 3\sigma_{\mathrm{r}\vartheta}] + \omega^2\rho_{\mathrm{s}}u_\vartheta = 0 \tag{B.11}$$

$$\frac{\partial\sigma_{\mathrm{r}\varphi}}{\partial r} + \frac{1}{r}\frac{\partial\sigma_{\vartheta\varphi}}{\partial\vartheta} + \frac{1}{r\sin\vartheta}\frac{\partial\sigma_{\varphi\varphi}}{\partial\varphi} + \frac{1}{r}(2\sigma_{\vartheta\varphi}\cot\vartheta + 3\sigma_{\mathrm{r}\varphi}) + \omega^2\rho_{\mathrm{s}}u_\varphi = 0. \tag{B.12}$$

C. Fundamental functions

Exact solutions for scattering problems on spherical symmetric scatterers are heavily based on the spherical coordinate system defined in Appendix A. Some fundamental functions then naturally arise, and the notation will briefly be presented in the following.

C.1. Legendre polynomials

The Legendre polynomials are defined recursively by (cf. [45, p. 332])

$$(n+1)\mathrm{P}_{n+1}(x) = (2n+1)x\mathrm{P}_n(x) - n\mathrm{P}_{n-1}(x) \tag{C.1}$$

starting with $\mathrm{P}_0(x) = 1$ and $\mathrm{P}_1(x) = x$. From orthogonality property [43, 05.03.21.0006.01]

$$\int_{-1}^{1} \mathrm{P}_m(x)\mathrm{P}_n(x)\,\mathrm{d}x = \frac{2}{2n+1}\delta_{mn}, \tag{C.2}$$

with δ_{mn} being the Kronecker delta function, one can do a simple substitution to obtain the following expression

$$\int_{0}^{\pi} \mathrm{P}_m(\cos\vartheta)\mathrm{P}_n(\cos\vartheta)\sin\vartheta\,\mathrm{d}\vartheta = \frac{2}{2n+1}\delta_{mn}. \tag{C.3}$$

Note the following identity from the expanded Legendre equation

$$\frac{\mathrm{d}^2}{\mathrm{d}\vartheta^2}\mathrm{P}_n(\cos\vartheta) + \cot\vartheta\frac{\mathrm{d}}{\mathrm{d}\vartheta}\mathrm{P}_n(\cos\vartheta) = -n(n+1)\mathrm{P}_n(\cos\vartheta). \tag{C.4}$$

The associated Legendre polynomials is a generalization of the Legendre polynomials as they are defined by

$$\mathrm{P}_n^m(x) = (-1)^m(1-x^2)^{\frac{m}{2}}\frac{\partial^m}{\partial x^m}\mathrm{P}_n(x). \tag{C.5}$$

A convenient result of this is the following relation

$$\mathrm{P}_n^1(\cos\vartheta) = \frac{\mathrm{d}}{\mathrm{d}\vartheta}\mathrm{P}_n(\cos\vartheta). \tag{C.6}$$

Let $\left\{Q_n^{(j)}\right\}_{j\in\mathbb{N}}$ be a set of functions defined by

$$Q_n^{(j)}(\vartheta) = \frac{\mathrm{d}^j}{\mathrm{d}\vartheta^j}\mathrm{P}_n(\cos\vartheta), \tag{C.7}$$

the first four of which are given by

$$\begin{aligned}
Q_n^{(0)}(\vartheta) &= \mathrm{P}_n(\cos\vartheta) \\
Q_n^{(1)}(\vartheta) &= -\mathrm{P}'_n(\cos\vartheta)\sin\vartheta \\
Q_n^{(2)}(\vartheta) &= -\mathrm{P}'_n(\cos\vartheta)\cos\vartheta + \mathrm{P}''_n(\cos\vartheta)\sin^2\vartheta \\
Q_n^{(3)}(\vartheta) &= \mathrm{P}'_n(\cos\vartheta)\sin\vartheta + \frac{3}{2}\mathrm{P}''_n(\cos\vartheta)\sin 2\vartheta - \mathrm{P}'''_n(\cos\vartheta)\sin^3\vartheta
\end{aligned} \tag{C.8}$$

where the derivatives are found by the recursion relations

$$(n+1)\mathrm{P}'_{n+1}(x) = (2n+1)\big[\mathrm{P}_n(x) + x\mathrm{P}'_n(x)\big] - n\mathrm{P}'_{n-1}(x) \tag{C.9}$$
$$(n+1)\mathrm{P}''_{n+1}(x) = (2n+1)\big[2\mathrm{P}'_n(x) + x\mathrm{P}''_n(x)\big] - n\mathrm{P}''_{n-1}(x) \tag{C.10}$$
$$(n+1)\mathrm{P}'''_{n+1}(x) = (2n+1)\big[3\mathrm{P}''_n(x) + x\mathrm{P}'''_n(x)\big] - n\mathrm{P}'''_{n-1}(x) \tag{C.11}$$

starting with

$$\begin{aligned}
&\mathrm{P}'_0(x) = 0, \quad \mathrm{P}'_1(x) = 1, \quad \mathrm{P}'_2(x) = 3x \\
&\mathrm{P}''_0(x) = 0, \quad \mathrm{P}''_1(x) = 0, \quad \mathrm{P}''_2(x) = 3, \quad \mathrm{P}''_3(x) = 15x \\
&\mathrm{P}'''_0(x) = 0, \quad \mathrm{P}'''_1(x) = 0, \quad \mathrm{P}'''_2(x) = 0, \quad \mathrm{P}'''_3(x) = 15, \quad \mathrm{P}'''_4(x) = 105x.
\end{aligned}$$

Note that the formulas in Eq. (C.8) can be rewritten in the following way

$$Q_n^{(1)}(\vartheta) = \frac{n}{\sin\vartheta}[\mathrm{P}_n(\cos\vartheta)\cos\vartheta - \mathrm{P}_{n-1}(\cos\vartheta)] \tag{C.12}$$
$$Q_n^{(2)}(\vartheta) = \frac{n}{\sin^2\vartheta}\Big[-\Big(n\sin^2\vartheta + 1\Big)\mathrm{P}_n(\cos\vartheta) - \mathrm{P}_{n-1}(\cos\vartheta)\cos\vartheta\Big]. \tag{C.13}$$

From Eq. (C.4) the following relations can be obtained

$$Q_n^{(2)}(\vartheta) = -Q_n^{(1)}(\vartheta)\cot\vartheta - n(n+1)Q_n^{(0)}(\vartheta) \tag{C.14}$$
$$Q_n^{(3)}(\vartheta) = -Q_n^{(2)}(\vartheta)\cot\vartheta + Q_n^{(1)}(\vartheta)\cot^2\vartheta + (-n^2 - n + 1)Q_n^{(1)}(\vartheta). \tag{C.15}$$

C.2. Spherical Bessel and Hankel functions

The Bessel functions of the first kind can be defined by [45, p. 360]

$$\mathrm{J}_\upsilon(x) = \sum_{m=0}^{\infty} \frac{(-1)^m}{m!\Gamma(m+\upsilon+1)}\left(\frac{x}{2}\right)^{2m+\upsilon}, \tag{C.16}$$

while the Bessel functions of the second kind are defined by

$$\mathrm{Y}_\upsilon(x) = \frac{\mathrm{J}_\upsilon(x)\cos(\upsilon\pi) - \mathrm{J}_{-\upsilon}(x)}{\sin(\upsilon\pi)}, \tag{C.17}$$

where

$$\mathrm{Y}_n(x) = \lim_{\upsilon \to n} \mathrm{Y}_\upsilon(x) \tag{C.18}$$

whenever $n \in \mathbb{Z}$ (cf. [45, p. 358]). These definitions may be used to define the *spherical Bessel functions*. The spherical Bessel functions of the first kind are defined by (cf. [45, p. 437])

$$\mathrm{j}_n(x) = \sqrt{\frac{\pi}{2x}}\mathrm{J}_{n+\frac{1}{2}}(x) \tag{C.19}$$

and the second kind are defined by

$$\mathrm{y}_n(x) = \sqrt{\frac{\pi}{2x}}\mathrm{Y}_{n+\frac{1}{2}}(x). \tag{C.20}$$

Some important limits of the spherical Bessel function of the first kind at the origin are [43, 03.21.20.0016.01 and 03.21.20.0017.01]

$$\lim_{x\to 0} \mathrm{j}_0(x) = 1, \quad \lim_{x\to 0} \mathrm{j}_n(x) = 0 \quad \forall n \in \mathbb{N}^* \tag{C.21}$$

$$\lim_{x\to 0} \frac{\mathrm{d}}{\mathrm{d}x}\mathrm{j}_1(x) = \frac{1}{3}, \quad \lim_{x\to 0} \frac{\mathrm{d}}{\mathrm{d}x}\mathrm{j}_n(x) = 0 \quad \forall n \in \mathbb{N} \setminus \{1\} \tag{C.22}$$

$$\lim_{x\to 0} \frac{\mathrm{d}^2}{\mathrm{d}x^2}\mathrm{j}_0(x) = -\frac{1}{3}, \quad \lim_{x\to 0} \frac{\mathrm{d}^2}{\mathrm{d}x^2}\mathrm{j}_2(x) = \frac{2}{15}, \quad \lim_{x\to 0} \frac{\mathrm{d}^2}{\mathrm{d}x^2}\mathrm{j}_n(x) = 0 \quad \forall n \in \mathbb{N} \setminus \{0, 2\}. \tag{C.23}$$

From this the following limits are obtained

$$\lim_{x\to 0^+} \frac{\mathrm{j}_n(x)}{x} = \begin{cases} \infty & n = 0 \\ \frac{1}{3} & n = 1 \\ 0 & n > 1 \end{cases} \tag{C.24}$$

and

$$\lim_{x\to 0^+} \frac{\mathrm{j}_n(x)}{x^2} = \begin{cases} \infty & n = 0, 1 \\ \frac{1}{15} & n = 2 \\ 0 & n > 2. \end{cases} \tag{C.25}$$

A couple of convenient identities involving the derivatives of the spherical Bessel functions are given by [43, 03.21.20.0007.01 and 03.21.20.0008.01]

$$\frac{\mathrm{d}}{\mathrm{d}x} Z_n^{(i)}(x) = Z_{n-1}^{(i)}(x) - \frac{n+1}{x} Z_n^{(i)}(x) \tag{C.26}$$

$$\frac{\mathrm{d}}{\mathrm{d}x} Z_n^{(i)}(x) = \frac{n}{x} Z_n^{(i)}(x) - Z_{n+1}^{(i)}(x) \tag{C.27}$$

for $i = 1, 2$. By combining these two formulas, one can compute higher order derivatives. For example

$$\frac{\mathrm{d}^2}{\mathrm{d}x^2} Z_n^{(i)}(x) = \left[\frac{n(n-1)}{x^2} - 1\right] Z_n^{(i)}(x) + \frac{2}{x} Z_{n+1}^{(i)}(x). \tag{C.28}$$

The spherical Hankel functions of the first and second kind can now be expressed by

$$\mathrm{h}_n^{(1)}(x) = \mathrm{j}_n(x) + \mathrm{i}\mathrm{y}_n(x) \tag{C.29}$$

and

$$\mathrm{h}_n^{(2)}(x) = \mathrm{j}_n(x) - \mathrm{i}\mathrm{y}_n(x). \tag{C.30}$$

respectively. Two important limits for spherical Hankel functions are [37, p. 25]

$$\lim_{x\to\infty} x\mathrm{e}^{-\mathrm{i}x}\mathrm{h}_n^{(1)}(x) = \mathrm{i}^{-n-1} \tag{C.31}$$

$$\lim_{x\to\infty} x\mathrm{e}^{\mathrm{i}x}\mathrm{h}_n^{(2)}(x) = \mathrm{i}^{n+1} \tag{C.32}$$

One can trivially show that the Eqs. (C.26) to (C.28) holds for spherical Hankel functions as well

$$\frac{\mathrm{d}}{\mathrm{d}x}\mathrm{h}_n^{(i)}(x) = \mathrm{h}_{n-1}^{(i)}(x) - \frac{n+1}{x}\mathrm{h}_n^{(i)}(x) \tag{C.33}$$

$$\frac{\mathrm{d}}{\mathrm{d}x}\mathrm{h}_n^{(i)}(x) = \frac{n}{x}\mathrm{h}_n^{(i)}(x) - \mathrm{h}_{n+1}^{(i)}(x) \tag{C.34}$$

$$\frac{\mathrm{d}^2}{\mathrm{d}x^2}\mathrm{h}_n^{(i)}(x) = \left[\frac{n(n-1)}{x^2} - 1\right]\mathrm{h}_n^{(i)}(x) + \frac{2}{x}\mathrm{h}_{n+1}^{(i)}(x), \tag{C.35}$$

for $i = 1, 2$.

D. The incident wave

The coefficients $F_n^{(1)}$ and $F_n^{(2)}$ in Eq. (74) may be computed by using the orthogonality property of the Legendre polynomials in Eq. (C.3). In fact, any square integrable function $\Psi(\vartheta)$ on the interval $[0, \pi]$ can be written as (see [37, p. 27])

$$\Psi(\vartheta) = \sum_{n=0}^{\infty} \Psi_n \mathrm{P}_n(\cos\vartheta) \tag{D.1}$$

where

$$\Psi_n = \frac{2n+1}{2} \int_0^{\pi} \Psi(\vartheta)\mathrm{P}_n(\cos\vartheta)\sin\vartheta\,\mathrm{d}\vartheta. \tag{D.2}$$

For example, a plane wave traveling along the x_3-axis can be expanded as [45, 10.1.47]

$$\begin{aligned} p_{\mathrm{inc}}(\boldsymbol{x},\omega) &= P_{\mathrm{inc}}(\omega)\mathrm{e}^{\mathrm{i}k_1 x_3} = P_{\mathrm{inc}}(\omega)\mathrm{e}^{\mathrm{i}k_1 r\cos\vartheta} \\ &= P_{\mathrm{inc}}(\omega)\sum_{n=0}^{\infty}(2n+1)\mathrm{i}^n j_n(k_1 r)\mathrm{P}_n(\cos\vartheta) \end{aligned} \tag{D.3}$$

such that

$$F_n^{(1)} = P_{\mathrm{inc}}(\omega)(2n+1)\mathrm{i}^n j_n(k_1 R_{0,1}) \tag{D.4}$$

$$F_n^{(2)} = P_{\mathrm{inc}}(\omega)(2n+1)\mathrm{i}^n k_1 j_n'(k_1 R_{0,1}). \tag{D.5}$$

Another example of an incident wave satisfying the axisymmetry property, is a wave due to a point source located at $\boldsymbol{x}_{\mathrm{s}} = -r_{\mathrm{s}}\boldsymbol{e}_3$. The incident wave can then be expressed with the fundamental solution of the Helmholtz equation

$$p_{\mathrm{inc}}(\boldsymbol{x},\omega) = P_{\mathrm{inc}}(\omega)\frac{r_{\mathrm{s}}}{|\boldsymbol{x}_{\mathrm{s}}-\boldsymbol{x}|}\mathrm{e}^{\mathrm{i}k_1|\boldsymbol{x}_{\mathrm{s}}-\boldsymbol{x}|}, \quad |\boldsymbol{x}_{\mathrm{s}}-\boldsymbol{x}| = \sqrt{r^2+2r_{\mathrm{s}}r\cos\vartheta+r_{\mathrm{s}}^2}. \tag{D.6}$$

By a simple substitution $v = \cos\vartheta$ in Eq. (D.2) one gets

$$\begin{aligned} F_n^{(1)} &= P_{\mathrm{inc}}(\omega)\frac{2n+1}{2}r_{\mathrm{s}}\int_{-1}^{1}\frac{\mathrm{e}^{\mathrm{i}k_1 q(v)}}{q(v)}\mathrm{P}_n(v)\,\mathrm{d}v \\ F_n^{(2)} &= P_{\mathrm{inc}}(\omega)\frac{2n+1}{2}r_{\mathrm{s}}\int_{-1}^{1}(R_{0,1}+r_{\mathrm{s}}v)\frac{\mathrm{e}^{\mathrm{i}k_1 q(v)}}{q^3(v)}[\mathrm{i}k_1 q(v)-1]\mathrm{P}_n(v)\,\mathrm{d}v \end{aligned} \tag{D.7}$$

where

$$q(v) = \sqrt{R_{0,1}^2+2r_{\mathrm{s}}R_{0,1}v+r_{\mathrm{s}}^2}.$$

One can obtain simple expressions for some of these coefficients, for example

$$F_0^{(1)} = P_{\mathrm{inc}}(\omega)\,\mathrm{sinc}(k_1 R_{0,1})\mathrm{e}^{\mathrm{i}k_1 r_{\mathrm{s}}}.$$

But in general, one needs to use a numerical routine to evaluate the integrals in Eq. (D.7).

References

[1] V. C. Anderson, Sound scattering from a fluid sphere, *The Journal of the Acoustical Society of America*, 22:426–431 (1950).

[2] J. J. Faran, Sound scattering by solid cylinders and spheres, *The Journal of the Acoustical Society of America*, 23:405–418 (1951).

[3] R. E. Anderson, Scattering of acoustic pulses by a solid sphere in air, *The Journal of the Acoustical Society of America*, 27:1006–1006 (1955).

[4] R. Hickling, Analysis of echoes from a solid elastic sphere in water, *The Journal of the Acoustical Society of America*, 34:1582–1592 (1962).

[5] R. D. Doolittle, H. Überall, P. Uginčius, Sound scattering by elastic cylinders, *The Journal of the Acoustical Society of America*, 43:1–14 (1968).

[6] L. Flax, L. R. Dragonette, H. Überall, Theory of elastic resonance excitation by sound scattering, *The Journal of the Acoustical Society of America*, 63:723–731 (1978).

[7] G. C. Gaunaurd, H. Überall, RST analysis of monostatic and bistatic acoustic echoes from an elastic sphere, *The Journal of the Acoustical Society of America*, 73:1–12 (1983).

[8] R. Hickling, Analysis of echoes from a hollow metallic sphere in water, *The Journal of the Acoustical Society of America*, 36:1124–1137 (1964).

[9] R. D. Doolittle, H. Überall, Sound scattering by elastic cylindrical shells, *The Journal of the Acoustical Society of America*, 39:272–275 (1966).

[10] G. C. Gaunaurd, M. F. Werby, Lamb and creeping waves around submerged spherical shells resonantly excited by sound scattering, *The Journal of the Acoustical Society of America*, 82:2021–2033 (1987).

[11] G. C. Gaunaurd, M. F. Werby, Sound scattering by resonantly excited, fluid-loaded, elastic spherical shells, *The Journal of the Acoustical Society of America*, 90:2536–2550 (1991).

[12] G. Kaduchak, C. Loeffler, Relationship between material parameters and target strength of fluid-filled spherical shells in water: calculations and observations, *IEEE Journal of Oceanic Engineering*, 23:26–30 (1998).

[13] Y. C. Chang, L. Demkowicz, *Vibrations of a spherical shell comparison of 3-D elasticity and Kirchhoff shell theory results*, no. 6 in TICAM report, Texas Institute for Computational and Applied Mathematics, University of Texas at Austin, 1994.

[14] Y. C. Chang, L. Demkowicz, *Scattering on a Spherical Shell Problem: Comparison of 3-D Elasticity and Kirchhoff Shell Theory Results*, no. 12 in TICAM report, Texas Institute for Computational and Applied Mathematics, University of Texas at Austin, 1994.

[15] W. F. Fender, Scattering from an elastic spherical shell, Tech. rep., DTIC Document (1972).

[16] L. Flax, G. C. Gaunaurd, H. Überall, *Physical Acoustics*, vol. XV, Academic Press, 1981, ch. Theory of Resonance Scattering.

[17] W. H. Lin, A. C. Raptis, Acoustic scattering by elastic solid cylinders and spheres in viscous fluids, *The Journal of the Acoustical Society of America*, 73:736–748 (1983).

[18] S. Hasheminejad, N. Safari, Acoustic scattering from viscoelastically coated spheres and cylinders in viscous fluids, *Journal of Sound and Vibration*, 280:101–125 (2005).

[19] X. Bao, H. Cao, H. Überall, Resonances and surface waves in the scattering of an obliquely incident acoustic field by an infinite elastic cylinder, *The Journal of the Acoustical Society of America*, 87:106–110 (1990).

[20] K. Daneshjou, R. Talebitooti, A. Tarkashvand, An exact solution of three-dimensional elasticity for sound transmission loss through FG cylinder in presence of subsonic external flow, *International Journal of Mechanical Sciences*, 120:105–119 (2017).

[21] P. L. Marston, Acoustic beam scattering and excitation of sphere resonance: Bessel beam example, *The Journal of the Acoustical Society of America*, 122:247–252 (2007).

[22] Z. Gong, W. Li, F. G. Mitri, Y. Chai, Y. Zhao, Arbitrary scattering of an acoustical bessel beam by a rigid spheroid with large aspect-ratio, *Journal of Sound and Vibration*, 383:233–247 (2016).

[23] J. A. Fawcett, Scattering from a partially fluid-filled, elastic-shelled sphere, *The Journal of the Acoustical Society of America*, 109:508–513 (2001).

[24] G. Elias, P. Malbéqui, Scattering by an open sphere: Exact solution and comparison with a boundary integral method, *The Journal of the Acoustical Society of America*, 90:2368–2369 (1991).

[25] P. Gabrielli, M. Mercier-Finidori, Acoustic scattering by two spheres: Multiple scattering and symmetry considerations, *Journal of Sound and Vibration*, 241:423–439 (2001).

[26] J. Wu, A. Liu, H. Chen, T. Chen, Multiple scattering of a spherical acoustic wave from fluid spheres, *Journal of Sound and Vibration*, 290:17–33 (2006).

[27] M. Zampolli, F. B. Jensen, A. Tesei, Benchmark problems for acoustic scattering from elastic objects in the free field and near the seafloor, *The Journal of the Acoustical Society of America*, 125:89–98 (2009).

[28] T. K. Stanton, P. H. Wiebe, D. Chu, Differences between sound scattering by weakly scattering spheres and finite-length cylinders with applications to sound scattering by zooplankton, *The Journal of the Acoustical Society of America*, 103:254–264 (1998).

[29] T. K. Stanton, D. Chu, P. H. Wiebe, R. L. Eastwood, J. D. Warren, Acoustic scattering by benthic and planktonic shelled animals, *The Journal of the Acoustical Society of America*, 108:535–550 (2000).

[30] J. Sessarego, J. Sageloli, R. Guillermin, H. Überall, Scattering by an elastic sphere embedded in an elastic isotropic medium, *The Journal of the Acoustical Society of America*, 104:2836–2844 (1998).

[31] P. N. T. Wells, Ultrasound imaging, *Physics in Medicine and Biology*, 51:R83–R98 (2006).

[32] V. M. Ayres, G. C. Gaunaurd, Inverse acoustic scattering from an elastic sphere, *The Journal of the Acoustical Society of America*, 82:1291–1302 (1987).

[33] E. Avital, T. Miloh, Sound scattering and its cancellation by an elastic spherical shell in free space and near a free surface, *Wave Motion*, 55:35–47 (2015).

[34] R. Talebitooti, M. Zarastvand, M. Gheibi, Acoustic transmission through laminated composite cylindrical shell employing third order shear deformation theory in the presence of subsonic flow, *Composite Structures*, 157:95–110 (2016).

[35] T. Jenserud, D. Tollefsen, Acoustic resonance scattering from multilayered objects - a normal mode model, Tech. rep., FFI (1990).

[36] H. Schmidt, F. B. Jensen, A full wave solution for propagation in multilayered viscoelastic media with application to Gaussian beam reflection at fluid–solid interfaces, *The Journal of the Acoustical Society of America*, 77:813–825 (1985).

[37] F. Ihlenburg, *Finite Element Analysis of Acoustic Scattering*, vol. 132 of *Applied Mathematical Sciences*, Springer, New York, USA, 1998.

[38] W. S. Slaughter, *The Linearized Theory of Elasticity*, Birkhäuser Boston, Boston, USA, 2002.

[39] ISO, Quantities and units - Part 2: Mathematical signs and symbols to be used in the natural sciences and technology, Tech. rep., International Organization for Standardization, Geneva, Switzerland (2009).

[40] F. B. Jensen, W. A. Kuperman, M. B. Porter, H. Schmidt, *Computational Ocean Acoustics*, 2nd edition, Springer New York, 2011.

[41] R. R. Goodman, R. Stern, Reflection and transmission of sound by elastic spherical shells, *The Journal of the Acoustical Society of America*, 34:338–344 (1962).

[42] A. Sommerfeld, *Partial differential equations in physics*, vol. 1, Academic press, 1949.

[43] Wolfram Research, Inc., Mathematica.

[44] P. L. Gould, *Introduction to Linear Elasticity*, Springer New York, New York, USA, 1994.

[45] M. Abramowitz, I. A. Stegun, *Handbook of Mathematical Function: With Formulas, Graphs, and Mathematical Tables*, Dover, New York, USA, 1965.

Paper II

Isogeometric Analysis of Acoustic Scattering using Infinite Elements

Jon Vegard Venås, Trond Kvamsdal and Trond Jenserud

Published in *Computer Methods in Applied Mechanics and Engineering*
(2018) **335**:152–193

Isogeometric Analysis of Acoustic Scattering using Infinite Elements

Jon Vegard Venås[a,*], Trond Kvamsdal[a], Trond Jenserud[b]

[a] *Department of Mathematical Sciences, Norwegian University of Science and Technology, Alfred Getz' vei 1, 7034 Trondheim, Norway*
[b] *Department of Marine Systems, Norwegian Defence Research Establishment, Postboks 115, 3191 Horten, Norway*

Abstract

Isogeometric analysis (IGA) has proven to be an improvement on the classical finite element method (FEM) in several fields, including structural mechanics and fluid dynamics. In this paper, the performance of IGA coupled with the infinite element method (IEM) for some acoustic scattering problems is investigated. In particular, the simple problem of acoustic scattering by a rigid sphere, and the scattering of acoustic waves by an elastic spherical shell with fluid domains both inside and outside, representing a full acoustic-structure interaction (ASI) problem. Finally, a mock shell and a simplified submarine benchmark are investigated. The numerical examples include comparisons between IGA and the FEM. Our main finding is that the usage of IGA significantly increases the accuracy compared to the usage of C^0 FEM due to increased inter-element continuity of the spline basis functions.

1. Introduction

Acoustic scattering is the physical phenomena of how sound interacts with objects and medium fluctuations. When an acoustic wave hits a rigid object, it is totally reflected, and the object is left in a quiescent state. In the case of an elastic object, part of the sound is transmitted into the object, which is set into motion and starts radiating sound. This leads to a coupled acoustic-structure interaction (ASI) problem. Applications include underwater acoustics [1] and noise propagation in air [2]. Inverse problems are also of interest, such as shape optimization of membranes [3] and the problem of designing submarines with low scattering strength. Assuming harmonic time dependency, the fluid and solid media can be

*Corresponding author.
Email addresses: Jon.Venas@ntnu.no (J.V. Venås), Trond.Kvamsdal@ntnu.no (T. Kvamsdal), Trond.Jenserud@ffi.no (T. Jenserud).

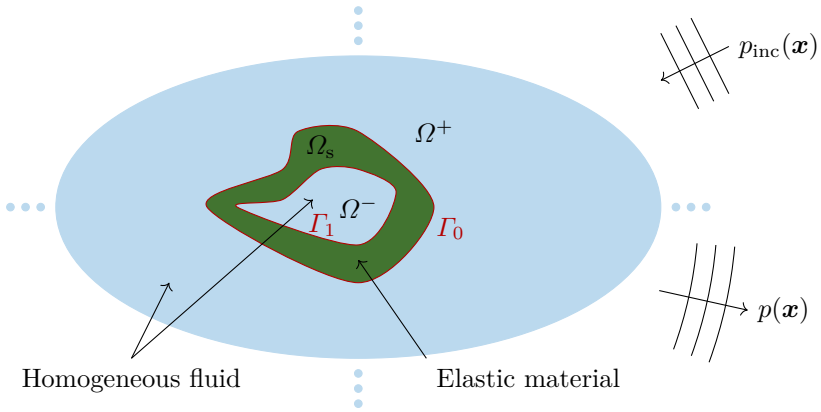

Figure 1: Illustration of the physical problem. A plane incident wave, $p_{\text{inc}}(\boldsymbol{x})$, is scattered by the scatterer, Ω_{s}, in an unbounded domain, Ω^+, resulting in the scattered wave, $p(\boldsymbol{x})$. The scatterer, which is bounded by the boundaries Γ_0 and Γ_1, envelops a fluid domain, Ω^-.

modeled using the scalar and vector Helmholtz equations, respectively. The vector Helmholtz equation can be used to model electromagnetic waves [4], such that the work presented herein can also be used for electromagnetic scattering.

Herein, the acoustic scattering characterized by sound waves reflected by man-made elastic objects will be addressed. Shape optimization for optimal acoustic scattering on man-made objects, e.g. antennas, submarines etc., is a typical problem facing design engineers.

Isogeometric analysis (IGA) is basically an extension of the finite element method (FEM) using non-uniform rational B-splines (NURBS) as basis functions not only representing the solution space, but also the geometry. Being introduced in 2005 by Hughes et al. [5], followed by the book [6] in 2009, IGA tries to bridge the gap between finite element analysis (FEA) and computer aided design (CAD) tools. The important feature of IGA is that it uses the same basis as CAD software for describing the given geometry, and thus exact representation of the model is possible.

The physical problem is illustrated in Figure 1 where the incoming sound waves, p_{inc}, originate from a point source far from this object, such that the (spherical) sound waves are quite accurately approximated by plane waves when the waves reaches the proximity of the object. For rigid objects of irregular shape, the incoming wave may be reflected multiple times before leaving the object. When the object is elastic a coupled ASI problem results. The goal is then to calculate the scattered wave p at an arbitrary far field point. Finally, to use the FEM or IGA the domain must be finite. A fictitious boundary is thus introduced, which must be implemented in such a way that outgoing waves reaching this boundary

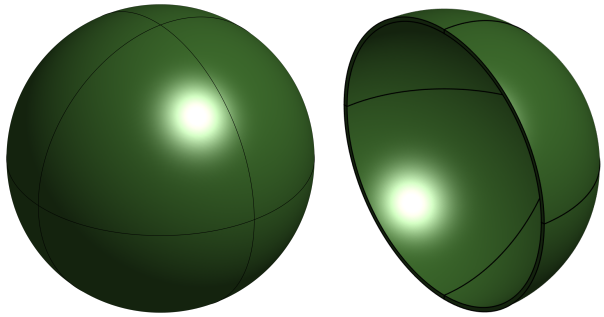

Figure 2: Exact geometry of a spherical shell using 8 elements.

are absorbed.

The problem at hand is time dependent. However, harmonic time dependency will be assumed, such that all time dependent functions may be written as $\breve{F} = \breve{F}(\boldsymbol{x}, t) = F(\boldsymbol{x})\mathrm{e}^{-\mathrm{i}\omega t}$ where ω is the angular frequency and $\mathrm{i} = \sqrt{-1}$ the imaginary unit. This enables us to model the pressure p in the fluid with the Helmholtz equation given by

$$\nabla^2 p + k^2 p = 0 \tag{1}$$

with the wave number $k = \frac{\omega}{c_\mathrm{f}}$ (where c_f is the wave speed in the fluid). Other important quantities include the frequency $f = \frac{\omega}{2\pi}$ and the wavelength $\lambda = \frac{2\pi}{k}$.

The geometry of the elastic object may be quite complex but is typically exactly represented using NURBS. This fact is one of the motivating factors for using IGA, as it uses the same functions as basis functions for analysis. The spherical shell depicted in Figure 2 is an example of a geometry that has an exact representation using NURBS but is outside the space of standard (Lagrangian) FEM geometries.

It has been shown that the continuity of the basis functions plays an important role for the accuracy of solving elliptical problems (for instance the Helmholtz equation), see [7] and [8]. This motivates the use of IGA even further, as IGA enables control of the continuity of the basis function up to C^{p-1} (in contrast with the C^0-continuity restriction in FEA). IGA has proven to be promising in a host of areas related to the problem at hand, which yields further motivation in the use of IGA. For instance, in [9] the method was shown to be suited for the more complex scenario of sound propagation through laminar flow.

In addition to IGA, the so-called infinite element method (IEM) has been chosen to handle the boundary conditions at the artificial boundary. Typically, the boundary element method (BEM) [10, 11] has been used for this purpose. However, for higher frequencies and complex geometries, BEM becomes computationally expensive (although improvement in performance has been done in the recent decades [12]). The main motivation for the infinite element method is computational efficiency as reported by Burnett [13] and Gerdes and Demkowicz [14].

Before starting on the full ASI problem, it is important to establish good results for the IEM. This method only applies for the outer fluid, and it would thus be natural to first investigate the scattering problem on rigid objects (that is, no acoustic-structure interaction occurs). An introduction to the IEM is presented in Section 2. The extension to ASI problems (presented in Section 3) naturally follows from the implementation of rigid scattering using IEM. In Section 4 the results obtained for both rigid and elastic scattering on a spherical shell is presented. Results for rigid scattering from a mock shell are included to investigate condition numbers. Moreover, results for a simplified submarine is presented to illustrate the performance of the implementation on complex geometries. Finally, conclusions and suggested future work can be found in Section 5.

2. Exterior Helmholtz problems

Scattering problems involve *unbounded exterior domains*, Ω^+. A common method for solving such problems with the FEM is to introduce an artificial boundary that encloses the scatterer. On the artificial boundary some sort of absorbing boundary condition (ABC) is prescribed. The problem is then reduced to a finite domain, and both the elastic scatterer and the bounded domain between the scatterer and the artificial boundary can be discretized with finite elements. Several methods exist for handling the exterior Helmholtz problem (on unbounded domain), including

- the perfectly matched layer (PML) method after Bérenger [15, 16]
- the boundary element method [10, 11, 17, 18]
- Dirichlet to Neumann-operators (DtN-operators) [19]
- local differential ABC operators [20–23]
- the infinite element method. [24, 25]

Herein, the infinite element method is chosen. For the IEM, the unbounded domain Ω^+ is partitioned into two domains by the artificial boundary Γ_a; Ω_a and Ω_a^+ (see Figure 3). These domains are discretized by finite and infinite elements, respectively. A convergence analysis of a coupled FEM-IEM can be found in [26].

The exterior Helmholtz problem is given by

$$\nabla^2 p + k^2 p = 0 \qquad \text{in} \quad \Omega^+, \tag{2}$$

$$\partial_n p = g \qquad \text{on} \quad \Gamma_0, \tag{3}$$

$$\frac{\partial p}{\partial r} - \mathrm{i}kp = o\Big(r^{-1}\Big) \quad \text{with} \quad r = |\boldsymbol{x}| \tag{4}$$

where the Sommerfeld condition [27] in Eq. (4) restricts the field in the limit $r \to \infty$ uniformly in $\hat{\boldsymbol{x}} = \frac{\boldsymbol{x}}{r}$, such that no waves originate from infinity. The

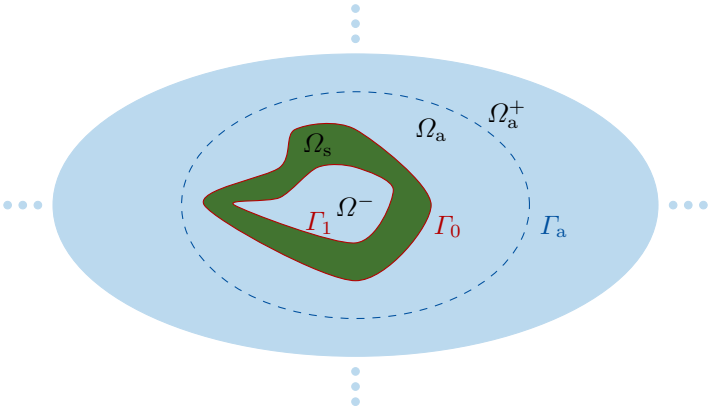

Figure 3: An artificial boundary Γ_a is introduced such that the exterior domain Ω^+ is decomposed by the two domains Ω_a (which is bounded by Γ_0 and Γ_a) and Ω_a^+. Thus, $\Omega^+ = \Omega_a \cup \Omega_a^+$.

Neumann condition given by the function g will in the case of rigid scattering be given by the incident wave p_{inc}. Zero displacement of the fluid normal on the scatterer (rigid scattering) implies that $\partial_n(p + p_{inc}) = 0$ where ∂_n denotes the partial derivative in the normal direction on the surface Γ_0 (pointing "out" from Ω^+), which implies that

$$g = -\frac{\partial p_{inc}}{\partial n}. \tag{5}$$

Plane incident waves (with amplitude P_{inc}) traveling in the direction $\boldsymbol{d}_s$ can be written as

$$p_{inc} = P_{inc} e^{ik\boldsymbol{d}_s \cdot \boldsymbol{x}}. \tag{6}$$

The normal derivative on the surface of any smooth geometry may then be computed by

$$\frac{\partial p_{inc}}{\partial n} = \boldsymbol{n} \cdot \nabla p_{inc} = ik\boldsymbol{d}_s \cdot \boldsymbol{n} p_{inc}. \tag{7}$$

2.1. Weak formulation for the Helmholtz equation

In order to choose the correct solution space in the infinite element method, the asymptotic behavior of the scattered pressure p at large radii[1] r must be examined. In [28], Wilcox shows that the scalar pressure field $p(\boldsymbol{x})$ satisfying the Helmholtz

[1]Here, r is referred to as the radius even though it does not necessarily represent the radius in spherical coordinates.

equation and the Sommerfeld radiation conditions can be written in the form[2]

$$p(\boldsymbol{x}) = \frac{\mathrm{e}^{\mathrm{i}kr}}{r} \sum_{n=0}^{\infty} \frac{p_n(\vartheta, \varphi)}{r^n}, \tag{8}$$

which implies that $|p| = \mathcal{O}(r^{-1})$ asymptotically for large r. Considering a function which represents this asymptotic property

$$\Psi(r) = \frac{\mathrm{e}^{\mathrm{i}kr}}{r}, \tag{9}$$

one can observe that the L^2 Hermitian inner product does not exist. Indeed, if Γ_0 is the unit sphere then

$$(\Psi, \Psi)_{L^2} = \int_{\Omega^+} \frac{\mathrm{e}^{\mathrm{i}kr}}{r} \frac{\mathrm{e}^{-\mathrm{i}kr}}{r} \,\mathrm{d}\Omega = 4\pi \int_1^{\infty} \frac{1}{r^2} r^2 \,\mathrm{d}r,$$

which is not finite. The solution to the problem is to introduce weighted norms by defining the inner product

$$(p, q)_w = \int_{\Omega^+} w p \bar{q} \,\mathrm{d}\Omega, \qquad \text{with} \quad w = \frac{1}{r^2}. \tag{10}$$

The following norm may then be induced

$$\|p\|_{1,w} = \sqrt{(p, p)_w + (\nabla p, \nabla p)_w} \tag{11}$$

such that the trial functions satisfy $\|p\|_{1,w} < \infty$. The integrals

$$\int_{\Omega^+} p \bar{q} \,\mathrm{d}\Omega \quad \text{and} \quad \int_{\Omega^+} \nabla p \cdot \nabla \bar{q} \,\mathrm{d}\Omega \tag{12}$$

are well defined if the test functions q are such that

$$(q, q)_{w^*} < \infty \quad \text{and} \quad (\nabla q, \nabla q)_{w^*} < \infty \tag{13}$$

with the inner product

$$(p, q)_{w^*} = \int_{\Omega^+} w^* p \bar{q} \,\mathrm{d}\Omega, \qquad \text{with} \quad w^* = r^2, \tag{14}$$

and the corresponding norm

$$\|p\|_{1,w^*} = \sqrt{(p, p)_{w^*} + (\nabla p, \nabla p)_{w^*}}. \tag{15}$$

[2] In some appropriate coordinate system (r, ϑ, φ) with the "radial variable", r, extending to infinity. Typically, some degeneration of the ellipsoidal (in 3D) coordinate system.

Define now the following *weighted Sobolev spaces* for the trial- and test spaces

$$H^1_w(\Omega^+) = \{p \,:\, \|p\|_{1,w} < \infty\} \quad \text{and} \quad H^1_{w^*}(\Omega^+) = \{q \,:\, \|q\|_{1,w^*} < \infty\}, \tag{16}$$

respectively. These definitions will not ensure that all trial function satisfy the Sommerfeld condition. Leis solved this problem in [29] by modifying the trial space to be

$$H^{1+}_w(\Omega^+) = \{p \,:\, \|p\|^+_{1,w} < \infty\} \tag{17}$$

where

$$\|p\|^+_{1,w} = \sqrt{\|p\|^2_{1,w} + \int_{\Omega^+} \left| \frac{\partial p}{\partial r} - \mathrm{i}kp \right|^2 \mathrm{d}\Omega}. \tag{18}$$

For a more detailed discussion of the functional analysis involved in these spaces refer to the book by Ihlenburg [30, pp. 41-43].

The weak form of the Helmholtz equation may now be found by multiplying Eq. (2) with a test function and integration over the domain

$$\int_{\Omega^+} \left[q\nabla^2 p + k^2 qp \right] \mathrm{d}\Omega = 0.$$

Using Greens first identity this can be written as

$$-\int_{\Omega^+} \nabla q \cdot \nabla p \,\mathrm{d}\Omega + \int_{\partial\Omega^+} q\nabla p \cdot \boldsymbol{n} \,\mathrm{d}\Gamma + k^2 \int_{\Omega^+} qp \,\mathrm{d}\Omega = 0.$$

Thus,

$$\int_{\Omega^+} \nabla q \cdot \nabla p \,\mathrm{d}\Omega - k^2 \int_{\Omega^+} qp \,\mathrm{d}\Omega = \int_{\partial\Omega^+} qg \,\mathrm{d}\Gamma. \tag{19}$$

The weak formulation then becomes:

$$\text{Find} \quad p \in H^{1+}_w(\Omega^+) \quad \text{such that} \quad B(q,p) = L(q), \qquad \forall q \in H^1_{w^*}(\Omega^+), \tag{20}$$

where the bilinear form is given by

$$B(q,p) = \int_{\Omega^+} \left[\nabla q \cdot \nabla p - k^2 qp \right] \mathrm{d}\Omega$$

and the corresponding linear form is given by

$$L(q) = \int_{\Gamma_0} qg \,\mathrm{d}\Gamma.$$

2.2. Infinite elements

In the following, a derivation of the weak formulation for infinite elements using a prolate spheroidal coordinate system is presented (cf. [13]). The IEM is typically presented with four infinite element formulations:

- Petrov–Galerkin conjugated (PGC)
- Petrov–Galerkin unconjugated (PGU)
- Bubnov–Galerkin conjugated (BGC)
- Bubnov–Galerkin unconjugated (BGU)

The Petrov–Galerkin formulations are based on the weighted Sobolev spaces after Leis [29]. It turns out that it is possible to create Bubnov–Galerkin formulations as well when the integration in the weak formulation is understood in the sense of the Cauchy principal value (consider [13] and [31] for details). These spaces differ compared to the Petrov–Galerkin counterpart in that the test space and trial space are equal. The difference between the conjugated formulations and the unconjugated formulations is simply conjugations of the test functions in the weak formulation. The accuracy of these formulations has been assessed in the overview in [32].

The idea of the IEM is to partition the unbounded domain Ω^+ into Ω_a and Ω_a^+ separated by an artificial boundary Γ_a (cf. Figure 3). These two domains can then be discretized with finite elements and infinite elements, respectively. The boundary of the scatterer is assumed to be parameterized using 3D NURBS surface patches, such that the domain Ω_a can be parameterized using 3D NURBS volume patches. Denote by $\mathcal{V}_h(\Omega_\mathrm{a})$, the space spanned by these trivariate NURBS-basis functions. As the 3D NURBS volume representation of Ω_a reduces to a NURBS surface parametrization at Γ_a, a natural partition of Γ_a into surface elements arises. Denote by $\mathcal{V}_h(\Gamma_\mathrm{a})$, the space spanned by the resulting bivariate basis functions. Consider now the following basis of the *radial shape functions* which is motivated by the Wilcox expansion in Eq. (8)

$$\mathcal{I}_{N,w}^{+} = \operatorname{span}\left(\left\{ \frac{\mathrm{e}^{\mathrm{i}kr}}{r^n} \right\}_{n=1,\dots,N} \right). \tag{21}$$

Moreover, define corresponding spaces for the test-space

$$\mathcal{I}_{N,w^*}^{+} = \begin{cases} \mathcal{I}_{N,w}^{+} & \text{for Bubnov–Galerkin formulations} \\ \operatorname{span}\left(\left\{ \frac{\mathrm{e}^{\mathrm{i}kr}}{r^{n+2}} \right\}_{n=1,\dots,N} \right) & \text{for Petrov–Galerkin formulations.} \end{cases} \tag{22}$$

The trial- and test spaces for the infinite elements can then be defined by

$$\mathcal{I}^+_{h,w} = \mathcal{V}_h(\Gamma_\mathrm{a}) \times \mathcal{I}^+_{N,w}, \tag{23}$$

$$\mathcal{I}^+_{h,w^*} = \mathcal{V}_h(\Gamma_\mathrm{a}) \times \mathcal{I}^+_{N,w^*}, \tag{24}$$

respectively. Finally, the trial- and test spaces for the coupled FEM-IEM can be written as

$$\mathcal{F}^+_{h,w} = \left\{ p \in H^{1+}_w(\Omega^+);\, p\big|_{\Omega_\mathrm{a}} \in \mathcal{V}_h(\Omega_\mathrm{a}) \quad \text{and} \quad p\big|_{\Omega^+_\mathrm{a}} \in \mathcal{I}^+_{h,w} \right\}, \tag{25}$$

$$\mathcal{F}^+_{h,w^*} = \left\{ q \in H^{1+}_{w^*}(\Omega^+);\, q\big|_{\Omega_\mathrm{a}} \in \mathcal{V}_h(\Omega_\mathrm{a}) \quad \text{and} \quad q\big|_{\Omega^+_\mathrm{a}} \in \mathcal{I}^+_{h,w^*} \right\}, \tag{26}$$

respectively. Note that $\mathcal{F}^+_{h,w^*} = \mathcal{F}^+_{h,w}$ for Bubnov–Galerkin formulations.

For the unconjugated formulations the Galerkin formulations now takes the form:

$$\text{Find} \quad p_h \in \mathcal{F}^+_{h,w} \quad \text{such that} \quad B_\mathrm{uc}(q_h, p_h) = L(q_h), \qquad \forall q_h \in \mathcal{F}^+_{h,w^*} \tag{27}$$

where the bilinear form and linear form are respectively given by

$$B_\mathrm{uc}(q,p) = \lim_{\gamma\to\infty} \left(\int_{\Omega^\gamma} \left[\nabla q \cdot \nabla p - k^2 q p \right] \mathrm{d}\Omega - \int_{S^\gamma} q \partial_n p \, \mathrm{d}\Gamma \right), \tag{28}$$

$$L(q) = \int_{\Gamma_0} q g \, \mathrm{d}\Gamma.$$

Here, S^γ is the surface at $r = \gamma$ (and Ω^γ is the domain bounded by Γ_0 and S^γ, such that $\lim_{\gamma\to\infty} \Omega^\gamma = \Omega^+$) and the full domain can then be recovered by letting $\gamma \to \infty$ (see Figure 4). Recall that $\partial_n p = \frac{\partial p}{\partial n} = \boldsymbol{n} \cdot \nabla p$ where $\boldsymbol{n}$ is pointing "out" of Ω^γ. In the conjugated formulations the test functions q_h are conjugated.

Let r_a be the radius in the prolate spheroidal coordinate system at the artificial boundary Γ_a. Moreover, let the radial shape functions ϕ be defined by

$$\phi_m(r) = \mathrm{e}^{\mathrm{i}k(r-r_\mathrm{a})} Q_m\left(\frac{r_\mathrm{a}}{r}\right), \quad m = 1, \ldots, N \tag{29}$$

where

$$Q_m(x) = \sum_{\tilde{m}=1}^{N} D_{m\tilde{m}} x^{\tilde{m}} \tag{30}$$

is a set of polynomial functions defined on the half open interval $(0, 1]$. To obtain optimal sparsity of the global matrix, one should choose the polynomials such that $Q_m(1) = \delta_{m1}$, with the Kronecker delta function defined by

$$\delta_{ij} = \begin{cases} 1 & \text{if} \quad i = j \\ 0 & \text{if} \quad i \neq j \end{cases} \tag{31}$$

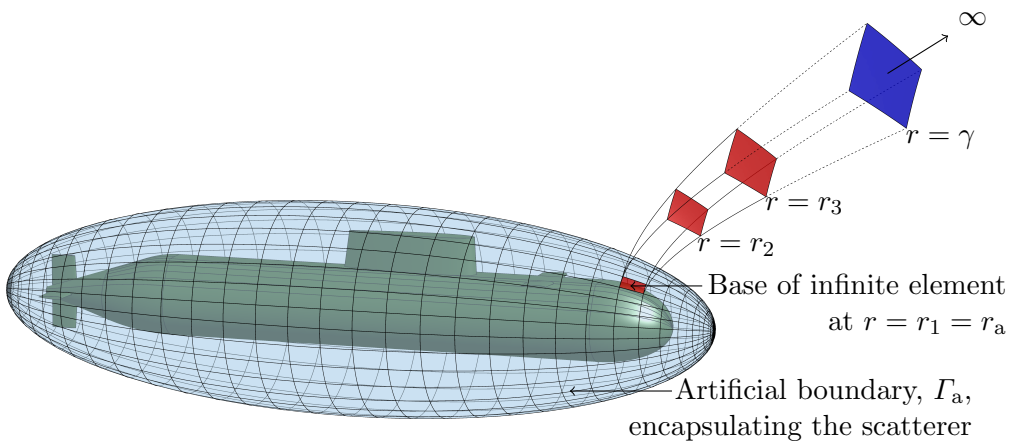

Figure 4: Illustration of an infinite element (with $N = 3$) where the radial shape functions have the Kronecker delta property at radii $r_1 = r_a$, $r_2 = \frac{5}{4}r_a$ and $r_3 = \frac{6}{4}r_a$. The (green) scatterer inside Γ_a is the BeTSSi submarine which originates from the BeTSSi workshops [1]. Note that the volume elements discretizing the domain Ω_a (bounded by the scatterer and the artificial boundary) are not shown here.

which implies that $\phi_m(r_a) = \delta_{m1}$. In [13] Burnett includes the restrictions $\phi_m(r_n) = \delta_{mn}$ with radii r_n, $n = 1, \ldots, N$ (see Figure 4). Alternatively, one could use the shifted Chebyshev polynomials as done by Shirron and Dey in [33]. These polynomials are defined by the three-term recurrence relation

$$\tilde{T}_{m+1}(x) = 2(2x-1)\tilde{T}_m(x) - \tilde{T}_{m-1}(x) \tag{32}$$

for $m \geqslant 1$ starting with

$$\tilde{T}_0(x) = 1 \quad \text{and} \quad \tilde{T}_1(x) = 2x - 1. \tag{33}$$

Let

$$Q_m(x) = \begin{cases} x\Big(\tilde{T}_{m-1}(x) - 1\Big) & m > 1 \\ x & m = 1. \end{cases} \tag{34}$$

Then the coefficients $D_{m\tilde{m}}$ in Eq. (30) can be collected in the matrix (for $N \leqslant 6$)

$$\boldsymbol{D} = \begin{bmatrix} 1 & 0 & 0 & 0 & 0 & 0 \\ -2 & 2 & 0 & 0 & 0 & 0 \\ 0 & -8 & 8 & 0 & 0 & 0 \\ -2 & 18 & -48 & 32 & 0 & 0 \\ 0 & -32 & 160 & -256 & 128 & 0 \\ -2 & 50 & -400 & 1120 & -1280 & 512 \end{bmatrix}.$$

For the Petrov–Galerkin formulations, a second set of shape functions (for the test space) must be created, namely

$$\psi_n(r) = \mathrm{e}^{\mathrm{i}k(r-r_\mathrm{a})}\tilde{Q}_n\left(\frac{r_\mathrm{a}}{r}\right), \quad n = 1, \ldots, N \tag{35}$$

using

$$\tilde{Q}_n(x) = \sum_{\tilde{n}=1}^{N} \tilde{D}_{n\tilde{n}} x^{\tilde{n}+2} \tag{36}$$

where it is natural to choose $\tilde{D}_{n\tilde{n}} = D_{n\tilde{n}}$. The Bubnov–Galerkin formulations use the same shape functions for the test space, i.e., $\psi_n = \phi_n$.

Alternatively, the polynomials Q can be based upon the Bernstein basis of order $\check{p} = N - 1$ by

$$Q_m(x) = x b_{p-m+1,\check{p}}(x) \qquad m = 1, \ldots N \tag{37}$$

where

$$b_{i,\check{p}}(x) = \binom{n}{i}(1-x)^{\check{p}-i}x^i = \sum_{j=0}^{\check{p}-i}(-1)^j\binom{\check{p}}{i}\binom{\check{p}-i}{j}x^{i+j}, \qquad i = 0, \ldots, \check{p}. \tag{38}$$

For completeness, note that the coefficients for the radial shape functions used by Burnett [13] (for the Bubnov–Galerkin formulations) can be found by solving $\boldsymbol{DB} = \boldsymbol{E}$ where

$$\boldsymbol{B} = \begin{bmatrix} x_1 & x_2 & \ldots & x_N \\ x_1^2 & x_2^2 & \ldots & x_N^2 \\ \vdots & \vdots & \ddots & \vdots \\ x_1^N & x_2^N & \ldots & x_N^N \end{bmatrix}, \quad \boldsymbol{E} = \begin{bmatrix} 1 & & & \\ & \mathrm{e}^{\mathrm{i}k(r_\mathrm{a}-r_2)} & & \\ & & \ddots & \\ & & & \mathrm{e}^{\mathrm{i}k(r_\mathrm{a}-r_N)} \end{bmatrix}, \quad x_n = \frac{r_\mathrm{a}}{r_n}.$$

The coefficients $D_{m\tilde{m}}$ are thus given by $\boldsymbol{D} = \boldsymbol{E}\boldsymbol{B}^{-1}$. For Petrov–Galerkin formulations, the coefficients $\tilde{D}_{n\tilde{n}}$ are found in the same way, but now with the matrix

$$\tilde{\boldsymbol{B}} = \begin{bmatrix} x_1^3 & x_2^3 & \ldots & x_N^3 \\ x_1^4 & x_2^4 & \ldots & x_N^4 \\ \vdots & \vdots & \ddots & \vdots \\ x_1^{N+2} & x_2^{N+2} & \ldots & x_N^{N+2} \end{bmatrix}$$

instead of $\boldsymbol{B}$. So, with the notation presented, these basis functions are based on the Lagrange polynomials with polynomial order[3] $\check{p} = N - 1$

$$l_n(x) = \prod_{\substack{0 \leqslant n \leqslant \check{p} \\ n \neq m}} \frac{x - x_n}{x_m - x_n}, \tag{39}$$

[3]The usage of a check sign above the polynomial order p is to avoid ambiguity between the polynomial order and the scattered pressure.

since the polynomials Q_m can be written as

$$Q_m(x) = \mathrm{e}^{\mathrm{i}k(r_\mathrm{a}-r_m)}\frac{r_m}{r_\mathrm{a}} x l_m(x)$$

such that

$$\phi_m(r) = \mathrm{e}^{\mathrm{i}k(r-r_m)}\frac{r_m}{r} l_m\left(\frac{r_\mathrm{a}}{r}\right).$$

The radial shape functions in the test space for the Petrov–Galerkin formulations take the form

$$\psi_n(r) = \mathrm{e}^{\mathrm{i}k(r-r_n)}\left(\frac{r_n}{r}\right)^3 l_n\left(\frac{r_\mathrm{a}}{r}\right).$$

As all these sets of basis functions span the same space, they should only affect the conditioning of the system. Note that the sets of basis functions are identical for $N = 1$.

The trial- and test functions now take the form

$$p_h(\boldsymbol{x}) = \begin{cases} \displaystyle\sum_{J\in\boldsymbol{\kappa}_\mathrm{a}}\sum_{m=1}^{N} d_{m,J}\phi_m(r)R_J(\xi,\eta,\zeta)\big|_{\Gamma_\mathrm{a}} & \boldsymbol{x}\in\Omega_\mathrm{a}^+ \\ \displaystyle\sum_{J\in\boldsymbol{\kappa}} d_{1,J}R_J(\xi,\eta,\zeta) & \boldsymbol{x}\in\Omega_\mathrm{a} \end{cases} \tag{40}$$

and

$$q_h(\boldsymbol{x}) = \begin{cases} \displaystyle\sum_{I\in\boldsymbol{\kappa}_\mathrm{a}}\sum_{n=1}^{N} c_{n,I}\psi_n(r)R_I(\xi,\eta,\zeta)\big|_{\Gamma_\mathrm{a}} & \boldsymbol{x}\in\Omega_\mathrm{a}^+ \\ \displaystyle\sum_{I\in\boldsymbol{\kappa}} c_{1,I}R_I(\xi,\eta,\zeta) & \boldsymbol{x}\in\Omega_\mathrm{a}, \end{cases} \tag{41}$$

respectively. Here, $\boldsymbol{\kappa}$ is the collection of the global indices of the NURBS basis functions and $\boldsymbol{\kappa}_\mathrm{a}$ the corresponding indices of the non-zero NURBS function at the surface Γ_a. Moreover, $R_I(\xi,\eta,\zeta)$ is the set of NURBS basis functions. The system of equations will now be obtained by inserting the functions in Eq. (40) and Eq. (41) into the bilinear form (or sesquilinear form for the BGC and PGC formulations, i.e. the bilinear form with conjugated test functions).

Before the insertion, it is advantageous to split the bilinear form in Eq. (28) as

$$B_\mathrm{uc}(q,p) = B_\mathrm{a}(q,p) + B^+_\mathrm{uc,a}(q,p) \tag{42}$$

where

$$\begin{aligned} B_\mathrm{a}(q,p) &= \int_{\Omega_\mathrm{a}} \Big[\nabla q\cdot\nabla p - k^2 qp\Big]\,\mathrm{d}\Omega \\ B^+_\mathrm{uc,a}(q,p) &= \lim_{\gamma\to\infty}\left(\int_{\Omega_\mathrm{a}^\gamma}\Big[\nabla q\cdot\nabla p - k^2 qp\Big]\,\mathrm{d}\Omega - \int_{S^\gamma} q\partial_n p\,\mathrm{d}\Gamma\right). \end{aligned} \tag{43}$$

Insertion of Eq. (40) and Eq. (41) into Eq. (27) (using the splitting in Eq. (42)) results in the following system of equations

$$(\boldsymbol{A}_{\mathrm{a}} + \boldsymbol{A}^{+}_{\mathrm{uc,a}})\boldsymbol{d} = \boldsymbol{F} \tag{44}$$

with components

$$\begin{aligned} \boldsymbol{A}_{\mathrm{a}}[I,J] &= B_{\mathrm{a}}(R_I, R_J) && I,J = 1,\ldots,|\boldsymbol{\kappa}| \\ \boldsymbol{F}[I] &= L(R_I) && I = 1,\ldots,|\boldsymbol{\kappa}| \\ \boldsymbol{d}[J] &= d_{1,J} && J = 1,\ldots,|\boldsymbol{\kappa}| \end{aligned}$$

and

$$\begin{aligned} \boldsymbol{A}^{+}_{\mathrm{uc,a}}[\tilde{I},\tilde{J}] &= B^{+}_{\mathrm{uc,a}}(R_I\psi_n, R_J\phi_m) \\ \boldsymbol{d}[\tilde{J}] &= d_{m,J} \end{aligned}$$

where $I = \boldsymbol{\kappa}_{\mathrm{a}}[\tilde{i}]$ and $J = \boldsymbol{\kappa}_{\mathrm{a}}[\tilde{j}]$ for $\tilde{i},\tilde{j} = 1,\ldots,|\boldsymbol{\kappa}_{\mathrm{a}}|$ and $m,n = 1,\ldots,N$, and

$$\tilde{I} = \begin{cases} \boldsymbol{\kappa}_{\mathrm{a}}[\tilde{i}] & n = 1 \\ |\boldsymbol{\kappa}| + (n-2)|\boldsymbol{\kappa}_{\mathrm{a}}| + \tilde{i} & n > 1 \end{cases}$$

$$\tilde{J} = \begin{cases} \boldsymbol{\kappa}_{\mathrm{a}}[\tilde{j}] & m = 1 \\ |\boldsymbol{\kappa}| + (m-2)|\boldsymbol{\kappa}_{\mathrm{a}}| + \tilde{j} & m > 1. \end{cases}$$

Note that $\boldsymbol{A}_{\mathrm{a}}$ and $\boldsymbol{F}$ are independent of the IEM and that there are $|\boldsymbol{\kappa}|+|\boldsymbol{\kappa}_{\mathrm{a}}|(N-1)$ linear equations. The matrices are assembled as in the classical FEM. That is, instead of looping through the indices, one loops through the elements. A formula for $B^{+}_{\mathrm{uc,a}}(R_I\psi_n, R_J\phi_m)$ for the Petrov Galerkin formulation is derived in Appendix A and the final bilinear form is given in Eq. (A.19). The final formulas for the other three formulations are also added in this appendix.

2.3. Far field pattern

The problem is solved inside an artificial boundary, computing the so-called near field. However, the far field is also often of interest. To solve this issue, one uses the integral solution given by[4] (cf. [18, Theorem 2.21])

$$p(\boldsymbol{x}) = \int_{\Gamma_0} \left[p(\boldsymbol{y}) \frac{\partial \Phi_k(\boldsymbol{x},\boldsymbol{y})}{\partial n(\boldsymbol{y})} - \Phi_k(\boldsymbol{x},\boldsymbol{y}) \frac{\partial p(\boldsymbol{y})}{\partial n(\boldsymbol{y})} \right] \mathrm{d}\Gamma(\boldsymbol{y}) \tag{45}$$

[4]For the conjugated formulations one may also compute the far field using the radial shape functions in the infinite elements, but for the unconjugated formulations it is mentioned in [34, p. 137] that the expansion does not converge in the far field, such that it must be computed by other means.

where $\boldsymbol{y}$ is a point on the surface Γ_0, n lies on Γ_0 pointing "into" Ω^+ at $\boldsymbol{y}$ and Φ_k is the free space Green's function for the Helmholtz equation in Eq. (2) given (in 3D) by

$$\Phi_k(\boldsymbol{x}, \boldsymbol{y}) = \frac{\mathrm{e}^{\mathrm{i}kR}}{4\pi R}, \quad \text{where} \quad R = |\boldsymbol{x} - \boldsymbol{y}|. \tag{46}$$

The derivative of both Green's function and the numerical solution for the pressure is therefore needed

$$\frac{\partial \Phi_k(\boldsymbol{x}, \boldsymbol{y})}{\partial n(\boldsymbol{y})} = \frac{\Phi_k(\boldsymbol{x}, \boldsymbol{y})}{R}(\mathrm{i}kR - 1)\frac{\partial R}{\partial n(\boldsymbol{y})}, \quad \text{where} \quad \frac{\partial R}{\partial n(\boldsymbol{y})} = -\frac{(\boldsymbol{x} - \boldsymbol{y}) \cdot \boldsymbol{n}(\boldsymbol{y})}{R}. \tag{47}$$

Note that for sound-hard scattering (where $\partial_n(p + p_{\mathrm{inc}}) = 0$) the values for $\partial_n p$ are known at the boundary Γ_0 (given by Eq. (3)). To use the exact expression for the derivative seems to give better results and is for this reason used in the sound-hard scattering cases when computing the field outside the artificial boundary.

The *far field pattern* for the scattered pressure p, is now defined by

$$p_0(\hat{\boldsymbol{x}}) = \lim_{r \to \infty} r\mathrm{e}^{-\mathrm{i}kr} p(r\hat{\boldsymbol{x}}), \tag{48}$$

with $r = |\boldsymbol{x}|$ and $\hat{\boldsymbol{x}} = \boldsymbol{x}/|\boldsymbol{x}|$. Using the limits

$$\lim_{r \to \infty} r\mathrm{e}^{-\mathrm{i}kr} \Phi_k(r\hat{\boldsymbol{x}}, \boldsymbol{y}) = \frac{1}{4\pi}\mathrm{e}^{-\mathrm{i}k\hat{\boldsymbol{x}} \cdot \boldsymbol{y}} \tag{49}$$

and

$$\lim_{r \to \infty} r\mathrm{e}^{-\mathrm{i}kr} \frac{\partial \Phi_k(r\hat{\boldsymbol{x}}, \boldsymbol{y})}{\partial n(\boldsymbol{y})} = -\frac{\mathrm{i}k}{4\pi}\mathrm{e}^{-\mathrm{i}k\hat{\boldsymbol{x}} \cdot \boldsymbol{y}} \hat{\boldsymbol{x}} \cdot \boldsymbol{n}(\boldsymbol{y}) \tag{50}$$

the formula in Eq. (45) simplifies in the far field to (cf. [30, p. 32])

$$p_0(\hat{\boldsymbol{x}}) = -\frac{1}{4\pi} \int_{\Gamma_0} \left[\mathrm{i}kp(\boldsymbol{y}) \hat{\boldsymbol{x}} \cdot \boldsymbol{n}(\boldsymbol{y}) + \frac{\partial p(\boldsymbol{y})}{\partial n(\boldsymbol{y})} \right] \mathrm{e}^{-\mathrm{i}k\hat{\boldsymbol{x}} \cdot \boldsymbol{y}} \, \mathrm{d}\Gamma(\boldsymbol{y}). \tag{51}$$

From the far field pattern, the *target strength*, TS, can be computed. It is defined by

$$\mathrm{TS} = 20 \log_{10}\left(\frac{|p_0(\hat{\boldsymbol{x}})|}{|P_{\mathrm{inc}}|} \right) \tag{52}$$

where P_{inc} is the amplitude of the incident wave at the geometric center of the scatterer (i.e. the origin). Note that TS is independent of P_{inc}, which is a result of the linear dependency of the amplitude of the incident wave in scattering problems (i.e. doubling the amplitude of the incident wave will double the amplitude of the scattered wave).

3. Acoustic-structure interaction

In [30, pp. 13-14] Ihlenburg briefly derives the governing equations for the ASI problem. Building upon this the formulas are generalized to include an interior fluid domain Ω^-. The pressure in the exterior and interior fluid domain are now denoted by p_1 and p_2 (see Figure 3).

$$\nabla^2 p_1 + k_1^2 p_1 = 0 \qquad \text{in} \quad \Omega^+ \tag{53}$$

$$\frac{\partial p(\boldsymbol{x},\omega)}{\partial r} - \mathrm{i}kp(\boldsymbol{x},\omega) = o\Big(r^{-1}\Big) \qquad \text{with} \quad r = |\boldsymbol{x}| \tag{54}$$

$$\rho_{\mathrm{f},1}\omega^2 u_i n_i - \frac{\partial p_1}{\partial n} = \frac{\partial p_{\mathrm{inc}}}{\partial n} \qquad \text{on} \quad \Gamma_0 \tag{55}$$

$$\sigma_{ij} n_i n_j + p_1 = -p_{\mathrm{inc}} \qquad \text{on} \quad \Gamma_0 \tag{56}$$

$$\sigma_{ij,j} + \omega^2 \rho_{\mathrm{s}} u_i = 0 \qquad \text{in} \quad \Omega_{\mathrm{s}} \tag{57}$$

$$\rho_{\mathrm{f},2}\omega^2 u_i n_i - \frac{\partial p_2}{\partial n} = 0 \qquad \text{on} \quad \Gamma_1 \tag{58}$$

$$\sigma_{ij} n_i n_j + p_2 = 0 \qquad \text{on} \quad \Gamma_1 \tag{59}$$

$$\nabla^2 p_2 + k_2^2 p_2 = 0 \qquad \text{in} \quad \Omega^-. \tag{60}$$

The first two equations represent the Helmholtz equation and Sommerfeld conditions, respectively, for the exterior domain. The wave numbers in the exterior and interior fluid domain are denoted by k_1 and k_2. The elasticity equation in Eq. (57) comes from momentum conservation (Newton's second law), while Eqs. (55), (56), (58) and (59) represent the coupling equations and come from the continuity requirement of the displacement and pressures at the boundaries Γ_m. The final formula is simply the Helmholtz equation for the internal fluid domain. The function p_{inc} represents the incident plane wave in Eq. (6) (in the exterior domain). The mass densities of the solid and the fluid are denoted by ρ_{s} and ρ_{f}, respectively, and $\sigma_{ij}(\boldsymbol{u})$ represents the stress components as a function of the displacement $\boldsymbol{u} = u_i \boldsymbol{e}_i$ in the solid.

For the domain of the scatterer, Ω_{s}, it can be shown that the following weak formulation is obtained from the strong form in Eq. (57) (see for example [30])

$$\int_{\Omega_{\mathrm{s}}} \Big[v_{i,j}\sigma_{ij} - \rho_{\mathrm{s}}\omega^2 u_i \bar{v}_i \Big] \,\mathrm{d}\Omega = \int_{\Gamma_0} v_i(\sigma_{ij} n_j) \,\mathrm{d}\Gamma + \int_{\Gamma_1} v_i(\sigma_{ij} n_j) \,\mathrm{d}\Gamma. \tag{61}$$

where the normal vectors point out of Ω_{s}. The integrands on the right-hand side may be rewritten using Eqs. (56) and (59) in the following way. Consider a point $\boldsymbol{P}$ on Γ_0 or Γ_1, with normal vector $\boldsymbol{n} = n_i \boldsymbol{e}_i$. Let T_i be the components (in Cartesian coordinates) of the exterior traction vector $\boldsymbol{T}$. That is to say, $T_i = \sigma_{ij} n_j$. One can then create a local orthogonal coordinate system at this point with unit vectors $\boldsymbol{e}_\perp$, $\boldsymbol{e}_{\parallel_1}$ and $\boldsymbol{e}_{\parallel_2}$, where the latter two vectors represent basis vectors for the tangential

plane of the surface at $\boldsymbol{P}$ (and $\boldsymbol{e}_\perp$ represents the normal unit vector on this plane at $\boldsymbol{P}$).

As the scalar product is invariant to orthogonal transformations, the following holds

$$T_i v_i = T_x v_x + T_y v_y + T_z v_z = T_\perp v_\perp + T_{\parallel_1} v_{\parallel_1} + T_{\parallel_2} v_{\parallel_2}.$$

Since the acoustic pressure from the fluid only exerts forces normal to the surfaces Γ_0 and Γ_1, the static equilibrium conditions for the traction at $\boldsymbol{P}$ are given by

$$T_{\parallel_1} = 0, \qquad T_{\parallel_2} = 0, \quad \text{and} \quad T_\perp = -p_{\mathrm{tot},m},$$

where the total pressure is given by

$$p_{\mathrm{tot},m} = \begin{cases} p_{\mathrm{inc}} + p_1 & m = 1 \\ p_2 & m = 2. \end{cases}$$

The scalar product may therefore be written as

$$T_i v_i = -p_{\mathrm{tot},m} v_\perp = -p_{\mathrm{tot},m} v_i n_i.$$

Eq. (61) can thus be rewritten as

$$\int_{\Omega_\mathrm{s}} \left[v_{i,j}\sigma_{ij} - \rho_\mathrm{s}\omega^2 u_i v_i \right] \mathrm{d}\Omega = -\int_{\Gamma_0} (p_{\mathrm{inc}} + p_1) v_i n_i \,\mathrm{d}\Gamma - \int_{\Gamma_1} p_2 v_i n_i \,\mathrm{d}\Gamma. \tag{62}$$

Moreover, from Eq. (19) one obtains

$$\int_{\Omega^+} \left[\nabla q_1 \cdot \nabla p_1 - k_1^2 q_1 p_1 \right] \mathrm{d}\Omega = -\int_{\Gamma_0} q_1 \frac{\partial p_1}{\partial n} \,\mathrm{d}\Gamma$$

and

$$\int_{\Omega^-} \left[\nabla q_2 \cdot \nabla p_2 - k_2^2 q_2 p_2 \right] \mathrm{d}\Omega = -\int_{\Gamma_1} q_2 \frac{\partial p_2}{\partial n} \,\mathrm{d}\Gamma$$

where the sign of the right-hand side must be changed in order to get a normal vector that points out of Ω_s. Using now Eqs. (55) and (58)

$$\frac{1}{\rho_{\mathrm{f},1}\omega^2} \int_{\Omega^+} \left[\nabla q_1 \cdot \nabla p_1 - k_1^2 q_1 p_1 \right] \mathrm{d}\Omega = -\int_{\Gamma_0} q_1 \left(u_i n_i - \frac{1}{\rho_{\mathrm{f},1}\omega^2} \frac{\partial p_{\mathrm{inc}}}{\partial n} \right) \mathrm{d}\Gamma \tag{63}$$

and

$$\frac{1}{\rho_{\mathrm{f},2}\omega^2} \int_{\Omega^-} \left[\nabla q_2 \cdot \nabla p_2 - k_2^2 q_2 p_2 \right] \mathrm{d}\Omega = -\int_{\Gamma_1} q_2 u_i n_i \,\mathrm{d}\Gamma. \tag{64}$$

Adding Eqs. (62) to (64)

$$\begin{aligned} &\frac{1}{\rho_{\mathrm{f},1}\omega^2} \int_{\Omega^+} \left[\nabla q_1 \cdot \nabla p_1 - k_1^2 q_1 p_1 \right] \mathrm{d}\Omega + \int_{\Gamma_0} \left[q_1 u_i n_i + p_1 v_i n_i \right] \mathrm{d}\Gamma \\ &+ \frac{1}{\rho_{\mathrm{f},2}\omega^2} \int_{\Omega^-} \left[\nabla q_2 \cdot \nabla p_2 - k_2^2 q_2 p_2 \right] \mathrm{d}\Omega + \int_{\Gamma_1} \left[q_2 u_i n_i + p_2 v_i n_i \right] \mathrm{d}\Gamma \\ &+ \int_{\Omega_\mathrm{s}} \left[v_{i,j}\sigma_{ij} - \rho_\mathrm{s}\omega^2 u_i v_i \right] \mathrm{d}\Omega = \int_{\Gamma_0} \left[\frac{1}{\rho_{\mathrm{f},1}\omega^2} q_1 \frac{\partial p_{\mathrm{inc}}}{\partial n} - p_{\mathrm{inc}} v_i n_i \right] \mathrm{d}\Gamma \end{aligned}$$

where $\boldsymbol{n} = \{n_1, n_2, n_3\}$ points outwards from the solid. Defining the Sobolev spaces $\boldsymbol{\mathcal{H}}_w = \boldsymbol{\mathcal{S}} \times H^{1+}_w(\Omega^+) \times H^1(\Omega^-)$ and $\boldsymbol{\mathcal{H}}_{w^*} = \boldsymbol{\mathcal{S}} \times H^1_{w^*}(\Omega^+) \times H^1(\Omega^-)$ where $\boldsymbol{\mathcal{S}} = \{\boldsymbol{u} : u_i \in H^1(\Omega_\mathrm{s})\}$, the weak formulation for the ASI problem then becomes (with the notation $U = \{\boldsymbol{u}, p_1, p_2\}$ and $V = \{\boldsymbol{v}, q_1, q_2\}$):

$$\text{Find} \quad U \in \boldsymbol{\mathcal{H}}_w \quad \text{such that} \quad B_\mathrm{ASI}(V, U) = L_\mathrm{ASI}(V), \quad \forall V \in \boldsymbol{\mathcal{H}}_{w^*} \tag{65}$$

where

$$\begin{aligned} B_\mathrm{ASI}(V,U) = \frac{1}{\rho_{\mathrm{f},1}\omega^2} \int_{\Omega^+} \Big[\nabla q_1 \cdot \nabla p_1 - k_1^2 q_1 p_1\Big] \,\mathrm{d}\Omega + \int_{\Gamma_0} [q_1 u_i n_i + p_1 v_i n_i] \,\mathrm{d}\Gamma \\ + \int_{\Omega_\mathrm{s}} \Big[v_{i,j}\sigma_{ij} - \rho_\mathrm{s}\omega^2 u_i v_i\Big] \,\mathrm{d}\Omega \\ + \frac{1}{\rho_{\mathrm{f},2}\omega^2} \int_{\Omega^-} \Big[\nabla q_2 \cdot \nabla p_2 - k_2^2 q_2 p_2\Big] \,\mathrm{d}\Omega + \int_{\Gamma_1} [q_2 u_i n_i + p_2 v_i n_i] \,\mathrm{d}\Gamma \end{aligned}$$

and

$$L_\mathrm{ASI}(V) = \int_{\Gamma_0} \left[\frac{1}{\rho_{\mathrm{f},1}\omega^2} q_1 \frac{\partial p_\mathrm{inc}}{\partial n} - p_\mathrm{inc} v_i n_i\right] \mathrm{d}\Gamma.$$

Let $\boldsymbol{\mathcal{S}}_h = \{\boldsymbol{u} : u_i \in \mathcal{V}(\Omega_\mathrm{s})\} \subset \boldsymbol{\mathcal{S}}$ where $\mathcal{V}(\Omega_\mathrm{s})$ is the space spanned by the NURBS basis functions used to parameterize $\mathcal{V}(\Omega_\mathrm{s})$, and correspondingly for $\mathcal{F}^-_h = \{p_2 : p_2 \in \mathcal{V}(\Omega^-)\} \subset H^1(\Omega^-)$. Moreover, define the spaces $\boldsymbol{\mathcal{H}}_{h,w} = \boldsymbol{\mathcal{S}}_h \times \mathcal{F}^+_{h,w} \times \mathcal{F}^-_h$ and $\boldsymbol{\mathcal{H}}_{h,w^*} = \boldsymbol{\mathcal{S}}_h \times \mathcal{F}^+_{h,w^*} \times \mathcal{F}^-_h$. The Galerkin formulation for the ASI problem then becomes:

$$\text{Find} \quad U_h \in \boldsymbol{\mathcal{H}}_{h,w} \quad \text{such that} \quad B_\mathrm{ASI}(V_h, U_h) = L_\mathrm{ASI}(V_h), \quad \forall V_h \in \boldsymbol{\mathcal{H}}_{h,w^*}. \tag{66}$$

As the bilinear forms treated in this work are not V-elliptic [30, p. 46], they do not induce a well-defined energy-norm. For this reason, the energy norm for the fluid domains Ω_a are defined by

$$|||p_1|||_{\Omega_\mathrm{a}} = \sqrt{\int_{\Omega_\mathrm{a}} |\nabla p_1|^2 + k_1^2 |p_1|^2 \,\mathrm{d}\Omega} \quad \text{and} \quad |||p_2|||_{\Omega^-} = \sqrt{\int_{\Omega^-} |\nabla p_2|^2 + k_2^2 |p_2|^2 \,\mathrm{d}\Omega} \tag{67}$$

and for the solid domain (using Einstein summation convention)

$$|||\boldsymbol{u}|||_{\Omega_\mathrm{s}} = \sqrt{\int_{\Omega_\mathrm{s}} u_{(i,j)} c_{ijkl} \bar{u}_{(k,l)} + \rho_\mathrm{s}\omega^2 |\boldsymbol{u}|^2 \,\mathrm{d}\Omega} \tag{68}$$

where

$$u_{(i,j)} = \frac{1}{2}\left(\frac{\partial u_i}{\partial x_j} + \frac{\partial u_j}{\partial x_i}\right)$$

and elastic coefficients expressed in terms of Young's modulus, E, and the Poisson's ratio, ν, as [6, p. 110]

$$c_{ijkl} = \frac{\nu E}{(1+\nu)(1-2\nu)}\delta_{ij}\delta_{kl} + \frac{E}{2(1+\nu)}(\delta_{ik}\delta_{jl} + \delta_{il}\delta_{jk}).$$

The energy norm for the coupled problem with $\Omega = \Omega_\mathrm{a} \cup \Omega_\mathrm{s} \cup \Omega^-$ is then defined by

$$|||U|||_\Omega = \sqrt{\frac{1}{\rho_{\mathrm{f},1}\omega^2}|||p_1|||^2_{\Omega_\mathrm{a}} + |||\boldsymbol{u}|||^2_{\Omega_\mathrm{s}} + \frac{1}{\rho_{\mathrm{f},2}\omega^2}|||p_2|||^2_{\Omega^-}}. \tag{69}$$

As the unconjugated formulations do not converge in the far field, the norm in the exterior domain is taken over the Ω_a instead of Ω^+.

4. Numerical examples

Rigid scattering on a sphere and elastic scattering on a spherical shell are investigated in the following. These problems possess analytic solutions [35] and are for this reason often used to verify numerical methods in acoustic scattering, e.g. [14, 30, 31, 36–38].

The mock shell is analyzed to investigate the infinite element formulations, and we end this section by analyzing a simplified submarine benchmark.

In this work, the test setting is chosen so that the present approach can be compared to other methods. In particular, the scattering on a rigid sphere example found in [36] and the scattering on a spherical shell used in [30] are addressed. The latter problem will be investigated in depth and we shall build upon this problem to include both rigid scattering and scattering with full ASI on both sides of the shell.

The direction of the incident wave is along the x-axis while the symmetry of the parametrization of the domain is around the z-axis (to avoid exploitation of the symmetry of the problems).

We define the *SAV index* by

$$I_\mathrm{SAV} = \frac{L_{\Gamma_\mathrm{a}}}{2}\frac{|\Gamma_0|}{|\Omega_\mathrm{a}|} \tag{70}$$

where L_{Γ_a} is the characteristic length of the artificial boundary, $|\Gamma_0|$ is the surface area of the scatterer and $|\Omega_\mathrm{a}|$ is the volume of the discretized fluid between Γ_0 and Γ_a. The SAV index is based on a scaled surface-area-to-volume ratio (SA/V) such that the domain of computation is fitted in a unit sphere. It can be thought of as an efficiency index for the IEM compared to BEM, as problems with low I_SAV will be more suited for BEM, while high values of I_SAV will be more suited for IEM. If

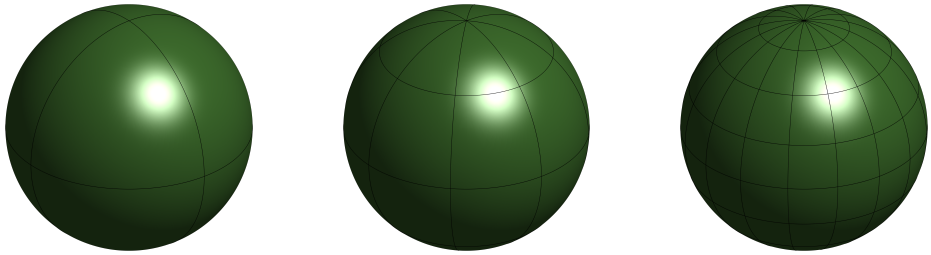

(a) Mesh $\mathcal{M}^{\text{IGA}}_{1,\check{p},\check{k}}$ (b) Mesh $\mathcal{M}^{\text{IGA}}_{2,\check{p},\check{k}}$ (c) Mesh $\mathcal{M}^{\text{IGA}}_{3,\check{p},\check{k}}$

Figure 5: **Numerical examples**: Illustration of the first three meshes, using two successive refinements from the coarse mesh $\mathcal{M}^{\text{IGA}}_{1,\check{p},\check{k}}$.

we for the sphere example place the artificial boundary, Γ_{a}, at $r_{\text{a}} = sR_0$, where R_0 is the outer radius of the scatterer, then the SAV index is given by

$$I_{\text{SAV}} = \frac{3s}{s^3 - 1}. \tag{71}$$

The IEM is optimal for the sphere problem in the sense that the SAV index can be arbitrarily large. In fact, the infinite elements can be attached directly onto the scatterer (such that $I_{\text{SAV}} = \infty$) as done in [33]. This, however, is not the case for more complex geometries.

A typical SAV index for submarines like the one depicted in Figure 4 is approximately 5, so by choosing $s > 1$, the SAV index can be adjusted for a fairer comparison with methods like BEM. In the numerical experiments on spherical shells we use $s = \frac{32+\pi}{32-\pi} \approx 1.2$ (such that the aspect ratio of the elements in the tensor product meshes are minimal), resulting in $I_{\text{SAV}} \approx 4.5$.

The meshes will be generated from a standard discretization of a sphere using NURBS as seen in Figure 5. We shall denote by $\mathcal{M}^{\text{IGA}}_{m,\check{p},\check{k}}$, mesh number m with polynomial order $\check{p}$ and continuity $\check{k}$ across element boundaries[5]. For the corresponding FEM meshes we denote by $\mathcal{M}^{\text{FEM}}_{m,\check{p},\text{s}}$ and $\mathcal{M}^{\text{FEM}}_{m,\check{p},\text{i}}$ the subparametric and isoparametric FEM meshes, respectively. The construction of NURBS meshes are illustrated in Figure 5. The initial mesh is depicted as mesh $\mathcal{M}^{\text{IGA}}_{1,\check{p},\check{k}}$ in Figure 5a and is refined only in the angular directions for the first 3 refinements (that is, mesh $\mathcal{M}^{\text{IGA}}_{4,\check{p},\check{k}}$ only have one element thickness in the radial direction). Mesh $\mathcal{M}^{\text{IGA}}_{m,\check{p},\check{k}}$, $m = 5, 6, 7$, have 2, 4 and 8 elements in its thickness, respectively. This is done to obtain low aspect ratios for the elements. All the meshes will then be nested and the refinements are done uniformly. We shall use the same polynomial order in all parameter directions; $\check{p}_\xi = \check{p}_\eta = \check{p}_\zeta$.

Unless otherwise stated, we shall use the BGU formulation and $N = 4$ basis functions in the radial direction of the infinite elements.

[5]Except for some possible C^0 lines in the initial CAD geometry.

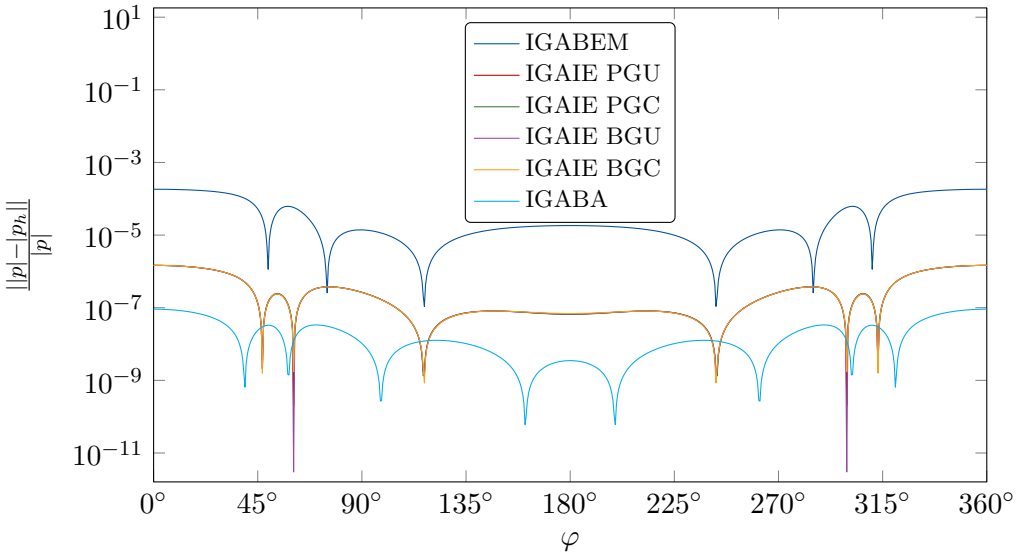

Figure 6: **Simpson benchmark**: The relative error in the modulus of the pressure is plotted on a circle (azimuth direction, φ) in the xy-plane at $r = 5\,\mathrm{m}$. All simulations were computed on mesh $\mathcal{M}^{\mathrm{IGA}}_{3,3,2}$. The IGAIE formulations here produce roughly the same result.

4.1. Simpson benchmark

The configuration presented by Simpson et al. [36] is considered: a rigid sphere of radius $R_0 = 0.5\,\mathrm{m}$ is impinged by an incident plane wave and the total pressure is measured at a distance $r = 5\,\mathrm{m}$ from the origin.

This is a low frequency problem with $k = 2\,\mathrm{m}^{-1}$. It is emphasized that the trace of the NURBS discretization of the domain Ω_a at the surface Γ_0 reduces to the exact same NURBS discretization used in [36] to discretize the boundary Γ_0.

From Figure 6 we observe that the IGA infinite element method (IGAIE) exploits the available degrees of freedom at Γ_0 more effectively than the IGA boundary element method (IGABEM) in [36][6].

By projecting the analytic solution onto this set of NURBS basis functions at Γ_0 (the best approximation in the L_2-norm by least squares projection, IGA best approximation, IGABA), it is revealed that even more accuracy can potentially be made. This is an inherent problem for Galerkin FEM when solving the Helmholtz equation and is related to the pollution effect [39]. All IEM formulations (PGU, PGC, BGU and BGC) gave approximately the same result in this case.

[6]Due to low resolution of the plots in [36, Fig. 17], the results were reproduced and sampled at 3601 points (rather than 30 points) using our own IGABEM implementation.

Table 1: **Ihlenburg benchmark**: Parameters for the Ihlenburg benchmark problems.

Parameter	Description
$P_{\text{inc}} = 1\,\text{Pa}$	Amplitude of incident wave
$E = 2.07 \cdot 10^{11}\,\text{Pa}$	Young's modulus
$\nu = 0.3$	Poisson's ratio
$\rho_{\text{s}} = 7669\,\text{kg}\,\text{m}^{-3}$	Density of solid
$\rho_{\text{f}} = 1000\,\text{kg}\,\text{m}^{-3}$	Density of water
$c_{\text{f}} = 1524\,\text{m}\,\text{s}^{-1}$	Speed of sound in water
$R_0 = 5.075\,\text{m}$	Outer radius
$R_1 = 4.925\,\text{m}$	Inner radius

4.2. Ihlenburg benchmark

Three benchmark solutions based on the model problem after Ihlenburg [30, p. 191] with parameters given in Table 1, are investigated. The parameters for the fluid domains are the speed of sound in water c_{f} and the fluid density ρ_{f}, and the parameters for the solid domain are the Young's modulus, E, the Poisson's ratio ν and the solid density ρ_{s}. The first benchmark is a simple rigid scattering case (with sound-hard boundary conditions, SHBC) on a sphere with radius R_0. The second benchmark problem on a spherical shell has ASI conditions at the outer radius, R_0, and homogeneous Neumann condition at the inner radius, R_1 (sound-soft boundary conditions, SSBC). This case can be thought of as an approximation of a scattering problem on a spherical shell with an internal fluid with very low density. The third and final benchmark is a further extension with ASI conditions on both sides of the spherical shell (Neumann-Neumann conditions on both surfaces of the shell, NNBC). All of these benchmarks have analytic solutions [35] (see Figures 7 and 8), which enables computation of the error in the energy norm. As we use the same parameters in both fluids, we denote the common wave number in these fluids by $k = k_1 = k_2$. For each experiment, we use the same NURBS order everywhere. Denote by $\check{p}_\xi = \check{p}_{\xi,\text{f}} = \check{p}_{\xi,\text{s}}$ the common NURBS order in the fluid and the solid in the ξ-direction. Similarly $\check{p}_\eta = \check{p}_{\eta,\text{f}} = \check{p}_{\eta,\text{s}}$ and $\check{p}_\zeta = \check{p}_{\zeta,\text{f}} = \check{p}_{\zeta,\text{s}}$. Moreover, we denote by $\check{p} = \check{p}_\xi = \check{p}_\eta = \check{p}_\zeta$ the common polynomial orders in all domains.

In order to compare C^0 FEM and IGA on the scattering problem, we shall transform the NURBS mesh to a C^0 FEM mesh. We use the technique described in Appendix D to get an isoparametric B-spline approximation of the geometry (isoparametric FEM). This parametrization will have C^0 continuity at element boundaries and correspondingly G^0 continuity of the geometry representation (i.e. with kinks). The geometric approximation error is of one order higher than the

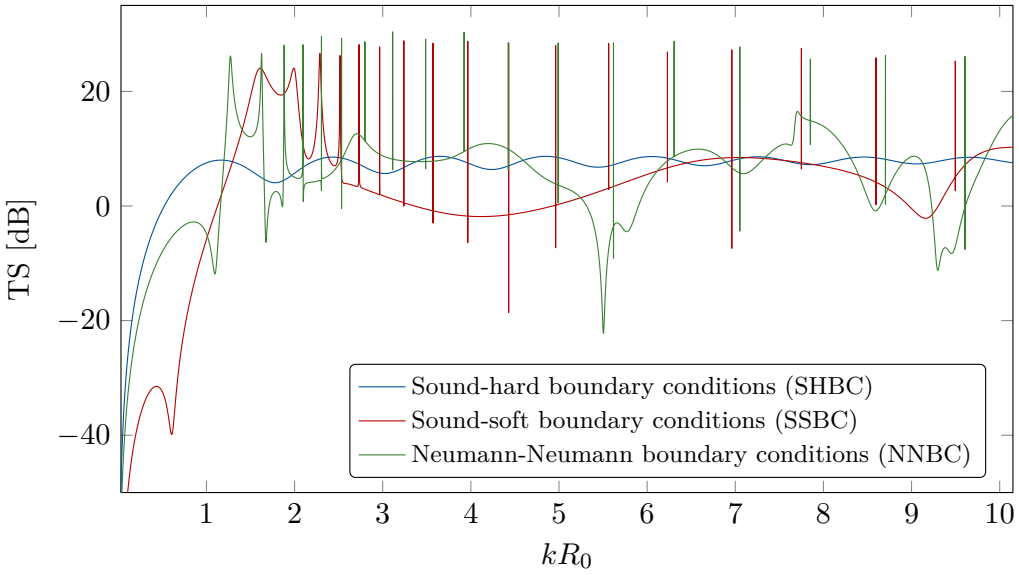

Figure 7: **Ihlenburg benchmark**: Analytic solutions to the scattering problem on a spherical shell with parameters given in Table 1. The far field pattern of backscattered pressure is plotted against the wave number k. A single Neumann condition at the outer radius, R_0, corresponds to the rigid scattering case with $\boldsymbol{u} = \mathbf{0}$ and $p_2 = 0$. ASI at R_0 and Neumann at R_1 models $p_2 = 0$. Note that Ihlenburg [30, p. 192] plots the far field pattern in Eq. (48) instead of the target strength, TS, in Eq. (52).

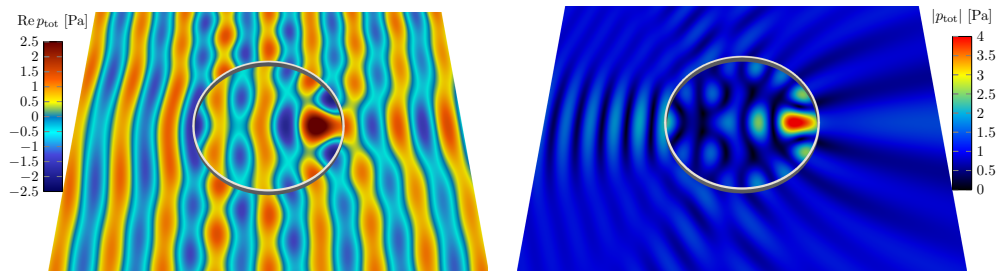

(a) Plot of the real part of the total pressure. (b) Plot of the modulus of the total pressure.

Figure 8: **Ihlenburg benchmark with NNBC**: The analytic solution with ASI at both R_0 and R_1 with $kR_0 = 10.15$ is plotted in the xy-plane. The solid domain is cut open for visualization purposes.

finite element approximation of the solution [40], so one could expect the C^0-IGA meshes (with $\check{k} = 0$) to produce the same accuracy as the isoparametric FEM meshes of higher order ($\check{p} \geqslant 2$). It should be noted that the FEM analysis would then use the Bernstein basis instead of the classical Lagrange basis. However, both of these set of functions spans the same spaces, such that the results should be identical in the absence of round-off errors.

In Figure 9 we illustrate h-refinement through the error in the energy norm for the first benchmark example (rigid scattering). Predicted convergence rates are not obtained until the aspect ratio of the elements are reduced sufficiently (that is, from mesh $\mathcal{M}_4$ and onward). By comparing the results of mesh $\mathcal{M}^{\text{FEM}}_{m,2,\text{i}}$ and mesh $\mathcal{M}^{\text{IGA}}_{m,2,0}$ it can be concluded that the geometry error of mesh $\mathcal{M}^{\text{FEM}}_{m,2,\text{i}}$ has almost no impact on the accuracy. However, when using maximum continuity, we get significantly better results. Expected convergence rates are visualized in Figure 10 where we now plot the energy norm against $\lambda/h_{\max}$ (corresponding to the number of elements per wave) with λ being the wavelength $\lambda = 2\pi/k$. A key observation is that the number of elements per wave (needed to obtain a given accuracy) is greatly reduced with higher order IGA methods compared to the classical linear FEM (where 10 elements per wavelength is typically desired for engineering precision, [30, p. 182]). The result for the subparametric meshes $\mathcal{M}^{\text{FEM}}_{m,2,\text{s}}$ indicates that the convergence rate is reduced due to the reduced accuracy in the geometric representation. This is to be expected as shown in [40, p. 202].

Approaching the ASI problems, we illustrate some meshes in Figure 11 for the full ASI problem. The corresponding meshes for the SSBC problem (with $p_2 = 0$) are obtained by removing the mesh inside the solid domain. In Figures 12 to 17 the target strength, TS, and the error in the energy norm is plotted against the scaled wave number, kR_0, in all of the three Ihlenburg benchmarks. As each frequency sweep is computed with a different number of degrees of freedom, one should draw the conclusions based on comparing both the accuracy of the results and the related computational costs.

Some data from simulations at $k = 1\,\text{m}^{-1}$ are reported in Table 2 (simulation run with 12 processors of the type Intel(R) Xeon(R) CPU E5-4650 2.70GHz). It should be noted that all simulations were done using the same code, such that the computational time for the FEM simulations can be optimized. However, this is actually the case for the IGA code as well since the implementation does not utilize optimized quadrature rules. The integration is done with $(\check{p}+1)^3$ quadrature points per element when building the system. For higher order splines spaces this is significantly more quadrature point than what is needed for exact integration (on meshes with affine geometry mapping[7]). In [42, 43], it is shown that the optimal number of quadrature points is half the number of degrees of freedom of

[7]Using the same quadrature scheme on truly isoparametric elements will according to [41, p. 256] give a numerical integration error of the same order as the finite element discretization error. Thus, the argument for optimal quadrature scheme also holds for isoparametric elements as well.

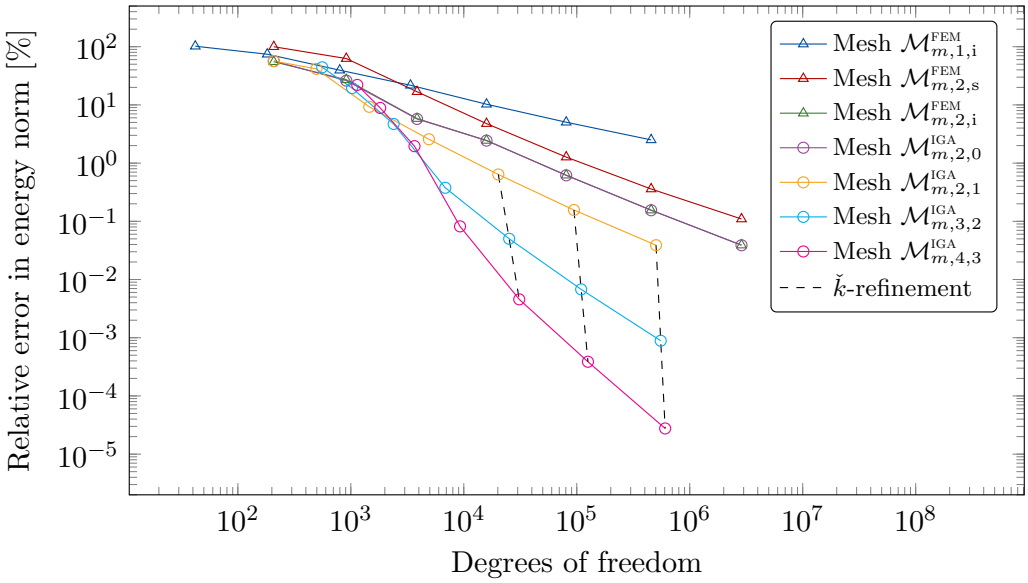

Figure 9: **Ihlenburg benchmark with SHBC**: Convergence analysis on the rigid scattering case with $k = 1\,\mathrm{m}^{-1}$ and mesh $\mathcal{M}_m$, $m = 1, \ldots, 7$, using $N = 6$. The relative energy error (Eq. (67)) is plotted against the degrees of freedom.

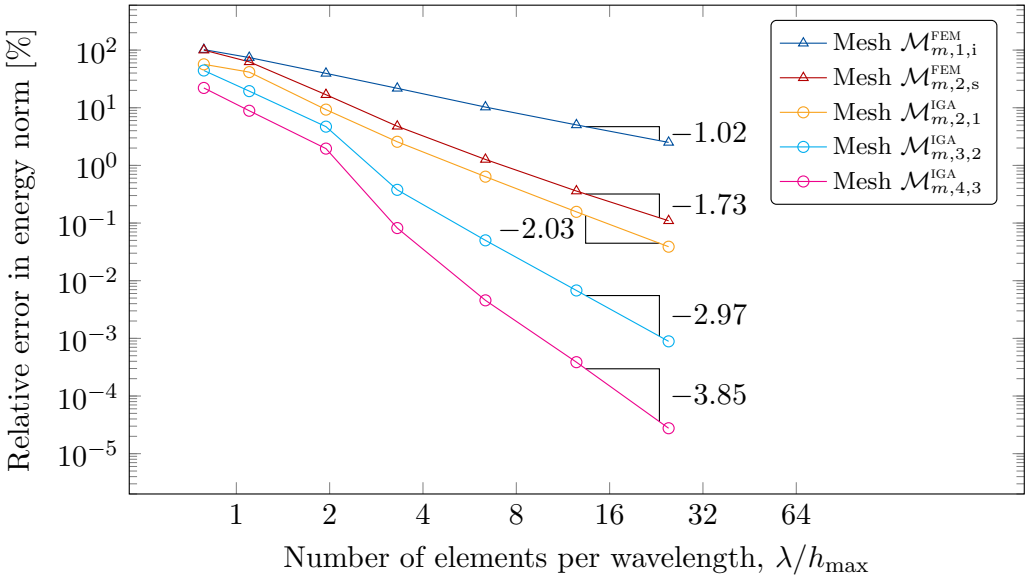

Figure 10: **Ihlenburg benchmark with SHBC**: Convergence analysis on the rigid scattering case with $k = 1\,\mathrm{m}^{-1}$ and mesh $\mathcal{M}_m$, $m = 1, \ldots, 7$, using $N = 6$. The relative energy error (Eq. (67)) is plotted against the number of elements per wave.

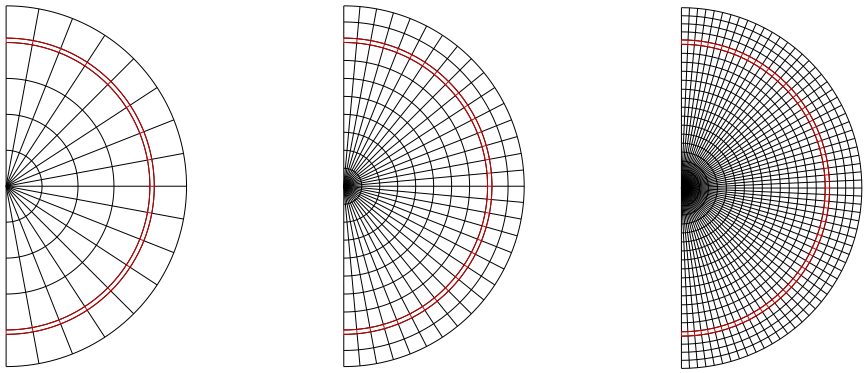

(a) Mesh $\mathcal{M}^{\text{IGA}}_{4,\check{p},\check{k}}$ (b) Mesh $\mathcal{M}^{\text{IGA}}_{5,\check{p},\check{k}}$ (c) Mesh $\mathcal{M}^{\text{FEM}}_{6,1,\text{i}}$

Figure 11: **Ihlenburg benchmark with NNBC**: Illustration of some meshes for the full ASI problem in the xz-plane ($x > 0$), where the mesh lines for the solid domain is colored red. The full mesh is obtained by rotation around the z-axis. Mesh $\mathcal{M}^{\text{FEM}}_{5,2,\text{i}}$ is visually indistinguishable from $\mathcal{M}^{\text{IGA}}_{5,\check{p},\check{k}}$.

the splines space under consideration. That is, the number of quadrature points in the IGA 3D tensor product meshes can be reduced by a factor up to $2^3(\check{p}+1)^3$ for meshes with maximal continuity. Thus, the efficiency of the IGA simulation may be improved significantly.

A particular interesting observation is that IGA obtains roughly the same accuracy as FEM when the same number of elements is used, even though this corresponds to far less degrees of freedom for the IGA simulation. Moreover, even better result can be obtained with less degrees of freedom if the polynomial degree is increased in the IGA simulations. This, however, only occurs when the mesh resolves the number of waves per element. When the mesh is sufficiently resolved, one order of magnitude improvement in the accuracy is obtained by increasing the polynomial degree. Since another magnitude of accuracy is obtained by using higher order elements in FEM/IGA, the IGA offers several orders of magnitude better accuracy than classical linear FEM.

The peaks in the frequency sweeps represent eigenmodes. The quality of the numerical approximation of the corresponding frequencies is reduced for higher frequencies, resulting in fictitious modes. This typically does not pose that much of a problem as the bandwidth of these eigenmodes becomes very small, with a corresponding reduction in the energy they represent. Note that mesh $\mathcal{M}^{\text{IGA}}_{4,3,2}$ performs particularly poorly on the partial ASI problem due to a fictitious mode at $k = 1\,\text{m}^{-1}$ for this mesh. The improvement offered by IGA concerning the accuracy in the eigenmodes is investigated in [44].

It should be noted that the meshes used throughout this work are not optimal. This is in particular the case for the full ASI problem where the density of elements

becomes large at the origin. These meshes were used as they naturally arise from tensor product NURBS meshes of spherical shells and spheres. One could thus obtain increased performance for the FEM solutions using standard meshing of the domain. However, locally refined meshes can also be obtained with the IGA method, for example using LR B-splines [45].

In Figure 18 we visualize the distribution of the error of the full ASI problem. The error is observed to be largest at element boundaries where the continuity is reduced. Since second order basis functions are used and the error in the velocity/stress dominates the error in the pressure/displacement, the results are in agreement with what was observed in [46], i.e., that the error in the derivative of the primary solution is largest at the element boundaries.

4.3. Radial pulsation from a mock shell

By construction of the fundamental solution of the Helmholtz equation ($\Phi_k(\boldsymbol{x}, \boldsymbol{y})$ in Eq. (46)), the function $p(\boldsymbol{x}) = \Phi_k(\boldsymbol{x}, \boldsymbol{y})$ is a solution to Eqs. (2) to (4) whenever $\boldsymbol{y} \in \mathbb{R}^3 \setminus \overline{\Omega^+}$ and for the Neumann boundary condition $g(\boldsymbol{x}) = \partial_n \Phi_k(\boldsymbol{x}, \boldsymbol{y})$ on Γ_0. Hence, we have an exact reference solution for the exterior Helmholtz problem for arbitrary geometries Γ_0 which encloses the point $\boldsymbol{y}$. It is emphasized that this solution is non-physical for non-spherical geometries Γ_0. General solutions may be constructed by separation of variables (cf. [30, p. 26])

$$p(\boldsymbol{x}) = \sum_{n=0}^{\infty} \sum_{m=-n}^{n} C_{nm} \mathrm{h}_n^{(1)}(kR) \mathrm{P}_n^{|m|}(\cos\vartheta) \mathrm{e}^{\mathrm{i}m\varphi} \tag{72}$$

with

$$R = |\boldsymbol{x} - \boldsymbol{y}|, \quad \vartheta = \arccos\left(\frac{x_3 - y_3}{R}\right), \quad \varphi = \operatorname{atan2}(x_2 - y_2, x_1 - y_1)$$

where $\mathrm{h}_n^{(1)}$ is the n^{th} spherical Hankel function of first kind and P_n^m are the associated Legendre functions. In fact, the solution $p(\boldsymbol{x}) = \Phi_k(\boldsymbol{x}, \boldsymbol{y})$ is a special case of this general form with

$$C_{nm} = \begin{cases} \frac{\mathrm{i}k}{4\pi} & n = 0,\ m = 0 \\ 0 & \text{otherwise.} \end{cases} \tag{73}$$

The complexity of this problem setup does not scale with the complexity of the model as it is independent of Γ_0. However, it preserves two important properties of acoustic scattering, namely the radial decay and the oscillatory nature. Thus, this problem setup represents a general way of constructing manufactured solutions, that can be utilized to verify the correctness of the implemented code for solving the Helmholtz equation. A special case of this general setup is the pulsating sphere example in [36].

Table 2: **Ihlenburg benchmark**: Data for some simulations on the rigid scattering problem with $k = 1\,\mathrm{m}^{-1}$. The errors are given in the energy norm (Eq. (69)). For each simulation, the mesh number, the polynomial order, $\check{p}$, the number of mesh elements n_{el} (not including the infinite elements) and the number of degrees of freedom n_{dof}, is reported. The elapsed times for building the system t_{sys} and for solving the system t_{sol} (using LU-factorization) are also included (times in seconds). Finally, the relative error in the energy norm is given in percentage.

(a) Sound-hard boundary conditions (SHBC).

	n_{el}	n_{dof}	t_{sys} [s]	t_{sol} [s]	Relative energy error [%]
Mesh $\mathcal{M}^{\mathrm{FEM}}_{6,1,\mathrm{i}}$	32 768	56 462	7.7	26.5	5.04
Mesh $\mathcal{M}^{\mathrm{FEM}}_{5,2,\mathrm{i}}$	4096	56 462	5.1	20.5	0.62
Mesh $\mathcal{M}^{\mathrm{IGA}}_{5,2,1}$	4096	13 476	4.8	4.3	0.64
Mesh $\mathcal{M}^{\mathrm{IGA}}_{4,3,2}$	512	4572	3.1	1.6	0.38
Mesh $\mathcal{M}^{\mathrm{IGA}}_{5,3,2}$	4096	17 654	14.8	8.3	0.05

(b) Sound-soft boundary conditions (SSBC).

	n_{el}	n_{dof}	t_{sys} [s]	t_{sol} [s]	Relative energy error [%]
Mesh $\mathcal{M}^{\mathrm{FEM}}_{6,1,\mathrm{i}}$	40 960	104 858	13.7	75.3	7.66
Mesh $\mathcal{M}^{\mathrm{FEM}}_{5,2,\mathrm{i}}$	6144	129 056	15.9	106.1	1.35
Mesh $\mathcal{M}^{\mathrm{IGA}}_{5,2,1}$	6144	33 690	13.4	34.7	0.99
Mesh $\mathcal{M}^{\mathrm{IGA}}_{4,3,2}$	1024	13 716	11.8	9.0	41.30
Mesh $\mathcal{M}^{\mathrm{IGA}}_{5,3,2}$	6144	47 918	52.0	69.9	0.09

(c) Neumann-Neumann boundary conditions (NNBC).

	n_{el}	n_{dof}	t_{sys} [s]	t_{sol} [s]	Relative energy error [%]
Mesh $\mathcal{M}^{\mathrm{FEM}}_{6,1,\mathrm{i}}$	172 032	233 915	27.8	429.5	6.55
Mesh $\mathcal{M}^{\mathrm{FEM}}_{5,2,\mathrm{i}}$	22 528	258 113	31.1	462.7	0.53
Mesh $\mathcal{M}^{\mathrm{IGA}}_{5,2,1}$	22 528	53 905	22.5	64.9	0.71
Mesh $\mathcal{M}^{\mathrm{IGA}}_{4,3,2}$	3072	18 289	17.1	17.3	1.47
Mesh $\mathcal{M}^{\mathrm{IGA}}_{5,3,2}$	22 528	73 139	93.2	145.7	0.05

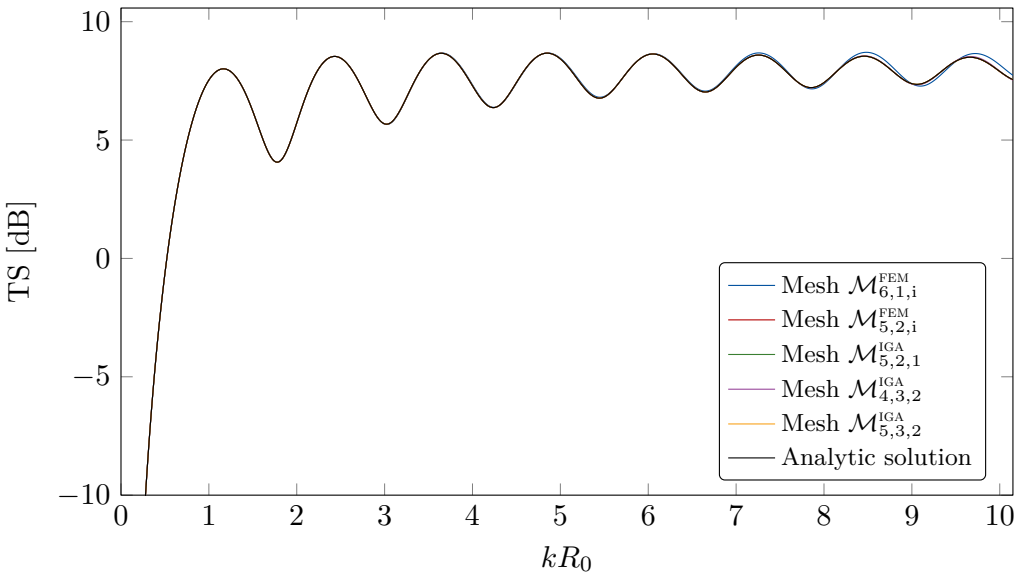

Figure 12: **Ihlenburg benchmark with SHBC**: The target strength (TS) in Eq. (52) is plotted against kR_0.

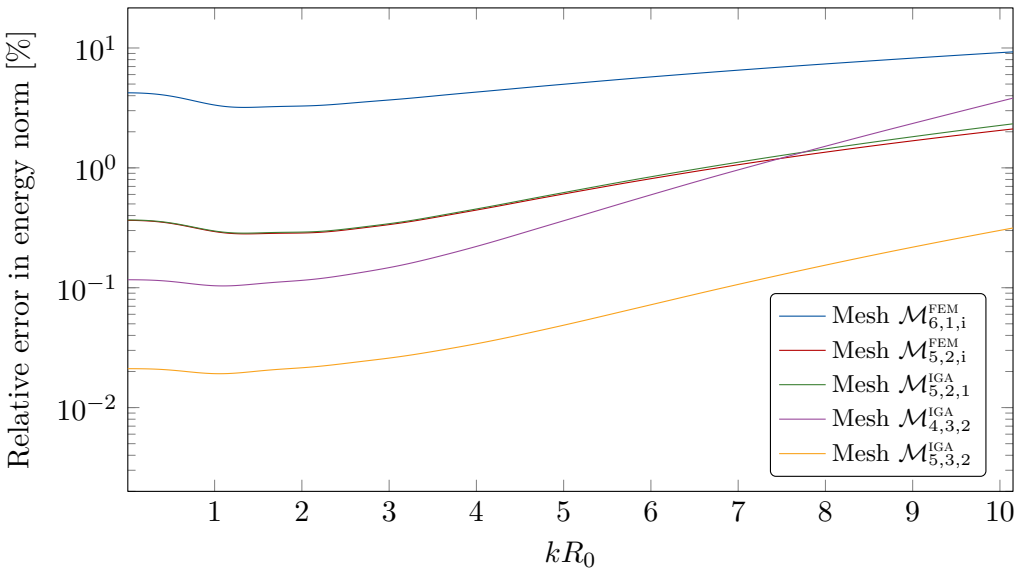

Figure 13: **Ihlenburg benchmark with SHBC**: The relative energy norm (Eq. (69)) is plotted against kR_0.

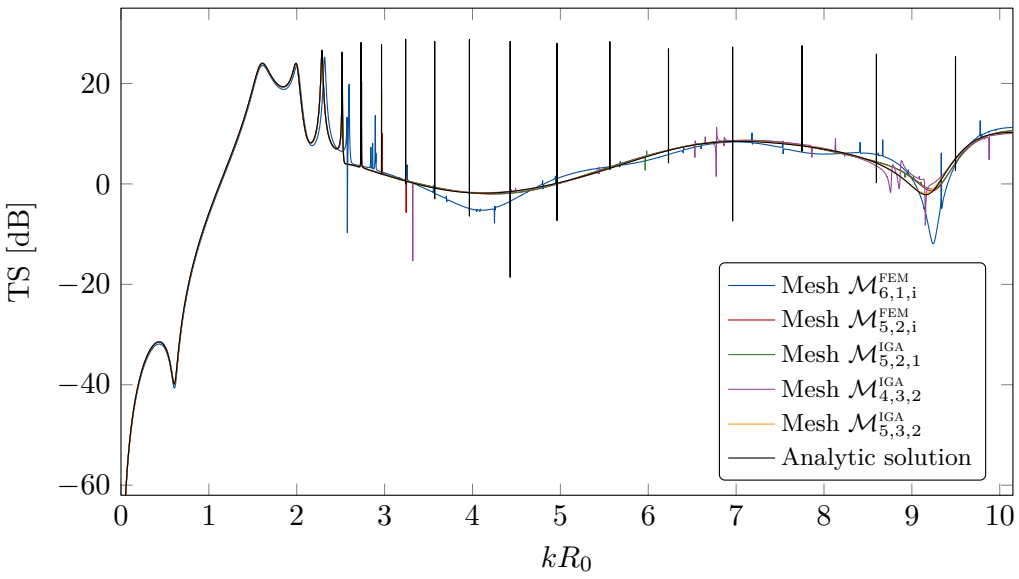

Figure 14: **Ihlenburg benchmark with SSBC**: ASI problem with the internal pressure modeled to be $p_2 = 0$. The target strength (TS) in Eq. (52) is plotted against kR_0.

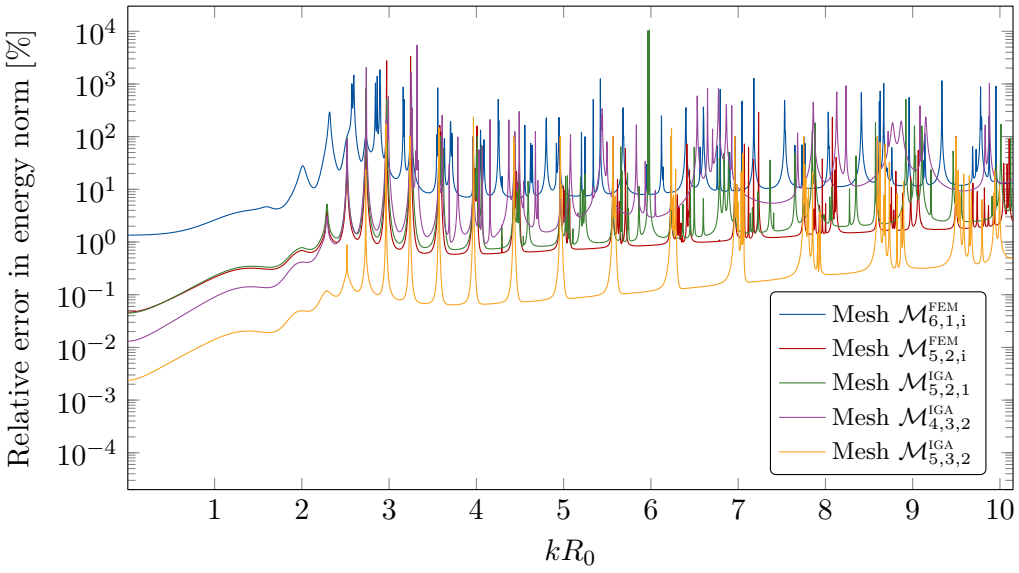

Figure 15: **Ihlenburg benchmark with SSBC**: ASI problem with the internal pressure modeled to be $p_2 = 0$. The relative energy norm (Eq. (69)) is plotted against kR_0.

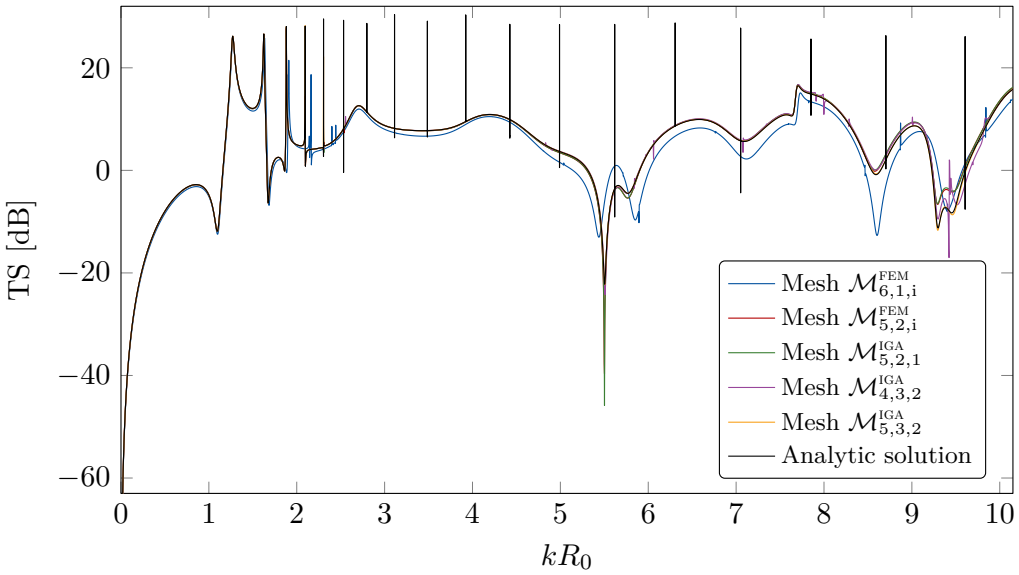

Figure 16: **Ihlenburg benchmark with NNBC**: The target strength (TS) in Eq. (52) is plotted against kR_0.

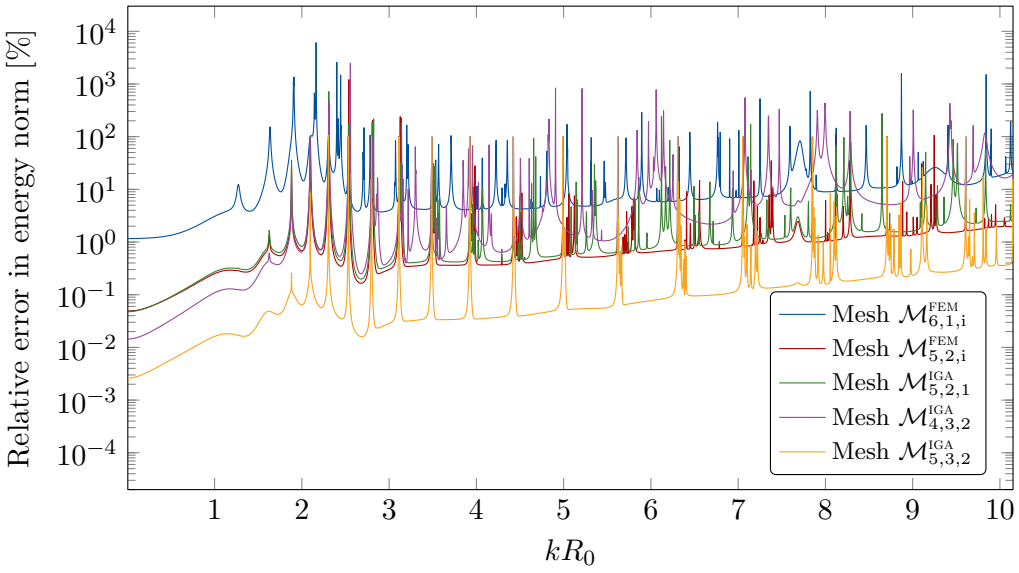

Figure 17: **Ihlenburg benchmark with NNBC**: The relative energy norm (Eq. (69)) is plotted against kR_0.

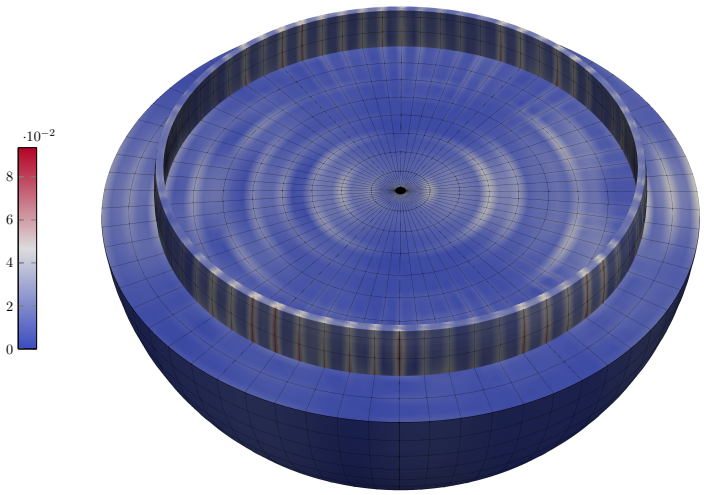

Figure 18: **Ihlenburg benchmark with NNBC**: Simulation of the full ASI problem on mesh $\mathcal{M}^{\mathrm{IGA}}_{5,2,1}$. Pointwise evaluation of the square root of the integrand of the volume integrals in the energy norm $|||U - U_h|||_\Omega$ in Eq. (69) with $k = 2\,\mathrm{m}^{-1}$ (error in the infinite elements in Ω_{a}^+ is not shown) is here visualized, where U is the set of analytic solutions in both fluid domains and the solid domain, and U_h is the corresponding numerical solution. The values are scaled by the square root of the maximum of the corresponding integrand values of $|||U|||_\Omega$. Both fluid domains are cut open at the xy-plane (at $z = 0$), and the solid domain is cut open at $z = 1.1\,\mathrm{m}$.

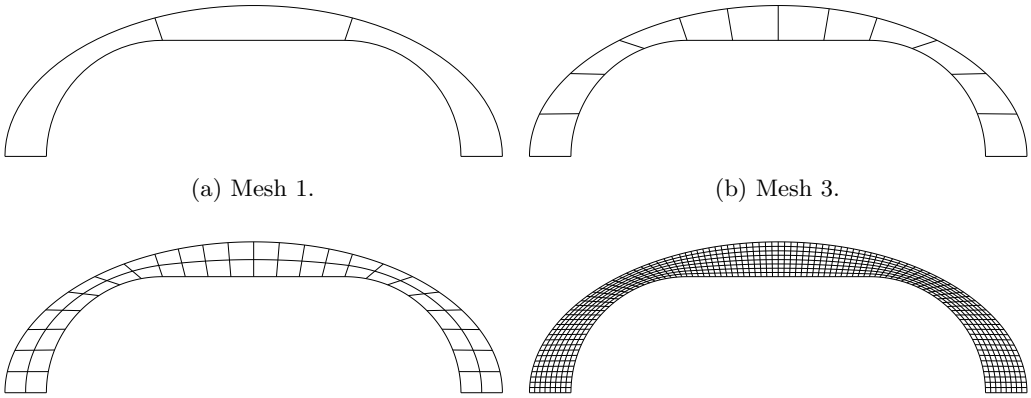

(a) Mesh 1. (b) Mesh 3.

(c) Mesh 4. (d) Mesh 6.

Figure 19: **Radial pulsation from a mock shell**: Meshes for the fluid domain between the scatterer and the artificial boundary. The meshes are constructed from the initial mesh 1, which is rotated around the axis of symmetry using four elements. Mesh 2 and 3 are refined only in the angular direction, while the more refined meshes also refine in the radial direction to obtain smallest aspect ratio. The meshes are nested.

From the first limit of Eqs. (49) and (50), the far field is given by $p_0(\hat{\boldsymbol{x}}) = \frac{1}{4\pi}\mathrm{e}^{-\mathrm{i}k\hat{\boldsymbol{x}}\cdot\boldsymbol{y}}$. Thus, the target strength is a constant, $\mathrm{TS} = -20\log_{10}(4\pi) \approx -21.984$ (where we define $P_{\mathrm{inc}} = 1\,\mathrm{Pa}$ in Eq. (52) for this problem).

Consider the case $\boldsymbol{y} = \frac{R_0}{4}(1,1,1)$ and the boundary Γ_0 given by a *mock shell* composed of a cylinder with hemispherical endcaps (with axis of symmetry along the x-axis such that the center of the spherical endcaps are located at $x = 0$ and $x = -L$). The cylinder has radius $R_0 = 1\,\mathrm{m}$ and length $L = \frac{\pi}{2}R_0$. The analytic solution is given by

$$p(\boldsymbol{x}) = \frac{\mathrm{e}^{\mathrm{i}kR}}{4\pi R}, \quad R = |\boldsymbol{x} - \boldsymbol{y}| \tag{74}$$

and the Neumann condition is then

$$g(\boldsymbol{x}) = \frac{\mathrm{e}^{\mathrm{i}kR}}{4\pi R^3}(\mathrm{i}kR - 1)(\boldsymbol{x} - \boldsymbol{y}) \cdot \boldsymbol{n}(\boldsymbol{x}). \tag{75}$$

This example is used to illustrate the differences of the infinite element formulations using the prolate ellipsoidal elements after Burnett [13]. The mesh construction is illustrated in Figure 19, and an illustration of the solution is presented in Figure 20. Convergence plots are shown in Figure 21. Gerdes did a similar comparison in [31] where scattering on a sphere was investigated. Our results verify these findings, namely lower errors for the unconjugated formulations (cf. Figure 21). Good results can be obtained using only a single radial shape

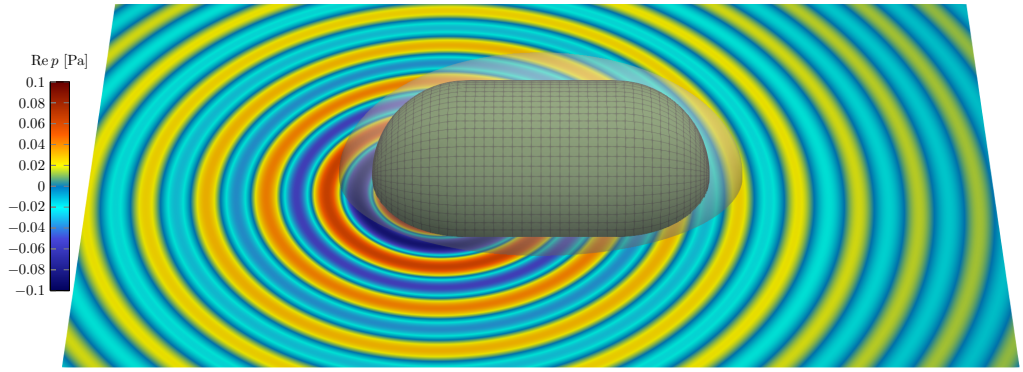

Figure 20: **Radial pulsation from a mock shell**: Visualization of numerical solution in the xy-plane using BGU with $N = 6$ on mesh 5.

function in case of unconjugated formulations. For the conjugated versions, on the other hand, $N > 6$ functions are needed to obtain similar accuracy and more degrees of freedom are required to get an asymptotic behavior.

In Figure 22 and Figure 23 the condition number is investigated for the different formulations and basis functions in the radial shape functions. The condition number for the unconjugated versions increases more rapidly as a function of N compared to the corresponding formulations in the conjugated case. The condition number of the Lagrange basis increases particularly fast with N, making it useless[8] for the conjugated formulations. However, the Lagrange basis yields the best result for the unconjugated formulations for small N. The Chebyshev basis seems to give the best condition numbers for the conjugated formulations for large N (which is required for acceptable results). The unconjugated formulations perform quite similar, both in terms of the condition numbers and the error. The BGU formulation has the additional advantage of producing symmetric matrices and reduces the memory requirement.

It is clear that the choice of basis functions in the infinite elements plays a crucial role for the condition number, and more research is required to find the optimal set of basis functions. Based on the findings in this work, it is recommended to use the BGU formulation alongside the Lagrange basis (in the radial direction) in the infinite elements. However, if larger N is needed for accuracy, the Chebyshev basis is recommended.

4.4. Stripped BeTSSi submarine

Finally, we consider the *stripped BeTSSi submarine*[9] described in Appendix C.

[8] In the case of $r_n = nr_a$.

[9] Based upon the BeTSSi submarine which originates from the BeTSSi workshops [1].

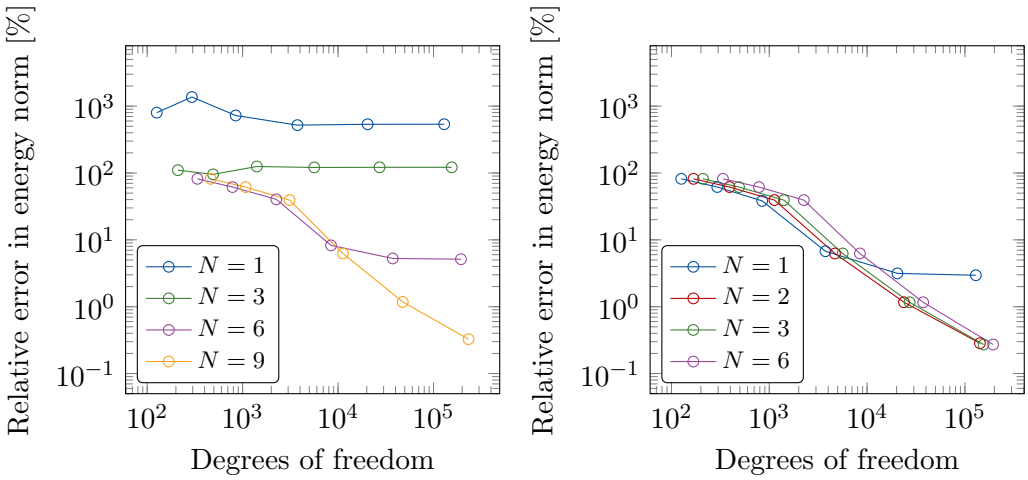

(a) BGC (b) BGU

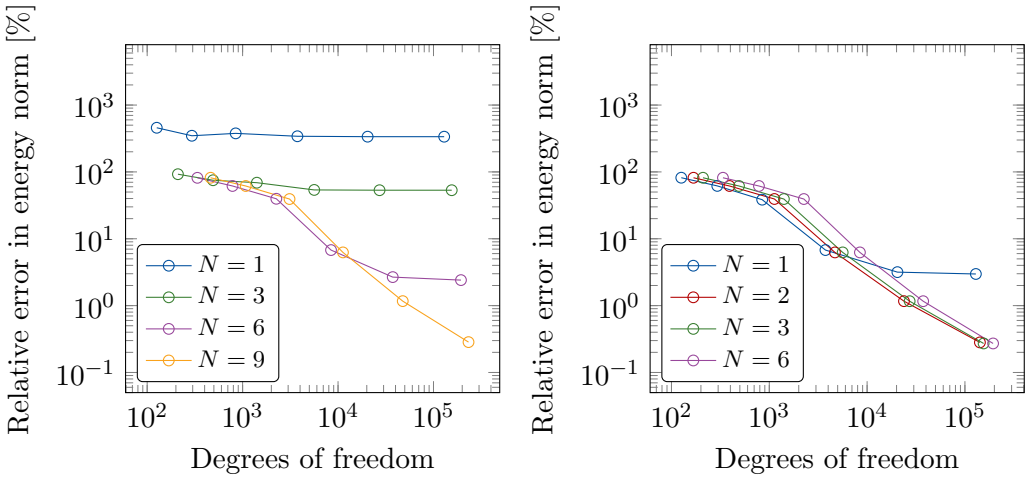

(c) PGC (d) PGU

Figure 21: **Radial pulsation from a mock shell**: Convergence plots for the four infinite element formulations. The relative error in the energy norm (Eq. (67)) is plotted against the number of degrees of freedom.

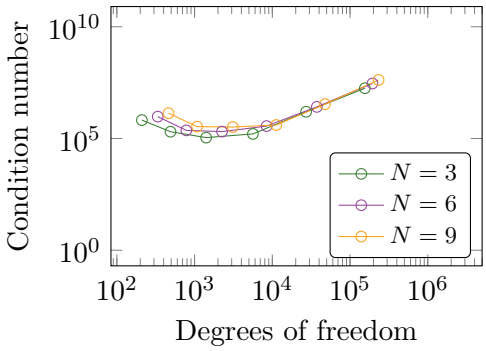

(a) BGC with the shifted Chebyshev basis

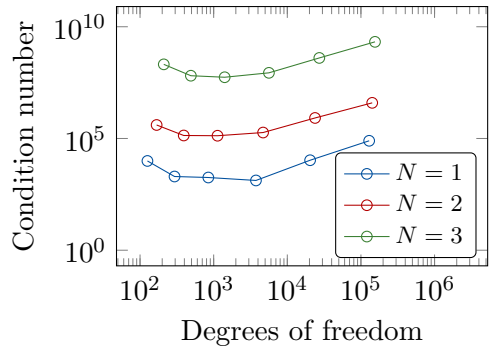

(b) BGU with the shifted Chebyshev basis

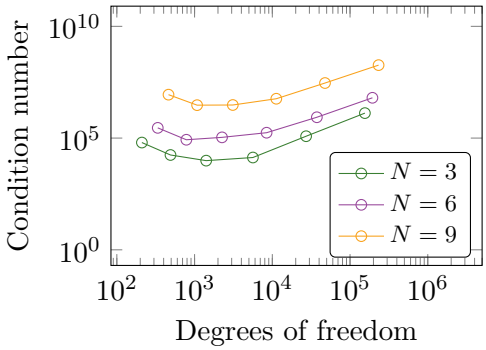

(c) BGC with the Bernstein basis

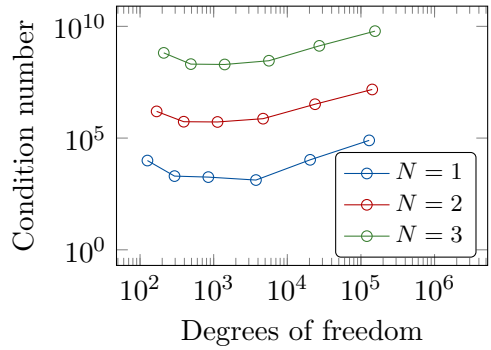

(d) BGU with the Bernstein basis

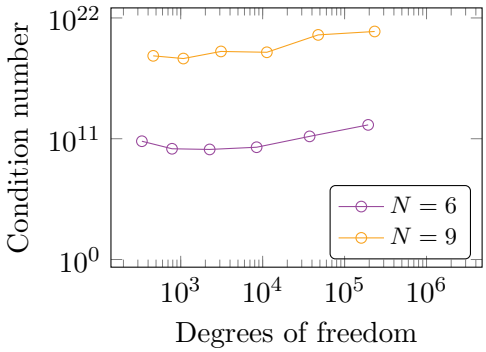

(e) BGC with the Lagrange basis

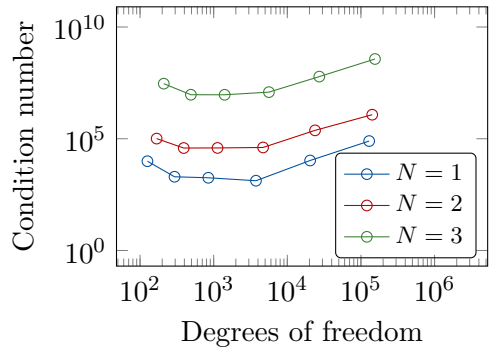

(f) BGU with the Lagrange basis

Figure 22: **Radial pulsation from a mock shell**: Convergence plots for the BGC and BGU formulations using three different sets of radial shape functions (Chebyshev, Bernstein and Lagrange). The condition number (1-norm condition number estimate provided by `condest` in MATLAB) is plotted against the number of degrees of freedom.

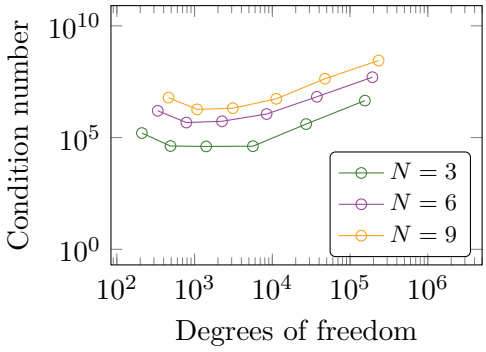

(a) PGC with the shifted Chebyshev basis

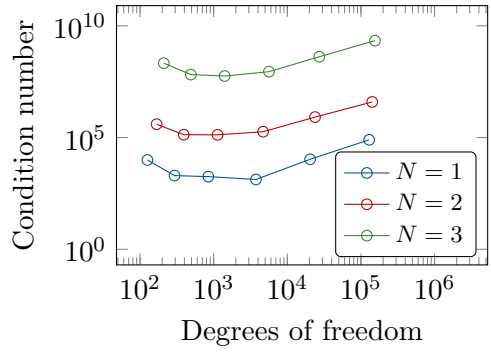

(b) PGU with the shifted Chebyshev basis

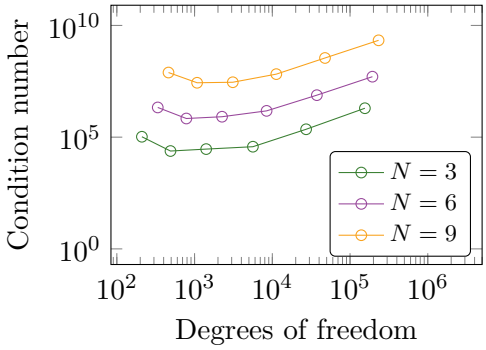

(c) PGC with the Bernstein basis

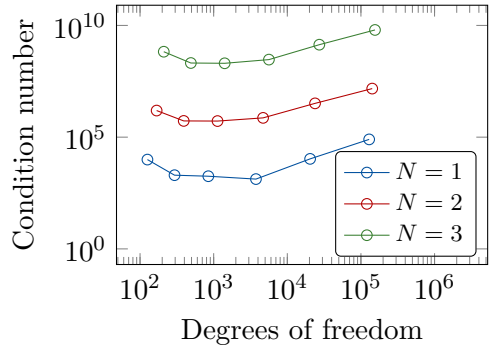

(d) PGU with the Bernstein basis

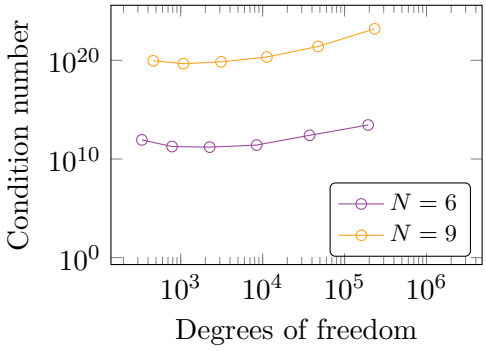

(e) PGC with the Lagrange basis

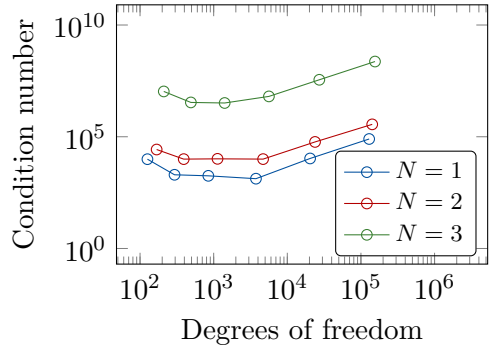

(f) PGU with the Lagrange basis

Figure 23: **Radial pulsation from a mock shell**: Convergence plots for the PGC and PGU formulations using three different sets of radial shape functions (Chebyshev, Bernstein and Lagrange). The condition number (1-norm condition number estimate provided by `condest` in MATLAB) is plotted against the number of degrees of freedom.

Let a plane wave, with the direction of incidence given by

$$\boldsymbol{d}_{\mathrm{s}} = -\begin{bmatrix} \cos\beta_{\mathrm{s}} \cos\alpha_{\mathrm{s}} \\ \cos\beta_{\mathrm{s}} \sin\alpha_{\mathrm{s}} \\ \sin\beta_{\mathrm{s}} \end{bmatrix}, \quad \text{where} \quad \alpha_{\mathrm{s}} = 240^{\circ},\ \beta_{\mathrm{s}} = 0^{\circ}, \tag{76}$$

be scattered by this submarine. The CAD model is given in Figure 24 alongside computational meshes. Again, we shall denote by $\mathcal{M}^{\mathrm{IGA}}_{m,\check{p},\check{k}}$, mesh number m with polynomial order $\check{p}$ and continuity $\check{k}$ across element boundaries of the NURBS parametrization.

The near field at $f = 1000\,\mathrm{Hz}$ is visualized in Figure 25. The low frequency problem at $f = 100\,\mathrm{Hz}$ is considered in Figure 26. In this case, mesh $\mathcal{M}^{\mathrm{IGA}}_{1,2,1}$ resolves this frequency, but the solution slightly deviates from the reference solution computed by IGABEM on a fine mesh. The reason for this is that N is too low. Although $N = 3$ was enough for engineering precision (below 1%) in the mock shell example, it does not suffice for the more complicated geometry like the stripped BeTSSi submarine. Consider the relative error for the far field at the well resolved mesh $\mathcal{M}^{\mathrm{IGA}}_{2,3,2}$. In this case the error will originate from the low resolution (governed by N) in the radial direction for the infinite elements. As illustrated in Figure 27 an order of magnitude in accuracy is gained by increasing N. This effect was also observed by the verification test in Subsection 4.3 applied to the stripped BeTSSi submarine. In Figure 28 the target strength is plotted for $f = 500\,\mathrm{Hz}$ and $f = 1000\,\mathrm{Hz}$. A reference solution (using IGABEM) is added for the $f = 500\,\mathrm{Hz}$ case, and illustrates again the pollution of low N. The IGA mesh 1 resolves the frequency $f = 500\,\mathrm{Hz}$ quite well using only about 5 elements per wavelength. This corresponds to about 5 dofs per wavelength in each dimensional direction compared to the classical 10-12 dofs per wavelength needed for FEM methods.

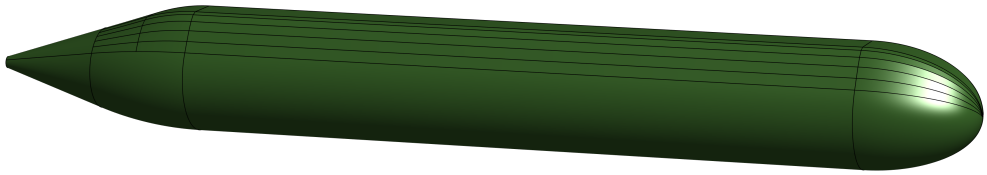

(a) CAD model.

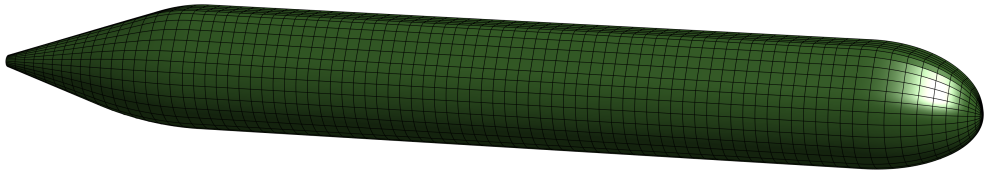

(b) Surface mesh for mesh $\mathcal{M}^{\mathrm{IGA}}_{1,\check{p},\check{k}}$

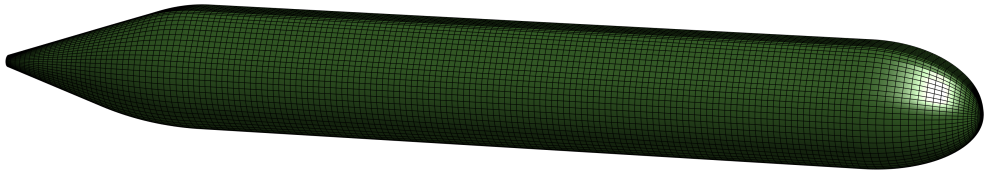

(c) Surface mesh for mesh $\mathcal{M}^{\mathrm{IGA}}_{2,\check{p},\check{k}}$.

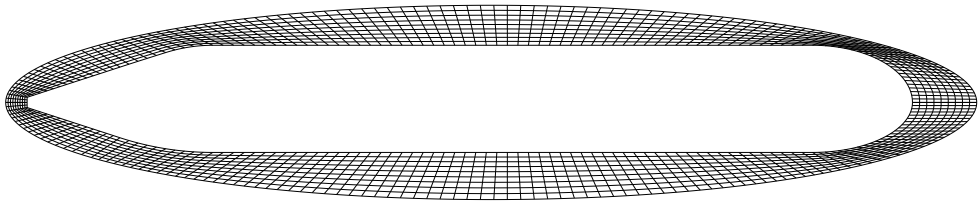

(d) Cross section in the xz-plane for mesh $\mathcal{M}^{\mathrm{IGA}}_{1,\check{p},\check{k}}$.

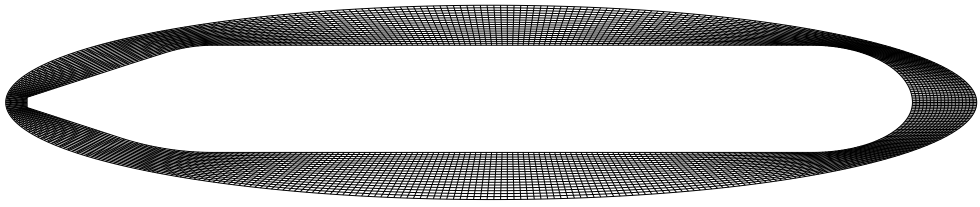

(e) Cross section in the xz-plane for mesh $\mathcal{M}^{\mathrm{IGA}}_{2,\check{p},\check{k}}$.

Figure 24: **Stripped BeTSSi submarine**: CAD model and meshes used for computations.

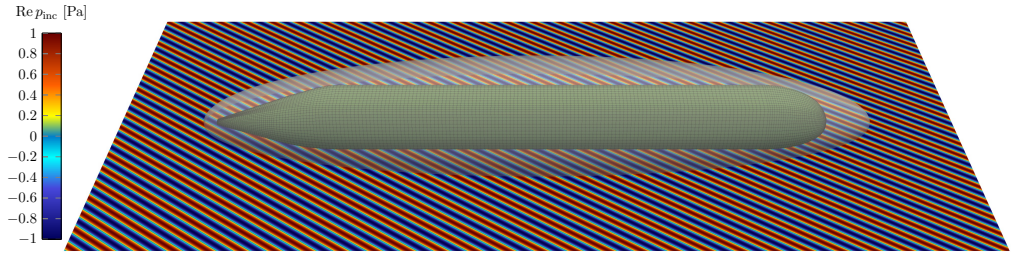

(a) Real part of the incident wave $p_{\text{inc}}(\boldsymbol{x}) = P_{\text{inc}} \mathrm{e}^{\mathrm{i}k\boldsymbol{d}_{\text{s}}\cdot\boldsymbol{x}}$.

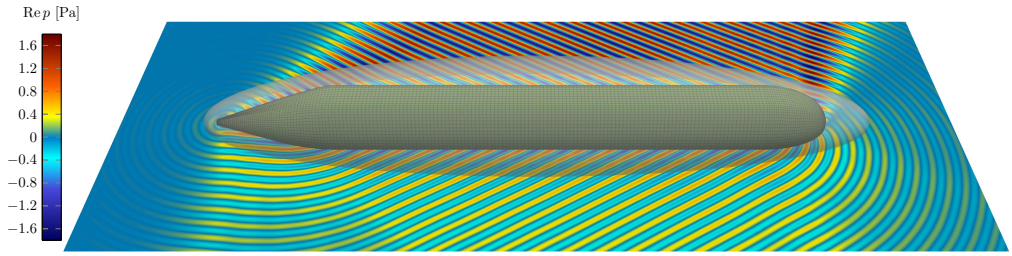

(b) Real part of the scattered pressure $p(\boldsymbol{x})$.

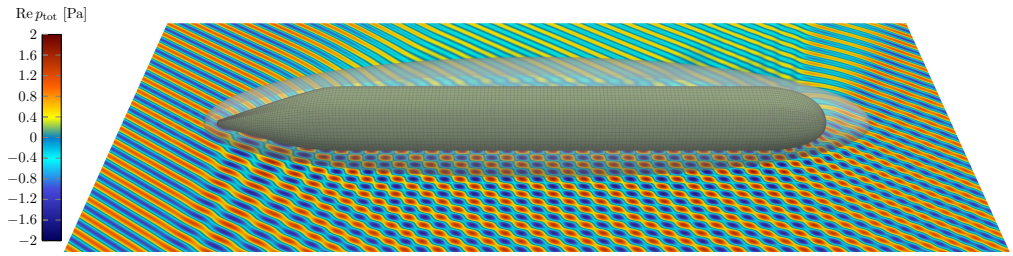

(c) Real part of the total pressure $p_{\text{tot}}(\boldsymbol{x}) = p_{\text{inc}}(\boldsymbol{x}) + p(\boldsymbol{x})$.

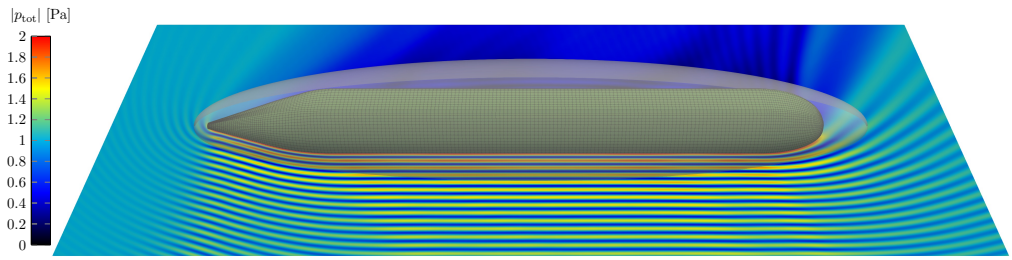

(d) Modulus of the total pressure $p_{\text{tot}}(\boldsymbol{x}) = p_{\text{inc}}(\boldsymbol{x}) + p(\boldsymbol{x})$.

Figure 25: **Stripped BeTSSi submarine with SHBC**: The simulation at $f = 1000\,\text{Hz}$ is visualized in the xy-plane, and is computed on mesh $\mathcal{M}_{2,3,2}^{\text{IGA}}$ and the BGU formulation with $N = 4$. The numerical evaluations outside the (transparent) prolate ellipsoidal artificial boundary are evaluated with Eq. (45).

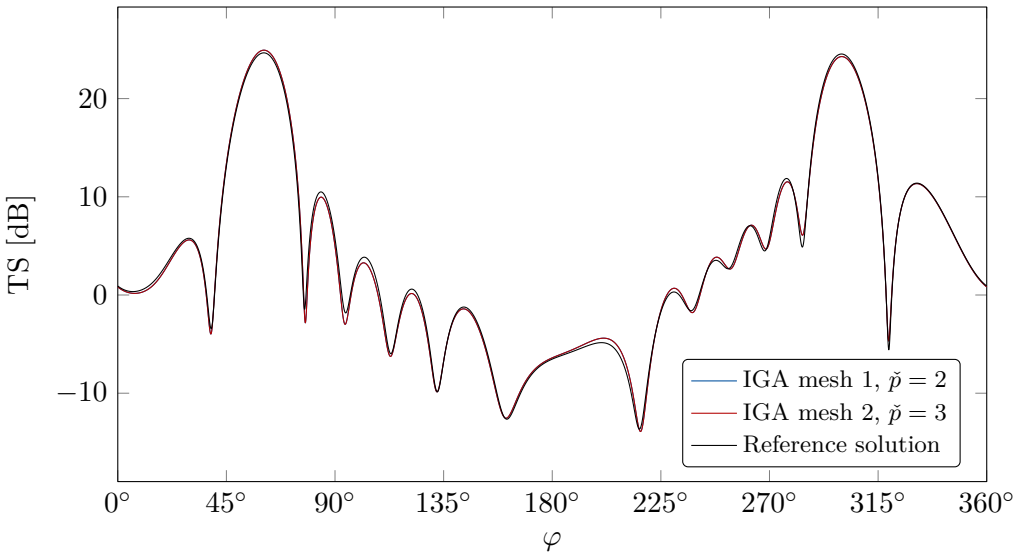

Figure 26: **Stripped BeTSSi submarine with SHBC**: Computation of target strength (Eq. (52)) at $f = 100\,\mathrm{Hz}$ as a function of the azimuth angle in the spherical coordinate system. The two IGA results (both using $N = 3$) are visually indistinguishable meaning that mesh $\mathcal{M}^{\mathrm{IGA}}_{1,2,1}$ is well resolved for this frequency.

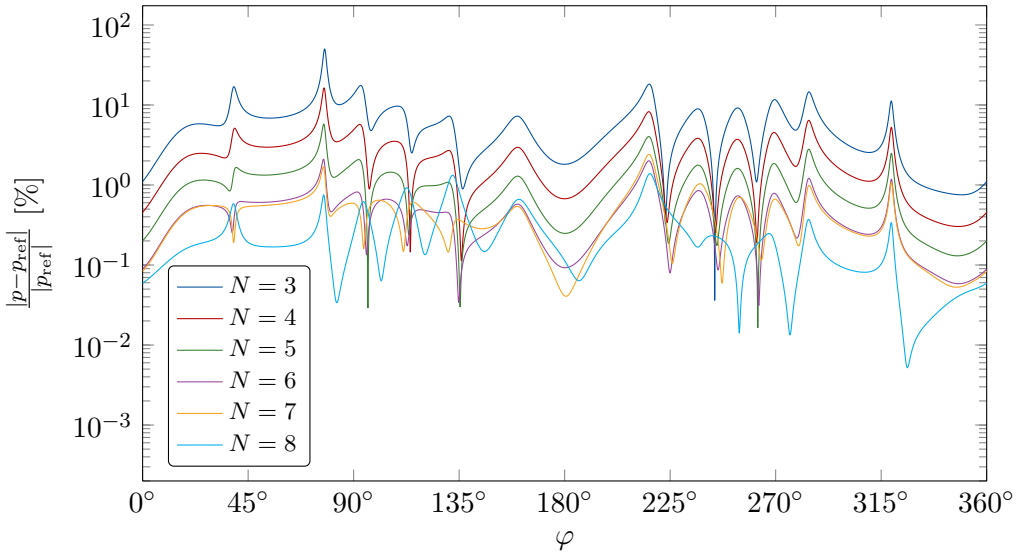

Figure 27: **Stripped BeTSSi submarine with SHBC**: Computation of the relative error in the far field (Eq. (45)) compared to a reference solution at $f = 100\,\mathrm{Hz}$. The computations are done using IGA on mesh $\mathcal{M}^{\mathrm{IGA}}_{2,3,2}$ using the BGU formulation.

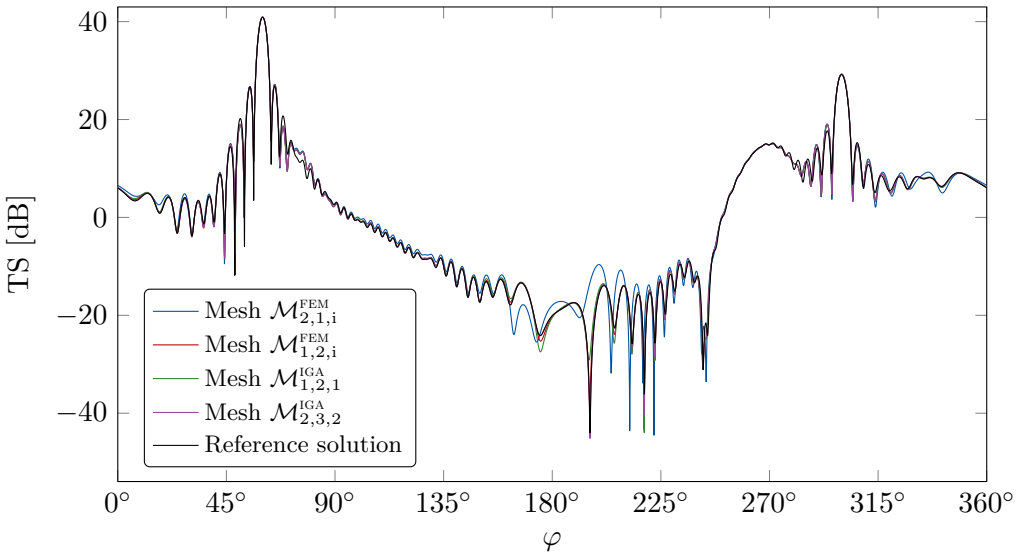

(a) $f = 500\,\text{Hz}$

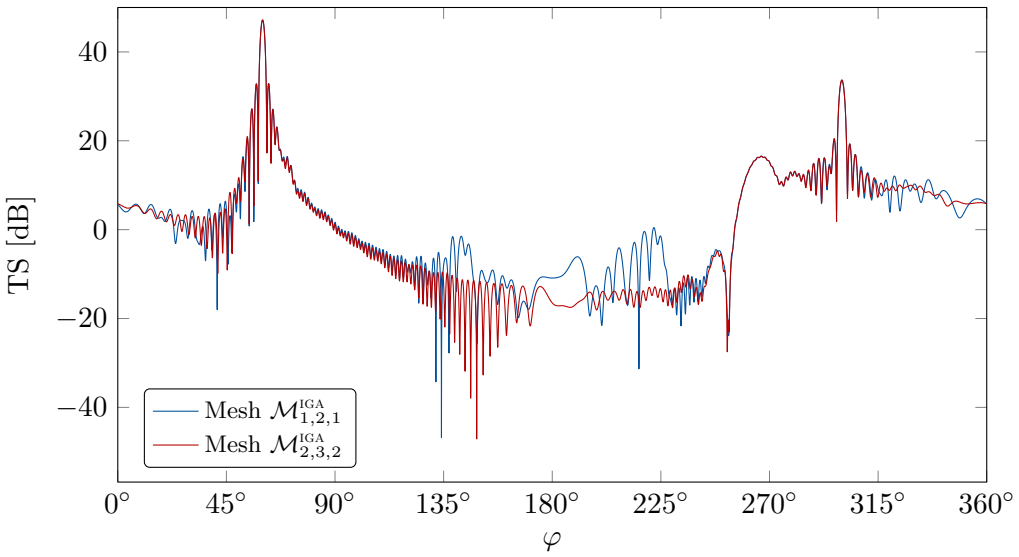

(b) $f = 1000\,\text{Hz}$

Figure 28: **Stripped BeTSSi submarine with SHBC**: Computation of target strength (Eq. (52)) as a function of the azimuth angle in the spherical coordinate system. The numerical evaluations are evaluated with Eq. (52).

5. Conclusions

This article addresses acoustic scattering characterized by sound waves reflected by man-made elastic objects. The present approach is characterized by:

- The fluid surrounding (inside and in the vicinity outside) the solid scatterer is discretized by using isogeometric analysis (IGA).
- The unbounded domain outside the artificial boundary circumscribing the scatterer is handled by use of the infinite element method (IEM).
- The elastic scatterer is discretized by using IGA.
- The coupled acoustic structure interaction (ASI) problem is solved as a monolithic problem.

The main finding of the present study is that the use of IGA significantly increases the accuracy compared to the use of C^0 finite element analysis (FEA) due to increased inter-element continuity of the spline basis functions.

Furthermore, the following observations are made

- IGA and the four presented IEM formulations work well on acoustic scattering for low frequencies. Among the infinite element formulations, the unconjugated version seems to give the best results.
- IGA's ability to represent the geometry exactly was observed to be of less importance for accuracy when comparing to higher order ($\check{p} \geqslant 2$) isoparametric FEA. However, a more significant improvement offered by IGA is due to higher continuity of the spline basis functions in the solution space.
- The IGA framework enables roughly the same accuracy per element (compared to higher order isoparametric FEA) even though the number of degrees of freedom is significantly reduced.
- IGA is more computationally efficient than FEA to obtain highly accurate solutions. That is, when the mesh is sufficiently resolved, a given accuracy is obtained computationally faster using IGA.
- As for the FEA, IGA also suffers from the pollution effect at high frequencies. This will always be a problem, and for the higher frequency spectrum, the methods must be extended correspondingly. The XIBEM [47, 48] (extended isogeometric boundary element method) is such an extension for the boundary element method. This technique (and similar enrichment strategies) could be applied to IEM as well and is suggested as future work.

- The IEM suffers from high condition numbers when the number of radial shape functions in the infinite elements (N) is large. This becomes a problem for more complex geometries as N must be increased to achieve higher precision.

The main disadvantages of using IGA with IEM is the need for a surface-to-volume parametrization between the scatterer and the artificial boundary, Ω_{a}. In this paper, the scatterer has been simple enough to discretize Ω_{a} using a single 3D NURBS patch. For more complex geometries, this becomes more involved, and is a topic of active research to this date in the IGA community [49–51]. The surface-to-volume parametrization and the conditioning are the main open issues of IGA with IEM and should be explored in future research.

Acknowledgements

This work was supported by the Department of Mathematical Sciences at the Norwegian University of Science and Technology and by the Norwegian Defence Research Establishment.

The stripped BeTSSi submarine simulations were performed on resources provided by UNINETT Sigma2 — the National Infrastructure for High Performance Computing and Data Storage in Norway (reference number: NN9322K/4317).

The authors would like to thank the reviewers for detailed response and many constructive comments.

A. Derivation of bilinear form in infinite elements

In this appendix, the integrals in the bilinear forms for the infinite elements will be separated for the PGU case[10]. For generality, the derivation is done in the prolate spheroidal coordinate system.

A.1. The prolate spheroidal coordinate system

The prolate spheroidal coordinate system is an extension of the spherical coordinate system. It is defined by the relations

$$x = \sqrt{r^2 - \Upsilon^2}\sin\vartheta\cos\varphi \tag{A.1}$$

$$y = \sqrt{r^2 - \Upsilon^2}\sin\vartheta\sin\varphi \tag{A.2}$$

$$z = r\cos\vartheta \tag{A.3}$$

with foci located at $z = \pm\Upsilon$ and $r \geqslant \Upsilon$. Note that the coordinate system reduces to the spherical coordinate system when $\Upsilon = 0$. the following inverse formulas may be derived

$$\begin{aligned} r &= \frac{1}{2}(d_1 + d_2) \\ \vartheta &= \arccos\left(\frac{z}{r}\right) \\ \varphi &= \operatorname{atan2}(y, x) \end{aligned} \tag{A.4}$$

where

$$d_1 = d_1(x, y, z) = \sqrt{x^2 + y^2 + (z + \Upsilon)^2}$$

$$d_2 = d_2(x, y, z) = \sqrt{x^2 + y^2 + (z - \Upsilon)^2}$$

and

$$\operatorname{atan2}(y, x) = \begin{cases} \arctan(\frac{y}{x}) & \text{if } x > 0 \\ \arctan(\frac{y}{x}) + \pi & \text{if } x < 0 \text{ and } y \geq 0 \\ \arctan(\frac{y}{x}) - \pi & \text{if } x < 0 \text{ and } y < 0 \\ \frac{\pi}{2} & \text{if } x = 0 \text{ and } y > 0 \\ -\frac{\pi}{2} & \text{if } x = 0 \text{ and } y < 0 \\ \text{undefined} & \text{if } x = 0 \text{ and } y = 0. \end{cases}$$

[10]The other three formulations have been derived in [44]. For the more general ellipsoidal coordinate system, refer to [52].

The derivatives are found to be

$$\begin{aligned}
&\frac{\partial x}{\partial r} = \frac{r\sin\vartheta\cos\varphi}{\sqrt{r^2-\Upsilon^2}}, && \frac{\partial y}{\partial r} = \frac{r\sin\vartheta\sin\varphi}{\sqrt{r^2-\Upsilon^2}}, && \frac{\partial z}{\partial r} = \cos\vartheta\\
&\frac{\partial x}{\partial \vartheta} = \sqrt{r^2-\Upsilon^2}\cos\vartheta\cos\varphi, && \frac{\partial y}{\partial \vartheta} = \sqrt{r^2-\Upsilon^2}\cos\vartheta\sin\varphi, && \frac{\partial z}{\partial \vartheta} = -r\sin\vartheta\\
&\frac{\partial x}{\partial \varphi} = -\sqrt{r^2-\Upsilon^2}\sin\vartheta\sin\varphi, && \frac{\partial y}{\partial \varphi} = \sqrt{r^2-\Upsilon^2}\sin\vartheta\cos\varphi, && \frac{\partial z}{\partial \varphi} = 0
\end{aligned} \tag{A.5}$$

and

$$\begin{aligned}
&\frac{\partial r}{\partial x} = \frac{x(d_1+d_2)}{2d_1d_2}, && \frac{\partial r}{\partial y} = \frac{y(d_1+d_2)}{2d_1d_2}\\
&\frac{\partial r}{\partial z} = \frac{z(d_1+d_2)+\Upsilon(d_2-d_1)}{2d_1d_2}\\
&\frac{\partial \vartheta}{\partial x} = \frac{xz}{d_1d_2\sqrt{r^2-z^2}}, && \frac{\partial \vartheta}{\partial y} = \frac{yz}{d_1d_2\sqrt{r^2-z^2}}\\
&\frac{\partial \vartheta}{\partial z} = \frac{1}{\sqrt{r^2-z^2}}\left(\frac{z^2}{d_1d_2}+\frac{\Upsilon z(d_2-d_1)}{d_1d_2(d_1+d_2)}-1\right)\\
&\frac{\partial \varphi}{\partial x} = -\frac{y}{x^2+y^2}, && \frac{\partial \varphi}{\partial y} = \frac{x}{x^2+y^2}, && \frac{\partial \varphi}{\partial z} = 0.
\end{aligned} \tag{A.6}$$

The general nabla operator can be written as

$$\nabla = \frac{\boldsymbol{e}_{\mathrm{r}}}{h_{\mathrm{r}}}\frac{\partial}{\partial r} + \frac{\boldsymbol{e}_{\vartheta}}{h_{\vartheta}}\frac{\partial}{\partial \vartheta} + \frac{\boldsymbol{e}_{\varphi}}{h_{\varphi}}\frac{\partial}{\partial \varphi} \tag{A.7}$$

where

$$\boldsymbol{e}_{\mathrm{r}} = \frac{1}{h_{\mathrm{r}}}\left[\frac{\partial x}{\partial r}, \frac{\partial y}{\partial r}, \frac{\partial z}{\partial r}\right]^{\top}, \quad \boldsymbol{e}_{\vartheta} = \frac{1}{h_{\vartheta}}\left[\frac{\partial x}{\partial \vartheta}, \frac{\partial y}{\partial \vartheta}, \frac{\partial z}{\partial \vartheta}\right]^{\top}, \quad \boldsymbol{e}_{\varphi} = \frac{1}{h_{\varphi}}\left[\frac{\partial x}{\partial \varphi}, \frac{\partial y}{\partial \varphi}, \frac{\partial z}{\partial \varphi}\right]^{\top}$$

and

$$\begin{aligned}
h_{\mathrm{r}} &= \sqrt{\frac{r^2-\Upsilon^2\cos^2\vartheta}{r^2-\Upsilon^2}}\\
h_{\vartheta} &= \sqrt{r^2-\Upsilon^2\cos^2\vartheta}\\
h_{\varphi} &= \sqrt{r^2-\Upsilon^2}\sin\vartheta.
\end{aligned}$$

The Jacobian determinant (for the mapping from Cartesian coordinates to prolate spheroidal coordinates) may now be written as

$$J_1 = h_{\mathrm{r}}h_{\vartheta}h_{\varphi} = \left(r^2-\Upsilon^2\cos^2\vartheta\right)\sin\vartheta. \tag{A.8}$$

As any normal vector at a surface with constant radius $r=\gamma$ can be written as $\boldsymbol{n} = \boldsymbol{e}_{\vartheta}\times\boldsymbol{e}_{\phi} = \boldsymbol{e}_{\mathrm{r}}$

$$\partial_n p = \boldsymbol{n}\cdot\nabla p = \boldsymbol{e}_{\mathrm{r}}\cdot\nabla p = \frac{1}{h_{\mathrm{r}}}\frac{\partial p}{\partial r}. \tag{A.9}$$

The surface Jacobian determinant at a given (constant) $r = \gamma$ is

$$J_S = h_\vartheta h_\varphi = \sqrt{r^2 - \Upsilon^2 \cos^2\vartheta}\sqrt{r^2 - \Upsilon^2}\sin\vartheta, \tag{A.10}$$

such that

$$q\partial_n p J_S = \mathcal{O}\Big(r^{-3}\Big) \quad \text{whenever} \quad q = \mathcal{O}\Big(r^{-3}\Big) \quad \text{and} \quad p = \mathcal{O}\Big(r^{-1}\Big). \tag{A.11}$$

That is, for the Petrov–Galerkin formulations

$$\lim_{\gamma\to\infty} \int_{S^\gamma} q\partial_n p \,\mathrm{d}\Gamma = \lim_{\gamma\to\infty} \int_0^{2\pi}\int_0^{\pi} q\partial_n p J_S \,\mathrm{d}\vartheta \,\mathrm{d}\varphi = 0. \tag{A.12}$$

A.2. Bilinear form for unconjugated Petrov–Galerkin formulation

The bilinear form (in the domain outside the artificial boundary) in Eq. (43) (in the unconjugated case) can in the Petrov–Galerkin formulations be simplified to

$$\begin{aligned} B_{\mathrm{PGU}}(R_I\psi_n, R_J\phi_m) &= \lim_{\gamma\to\infty} \int_{\Omega_{\mathrm{a}}^\gamma} \Big[\nabla(R_I\psi_n)\cdot\nabla(R_J\phi_m) - k^2 R_I\psi_n R_J\phi_m\Big]\,\mathrm{d}\Omega \\ &= \int_{\Omega_{\mathrm{a}}^+} \Big[\nabla(R_I\psi_n)\cdot\nabla(R_J\phi_m) - k^2 R_I\psi_n R_J\phi_m\Big]\,\mathrm{d}\Omega \end{aligned} \tag{A.13}$$

as the mentioned surface integral in the far field vanishes (this is however not the case for the Bubnov–Galerkin formulations). Recall that the radial shape functions are given by

$$\begin{aligned} \phi_m(r) &= \mathrm{e}^{\mathrm{i}k(r-r_{\mathrm{a}})} Q_m\Big(\frac{r_{\mathrm{a}}}{r}\Big), \quad m = 1,\dots,N \\ \psi_n(r) &= \mathrm{e}^{\mathrm{i}k(r-r_{\mathrm{a}})} \tilde{Q}_n\Big(\frac{r_{\mathrm{a}}}{r}\Big), \quad n = 1,\dots,N \end{aligned}$$

such that the derivative can be computed by

$$\frac{\mathrm{d}\phi_m}{\mathrm{d}r} = \Big[\mathrm{i}kQ_m\Big(\frac{r_{\mathrm{a}}}{r}\Big) - \frac{r_{\mathrm{a}}}{r^2}Q_m'\Big(\frac{r_{\mathrm{a}}}{r}\Big)\Big]\mathrm{e}^{\mathrm{i}k(r-r_{\mathrm{a}})}$$

and corresponding expression for ψ_n. Using the expression for the nabla operator found in Eq. (A.7)

$$\begin{aligned} \nabla(R_I\psi_n)\cdot\nabla(R_J\phi_m) &= \frac{1}{h_{\mathrm{r}}^2}\frac{\partial(R_I\psi_n)}{\partial r}\frac{\partial(R_J\phi_m)}{\partial r} + \frac{1}{h_{\vartheta}^2}\frac{\partial(R_I\psi_n)}{\partial\vartheta}\frac{\partial(R_J\phi_m)}{\partial\vartheta} \\ &\qquad + \frac{1}{h_{\varphi}^2}\frac{\partial(R_I\psi_n)}{\partial\varphi}\frac{\partial(R_J\phi_m)}{\partial\varphi} \\ &= \frac{1}{h_{\mathrm{r}}^2}\frac{\partial\psi_n}{\partial r}\frac{\partial\phi_m}{\partial r}R_IR_J + \frac{1}{h_{\vartheta}^2}\psi_n\phi_m\frac{\partial R_I}{\partial\vartheta}\frac{\partial R_J}{\partial\vartheta} \\ &\qquad + \frac{1}{h_{\varphi}^2}\psi_n\phi_m\frac{\partial R_I}{\partial\varphi}\frac{\partial R_J}{\partial\varphi} \end{aligned}$$

which multiplied with the Jacobian J_1 yields

$$\nabla(R_I\psi_n)\cdot\nabla(R_J\phi_m)J_1 = \Bigg[\Big(r^2-\Upsilon^2\Big)\frac{\partial\psi_n}{\partial r}\frac{\partial\phi_m}{\partial r}R_IR_J + \psi_n\phi_m\frac{\partial R_I}{\partial\vartheta}\frac{\partial R_J}{\partial\vartheta} + \frac{r^2-\Upsilon^2\cos^2\vartheta}{(r^2-\Upsilon^2)\sin^2\vartheta}\psi_n\phi_m\frac{\partial R_I}{\partial\varphi}\frac{\partial R_J}{\partial\varphi}\Bigg]\sin\vartheta$$

Combining all of this into Eq. (A.13) yields

$$B_{\mathrm{PGU}}(R_I\psi_n, R_J\phi_m) = \int_0^{2\pi}\int_0^{\pi} K(\vartheta,\varphi)\sin\vartheta\,\mathrm{d}\vartheta\,\mathrm{d}\varphi \tag{A.14}$$

where

$$K(\vartheta,\varphi) = \int_{r_\mathrm{a}}^{\infty}\Big\{\Big(r^2-\Upsilon^2\Big)\frac{\partial\psi_n}{\partial r}\frac{\partial\phi_m}{\partial r}R_IR_J + \psi_n\phi_m\frac{\partial R_I}{\partial\vartheta}\frac{\partial R_J}{\partial\vartheta} + \frac{r^2-\Upsilon^2\cos^2\vartheta}{(r^2-\Upsilon^2)\sin^2\vartheta}\psi_n\phi_m\frac{\partial R_I}{\partial\varphi}\frac{\partial R_J}{\partial\varphi} - k^2(r^2-\Upsilon^2\cos^2\vartheta)\psi_n\phi_m R_IR_J\Big\}\,\mathrm{d}r.$$

Inserting the expressions for the radial shape functions ϕ and ψ (with Einstein's summation convention) with their corresponding derivatives one obtains the following expression using the substitution $\rho = \frac{r}{r_\mathrm{a}}$ and the notation $\varrho_1 = \Upsilon/r_\mathrm{a}$ (the eccentricity of the infinite-element spheroid), $\varrho_2 = kr_\mathrm{a}$ and $\varrho_3 = k\Upsilon$

$$\begin{aligned}K(\vartheta,\varphi) = \Bigg\{ R_IR_J\Bigg[&-2\varrho_2^2B^{(1)}_{\tilde n+\tilde m} - \mathrm{i}\varrho_2(\tilde n+\tilde m+2)B^{(1)}_{\tilde n+\tilde m+1}\\ &+\Big[\tilde m(\tilde n+2)+\varrho_3^2\Big]B^{(1)}_{\tilde n+\tilde m+2} + \mathrm{i}\varrho_1^2\varrho_2(\tilde n+\tilde m+2)B^{(1)}_{\tilde n+\tilde m+3}\\ &-\tilde m(\tilde n+2)\varrho_1^2B^{(1)}_{\tilde n+\tilde m+4} + \varrho_3^2\cos^2\vartheta B^{(1)}_{\tilde n+\tilde m+2}\Bigg]\\ &+\frac{\partial R_I}{\partial\vartheta}\frac{\partial R_J}{\partial\vartheta}B^{(1)}_{\tilde n+\tilde m+2}\\ &+\frac{\partial R_I}{\partial\varphi}\frac{\partial R_J}{\partial\varphi}\frac{1}{\sin^2\vartheta}\Big(B^{(2)}_{\tilde n+\tilde m+1} - \varrho_1^2\cos^2\vartheta B^{(2)}_{\tilde n+\tilde m+3}\Big)\Bigg\} r_\mathrm{a}\mathrm{e}^{-2\mathrm{i}\varrho_2}\tilde D_{n\tilde n}D_{m\tilde m}\end{aligned}$$

where the radial integrals

$$B_n^{(1)} = \int_1^\infty \frac{\mathrm{e}^{2\mathrm{i}\varrho_2\rho}}{\rho^n}\,\mathrm{d}\rho \qquad B_n^{(2)} = \int_1^\infty \frac{\mathrm{e}^{2\mathrm{i}\varrho_2\rho}}{(\rho^2-\varrho_1^2)\rho^{n-1}}\,\mathrm{d}\rho, \qquad n\geqslant 1$$

can be evaluated according to formulas in Appendix B.

Assume that the artificial boundary Γ_a is parameterized by ξ and η. As Γ_a is a surface with constant radius, $r = r_\mathrm{a}$, in the prolate spheroidal coordinate system, it may also be parameterized by ϑ and φ. Therefore,

$$\mathrm{d}\vartheta\mathrm{d}\varphi = \begin{vmatrix}\frac{\partial\vartheta}{\partial\xi} & \frac{\partial\varphi}{\partial\xi}\\ \frac{\partial\vartheta}{\partial\eta} & \frac{\partial\varphi}{\partial\eta}\end{vmatrix}\mathrm{d}\xi\mathrm{d}\eta \tag{A.15}$$

where

$$\frac{\partial\vartheta}{\partial\xi} = \frac{\partial\vartheta}{\partial x}\frac{\partial x}{\partial\xi} + \frac{\partial\vartheta}{\partial y}\frac{\partial y}{\partial\xi} + \frac{\partial\vartheta}{\partial z}\frac{\partial z}{\partial\xi}, \qquad \frac{\partial\vartheta}{\partial\eta} = \frac{\partial\vartheta}{\partial x}\frac{\partial x}{\partial\eta} + \frac{\partial\vartheta}{\partial y}\frac{\partial y}{\partial\eta} + \frac{\partial\vartheta}{\partial z}\frac{\partial z}{\partial\eta}$$
$$\frac{\partial\varphi}{\partial\xi} = \frac{\partial\varphi}{\partial x}\frac{\partial x}{\partial\xi} + \frac{\partial\varphi}{\partial y}\frac{\partial y}{\partial\xi} + \frac{\partial\varphi}{\partial z}\frac{\partial z}{\partial\xi}, \qquad \frac{\partial\varphi}{\partial\eta} = \frac{\partial\varphi}{\partial x}\frac{\partial x}{\partial\eta} + \frac{\partial\varphi}{\partial y}\frac{\partial y}{\partial\eta} + \frac{\partial\varphi}{\partial z}\frac{\partial z}{\partial\eta}$$

and the inverse partial derivatives with respect to the coordinate transformation (from the prolate spheroidal coordinate system to the Cartesian coordinate system) is found in Eq. (A.6). This Jacobian matrix may be evaluated by

$$J_3 = \begin{bmatrix} \frac{\partial\vartheta}{\partial\xi} & \frac{\partial\vartheta}{\partial\eta} \\ \frac{\partial\varphi}{\partial\xi} & \frac{\partial\varphi}{\partial\eta} \end{bmatrix} = \begin{bmatrix} \frac{\partial\vartheta}{\partial x} & \frac{\partial\vartheta}{\partial y} & \frac{\partial\vartheta}{\partial z} \\ \frac{\partial\varphi}{\partial x} & \frac{\partial\varphi}{\partial y} & \frac{\partial\varphi}{\partial z} \end{bmatrix} \begin{bmatrix} \frac{\partial x}{\partial\xi} & \frac{\partial x}{\partial\eta} \\ \frac{\partial y}{\partial\xi} & \frac{\partial y}{\partial\eta} \\ \frac{\partial z}{\partial\xi} & \frac{\partial z}{\partial\eta} \end{bmatrix} \tag{A.16}$$

and the derivatives of the basis functions may then be computed by

$$\begin{bmatrix} \frac{\partial R_I}{\partial\vartheta} \\ \frac{\partial R_I}{\partial\varphi} \end{bmatrix} = J_3^{-\top} \begin{bmatrix} \frac{\partial R_I}{\partial\xi} \\ \frac{\partial R_I}{\partial\eta} \end{bmatrix}. \tag{A.17}$$

Defining the angular integrals

$$\begin{aligned} A_{IJ}^{(1)} &= \int_0^{2\pi}\int_0^{\pi} R_I R_J \sin\vartheta \,\mathrm{d}\vartheta \,\mathrm{d}\varphi, & A_{IJ}^{(2)} &= \int_0^{2\pi}\int_0^{\pi} \frac{\partial R_I}{\partial\vartheta}\frac{\partial R_J}{\partial\vartheta}\sin\vartheta \,\mathrm{d}\vartheta \,\mathrm{d}\varphi \\ A_{IJ}^{(3)} &= \int_0^{2\pi}\int_0^{\pi} R_I R_J \cos^2\vartheta \sin\vartheta \,\mathrm{d}\vartheta \,\mathrm{d}\varphi, & A_{IJ}^{(4)} &= \int_0^{2\pi}\int_0^{\pi} \frac{\partial R_I}{\partial\varphi}\frac{\partial R_J}{\partial\varphi}\frac{1}{\sin\vartheta} \,\mathrm{d}\vartheta \,\mathrm{d}\varphi \\ A_{IJ}^{(5)} &= \int_0^{2\pi}\int_0^{\pi} \frac{\partial R_I}{\partial\varphi}\frac{\partial R_J}{\partial\varphi}\frac{\cos^2\vartheta}{\sin\vartheta} \,\mathrm{d}\vartheta \,\mathrm{d}\varphi \end{aligned} \tag{A.18}$$

the bilinear form may then finally be written as (Einstein's summation convention is used for the indices $\tilde{n}$ and $\tilde{m}$)

$$\begin{aligned} &B_{\mathrm{PGU}}(R_I\psi_n, R_J\phi_m) \\ &= \Big\{ A_{IJ}^{(1)} \Big[-2\varrho_2^2 B_{\tilde{n}+\tilde{m}}^{(1)} - \mathrm{i}\varrho_2(\tilde{n}+\tilde{m}+2) B_{\tilde{n}+\tilde{m}+1}^{(1)} + \Big[(\tilde{n}+2)\tilde{m} + \varrho_3^2\Big] B_{\tilde{n}+\tilde{m}+2}^{(1)} \\ &\qquad + \mathrm{i}\varrho_1\varrho_3(\tilde{n}+\tilde{m}+2) B_{\tilde{n}+\tilde{m}+3}^{(1)} - \varrho_1^2(\tilde{n}+2)\tilde{m} B_{\tilde{n}+\tilde{m}+4}^{(1)} \Big] \\ &\quad + A_{IJ}^{(2)} B_{\tilde{n}+\tilde{m}+2}^{(1)} + \varrho_3^2 A_{IJ}^{(3)} B_{\tilde{n}+\tilde{m}+2}^{(1)} \\ &\quad + A_{IJ}^{(4)} B_{\tilde{n}+\tilde{m}+1}^{(2)} - \varrho_1^2 A_{IJ}^{(5)} B_{\tilde{n}+\tilde{m}+3}^{(2)} \Big\} r_{\mathrm{a}} \mathrm{e}^{-2\mathrm{i}\varrho_2} D_{m\tilde{m}} \tilde{D}_{n\tilde{n}}. \end{aligned} \tag{A.19}$$

For completeness, the formulas for the other three formulations are included

$$
\begin{aligned}
&B_{\mathrm{BGU}}(R_I\psi_n, R_J\phi_m)\\
&= \Big\{A_{IJ}^{(1)}\Big[-2\varrho_2^2 B_{\tilde{n}+\tilde{m}-2}^{(1)}(1-\delta_{\tilde{n}1}\delta_{\tilde{m}1}) - \mathrm{i}\varrho_2(\tilde{n}+\tilde{m})B_{\tilde{n}+\tilde{m}-1}^{(1)} + \Big(\tilde{n}\tilde{m}+\varrho_3^2\Big)B_{\tilde{n}+\tilde{m}}^{(1)}\\
&\qquad +\mathrm{i}\varrho_1\varrho_3(\tilde{n}+\tilde{m})B_{\tilde{n}+\tilde{m}+1}^{(1)} - \varrho_1^2\tilde{n}\tilde{m}B_{\tilde{n}+\tilde{m}+2}^{(1)}\Big]\\
&\quad +A_{IJ}^{(2)}B_{\tilde{n}+\tilde{m}}^{(1)} + \varrho_3^2 A_{IJ}^{(3)}B_{\tilde{n}+\tilde{m}}^{(1)}\\
&\quad +A_{IJ}^{(4)}B_{\tilde{n}+\tilde{m}-1}^{(2)} - \varrho_1^2 A_{IJ}^{(5)}B_{\tilde{n}+\tilde{m}+1}^{(2)}\Big\}r_{\mathrm{a}}\mathrm{e}^{-2\mathrm{i}\varrho_2}D_{m\tilde{m}}\tilde{D}_{n\tilde{n}}\\
&\quad -\mathrm{i}\varrho_2 r_{\mathrm{a}}D_{m1}\tilde{D}_{n1}A_{IJ}^{(1)}
\end{aligned}
\tag{A.20}
$$

$$
\begin{aligned}
&B_{\mathrm{PGC}}(R_I\psi_n, R_J\phi_m)\\
&= \Big\{A_{IJ}^{(1)}\Big[-\mathrm{i}\varrho_2(\tilde{n}-\tilde{m}+2)B_{\tilde{n}+\tilde{m}+1}^{(1)} + \Big[(\tilde{n}+2)\tilde{m}-\varrho_3^2\Big]B_{\tilde{n}+\tilde{m}+2}^{(1)}\\
&\qquad +\mathrm{i}\varrho_1\varrho_3(\tilde{n}-\tilde{m}+2)B_{\tilde{n}+\tilde{m}+3}^{(1)} - \varrho_1^2(\tilde{n}+2)\tilde{m}B_{\tilde{n}+\tilde{m}+4}^{(1)}\Big]\\
&\quad +A_{IJ}^{(2)}B_{\tilde{n}+\tilde{m}+2}^{(1)} + \varrho_3^2 A_{IJ}^{(3)}B_{\tilde{n}+\tilde{m}+2}^{(1)}\\
&\quad +A_{IJ}^{(4)}B_{\tilde{n}+\tilde{m}+1}^{(2)} - \varrho_1^2 A_{IJ}^{(5)}B_{\tilde{n}+\tilde{m}+3}^{(2)}\Big\}r_{\mathrm{a}}D_{m\tilde{m}}\tilde{D}_{n\tilde{n}}
\end{aligned}
\tag{A.21}
$$

$$
\begin{aligned}
B_{\mathrm{BGC}}(R_I\psi_n, R_J\phi_m) = &\Big\{A_{IJ}^{(1)}\Big[-\mathrm{i}\varrho_2(\tilde{n}-\tilde{m})B_{\tilde{n}+\tilde{m}-1}^{(1)} + \Big(\tilde{n}\tilde{m}-\varrho_3^2\Big)B_{\tilde{n}+\tilde{m}}^{(1)}\\
&\qquad +\mathrm{i}\varrho_1\varrho_3(\tilde{n}-\tilde{m})B_{\tilde{n}+\tilde{m}+1}^{(1)} - \varrho_1^2\tilde{n}\tilde{m}B_{\tilde{n}+\tilde{m}+2}^{(1)}\Big]\\
&\quad +A_{IJ}^{(2)}B_{\tilde{n}+\tilde{m}}^{(1)} + \varrho_3^2 A_{IJ}^{(3)}B_{\tilde{n}+\tilde{m}}^{(1)}\\
&\quad +A_{IJ}^{(4)}B_{\tilde{n}+\tilde{m}-1}^{(2)} - \varrho_1^2 A_{IJ}^{(5)}B_{\tilde{n}+\tilde{m}+1}^{(2)}\Big\}r_{\mathrm{a}}D_{m\tilde{m}}\tilde{D}_{n\tilde{n}}\\
&\quad -\mathrm{i}r_{\mathrm{a}}\varrho_2 D_{m1}\tilde{D}_{n1}A_{IJ}^{(1)}
\end{aligned}
\tag{A.22}
$$

where δ_{ij} is the Kronecker delta function in Eq. (31).

B. Evaluation of radial integrals

The exponential integral

$$
E_n(z) = \int_1^\infty \frac{\mathrm{e}^{-z\rho}}{\rho^n}\,\mathrm{d}\rho, \qquad \mathrm{Re}(z) \geqslant 0 \tag{B.1}
$$

is of great importance for the unconjugated formulations in the IEM. It is therefore important to be able to evaluate the integral accurately and efficiently, also for large (absolute) values of z (which will correspond to high frequencies). In [53, p. 229,

5.1.12] the series representation for evaluation of these functions can be found[11]

$$E_n(z) = \frac{(-z)^{n-1}}{(n-1)!}\left[-\ln z - \gamma + \sum_{m=1}^{n-1}\frac{1}{m}\right] - \sum_{\substack{m=0\\ m\neq n-1}}^{\infty}\frac{(-z)^m}{(m-n+1)m!} \tag{B.2}$$

with the empty sum interpreted to be zero. Moreover, using the continued fraction notation

$$b_0 + \frac{a_1}{b_1+}\frac{a_2}{b_2+}\frac{a_3}{b_3+}\cdots = b_0 + \cfrac{a_1}{b_1 + \cfrac{a_2}{b_2 + \cfrac{a_3}{b_3 + \cdots}}} \tag{B.3}$$

the continued fraction representation of these functions is given by [53, p. 229, 5.1.22]

$$E_n(z) = \mathrm{e}^{-z}\left(\frac{1}{z+}\frac{n}{1+}\frac{1}{z+}\frac{n+1}{1+}\frac{2}{z+}\frac{n+2}{1+}\frac{3}{z+}\cdots\right). \tag{B.4}$$

In [54, p. 222] Press et al. present an even faster converging continued fraction given by

$$E_n(z) = \mathrm{e}^{-z}\left(\frac{1}{z+n-}\frac{1\cdot n}{z+n+2-}\frac{2(n+1)}{z+n+4-}\frac{3(n+2)}{z+n+6-}\cdots\right). \tag{B.5}$$

It is here suggested to use Eq. (B.2) when $|z| \lesssim 1$ and Eq. (B.4) or Eq. (B.5) when $|z| \gtrsim 1$. Press et al. then continue to present efficient algorithms for evaluation of these formulas.

Using series expansions at infinity

$$\frac{1}{\rho^2 - \varrho_1^2} = \frac{1}{\varrho_1^2}\sum_{j=1}^{\infty}\left(\frac{\varrho_1}{\rho}\right)^{2j}, \tag{B.6}$$

the radial integrals for 3D infinite elements may be computed by

$$\int_1^{\infty}\frac{1}{\rho^n}\,\mathrm{d}\rho = \frac{1}{n-1} \tag{B.7}$$

$$\int_1^{\infty}\frac{1}{(\rho^2-\varrho_1^2)\rho^{n-1}}\,\mathrm{d}\rho = \sum_{j=0}^{\infty}\frac{\varrho_1^{2j}}{2j+n} \tag{B.8}$$

[11] Here, γ is the Euler-Mascheroni constant which is defined by

$$\gamma = \lim_{n\to\infty}\left[-\ln(n) + \sum_{m=1}^{n}\frac{1}{m}\right] = 0.57721566490153286060651209008 2\ldots.$$

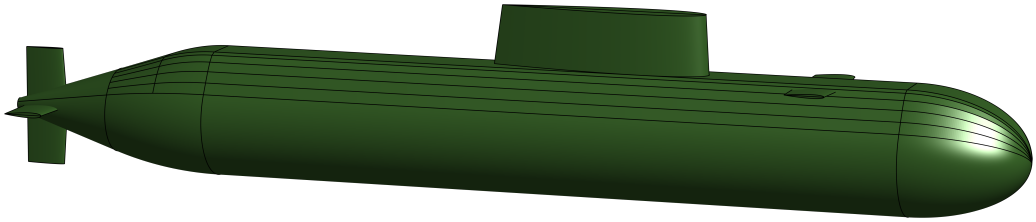

Figure C29: Outer pressure hull for BeTSSi submarine.

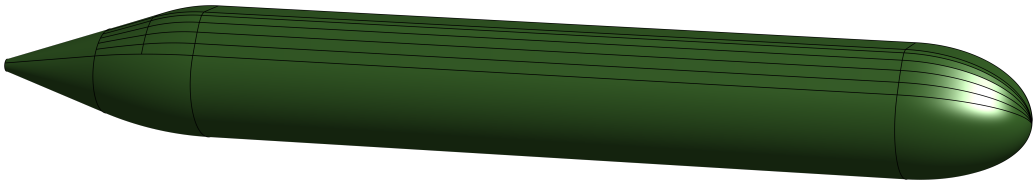

Figure C30: The stripped BeTSSi submarine model.

in the conjugated case and

$$\int_1^\infty \frac{\mathrm{e}^{2\mathrm{i}\varrho_2\rho}}{\rho^n}\,\mathrm{d}\rho = E_n(-2\mathrm{i}\varrho_2) \tag{B.9}$$

$$\int_1^\infty \frac{\mathrm{e}^{2\mathrm{i}\varrho_2\rho}}{(\rho^2-\varrho_1^2)\rho^{n-1}}\,\mathrm{d}\rho = \sum_{j=0}^{\infty} \varrho_1^{2j} E_{2j+n+1}(-2\mathrm{i}\varrho_2) \tag{B.10}$$

in the unconjugated case.

C. The stripped BeTSSi submarine model

In this section a simplified version of the BeTSSi submarine model (depicted in Figure C29) will be presented. Namely a *stripped BeTSSi submarine model* without sail and rudders as in Figure C30. The relevant BeTSSi parameters for the work presented herein are given in Table 3. The model is symmetric about the xz-plane and has rotational symmetry for the lower part as described in Figure C31. The transition from this axisymmetric part to the deck is described in Figure C32. This transition as well as the deck itself, contains a set of rectangular panels of length L. The polynomial $P(y)$, is uniquely defined by the requirement that it defines a smooth transition between the hull and the deck. More precisely, the following requirement must be satisfied:

$$P(s) = c, \quad P\left(b\sin\frac{\beta}{2}\right) = -b\cos\frac{\beta}{2}$$

$$P'(s) = 0, \quad P'\left(b\sin\frac{\beta}{2}\right) = \tan\frac{\beta}{2}$$

Table 3: **BeTSSi submarine:** Parameters for the BeTSSi submarine benchmark.

Parameter	Description
$P_{\text{inc}} = 1\,\text{Pa}$	Amplitude of incident wave
$E = 2.10 \cdot 10^{11}\,\text{Pa}$	Young's modulus
$\nu = 0.3$	Poisson's ratio
$\rho_{\text{s}} = 7850\,\text{kg}\,\text{m}^{-3}$	Density of solid
$\rho_{\text{f}} = 1000\,\text{kg}\,\text{m}^{-3}$	Density of water
$c_{\text{f}} = 1500\,\text{m}\,\text{s}^{-1}$	Speed of sound in water
$t = 0.01\,\text{m}$	Thickness of pressure hull
$\alpha = 18°$	Arc angle of transition to the tail cone
$\beta = 240°$	Rotational angle for the axisymmetric lower part
$g_2 = 6.5\,\text{m}$	Distance in x-direction of transition to the tail cone
$g_3 = 6.5\,\text{m}$	Distance in x-direction of the tail cone
$L = 42\,\text{m}$	Length of the deck
$a = 7\,\text{m}$	Semi-major axis of bow
$b = 3.5\,\text{m}$	Semi-major axis of bow
$c = 4\,\text{m}$	Height from x-axis to the deck
$s = 1.2\,\text{m}$	Half of the width of the deck

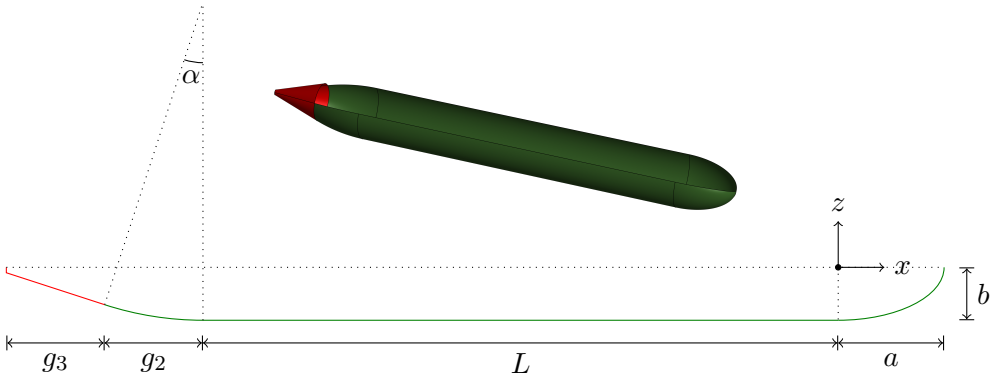

Figure C31: The sideline of the lower part of the BeTSSi submarine. The sidelines are formed (from the right) by an ellipse with semi-major axis a and semi-minor axis b, followed by a straight line of length L, then an arc of angle α and finally two straight lines. The latter two straight lines (in red) are rotated about the x-axis and the remaining part (in green) are rotated an angle β around the x-axis.

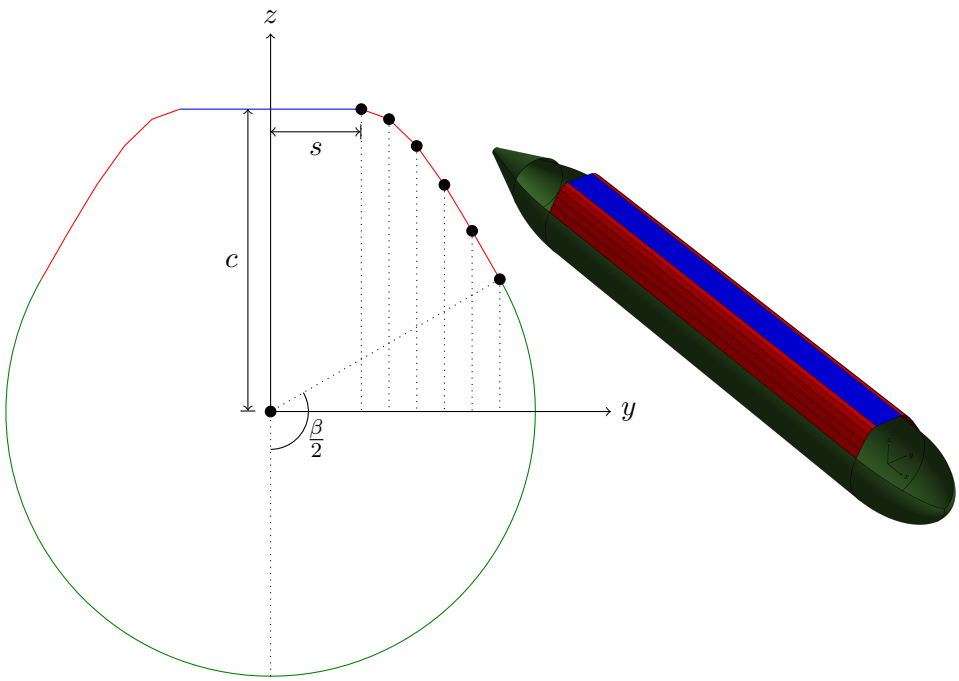

Figure C32: The transition (red line) from the axisymmetric hull (green line) to the deck (blue line) is given by sampling a cubic polynomial, $P(y)$, at 6 equidistant points in the y-direction and connecting the resulting points with straight lines (corresponding 6 points are found for negative values y-values, $(0, y, P(|y|))$).

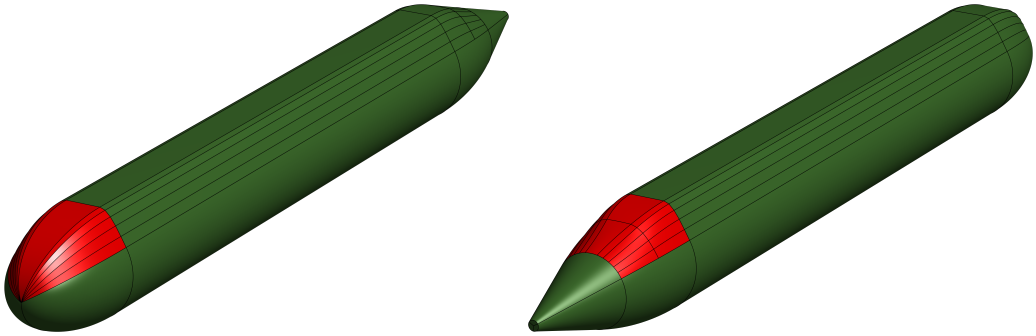

(a) Illustration of upper bow part. (b) Illustration of upper transition part.

Figure C33: Final patches for the stripped BeTSSi submarine.

which gives the polynomial

$$P(y) = c + C_1(y-s)^2 + C_2(y-s)^3 \tag{C.1}$$

where

$$C_1 = -\frac{3C_4 + C_3 \tan\frac{\beta}{2}}{C_3^2}, \quad C_2 = \frac{2C_4 + C_3 \tan\frac{\beta}{2}}{C_3^3},$$
$$C_3 = b\sin\frac{\beta}{2} - s, \quad C_4 = c + b\cos\frac{\beta}{2}.$$

The upper part of the bow (highlighted in Figure C33a) is obtained by linear lofting of elliptic curves from the 12 points described in Figure C32 to the tip of the bow. The upper part of the tail section (highlighted in Figure C33b) is connected using a tensor NURBS surface of degree 2 such that it defines a smooth transition from the axisymmetric cone to the deck. More precisely, the upper part of the cone tail is divided into 12 arcs with angle $\frac{2\pi-\beta}{12}$, and the resulting points are connected to corresponding points on the transition to the deck from the axisymmetric hull. As illustrated in Figure C34a, the NURBS patch is given by 22 elements. Thus, $4 \cdot 23 = 92$ control points, $\boldsymbol{P}_{i,j}$, is needed as shown in Figure C34b (23 and 4 control points in the ξ direction and η direction, respectively). The control points $\boldsymbol{P}_{1,j}$ and $\boldsymbol{P}_{23,j}$ for $j = 1, 2, 3, 4$ must be defined as in Figure C35b, while the control points $\boldsymbol{P}_{i,1}$ must be defined as in Figure C35a (with corresponding weights). For $2 \leqslant i \leqslant 22$ the weights are defined by $w_{i,j} = w_{i,1}$ for $j = 2, 3, 4$. That is,

$$w_{i,j} = \begin{cases} 1 & i \text{ odd} \\ \cos\left(\frac{2\pi-\beta}{24}\right) & i \text{ even}, \ i \neq 12 \\ \cos\left(\frac{2\pi-\beta}{12}\right) & i = 12 \end{cases} \tag{C.2}$$

The location of the control points $\boldsymbol{P}_{i,j}$, $j = 2, 3$ and $2 \leqslant i \leqslant 22$, are determined by the requirement that the x component is the same as $\boldsymbol{P}_{1,j}$ and the fact that the

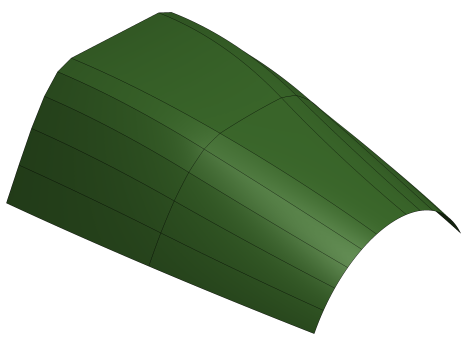

(a) Illustration of the mesh.

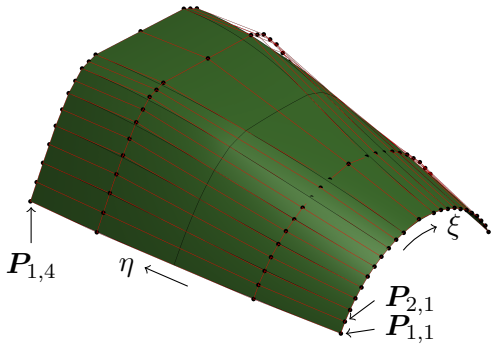

(b) Illustration of the control polygon mesh.

Figure C34: Illustration of the upper transition part of the tail.

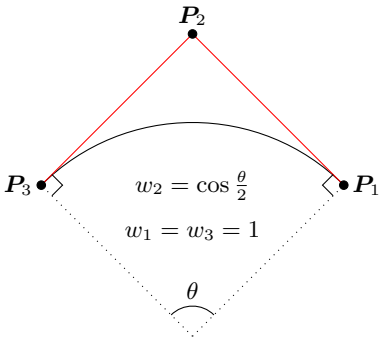

(a) NURBS parametrization of arc of angle θ using three control points $\{\boldsymbol{P}_i\}_{i=1}^3$, the weights $\{w_i\}_{i=1}^3$ and the open knot vector $\boldsymbol{t}_\xi = \{0, 0, 0, 1, 1, 1\}$.

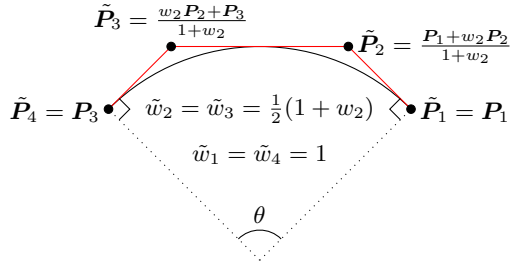

(b) NURBS parametrization of arc of angle θ using four control points $\{\tilde{\boldsymbol{P}}_i\}_{i=1}^4$, the weights $\{\tilde{w}_i\}_{i=1}^4$ and the open knot vector $\tilde{\boldsymbol{t}}_\xi = \{0, 0, 0, 0.5, 1, 1, 1\}$.

Figure C35: Two ways of parametrizing an arc using NURBS [55, p. 315].

control polygon lines must be tangential to the surface both at the deck and the cone tail.

The inner surface of the BeTSSi submarine is generated by scaling a copy of the outer surface with the following change in the parameters $a \to a - t$, $b \to b - t$, $c \to c - t$, $s \to s - t/2$, $g_2 \to g_2 - t/2$ and $g_3 \to g_3 - t/2$ (α, β and l remain unchanged).

D. Approximating NURBS parametrizations with B-spline parametrizations

Starting with any NURBS parametrizations of a geometry where every internal knot has multiplicity $m = \check{p}_\xi$ in the ξ-direction and correspondingly in the other two parameter directions, we want to transform the NURBS parametrization of the exact geometry, to a B-spline representation. This representation approximates the geometry by interpolating the geometry at $n_\xi \cdot n_\eta \cdot n_\zeta$ (not necessarily unique) physical points resulting from a grid in the parametric space.

Let $\boldsymbol{X}$ be the NURBS parametrization of the geometry

$$\boldsymbol{X}(\xi,\eta,\zeta) = \sum_{i=1}^{n_\xi}\sum_{j=1}^{n_\eta}\sum_{l=1}^{n_\zeta} R_{i,j,l}(\xi,\eta,\zeta)\boldsymbol{P}_{i,j,l}, \tag{D.1}$$

with knot vectors $\boldsymbol{t}_\xi$, $\boldsymbol{t}_\eta$ and $\boldsymbol{t}_\zeta$, polynomial order $\check{p}_\xi$, $\check{p}_\eta$ and $\check{p}_\zeta$. For each control point $\boldsymbol{P}_{i,j,l}$ we will need a corresponding interpolating point $\boldsymbol{Q}_{i,j,l}$ which will be located at the grid point $\left(\tilde{\xi}_i, \tilde{\eta}_j, \tilde{\zeta}_l\right)$. These points in the parameter domain are chosen to be the Greville abscissae

$$\tilde{\xi}_i = \frac{1}{\check{p}_\xi}\sum_{\tilde{i}=i+1}^{i+\check{p}_\xi} \xi_{\tilde{i}}, \quad i = 1,\dots,n_\xi \tag{D.2}$$

$$\tilde{\eta}_j = \frac{1}{\check{p}_\eta}\sum_{\tilde{j}=j+1}^{j+\check{p}_\eta} \eta_{\tilde{j}}, \quad j = 1,\dots,n_\eta \tag{D.3}$$

$$\tilde{\zeta}_l = \frac{1}{\check{p}_\zeta}\sum_{\tilde{l}=l+1}^{l+\check{p}_\zeta} \zeta_{\tilde{l}}, \quad l = 1,\dots,n_\zeta, \tag{D.4}$$

where ξ_i, η_j and ζ_l are the knots of the knot vectors $\boldsymbol{t}_\xi$, $\boldsymbol{t}_\eta$ and $\boldsymbol{t}_\zeta$, respectively.

We can now compute the interpolation points $\boldsymbol{Q}_{i,j,l}$ by

$$\boldsymbol{Q}_{i,j,l} = \boldsymbol{X}(\tilde{\xi}_i, \tilde{\eta}_j, \tilde{\zeta}_l). \tag{D.5}$$

To find a B-spline approximation of the geometry which interpolates the points $\boldsymbol{Q}_{i,j,l}$, we want this new parametrization $\tilde{\boldsymbol{X}}$ to be based on $\boldsymbol{X}$ such that their order and knot vectors are equal. As all weights will be set to 1 (to get a B-spline parametrization), we are only left with dofs in the control points, $\tilde{\boldsymbol{P}}_{i,j,l}$, of the B-spline parametrization. To find these points we require

$$\tilde{\boldsymbol{X}}(\tilde{\xi}_i, \tilde{\eta}_j, \tilde{\zeta}_l) = \sum_{\tilde{i}=1}^{n_\xi}\sum_{\tilde{j}=1}^{n_\eta}\sum_{\tilde{l}=1}^{n_\zeta} B_{\tilde{i},\check{p}_\xi,\boldsymbol{t}_\xi}(\tilde{\xi}_i) B_{\tilde{j},\check{p}_\eta,\boldsymbol{t}_\eta}(\tilde{\eta}_j) B_{\tilde{l},\check{p}_\zeta,\boldsymbol{t}_\zeta}(\tilde{\zeta}_l) \tilde{\boldsymbol{P}}_{\tilde{i},\tilde{j},\tilde{l}} = \boldsymbol{Q}_{i,j,l} \tag{D.6}$$

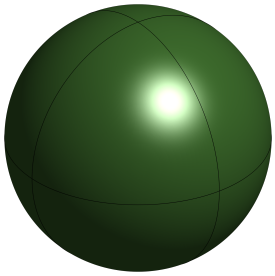

(a) Exact geometry.

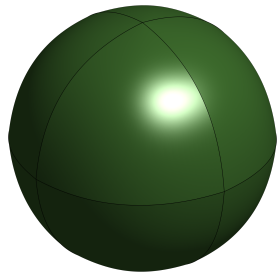

(b) Approximation using $\check{p}_\xi = \check{p}_\eta = 2$.

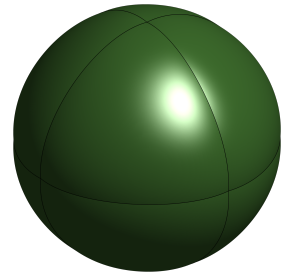

(c) Approximation using $\check{p}_\xi = \check{p}_\eta = 3$.

Figure D36: Transformation of an exact NURBS parametrization of a spherical shell to a B-spline approximation of the same geometry.

for all $i = 1, \ldots, n_\xi$, $j = 1, \ldots, n_\eta$ and $l = 1, \ldots, n_\zeta$. We may therefore find $\tilde{\boldsymbol{P}}_{i,j,l}$ by solving a system of $3n_\xi \cdot n_\eta \cdot n_\zeta$ equations.

Application of this algorithm to the spherical shell parametrization using NURBS is illustrated in Figure D36.

References

[1] L. Gilroy, C. de Jong, B. Nolte, I. Schäfer, BeTSSi II Benchmark Target Strength Simulation, Technical Report (WTD71 0029/2013 WB), Wehrtechnische Dienststelle für Schiffe und Marinewaffen der Bundeswehr, Maritime Technologie und Forschung (WTD 71), Eckenförde, Germany (2013).

[2] P. Bouillard, F. Ihlenburg, Error estimation and adaptivity for the finite element method in acoustics: 2D and 3D applications, *Computer Methods in Applied Mechanics and Engineering*, 176:147–163 (1999).

[3] N. D. Manh, A. Evgrafov, A. R. Gersborg, J. Gravesen, Isogeometric shape optimization of vibrating membranes, *Computer Methods in Applied Mechanics and Engineering*, 200:1343–1353 (2011).

[4] N. D. Manh, Isogeometric analysis and shape optimization in electromagnetism, Ph.D. thesis, Technical University of Denmark, Department of Informatics and Mathematical Modeling (2012).

[5] T. Hughes, J. Cottrell, Y. Bazilevs, Isogeometric analysis: CAD, finite elements, NURBS, exact geometry and mesh refinement, *Computer Methods in Applied Mechanics and Engineering*, 194:4135–4195 (2005).

[6] J. Cottrell, T. Hughes, Y. Bazilevs, *Isogeometric Analysis: Toward Integration of CAD and FEA*, Wiley, 2009.

[7] L. Beirão da Veiga, A. Buffa, J. Rivas, G. Sangalli, Some estimates for h–p–k-refinement in isogeometric analysis, *Numerische Mathematik*, 118:271–305 (2011).

[8] L. Beirão da Veiga, A. Buffa, G. Sangalli, R. Vázquez, Mathematical analysis of variational isogeometric methods, *Acta Numerica*, 23:157–287 (2014).

[9] P. Nørtoft, J. Gravesen, M. Willatzen, Isogeometric analysis of sound propagation through laminar flow in 2-dimensional ducts, *Computer Methods in Applied Mechanics and Engineering*, 284:1098–1119 (2015).

[10] S. A. Sauter, C. Schwab, *Boundary Element Methods*, Springer Berlin Heidelberg, Berlin, Heidelberg, 2011, pp. 183–287.

[11] M. Schanz, O. Steinbach, *Boundary Element Analysis: Mathematical Aspects and Applications*, Lecture Notes in Applied and Computational Mechanics, Springer Berlin Heidelberg, 2007.

[12] Y. J. Liu, S. Mukherjee, N. Nishimura, M. Schanz, W. Ye, A. Sutradhar, E. Pan, N. A. Dumont, A. Frangi, A. Saez, Recent advances and emerging applications of the boundary element method, *Applied Mechanics Reviews*, 64:030802 (2012).

[13] D. S. Burnett, A three-dimensional acoustic infinite element based on a prolate spheroidal multipole expansion, *The Journal of the Acoustical Society of America*, 96:2798–2816 (1994).

[14] K. Gerdes, L. Demkowicz, Solution of 3D-Laplace and Helmholtz equations in exterior domains using *hp*-infinite elements, *Computer Methods in Applied Mechanics and Engineering*, 137:239–273 (1996).

[15] J.-P. Berenger, A perfectly matched layer for the absorption of electromagnetic waves, *Journal of Computational Physics*, 114:185–200 (1994).

[16] J.-P. Berenger, Perfectly matched layer for the FDTD solution of wave-structure interaction problems, *IEEE Transactions on Antennas and Propagation*, 44:110–117 (1996).

[17] S. Marburg, B. Nolte, *Computational Acoustics of Noise Propagation in Fluids-Finite and Boundary Element Methods*, vol. 578, Springer, 2008.

[18] S. N. Chandler-Wilde, I. G. Graham, S. Langdon, E. A. Spence, Numerical-asymptotic boundary integral methods in high-frequency acoustic scattering, *Acta Numerica*, 21:89–305 (2012).

[19] D. Givoli, *Numerical methods for problems in infinite domains*, vol. 33, Elsevier, 2013.

[20] J. J. Shirron, Solution of exterior Helmholtz problems using finite and infinite elements, Ph.D. thesis, University of Maryland College Park (1995).

[21] A. Bayliss, M. Gunzburger, E. Turkel, Boundary conditions for the numerical solution of elliptic equations in exterior regions, *SIAM Journal on Applied Mathematics*, 42:430–451 (1982).

[22] T. Hagstrom, S. Hariharan, A formulation of asymptotic and exact boundary conditions using local operators, *Applied Numerical Mathematics*, 27:403–416 (1998), Special Issue on Absorbing Boundary Conditions.

[23] R. Tezaur, A. Macedo, C. Farhat, R. Djellouli, Three-dimensional finite element calculations in acoustic scattering using arbitrarily shaped convex artificial boundaries, *International Journal for Numerical Methods in Engineering*, 53:1461–1476 (2001).

[24] P. Bettess, Infinite elements, *International Journal for Numerical Methods in Engineering*, 11:53–64 (1977).

[25] P. Bettess, O. C. Zienkiewicz, Diffraction and refraction of surface waves using finite and infinite elements, *International Journal for Numerical Methods in Engineering*, 11:1271–1290 (1977).

[26] L. Demkowicz, F. Ihlenburg, Analysis of a coupled finite-infinite element method for exterior Helmholtz problems, *Numerische Mathematik*, 88:43–73 (2001).

[27] A. Sommerfeld, *Partial differential equations in physics*, vol. 1, Academic press, 1949.

[28] C. H. Wilcox, An expansion theorem for electromagnetic fields, *Communications on Pure and Applied Mathematics*, 9:115–134 (1956).

[29] R. Leis, *Initial Boundary Value Problems in Mathematical Physics*, J. Wiley & Teubner Verlag, Stuttgart, 1986.

[30] F. Ihlenburg, *Finite Element Analysis of Acoustic Scattering*, vol. 132 of *Applied Mathematical Sciences*, Springer, New York, USA, 1998.

[31] K. Gerdes, The conjugated vs. the unconjugated infinite element method for the Helmholtz equation in exterior domains, *Computer Methods in Applied Mechanics and Engineering*, 152:125–145 (1998).

[32] R. J. Astley, Infinite elements for wave problems: a review of current formulations and an assessment of accuracy, *International Journal for Numerical Methods in Engineering*, 49:951–976 (2000).

[33] J. J. Shirron, S. Dey, Acoustic infinite elements for non-separable geometries, *Computer Methods in Applied Mechanics and Engineering*, 191:4123–4139 (2002).

[34] J. J. Shirron, I. Babuška, A comparison of approximate boundary conditions and infinite element methods for exterior Helmholtz problems, *Computer Methods in Applied Mechanics and Engineering*, 164:121–139 (1998).

[35] J. V. Venås, T. Jenserud, Exact 3D scattering solutions for spherical symmetric scatterers, *Journal of Sound and Vibration*, 440:439–479 (2019).

[36] R. Simpson, M. Scott, M. Taus, D. Thomas, H. Lian, Acoustic isogeometric boundary element analysis, *Computer Methods in Applied Mechanics and Engineering*, 269:265–290 (2014).

[37] K. Gerdes, F. Ihlenburg, On the pollution effect in FE solutions of the 3D-Helmholtz equation, *Computer Methods in Applied Mechanics and Engineering*, 170:155–172 (1999).

[38] L. Coox, O. Atak, D. Vandepitte, W. Desmet, An isogeometric indirect boundary element method for solving acoustic problems in open-boundary domains, *Computer Methods in Applied Mechanics and Engineering*, 316:186–208 (2017).

[39] I. Babuška, F. Ihlenburg, E. T. Paik, S. A. Sauter, A generalized finite element method for solving the Helmholtz equation in two dimensions with minimal pollution, *Computer Methods in Applied Mechanics and Engineering*, 128:325–359 (1995).

[40] G. Strang, G. J. Fix, *An analysis of the finite element method*, vol. 212, Prentice-Hall Englewood Cliffs, NJ, 1973.

[41] P. G. Ciarlet, *Basic Error Estimates for Elliptic Problems*, vol. 2, North-Holland, Amsterdam, The Netherlands, 1991.

[42] T. Hughes, A. Reali, G. Sangalli, Efficient quadrature for NURBS-based isogeometric analysis, *Computer Methods in Applied Mechanics and Engineering*, 199:301–313 (2010), Computational Geometry and Analysis.

[43] K. A. Johannessen, Optimal quadrature for univariate and tensor product splines, *Computer Methods in Applied Mechanics and Engineering*, 316:84–99 (2017), Special Issue on Isogeometric Analysis: Progress and Challenges.

[44] J. V. Venås, Isogeometric analysis of acoustic scattering, Master's thesis, Norwegian University of Science and Technology, Trondheim, Norway (2015).

[45] K. A. Johannessen, T. Kvamsdal, T. Dokken, Isogeometric analysis using LR B-splines, *Computer Methods in Applied Mechanics and Engineering*, 269:471–514 (2014).

[46] M. Kumar, T. Kvamsdal, K. A. Johannessen, Superconvergent patch recovery and a posteriori error estimation technique in adaptive isogeometric analysis, *Computer Methods in Applied Mechanics and Engineering*, 316:1086–1156 (2017).

[47] M. Peake, J. Trevelyan, G. Coates, Extended isogeometric boundary element method (XIBEM) for two-dimensional Helmholtz problems, *Computer Methods in Applied Mechanics and Engineering*, 259:93–102 (2013).

[48] M. Peake, J. Trevelyan, G. Coates, Extended isogeometric boundary element method (XIBEM) for three-dimensional medium-wave acoustic scattering

problems, *Computer Methods in Applied Mechanics and Engineering*, 284:762–780 (2015), Isogeometric Analysis Special Issue.

[49] L. Engvall, J. A. Evans, Isogeometric triangular Bernstein–Bézier discretizations: Automatic mesh generation and geometrically exact finite element analysis, *Computer Methods in Applied Mechanics and Engineering*, 304:378–407 (2016).

[50] L. Engvall, J. A. Evans, Isogeometric unstructured tetrahedral and mixed-element Bernstein–Bézier discretizations, *Computer Methods in Applied Mechanics and Engineering*, 319:83–123 (2017).

[51] S. Xia, X. Qian, Isogeometric analysis with Bézier tetrahedra, *Computer Methods in Applied Mechanics and Engineering*, 316:782–816 (2017), Special Issue on Isogeometric Analysis: Progress and Challenges.

[52] D. S. Burnett, R. L. Holford, An ellipsoidal acoustic infinite element, *Computer Methods in Applied Mechanics and Engineering*, 164:49–76 (1998).

[53] M. Abramowitz, I. A. Stegun, *Handbook of Mathematical Function: With Formulas, Graphs, and Mathematical Tables*, Dover, New York, USA, 1965.

[54] W. H. Press, S. A. Teukolsky, W. T. Vetterling, B. P. Flannery, *Numerical recipes in C*, vol. 2, Cambridge Univ Press, 1988.

[55] L. Piegl, W. Tiller, *The NURBS book*, Springer Science & Business Media, 1997.

Paper III

Isogeometric Boundary Element Method for Acoustic Scattering by a Submarine

Jon Vegard Venås and Trond Kvamsdal

Accepted in *Computer Methods in Applied Mechanics and Engineering*

Isogeometric Boundary Element Method for Acoustic Scattering by a Submarine

Jon Vegard Venås[a,*], Trond Kvamsdal[a]

[a] *Department of Mathematical Sciences, Norwegian University of Science and Technology, Alfred Getz' vei 1, 7034 Trondheim, Norway*

Abstract

Isogeometric analysis with the boundary element method (IGABEM) has recently gained interest. In this paper, the approximability of IGABEM on 3D acoustic scattering problems will be investigated and a new improved BeTSSi submarine will be presented as a benchmark example. Both Galerkin and collocation are considered in combination with several boundary integral equations (BIE). In addition to the conventional BIE, regularized versions of this BIE will be considered. Moreover, the hyper-singular BIE and the Burton–Miller formulation are also considered. A new adaptive integration routine is presented, and the numerical examples show the importance of the integration procedure in the boundary element method. The numerical examples also include comparison between standard BEM and IGABEM, which again verifies the higher accuracy obtained from the increased inter-element continuity of the spline basis functions. One of the main objectives in this paper is benchmarking acoustic scattering problems, and the method of manufactured solution will be used frequently in this regard.

1. Introduction

Isogeometric analysis (IGA) was introduced in 2005 by Hughes et al. [1], followed by the book [2] in 2009. Since then, IGA has received a great deal of attention in the effort of bridging the gap between finite element analysis (FEA) and computer aided design (CAD) tools. The initial problem that sparked the IGA movement was the cumbersome mesh generating process when converting the design models from CAD into the FEA programs, and the analysis could often imply a rerun of this tedious process. The problem being that the geometry is represented differently in CAD and FEA.

*Corresponding author.
Email addresses: Jon.Venas@ntnu.no (J.V. Venås), Trond.Kvamsdal@ntnu.no (T. Kvamsdal).

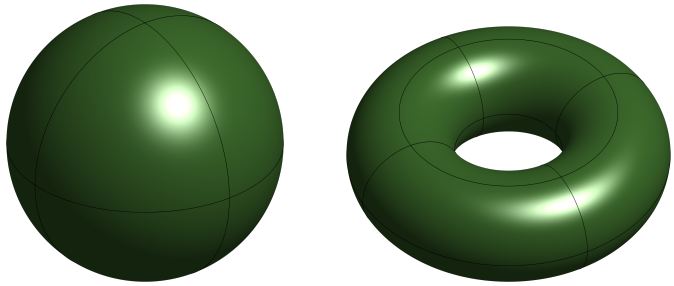

(a) A sphere with 8 elements. (b) A torus with 16 elements.

Figure 1: Examples of exact NURBS geometries of second degree.

An example is the geometries illustrated in Figure 1 which can be represented exactly using NURBS but is outside the space of standard (Lagrangian) FEM geometries. Using the same geometry representation as in CAD, IGA features exact geometry, which remains true in all mesh refinement procedures. Moreover, it turns out that using the non-uniform rational B-splines (NURBS) as basis functions not only for representing the geometry, but also the solution space, greatly enhances the numerical accuracy, see [3] and [4]. This motivates the use of IGA even further, as IGA enables control of the continuity of the basis function up to $C^{\check{p}-1}$ where $\check{p}$ is the polynomial degree (in contrast with the C^0-continuity restriction in classical FEA).

For exterior problems, one can introduce an artificial boundary to obtain a bounded domain introducing the difficulty of surface-to-volume parametrization. The boundary element method (BEM) avoids this issue entirely as it only relies on a computational domain on the surface of the scatterer. Moreover, solid domains are usually represented by surfaces in CAD-systems, such that if modeling of an elastic scatterer is required, the BEM solves this problem as well without the need of surface-to-volume parametrization. This then represents an even further improvement of the quality of the design-analysis bridging development.

This work is only concerned with 3D acoustic scattering (with $d = 3$). The main objective is scattering by plane waves, p_{inc}, as illustrated in Figure 2. In scattering problems, it is often of interest to compute the target strength, TS, of the scatterer in the far field. As an application of this work, the target strength is the quantity of interest for the acoustical aspects of constructing a submarine and is for this reason investigated in this work.

Assuming harmonic time dependency, all time dependent functions may be written as $\breve{F} = \breve{F}(\boldsymbol{x}, t) = F(\boldsymbol{x})\mathrm{e}^{-\mathrm{i}\omega t}$ where ω is the angular frequency and $\mathrm{i} = \sqrt{-1}$ the imaginary unit. This enables us to model the pressure p in the fluid with the Helmholtz equation given by

$$\nabla^2 p + k^2 p = 0 \tag{1}$$

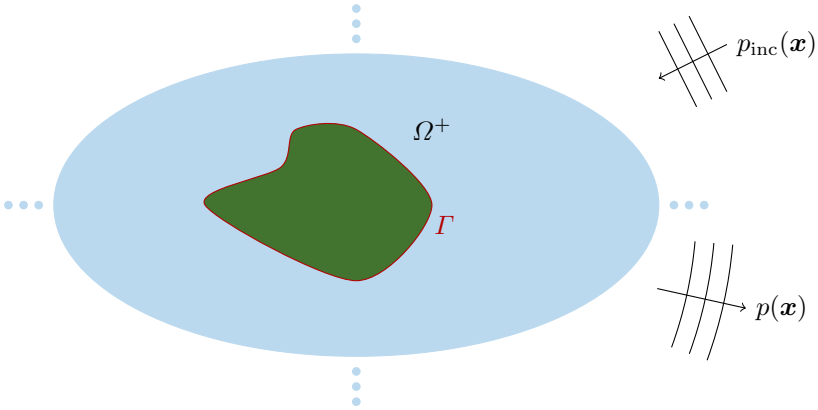

Figure 2: Illustration of the physical problem. A plane incident wave, $p_{\text{inc}}(\boldsymbol{x})$, is scattered by the scatterer, represented by the closed boundary Γ, in an unbounded domain, $\Omega^+ \subset \mathbb{R}^d$, resulting in the scattered pressure, $p(\boldsymbol{x})$.

with the wave number $k = \frac{\omega}{c_{\text{f}}}$ (where c_{f} is the wave speed in the fluid[1]). Other important quantities include the frequency $f = \frac{\omega}{2\pi}$ and the wavelength $\lambda = \frac{2\pi}{k}$.

Some literature already exists for solving acoustic problems using IGABEM including [5–15]. Arguably there is a lack of work in the approximability for IGABEM simulations for more complex geometries, and one of the aims of this work is to contribute to fill this gap.

The exterior Helmholtz problem is presented in Section 2, and the corresponding boundary integral equations are given in Section 3. Discretization of these integral equations either with the use of collocation or a Galerkin approach yields the boundary element method which is presented in Section 4. The weakly singular boundary integral equation requires care when using numerical quadrature and is discussed in Section 5. In Section 6 the results for several benchmark problems are presented. Not only are these benchmark problems important in bug testing for code development, but it is also important to establish reliable results for several geometries ranging in complexity. Finally, conclusions and suggested future work can be found in Section 7.

2. Helmholtz problems

The Helmholtz problem is given by

$$\nabla^2 p + k^2 p = 0 \quad \text{in} \quad \Omega, \tag{2}$$

$$\partial_n p = g \quad \text{on} \quad \Gamma, \tag{3}$$

[1]Throughout this work we shall use $c_{\text{f}} = 1500\,\text{m/s}$.

where ∂_n denotes the partial derivative in the normal direction, $\boldsymbol{n}$, on the surface Γ. Throughout this work, $\boldsymbol{n}$ is always pointing "into" Ω^+. If $\Omega = \Omega^-$ is inside a closed boundary Γ, the problem is referred to as an interior problem. If, on the other hand, $\Omega = \Omega^+$ is the unbounded domain outside Γ (as illustrated in Figure 2), the problem is referred to as an exterior problem where we must impose the Sommerfeld condition [16]

$$\frac{\partial p}{\partial r} - \mathrm{i}kp = o\Big(r^{-1}\Big) \quad \text{with} \quad r = |\boldsymbol{x}| \tag{4}$$

in order to restrict the field in the limit $r \to \infty$ uniformly in $\hat{\boldsymbol{x}} = \frac{\boldsymbol{x}}{r}$, such that no waves originate from infinity (to obtain uniqueness of the solution p).

A common approach for solving unbounded scattering problems with the FEM is to introduce an artificial boundary that encloses the scatterer. On the artificial boundary some sort of absorbing boundary condition (ABC) is prescribed. The problem is then reduced to a finite domain problem, and the bounded domain between the scatterer and the artificial boundary can be discretized with finite elements. Several methods exist for handling the exterior Helmholtz problem (on unbounded domain), including

- the perfectly matched layer (PML) method after Bérenger [17, 18]
- the boundary element method [19–22]
- Dirichlet to Neumann-operators (DtN-operators) [23]
- local differential ABC operators [24–27]
- the infinite element method. [28, 29]

Due to the complexity of the BeTSSi geometry considered in this work we conveniently consider the boundary element method to solve the Helmholtz problem in order to avoid the surface-to-volume parametrization discussed in the introduction.

The Neumann condition (in Eq. (3)), given by the function g, will in the case of rigid scattering be given in terms of the incident wave p_{inc}. Zero displacement of the fluid normally on the scatterer (rigid scattering) implies that $\partial_n(p + p_{\mathrm{inc}}) = 0$, and hence

$$g = -\frac{\partial p_{\mathrm{inc}}}{\partial n}. \tag{5}$$

Plane incident waves (with amplitude P_{inc}) traveling in the direction $\boldsymbol{d}_{\mathrm{s}}$ can be written as

$$p_{\mathrm{inc}} = P_{\mathrm{inc}} \mathrm{e}^{\mathrm{i}k\boldsymbol{d}_{\mathrm{s}}\cdot\boldsymbol{x}}. \tag{6}$$

The normal derivative on the surface of any smooth geometry may then be computed by

$$\frac{\partial p_{\mathrm{inc}}}{\partial n} = \boldsymbol{n} \cdot \nabla p_{\mathrm{inc}} = \mathrm{i}k\boldsymbol{d}_{\mathrm{s}} \cdot \boldsymbol{n} p_{\mathrm{inc}}. \tag{7}$$

2.1. Far field pattern

If the field at the scatterer is known, one can compute the solution in the exterior domain, Ω^+, using the following integral solution (cf. [22, Theorem 2.21])

$$p(\boldsymbol{x}) = \int_\Gamma \Big[p(\boldsymbol{y}) \frac{\partial \Phi_k(\boldsymbol{x},\boldsymbol{y})}{\partial n(\boldsymbol{y})} - \Phi_k(\boldsymbol{x},\boldsymbol{y}) \frac{\partial p(\boldsymbol{y})}{\partial n(\boldsymbol{y})} \Big] \,\mathrm{d}\Gamma(\boldsymbol{y}), \quad \boldsymbol{x} \in \Omega^+ \tag{8}$$

where $\boldsymbol{y}$ is a point on the surface Γ, $\boldsymbol{n}$ lies on Γ pointing "into" Ω^+ at $\boldsymbol{y}$, and Φ_k is the free space Green's function for the Helmholtz equation in Eq. (2) given (in 3D) by

$$\Phi_k(\boldsymbol{x},\boldsymbol{y}) = \frac{\mathrm{e}^{\mathrm{i}kR}}{4\pi R}, \quad \text{where} \quad R = |\boldsymbol{x}-\boldsymbol{y}|. \tag{9}$$

For later convenience, we note that

$$\begin{aligned}
\frac{\partial \Phi_k(\boldsymbol{x},\boldsymbol{y})}{\partial n(\boldsymbol{y})} &= \frac{\Phi_k(\boldsymbol{x},\boldsymbol{y})}{R}(\mathrm{i}kR-1)\frac{\partial R}{\partial n(\boldsymbol{y})} \\
\frac{\partial \Phi_k(\boldsymbol{x},\boldsymbol{y})}{\partial n(\boldsymbol{x})} &= \frac{\Phi_k(\boldsymbol{x},\boldsymbol{y})}{R}(\mathrm{i}kR-1)\frac{\partial R}{\partial n(\boldsymbol{x})} \\
\frac{\partial^2 \Phi_k(\boldsymbol{x},\boldsymbol{y})}{\partial \boldsymbol{n}(\boldsymbol{y}) \partial \boldsymbol{n}(\boldsymbol{x})} &= -\frac{\Phi_k(\boldsymbol{x},\boldsymbol{y})}{R^2}\Big[\boldsymbol{n}(\boldsymbol{x})\cdot\boldsymbol{n}(\boldsymbol{y})(\mathrm{i}kR-1) \\
&\qquad + \Big(k^2R^2 + 3(\mathrm{i}kR-1)\Big)\frac{\partial R}{\partial n(\boldsymbol{x})}\frac{\partial R}{\partial n(\boldsymbol{y})}\Big]
\end{aligned}$$

where

$$\frac{\partial R}{\partial n(\boldsymbol{x})} = \frac{(\boldsymbol{x}-\boldsymbol{y})\cdot\boldsymbol{n}(\boldsymbol{x})}{R} \quad \text{and} \quad \frac{\partial R}{\partial n(\boldsymbol{y})} = -\frac{(\boldsymbol{x}-\boldsymbol{y})\cdot\boldsymbol{n}(\boldsymbol{y})}{R}.$$

The *far field pattern* for the scattered pressure p, is defined by

$$p_0(\hat{\boldsymbol{x}}) = \lim_{r\to\infty} r\mathrm{e}^{-\mathrm{i}kr} p(r\hat{\boldsymbol{x}}), \tag{10}$$

with $r = |\boldsymbol{x}|$ and $\hat{\boldsymbol{x}} = \boldsymbol{x}/|\boldsymbol{x}|$. Using the limits

$$\begin{aligned}
\lim_{r\to\infty} r\mathrm{e}^{-\mathrm{i}kr}\Phi_k(r\hat{\boldsymbol{x}},\boldsymbol{y}) &= \frac{1}{4\pi}\mathrm{e}^{-\mathrm{i}k\hat{\boldsymbol{x}}\cdot\boldsymbol{y}} \\
\lim_{r\to\infty} r\mathrm{e}^{-\mathrm{i}kr}\frac{\partial \Phi_k(r\hat{\boldsymbol{x}},\boldsymbol{y})}{\partial n(\boldsymbol{y})} &= -\frac{\mathrm{i}k}{4\pi}\mathrm{e}^{-\mathrm{i}k\hat{\boldsymbol{x}}\cdot\boldsymbol{y}}\hat{\boldsymbol{x}}\cdot\boldsymbol{n}(\boldsymbol{y})
\end{aligned} \tag{11}$$

the formula in Eq. (8) simplifies in the far field to (cf. [30, p. 32])

$$p_0(\hat{\boldsymbol{x}}) = -\frac{1}{4\pi}\int_\Gamma \Big[\mathrm{i}kp(\boldsymbol{y})\hat{\boldsymbol{x}}\cdot\boldsymbol{n}(\boldsymbol{y}) + \frac{\partial p(\boldsymbol{y})}{\partial n(\boldsymbol{y})}\Big]\mathrm{e}^{-\mathrm{i}k\hat{\boldsymbol{x}}\cdot\boldsymbol{y}}\,\mathrm{d}\Gamma(\boldsymbol{y}). \tag{12}$$

From the far field pattern, the *target strength*, TS, can be computed. It is defined by

$$\mathrm{TS} = 20\log_{10}\Big(\frac{|p_0(\hat{\boldsymbol{x}})|}{|P_{\mathrm{inc}}|}\Big) \tag{13}$$

where P_{inc} is the amplitude of the incident wave at the geometric center of the scatterer (i.e. the origin). Note that the TS is independent of P_{inc}, which is a result of the linear dependency of the amplitude of the incident wave in scattering problems (i.e. doubling the amplitude of the incident wave will double the amplitude of the scattered wave).

3. Boundary integral equations

We adopt the following notation from [22]. The single- and double layer potential operator are given by

$$\mathcal{S}_k\phi(\boldsymbol{x}) = \int_\Gamma \Phi_k(\boldsymbol{x},\boldsymbol{y})\phi(\boldsymbol{y})\,\mathrm{d}\Gamma(\boldsymbol{y}) \qquad \boldsymbol{x}\in\mathbb{R}^d\setminus\Gamma,$$

and

$$\mathcal{D}_k\phi(\boldsymbol{x}) = \int_\Gamma \frac{\partial\Phi_k(\boldsymbol{x},\boldsymbol{y})}{\partial n(\boldsymbol{y})}\phi(\boldsymbol{y})\,\mathrm{d}\Gamma(\boldsymbol{y}) \qquad \boldsymbol{x}\in\mathbb{R}^d\setminus\Gamma,$$

respectively. Here, the normal vector $\boldsymbol{n}$ at the surface Γ always points from the interior domain Ω^- into the exterior domain Ω^+.

For $D\subset\mathbb{R}^d$, define the spaces (for details see [22])

$$\begin{aligned}
L^2_{\text{loc}}(D) &= \Big\{u|_G\in L^2(G)\,:\,\forall G\subset D,\, G \text{ bounded and measurable}\Big\}\\
H^1_{\text{loc}}(D) &= \Big\{u\in L^2_{\text{loc}}(D)\,:\,vu\in H^1(D),\, v\in C^\infty_{\text{comp}}(\overline{D})\Big\}\\
H^1_{\text{loc}}(D;\nabla) &= \Big\{u\in L^2_{\text{loc}}(D)\,:\,\nabla u\in\Big[L^2_{\text{loc}}(D)\Big]^d,\,\nabla^2 u\in L^2_{\text{loc}}(D)\Big\}\\
H^s(\mathbb{R}^d) &= \Big\{u\in L^2(\mathbb{R}^d)\,:\,\mathcal{F}^{-1}\Big[\Big(1+|\boldsymbol{\xi}|^2\Big)^s\mathcal{F}\,u\Big]\in L^2(\mathbb{R}^d)\Big\}\\
H^s(D) &= \Big\{u|_D\,:\,u\in H^s(\mathbb{R}^d)\Big\}\\
H^s(\Gamma) &= \Big\{\phi\in L^2(\Gamma)\,:\,\phi_f\in H^s(\mathbb{R}^{d-1})\Big\}
\end{aligned}$$

with the Fourier transform

$$(\mathcal{F}\,u)(\boldsymbol{\xi}) = (2\pi)^{-d/2}\int_{\mathbb{R}^d}\mathrm{e}^{-\mathrm{i}\boldsymbol{x}\cdot\boldsymbol{\xi}}u(\boldsymbol{x})\,\mathrm{d}\Omega(\boldsymbol{x}),\quad \boldsymbol{\xi}\in\mathbb{R}^d.$$

By defining $\gamma^\pm$ to be the trace operator from $H^s(\Omega^\pm)\to H^{s-1/2}(\Gamma)$ for $\frac{1}{2}<s<\frac{3}{2}$ and $\partial_n^\pm$ to be the normal derivative from $H^1(\Omega^\pm;\nabla)\to H^{1/2}(\Gamma)$, we restate two important theorems for BEM analysis from [22], namely theorem 2.20 and 2.21:

Theorem 1. *If $p\in H^1(\Omega^-)\cup C^2(\Omega^-)$ and, for some $k\geqslant 0$, $\nabla^2 p+k^2p=0$ in Ω^-, then*

$$\mathcal{S}_k\partial_n^-p(\boldsymbol{x})-\mathcal{D}_k\gamma^-p(\boldsymbol{x}) = \begin{cases} p(\boldsymbol{x}), & x\in\Omega^-,\\ 0 & x\in\Omega^+.\end{cases}$$

Theorem 2. *If $p \in H^1_{\mathrm{loc}}(\Omega^+) \cup C^2(\Omega^+)$ and, for some $k > 0$, $\nabla^2 p + k^2 p = 0$ in Ω^+ and p satisfies the Sommerfeld radiation condition in Ω^+, that is,*

$$\frac{\partial p(\boldsymbol{x})}{\partial r} - \mathrm{i}kp(\boldsymbol{x}) = o\Big(r^{-\frac{d-1}{2}}\Big) \quad r = |\boldsymbol{x}|$$

as $r \to \infty$ uniformly in $\hat{\boldsymbol{x}} = \frac{\boldsymbol{x}}{r}$, then

$$-\mathcal{S}_k \partial_n^+ p(\boldsymbol{x}) + \mathcal{D}_k \gamma^+ p(\boldsymbol{x}) = \begin{cases} p(\boldsymbol{x}), & x \in \Omega^+, \\ 0 & x \in \Omega^-. \end{cases}$$

The *acoustic* single- and double layer potential operator are respectively given by

$$S_k \phi(\boldsymbol{x}) = \int_\Gamma \Phi_k(\boldsymbol{x}, \boldsymbol{y}) \phi(\boldsymbol{y}) \, \mathrm{d}\Gamma(\boldsymbol{y}) \qquad \boldsymbol{x} \in \Gamma$$

and

$$D_k \phi(\boldsymbol{x}) = \int_\Gamma \frac{\partial \Phi_k(\boldsymbol{x}, \boldsymbol{y})}{\partial n(\boldsymbol{y})} \phi(\boldsymbol{y}) \, \mathrm{d}\Gamma(\boldsymbol{y}) \qquad \boldsymbol{x} \in \Gamma$$

and the acoustic adjoint double-layer operator and the hypersingular operator are respectively given by

$$D_k' \phi(\boldsymbol{x}) = \int_\Gamma \frac{\partial \Phi_k(\boldsymbol{x}, \boldsymbol{y})}{\partial n(\boldsymbol{x})} \phi(\boldsymbol{y}) \, \mathrm{d}\Gamma(\boldsymbol{y}) \qquad \boldsymbol{x} \in \Gamma$$

and

$$H_k \phi(\boldsymbol{x}) = \int_\Gamma \frac{\partial^2 \Phi_k(\boldsymbol{x}, \boldsymbol{y})}{\partial \boldsymbol{n}(\boldsymbol{y}) \partial \boldsymbol{n}(\boldsymbol{x})} \phi(\boldsymbol{y}) \, \mathrm{d}\Gamma(\boldsymbol{y}) \qquad \boldsymbol{x} \in \Gamma.$$

By following the notation in [22, p. 117] we let

$$M_k = \begin{bmatrix} D_k & -S_k \\ H_k & -D_k' \end{bmatrix} \quad \text{and} \quad c^\pm p = \begin{bmatrix} \gamma^\pm p \\ \partial_n^\pm p \end{bmatrix}$$

such that the boundary integral equations (BIE) for the exterior- and interior problem are respectively given by

$$\mp \frac{1}{2} c^\pm p = M_k c^\pm p.$$

We can write this more explicitly as

$$\mp \frac{1}{2} p(\boldsymbol{x}) + \int_\Gamma \frac{\partial \Phi_k(\boldsymbol{x}, \boldsymbol{y})}{\partial n(\boldsymbol{y})} p(\boldsymbol{y}) \, \mathrm{d}\Gamma(\boldsymbol{y}) = \int_\Gamma \Phi_k(\boldsymbol{x}, \boldsymbol{y}) \frac{\partial p(\boldsymbol{y})}{\partial n(\boldsymbol{y})} \, \mathrm{d}\Gamma(\boldsymbol{y})$$

$$\mp \frac{1}{2} \frac{\partial p(\boldsymbol{x})}{\partial n(\boldsymbol{x})} + \int_\Gamma \frac{\partial^2 \Phi_k(\boldsymbol{x}, \boldsymbol{y})}{\partial \boldsymbol{n}(\boldsymbol{y}) \partial \boldsymbol{n}(\boldsymbol{x})} p(\boldsymbol{y}) \, \mathrm{d}\Gamma(\boldsymbol{y}) = \int_\Gamma \frac{\partial \Phi_k(\boldsymbol{x}, \boldsymbol{y})}{\partial n(\boldsymbol{x})} \frac{\partial p(\boldsymbol{y})}{\partial n(\boldsymbol{y})} \, \mathrm{d}\Gamma(\boldsymbol{y})$$

for almost all $\boldsymbol{x} \in \Gamma$. These integral equations need a modification if Γ is not smooth at $\boldsymbol{x}$. With the jump term defined as (cf. [31])

$$C^{\pm}(\boldsymbol{x}) = \begin{cases} -\frac{1}{2}(1 \pm 1) & \boldsymbol{x} \in \Omega^{+} \\ -\frac{1}{2}(1 \pm 1) - \int_{\Gamma} \frac{\partial \Phi_0(\boldsymbol{x},\boldsymbol{y})}{\partial n(\boldsymbol{y})} \, \mathrm{d}\Gamma(\boldsymbol{y}) & \boldsymbol{x} \in \Gamma \\ \frac{1}{2}(1 \mp 1) & \boldsymbol{x} \in \Omega^{-} \end{cases} \tag{14}$$

the conventional BIE (CBIE) and hypersingular BIE (HBIE) are respectively given by

$$C^{\pm}(\boldsymbol{x}) p(\boldsymbol{x}) + \int_{\Gamma} \frac{\partial \Phi_k(\boldsymbol{x},\boldsymbol{y})}{\partial n(\boldsymbol{y})} p(\boldsymbol{y}) \, \mathrm{d}\Gamma(\boldsymbol{y}) = \int_{\Gamma} \Phi_k(\boldsymbol{x},\boldsymbol{y}) \frac{\partial p(\boldsymbol{y})}{\partial n(\boldsymbol{y})} \, \mathrm{d}\Gamma(\boldsymbol{y}) \tag{15}$$

$$C^{\pm}(\boldsymbol{x}) \frac{\partial p(\boldsymbol{x})}{\partial n(\boldsymbol{x})} + \int_{\Gamma} \frac{\partial^2 \Phi_k(\boldsymbol{x},\boldsymbol{y})}{\partial \boldsymbol{n}(\boldsymbol{y}) \partial \boldsymbol{n}(\boldsymbol{x})} p(\boldsymbol{y}) \, \mathrm{d}\Gamma(\boldsymbol{y}) = \int_{\Gamma} \frac{\partial \Phi_k(\boldsymbol{x},\boldsymbol{y})}{\partial n(\boldsymbol{x})} \frac{\partial p(\boldsymbol{y})}{\partial n(\boldsymbol{y})} \, \mathrm{d}\Gamma(\boldsymbol{y}). \tag{16}$$

Note that using the divergence theorem it is possible to show the following (cf. [19, p. 126])

$$\int_{\Gamma} \frac{\partial \Phi_0(\boldsymbol{x},\boldsymbol{y})}{\partial n(\boldsymbol{y})} \, \mathrm{d}\Gamma(\boldsymbol{y}) = \begin{cases} 0 & \boldsymbol{x} \in \Omega^{+} \\ -\frac{1}{2} & \boldsymbol{x} \in \Gamma, \text{ if } \Gamma \text{ is smooth at } \boldsymbol{x} \\ -1 & \boldsymbol{x} \in \Omega^{-}. \end{cases}$$

This result may be generalized for the case that Γ is not smooth at $\boldsymbol{x}$, namely in terms of the solid angle [32]

$$\int_{\Gamma} \frac{\partial \Phi_0(\boldsymbol{x},\boldsymbol{y})}{\partial n(\boldsymbol{y})} \, \mathrm{d}\Gamma(\boldsymbol{y}) = -\frac{c_0}{4\pi} \tag{17}$$

where the solid angle c_0 can be computed by

$$c_0 = \lim_{\epsilon \to 0^{+}} \frac{|\partial B_{\epsilon}(\boldsymbol{x}) \cap \Omega^{-}|}{\epsilon^2}$$

where $B_{\epsilon}(\boldsymbol{x})$ is a ball of radius ϵ centered at $\boldsymbol{x}$. In other words, the integral in Eq. (17) is given by the negative relative size of the surface of a infinitesimal small sphere centered at $\boldsymbol{x}$ that is inside Ω^{-}. This enables simple exact calculation of this integral for most standard geometries. For example, if Ω^{-} is a cube, the integral in Eq. (17) takes the value $-\frac{1}{4}$ and $-\frac{1}{8}$ if $\boldsymbol{x}$ is at an edge or at a vertex, respectively. This can be used to test the numerical integration involved in solving BIEs.

Combining the CBIE in Eq. (15) and the HBIE in Eq. (16) yields the Burton–Miller (BM) formulation which can conceptually be written as

$$\text{CBIE} + \alpha \cdot \text{HBIE} = 0$$

with the usual choice of the coupling parameter $\alpha = \frac{\mathrm{i}}{k}$ [33]. More precisely, the BM formulation is given by

$$\begin{aligned} &C^{\pm}(\boldsymbol{x})p(\boldsymbol{x}) + \int_{\Gamma} \frac{\partial \Phi_k(\boldsymbol{x},\boldsymbol{y})}{\partial n(\boldsymbol{y})} p(\boldsymbol{y})\,\mathrm{d}\Gamma(\boldsymbol{y}) + \alpha \int_{\Gamma} \frac{\partial^2 \Phi_k(\boldsymbol{x},\boldsymbol{y})}{\partial \boldsymbol{n}(\boldsymbol{y})\partial \boldsymbol{n}(\boldsymbol{x})} p(\boldsymbol{y})\,\mathrm{d}\Gamma(\boldsymbol{y}) \\ &= \int_{\Gamma} \Phi_k(\boldsymbol{x},\boldsymbol{y}) \frac{\partial p(\boldsymbol{y})}{\partial n(\boldsymbol{y})}\,\mathrm{d}\Gamma(\boldsymbol{y}) + \alpha \int_{\Gamma} \frac{\partial \Phi_k(\boldsymbol{x},\boldsymbol{y})}{\partial n(\boldsymbol{x})} \frac{\partial p(\boldsymbol{y})}{\partial n(\boldsymbol{y})}\,\mathrm{d}\Gamma(\boldsymbol{y}) - \alpha C^{\pm}(\boldsymbol{x}) \frac{\partial p(\boldsymbol{x})}{\partial n(\boldsymbol{x})}. \end{aligned} \tag{18}$$

As in [5], we restrict our analysis to direct IGABEM formulations (indirect IGABEM formulations are considered in [10, 13, 15]).

3.1. Regularization techniques

Using Eq. (14) the CBIE can be regularized as follows

$$\begin{aligned} -\frac{1}{2}p(\boldsymbol{x})(1 \pm 1) + \int_{\Gamma} \frac{\partial \Phi_k(\boldsymbol{x},\boldsymbol{y})}{\partial n(\boldsymbol{y})} p(\boldsymbol{y}) - \frac{\partial \Phi_0(\boldsymbol{x},\boldsymbol{y})}{\partial n(\boldsymbol{y})} p(\boldsymbol{x})\,\mathrm{d}\Gamma(\boldsymbol{y}) \\ = \int_{\Gamma} \Phi_k(\boldsymbol{x},\boldsymbol{y}) \frac{\partial p(\boldsymbol{y})}{\partial n(\boldsymbol{y})}\,\mathrm{d}\Gamma(\boldsymbol{y}). \end{aligned} \tag{19}$$

The regularization of the HBIE is slightly more comprehensive. Let $\boldsymbol{v}_j$ (cf. [5, Fig. 2]) be an orthonormal set of (unit) vectors at $\boldsymbol{x}$ such that $\boldsymbol{v}_3 = \boldsymbol{n}$, $\boldsymbol{v}_1 = \boldsymbol{e}_\xi$ and $\boldsymbol{v}_2 = \boldsymbol{v}_3 \times \boldsymbol{v}_1$ with the following notation

$$\boldsymbol{e}_\xi = \frac{1}{h_\xi}\frac{\partial \boldsymbol{x}}{\partial \xi}, \quad \boldsymbol{e}_\eta = \frac{1}{h_\eta}\frac{\partial \boldsymbol{x}}{\partial \eta}, \quad h_\xi = \left|\frac{\partial \boldsymbol{x}}{\partial \xi}\right|, \quad h_\eta = \left|\frac{\partial \boldsymbol{x}}{\partial \eta}\right|.$$

Here, ξ and η are the parameters for the surface parametrization. Note that [34, p. 219]

$$\begin{aligned} \frac{\partial p(\boldsymbol{x})}{\partial v_1} &= \frac{1}{h_\xi}\frac{\partial p(\boldsymbol{x})}{\partial \xi} \\ \frac{\partial p(\boldsymbol{x})}{\partial v_2} &= -\frac{1}{h_\xi}\frac{\cos\theta}{\sin\theta}\frac{\partial p(\boldsymbol{x})}{\partial \xi} + \frac{1}{h_\eta}\frac{1}{\sin\theta}\frac{\partial p(\boldsymbol{x})}{\partial \eta} \end{aligned}$$

where θ is the angle between $\boldsymbol{e}_\xi$ and $\boldsymbol{e}_\eta$.

With the identities [35]

$$\int_{\Gamma} \frac{\partial^2 \Phi_0(\boldsymbol{x},\boldsymbol{y})}{\partial \boldsymbol{n}(\boldsymbol{y})\partial \boldsymbol{n}(\boldsymbol{x})}(\boldsymbol{y}-\boldsymbol{x})\,\mathrm{d}\Gamma(\boldsymbol{y}) = \int_{\Gamma} \frac{\partial \Phi_0(\boldsymbol{x},\boldsymbol{y})}{\partial n(\boldsymbol{x})}\boldsymbol{n}(\boldsymbol{y}) + \frac{\partial \Phi_0(\boldsymbol{x},\boldsymbol{y})}{\partial n(\boldsymbol{y})}\boldsymbol{n}(\boldsymbol{x})\,\mathrm{d}\Gamma(\boldsymbol{y})$$

and

$$\int_{\Gamma} \frac{\partial^2 \Phi_0(\boldsymbol{x},\boldsymbol{y})}{\partial \boldsymbol{n}(\boldsymbol{y})\partial \boldsymbol{n}(\boldsymbol{x})}\,\mathrm{d}\Gamma(\boldsymbol{y}) = 0$$

the regularization of the HBIE is now given by

$$
\begin{aligned}
&\int_\Gamma \left[\frac{\partial^2 \Phi_k(\boldsymbol{x},\boldsymbol{y})}{\partial \boldsymbol{n}(\boldsymbol{y})\partial \boldsymbol{n}(\boldsymbol{x})} - \frac{\partial^2 \Phi_0(\boldsymbol{x},\boldsymbol{y})}{\partial \boldsymbol{n}(\boldsymbol{y})\partial \boldsymbol{n}(\boldsymbol{x})}\right] p(\boldsymbol{y})\,\mathrm{d}\Gamma(\boldsymbol{y}) \\
&+ \int_\Gamma \frac{\partial^2 \Phi_0(\boldsymbol{x},\boldsymbol{y})}{\partial \boldsymbol{n}(\boldsymbol{y})\partial \boldsymbol{n}(\boldsymbol{x})}\left[p(\boldsymbol{y}) - p(\boldsymbol{x}) - \frac{\partial p(\boldsymbol{x})}{\partial v_j}\boldsymbol{v}_j\cdot(\boldsymbol{y}-\boldsymbol{x})\right]\mathrm{d}\Gamma(\boldsymbol{y}) \\
&+ \frac{\partial p(\boldsymbol{x})}{\partial v_j}\int_\Gamma \frac{\partial \Phi_0(\boldsymbol{x},\boldsymbol{y})}{\partial n(\boldsymbol{x})}\boldsymbol{v}_j\cdot\boldsymbol{n}(\boldsymbol{y}) + \frac{\partial \Phi_0(\boldsymbol{x},\boldsymbol{y})}{\partial n(\boldsymbol{y})}\boldsymbol{v}_j\cdot\boldsymbol{n}(\boldsymbol{x})\,\mathrm{d}\Gamma(\boldsymbol{y}) \\
&= \int_\Gamma \left[\frac{\partial \Phi_k(\boldsymbol{x},\boldsymbol{y})}{\partial n(\boldsymbol{x})} + \frac{\partial \Phi_0(\boldsymbol{x},\boldsymbol{y})}{\partial n(\boldsymbol{y})}\right]\frac{\partial p(\boldsymbol{y})}{\partial n(\boldsymbol{y})}\,\mathrm{d}\Gamma(\boldsymbol{y}) \\
&\quad - \int_\Gamma \frac{\partial \Phi_0(\boldsymbol{x},\boldsymbol{y})}{\partial n(\boldsymbol{y})}\left[\frac{\partial p(\boldsymbol{y})}{\partial n(\boldsymbol{y})} - \frac{\partial p(\boldsymbol{x})}{\partial n(\boldsymbol{x})}\right]\mathrm{d}\Gamma(\boldsymbol{y}) + \frac{1}{2}\frac{\partial p(\boldsymbol{x})}{\partial n(\boldsymbol{x})}(1\pm 1) \\
&\quad - \frac{\partial p(\boldsymbol{x})}{\partial n(\boldsymbol{x})}\left[\int_\Gamma \frac{\partial \Phi_0(\boldsymbol{x},\boldsymbol{y})}{\partial n(\boldsymbol{x})}\boldsymbol{n}(\boldsymbol{x})\cdot\boldsymbol{n}(\boldsymbol{y}) + \frac{\partial \Phi_0(\boldsymbol{x},\boldsymbol{y})}{\partial n(\boldsymbol{y})}\,\mathrm{d}\Gamma(\boldsymbol{y})\right. \\
&\qquad\qquad \left. - \int_\Gamma \frac{\partial^2 \Phi_0(\boldsymbol{x},\boldsymbol{y})}{\partial \boldsymbol{n}(\boldsymbol{y})\partial \boldsymbol{n}(\boldsymbol{x})}\boldsymbol{n}(\boldsymbol{x})\cdot(\boldsymbol{y}-\boldsymbol{x})\,\mathrm{d}\Gamma(\boldsymbol{y})\right]
\end{aligned}
\tag{20}
$$

where the summation over the indices $j = 1, 2$ is implied. The integrals in Eqs. (19) and (20) are at most weakly singular.

In practice [34], the integrals in the BIEs are discretized individually using the same quadrature points making several terms cancel.

Another approach for regularizing the CBIE in Eq. (15) is presented in [32]. Consider the function

$$
\Psi(\boldsymbol{y}) = p(\boldsymbol{x})\Psi_1(\boldsymbol{y}) + \frac{\partial p}{\partial n}\Big|_{\boldsymbol{y}=\boldsymbol{x}}\Psi_2(\boldsymbol{y})
$$

where $\Psi_1(\boldsymbol{y})$ and $\Psi_2(\boldsymbol{y})$ solve

$$
\nabla^2\Psi_1(\boldsymbol{y}) + k^2\Psi_1(\boldsymbol{y}) = 0, \quad \Psi_1(\boldsymbol{x}) = 1 \quad \nabla\Psi_1(\boldsymbol{x})\cdot\boldsymbol{n}(\boldsymbol{x}) = 0
$$

and

$$
\nabla^2\Psi_2(\boldsymbol{y}) + k^2\Psi_2(\boldsymbol{y}) = 0, \quad \Psi_2(\boldsymbol{x}) = 0 \quad \nabla\Psi_2(\boldsymbol{x})\cdot\boldsymbol{n}(\boldsymbol{x}) = 1.
$$

The idea is that $\Psi(\boldsymbol{y})$ also solves BIEs such that a subtraction of two such BIEs yields regularization of the integrand. There exist a lot of freedom in choosing functions Ψ_1 and Ψ_2 that satisfy these constraints. The original ones suggested by [32] are given by

$$
\begin{aligned}
\Psi_1^{(1)}(\boldsymbol{y}) &= \frac{C_1\cos[k(R_1 - C_1)]}{R_1} + \frac{\sin[k(R_1 - C_1)]}{kR_1} \\
\Psi_2^{(1)}(\boldsymbol{y}) &= \frac{C_1^2\sin[k(R_1 - C_1)]}{C_2 kR_1}
\end{aligned}
\tag{21}
$$

where

$$R_1(\boldsymbol{y}) = |\boldsymbol{y} - \boldsymbol{x}_1|, \quad C_1 = |\boldsymbol{x} - \boldsymbol{x}_1|, \quad C_2 = (\boldsymbol{x} - \boldsymbol{x}_1) \cdot \boldsymbol{n}(\boldsymbol{x}).$$

The point $\boldsymbol{x}_1$ must lie outside the solution domain and chosen such that $C_2 \neq 0$ (for the sphere and the torus geometry in this work, we use $\boldsymbol{x}_1 = \boldsymbol{x} - \boldsymbol{n}(\boldsymbol{x})$). However, these functions do not satisfy an exterior problem (as they do not satisfy the Sommerfeld radiation condition). This problem is resolved by adding a non-vanishing integral at infinity as described in [32].

One can easily create functions that also satisfy the Sommerfeld radiation condition, simply by basing the functions on the fundamental solutions in Eq. (9)

$$\begin{aligned} \Psi_1^{(2)}(\boldsymbol{y}) &= \frac{1}{C_1}\frac{\Phi_k(\boldsymbol{x}_1, \boldsymbol{y})}{\Phi_k(\boldsymbol{x}_1, \boldsymbol{x})} + \left(1 - \frac{1}{C_1}\right)\frac{\Phi_k(\boldsymbol{x}_2, \boldsymbol{y})}{\Phi_k(\boldsymbol{x}_2, \boldsymbol{x})} \\ \Psi_2^{(2)}(\boldsymbol{y}) &= \frac{1}{C_2}\left[\frac{\Phi_k(\boldsymbol{x}_1, \boldsymbol{y})}{\Phi_k(\boldsymbol{x}_1, \boldsymbol{x})} - \frac{\Phi_k(\boldsymbol{x}_2, \boldsymbol{y})}{\Phi_k(\boldsymbol{x}_2, \boldsymbol{x})}\right] \end{aligned} \tag{22}$$

where

$$C_1 = 1 - \frac{r_2^2(\mathrm{i}kr_1 - 1)(\boldsymbol{x}_1 - \boldsymbol{x}) \cdot \boldsymbol{n}(\boldsymbol{x})}{r_1^2(\mathrm{i}kr_2 - 1)(\boldsymbol{x}_2 - \boldsymbol{x}) \cdot \boldsymbol{n}(\boldsymbol{x})}, \qquad C_2 = \frac{C_1}{r_2^2}(\mathrm{i}kr_2 - 1)(\boldsymbol{x}_2 - \boldsymbol{x}) \cdot \boldsymbol{n}(\boldsymbol{x})$$

and

$$r_1 = |\boldsymbol{x}_1 - \boldsymbol{x}|, \qquad r_2 = |\boldsymbol{x}_2 - \boldsymbol{x}|.$$

The points $\boldsymbol{x}_1$ and $\boldsymbol{x}_2$ must lie outside the solution domain and chosen such that $C_1 \neq 0$ and $C_2 \neq 0$ (for the sphere and the torus geometry in this work, we use $\boldsymbol{x}_1 = \boldsymbol{x} - \frac{1}{2}\boldsymbol{n}(\boldsymbol{x})$ and $\boldsymbol{x}_2 = \boldsymbol{x} - \boldsymbol{n}(\boldsymbol{x})$, respectively).

Alternatively, for the interior problem one could choose

$$\begin{aligned} \Psi_1^{(3)}(\boldsymbol{y}) &= \frac{\boldsymbol{k}_2 \cdot \boldsymbol{n}(\boldsymbol{x})\mathrm{e}^{\mathrm{i}\boldsymbol{k}_1 \cdot (\boldsymbol{y} - \boldsymbol{x})} - \boldsymbol{k}_1 \cdot \boldsymbol{n}(\boldsymbol{x})\mathrm{e}^{\mathrm{i}\boldsymbol{k}_2 \cdot (\boldsymbol{y} - \boldsymbol{x})}}{(\boldsymbol{k}_2 - \boldsymbol{k}_1) \cdot \boldsymbol{n}(\boldsymbol{x})} \\ \Psi_2^{(3)}(\boldsymbol{y}) &= \frac{\mathrm{e}^{\mathrm{i}\boldsymbol{k}_2 \cdot (\boldsymbol{y} - \boldsymbol{x})} - \mathrm{e}^{\mathrm{i}\boldsymbol{k}_1 \cdot (\boldsymbol{y} - \boldsymbol{x})}}{\mathrm{i}(\boldsymbol{k}_2 - \boldsymbol{k}_1) \cdot \boldsymbol{n}(\boldsymbol{x})} \end{aligned}$$

where $\boldsymbol{k}_2 = k\boldsymbol{d}_2$ and $\boldsymbol{k}_1 = k\boldsymbol{d}_1$ are the wave vectors for the plane wave in the direction of the unit vectors $\boldsymbol{d}_1$ and $\boldsymbol{d}_2$, respectively. Choosing $\boldsymbol{d}_2 = \boldsymbol{d}_1 + \boldsymbol{n}(\boldsymbol{x})$ we get (with $|\boldsymbol{n}(\boldsymbol{x})| = 1$)

$$\Psi_1^{(3)}(\boldsymbol{y}) = (\boldsymbol{d}_1 \cdot \boldsymbol{n}(\boldsymbol{x}) + 1)\mathrm{e}^{\mathrm{i}k\boldsymbol{d}_1(\boldsymbol{y} - \boldsymbol{x})} - \boldsymbol{d}_1 \cdot \boldsymbol{n}(\boldsymbol{x})\mathrm{e}^{\mathrm{i}k(\boldsymbol{d}_1 + \boldsymbol{n}(\boldsymbol{x}))(\boldsymbol{y} - \boldsymbol{x})}$$

and

$$\Psi_2^{(3)}(\boldsymbol{y}) = \frac{\mathrm{i}}{k}\left(\mathrm{e}^{\mathrm{i}k\boldsymbol{d}_1 \cdot (\boldsymbol{y} - \boldsymbol{x})} - \mathrm{e}^{\mathrm{i}k(\boldsymbol{d}_1 + \boldsymbol{n}(\boldsymbol{x})) \cdot (\boldsymbol{y} - \boldsymbol{x})}\right)$$

where

$$\boldsymbol{d}_1 = \begin{cases} \frac{\sqrt{3}}{2\sqrt{1-n_1(\boldsymbol{x})^2}} \begin{bmatrix} (1-n_1(\boldsymbol{x})^2)\cos\theta_1 \\ -n_1(\boldsymbol{x})n_2(\boldsymbol{x})\cos\theta_1 + n_3(\boldsymbol{x})\sin\theta_1 \\ -n_1(\boldsymbol{x})n_3(\boldsymbol{x})\cos\theta_1 - n_2(\boldsymbol{x})\sin\theta_1 \end{bmatrix} - \frac{1}{2}\boldsymbol{n}(\boldsymbol{x}) & |n_1(\boldsymbol{x})| < \frac{1}{\sqrt{2}} \\ \frac{\sqrt{3}}{2\sqrt{1-n_2(\boldsymbol{x})^2}} \begin{bmatrix} -n_1(\boldsymbol{x})n_2(\boldsymbol{x})\sin\theta_2 - n_3(\boldsymbol{x})\cos\theta_2 \\ (1-n_2(\boldsymbol{x})^2)\sin\theta_2 \\ -n_2(\boldsymbol{x})n_3(\boldsymbol{x})\sin\theta_2 + n_1(\boldsymbol{x})\cos\theta_2 \end{bmatrix} - \frac{1}{2}\boldsymbol{n}(\boldsymbol{x}) & \text{otherwise,} \end{cases} \tag{23}$$

for some free parameters θ_1 and θ_2. Choosing $\theta_1 = -\pi/2$ and $\theta_2 = -\pi$ yields

$$\boldsymbol{d}_1 = \begin{cases} \frac{\sqrt{3}}{2\sqrt{1-n_1(\boldsymbol{x})^2}}\boldsymbol{e}_1 \times \boldsymbol{n}(\boldsymbol{x}) - \frac{1}{2}\boldsymbol{n}(\boldsymbol{x}) & |n_1(\boldsymbol{x})| < \frac{1}{\sqrt{2}} \\ \frac{\sqrt{3}}{2\sqrt{1-n_2(\boldsymbol{x})^2}}\boldsymbol{e}_2 \times \boldsymbol{n}(\boldsymbol{x}) - \frac{1}{2}\boldsymbol{n}(\boldsymbol{x}) & \text{otherwise.} \end{cases} \tag{24}$$

Then, $\boldsymbol{d}_1 \cdot \boldsymbol{n}(\boldsymbol{x}) = -\frac{1}{2}$ and

$$\begin{aligned} \Psi_1^{(3)}(\boldsymbol{y}) &= \frac{1}{2}\Big(\mathrm{e}^{\mathrm{i}k\boldsymbol{d}_1(\boldsymbol{y}-\boldsymbol{x})} + \mathrm{e}^{\mathrm{i}k\boldsymbol{d}_2(\boldsymbol{y}-\boldsymbol{x})}\Big) \\ \Psi_2^{(3)}(\boldsymbol{y}) &= \frac{\mathrm{i}}{k}\Big(\mathrm{e}^{\mathrm{i}k\boldsymbol{d}_1\cdot(\boldsymbol{y}-\boldsymbol{x})} - \mathrm{e}^{\mathrm{i}k\boldsymbol{d}_2\cdot(\boldsymbol{y}-\boldsymbol{x})}\Big). \end{aligned} \tag{25}$$

The advantage of this choice over the former two choices is that it does not require finding points ($\boldsymbol{x}_1$ and $\boldsymbol{x}_2$) outside the solution domain that satisfy a given criterion.

If

$$\Psi(\boldsymbol{y}) = p(\boldsymbol{x})\Psi_1^{(1)}(\boldsymbol{y}) + \frac{\partial p}{\partial n}\Big|_{\boldsymbol{y}=\boldsymbol{x}}\Psi_2^{(1)}(\boldsymbol{y})$$

then[2] (cf. [32])

$$\begin{aligned} &\frac{1}{2}p(\boldsymbol{x})\Big[1 \mp 1 - \Big(1 + \frac{\mathrm{i}}{kC_1}\Big)\Big(1 - \mathrm{e}^{2\mathrm{i}kC_1}\Big)\Big] \\ &+ \int_\Gamma \Big(p(\boldsymbol{y}) - p(\boldsymbol{x})\Psi_1(\boldsymbol{y}) - \frac{\partial p}{\partial n}\Big|_{\boldsymbol{y}=\boldsymbol{x}}\Psi_2(\boldsymbol{y})\Big)\frac{\partial \Phi_k(\boldsymbol{x},\boldsymbol{y})}{\partial n(\boldsymbol{y})}\,\mathrm{d}\Gamma(\boldsymbol{y}) \\ &\quad = \frac{\mathrm{i}C_1}{2kC_2}\Big(1 - \mathrm{e}^{2\mathrm{i}kC_1}\Big)\frac{\partial p}{\partial n}\Big|_{\boldsymbol{y}=\boldsymbol{x}} \\ &\qquad + \int_\Gamma \Big(\frac{\partial p(\boldsymbol{y})}{\partial n(\boldsymbol{y})} - p(\boldsymbol{x})\frac{\partial \Psi_1(\boldsymbol{y})}{\partial n(\boldsymbol{y})} - \frac{\partial p}{\partial n}\Big|_{\boldsymbol{y}=\boldsymbol{x}}\frac{\partial \Psi_2(\boldsymbol{y})}{\partial n(\boldsymbol{y})}\Big)\Phi_k(\boldsymbol{x},\boldsymbol{y})\,\mathrm{d}\Gamma(\boldsymbol{y}). \end{aligned} \tag{26}$$

We refer to this integral equation as the first regularized CBIE (RCBIE1). If

$$\Psi(\boldsymbol{y}) = p(\boldsymbol{x})\Psi_1^{(2)}(\boldsymbol{y}) + \frac{\partial p}{\partial n}\Big|_{\boldsymbol{y}=\boldsymbol{x}}\Psi_2^{(2)}(\boldsymbol{y})$$

[2]Recall that the upper plus sign in $\pm$ (and negative sign for $\mp$) is chosen for the exterior problem while the negative sign in $\pm$ (and positive sign for $\mp$) is chosen for the interior problem.

then $\Psi(\boldsymbol{y})$ solves the exterior problem of Eq. (15) such that

$$\begin{aligned}\frac{1}{2}p(\boldsymbol{x})(1\mp 1)+\int_\Gamma\Big(p(\boldsymbol{y})-p(\boldsymbol{x})\Psi_1(\boldsymbol{y})-\frac{\partial p}{\partial n}\Big|_{\boldsymbol{y}=\boldsymbol{x}}\Psi_2(\boldsymbol{y})\Big)\frac{\partial\Phi_k(\boldsymbol{x},\boldsymbol{y})}{\partial n(\boldsymbol{y})}\,\mathrm{d}\Gamma(\boldsymbol{y})\\ =\int_\Gamma\Big(\frac{\partial p(\boldsymbol{y})}{\partial n(\boldsymbol{y})}-p(\boldsymbol{x})\frac{\partial\Psi_1(\boldsymbol{y})}{\partial n(\boldsymbol{y})}-\frac{\partial p}{\partial n}\Big|_{\boldsymbol{y}=\boldsymbol{x}}\frac{\partial\Psi_2(\boldsymbol{y})}{\partial n(\boldsymbol{y})}\Big)\Phi_k(\boldsymbol{x},\boldsymbol{y})\,\mathrm{d}\Gamma(\boldsymbol{y}).\end{aligned}\tag{27}$$

We refer to this integral equation as the second regularized CBIE (RCBIE2). If

$$\Psi(\boldsymbol{y})=p(\boldsymbol{x})\Psi_1^{(3)}(\boldsymbol{y})+\frac{\partial p}{\partial n}\Big|_{\boldsymbol{y}=\boldsymbol{x}}\Psi_2^{(3)}(\boldsymbol{y})$$

then $\Psi(\boldsymbol{y})$ solves the interior problem of Eq. (15) such that

$$\begin{aligned}-\frac{1}{2}p(\boldsymbol{x})(1\pm 1)+\int_\Gamma\Big(p(\boldsymbol{y})-p(\boldsymbol{x})\Psi_1(\boldsymbol{y})-\frac{\partial p}{\partial n}\Big|_{\boldsymbol{y}=\boldsymbol{x}}\Psi_2(\boldsymbol{y})\Big)\frac{\partial\Phi_k(\boldsymbol{x},\boldsymbol{y})}{\partial n(\boldsymbol{y})}\,\mathrm{d}\Gamma(\boldsymbol{y})\\ =\int_\Gamma\Big(\frac{\partial p(\boldsymbol{y})}{\partial n(\boldsymbol{y})}-p(\boldsymbol{x})\frac{\partial\Psi_1(\boldsymbol{y})}{\partial n(\boldsymbol{y})}-\frac{\partial p}{\partial n}\Big|_{\boldsymbol{y}=\boldsymbol{x}}\frac{\partial\Psi_2(\boldsymbol{y})}{\partial n(\boldsymbol{y})}\Big)\Phi_k(\boldsymbol{x},\boldsymbol{y})\,\mathrm{d}\Gamma(\boldsymbol{y}).\end{aligned}\tag{28}$$

We refer to this integral equation as the third regularized CBIE (RCBIE3). These integrals have bounded integrands [36] and are thus a further regularization of Eq. (19).

3.2. Rigid scattering problems

For rigid (exterior) scattering problems the boundary integral equations are simplified somewhat. Consider an incident plane wave

$$p_{\mathrm{inc}}(\boldsymbol{x})=P_{\mathrm{inc}}\mathrm{e}^{\mathrm{i}\boldsymbol{k}\cdot\boldsymbol{x}}$$

scattered by the boundary Γ. Here, P_{inc} is the amplitude, and $\boldsymbol{k}$ is the wave vector. Combining Theorem 1 and Theorem 2 we can write

$$p_{\mathrm{tot}}(\boldsymbol{x})=p_{\mathrm{inc}}(\boldsymbol{x})+\mathcal{D}_k\gamma^+p_{\mathrm{tot}}(\boldsymbol{x})-\mathcal{S}_k\partial_n^+p_{\mathrm{tot}}(\boldsymbol{x})$$

where $p_{\mathrm{tot}}=p+p_{\mathrm{inc}}$ is the total field and p is the scattered field satisfying the assumptions of Theorem 2.

For rigid scattering we have $\partial_n^+p_{\mathrm{tot}}(\boldsymbol{x})=0$, such that the regularized CBIE in Eq. (19) and HBIE in Eq. (20) reduce to[3]

$$-p_{\mathrm{tot}}(\boldsymbol{x})+\int_\Gamma\frac{\partial\Phi_k(\boldsymbol{x},\boldsymbol{y})}{\partial n(\boldsymbol{y})}p_{\mathrm{tot}}(\boldsymbol{y})-\frac{\partial\Phi_0(\boldsymbol{x},\boldsymbol{y})}{\partial n(\boldsymbol{y})}p_{\mathrm{tot}}(\boldsymbol{x})\,\mathrm{d}\Gamma(\boldsymbol{y})=-p_{\mathrm{inc}}(\boldsymbol{x})\tag{29}$$

[3]Note that this CBIE formulation no longer contains weakly singular integrals (only integrals with bounded integrands).

and

$$\int_\Gamma \left[\frac{\partial^2 \Phi_k(\boldsymbol{x},\boldsymbol{y})}{\partial \boldsymbol{n}(\boldsymbol{y})\partial \boldsymbol{n}(\boldsymbol{x})} - \frac{\partial^2 \Phi_0(\boldsymbol{x},\boldsymbol{y})}{\partial \boldsymbol{n}(\boldsymbol{y})\partial \boldsymbol{n}(\boldsymbol{x})}\right] p_{\text{tot}}(\boldsymbol{y})\,\mathrm{d}\Gamma(\boldsymbol{y})$$
$$+ \int_\Gamma \frac{\partial^2 \Phi_0(\boldsymbol{x},\boldsymbol{y})}{\partial \boldsymbol{n}(\boldsymbol{y})\partial \boldsymbol{n}(\boldsymbol{x})}\left[p_{\text{tot}}(\boldsymbol{y}) - p_{\text{tot}}(\boldsymbol{x}) - \frac{\partial p_{\text{tot}}(\boldsymbol{x})}{\partial v_j}\boldsymbol{v}_j \cdot (\boldsymbol{y}-\boldsymbol{x})\right]\mathrm{d}\Gamma(\boldsymbol{y})$$
$$+ \frac{\partial p_{\text{tot}}(\boldsymbol{x})}{\partial v_j}\int_\Gamma \frac{\partial \Phi_0(\boldsymbol{x},\boldsymbol{y})}{\partial n(\boldsymbol{x})}\boldsymbol{v}_j \cdot \boldsymbol{n}(\boldsymbol{y}) + \frac{\partial \Phi_0(\boldsymbol{x},\boldsymbol{y})}{\partial n(\boldsymbol{y})}\boldsymbol{v}_j \cdot \boldsymbol{n}(\boldsymbol{x})\,\mathrm{d}\Gamma(\boldsymbol{y}) = -\frac{\partial p_{\text{inc}}(\boldsymbol{x})}{\partial n(\boldsymbol{x})},$$

respectively. In a similar fashion Eq. (26), Eq. (27) and Eq. (28) can be reformulated as

$$-\frac{1}{2}p_{\text{tot}}(\boldsymbol{x})\left(1+\frac{\mathrm{i}}{kC_1}\right)\left(1-\mathrm{e}^{2\mathrm{i}kC_1}\right)$$
$$+\int_\Gamma (p_{\text{tot}}(\boldsymbol{y}) - p_{\text{tot}}(\boldsymbol{x})\Psi_1(\boldsymbol{y}))\frac{\partial \Phi_k(\boldsymbol{x},\boldsymbol{y})}{\partial n(\boldsymbol{y})} + p_{\text{tot}}(\boldsymbol{x})\frac{\partial \Psi_1(\boldsymbol{y})}{\partial n(\boldsymbol{y})}\Phi_k(\boldsymbol{x},\boldsymbol{y})\,\mathrm{d}\Gamma(\boldsymbol{y})$$
$$= -p_{\text{inc}}(\boldsymbol{x}),$$

$$\int_\Gamma (p_{\text{tot}}(\boldsymbol{y}) - p_{\text{tot}}(\boldsymbol{x})\Psi_1(\boldsymbol{y}))\frac{\partial \Phi_k(\boldsymbol{x},\boldsymbol{y})}{\partial n(\boldsymbol{y})} + p_{\text{tot}}(\boldsymbol{x})\frac{\partial \Psi_1(\boldsymbol{y})}{\partial n(\boldsymbol{y})}\Phi_k(\boldsymbol{x},\boldsymbol{y})\,\mathrm{d}\Gamma(\boldsymbol{y}) = -p_{\text{inc}}(\boldsymbol{x})$$

and

$$-p_{\text{tot}}(\boldsymbol{x}) + \int_\Gamma \Big[(p_{\text{tot}}(\boldsymbol{y}) - p_{\text{tot}}(\boldsymbol{x})\Psi_1(\boldsymbol{y}))\frac{\partial \Phi_k(\boldsymbol{x},\boldsymbol{y})}{\partial n(\boldsymbol{y})}$$
$$+p_{\text{tot}}(\boldsymbol{x})\frac{\partial \Psi_1(\boldsymbol{y})}{\partial n(\boldsymbol{y})}\Phi_k(\boldsymbol{x},\boldsymbol{y})\Big]\,\mathrm{d}\Gamma(\boldsymbol{y}) = -p_{\text{inc}}(\boldsymbol{x}),$$

respectively.

4. Collocation and Galerkin formulations

For the discretization procedure we consider a finite dimensional trial space $V_h \subset V = H^{1/2}(\Gamma)$ which is built up by the same NURBS basis functions used to represent the CAD geometry. In this work, the geometry is assumed to be constructed by tensorial NURBS patches such that the geometry for each patch can be written as

$$\boldsymbol{X}(\xi,\eta) = \sum_{i=1}^{n}\sum_{j=1}^{m} R_{i,j}^{\check{p},\check{q}}(\xi,\eta)$$

with notation taken from and explained in [37, p. 51]. For convenience we simplify the notation $R_{i,j}^{\check{p},\check{q}}$ to $R_{\tilde{i}}$ where the index $\tilde{i}$ represents a map from local indices to global indices (over all patches).

For the collocation formulations, we evaluate the BIEs at n_{dofs} collocation points, $\boldsymbol{x}_i \in \Gamma$. This forms an algebraic system of equations which can be solved to obtain the numerical solution. Throughout this work, the collocation points are chosen to be the Greville abscissae as described in [34].

The Galerkin formulations are obtained by multiplying the BIEs with a test function $q_{\text{tot}}(\boldsymbol{x})$ and integrating over Γ. For brevity we only here consider rigid scattering problems with the CBIE formulation in Eq. (29)

$$
\begin{aligned}
&-\int_\Gamma p_{\text{tot}}(\boldsymbol{x}) q_{\text{tot}}(\boldsymbol{x}) \,\mathrm{d}\Gamma(\boldsymbol{x}) \\
&+\int_\Gamma q_{\text{tot}}(\boldsymbol{x}) \int_\Gamma \frac{\partial \Phi_k(\boldsymbol{x},\boldsymbol{y})}{\partial n(\boldsymbol{y})} p_{\text{tot}}(\boldsymbol{y}) - \frac{\partial \Phi_0(\boldsymbol{x},\boldsymbol{y})}{\partial n(\boldsymbol{y})} p_{\text{tot}}(\boldsymbol{x}) \,\mathrm{d}\Gamma(\boldsymbol{y}) \,\mathrm{d}\Gamma(\boldsymbol{x}) \\
&\qquad\qquad = -\int_\Gamma p_{\text{inc}}(\boldsymbol{x}) q_{\text{tot}}(\boldsymbol{x}) \,\mathrm{d}\Gamma(\boldsymbol{x}).
\end{aligned}
$$

Letting

$$
p_{\text{tot}}(\boldsymbol{x}) = \sum_{j=1}^{n_{\text{dofs}}} u_j R_j(\boldsymbol{x}),
$$

we get (by choosing $q_{\text{tot}}(\boldsymbol{x}) = R_i(\boldsymbol{x})$)

$$
\begin{aligned}
-\sum_{j=1}^{n_{\text{dofs}}} u_j \Bigg[&\int_\Gamma R_j(\boldsymbol{x}) R_i(\boldsymbol{x}) \,\mathrm{d}\Gamma(\boldsymbol{x}) + \int_\Gamma R_i(\boldsymbol{x}) \int_\Gamma \frac{\partial \Phi_k(\boldsymbol{x},\boldsymbol{y})}{\partial n(\boldsymbol{y})} R_j(\boldsymbol{y}) \,\mathrm{d}\Gamma(\boldsymbol{y}) \,\mathrm{d}\Gamma(\boldsymbol{x}) \\
&- \int_\Gamma R_i(\boldsymbol{x}) R_j(\boldsymbol{x}) \int_\Gamma \frac{\partial \Phi_0(\boldsymbol{x},\boldsymbol{y})}{\partial n(\boldsymbol{y})} \,\mathrm{d}\Gamma(\boldsymbol{y}) \,\mathrm{d}\Gamma(\boldsymbol{x}) \Bigg] \\
&= -\int_\Gamma p_{\text{inc}}(\boldsymbol{x}) R_i(\boldsymbol{x}) \,\mathrm{d}\Gamma(\boldsymbol{x}), \quad \forall i = 1, \ldots, n_{\text{dofs}},
\end{aligned}
$$

which results in a linear system of n_{dofs} equations. Instead of looping through all basis functions $R_i(\boldsymbol{x})$, it is advantageous to loop through the elements as done in finite element methods [5].

For the collocation formulations we prepend a letter "C" (i.e. CCBIE, CBM, CRCBIE1, etc.) and for the Galerkin formulations we prepend a letter "G" (i.e. GCBIE, GBM, GRCBIE1, etc.).

5. Numerical evaluation of the boundary integrals

In [5, p. 286] an adaptive integration technique is used around the collocation points in order to resolve the singular behavior of the integrand. Every element not containing the source point is divided into[4]

$$
n_{\text{div}} = \left(1 + \left\lfloor \frac{s_1 h}{l} \right\rceil \right)^{d-1} \tag{30}
$$

[4]Here, $\lfloor \cdot \rceil$ is the rounding function, i.e. $\lfloor x \rceil = \left\lfloor x + \frac{1}{2} \right\rfloor$, where $\lfloor x \rfloor = \max\{n \in \mathbb{Z} : n \leqslant x\}$.

sub elements at which standard quadrature is applied. Here, l is the distance from the center of the element to the source point[5], h is the element size (largest diagonal of the element) and s_1 is a user defined parameter controlling the adaptivity in terms of quadrature point density. For the element containing the source point, the element is divided into 2 to 4 (triangular) sub elements (depending on the location of the source point; at a corner, on an edge, or within an element) as described in [34]. A polar integration is then applied to each triangle such that the weakly singular integrands are regularized.

We use $\check{p}_\xi + 1 + n_{\text{eqp},1}$ quadrature points within each sub-element in the ξ-direction, and $\check{p}_\eta + 1 + n_{\text{eqp},1}$ in the η-direction. In the polar integration we use $\check{p}_{\max} + 1 + n_{\text{eqp},2}$ in each parameter direction where $\check{p}_{\max} = \max\{\check{p}_\xi, \check{p}_\eta\}$ for the Simpson method.

In this work we present a modification to this routine inspired by Taus et al. [11, 38]. For each element not containing the source point, each (sub) element is divided into 4 until $s_1 h/l < 1$ where h is the size of the (sub) element and l is the distance from the (sub) element center to the source point. Whenever a (sub) element fulfills this requirement, standard quadrature is used with $\lfloor(\check{p}_\xi + 1)(s_1 h/l + 1)\rceil$ quadrature points in the ξ-direction and $\lfloor(\check{p}_\eta + 1)(s_1 h/l + 1)\rceil$ quadrature points in the η-direction. An alternative approach to the polar integration is here used. It is based on the transformation in [39] (for details see [40]), which avoids the problem of awkward integration limits opposite to the triangle vertex containing the singularity. Each triangular sub element is bilinearly transformed into the unit square. Consider the i^{th} triangular sub element with vertices $\{(\xi_{\boldsymbol{x}}, \eta_{\boldsymbol{x}}), (\xi_{\text{v},i}, \eta_{\text{v},i}), (\xi_{\text{v},i+1}, \eta_{\text{v},i+1})\}$ in the parameter domain where $(\xi_{\boldsymbol{x}}, \eta_{\boldsymbol{x}})$ is the parametric coordinate of $\boldsymbol{x}$ and $(\xi_{\text{v},1}, \eta_{\text{v},1}) = (\xi_{\text{v},5}, \eta_{\text{v},5})$, $(\xi_{\text{v},2}, \eta_{\text{v},2})$, $(\xi_{\text{v},3}, \eta_{\text{v},3})$ and $(\xi_{\text{v},4}, \eta_{\text{v},4})$ are the parametric coordinates for the four vertices of the element (see Figure 3). The transformation is then given by ($\rho, \theta \in [0, 1]$)

$$\begin{aligned} \xi &= \xi_{\boldsymbol{x}} + \rho(\xi_{\text{v},i} - \xi_{\boldsymbol{x}} + (\xi_{\text{v},i+1} - \xi_{\text{v},i})\theta) \\ \eta &= \eta_{\boldsymbol{x}} + \rho(\eta_{\text{v},i} - \eta_{\boldsymbol{x}} + (\eta_{\text{v},i+1} - \eta_{\text{v},i})\theta) \end{aligned} \tag{31}$$

with Jacobian determinant given by

$$\begin{aligned} J_2 = \rho[&(\xi_{\text{v},i} - \xi_{\boldsymbol{x}} + (\xi_{\text{v},i+1} - \xi_{\text{v},i})\theta)(\eta_{\text{v},i+1} - \eta_{\text{v},i}) \\ &- (\eta_{\text{v},i} - \eta_{\boldsymbol{x}} + (\eta_{\text{v},i+1} - \eta_{\text{v},i})\theta)(\xi_{\text{v},i+1} - \xi_{\text{v},i})]. \end{aligned}$$

The factor ρ in the Jacobian determinant is responsible for regularizing the weakly singular integral. Note that $J_2 = 0$ for the collapsed triangle(s) when $\boldsymbol{x}$ lies on the edge (vertex) of the element. Each triangular sub element is divided into $n^{(i)}_{\text{div},\theta}$

[5] Arguably, a better choice for l would be the minimal distance between the source point and any point in the element as outlined in [11]. It is not clear to the authors if this is an optimization as it requires additional computational effort.

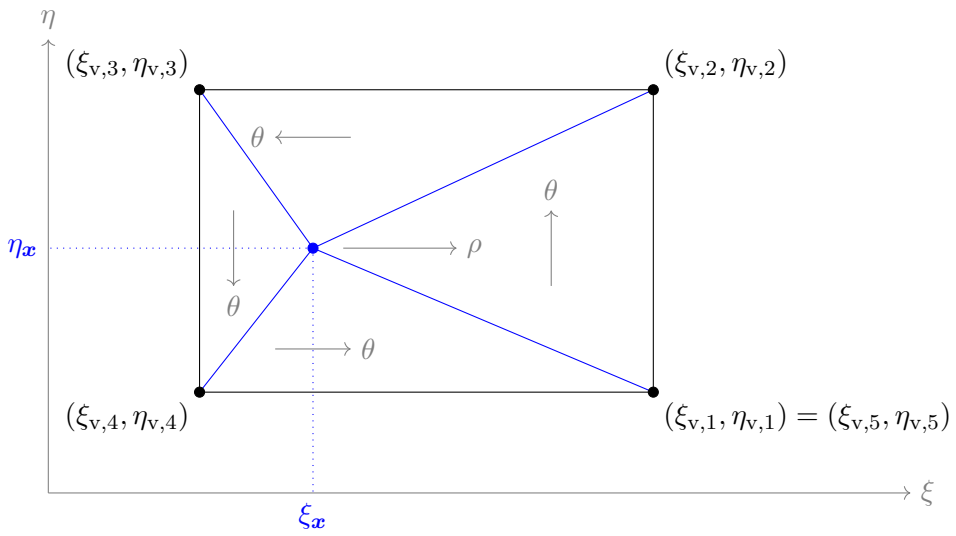

Figure 3: **Numerical evaluation of the boundary integral equations**: The element containing the source point $\boldsymbol{x}$ is divided in (up to) 4 triangles in the parameter domain.

sub elements (in the i^{th} triangle) in the θ-direction and $n_{\mathrm{div,r}}$ sub elements in the radial direction, where

$$n^{(i)}_{\mathrm{div},\theta} = \left\lceil s_2 \frac{\theta^{(i)}_{\mathrm{dir}}}{90^\circ} \right\rceil, \quad n_{\mathrm{div,r}} = \lceil s_2 \rceil, \quad s_2 = \frac{\check{p}_{\max} + 1 + n_{\mathrm{eqp},2}}{2(\check{p}_{\max} + 1)}.$$

Here, $\theta^{(i)}_{\mathrm{dir}}$ is the interior angle (in the parent domain) neighboring the source point of the initial sub triangle i. The reason for the subdivision of the triangles (as opposed to use high order quadrature) is that a high number of quadrature points is here needed (which will later be illustrated). This subdivision maps each sub element (in the (ρ, θ)-domain) to the reference domain $[-1, 1]^2$ by the linear transformation

$$\begin{aligned} \rho &= \rho_j + \frac{1}{2}(\rho_{j+1} - \rho_j)(\tilde{\rho} + 1), \qquad \rho_j = \frac{j}{n_{\mathrm{div,r}}}, \qquad j = 0, \ldots, n_{\mathrm{div,r}} - 1 \\ \theta &= \theta_l + \frac{1}{2}(\theta_{l+1} - \theta_l)(\tilde{\theta} + 1), \qquad \theta_l = \frac{l}{n^{(i)}_{\mathrm{div},\theta}}, \qquad l = 0, \ldots, n^{(i)}_{\mathrm{div},\theta} - 1 \end{aligned} \tag{32}$$

with Jacobian determinant $J_3 = 1/(4n^{(i)}_{\mathrm{div},\theta} n_{\mathrm{div,r}})$. Each of these sub elements are now evaluated using $2(\check{p}_{\max} + 1)$ quadrature points in both parametric directions.

For the Galerkin formulations the integral integrating the BIEs uses $(\check{p}_\xi + 1 + n_{\mathrm{eqp},1}) \times (\check{p}_\eta + 1 + n_{\mathrm{eqp},1})$ quadrature points over each element. If not otherwise stated, we shall use $n_{\mathrm{eqp},1} = 0$ throughout this work.

In Figures 4 and 5 the locations of the quadrature points are illustrated on the third uniform mesh refinement of the coarse mesh in Figure 1a (with $\check{p} = 2$).

6. Numerical examples

Acoustic scattering problems on a sphere are investigated in the following. These problems possess analytic solutions [41] and are for this reason often used to verify numerical methods in acoustic scattering, e.g. [5, 10, 30, 42–44]. In order to analyze convergence properties of IGABEM we also consider a torus, which can be represented by NURBS of polynomial order $\check{p} \geqslant 2$ with no poles in the parametrization. Also, a cube geometry will be investigated to check the behavior of the BIEs at G^0-geometries. We then continue be analyzing the BeTSSi[6] submarine. Before we consider the rigid scattering problem on this complex geometry, we present the method of manufactured solution. This method enables us to get some quality insurance of the underlying mesh to be used in the full scattering problem. Moreover, to some extent, the method can be used for quality insurance of the numerical solution of the scattering problem. Together with the benchmark problem on the sphere, these methods yield a solid basis for testing the correctness of the implemented code.

In this work, the test setting is chosen so that the present approach can be compared to other methods. In particular, the scattering on a rigid sphere example and the torus example is found in [5]. Scattering on the BeTSSi submarine has been addressed at three workshops in the past 18 years [45]. FWG[7] initiated the first workshop in 2001 (held in Kiel 2002) and delivered the generic BeTSSi submarine (for which the outer hull is described in Appendix C). The second workshop took place in Kiel in 2014 and the third in the Hague in 2016. The best of these results will be used as reference solutions in this work. Additionally, we create our own reference simulations using Comsol Multiphysics® [46]. This benchmarking exercise is a crucial step to obtain reliable solutions for even more complex models.

The aim of these numerical examples is to investigate the approximability of IGABEM and its formulations. Moreover, we aim to establish highly accurate solutions for the BeTSSi submarine for benchmarking purposes and compare the accuracy and computational complexity of these results to existing simulations.

With the use of the Galerkin method the following quasi-optimal error estimate exists for the BEM [22, Theorem 2.49] (with the Burton–Miller formulation)

$$\|p - p_h\|_{L^2(\Gamma)} \leqslant C_1 \inf_{q_h \in V_h} \|p - q_h\|_{L^2(\Gamma)} \leqslant C_2 (hk)^{\check{p}+1} \tag{33}$$

[6] Benchmark Target Strength Simulation.

[7] Forschungsanstalt für Wasserschall und Geophysik.

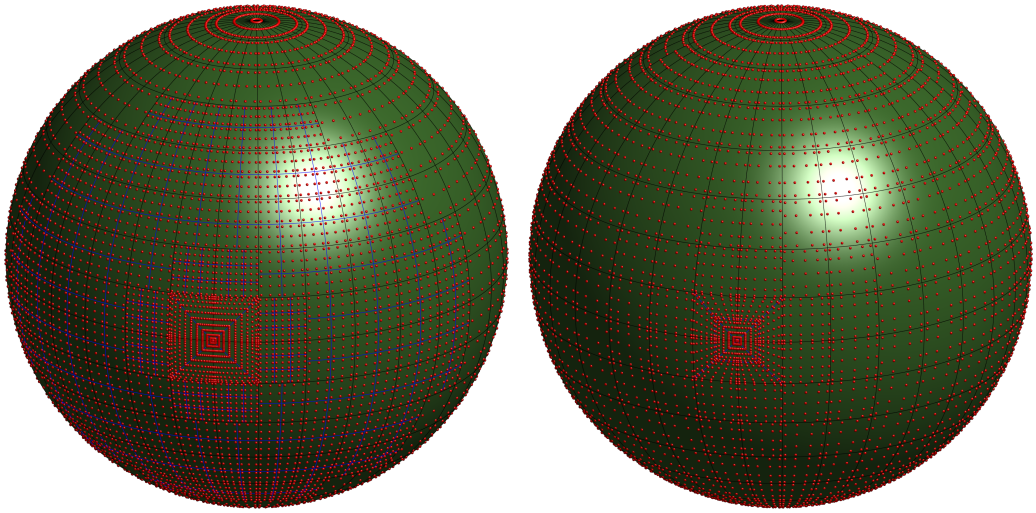

(a) The 317^{th} collocation point is at a vertex shared by four elements.

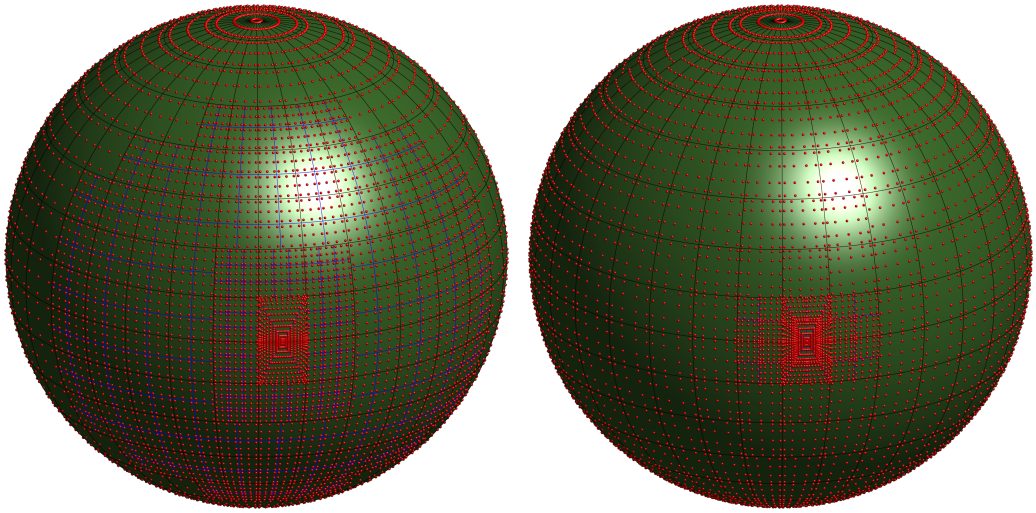

(b) The 319^{th} collocation point is on an element edge shared by two elements.

Figure 4: **Numerical evaluation of the boundary integral equations**: The figures to the left are the integration procedure in [5] (with $s_1 = 2$). The sub element divisions are here shown by blue lines (the black lines are the element edges). The red points are the quadrature points. Here, $n_{\text{eqp},1} = 0$ and $n_{\text{eqp},2} = 8$, and we thus get $(\check{p}_{\max}+1+n_{\text{eqp},2})\times(\check{p}_{\max}+1+n_{\text{eqp},2}) = 11\times 11$ quadrature in each sub element around the source point, and $(\check{p}_{\xi}+1+n_{\text{eqp},1})\times(\check{p}_{\eta}+1+n_{\text{eqp},1}) = 3\times 3$ in the remaining elements. The figures to the right are the new integration routine presented in this work with $s_1 = 1$.

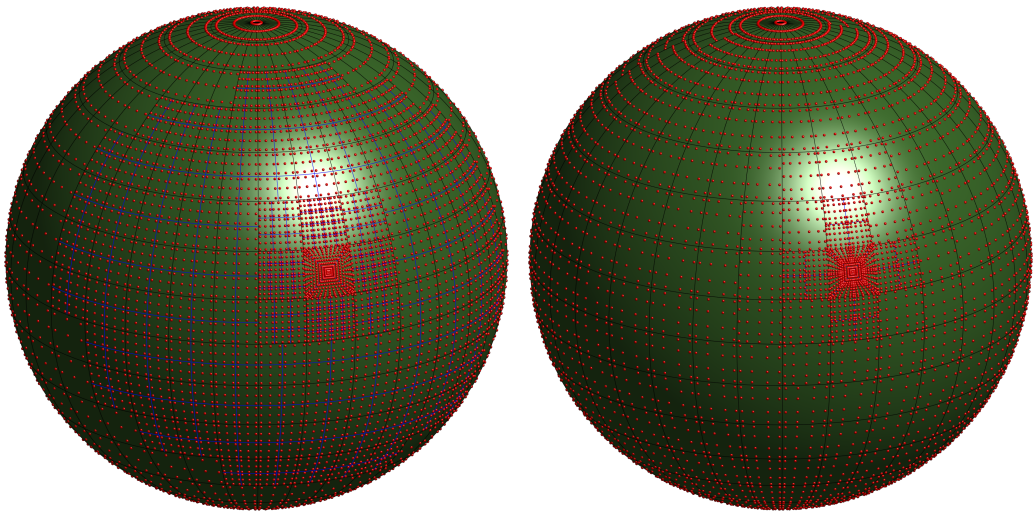

(a) The 392^{th} collocation point is at the center of an element.

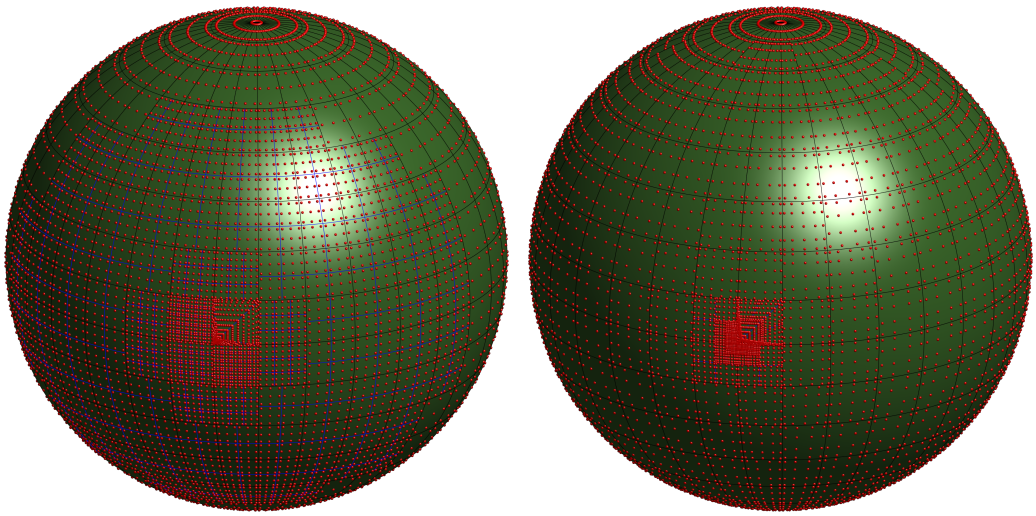

(b) The source point is the corner quadrature point for Galerkin formulations inside an element.

Figure 5: **Numerical evaluation of the boundary integral equations**: The figures to the left are the integration procedure in [5] (with $s_1 = 2$). The sub element divisions are here shown by blue lines (the black lines are the element edges). The red points are the quadrature points. Here, $n_{\text{eqp},1} = 0$ and $n_{\text{eqp},2} = 8$, and we thus get $(\check{p}_{\max}+1+n_{\text{eqp},2})\times(\check{p}_{\max}+1+n_{\text{eqp},2}) = 11\times 11$ quadrature in each sub element around the source point, and $(\check{p}_{\xi}+1+n_{\text{eqp},1})\times(\check{p}_{\eta}+1+n_{\text{eqp},1}) = 3\times 3$ in the remaining elements. The figures to the right are the new integration routine presented in this work with $s_1 = 1$.

Table 1: Overview of the boundary integral equation (BIE) formulations considered in this work.

Abbreviation	Name	Definition
CBIE	Conventional BIE	Eq. (15)
RCBIEi	The i^{th} regularized CBIE	Eqs. (26) to (28)
HBIE	Hypersingular BIE	Eq. (16)
BM	Burton–Miller	Eq. (18)

where V_h is the finite dimensional subspace in which the solution is sought and the constants C_1 and C_2 may depend on the analytic solution p, the boundary Γ and the wave number k. In this work we also aim to give numerical evidence for similar estimates for the other BEM formulations.

The simulations are based on the ASIGA[8] library written in MATLAB [47]. The integration is here vectorized over the quadrature points, such that the effect of increasing the number of quadrature points is of less significance due to the efficiency of vectorization in MATLAB. For this reason, we take the liberty of over integration the BIEs without suffering to much from computational cost. For optimization purposes, the library could be written in C/C++ which would require an accuracy-cost tradeoff study in this respect. Additionally, acceleration techniques exist for the boundary element method which have not been implemented in the ASIGA library. We refer to [12, 13, 48] for details. These optimizations are suggested as future work.

The BIE formulations listed in Table 1 will be investigated both in terms of approximability and the presence of fictitious eigenfrequencies.

The meshes will be generated from a coarse CAD model mesh (for example Figure 8a for the sphere) with mesh number $m = 1$. We shall denote by $\mathcal{M}^{\text{IGABEM}}_{m,\check{p},\check{k}}$, mesh number m with polynomial order $\check{p}$ and continuity $\check{k}$ across element boundaries[9]. For the corresponding FEM meshes we denote by $\mathcal{M}^{\text{FEMBEM}}_{m,\check{p},\text{s}}$ and $\mathcal{M}^{\text{FEMBEM}}_{m,\check{p},\text{i}}$ the subparametric and isoparametric FEM meshes, respectively. These meshes are constructed by the procedure outlined in [49, p. 191].

6.1. Pulsating sphere

Consider a pulsating unit sphere centered at the origin (cf. [5, 33]) with analytic solution given by

$$p(\boldsymbol{x}) = \frac{\mathrm{e}^{\mathrm{i}kR}}{4\pi R}, \quad R = |\boldsymbol{x}|, \quad \boldsymbol{x} \in \Omega^+ \tag{34}$$

[8]The ASIGA (Acoustic Scattering with IsoGeometric Analysis) library can be found at https://github.com/Zetison/ASIGA.

[9]Except for (potentially) some C^0 lines in the initial CAD geometry.

and with the (constant) Neumann condition

$$g(\boldsymbol{x}) = \frac{\mathrm{e}^{\mathrm{i}k}}{4\pi}(\mathrm{i}k - 1), \quad \boldsymbol{x} \in \Gamma. \tag{35}$$

This problem serves as a patch test for IGA as the analytic solution lies in the numerical solution space ($p(\boldsymbol{x})$ is constant at Γ). Contrary to FEM with affine mappings, (proper) Gaussian quadrature does not integrate the integrals in BEM exactly. Therefore, this example may be used to give some indication of the quality of the integration procedure. In Figures 6 and 7 we compare the two adaptive quadrature schemes (described in Section 5), where we set $n_{\mathrm{eqp},2} = 100$ to avoid error originating from the integration over the element containing the source points. The L^2-error of the numerical solution is here plotted against $n_{\mathrm{qp},1}$; the total number of quadrature points, excluding quadrature points in elements containing the source point. The simulations are done on the coarsest mesh of the second NURBS parametrization in Figure 8b (with $\check{p} = 4$). The BM and HBIE formulations (for both collocation and Galerkin) have more round-off errors and are for this reason further away from machine epsilon precision results compared to the other formulations. In all cases, the new adaptive quadrature scheme obtains better results. Interestingly CBIE obtains slightly better results using the new adaptive quadrature scheme compared to RCBIE3, the latter being the regularized version of the former. This might be due to the reduction of symmetry in the RCBIE3 compared to CBIE for this problem.

Note that for this problem using RCBIE1 or RCBIE2 (Eqs. (26) and (27)), results with machine epsilon precision are always obtained since the integrands are zero. This is due to the spherical symmetry of the problem and the functions involved.

Based on this study, a proper choice for the parameter s_1 is $s_1 = 1.4$ for the new adaptive method. If not otherwise stated, we shall use $s_1 = 1.4$ and $n_{\mathrm{eqp},2} = 50$, which in most cases results in over integration. As was mentioned before, the cost of this is not significant due to the current implementation in MATLAB.

6.2. Rigid scattering on a sphere

Consider a plane wave, with the direction of incidence given by

$$\boldsymbol{d}_{\mathrm{s}} = -\begin{bmatrix} \cos\beta_{\mathrm{s}} \cos\alpha_{\mathrm{s}} \\ \cos\beta_{\mathrm{s}} \sin\alpha_{\mathrm{s}} \\ \sin\beta_{\mathrm{s}} \end{bmatrix}, \tag{36}$$

with[10] $\alpha_{\mathrm{s}} = 240^\circ$ and $\beta_{\mathrm{s}} = 30^\circ$, scattered by a rigid sphere with radius $R_0 = 1\,\mathrm{m}$.

[10]The angles α and β are the so-called aspect and elevation angle, respectively. Note that the aspect angle is equal to the spherical coordinate φ (the azimuth angle).

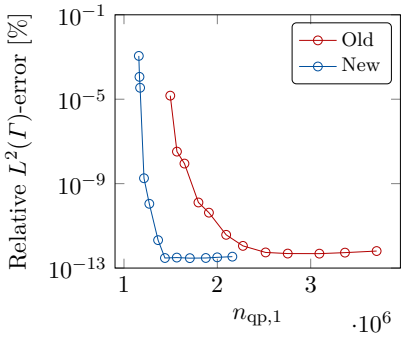

(a) CCBIE

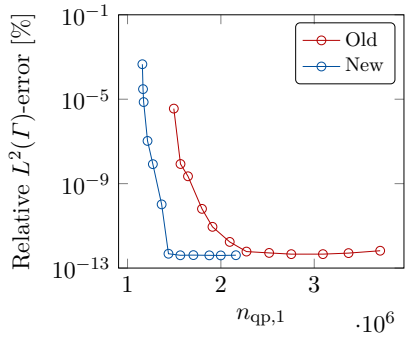

(b) CRCBIE3

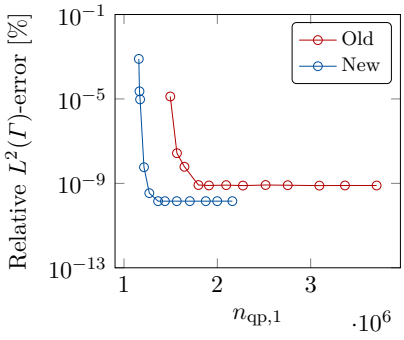

(c) CHBIE

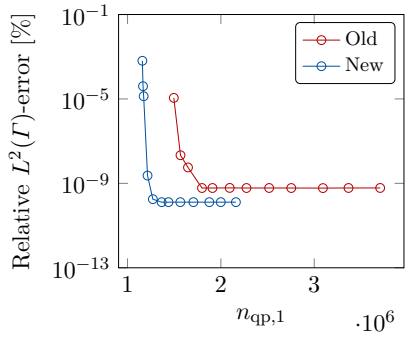

(d) CBM

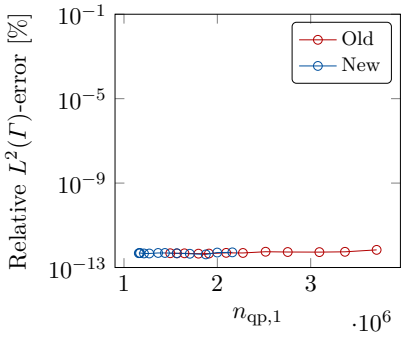

(e) CRCBIE1

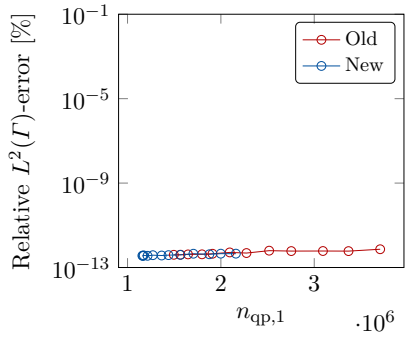

(f) CRCBIE2

Figure 6: **Pulsating sphere**: Surface error as a function of the total number of quadrature points $n_{\mathrm{qp},1}$ at $kR_0 = 1$. The old adaptive quadrature scheme presented by Simpson in [5] is compared to the new adaptive quadrature scheme presented in this work. The sample points correspond to $s_1 \in \{1, 2, \ldots, 12\}$ and $s_1 \in \{1, 2, \ldots, 12\}/5$ for the old and new method, respectively.

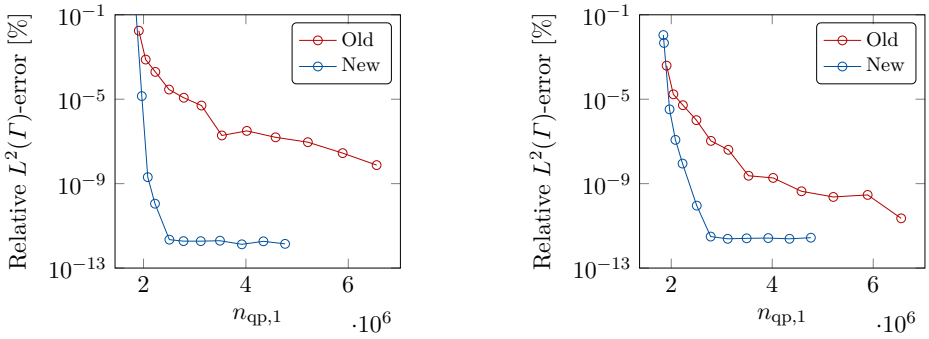

(a) GCBIE (b) GRCBIE3

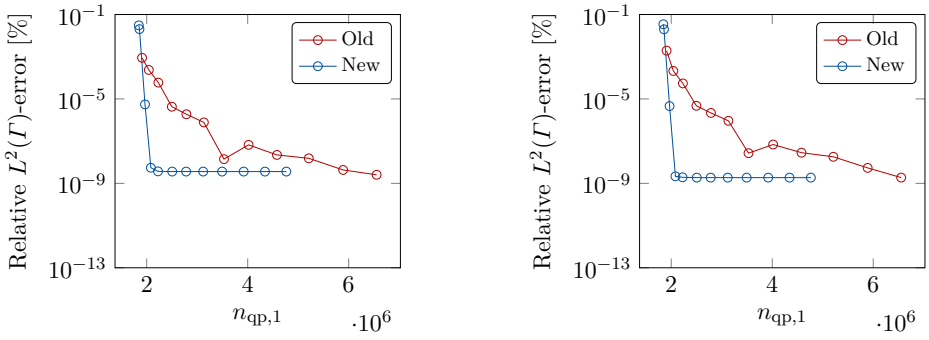

(c) GHBIE (d) GBM

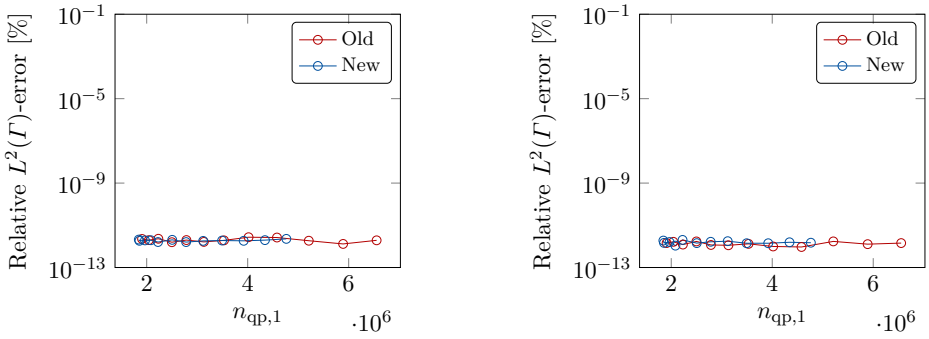

(e) GRCBIE1 (f) GRCBIE2

Figure 7: **Pulsating sphere**: Surface error as a function of the total number of quadrature points $n_{\mathrm{qp},1}$ at $kR_0 = 1$. The old adaptive quadrature scheme presented by Simpson in [5] is compared to the new adaptive quadrature scheme presented in this work. The sample points correspond to $s_1 \in \{1, 2, \ldots, 12\}$ and $s_1 \in \{1, 2, \ldots, 12\}/5$ for the old and new method, respectively.

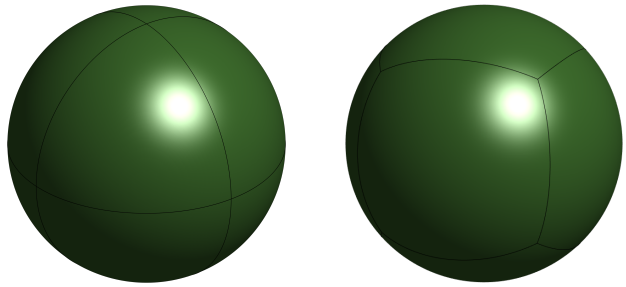

(a) Parametrization 1. (b) Parametrization 2.

Figure 8: Two exact NURBS parametrizations of the sphere. Parametrization 1 uses a single patch with 8 elements of degree $\check{p} \geqslant 2$ while parametrization 2 uses 6 patches of degree $\check{p} \geqslant 4$. Parametrization 1 is described in Subsection A.1 and parametrization 2 is described in Subsection A.2.

For the rigid scattering problems considered in this work, the error is computed of p_{tot} and the best approximation (BA) is obtained by performing an L^2-projection of p_{tot} onto the discretized solution space.

Continuing the study of numerical quadrature, we investigate the parameters s_1 and $n_{\text{eqp},2}$ also for rigid scattering. The study for the parameter s_1 uses $n_{\text{eqp},2} = 100$ and the study for $n_{\text{eqp},2}$ uses $s_1 = 0.7$.

For FEM/IGA using $\check{p}$+1 quadrature points in each parametric direction in each element ensures accurate numerical integration regardless of the computational mesh. As can be observed from Figures 9 to 11 this is not the case for BEM. Separate choices for the parameters $n_{\text{eqp},2}$ and s_1 need to be made for each formulation.

Contrary to FEM/IGA, the optimal quadrature rule seems to be depending on h-refinement (not only $\check{p}$-refinement). Although the integrals in the CBIE formulation are regularized to contain no singular integrals, the parameter s_1 may still not be set to zero. This could be expected due to the gradients around the source points.

For convenience we perturb the collocation points at the north and the south pole of the parametrization in Figure 8a in the HBIE and BM formulation for the ease of implementation. The perturbation is taken to be a distance $\frac{1}{2}|\Delta\eta_e|/\check{p}_\eta$ in the η-direction (in the parametric space), where $|\Delta\eta_e|$ is the element interval in the parametric domain in the η-direction. A similar strategy will be employed for the corresponding problematic areas on the BeTSSi submarine. This may be a sub optimal placement of collocation points, and as we can see from Figure 12b, the CBM formulation does not obtain the accuracy of the Galerkin formulation (Figure 12a). But this is also true for parametrization 2 (which contains no poles), and so this calls for an investigation of better placement of collocation points in

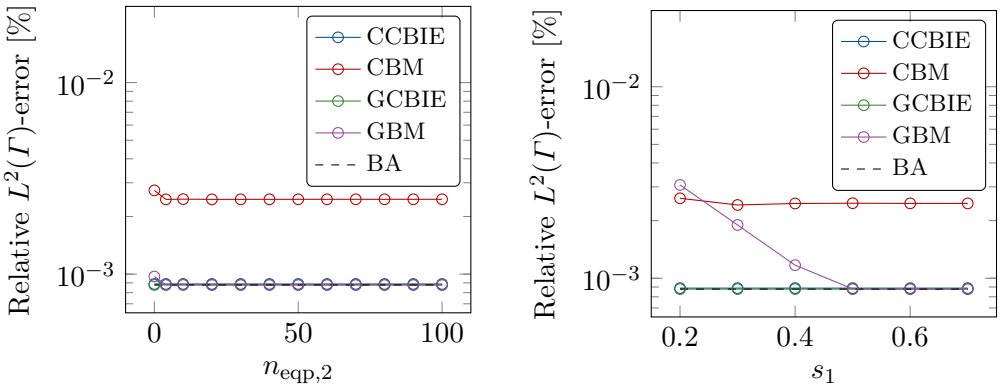

Figure 9: **Rigid scattering on a sphere**: Surface error as a function of the parameters $n_{\text{eqp},2}$ and s_1 to the left and right, respectively, on the mesh $\mathcal{M}_{5,2,1}^{\text{IGABEM}}$.

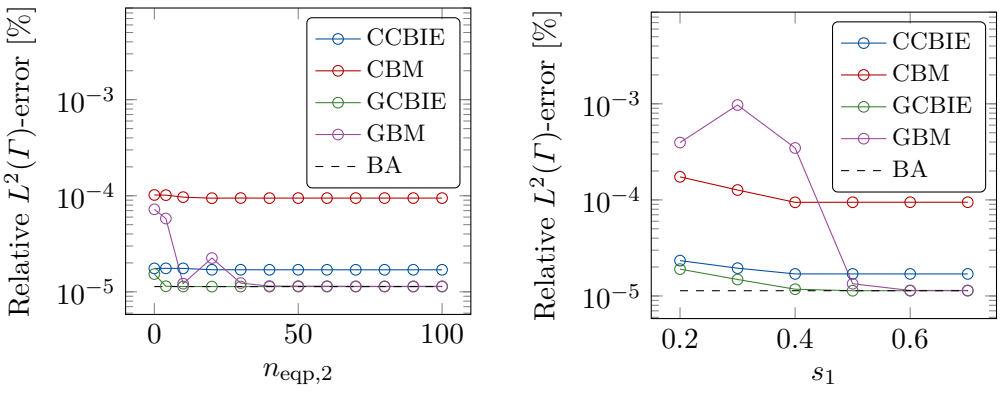

Figure 10: **Rigid scattering on a sphere**: Surface error as a function of the parameters $n_{\text{eqp},2}$ and s_1 to the left and right, respectively, on the mesh $\mathcal{M}_{4,5,4}^{\text{IGABEM}}$.

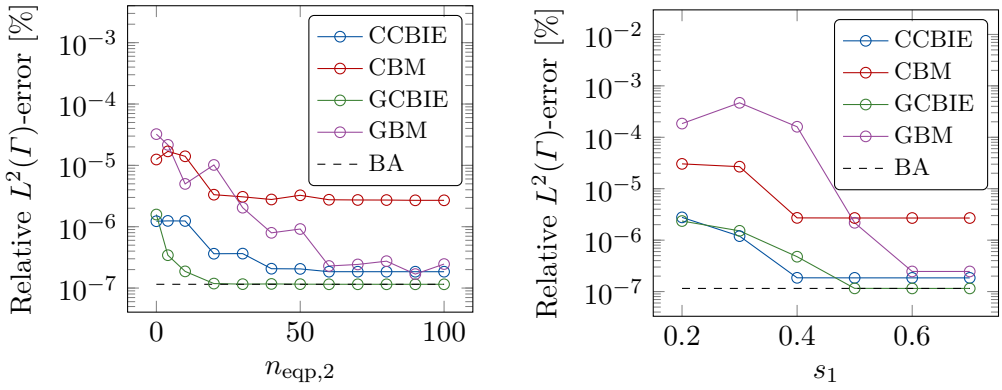

Figure 11: **Rigid scattering on a sphere**: Surface error as a function of the parameters $n_{\mathrm{eqp},2}$ and s_1 to the left and right, respectively, on the mesh $\mathcal{M}_{5,5,4}^{\mathrm{IGABEM}}$.

general for the CHBIE and CBM than that of the Greville abscissae. The CBM formulation for parametrization 1 is visibly polluted by round-off errors similar to those seen in Subsection 6.1.

In Figure 13 we can observe that CBM loses one order of convergence for the odd degree $\check{p} = 3$, which is similar to the effect discussed in [50]. However, this effect does not come into play in the same way for the CCBIE formulation, although it is still a significant difference between this simulation and the best approximation. This is in stark contrast to the CCBIE simulations of even degree which approaches the best approximation solution.

The plots in Figure 12 also show the impact a sub optimal parametrization may have. Parametrization 1 has roughly 8% higher errors compared to parametrization 2 in terms of degrees of freedom.

In Figure 14 we compare the classical boundary element method (FEMBEM) with IGA. For the subparametric second order FEMBEM mesh a full convergence order (see Figure 15) is lost in comparison with the best approximation for the same mesh (FEMBA). In fact, little is to be gained by increasing the polynomial order when using a linear approximation of the geometry. The exactness of the geometry is of less importance for isoparametric FEMBEM, which can be observed by comparing the results for mesh $\mathcal{M}_{m,2,\mathrm{i}}^{\mathrm{FEMBEM}}$ and mesh $\mathcal{M}_{m,2,0}^{\mathrm{IGABEM}}$. Increasing the continuity ($\check{k}$-refinement) of the basis functions, however, improves the accuracy significantly as obtained for infinite isogeometric finite elements [49].

As we can see from Figure 16a, the dimensionless fictitious eigenfrequencies in Tables 2 and 3 appear quite clearly for the CBIE and the HBIE, respectively, while the eigenvalues for the Burton–Miller formulation are shifted away from the real axis into the complex plane [33]. The fictitious eigenfrequencies are of course not present in the best approximation (BA) solution.

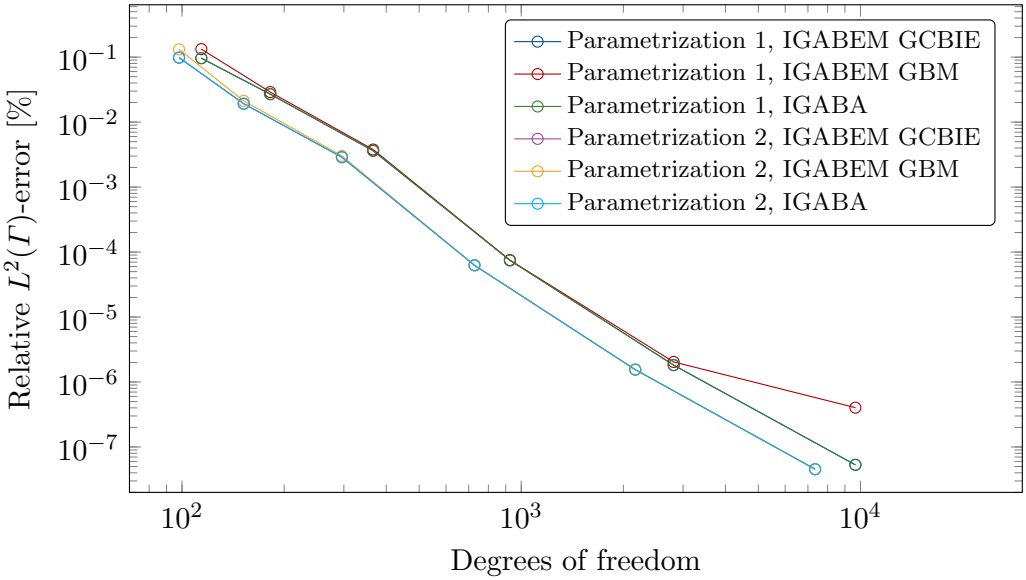

(a) Galerkin formulations

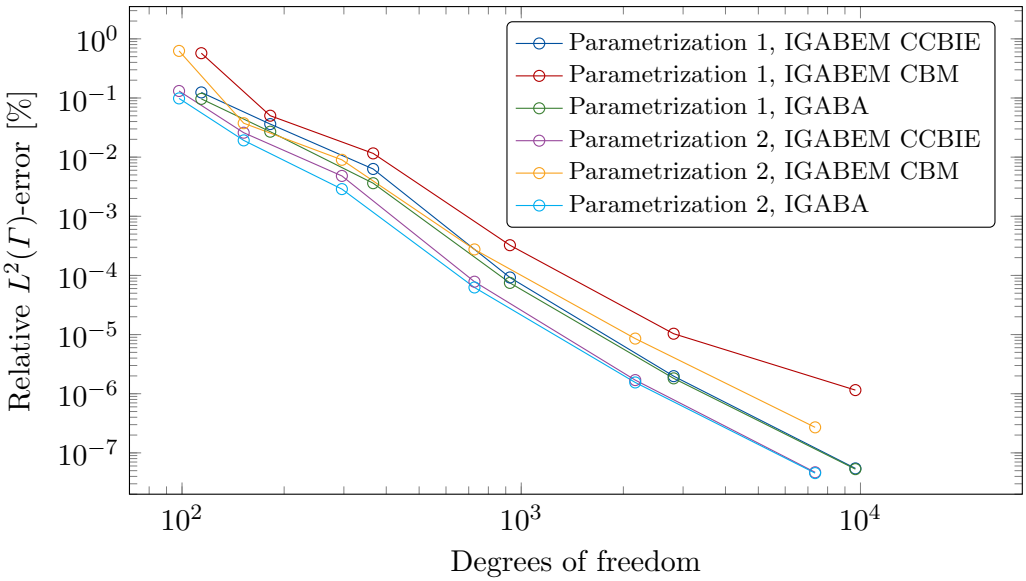

(b) Collocation formulations

Figure 12: **Rigid scattering on a sphere**: Convergence analysis with $\check{p} = 4$ and $kR_0 = 1$.

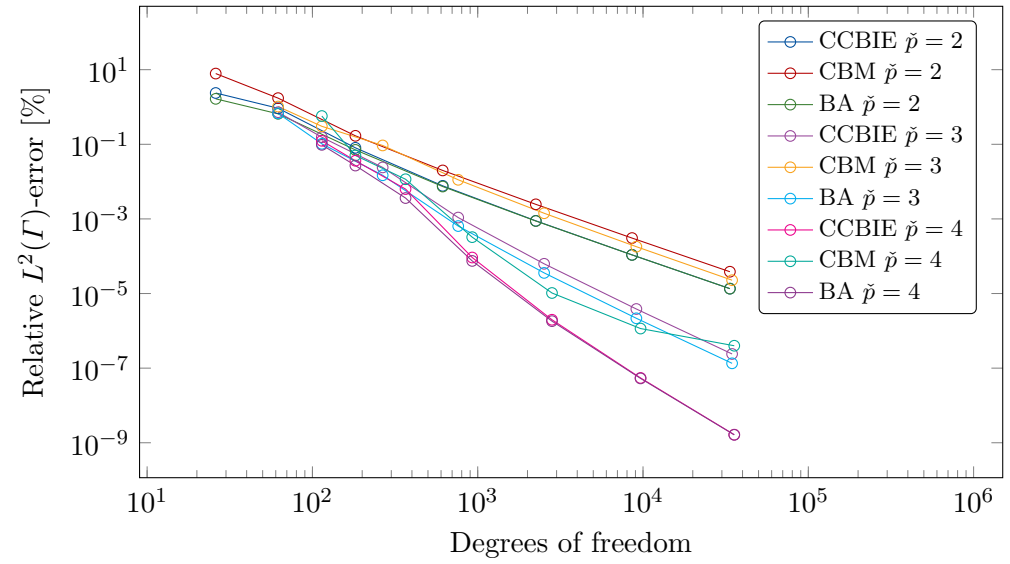

Figure 13: **Rigid scattering on a sphere**: Convergence analysis with $kR_0 = 1$.

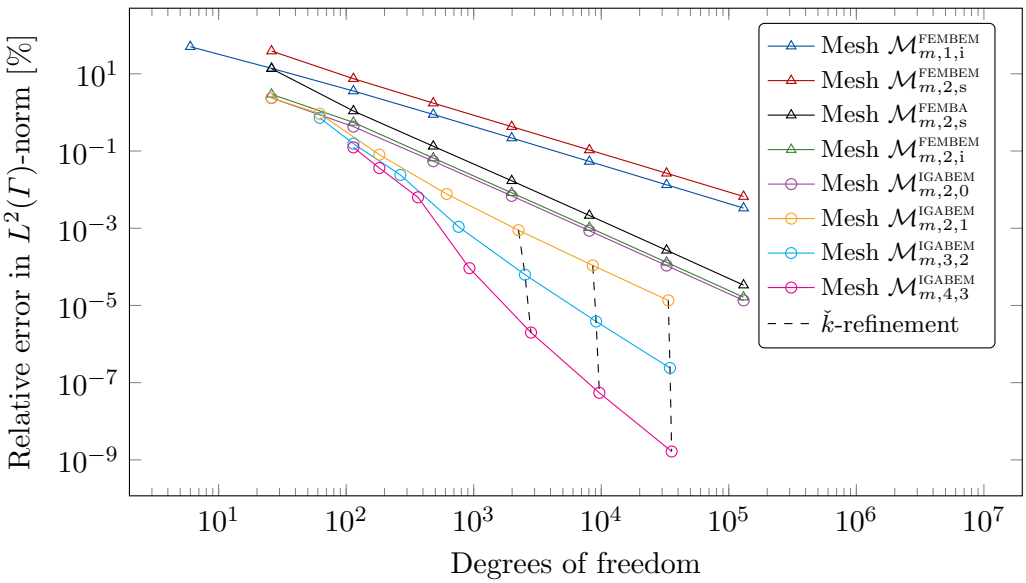

Figure 14: **Rigid scattering on a sphere**: Convergence analysis with the CCBIE formulation on parametrization 1 for $kR_0 = 1$.

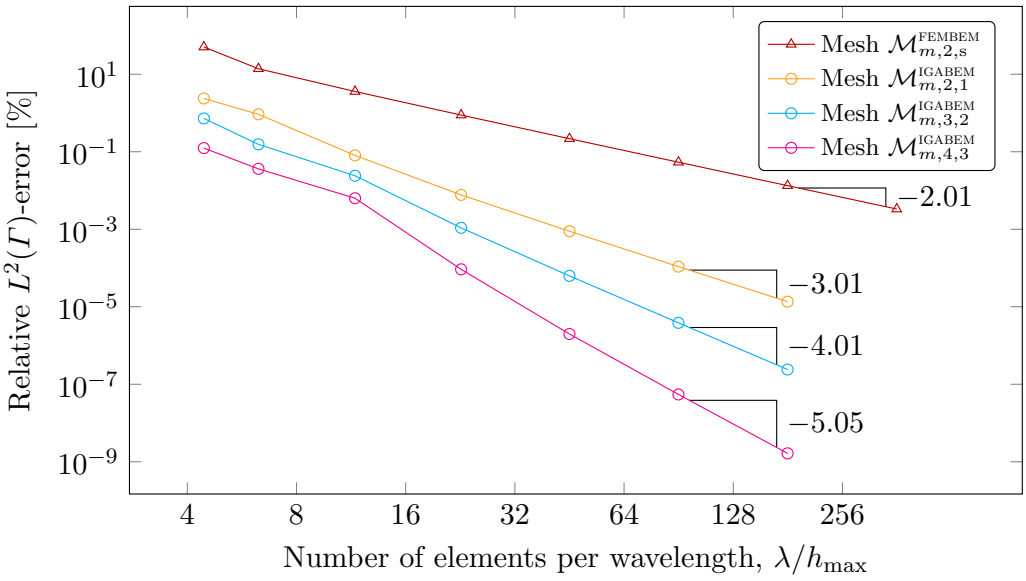

Figure 15: **Rigid scattering on a sphere**: Convergence analysis with the CCBIE formulation on parametrization 1 for $kR_0 = 1$.

Table 2: The non-zero dimensionless eigenvalues below $kR_0 = 10$ for the interior Dirichlet problem [33].

n	Roots of $\mathrm{j}_n(kR_0)$
0	π, 2π, 3π, ...
1	4.49340945790907, 7.72525183693771, ...
2	5.76345919689455, 9.09501133047635, ...
3	6.98793200050052, ...
4	8.18256145257124, ...
5	9.35581211104275, ...

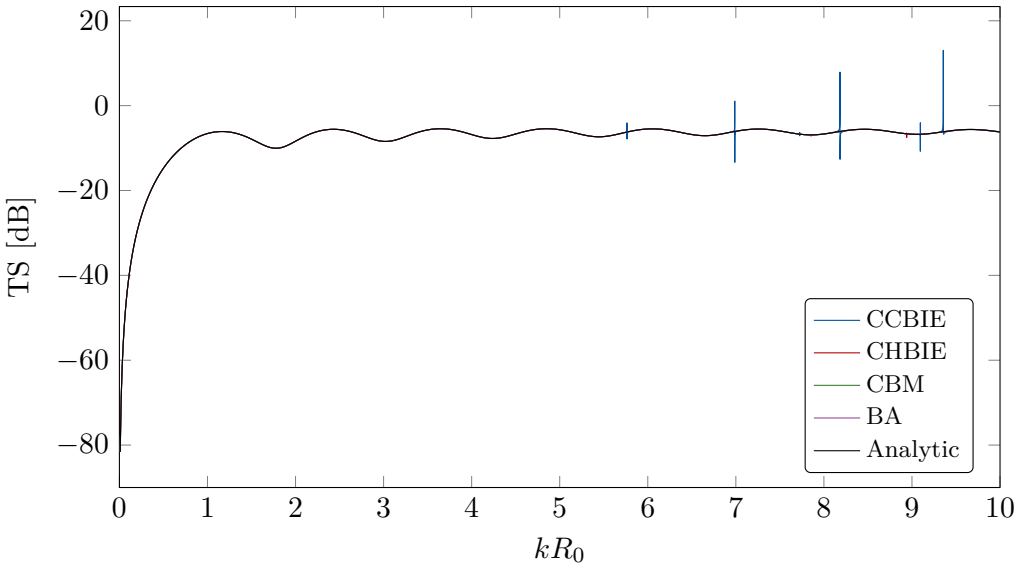

(a) Target strength of backscattered far field.

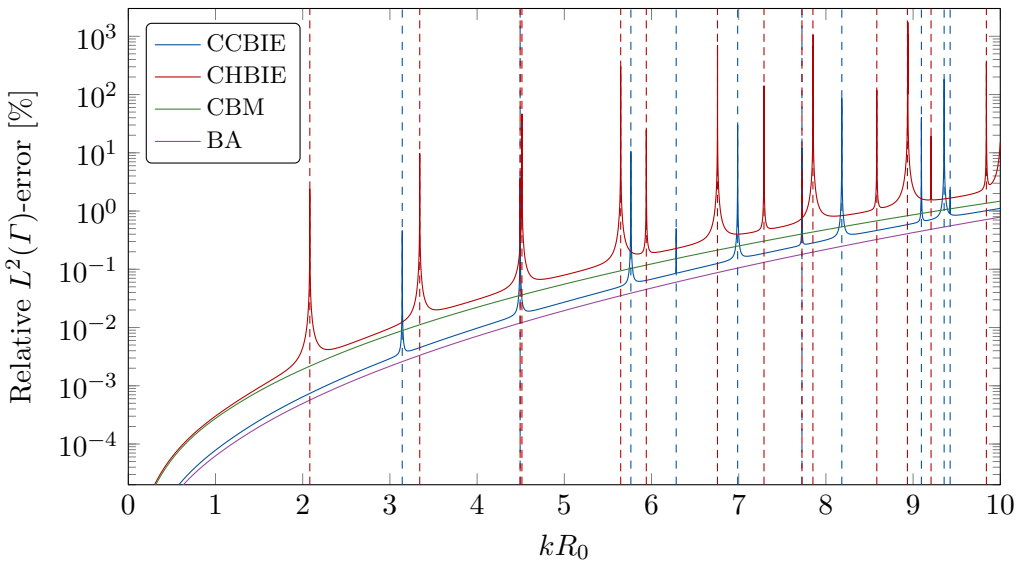

(b) Surface error on Γ.

Figure 16: **Rigid scattering on a sphere**: The plots show the instabilities around eigenfrequencies of the corresponding interior Dirichlet problem. All computations are done using the parametrization in Figure 8b refined uniformly three times with NURBS degree 4 (resulting in 384 elements and 728 degrees of freedom).

Table 3: The non-zero dimensionless eigenvalues below $kR_0 = 10$ for the interior Neumann problem [33].

n	Roots of $\mathrm{j}_n'(kR_0)$
0	4.49340945790907, 7.72525183693771, ...
1	2.08157597781810, 5.94036999057271, 9.20584014293667, ...
2	3.34209365736570, 7.28993230409335, ...
3	4.51409964703228, 8.58375495636577, ...
4	5.64670362043680, 9.84044604304014, ...
5	6.75645633020413, ...
6	7.85107767947440, ...
7	8.93483887835284, ...

6.3. Torus interior acoustic problem

Consider the Torus problem presented in [5]. This example sets the stage for optimal conditions for the a priori error estimate in Eq. (33) to be fulfilled. The geometry of the torus (with parametrization described in Appendix B) has G^∞ continuity and contains no polar singularities in the exact NURBS parametrization illustrated in Figure 1b (as opposed to the sphere parametrization in Figure 8a). The torus considered here has major radius $r_\mathrm{o} = 2$ and minor radius $r_\mathrm{i} = 1$.

Consider the exact solution

$$p(\boldsymbol{x}) = \sin\frac{kx_1}{\sqrt{3}}\sin\frac{kx_2}{\sqrt{3}}\sin\frac{kx_3}{\sqrt{3}}$$

with corresponding Neumann boundary conditions at the boundary Γ

$$\frac{\partial p}{\partial n} = \frac{k}{\sqrt{3}}\begin{bmatrix}\cos\frac{kx_1}{\sqrt{3}}\sin\frac{kx_2}{\sqrt{3}}\sin\frac{kx_3}{\sqrt{3}}\\ \sin\frac{kx_1}{\sqrt{3}}\cos\frac{kx_2}{\sqrt{3}}\sin\frac{kx_3}{\sqrt{3}}\\ \sin\frac{kx_1}{\sqrt{3}}\sin\frac{kx_2}{\sqrt{3}}\cos\frac{kx_3}{\sqrt{3}}\end{bmatrix}\cdot\boldsymbol{n}.$$

From Figure 17, the sharpness ($C_1 \approx 1$) of the a priori error estimate in Eq. (33) is demonstrated. The convergence rates for the best approximation (IGABA) are revealed quite clearly here.

Results for the same study using collocation formulation are given in Figure 18. The CCBIE formulation obtains very good results as it approaches the best approximation during refinement. Correct convergence rates are also obtained for the CBM formulation, but with a somewhat higher constant C_1 in Eq. (33).

In [5] Simpson projects the Neumann data onto the same basis used for the solution space. The accuracy for collocation formulations may be increased in some cases using this projection, but for Galerkin formulations projecting the Neumann data yields worse results. Moreover, if Γ is G^0 sub optimal results are obtained also for the collocation formulations.

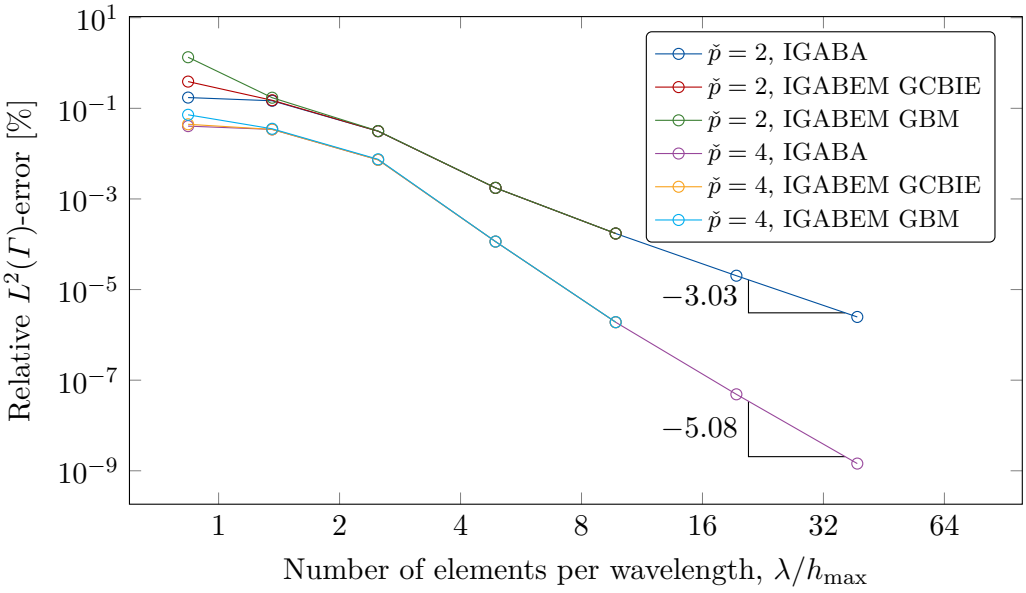

Figure 17: **Torus interior acoustic problem**: Convergence analysis at wave number $k = 2\,\mathrm{m}^{-1}$.

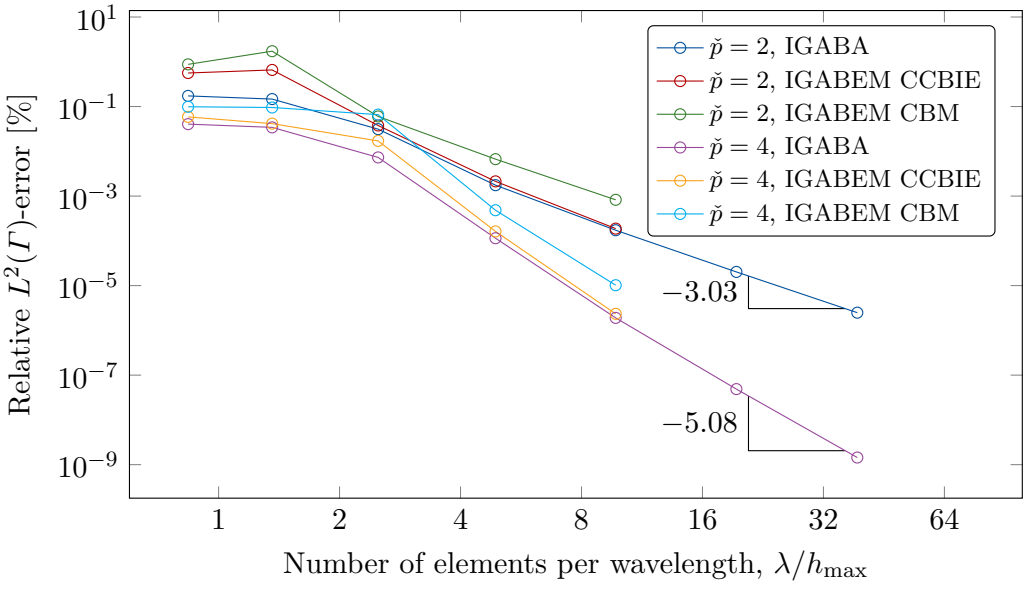

Figure 18: **Torus interior acoustic problem**: Convergence analysis at wave number $k = 2\,\mathrm{m}^{-1}$.

6.4. Manufactured solutions for complex geometries

In this section we shall consider the method of manufactured solutions (MMS). The idea behind MMS is explained in detail in [51].

By construction of the fundamental solution ($\Phi_k(\boldsymbol{x},\boldsymbol{y})$ in Eq. (9)), the function $p(\boldsymbol{x}) = \Phi_k(\boldsymbol{x},\boldsymbol{y})$ is a solution to Eqs. (2) to (4) whenever $\boldsymbol{y} \in \mathbb{R}^3 \setminus \overline{\Omega^+}$ and for the Neumann boundary condition $g(\boldsymbol{x}) = \partial_n \Phi_k(\boldsymbol{x},\boldsymbol{y})$ on Γ. Hence, we have an exact manufactured solution for the exterior Helmholtz problem for arbitrary geometries Γ which encloses the point $\boldsymbol{y}$. It is emphasized that this solution is non-physical for non-spherical geometries Γ (for the sphere, the solution represents a pulsating sphere [5]). General solutions may be constructed by separation of variables (cf. [30, p. 26])

$$p(\boldsymbol{x}) = \sum_{n=0}^{\infty} \sum_{m=-n}^{n} C_{nm} \mathrm{h}_n^{(1)}(kR) \mathrm{P}_n^{|m|}(\cos\vartheta) \mathrm{e}^{\mathrm{i}m\varphi} \tag{37}$$

with

$$R = |\boldsymbol{x}-\boldsymbol{y}|, \quad \vartheta = \arccos\left(\frac{x_3-y_3}{R}\right), \quad \varphi = \operatorname{atan2}(x_2-y_2, x_1-y_1)$$

where $\mathrm{h}_n^{(1)}$ is the n^{th} spherical Hankel function of first kind and P_n^m are the associated Legendre functions. In fact, the solution $p(\boldsymbol{x}) = \Phi_k(\boldsymbol{x},\boldsymbol{y})$ is a special case of this general form with

$$C_{nm} = \begin{cases} \frac{\mathrm{i}k}{4\pi} & n = 0,\ m = 0 \\ 0 & \text{otherwise.} \end{cases} \tag{38}$$

Inspired by the method of fundamental solutions [52], we can also use the solution

$$p(\boldsymbol{x}) = \sum_{n=1}^{N} C_n \Phi_k(\boldsymbol{x},\boldsymbol{y}_n) \tag{39}$$

for a set of N source points $\{\boldsymbol{y}_n\}_{n=1}^N$. To increase the complexity of the solution, we use $C_n = \cos(n-1)$ in this work.

The complexity of this problem setup does not scale with the complexity of the model as it is independent of Γ. However, it preserves two important properties of acoustic scattering, namely the radial decay and the oscillatory nature. Thus, this problem setup represents a general way of constructing manufactured solutions that can be utilized to verify the correctness of the implemented code for solving the Helmholtz equation. Moreover, as the boundary condition is the only condition that is altered from the original problem, one can solve the original system of equation with an extra appended column vector on the right-hand side (corresponding to the problem of finding the manufactured solution) with a small computational

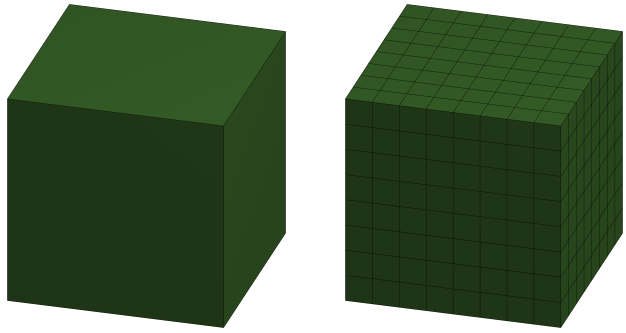

(a) Mesh 1. (b) Mesh 4.

Figure 19: Parametrization of a cube using 6 patches of degree $\check{p} \geqslant 1$.

effort. This gives some control over the correctness of the computed solution to the original problem. Since the fictitious eigenfrequencies are the same for both solutions, one can compute the error for the manufactured solution to give an indication whether the solution is polluted by such a frequency. If this is the case, one should resort to the somewhat more costly Burton–Miller formulation.

Note that from the first limit of Eq. (11), the far field of Eq. (39) is given by

$$p_0(\hat{\boldsymbol{x}}) = \frac{1}{4\pi} \sum_{n=1}^{N} C_n \mathrm{e}^{-\mathrm{i}k\hat{\boldsymbol{x}}\cdot\boldsymbol{y}_n}.$$

Whenever $\partial_n p_{\mathrm{tot}} \neq 0$ we must deal with an integral which is weakly singular, and the manufactured solution thus does not give the optimal test for the rigid body scattering problem as the CBIE formulation is free from such integrals in this case.

6.5. Manufactured solution with a cube

Consider a cube of side length a centered at the origin. Its interior Dirichlet problem has eigenfunctions (cf. [53, p. 52])

$$p(\boldsymbol{x}) = \prod_{i=1}^{d} \sin \frac{n_i \pi (x_i + a/2)}{a}, \quad \boldsymbol{x} \in \Omega^-$$

and the interior Neumann problem has eigenfunctions

$$p(\boldsymbol{x}) = \prod_{i=1}^{d} \cos \frac{n_i \pi (x_i + a/2)}{a}, \quad \boldsymbol{x} \in \Omega^-$$

where

$$\sum_{i=1}^{d} n_i^2 = \left(\frac{ka}{\pi}\right)^2 \quad \text{and} \quad \Omega^- = \left[-\frac{a}{2}, \frac{a}{2}\right]^d.$$

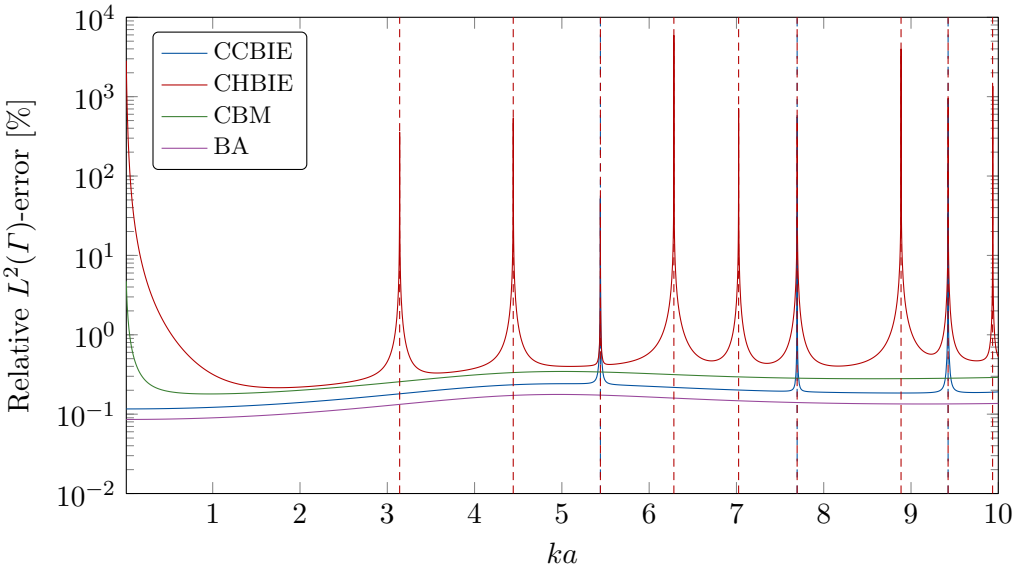

Figure 20: **Manufactured solution with a cube**: The plots show the instabilities around eigenfrequencies of the corresponding interior Dirichlet problem. All computations are done using the parametrization in Figure 19a refined uniformly three times with NURBS degree 4 (resulting in 384 elements and 728 degrees of freedom) as highlighted in Figure 19b.

The dimensionless eigenfrequencies are thus given by

$$ka = \pi \sqrt{\sum_{i=1}^{d} n_i^2},$$

where $n_i \in \mathbb{N}^*$ for the interior Dirichlet problem and $n_i \in \mathbb{N}$ for the interior Neumann problem. For the exterior problem these eigenfrequencies correspond to the fictitious eigenfrequencies for the CBIE formulation and the HBIE formulation, respectively. The dimensionless fictitious eigenfrequencies below $ka = 10$ are then $\pi\sqrt{3}$, $\pi\sqrt{6}$ and 3π for the CBIE formulation, and $\pi\sqrt{n}$ with $n \in \{0, 1, 2, 3, 4, 5, 6, 8, 9, 10\}$ for the HBIE formulation.

Consider the manufactured solution Eq. (39) with $N = 3^3 = 27$ source points

$$\boldsymbol{y}_n = \frac{a}{4}[c_i, c_j, c_l], \quad n = i + 3(j-1) + 3^2(l-1), \quad i, j, l = 1, 2, 3$$

where $c_1 = -1$, $c_2 = 0$ and $c_3 = 1$. In Figure 20 we again show a frequency sweep to illustrate the instability around the fictitious eigenfrequencies of the CBIE and HBIE formulations. From Figure 21a, the sharpness of the a priori error estimate in Eq. (33) is again demonstrated. Remarkably, the G^0 continuity of the cube

poses no problems for the Galerkin Burton–Miller formulation using $\check{p} \geqslant 2$, despite the problematic mathematical nature of the formulations with basis functions that are C^0 continuous [35]. Poor results are obtained for the BM formulation using $\check{p} = 1$ for both collocation and Galerkin formulation. This is in stark contrast to the CBIE which performs optimally for $\check{p} = 1$ in both cases. The CCBIE obtains good results in all cases and outperforms the CBM formulation.

6.6. Manufactured solution with the BeTSSi submarine

Consider now the BeTSSi submarine described in Appendix C. The BeTSSi meshes considered in this work are denoted by $\mathcal{M}^{\text{IGABEM}}_{m,\check{p},\check{k}}$, where m is the mesh number, and are illustrated in Figure 22 where $m = 1$ is the coarsest mesh, and $m = 2$ and $m = 3$ are uniformly refined meshes iterated on the coarsest mesh. Again, $\check{p}$ denotes the polynomial order and $\check{k}$ the continuity.

Consider the manufactured solution Eq. (39) on the BeTSSi submarine with $N = 16$ and where 16 source points are uniformly placed at the x-axis starting at $x = b$ and ending at $x = -L - 2b$ (parameters taken from Table 8). The analytic real part of the pressure, $\operatorname{Re} p$, is visualized on the surface of the scatterer in Figure 23. A simulation at $f = 100\,\text{Hz}$ on mesh $\mathcal{M}^{\text{IGABEM}}_{1,2,1}$ yields the error plots in Figure 24, which show good agreement between the best approximation and the BEM simulation. For more refined meshes in Figures 25 to 27 (especially Figure 27) the numerical quadrature around the source points is too inaccurate. At this level of numerical accuracy, one quickly runs into issues due to round-off errors. The non-Lipschitz domains do not in and of itself pose any analysis suitable issues as described in Appendix D, so the effect seen here is due to the numerical integration in the boundary element method. At $f = 1000\,\text{Hz}$ it is clear from Figure 28 that the IGABEM CCBIE simulation is polluted from a fictitious eigenfrequency. The remedy for this is to use the CBM formulation which obtains results with maximal error roughly twice the size of the best approximation. The meshes for the BeTSSi submarine in Figure 22 might give the impression of evenly distributed control points in some areas, in particular the area behind the sail ($-L < x < x_{\text{s}} - l_{\text{ls}}$). In this case there are additional knot insertions around the submarine to obtain the C^0 lines, which results in "bands" of slightly larger errors along the submarine. This effect will be larger for higher polynomial orders, particularly for mesh $\mathcal{M}^{\text{IGABEM}}_{2,5,4}$ in Figure 28a.

To assess the parameter s_1 in Eq. (30), a low frequency of $100\,\text{Hz}$ is now considered. In Figure 29 we illustrate the effect of different choices of the parameter s_1 for the more complex geometry of the BeTSSi submarine. Again, the optimal choice for s_1 is polynomial dependent. Moreover, even the regularized formulations CRCBIE1 and CRCBIE3 must have $s_1 > 0$ contrary to what was proposed in [32] (stating that the singular free integrals "can be evaluated by any convenient integration quadrature"). Whenever care is not taken for the numerical

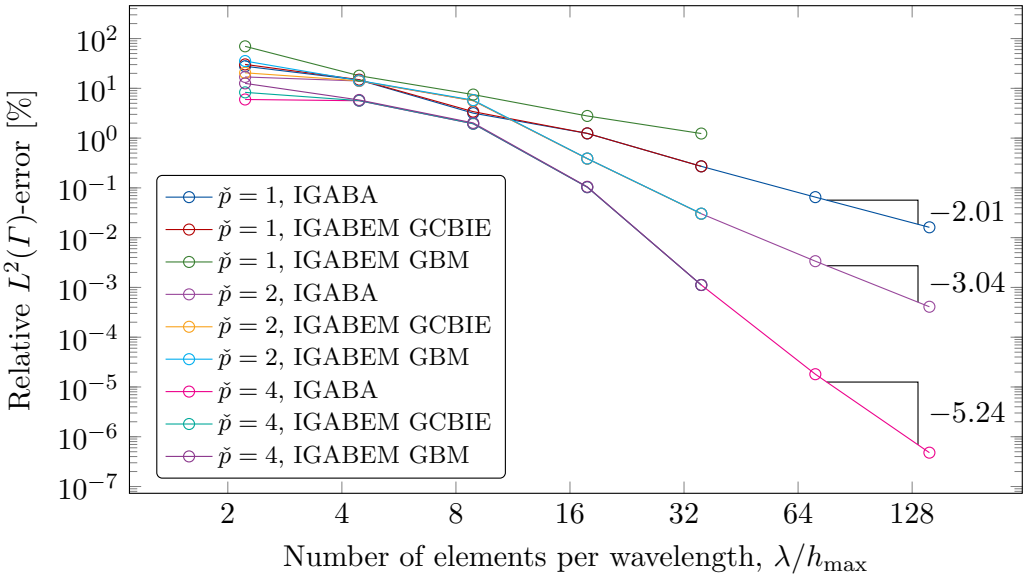

(a) Galerkin formulations

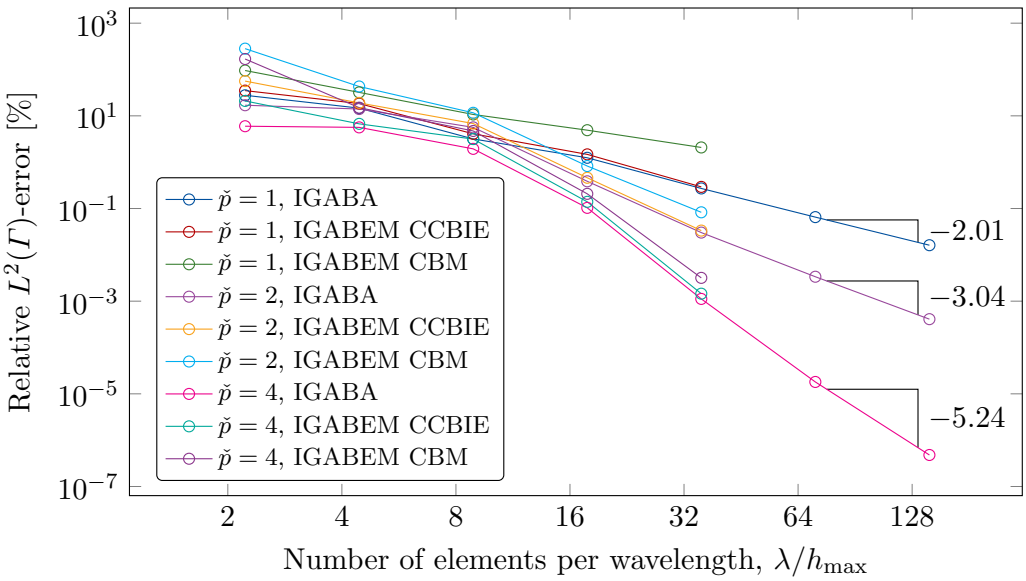

(b) Collocation formulations

Figure 21: **Manufactured solution with a cube**: Convergence analysis at $k = 2\,\mathrm{m}^{-1}$.

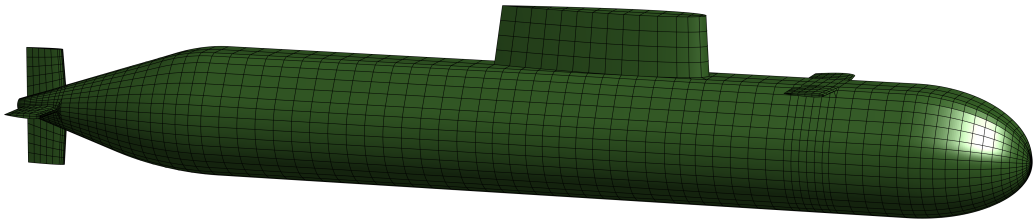

(a) $\mathcal{M}_{1,6,5}^{\text{IGABEM}}$ - 3718 elements

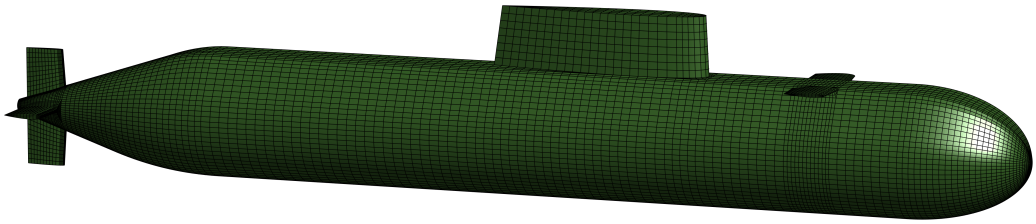

(b) $\mathcal{M}_{2,6,5}^{\text{IGABEM}}$ - 14872 elements

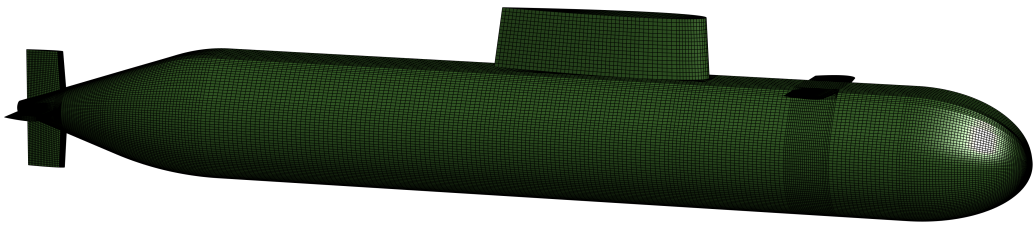

(c) $\mathcal{M}_{3,6,5}^{\text{IGABEM}}$ - 59488 elements

Figure 22: **The BeTSSi submarine**: Computational IGA meshes for $\Gamma_{\check{p}}$ with $\check{p} = 6$.

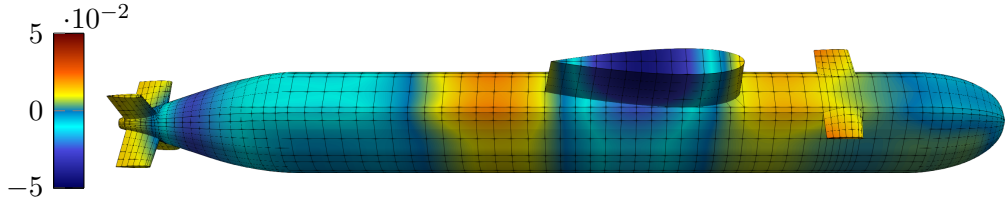

(a) $f = 100\,\mathrm{Hz}$

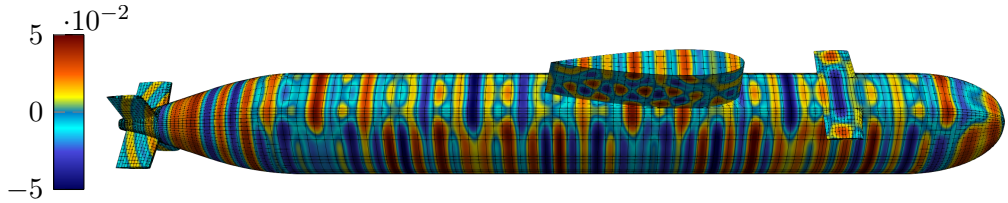

(b) $f = 1000\,\mathrm{Hz}$

Figure 23: **Manufactured solution with the BeTSSi submarine**: Analytic manufactured solution. Mesh 1 and mesh 2 are added to visualize elements to wavelength ratio for 100 Hz and 1000 Hz, respectively.

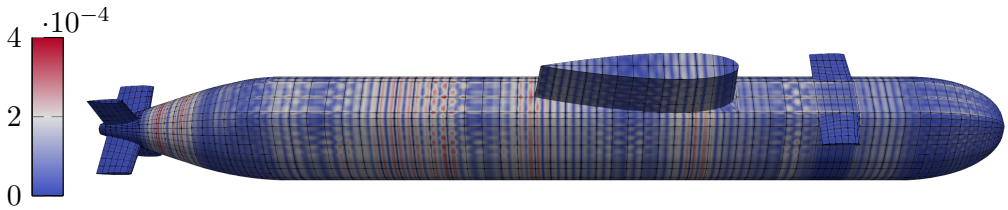

(a) IGABA: $\max\limits_{\boldsymbol{x}\in\Gamma_2} \dfrac{|p-p_h|}{|p|} = 3.8 \cdot 10^{-4}$

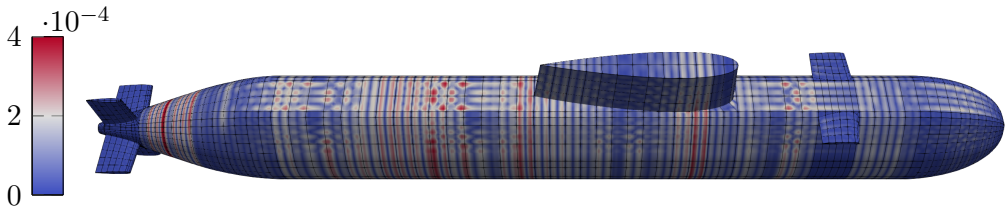

(b) IGABEM CCBIE: $\max\limits_{\boldsymbol{x}\in\Gamma_2} \dfrac{|p-p_h|}{|p|} = 4.0 \cdot 10^{-4}$

Figure 24: **Manufactured solution with the BeTSSi submarine**: Relative error on the surface of the scatterer at $f = 100\,\mathrm{Hz}$ on the mesh $\mathcal{M}_{1,2,1}^{\mathrm{IGABEM}}$.

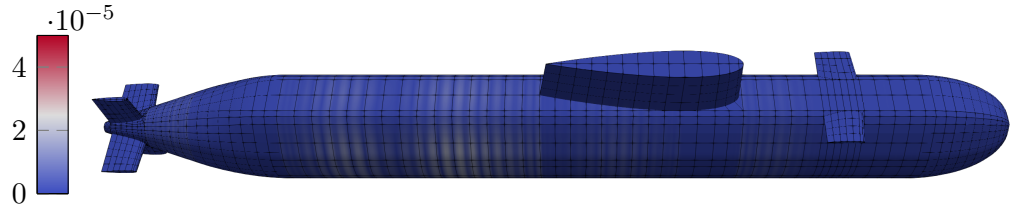

(a) IGABA: $\max_{\boldsymbol{x}\in\Gamma_5} \dfrac{|p-p_h|}{|p|} = 2.1 \cdot 10^{-5}$

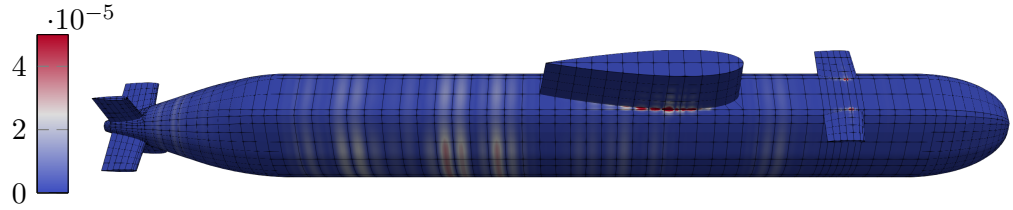

(b) IGABEM CCBIE: $\max_{\boldsymbol{x}\in\Gamma_5} \dfrac{|p-p_h|}{|p|} = 4.4 \cdot 10^{-4}$

Figure 25: **Manufactured solution with the BeTSSi submarine**: Relative error on the surface of the scatterer at $f = 100\,\mathrm{Hz}$ on the mesh $\mathcal{M}^{\mathrm{IGABEM}}_{1,5,4}$.

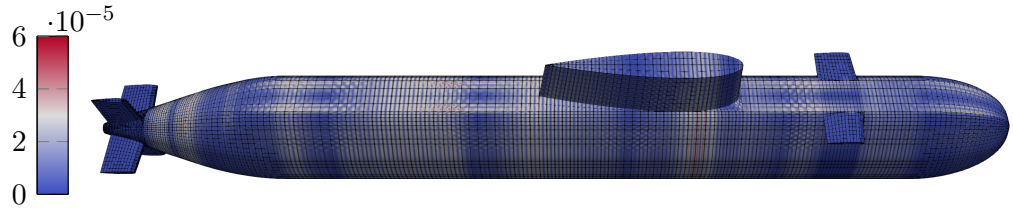

(a) IGABA: $\max_{\boldsymbol{x}\in\Gamma_2} \dfrac{|p-p_h|}{|p|} = 6.1 \cdot 10^{-5}$

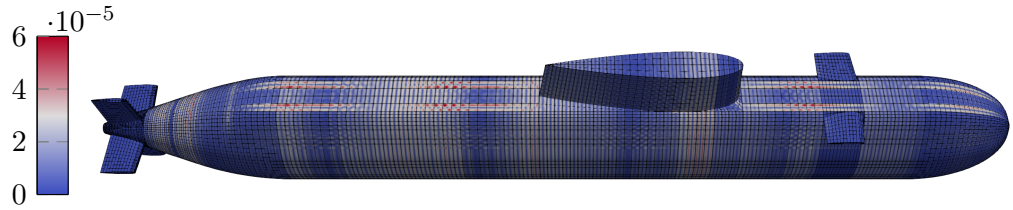

(b) IGABEM CCBIE: $\max_{\boldsymbol{x}\in\Gamma_2} \dfrac{|p-p_h|}{|p|} = 2.3 \cdot 10^{-4}$

Figure 26: **Manufactured solution with the BeTSSi submarine**: Relative error on the surface of the scatterer at $f = 100\,\mathrm{Hz}$ on the mesh $\mathcal{M}^{\mathrm{IGABEM}}_{2,2,1}$.

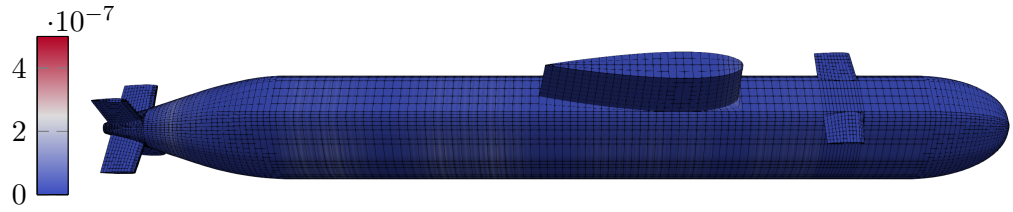

(a) IGABA: $\max_{\boldsymbol{x}\in\Gamma_5} \frac{|p-p_h|}{|p|} = 1.7 \cdot 10^{-7}$

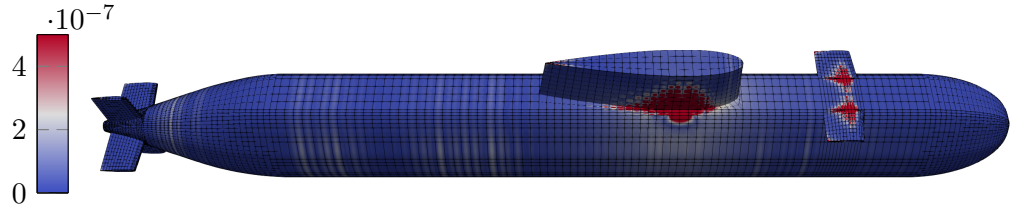

(b) IGABEM CCBIE: $\max_{\boldsymbol{x}\in\Gamma_5} \frac{|p-p_h|}{|p|} = 7.8 \cdot 10^{-4}$

Figure 27: **Manufactured solution with the BeTSSi submarine**: Relative error on the surface of the scatterer at $f = 100\,\text{Hz}$ on the mesh $\mathcal{M}_{2,5,4}^{\text{IGABEM}}$.

quadrature, incorrect conclusions may arise. This example illustrates the power of the manufactured solution as it enables computation of the best approximation such that the numerical integration may be controlled.

6.7. Rigid scattering on the BeTSSi submarine

Consider now a plane wave scattered by a rigid BeTSSi submarine. Throughout this section (motivated by the previous section) we use the CCBIE formulation at $f = 100\,\text{Hz}$ and the CBM formulation at $f = 1000\,\text{Hz}$. To verify our simulations, we compare with corresponding simulations done in Comsol Multiphysics®, with mesh and parameters as illustrated and described in Figure 30. Comparisons are also made with simulations done by WTD 71[11]. The polar plot in Figure 31 illustrates bistatic scattering where the incident wave is fixed, and the observation points for the far field computations sweep the aspect angles. A very good match is obtained, although some discrepancies are observed around the aft angles (around $\alpha = 180°$). One can argue that the logarithmic scale of the target strength (TS) yields a somewhat misguided conception of the numerical error in the pressure. The pressure at these angles is very low such that the global relative error in the pressure is not as bad as the plot may suggest. In Figure 32a

[11]Wehrtechnische Dienststelle für Schiffe und Marinewaffen, Maritime Technologie und Forschung.

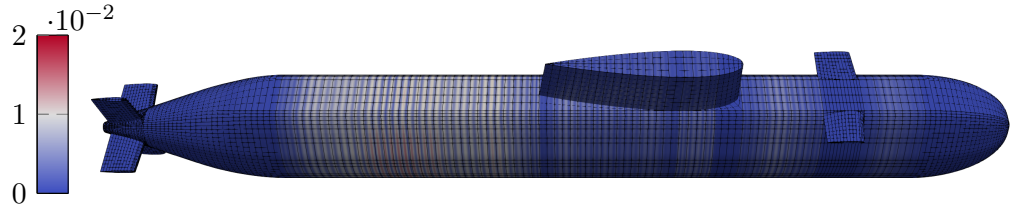

(a) IGABA: $\max_{\boldsymbol{x}\in\Gamma_5} \dfrac{|p-p_h|}{|p|} = 0.014$

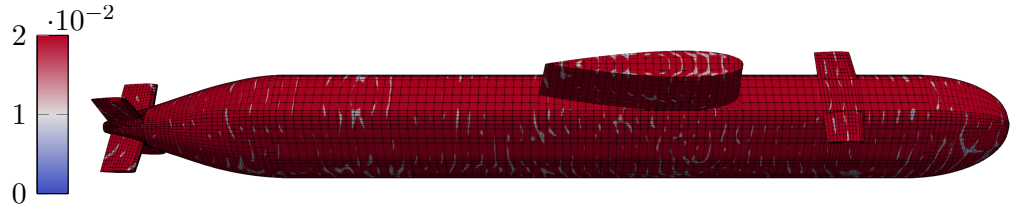

(b) IGABEM CCBIE: $\max_{\boldsymbol{x}\in\Gamma_5} \dfrac{|p-p_h|}{|p|} = 0.40$

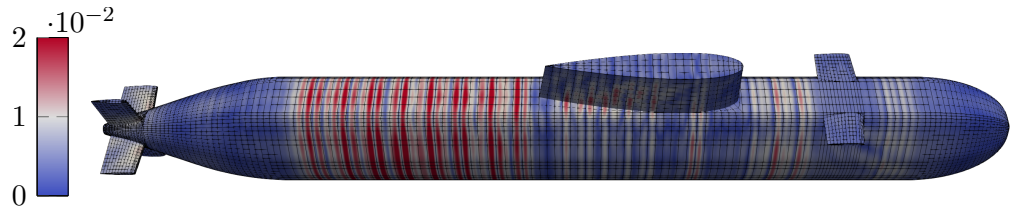

(c) IGABEM CBM: $\max_{\boldsymbol{x}\in\Gamma_5} \dfrac{|p-p_h|}{|p|} = 0.030$

Figure 28: **Manufactured solution with the BeTSSi submarine**: Relative error on the surface of the scatterer at $f = 1000\,\mathrm{Hz}$ on the mesh $\mathcal{M}_{2,5,4}^{\mathrm{IGABEM}}$.

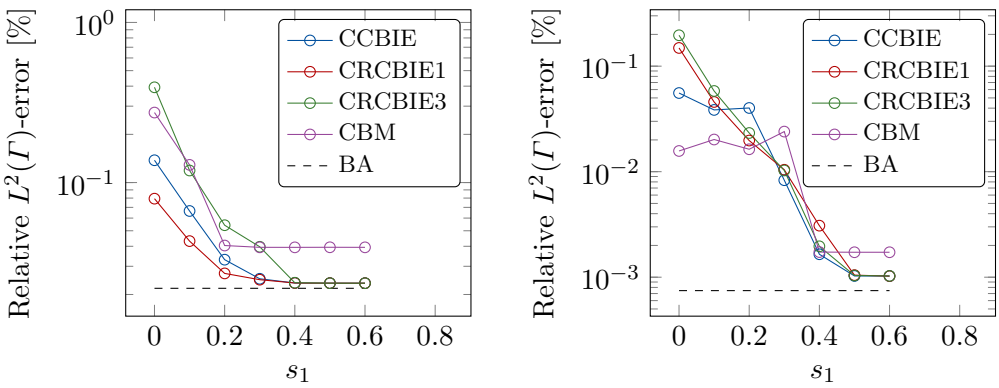

(a) $\check{p} = 2$ (b) $\check{p} = 5$

Figure 29: **Manufactured solution with the BeTSSi submarine**: Surface error as a function of the parameter s_1, on the mesh $\mathcal{M}^{\text{IGABEM}}_{1,\check{p},\check{p}-1}$.

and Figure 32b the corresponding xy-plots are given at 100 Hz and 1000 Hz, respectively. In Figure 32a (at 100 Hz) the IGA and Comsol Multiphysics® simulations are visually indistinguishable, such that error plots are in order. Let the simulation from $\mathcal{M}^{\text{IGABEM}}_{3,6,5}$, $\mathcal{M}^{\text{COMSOL}}_{4,2,0}$ and $\mathcal{M}^{\text{WTD}}_{6}$ be a reference solution for IGABEM, Comsol Multiphysics® and WTD71, respectively. In Figure 33 we compare the IGA results for lower resolved meshes. Convergence throughout the aspect angles is observed. In Figure 34 a corresponding comparison is done with the Comsol Multiphysics® simulations. Better convergence rates for higher polynomial degrees in the IGA simulations are not present. This is probably due to the problem of numerical integration over the non-Lipschitz domains as discussed in Subsection 6.6. Another reason could be the need for adaptive refinement, for example using LR B-splines [54] based on a posteriori error estimates, e.g. by exploiting k-refinement as presented in [55]. This might also be the reason that the Comsol Multiphysics® simulations converge to a different solution around $\varphi = 280°$ as illustrated in Figure 35. In Table 4 we present the computational complexity of the different simulations. The number of degrees of freedom per wavelength is denoted by τ. We shall use another definition of τ compared to the definition found in [9, p. 767][12], namely the minimal number of degrees of freedom per wavelength (instead of an average). This is arguably a better definition as it more precisely captures how well the frequency is resolved. We compute τ by

$$\tau = \frac{\lambda}{d_{\max}}, \quad d_{\max} = \max_{\boldsymbol{x} \in X} \min_{\boldsymbol{y} \in X \setminus \boldsymbol{x}} \|\boldsymbol{x} - \boldsymbol{y}\|$$

[12]Here, τ is defined as $\tau = \lambda\sqrt{n_{\text{dof}}/|\Gamma|}$.

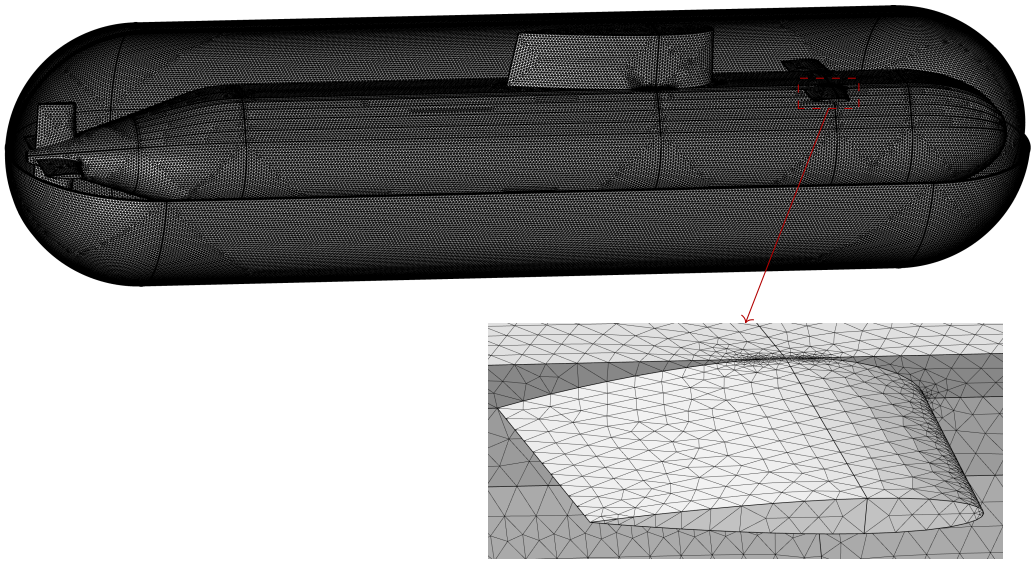

Figure 30: **Rigid scattering on the BeTSSi submarine**: Mesh used in COMSOL Multiphysics® simulations. The mesh consists of 27 614 929 second order finite elements including the elements in the PML (resulting in 43 431 671 degrees of freedom). This corresponds to 80 and 8 elements per wavelength for 100 Hz and 1000 Hz, respectively. The PML domain consists of a cylinder with two spherical end caps and are discretized by 10 layers of prismatic elements. The domain inside this PML is discretized with tetrahedral elements. The distance between the PML and the scatterer at the x-axis is $t_\mathrm{a} = 1\,\mathrm{m}$ at both ends. The thickness of the PML is the same as the maximal tetrahedral diameter $h_\mathrm{max} = 0.1875\,\mathrm{m}$. The PML cylinder starts at $x = -L - g_2 - g_3 + a$ and ends at $x = 0$. The radius of the PML cylinder and the PML spherical end caps are $r_\mathrm{a} = a + t_\mathrm{a}$. The PML uses a polynomial coordinate stretching type with scaling factor and scaling curvature equal to 1. The simulations use COMSOL Multiphysics® version 5.4 with the acoustics module (to enable the PML method) and the design module (to import the CAD model).

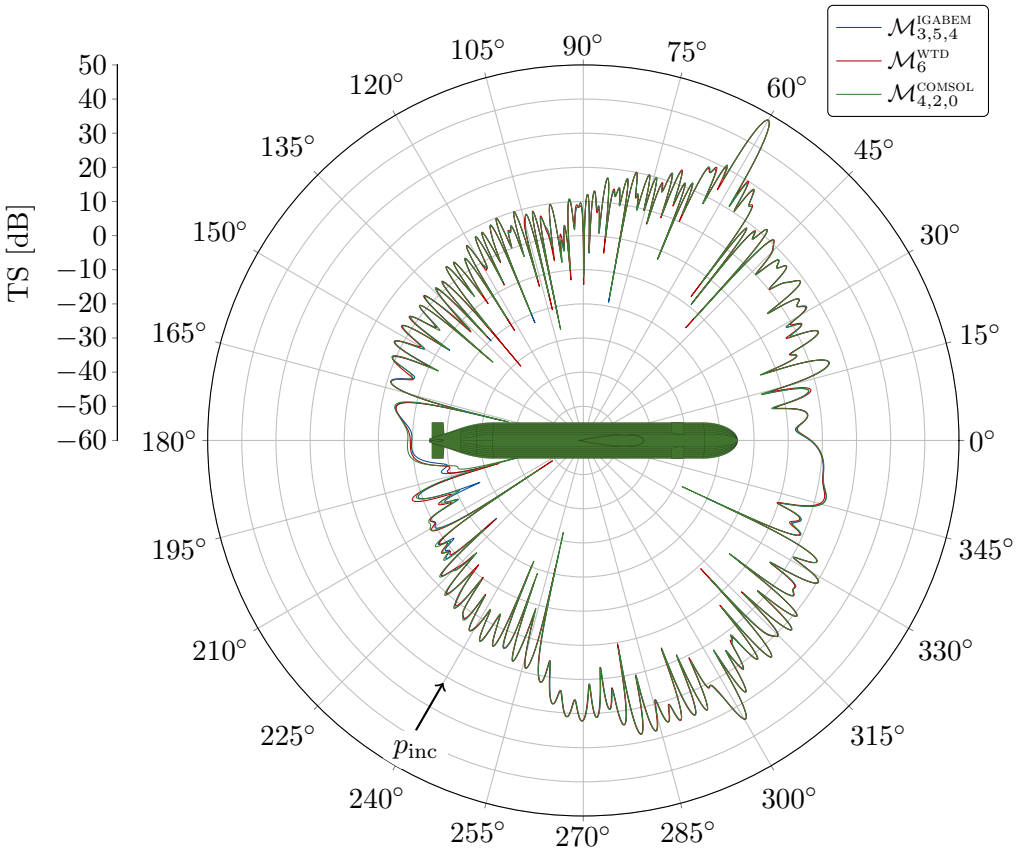

Figure 31: **Rigid scattering on the BeTSSi submarine**: Polar plot of the bistatic target strength (TS) plotted against the azimuth angle φ at $f = 1000\,\text{Hz}$. Direction of incident wave, p_{inc} is given by Eq. (36) with $\alpha_{\text{s}} = 240°$ and $\beta_{\text{s}} = 0°$. The IGA mesh here used is $\mathcal{M}_{3,5,4}^{\text{IGABEM}}$. The COMSOL Multiphysics® simulation used 3.8 hours on mesh $\mathcal{M}_{4,2,0}^{\text{COMSOL}}$. The WTD 71 simulation was made using a direct BEM collocation method with the Burton–Miller formulation on mesh $\mathcal{M}_{5}^{\text{WTD}}$ described in Appendix E with constant basis functions over each element.

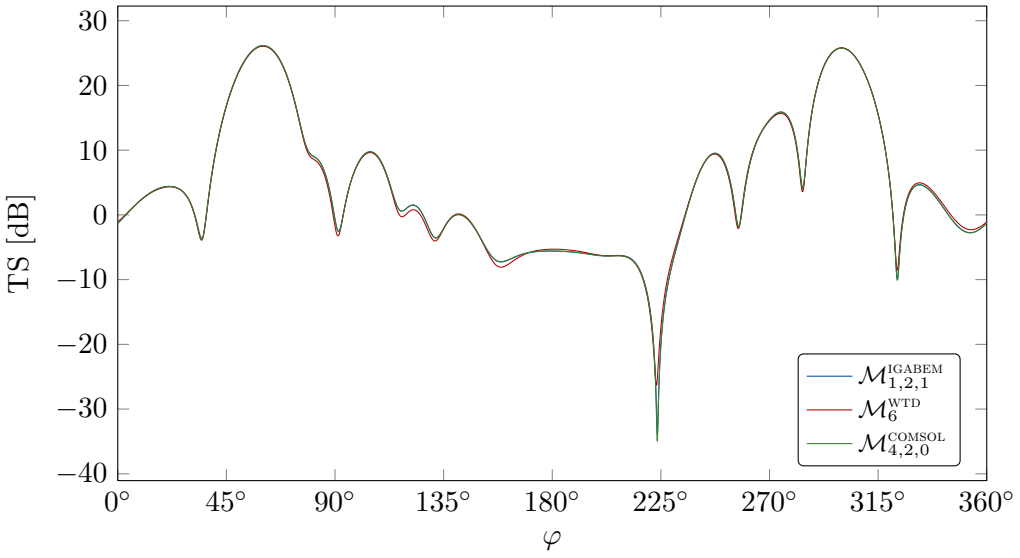

(a) $f = 100\,\text{Hz}$

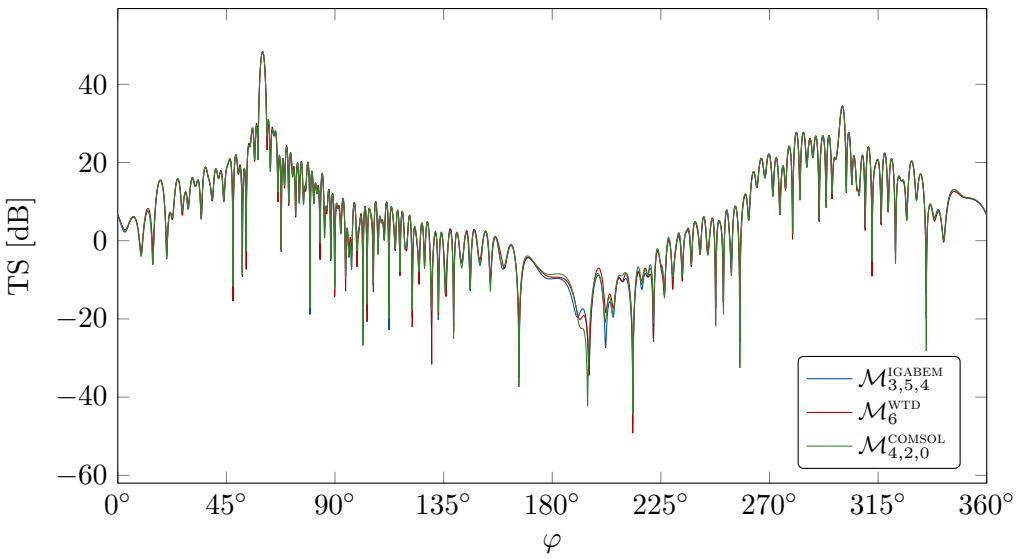

(b) $f = 1000\,\text{Hz}$

Figure 32: **Rigid scattering on the BeTSSi submarine**: The bistatic target strength (TS) plotted against the azimuth angle φ.

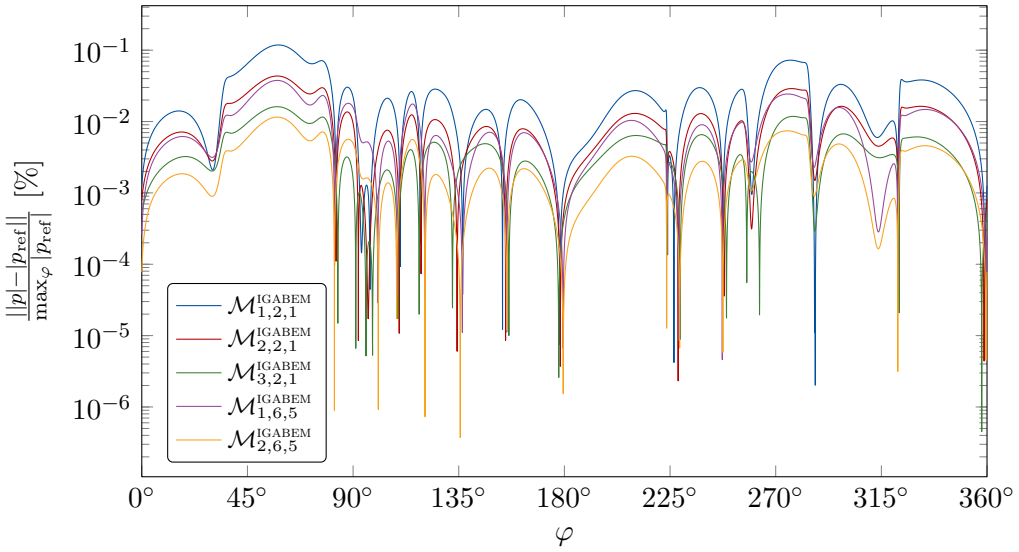

Figure 33: **Rigid scattering on the BeTSSi submarine**: The relative error in the far field absolute pressure plotted against the azimuth angle φ at $f = 100\,\text{Hz}$, with the simulations from $\mathcal{M}^{\text{IGABEM}}_{3,6,5}$ as reference solution.

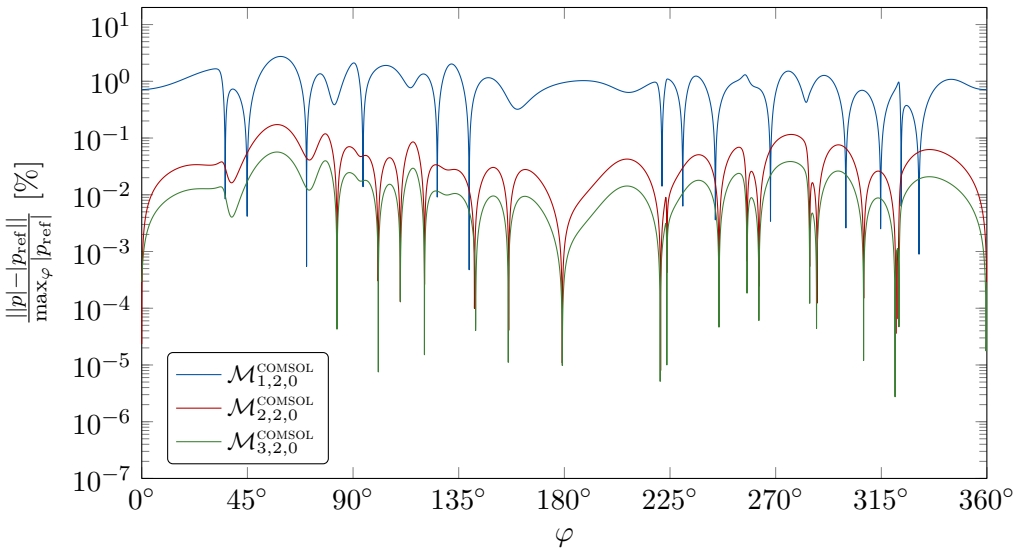

Figure 34: **Rigid scattering on the BeTSSi submarine**: The relative error in the far field absolute pressure plotted against the azimuth angle φ at $f = 100\,\text{Hz}$, with the simulations from $\mathcal{M}^{\text{COMSOL}}_{4,2,0}$ as reference solution.

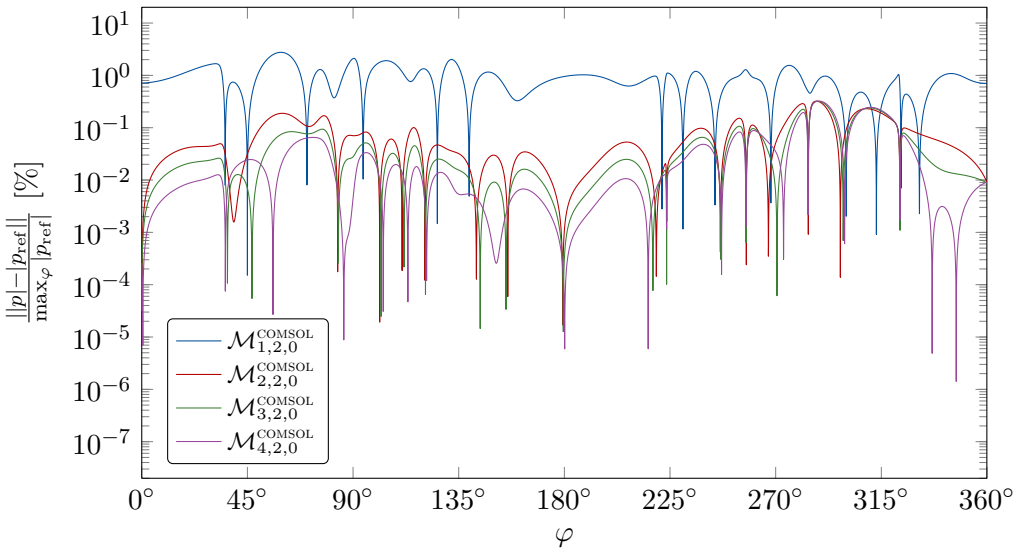

Figure 35: **Rigid scattering on the BeTSSi submarine**: The relative error in the far field absolute pressure plotted against the azimuth angle φ at $f = 100\,\text{Hz}$, with the simulations from $\mathcal{M}_{3,6,5}^{\text{IGABEM}}$ as reference solution.

where X is the set of nodes in the mesh. For IGA these nodes are chosen to be the Greville points in the physical domain (as the control points do not lie on the geometry). For the COMSOL Multiphysics® simulations we get $\tau = \frac{\lambda}{h_{\max}/2}$ and for constant triangular elements (WTD 71 simulations) we get $\tau = \frac{\lambda}{2h_{\max}/3}$. Considering the error as a function of τ, IGA outperforms the simulations from both COMSOL Multiphysics® and WTD 71. Even considering the error as a function of time usage, the IGA simulations obtain comparable results despite the sub-optimal implementation discussed earlier.

A monostatic[13] polar plot is shown in Figure 36 at $f = 1000\,\text{Hz}$. The results for $\mathcal{M}_{3,5,4}^{\text{IGABEM}}$ and $\mathcal{M}_{3,6,5}^{\text{IGABEM}}$ are practically indistinguishable in this plot. A comparison is made with a simulation done by WTD 71 showing good agreement. The l^2-error of the absolute far field pressure for $\mathcal{M}_{3,5,4}^{\text{IGABEM}}$ (with $\mathcal{M}_{3,6,5}^{\text{IGABEM}}$ as reference solution) is about 0.052%. The corresponding error for the WTD simulation is 5.5%. Using a direct solver for the IGA simulations, monostatic scattering can easily be solved with multiple right-hand sides (in the present case 3601 column vectors that correspond to 3601 distinct azimuth angles $\varphi \in [0, 180°]$ with steps of 0.5°). The time consumption for monostatic scattering is then increased by less than 1% compared to bistatic scattering since the most computationally complex operation here is to build the system of equations. The WTD 71 simulation solves

[13]The incident wave has the same origin as the far field point in a monostatic sweep.

Table 4: **Rigid scattering on the BeTSSi submarine**: Data for the meshes used in the BeTSSi simulations at $f = 100\,\text{Hz}$. The error is a relative l^2-error of the absolute far field pressure with the simulation from $\mathcal{M}_{3,6,5}^{\text{IGABEM}}$, $\mathcal{M}_{4,2,0}^{\text{COMSOL}}$ and $\mathcal{M}_{6}^{\text{WTD}}$ as a reference solution for IGABEM, COMSOL Multiphysics® and WTD71, respectively. The IGABEM and COMSOL Multiphysics® simulations were computed on 28 Intel CPUs (2×24-core Xeon 2.6 GHz) with 768 GB RAM available and the WTD71 simulations were computed on a 32 core Xeon computer with 2.3 GHz.

Mesh	n_{el}	n_{dofs}	$h_{\max}[\text{m}]$	τ [m^{-1}]	Error [%]	t_{tot} [s]
$\mathcal{M}_{1,2,1}^{\text{IGABEM}}$	3718	6725	1.65	17.0	0.1176	227
$\mathcal{M}_{2,2,1}^{\text{IGABEM}}$	14 872	20 521	0.83	30.6	0.0466	2611
$\mathcal{M}_{3,2,1}^{\text{IGABEM}}$	59 488	70 421	0.43	52.9	0.0185	34 244
$\mathcal{M}_{1,6,5}^{\text{IGABEM}}$	3718	27 537	1.65	25.5	0.0394	1789
$\mathcal{M}_{2,6,5}^{\text{IGABEM}}$	14 872	52 293	0.83	34.1	0.0122	11 860
$\mathcal{M}_{3,6,5}^{\text{IGABEM}}$	59 488	124 113	0.43	61.5	-	108 741
$\mathcal{M}_{1,2,0}^{\text{COMSOL}}$	100 436	250 638	2.21	13.6	3.3481	10
$\mathcal{M}_{2,2,0}^{\text{COMSOL}}$	550 300	1 167 195	1.14	26.3	0.1703	38
$\mathcal{M}_{3,2,0}^{\text{COMSOL}}$	3 729 303	6 654 972	0.60	50.0	0.0569	375
$\mathcal{M}_{4,2,0}^{\text{COMSOL}}$	27 614 929	43 431 671	0.32	93.8	-	5650
$\mathcal{M}_{1}^{\text{WTD}}$	4140	4140	1.89	11.9	2.4013	2
$\mathcal{M}_{2}^{\text{WTD}}$	10 406	10 406	1.00	22.4	1.8815	8
$\mathcal{M}_{3}^{\text{WTD}}$	31 104	31 104	0.50	45.1	1.2824	25
$\mathcal{M}_{4}^{\text{WTD}}$	106 888	106 888	0.26	87.6	1.0328	38
$\mathcal{M}_{5}^{\text{WTD}}$	400 886	400 886	0.13	173.0	0.6598	112
$\mathcal{M}_{6}^{\text{WTD}}$	1 584 014	1 584 014	0.07	325.4	-	400

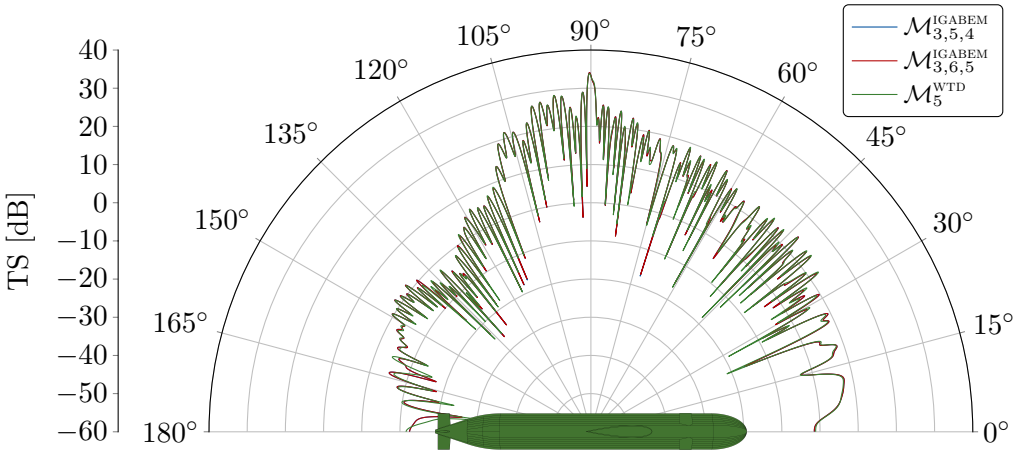

Figure 36: **Rigid scattering on the BeTSSi submarine**: Polar plot of the monostatic target strength (TS) at $f = 1000\,\text{Hz}$ plotted against the azimuth angle φ. All simulations use the CBM formulation.

the 3601 cases individually, resulting in a time consumption increase of about 1392% (the computations used 43.3 hours on a 32 core Xeon computer with 2.3 GHz). The reason that number is not 7201% (WTD 71 timings are here for all angles in $[0, 360°]$) is because WTD 71 uses a precondition matrix based on the result from 5 neighboring monostatic angles.

Finally, the near field at $f = 1000\,\text{Hz}$ is visualized in Figure 37. From Figure 37d one can observe that the incident wave is reflected multiple times beneath the right depth rudder.

7. Conclusions

This article addresses acoustic scattering characterized by sound waves reflected by man-made elastic objects. The present approach is characterized by:

- The scatterer is discretized using isogeometric analysis (IGA), which enables discretization directly from the basis functions used in the computer aided design (CAD) description of the model.

- Both collocation and Galerkin method are considered in combination with several boundary integral equation (BIE) formulations including the conventional (CBIE) formulation and the Burton–Miller (BM) formulation.

- The method of manufactured solution is used as a quality insurance.

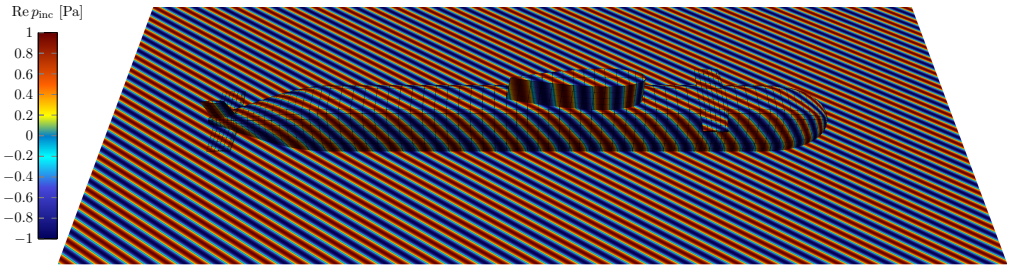

(a) Real part of the incident wave $p_{\text{inc}}(\boldsymbol{x}) = P_{\text{inc}} \mathrm{e}^{\mathrm{i}k\boldsymbol{d}_{\text{s}}\cdot\boldsymbol{x}}$.

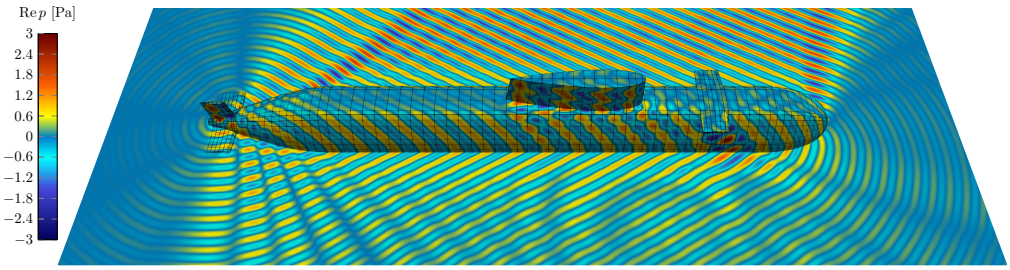

(b) Real part of the scattered pressure $p(\boldsymbol{x})$.

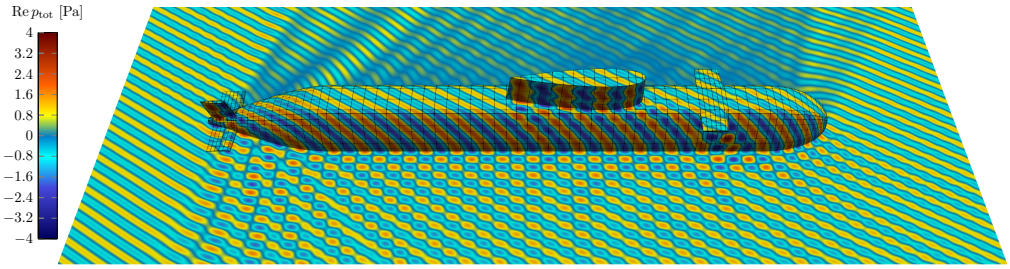

(c) Real part of the total pressure $p_{\text{tot}}(\boldsymbol{x}) = p_{\text{inc}}(\boldsymbol{x}) + p(\boldsymbol{x})$.

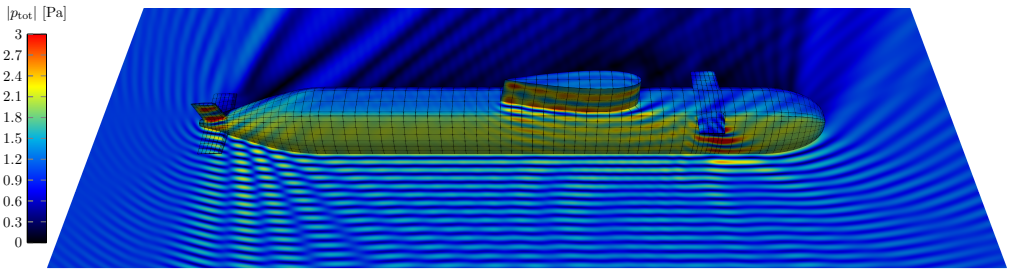

(d) Modulus of the total pressure $p_{\text{tot}}(\boldsymbol{x}) = p_{\text{inc}}(\boldsymbol{x}) + p(\boldsymbol{x})$.

Figure 37: **Rigid scattering on the BeTSSi submarine**: The simulation at $f = 1000\,\text{Hz}$ is visualized in the xy-plane (and on the scatterer), and is computed on mesh $\mathcal{M}_{3,5,4}^{\text{IGABEM}}$. For visualization purposes, the mesh $\mathcal{M}_{1,5,4}^{\text{IGABEM}}$ is here visualized.

The main finding of the present study is that the use of IGA significantly increases the accuracy compared to the use of C^0 finite element analysis (FEA) due to increased inter-element continuity of the spline basis functions.

Furthermore, the following observations are made

- IGA's ability to represent the geometry exactly was observed to be of less importance for accuracy when comparing to higher order ($\hat{p} \geqslant 2$) isoparametric FEA. However, a more significant improvement offered by IGA is due to higher continuity of the spline basis functions in the solution space.

- For linear approximation of the geometry using classical boundary element method (BEM) the convergence order is reduced for higher order sub parametric elements.

- For resolved meshes, the IGA framework enables roughly the same accuracy per element (compared to higher order isoparametric FEA) even though the number of degrees of freedom is significantly reduced.

- IGA is more computationally efficient than FEA to obtain highly accurate solutions. That is, when the mesh is sufficiently resolved, a given accuracy is obtained computationally faster using IGA.

- The collocation simulations have reduced accuracy compared to Galerkin simulations, especially for the hypersingular BIE (HBIE) formulation and BM formulation. Better located collocation points may remedy this difference and is suggested as future work.

- The method of manufactured solution enables a convenient method of checking the mesh quality and to some extent the numerical accuracy of the rigid body scattering problem. It can be used to check the presence of fictitious eigenfrequencies.

- The improved adaptive integration procedure presented in this work uses significantly less quadrature points than the integration procedure presented in [5] for a given accuracy.

- The presence of non-Lipschitz domain does not in principle cause problems for the analysis suitability of the problem as the best approximation is not significantly affected by such areas. However, for the boundary element method, the integral over singular kernels in such domain may cause problems. This is especially the case for highly accurate solution as round-off errors may become significant.

- Regularizing the weakly singular integrands in the BIEs does not eliminate the need for special quadrature rules around the source points. The small

reduction in the number of quadrature points needed for the three versions of the regularized conventional BIE (RCBIE1, RCBIE2 and RCBIE3) formulations compared to the CBIE formulation is arguable not significant.

- Using the collocation method, an advantage for the CBIE formulation compared with the regularized formulations (RCBIE1, RCBIE2 and RCBIE3) is that there is no need to compute the normal vector at the collocation point for the CBIE formulation which could be problematic if the geometric mapping is singular at that point (as is the case for the north and south pole of the parametrization in Figure 8a and several locations for the BeTSSi submarine).

- The Galerkin method obtains results remarkably close to the best approximation combined with any formulation, illustrating the sharpness of the a priori error estimate in Eq. (33).

The Burton-Miller formulation yields somewhat reduced accuracy in combination with the collocation method, which is the cost of removing fictitious eigenfrequencies. Another popular alternative is the combined Helmholtz integral formulation (CHIEF) framework which does not have this reduction in accuracy but has other downsides. By adding more constraints to the linear system of equations, the CHIEF method can remove fictitious eigenfrequencies with the cost of having to solve an over determined linear system of equations (using for example least squares). The main disadvantage with the CHIEF framework, however, is arguably the difficulty of finding interior points at which to evaluate the BIEs. This is especially problematic for high frequencies. An approach for solving this issue was made in [56]. The results in this work may be improved even further with the discontinuous IGABEM [14].

The boundary element method is the method of choice in the BeTSSi community for obtaining accurate results for the BeTSSi submarine, mainly to avoid surface-to-volume parametrization. Although IGABEM seems to be a prominent framework to solve acoustic scattering problems, there are still issues on the BeTSSi submarine that was not resolved in this paper, in particular the integration procedure over non-Lipschitz areas on the BeTSSi submarine.

Acknowledgements

This work was supported by the Department of Mathematical Sciences at the Norwegian University of Science and Technology and by the Norwegian Defence Research Establishment.

The publication of the BeTSSi models (storage of large data files) was provided by UNINETT Sigma2 — the National Infrastructure for High Performance Computing and Data Storage in Norway.

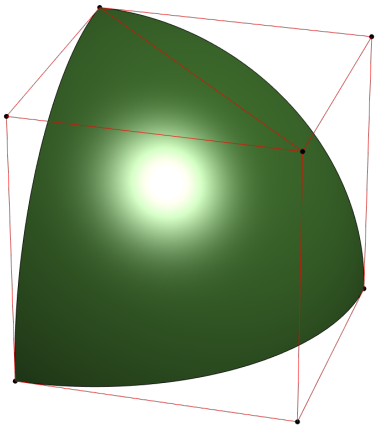

(a) Parametrization 1

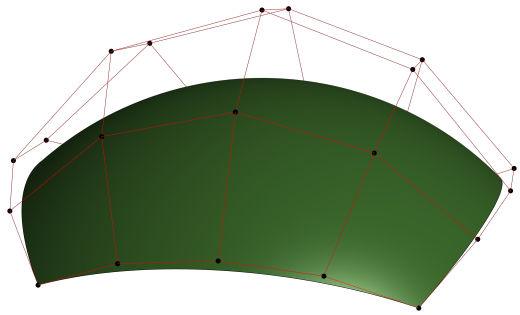

(b) Parametrization 2

Figure A38: **NURBS parametrization of the sphere**: Two NURBS parametrizations of the sphere. The control polygon is also shown.

The authors would like to thank Jan Ehrlich and Ingo Schaefer (WTD 71) for their simulations on the BeTSSi submarine and additional fruitful discussions.

The authors would also like to thank the reviewers for detailed response and many constructive comments.

A. NURBS parametrization of the sphere

Two standard ways of parametrizing a sphere using NURBS are given below for the unit sphere (a simple scaling generalizes this for spheres of arbitrary radii). The first is represented by 8 elements in a single patch (only one element is given below, as the others are obtained by symmetry), and the second is represented by 6 patches (only one patch is given below, as the others are obtained by symmetry).

A.1. Parametrization 1

The sphere can be exactly parametrized by 8 NURBS elements of degree 2. One of these elements with corresponding control points is illustrated in Figure A38a. The weights and control points are given in Table 5 (a parametrization of all elements in a single patch can be found in [57, p. 168]).

A.2. Parametrization 2

The sphere can be exactly parametrized [58, p. 11] by 6 NURBS patches of degree 4. One of these patches with corresponding control points is illustrated in Figure A38b. Some of the weights and weighted control points are given in

Table 5: **Parametrization 1**: Weights and control points for an element of a unit sphere.

i	j	$x_{i,j}$	$y_{i,j}$	$z_{i,j}$	$w_{i,j}$
1	1	1	0	0	1
2	1	1	1	0	$1/\sqrt{2}$
3	1	0	1	0	1
1	2	1	0	1	$1/\sqrt{2}$
2	2	1	1	1	$1/2$
3	2	0	1	1	$1/\sqrt{2}$
1	3	0	0	1	1
2	3	0	0	1	$1/\sqrt{2}$
3	3	0	0	1	1

Table 6. The remaining data is found by symmetry about the planes $x = 0$, $y = 0$, $y = x$ and $y = -x$. In particular (by symmetry about the $y = x$ plane)

$$x_{i,j} = y_{j,i}, \quad y_{i,j} = x_{j,i}, \quad z_{i,j} = z_{j,i}, \quad w_{i,j} = w_{j,i}$$

for the pairs $(i, j) \in \{(1, 2), (1, 3), (2, 3)\}$, and (by symmetry about the $y = 0$ plane)

$$x_{i,j} = -x_{6-i,j}, \quad y_{i,j} = y_{6-i,j}, \quad z_{i,j} = z_{6-i,j}, \quad w_{i,j} = w_{6-i,j}$$

for $i = 4, 5$ and $j = 1, 2, 3$, and then (by symmetry about the $x = 0$ plane)

$$x_{i,j} = x_{i,6-j}, \quad y_{i,j} = -y_{i,6-j}, \quad z_{i,j} = z_{i,6-j}, \quad w_{i,j} = w_{i,6-j}$$

for $i = 1, 2, 3, 4, 5$ and $j = 4, 5$.

B. NURBS parametrization of the torus

A torus with major radius r_o and minor radius r_i can be represented by a single NURBS patch with 16 elements (as visualized in Figure 1b). One of these elements is shown in Figure B39 with corresponding control polygon. The weights and control points are given in Table 7.

C. The BeTSSi submarine model

In this section the BeTSSi [45] submarine model (depicted in Figure C40) will be presented. The BeTSSi submarine contains many standard designing features

Table 6: **Parametrization 2**: Weights and weighted control points for a tile of a unit sphere.

i	j	$w_{i,j}x_{i,j}$	$w_{i,j}y_{i,j}$	$w_{i,j}z_{i,j}$	$w_{i,j}$
1	1	$4(1-\sqrt{3})$	$4(1-\sqrt{3})$	$4(\sqrt{3}-1)$	$4(3-\sqrt{3})$
2	1	$-\sqrt{2}$	$\sqrt{2}(\sqrt{3}-4)$	$\sqrt{2}(4-\sqrt{3})$	$\sqrt{2}(3\sqrt{3}-2)$
3	1	0	$4(1-2\sqrt{3})/3$	$4(2\sqrt{3}-1)/3$	$4(5-\sqrt{3})/3$
2	2	$-(3\sqrt{3}-2)/2$	$(2-3\sqrt{3})/2$	$(\sqrt{3}+6)/2$	$(\sqrt{3}+6)/2$
3	2	0	$\sqrt{2}(2\sqrt{3}-7)/3$	$5\sqrt{6}/3$	$\sqrt{2}(\sqrt{3}+6)/3$
3	3	0	0	$4(5-\sqrt{3})/3$	$4(5\sqrt{3}-1)/9$

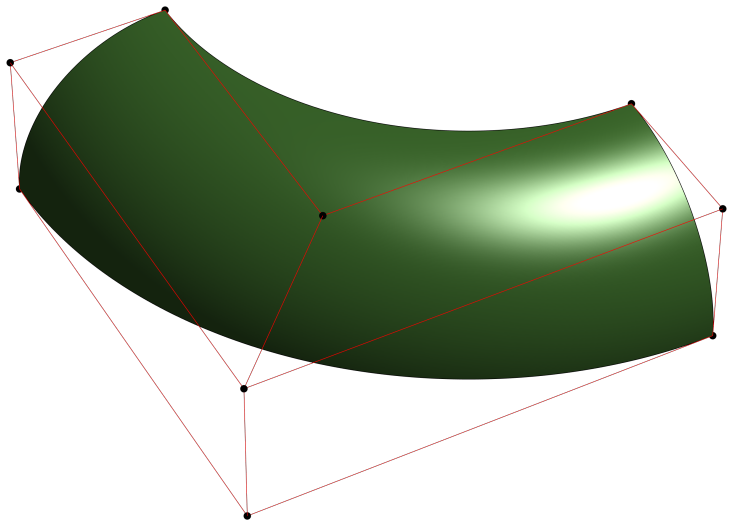

Figure B39: **NURBS parametrization of the torus**: A NURBS parametrization of a 1/16 of a torus. The control polygon is also shown.

Table 7: **NURBS parametrization of the torus**: Weights and control points for the torus.

i	j	$x_{i,j}$	$y_{i,j}$	$z_{i,j}$	$w_{i,j}$
1	1	$r_\mathrm{o} + r_\mathrm{i}$	0	0	1
2	1	$r_\mathrm{o} + r_\mathrm{i}$	$r_\mathrm{o} + r_\mathrm{i}$	0	$1/\sqrt{2}$
3	1	0	$r_\mathrm{o} + r_\mathrm{i}$	0	1
1	2	$r_\mathrm{o} + r_\mathrm{i}$	0	r_i	$1/\sqrt{2}$
2	2	$r_\mathrm{o} + r_\mathrm{i}$	$r_\mathrm{o} + r_\mathrm{i}$	r_i	$1/2$
3	2	0	$r_\mathrm{o} + r_\mathrm{i}$	r_i	$1/\sqrt{2}$
1	3	r_o	0	r_i	1
2	3	r_o	r_o	r_i	$1/\sqrt{2}$
3	3	0	r_o	r_i	1

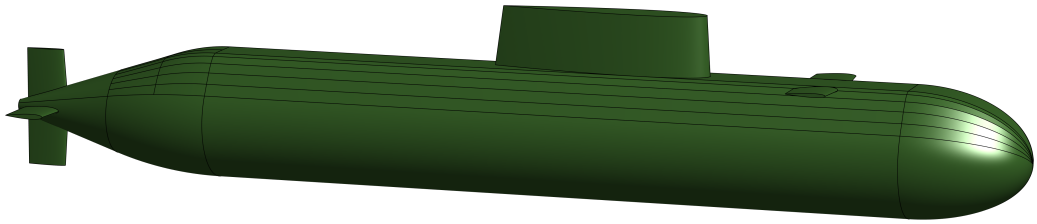

Figure C40: Outer pressure hull for BeTSSi submarine.

including circles, ellipses, straight panels, cylinders and cones. In addition, several NACA profiles are present giving a very nice benchmark model for sub-surface scattering. For the analysis part, it contains challenges such as trimming curves and non-Lipschitz domains [59]. All in all, a challenging benchmark without being too complex.

The original BeTSSi submarine model presented in [45] contains several discrepancies that is arguably not optimal for a benchmark model. First, the NACA profiles used to create the sail and the rudders are only given with 5 digits of accuracy. This in turn, results in for example the sail not being tangent to the side lines of the deck with an error of around 1 mm. This creates problems for the meshing procedure as this results in either very small elements in this area, or element with high aspect ratios. Second, the exact geometry for the upper transition from the deck to the rotationally symmetric cone tail, is hidden by an "internal routine in ANSYS". Not only is this hard to reproduce for anyone without an ANSYS license, but the available CAD file for this model does not represent the transition to the lower part exactly (as this curve should be a circular arc and

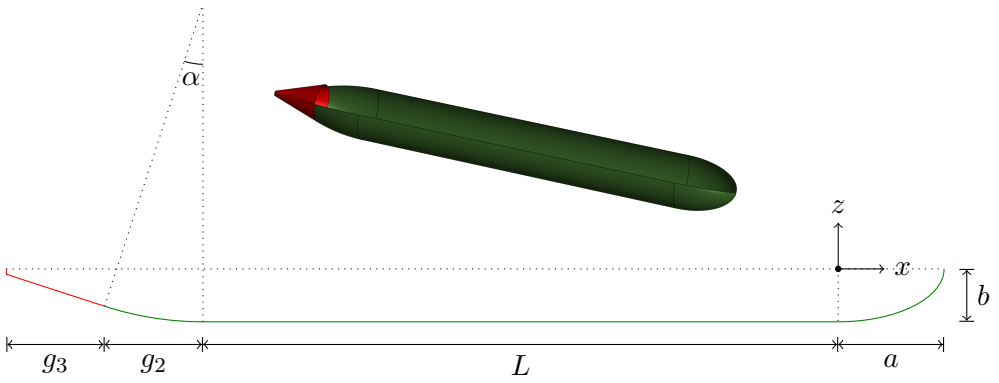

Figure C41: The sideline of the lower part of the BeTSSi submarine. The side lines are formed (from the right) by an ellipse with semi-major axis a and semi-minor axis b, followed by a straight line of length L, then an arc of angle α and finally two straight lines. The latter two straight lines (in red) are rotated about the x-axis and the remaining part (in green) are rotated an angle β around the x-axis.

is not represented by a NURBS curve). In order to create a watertight model, the available CAD file approximates the lower transition such that the side curves match.

The relevant BeTSSi parameters for the work presented herein are given in Table 8.

C.1. Main body

The model is symmetric about the xz-plane and has rotational symmetry for the lower part as described in Figure C41. The transition from this axisymmetric part to the deck is described in Figure C42. This transition as well as the deck itself, contains a set of rectangular panels of length L. The cubic polynomial $P_{\mathrm{p}}(y)$, is uniquely defined by the requirement that it defines a smooth transition between the hull and the deck. More precisely, the following requirement must be satisfied:

$$\begin{aligned} P_{\mathrm{p}}(s) &= c, \quad P_{\mathrm{p}}\left(b\sin\frac{\beta}{2}\right) = -b\cos\frac{\beta}{2} \\ P'_{\mathrm{p}}(s) &= 0, \quad P'_{\mathrm{p}}\left(b\sin\frac{\beta}{2}\right) = \tan\frac{\beta}{2} \end{aligned}$$

which gives the polynomial

$$P_{\mathrm{p}}(y) = c + C_1(y-s)^2 + C_2(y-s)^3$$

Table 8: **BeTSSi submarine:** Free parameters for the BeTSSi submarine benchmark.

Parameter	Description
$\alpha = 18°$	Arc angle of transition to the tail cone
$\beta = 240°$	Rotational angle for the axisymmetric lower part
$g_2 = 6.5\,\mathrm{m}$	Distance in the x-direction of transition to the tail cone
$g_3 = 6.5\,\mathrm{m}$	Distance in the x-direction of the tail cone
$L = 42\,\mathrm{m}$	Length of the deck
$a = 7\,\mathrm{m}$	Semi-major axis of bow
$b = 3.5\,\mathrm{m}$	Semi-minor axis of bow
$c = 4\,\mathrm{m}$	Height from the x-axis to the deck
$s = 1.2\,\mathrm{m}$	Half of the width of the deck
$l_{\mathrm{ls}} = 13\,\mathrm{m}$	Length of the lower cross-section of the sail
$l_{\mathrm{lm}} = 2.6\,\mathrm{m}$	Length of the lower cross-section of the main rudders
$l_{\mathrm{ld}} = 2.6\,\mathrm{m}$	Length of the lower cross-section of the depth rudders
$l_{\mathrm{us}} = 12.3\,\mathrm{m}$	Length of the upper cross-section of the sail
$l_{\mathrm{um}} = 2.35\,\mathrm{m}$	Length of the upper cross-section of the main rudders
$l_{\mathrm{ud}} = 2.35\,\mathrm{m}$	Length of the upper cross-section of the depth rudders
$b_{\mathrm{lm}} = 0.4\,\mathrm{m}$	Width of the lower cross-section of the main rudders
$b_{\mathrm{us}} = 2\,\mathrm{m}$	Width of the upper cross-section of the sail
$b_{\mathrm{um}} = 0.3\,\mathrm{m}$	Width of the upper cross-section of the main rudders
$b_{\mathrm{ud}} = 0.22\,\mathrm{m}$	Width of the upper cross-section of the depth rudders
$\delta_{\mathrm{s}} = 0.2\,\mathrm{m}$	Parameter for shifting cross-sections of the sail
$h_{\mathrm{s}} = 3.5\,\mathrm{m}$	Height of the sail
$h_{\mathrm{m}} = 3.5\,\mathrm{m}$	Height of the main rudders
$x_{\mathrm{s}} = -12\,\mathrm{m}$	Positioning of the sail
$x_{\mathrm{m}} = -51.9\,\mathrm{m}$	Positioning of the main rudders
$x_{\mathrm{d}} = -4\,\mathrm{m}$	Positioning of the depth rudders

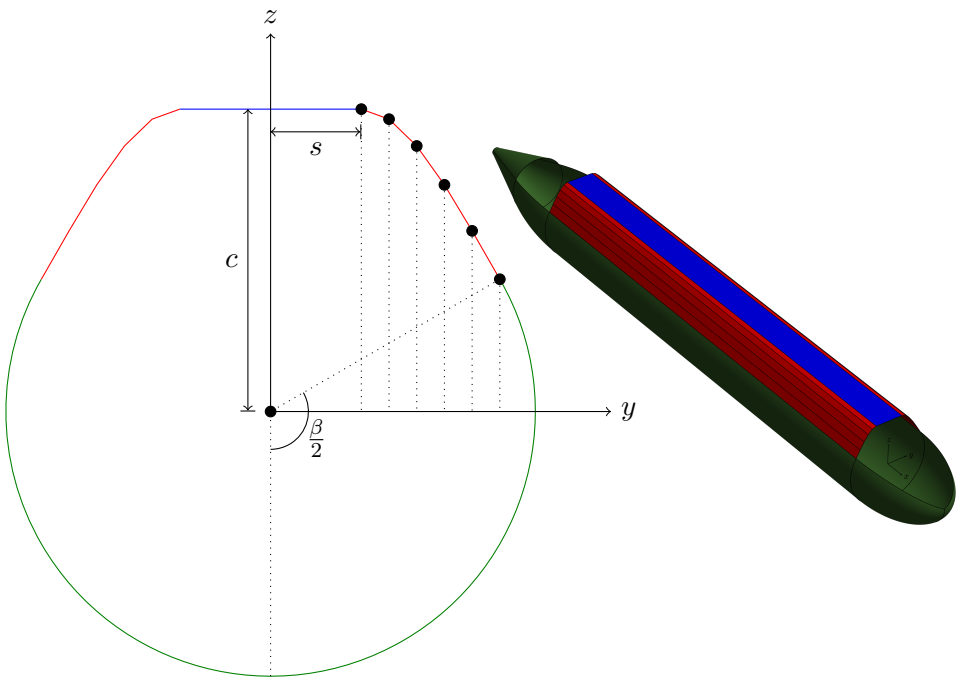

Figure C42: The transition (red line) from the axisymmetric hull (green line) to the deck (blue line) is given by sampling a cubic polynomial, $P_{\mathrm{p}}(y)$, at 6 equidistant points in the y-direction and connecting the resulting points with straight lines (corresponding 6 points are found for negative values y-values, $(0, y, P_{\mathrm{p}}(|y|))$).

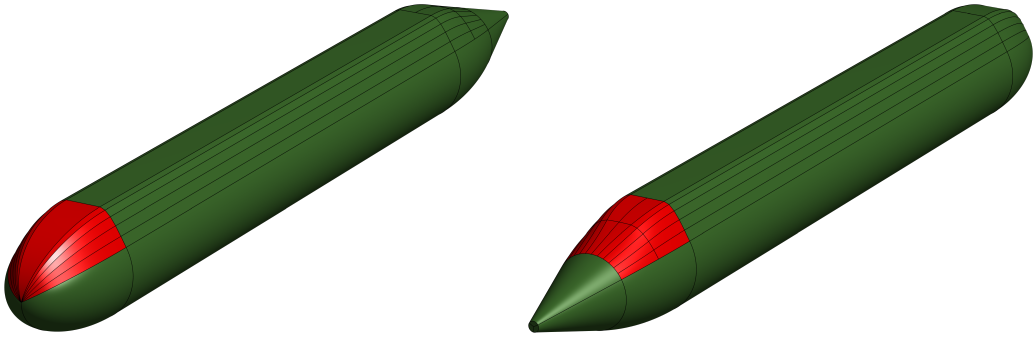

(a) Illustration of the upper bow part. (b) Illustration of the upper transition part.

Figure C43: Main body of BeTSSi submarine.

where

$$C_1 = -\frac{3C_4 + C_3 \tan\frac{\beta}{2}}{C_3^2}, \quad C_2 = \frac{2C_4 + C_3 \tan\frac{\beta}{2}}{C_3^3}$$
$$C_3 = b\sin\frac{\beta}{2} - s, \quad C_4 = c + b\cos\frac{\beta}{2}.$$

The upper part of the bow (highlighted in Figure C43a) is obtained by linear lofting of elliptic curves from the 12 points described in Figure C42 to the tip of the bow.

The upper part of the tail section (highlighted in Figure C43b) is connected using a tensor NURBS surface of degree 2 such that it defines a smooth transition from the axisymmetric cone to the deck. More precisely, the upper part of the cone tail is divided into 12 arcs with angle $\frac{2\pi-\beta}{12}$, and the resulting points are connected to corresponding points on the transition to the deck from the axisymmetric hull. As illustrated in Figure C44a, the NURBS patch is given by 24 elements. Thus, $4 \cdot 25 = 100$ control points, $\boldsymbol{P}_{i,j}$, are needed as shown in Figure C44b (25 and 4 control points in the ξ direction and η direction, respectively). The control points $\boldsymbol{P}_{1,j}$ and $\boldsymbol{P}_{25,j}$ for $j = 1, 2, 3, 4$ must be defined as in Figure C45b, while the control points $\boldsymbol{P}_{i,1}$ must be defined as in Figure C45a. The weights are defined by

$$w_{i,j} = \begin{cases} \tilde{w}_j & i \text{ odd} \\ \frac{\tilde{w}_j}{3}\left[(4-j)\cos\left(\frac{2\pi-\beta}{24}\right) + j - 1\right] & i \text{ even} \end{cases}$$

where

$$\tilde{w}_j = \begin{cases} 1 & j = 1, 4 \\ \frac{1}{2}(1 + \cos\frac{\alpha}{2}) & j = 2, 3. \end{cases}$$

The locations of the control points $\boldsymbol{P}_{i,j}$, $j = 2, 3$ and $2 \leqslant i \leqslant 24$, are determined by the requirement that the x component is the same as $\boldsymbol{P}_{1,j}$ and the fact that

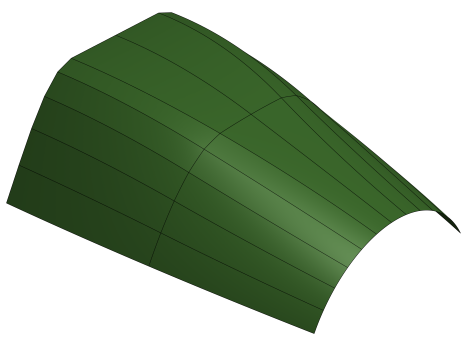

(a) Illustration of the mesh.

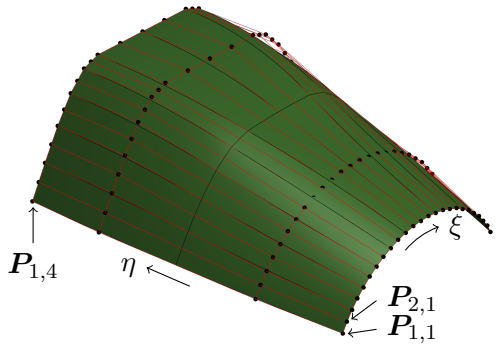

(b) Illustration of the control polygon mesh.

Figure C44: Illustration of the upper transition part of the tail.

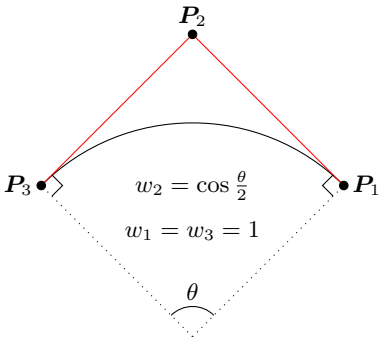

(a) NURBS parametrization of arc of angle θ using three control points $\{\boldsymbol{P}_i\}_{i=1}^3$, the weights $\{w_i\}_{i=1}^3$ and the open knot vector $\boldsymbol{t}_\xi = \{0, 0, 0, 1, 1, 1\}$.

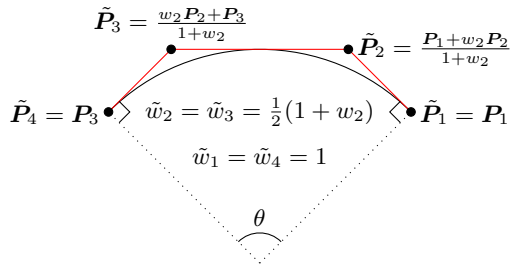

(b) NURBS parametrization of arc of angle θ using four control points $\{\tilde{\boldsymbol{P}}_i\}_{i=1}^4$, the weights $\{\tilde{w}_i\}_{i=1}^4$ and the open knot vector $\tilde{\boldsymbol{t}}_\xi = \{0, 0, 0, 0.5, 1, 1, 1\}$.

Figure C45: Two ways of parametrizing an arc using NURBS [60, p. 315].

the control polygon lines must be tangential to the surface both at the deck and the cone tail.

C.2. NACA profiles

The sail and the rudders are based on the NACA 00xx profiles [61, 62] (the first two digits indicate a symmetric airfoil, and the second two, the thickness-chord ratio). The NACA profiles are all based on the function

$$f_t(x) = 5t\Big(a_0\sqrt{x} + a_1 x + a_2 x^2 + a_3 x^3 + a_4 x^4\Big) \tag{C.1}$$

with t being the thickness of the rudder and a_i the coefficients determining the shape of the rudder.

This function satisfies the condition $f_t(0) = 0$ and should in addition satisfy

$$f_t(0.3) = \frac{t}{2}, \quad f_t'(0.3) = 0. \tag{C.2}$$

In [61, 62] the coefficients are computed to be

$$\begin{aligned} a_0 &= 0.2969 \\ a_1 &= -0.1260 \\ a_2 &= -0.3516 \\ a_3 &= 0.2843 \\ a_4 &= -0.1015. \end{aligned}$$

The conditions in Eq. (C.2) are approximated with a residual error of 0.0029% and 0.013%, respectively. Moreover, the additional condition $f_t(1) = 0.002$ is satisfied with a residual error of 0.01%. In order to have a zero-thickness trailing edge, i.e. $f_t(1) = 0$, the original BeTSSi coefficients slightly modify the NACA coefficients to be

$$\begin{aligned} a_0 &= 0.2969 \\ a_1 &= -0.1267 \\ a_2 &= -0.3523 \\ a_3 &= 0.2843 \\ a_4 &= -0.1022. \end{aligned}$$

The conditions in Eq. (C.2) are here approximated with a residual error of 0.025% and 0.013%, respectively. The fact that the conditions in Eq. (C.2) are approximated so poorly is problematic for an analysis suitable BeTSSi submarine as this results in tangential curves missing the NACA profiles with a significant error, resulting in elements with high aspect ratio or a redundant amount of elements in order to resolve these areas. This fact motivates a more precise definition of these coefficients.

Note that the leading-edge radius is given by

$$R_{\text{le}} = \lim_{x \to 0^+} \left| \frac{\left[1 + f_t'(x)^2\right]^{3/2}}{f_t''(x)} \right| = \frac{25}{2} a_0^2 t^2$$

and the included angle of the trailing edge by

$$\delta_{\text{te}} = 2 \tan^{-1} |f_t'(1)|.$$

Alternative conditions [62]

$$R_{\text{le}} = \frac{25}{2} 0.2969^2 t^2, \quad \delta_{\text{te}} = 2 \tan^{-1}(5t \cdot 0.23385) \tag{C.3}$$

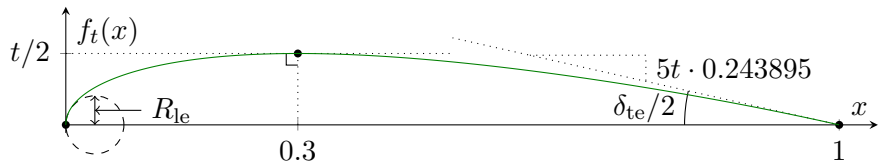

Figure C46: Illustration of the NACA profile used for the sail and the rudders. The five coefficients a_i in Eq. (C.1) are restricted by the conditions in Eq. (C.4) as illustrated here.

yield the coefficients (for usage in double precision)

$$\begin{aligned} a_0 &= 0.2969 \\ a_1 &\approx -0.128361732706295 \\ a_2 &\approx -0.335670924960620 \\ a_3 &\approx 0.251127048040123 \\ a_4 &\approx -0.083994390373209. \end{aligned}$$

Using

$$\delta_{\text{te}} = 2\tan^{-1}(5t \cdot 0.243895)$$

yields coefficients slightly closer to the original BeTSSi coefficients.

In summary, we shall use the conditions

$$f_t(1) = 0, \quad f_t(0.3) = \frac{t}{2}, \quad f_t'(0.3) = 0, \quad a_0 = 0.2969, \quad f_t'(1) = -5t \cdot 0.243895 \tag{C.4}$$

which are illustrated in Figure C46 and yields the coefficients (in double precision)

$$\begin{aligned} a_0 &= 0.2969 \\ a_1 &\approx -0.12651673270629464 \\ a_2 &\approx -0.34981592496061949 \\ a_3 &\approx 0.28392704804012290 \\ a_4 &\approx -0.10449439037320877. \end{aligned}$$

Computing the relative error in the L^2-norm of the NACA profile based on these coefficients and the original NACA profile for the BeTSSi submarine yields an error of about 0.54%. Note that $f_t(\xi^2)$ is a polynomial of degree 8, such that the NACA profile can be exactly represented by a spline curve based on the parametrization $\boldsymbol{C}(\xi) = [\xi^2, f_t(\xi^2)]$.

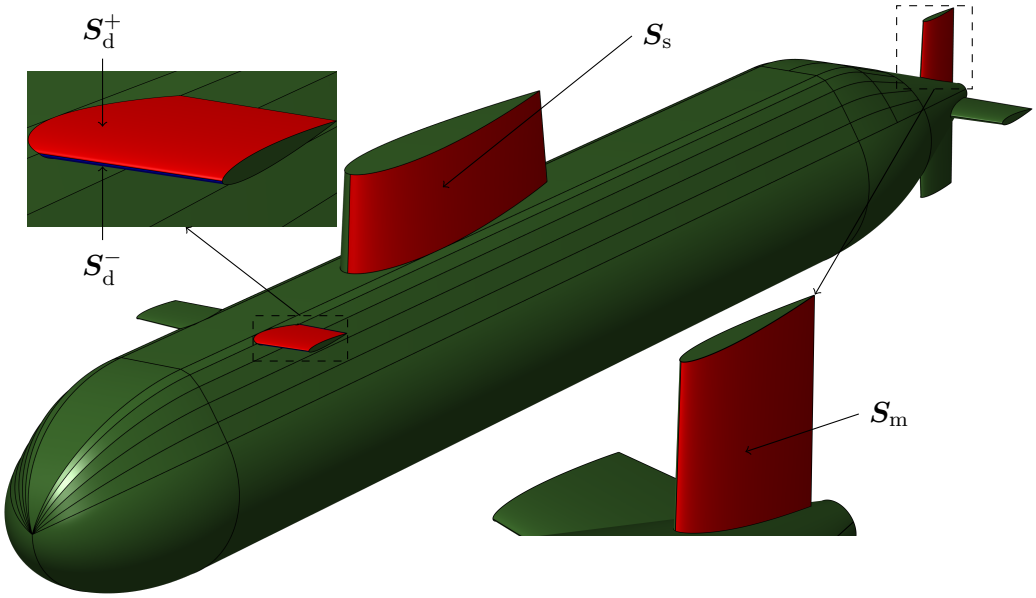

Figure C47: Illustration of the parametrizations $\boldsymbol{S}_\mathrm{s}$, $\boldsymbol{S}_\mathrm{m}$ and $\boldsymbol{S}_\mathrm{d}^\pm$ for the sail, the main rudders and the depth rudders, respectively.

C.3. Sail

Consider the port part ($y \geqslant 0$) of the sail. It can be parametrized by

$$\boldsymbol{S}_\mathrm{s}(\xi,\eta) = x_\mathrm{s}\boldsymbol{e}_\mathrm{x} + c\boldsymbol{e}_\mathrm{z} + \begin{bmatrix} -\left[l_\mathrm{ls}\xi^2 + \eta(\delta_\mathrm{s} - (l_\mathrm{ls} - l_\mathrm{us})\xi^2)\right] \\ l_\mathrm{ls} f_{t_\mathrm{ls}}(\xi^2) + \eta\left[l_\mathrm{us} f_{t_\mathrm{us}}(\xi^2) - l_\mathrm{ls} f_{t_\mathrm{ls}}(\xi^2)\right] \\ \eta h_\mathrm{s} \end{bmatrix} \tag{C.5}$$

where

$$0 \leqslant \xi \leqslant 1, \quad 0 \leqslant \eta \leqslant 1, \quad t_\mathrm{us} = \frac{b_\mathrm{us}}{l_\mathrm{us}}, \quad t_\mathrm{ls} = \frac{b_\mathrm{ls}}{l_\mathrm{ls}}, \quad \text{and} \quad b_\mathrm{ls} = 2s.$$

This parametrization is illustrated in Figure C47. The starboard part of the sail is obtained by mirroring the port side of the sail about the xz-plane. Finally, the roof is obtained by a linear loft between these two surfaces.

C.4. Main rudders

Consider the port part ($y \geqslant 0$) of the upper main rudder. It can be parametrized by

$$\boldsymbol{S}_\mathrm{m}(\xi,\eta) = x_\mathrm{m}\boldsymbol{e}_\mathrm{x} + \begin{bmatrix} -l_\mathrm{lm}\xi^2 - \delta_\mathrm{m}\eta(1-\xi^2) \\ l_\mathrm{lm} f_{t_\mathrm{lm}}(\xi^2) + \eta\left[l_\mathrm{um} f_{t_\mathrm{um}}(\xi^2) - l_\mathrm{lm} f_{t_\mathrm{lm}}(\xi^2)\right] \\ \eta h_\mathrm{m} \end{bmatrix}, \tag{C.6}$$

where

$$0 \leqslant \xi \leqslant 1, \quad g(\xi) \leqslant \eta \leqslant 1, \quad \delta_{\mathrm{m}} = l_{\mathrm{lm}} - l_{\mathrm{um}}, \quad t_{\mathrm{lm}} = \frac{b_{\mathrm{lm}}}{l_{\mathrm{lm}}}, \quad \text{and} \quad t_{\mathrm{um}} = \frac{b_{\mathrm{um}}}{l_{\mathrm{um}}}$$

for a function g (to be determined) representing the intersection between the rudder and the cone. The cone can be represented by

$$y^2 + z^2 = (x - x_{\mathrm{c}})^2 \tan^2 \alpha, \quad x_{\mathrm{c}} = -(L + g_2 + (b - h)\cot \alpha). \tag{C.7}$$

Then, inserting the components of $\boldsymbol{S}_{\mathrm{m}}(\xi, \eta)$ in Eq. (C.6) into Eq. (C.7) yields an equation in ξ and η. This equation is quadratic in η and has the solution $\eta = g(\xi)$ where

$$g(\xi) = \frac{-C_{\mathrm{b}}(\xi) + \sqrt{[C_{\mathrm{b}}(\xi)]^2 - 4C_{\mathrm{a}}(\xi)C_{\mathrm{c}}(\xi)}}{2C_{\mathrm{a}}(\xi)}$$

and

$$\begin{aligned}
C_{\mathrm{a}}(\xi) &= \Big[l_{\mathrm{um}} f_{t_{\mathrm{um}}}(\xi^2) - l_{\mathrm{lm}} f_{t_{\mathrm{lm}}}(\xi^2)\Big]^2 + h_{\mathrm{m}}^2 - \delta_{\mathrm{m}}^2 (1 - \xi^2)^2 \tan^2 \alpha \\
C_{\mathrm{b}}(\xi) &= 2 l_{\mathrm{lm}} f_{t_{\mathrm{lm}}}(\xi^2)\Big[l_{\mathrm{um}} f_{t_{\mathrm{um}}}(\xi^2) - l_{\mathrm{lm}} f_{t_{\mathrm{lm}}}(\xi^2)\Big] \\
&\quad + 2 \tan^2 \alpha \Big(x_{\mathrm{m}} - l_{\mathrm{lm}} \xi^2 - x_{\mathrm{c}}\Big) \delta_{\mathrm{m}} \Big(1 - \xi^2\Big) \\
C_{\mathrm{c}}(\xi) &= [l_{\mathrm{lm}} f_{t_{\mathrm{lm}}}(\xi^2)]^2 - \tan^2 \alpha \Big(x_{\mathrm{m}} - l_{\mathrm{lm}} \xi^2 - x_{\mathrm{c}}\Big)^2.
\end{aligned}$$

The trimming curve is then given by

$$\boldsymbol{r}_{\mathrm{m}}(\xi) = \boldsymbol{S}_{\mathrm{m}}(\xi, g(\xi)).$$

The parametrization $\boldsymbol{S}_{\mathrm{m}}$ is illustrated in Figure C47. The starboard side of the upper main rudder is given by mirroring the port side of the main upper rudder about the xz-plane, and the top part of the rudder is connected by linear lofting. The other main rudders are obtained by rotations by angles of 90°, 180° and 270° around the x-axis, respectively. Note that this trimming curve may not be represented exactly by NURBS basis functions, and hence, the BeTSSi submarine cannot be exactly represented by NURBS patches without trimming curves.

C.5. Depth rudders

Consider the port depth rudder ($y \geqslant 0$). The upper (+) part and lower (−) part can be parametrized by

$$\boldsymbol{S}_{\mathrm{d}}^{\pm}(\xi, \eta) = \begin{bmatrix} x_{\mathrm{d}} \\ s \\ c - \frac{b_{\mathrm{ld}}}{2} \end{bmatrix} + \begin{bmatrix} -l_{\mathrm{ld}} \xi^2 - \delta_{\mathrm{d}} \eta (1 - \xi^2) \\ \eta h_{\mathrm{d}} \\ \pm l_{\mathrm{ld}} f_{t_{\mathrm{ld}}}(\xi^2) \pm \eta \big[l_{\mathrm{ud}} f_{t_{\mathrm{ud}}}(\xi^2) - l_{\mathrm{ld}} f_{t_{\mathrm{ld}}}(\xi^2)\big] \end{bmatrix}, \tag{C.8}$$

where

$$0 \leqslant \xi \leqslant 1, \quad g^{\pm}(\xi) \leqslant \eta \leqslant 1, \delta_{\mathrm{d}} = l_{\mathrm{ld}} - l_{\mathrm{ud}}, \quad t_{\mathrm{ld}} = \frac{b_{\mathrm{ld}}}{l_{\mathrm{ld}}}, \quad t_{\mathrm{ud}} = \frac{b_{\mathrm{ud}}}{l_{\mathrm{ud}}},$$
$$h_{\mathrm{d}} = b - s \quad \text{and} \quad b_{\mathrm{ld}} = 2\left[c - P_{\mathrm{p}}\left(s + \frac{C_3}{5}\right)\right].$$

The two panels to be trimmed by this surface are given by

$$D_1^{\pm} y + D_2^{\pm} z = D_3^{\pm} \tag{C.9}$$

where

$$D_1^{+} = \frac{b_{\mathrm{ld}}}{2}, \quad D_2^{+} = \frac{C_3}{5}, \quad D_3^{+} = D_1^{+} s + D_2^{+} c$$

and

$$D_1^{-} = c - P_{\mathrm{p}}\left(s + \frac{2C_3}{5}\right) - \frac{b_{\mathrm{ld}}}{2}, \quad D_2^{-} = \frac{C_3}{5}, \quad D_3^{-} = D_1^{-}\left(s + \frac{C_3}{5}\right) + D_2^{-}\left(c - \frac{b_{\mathrm{ld}}}{2}\right).$$

Then, inserting the components of $\boldsymbol{S}_{\mathrm{d}}^{\pm}(\xi, \eta)$ in Eq. (C.8) into Eq. (C.9) yields an equation in ξ and η. This equation is linear in η and has the solution $\eta = g^{\pm}(\xi)$ where

$$g^{\pm}(\xi) = \frac{D_3^{\pm} - D_1^{\pm} s - D_2^{\pm}\left(c - \frac{b_{\mathrm{ld}}}{2} \pm l_{\mathrm{ld}} f_{t_{\mathrm{ld}}}(\xi^2)\right)}{D_1^{\pm} h_{\mathrm{d}} \pm D_2^{\pm}[l_{\mathrm{ud}} f_{t_{\mathrm{ud}}}(\xi^2) - l_{\mathrm{ld}} f_{t_{\mathrm{ld}}}(\xi^2)]}.$$

The trimming curves are then given by

$$\boldsymbol{r}_{\mathrm{d}}^{\pm}(\xi) = \boldsymbol{S}_{\mathrm{d}}^{\pm}(\xi, g^{\pm}(\xi)).$$

The parametrizations $\boldsymbol{S}_{\mathrm{d}}^{\pm}$ are illustrated in Figure C47. The side part is again obtained by linear lofting. The starboard depth rudder is given by mirroring the port depth rudder about the xz-plane.

D. An analysis suitable BeTSSi submarine

Most of the BeTSSi submarine can be exactly represented by second order NURBS basis functions and will need no approximation for our analysis. The areas around the trimming curves, however, needs special care. Instead of incorporating the trimming curves in the analysis of the BeTSSi submarine, a reparametrization of the problematic areas is considered. This enables the possibility to represent the NACA profile with polynomial orders less than 8, which would otherwise be a rather significant restriction of the computational efficiency. A third reason for reparametrizing the submarine is to obtain an analysis suitable mesh around the non-Lipschitz areas (sides of the sail at the deck and the upper part of the depth

rudders). The optimal way of parametrizing this area would be to have the same (we use linear) parametrization for the x-component as done in [59].

The approximations are done by performing least squares of the trimming curves. For the sail and the depth rudders, the surrounding areas are linear, and can be exactly represented based on the resulting NURBS-curve. For the main rudders, the surrounding areas are approximated by interpolation in such a way that the neighboring (exact) NURBS patches remain unaltered (illustrated in Figure D48). The interpolation was here preferred above the least squares as it resulted in more analysis suitable basis functions. The upper and lower curves of the sail/rudders are lofted linearly. Figures D49 and D50 show the exponential convergence to the exact geometry.

All NURBS patches are conforming such that there is no need to handle master/slave faces by adding constraint equations as described in [37, p. 87-91]. This results in redundant degrees of freedom, and the optimal mesh certainly requires a solution to this problem. Two very good alternatives include T-splines [63] and LR B-splines [54]).

For the sake of brevity, the authors refer to [64] instead of giving an exact description of every minor detail in constructing this approximation. The exact BeTSSi submarine as well as the approximate submarines for $\check{p} = 2, 3, 4$ are presented in the file formats `.step`, `.igs` and `.3dm` format.

By considering the manufactured solution in Subsection 6.6 the numerical evidence observed from Figure D51 indicates that the presence of non-Lipschitz domain does not affect the convergence rates (also observed in [59]).

E. Triangulation of the BeTSSi submarine

Triangularized versions of the exact BeTSSi submarine in `.stl` (both ASCII and binary) and `.bdf` format can be found in [64] where the triangulations is an optimization of meshes created in COMSOL Multiphysics® (surface mesh corresponding to the COMSOL Multiphysics® volume meshes considered in this work). An overview of the triangularization meshes can be found in Table 9. Since these meshes are used by WTD in the simulations they have provided for this work, they are denoted by $\mathcal{M}_m^{\text{WTD}}$. The *resolution* (res) parameter $\lambda/h_{\max}^{(2)}$ (at $f = 1\,\text{kHz}$) is used in the file names. In Table 9, $h_{\max}^{(1)}$ is defined as the maximum of the diameters of the smallest circle that inscribes the triangular element. For the i^{th} triangle with side lengths $l_{i,1}$, $l_{i,2}$ and $l_{i,3}$, it is given by

$$h_{\max}^{(1)} = \max_i \frac{2l_{i,1}l_{i,2}l_{i,3}}{\sqrt{(l_{i,1}+l_{i,2}+l_{i,3})(l_{i,1}+l_{i,2}-l_{i,3})(l_{i,1}+l_{i,3}-l_{i,2})(l_{i,2}+l_{i,3}-l_{i,1})}}.$$

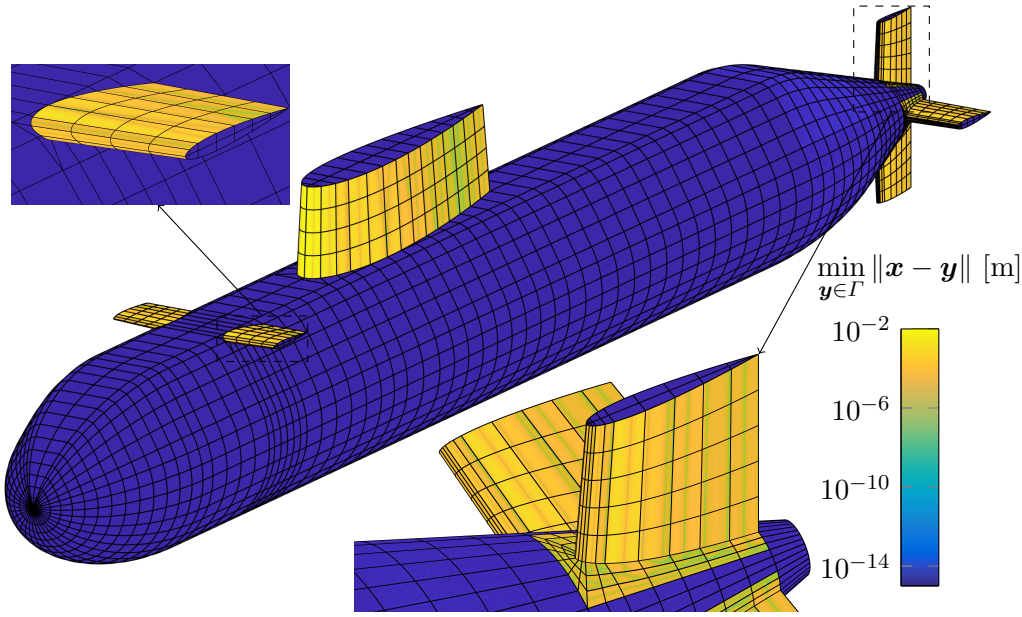

Figure D48: **An analysis suitable BeTSSi submarine**: The geometric surface approximation $\Gamma_{\check{p}}$ approximates the surface of the exact representation of the BeTSSi submarine Γ. Surface visualization of the mesh and geometric error for $\check{p} = 2$. Most parts of the approximation are exact to machine epsilon precision.

Table 9: **Triangularization of the BeTSSi submarine**: Data for the meshes.

Mesh	# triangles	# vertices	$h_{\max}^{(1)}$ [m]	$h_{\max}^{(2)}$ [m]	$R_{\max}$	$S_{\min}$
$\mathcal{M}_1^{\text{WTD}}$	4140	2072	2.109	1.893	28.4	0.0336
$\mathcal{M}_2^{\text{WTD}}$	10 406	5205	1.032	1.005	56.7	0.0168
$\mathcal{M}_3^{\text{WTD}}$	31 104	15 554	0.543	0.499	105.3	0.0091
$\mathcal{M}_4^{\text{WTD}}$	106 888	53 446	0.281	0.257	202.5	0.0047
$\mathcal{M}_5^{\text{WTD}}$	400 886	200 445	0.139	0.130	401.2	0.0024
$\mathcal{M}_6^{\text{WTD}}$	1 584 014	792 009	0.072	0.069	807.6	0.0012

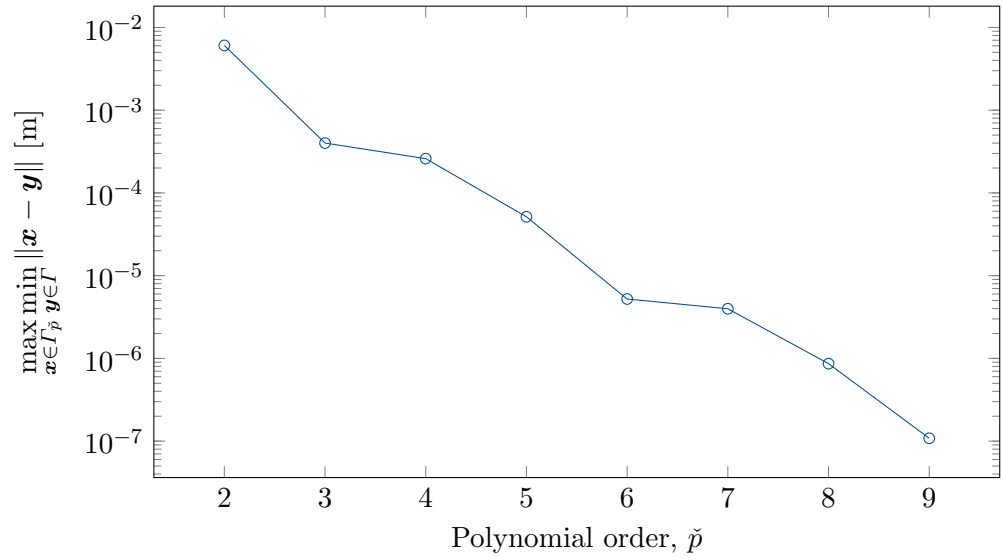

Figure D49: **An analysis suitable BeTSSi submarine**: The geometric surface approximation $\Gamma_{\check{p}}$ approximates the surface of the exact representation of the BeTSSi submarine Γ. Convergence plot showing exponential convergence to the exact geometry Γ.

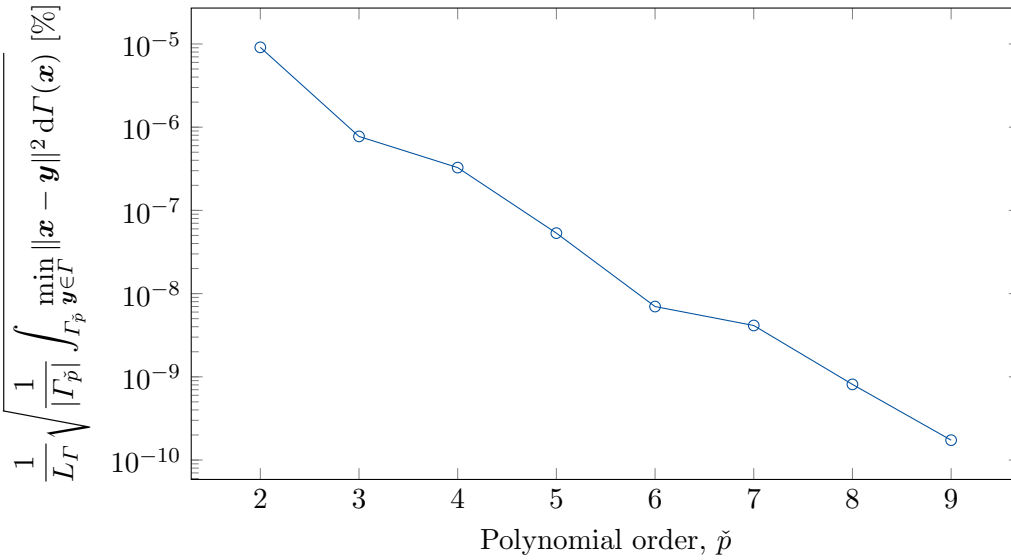

Figure D50: **An analysis suitable BeTSSi submarine**: Same as Figure D49 but in another norm. Here, the characteristic length of the geometry is given by $L_\Gamma = a + L + g_2 + g_3$.

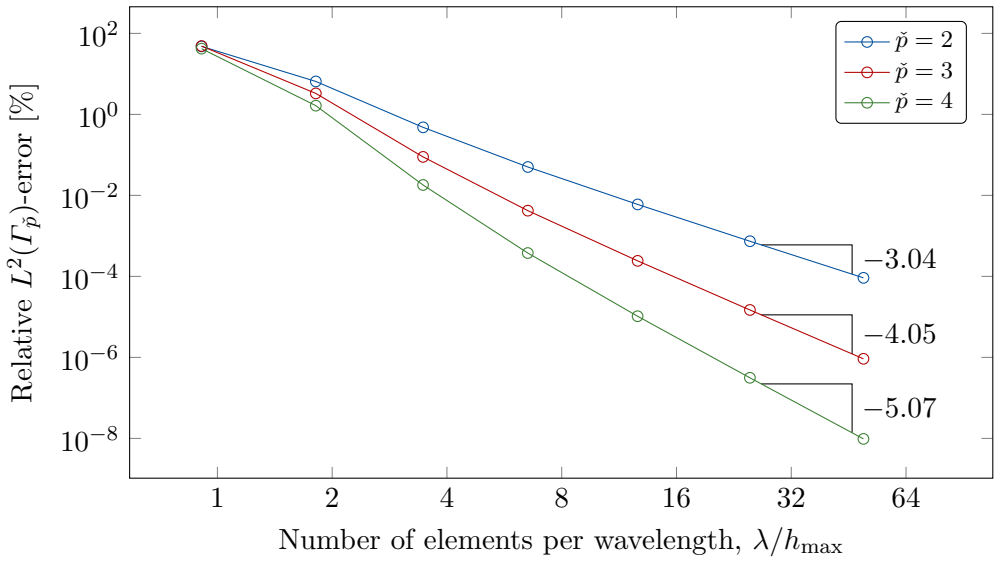

Figure D51: **An analysis suitable BeTSSi submarine**: Error of the best approximation for the manufactured solution presented in Subsection 6.6 on $\Gamma_{\check{p}}$.

Comsol Multiphysics® uses another common definition of the element size, namely the largest side length of the triangle

$$h_{\max}^{(2)} = \max_{i,j} l_{i,j}.$$

The three angles of a triangle may be computed by

$$\alpha_{i,1} = \cos^{-1}\left(\frac{l_{i,2}^2 + l_{i,3}^2 - l_{i,1}^2}{2 l_{i,2} l_{i,3}}\right), \quad \alpha_{i,2} = \cos^{-1}\left(\frac{l_{i,1}^2 + l_{i,3}^2 - l_{i,2}^2}{2 l_{i,1} l_{i,3}}\right)$$
$$\alpha_{i,3} = \cos^{-1}\left(\frac{l_{i,1}^2 + l_{i,2}^2 - l_{i,3}^2}{2 l_{i,1} l_{i,2}}\right),$$

such that the maximum and minimum angle are given by

$$\alpha_{\max} = \max_{i,j} \alpha_{i,j} \quad \text{and} \quad \alpha_{\min} = \min_{i,j} \alpha_{i,j},$$

respectively. The maximum aspect ratio is defined by

$$R_{\max} = \max_{i} \frac{\max_j l_{i,j}}{\min_j l_{i,j}}$$

and the minimum skewness is defined by

$$S_{\min} = \min_{i,j}\left[1 - \max\left(\frac{\alpha_{i,j} - \alpha_{\mathrm{e}}}{180° - \alpha_{\mathrm{e}}}, \frac{\alpha_{\mathrm{e}} - \alpha_{i,j}}{\alpha_{\mathrm{e}}}, \right)\right], \quad \alpha_{\mathrm{e}} = 60°.$$

The main take-away here is the inevitability of the increase in the aspect ratio (and the reduction in skewness) during refinement. This is because of the presence of non-Lipschitz domains.

References

[1] T. Hughes, J. Cottrell, Y. Bazilevs, Isogeometric analysis: CAD, finite elements, NURBS, exact geometry and mesh refinement, *Computer Methods in Applied Mechanics and Engineering*, 194:4135–4195 (2005).

[2] J. Cottrell, T. Hughes, Y. Bazilevs, *Isogeometric Analysis: Toward Integration of CAD and FEA*, Wiley, 2009.

[3] L. Beirão da Veiga, A. Buffa, J. Rivas, G. Sangalli, Some estimates for h–p–k-refinement in isogeometric analysis, *Numerische Mathematik*, 118:271–305 (2011).

[4] L. Beirão da Veiga, A. Buffa, G. Sangalli, R. Vázquez, Mathematical analysis of variational isogeometric methods, *Acta Numerica*, 23:157–287 (2014).

[5] R. Simpson, M. Scott, M. Taus, D. Thomas, H. Lian, Acoustic isogeometric boundary element analysis, *Computer Methods in Applied Mechanics and Engineering*, 269:265–290 (2014).

[6] S. Keuchel, N. C. Hagelstein, O. Zaleski, O. von Estorff, Evaluation of hypersingular and nearly singular integrals in the isogeometric boundary element method for acoustics, *Computer Methods in Applied Mechanics and Engineering*, 325:488–504 (2017).

[7] M. Peake, J. Trevelyan, G. Coates, Extended isogeometric boundary element method (XIBEM) for two-dimensional Helmholtz problems, *Computer Methods in Applied Mechanics and Engineering*, 259:93–102 (2013).

[8] M. Peake, Enriched and isogeometric boundary element methods for acoustic wave scattering, Ph.D. thesis, Durham University (2014).

[9] M. Peake, J. Trevelyan, G. Coates, Extended isogeometric boundary element method (XIBEM) for three-dimensional medium-wave acoustic scattering problems, *Computer Methods in Applied Mechanics and Engineering*, 284:762–780 (2015), Isogeometric Analysis Special Issue.

[10] L. Coox, O. Atak, D. Vandepitte, W. Desmet, An isogeometric indirect boundary element method for solving acoustic problems in open-boundary domains, *Computer Methods in Applied Mechanics and Engineering*, 316:186–208 (2017).

[11] M. F. Taus, Isogeometric analysis for boundary integral equations, Ph.D. thesis, The University of Texas at Austin (2015).

[12] J. Dölz, H. Harbrecht, M. Peters, An interpolation-based fast multipole method for higher-order boundary elements on parametric surfaces, *International Journal for Numerical Methods in Engineering*, 108:1705–1728 (2016).

[13] J. Dölz, H. Harbrecht, S. Kurz, S. Schöps, F. Wolf, A fast isogeometric BEM for the three dimensional Laplace- and Helmholtz problems, *Computer Methods in Applied Mechanics and Engineering*, 330:83–101 (2018).

[14] Y. Sun, J. Trevelyan, G. Hattori, C. Lu, Discontinuous isogeometric boundary element (IGABEM) formulations in 3D automotive acoustics, *Engineering Analysis with Boundary Elements*, 105:303–311 (2019).

[15] Y. Wu, C. Dong, H. Yang, Isogeometric indirect boundary element method for solving the 3D acoustic problems, *Journal of Computational and Applied Mathematics*, 363:273–299 (2020).

[16] A. Sommerfeld, *Partial differential equations in physics*, vol. 1, Academic press, 1949.

[17] J.-P. Berenger, A perfectly matched layer for the absorption of electromagnetic waves, *Journal of Computational Physics*, 114:185–200 (1994).

[18] J.-P. Berenger, Perfectly matched layer for the FDTD solution of wave-structure interaction problems, *IEEE Transactions on Antennas and Propagation*, 44:110–117 (1996).

[19] S. A. Sauter, C. Schwab, *Boundary Element Methods*, Springer Berlin Heidelberg, Berlin, Heidelberg, 2011, pp. 183–287.

[20] M. Schanz, O. Steinbach, *Boundary Element Analysis: Mathematical Aspects and Applications*, Lecture Notes in Applied and Computational Mechanics, Springer Berlin Heidelberg, 2007.

[21] S. Marburg, B. Nolte, *Computational Acoustics of Noise Propagation in Fluids-Finite and Boundary Element Methods*, vol. 578, Springer, 2008.

[22] S. N. Chandler-Wilde, I. G. Graham, S. Langdon, E. A. Spence, Numerical-asymptotic boundary integral methods in high-frequency acoustic scattering, *Acta Numerica*, 21:89–305 (2012).

[23] D. Givoli, *Numerical methods for problems in infinite domains*, vol. 33, Elsevier, 2013.

[24] J. J. Shirron, Solution of exterior Helmholtz problems using finite and infinite elements, Ph.D. thesis, University of Maryland College Park (1995).

[25] A. Bayliss, M. Gunzburger, E. Turkel, Boundary conditions for the numerical solution of elliptic equations in exterior regions, *SIAM Journal on Applied Mathematics*, 42:430–451 (1982).

[26] T. Hagstrom, S. Hariharan, A formulation of asymptotic and exact boundary conditions using local operators, *Applied Numerical Mathematics*, 27:403–416 (1998), Special Issue on Absorbing Boundary Conditions.

[27] R. Tezaur, A. Macedo, C. Farhat, R. Djellouli, Three-dimensional finite element calculations in acoustic scattering using arbitrarily shaped convex artificial boundaries, *International Journal for Numerical Methods in Engineering*, 53:1461–1476 (2001).

[28] P. Bettess, Infinite elements, *International Journal for Numerical Methods in Engineering*, 11:53–64 (1977).

[29] P. Bettess, O. C. Zienkiewicz, Diffraction and refraction of surface waves using finite and infinite elements, *International Journal for Numerical Methods in Engineering*, 11:1271–1290 (1977).

[30] F. Ihlenburg, *Finite Element Analysis of Acoustic Scattering*, vol. 132 of *Applied Mathematical Sciences*, Springer, New York, USA, 1998.

[31] W. S. Hwang, Hypersingular boundary integral equations for exterior acoustic problems, *The Journal of the Acoustical Society of America*, 101:3336–3342 (1997).

[32] Q. Sun, E. Klaseboer, B.-C. Khoo, D. Y. C. Chan, Boundary regularized integral equation formulation of the Helmholtz equation in acoustics, *Royal Society Open Science*, 2 (2015).

[33] C.-J. Zheng, H.-B. Chen, H.-F. Gao, L. Du, Is the Burton–Miller formulation really free of fictitious eigenfrequencies?, *Engineering Analysis with Boundary Elements*, 59:43–51 (2015).

[34] M. Scott, R. Simpson, J. Evans, S. Lipton, S. Bordas, T. Hughes, T. Sederberg, Isogeometric boundary element analysis using unstructured T-splines, *Computer Methods in Applied Mechanics and Engineering*, 254:197–221 (2013).

[35] Y. Liu, S. Chen, A new form of the hypersingular boundary integral equation for 3-D acoustics and its implementation with C^0 boundary elements, *Computer Methods in Applied Mechanics and Engineering*, 173:375–386 (1999).

[36] E. Klaseboer, Q. Sun, D. Y. C. Chan, Non-singular boundary integral methods for fluid mechanics applications, *Journal of Fluid Mechanics*, 696:468–478 (2012).

[37] J. Cottrell, A. Reali, Y. Bazilevs, T. Hughes, Isogeometric analysis of structural vibrations, *Computer Methods in Applied Mechanics and Engineering*, 195:5257–5296 (2006).

[38] M. Taus, G. J. Rodin, T. J. R. Hughes, Isogeometric analysis of boundary integral equations: High-order collocation methods for the singular and hypersingular equations, *Mathematical Models and Methods in Applied Sciences*, 26:1447–1480 (2016).

[39] M. G. Duffy, Quadrature over a pyramid or cube of integrands with a singularity at a vertex, *SIAM Journal on Numerical Analysis*, 19:1260–1262 (1982).

[40] S. A. Sauter, C. Schwab, Quadrature for *hp*-Galerkin BEM in $\mathbb{R}^3$, *Numerische Mathematik*, 78:211–258 (1997).

[41] J. V. Venås, T. Jenserud, Exact 3D scattering solutions for spherical symmetric scatterers, *Journal of Sound and Vibration*, 440:439–479 (2019).

[42] K. Gerdes, L. Demkowicz, Solution of 3D-Laplace and Helmholtz equations in exterior domains using *hp*-infinite elements, *Computer Methods in Applied Mechanics and Engineering*, 137:239–273 (1996).

[43] K. Gerdes, The conjugated vs. the unconjugated infinite element method for the Helmholtz equation in exterior domains, *Computer Methods in Applied Mechanics and Engineering*, 152:125–145 (1998).

[44] K. Gerdes, F. Ihlenburg, On the pollution effect in FE solutions of the 3D-Helmholtz equation, *Computer Methods in Applied Mechanics and Engineering*, 170:155–172 (1999).

[45] B. Nolte, I. Schäfer, C. de Jong, L. Gilroy, BeTSSi II benchmark on target strength simulation, in *Proceedings of Forum Acusticum*, 2014.

[46] Comsol Multiphysics® v. 5.4, `www.comsol.com`, COMSOL AB, Stockholm, Sweden.

[47] Matlab Release 2019a, `www.mathworks.com`, The MathWorks, Inc., Natick, Massachusetts, United States.

[48] G. Beer, I. Smith, C. Duenser, *The Boundary Element Method with Programming: For Engineers and Scientists*, Springer Vienna, 2008.

[49] J. V. Venås, T. Kvamsdal, T. Jenserud, Isogeometric analysis of acoustic scattering using infinite elements, *Computer Methods in Applied Mechanics and Engineering*, 335:152–193 (2018).

[50] H. Gomez, L. D. Lorenzis, The variational collocation method, *Computer Methods in Applied Mechanics and Engineering*, 309:152–181 (2016).

[51] C. J. Roy, Review of code and solution verification procedures for computational simulation, *Journal of Computational Physics*, 205:131–156 (2005).

[52] G. Fairweather, A. Karageorghis, P. Martin, The method of fundamental solutions for scattering and radiation problems, *Engineering Analysis with Boundary Elements*, 27:759–769 (2003), Special issue on Acoustics.

[53] H. A. Schenck, Improved integral formulation for acoustic radiation problems, *The Journal of the Acoustical Society of America*, 44:41–58 (1968).

[54] K. A. Johannessen, T. Kvamsdal, T. Dokken, Isogeometric analysis using LR B-splines, *Computer Methods in Applied Mechanics and Engineering*, 269:471–514 (2014).

[55] M. Kumar, T. Kvamsdal, K. A. Johannessen, Simple a posteriori error estimators in adaptive isogeometric analysis, *Computers & Mathematics with Applications*, 70:1555–1582 (2015).

[56] T. W. Wu, A. F. Seybert, A weighted residual formulation for the CHIEF method in acoustics, *The Journal of the Acoustical Society of America*, 90:1608–1614 (1991).

[57] J. V. Venås, Isogeometric analysis of acoustic scattering, Master's thesis, Norwegian University of Science and Technology, Trondheim, Norway (2015).

[58] J. E. Cobb, Tiling the sphere with rational Bézier patches, in *TR UUCS-88-009*, University of Utah USA, 1988.

[59] S. Lipton, J. Evans, Y. Bazilevs, T. Elguedj, T. Hughes, Robustness of isogeometric structural discretizations under severe mesh distortion, *Computer Methods in Applied Mechanics and Engineering*, 199:357–373 (2010), Computational Geometry and Analysis.

[60] L. Piegl, W. Tiller, *The NURBS book*, Springer Science & Business Media, 1997.

[61] C. L. Ladson, W. B. Jr. Cuyler, A. S. Hill, D. W. Sproles, Computer program to obtain ordinates for NACA airfoils, Tech. rep., NASA (1996).

[62] R. M. Cummings, W. H. Mason, S. A. Morton, D. R. McDaniel, *Geometry for aerodynamicists*, Cambridge Aerospace Series, Cambridge University Press, 2015, ch. Appendix A, pp. 731–765.

[63] M. A. Scott, T-splines as a design-through-analysis technology, Ph.D. thesis, The University of Texas at Austin (2011).

[64] J. V. Venås, Benchmark target strength simulation models (2019).

Paper IV

Isogeometric Kirchhoff Approximation using Numerical Steepest Descent

Jon Vegard Venås and Trond Kvamsdal

Work in progress

Isogeometric Kirchhoff Approximation using Numerical Steepest Descent

Jon Vegard Venås[a,*], Trond Kvamsdal[a]

[a] *Department of Mathematical Sciences, Norwegian University of Science and Technology, Alfred Getz' vei 1, 7034 Trondheim, Norway*

Abstract

The Kirchhoff approximation yields an accurate approximation of scattering problems on convex rigid bodies for high frequencies. The Kirchhoff–Helmholtz integral has usually been evaluated by discretizing the geometry by triangles, such that the integral may be evaluated exactly. However, this approach has frequency dependent accuracy and frequency dependent memory consumption. In this work, the integrals are evaluated numerically on the exact geometry using the method of numerical steepest descent. Both problems concerning the decreased accuracy and the increased memory consumption for higher frequencies are solved by this approach. The isogeoemtric framework eliminates the tessellation process and enables computations directly on the computer aided design (CAD) model.

1. Introduction

Acoustic scattering is a large field which has one of its application in the analysis of scattering on submarines. The scattering problem is by no means limited to submarines, as the physical phenomena occurs all around in nature. For instance, acoustic scattering may be used to calculate the number of fish in a fish farming net [1]. Moreover, the fluid to be analyzed is not limited to be water. For acoustic scattering problems, the Helmholtz equation represents the governing equation for the fluid medium. The same equation in vector form can govern electromagnetic waves (see [2]).

The problem at hand is time dependent. But we shall assume harmonic time dependency, such that all time dependent functions $\breve{F} = \breve{F}(\boldsymbol{x}, t)$ may be written as

$$\breve{F}(\boldsymbol{x}, t) = F(\boldsymbol{x})\mathrm{e}^{-\mathrm{i}\omega t} \tag{1}$$

*Corresponding author.
Email addresses: Jon.Venas@ntnu.no (J.V. Venås), Trond.Kvamsdal@ntnu.no (T. Kvamsdal).

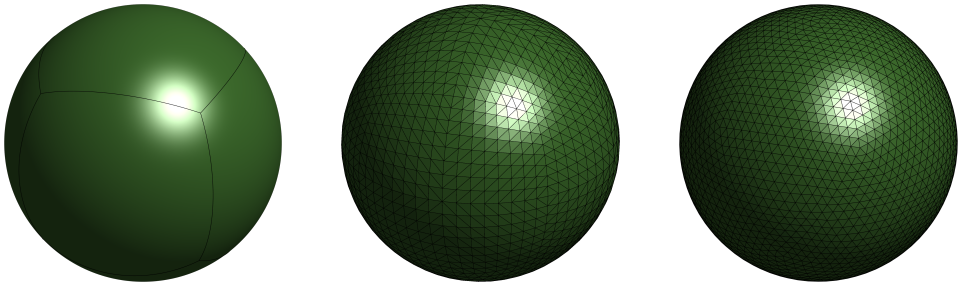

(a) Exact CAD model. (b) Triangulation with 3072 triangles. (c) Triangulation with 5120 triangles.

Figure 1: A CAD model often uses spline-based parametrization for modeling. Analysis are often made on an approximation of such a geometry. The surface of a sphere may be modeled by 6 patches using NURBS parametrizations.

where ω is the angular frequency and $\mathrm{i} = \sqrt{-1}$ the imaginary unit. This enables us to model the pressure p in the fluid with the Helmholtz equation given by

$$\nabla^2 p + k^2 p = 0 \tag{2}$$

with the wave number $k = \frac{\omega}{c_\mathrm{f}}$ (where c_f is the wave speed in the fluid). Other important quantities include the frequency $f = \frac{\omega}{2\pi}$ and the wavelength $\lambda = \frac{2\pi}{k}$.

By assuming the normal derivative of the total pressure at the boundary to be given by a physical optics approximation, the Kirchoff approximation enables efficient computation of the scattered pressure from objects. This approximation is best suited for smooth convex objects as edges and multiple reflections are not well approximated using this approach [3]. The Kirchhoff approximation has also been used to model problems in the time domain [3, 4]. For a more detailed introduction to this method, we refer to [5].

The geometry of the scatterer may be quite complex but is typically exactly represented using Non-Uniform Rational B-Splines (NURBS). This fact is one of the motivations of using the isogeometric analysis (IGA) concept as it uses the same functions as basis function for analysis. The sphere depicted in Figure 1a is an example of a geometry which has an exact representation using NURBS. A triangulation of such a geometry can easily be obtained by refining the CAD model, and then use the element corners as nodes for the triangulation as in Figure 1b. This may result in non-optimal triangulation as the triangles should be as close as possible to equilateral triangles of equal size (Figure 1c).

The approach of triangularization approximation has been used quite extensively in the BeTSSi[1] community [7–10] as the integration over triangles can be

[1]Benchmark Target Strength Simulation [6].

evaluated exactly. This approach is also taken in [11, 12]. As reported in [10] triangulating a submarine model for 30 kHz might result in a file size of several hundred GB. This is because the accuracy is frequency dependent when approximating the geometry. In [11] the integration was done using classical Gauss quadrature where they suggest the maximal point separation to be $\lambda/6$. A similar approach was taken in [13] where the maximal point separation was taken to be $\lambda/4$. This leads to computationally expensive calculations for high frequencies. An attempt to solve the problem of high memory consumption and low accuracy for high frequencies was made in [14] where a hybrid method was proposed using Gaussian quadrature on curvilinear facets. This approach seems to reduce the number of required facets by a significant amount (although still having frequency dependent accuracy). The main disadvantage is here arguably the requirement of tessellation of the CAD model into curvilinear facets.

In this work we will take the approach of using the exact geometry and using the numerical steepest descent to perform highly oscillatory integration, which is an attempt to solve the two problems of memory and accuracy dependency of large frequencies in addition to avoiding the tessellation process altogether using the IGA framework. The advantages of using curvilinear facets are covered indirectly in this work as one can choose to use classical Gauss-Legendre quadrature (on a refined IGA mesh) to evaluate the oscillatory integrals instead of the numerical steepest descent.

The integrals investigated in this work are related to the boundary integrals used in the boundary element method (BEM). Especially the approach by Peake et al. [15] where the NURBS basis functions are enriched with oscillatory plane waves. Peake evaluated the resulting integral using high order Gauss Legendre quadrature, which will be the bottleneck for high frequencies. This work sets a foundation for solving this problem using NSD.

The problem of highly oscillatory integration has long been an active research area. Especially integrals of the form

$$I[f, \Omega] = \int_{\Omega} f(\boldsymbol{x}) \mathrm{e}^{\mathrm{i}\omega g(\boldsymbol{x})} \, \mathrm{d}\Omega \tag{3}$$

are of major interest. Here $\Omega \subset \mathbb{R}^d$ is usually a bounded open domain with piece-wise smooth boundary, while the *amplitude function* f and the *oscillator* g are smooth. The integral in Eq. (3), is highly oscillatory for large values of $\omega \in \mathbb{R}$. Integration of such highly oscillatory integrals using classical Gaussian quadrature becomes prohibitively computationally expensive for large ω, and one should resort to other methods. Alternative methods such as asymptotic methods and Filon-type methods [16–18], Levin-type methods [19, 20], numerical steepest descent [21, 22], complex Gaussian quadrature [23, 24] have attained great interest during the last decade and we refer to the book by Deaño et al. [22] for more details.

In Section 2 we start by briefly presenting the Kirchhoff approximation, and continue by presenting the numerical steepest descent in Section 3. Numerical examples are presented in Section 4 followed by the conclusions in Section 5.

2. Kirchhoff approximation

The exterior Helmholtz problem is given by

$$\nabla^2 p + k^2 p = 0 \qquad \text{in} \quad \Omega^+, \tag{4}$$

$$\partial_n p = g \qquad \text{on} \quad \Gamma, \tag{5}$$

$$\frac{\partial p}{\partial r} - \mathrm{i}kp = o\Big(r^{-1}\Big) \quad \text{with} \quad r = |\boldsymbol{x}| \tag{6}$$

where the Sommerfeld condition in Eq. (6) restricts the field uniformly in $\hat{\boldsymbol{x}} = \frac{\boldsymbol{x}}{r}$, such that no waves originate from infinity.

By Kirchhoff's integral theorem we have (cf. [25, Theorem 2.21])

$$p(\boldsymbol{x}) = \int_\Gamma \left[p(\boldsymbol{y}) \frac{\partial \Phi_k(\boldsymbol{x},\boldsymbol{y})}{\partial n(\boldsymbol{y})} - \Phi_k(\boldsymbol{x},\boldsymbol{y}) \frac{\partial p(\boldsymbol{y})}{\partial n(\boldsymbol{y})} \right] \mathrm{d}\Gamma(\boldsymbol{y}) \tag{7}$$

where $\boldsymbol{y}$ is a point on the surface Γ, $\boldsymbol{n}$ lies on Γ pointing "into" Ω^+ at $\boldsymbol{y}$ and Φ_k is the free space Green's function for the Helmholtz equation in Eq. (4) given (in 3D) by

$$\Phi_k(\boldsymbol{x},\boldsymbol{y}) = \frac{\mathrm{e}^{\mathrm{i}kR}}{4\pi R}, \quad \text{where} \quad R = |\boldsymbol{x}-\boldsymbol{y}|. \tag{8}$$

The derivative of Green's function is given by

$$\frac{\partial \Phi_k(\boldsymbol{x},\boldsymbol{y})}{\partial n(\boldsymbol{y})} = \frac{\Phi_k(\boldsymbol{x},\boldsymbol{y})}{R}(\mathrm{i}kR - 1)\frac{\partial R}{\partial n(\boldsymbol{y})}, \quad \text{where} \quad \frac{\partial R}{\partial n(\boldsymbol{y})} = -\frac{(\boldsymbol{x}-\boldsymbol{y})\cdot \boldsymbol{n}(\boldsymbol{y})}{R}.$$

Moreover, for an incident wave p_{inc} satisfying the Helmholtz equation we have (using [25, Theorem 2.20])

$$\int_\Gamma \left[p_{\mathrm{inc}}(\boldsymbol{y}) \frac{\partial \Phi_k(\boldsymbol{x},\boldsymbol{y})}{\partial n(\boldsymbol{y})} - \Phi_k(\boldsymbol{x},\boldsymbol{y}) \frac{\partial p_{\mathrm{inc}}(\boldsymbol{y})}{\partial n(\boldsymbol{y})} \right] \mathrm{d}\Gamma(\boldsymbol{y}) = 0.$$

Thus, we can write Eq. (7) in terms of the total pressure $p_{\mathrm{tot}} = p + p_{\mathrm{inc}}$

$$p(\boldsymbol{x}) = \int_\Gamma \left[p_{\mathrm{tot}}(\boldsymbol{y}) \frac{\partial \Phi_k(\boldsymbol{x},\boldsymbol{y})}{\partial n(\boldsymbol{y})} - \Phi_k(\boldsymbol{x},\boldsymbol{y}) \frac{\partial p_{\mathrm{tot}}(\boldsymbol{y})}{\partial n(\boldsymbol{y})} \right] \mathrm{d}\Gamma(\boldsymbol{y}) \tag{9}$$

For rigid scattering with $\partial_n p_{\mathrm{tot}} = 0$ we therefore have

$$p(\boldsymbol{x}) = \int_\Gamma p_{\mathrm{tot}}(\boldsymbol{y}) \frac{\partial \Phi_k(\boldsymbol{x},\boldsymbol{y})}{\partial n(\boldsymbol{y})} \mathrm{d}\Gamma(\boldsymbol{y}) \tag{10}$$

The *far field pattern* for the scattered pressure p, is defined by

$$p_0(\hat{\boldsymbol{x}}) = \lim_{r\to\infty} r\mathrm{e}^{-\mathrm{i}kr} p(r\hat{\boldsymbol{x}}), \tag{11}$$

with $r = |\boldsymbol{x}|$ and $\hat{\boldsymbol{x}} = \boldsymbol{x}/|\boldsymbol{x}|$. Using the limits

$$\begin{aligned} \lim_{r\to\infty} r\mathrm{e}^{-\mathrm{i}kr} \Phi_k(r\hat{\boldsymbol{x}}, \boldsymbol{y}) &= \frac{1}{4\pi}\mathrm{e}^{-\mathrm{i}k\hat{\boldsymbol{x}}\cdot\boldsymbol{y}} \\ \lim_{r\to\infty} r\mathrm{e}^{-\mathrm{i}kr} \frac{\partial \Phi_k(r\hat{\boldsymbol{x}}, \boldsymbol{y})}{\partial n(\boldsymbol{y})} &= -\frac{\mathrm{i}k}{4\pi}\mathrm{e}^{-\mathrm{i}k\hat{\boldsymbol{x}}\cdot\boldsymbol{y}} \hat{\boldsymbol{x}}\cdot\boldsymbol{n}(\boldsymbol{y}) \end{aligned} \tag{12}$$

the formula in Eq. (7) simplifies in the far field to (cf. [26, p. 32])

$$p_0(\hat{\boldsymbol{x}}) = -\frac{1}{4\pi}\int_\Gamma \left[\mathrm{i}kp(\boldsymbol{y})\hat{\boldsymbol{x}}\cdot\boldsymbol{n}(\boldsymbol{y}) + \frac{\partial p(\boldsymbol{y})}{\partial n(\boldsymbol{y})}\right]\mathrm{e}^{-\mathrm{i}k\hat{\boldsymbol{x}}\cdot\boldsymbol{y}}\,\mathrm{d}\Gamma(\boldsymbol{y}). \tag{13}$$

For rigid scattering this is simplified to (from Eq. (10))

$$p_0(\hat{\boldsymbol{x}}) = -\frac{\mathrm{i}k}{4\pi}\int_\Gamma p_{\mathrm{tot}}(\boldsymbol{y})\hat{\boldsymbol{x}}\cdot\boldsymbol{n}(\boldsymbol{y})\mathrm{e}^{-\mathrm{i}k\hat{\boldsymbol{x}}\cdot\boldsymbol{y}}\,\mathrm{d}\Gamma(\boldsymbol{y}). \tag{14}$$

From the far field pattern, the *target strength*, TS, can be computed. It is defined by

$$\mathrm{TS} = 20\log_{10}\left(\frac{|p_0(\hat{\boldsymbol{x}})|}{|P_{\mathrm{inc}}|}\right) \tag{15}$$

where P_{inc} is the amplitude of the incident wave at the geometric center of the scatterer (i.e. the origin). Since the amplitude of the scattered pressure is proportional to the amplitude of the incident wave (due to the linearity of the Helmholtz equation), TS is independent of P_{inc}.

Kirchoff's diffraction formula is derived by assuming the values of p and $\partial_n p$ to be known at the boundary [3]. The value for the pressure p at the boundary Γ can be modeled by physical optics approximation [25, p. 147]. In this case, we have

$$p_{\mathrm{tot}} = \begin{cases} 2p_{\mathrm{inc}} & \text{on illuminated sides} \\ 0 & \text{on sides in shadow.} \end{cases}$$

By considering plane waves

$$p_{\mathrm{inc}} = P_{\mathrm{inc}}\mathrm{e}^{\mathrm{i}k\boldsymbol{d}_{\mathrm{s}}\cdot\boldsymbol{x}} \tag{16}$$

and defining Γ_{i} as the illuminated sides of Γ, Eq. (14) is then reduced to

$$p_0(\hat{\boldsymbol{x}}) \approx -\frac{\mathrm{i}kP_{\mathrm{inc}}}{2\pi}\int_{\Gamma_{\mathrm{i}}} \hat{\boldsymbol{x}}\cdot\boldsymbol{n}(\boldsymbol{y})\mathrm{e}^{\mathrm{i}k(\boldsymbol{d}_{\mathrm{s}}-\hat{\boldsymbol{x}})\cdot\boldsymbol{y}}\,\mathrm{d}\Gamma(\boldsymbol{y}). \tag{17}$$

For monostatic scattering we have $\boldsymbol{d}_{\mathrm{s}} = -\hat{\boldsymbol{x}}$, such that

$$p_0(\hat{\boldsymbol{x}}) \approx -\frac{\mathrm{i}kP_{\mathrm{inc}}}{2\pi}\int_{\Gamma_{\mathrm{i}}} \hat{\boldsymbol{x}}\cdot\boldsymbol{n}(\boldsymbol{y})\mathrm{e}^{-2\mathrm{i}k\hat{\boldsymbol{x}}\cdot\boldsymbol{y}}\,\mathrm{d}\Gamma(\boldsymbol{y}). \tag{18}$$

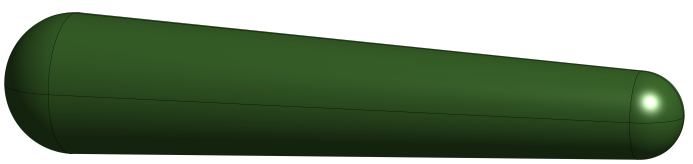

(a) The BeTSSi model 3

(b) The BeTSSi model 4

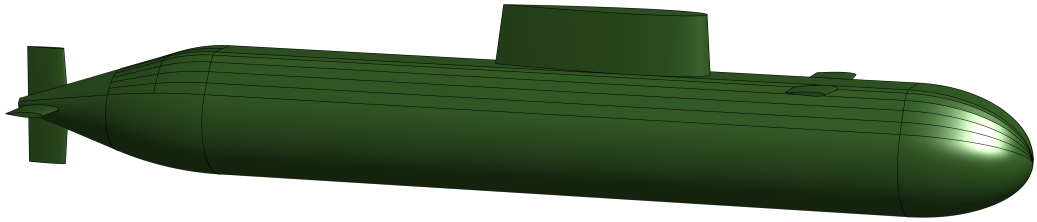

(c) The BeTSSi submarine

Figure 2: The BeTSSi model 3 is described and analyzed in [27] and the BeTSSi submarine is described and analyzed in [28].

In Figure 3 we illustrate the impact the convexity of a geometry has on two of the BeTSSi models [6] visualized in Figure 2. The reference solutions are computed by the ASIGA[2] library. The BeTSSi model 3 is nearly convex while the BeTSSi submarine is not. Despite this, good results are obtained for the BeTSSi submarine considering the simplicity of the Kirchhoff approximation method. The BEM simulation on the BeTSSi submarine was computed with 59 488 elements with basis functions of 6^{th} degree (resulting in 124 113 degrees of freedom) with the Burton-Miller formulation. The simulation used 126 650 seconds, and the Kirchhoff diffraction theory (KDT) simulation (with GL quadrature on IGA mesh) uses only 60 seconds on the same IGA mesh. This is reasonable since the complexity of a BEM solver is at least $\mathcal{O}(n_{\text{el}}^2)$ whereas the complexity of the KDT solver is only $\mathcal{O}(n_{\text{el}})$ assuming a given number of elements are needed for a given frequency and accuracy. Due to the exponential decay of the error in the numerical integration using Gauss–Legendre quadrature far less elements are needed for the KDT simulation compared to finite/boundary element methods (with algebraic convergence rates). The KDT simulation on only 3718 elements using $(\check{p}+1)^2 = 49$ GL points per element yields visually indistinguishable results for the BeTSSi submarine simulation with a computational timing of only a few seconds (not shown in Figure 3).

For the BeTSSi model 4 the results deviate much more as can be seen in Figure 4.

[2]The ASIGA (Acoustic Scattering with IsoGeometric Analysis) library can be found at https://github.com/Zetison/ASIGA.

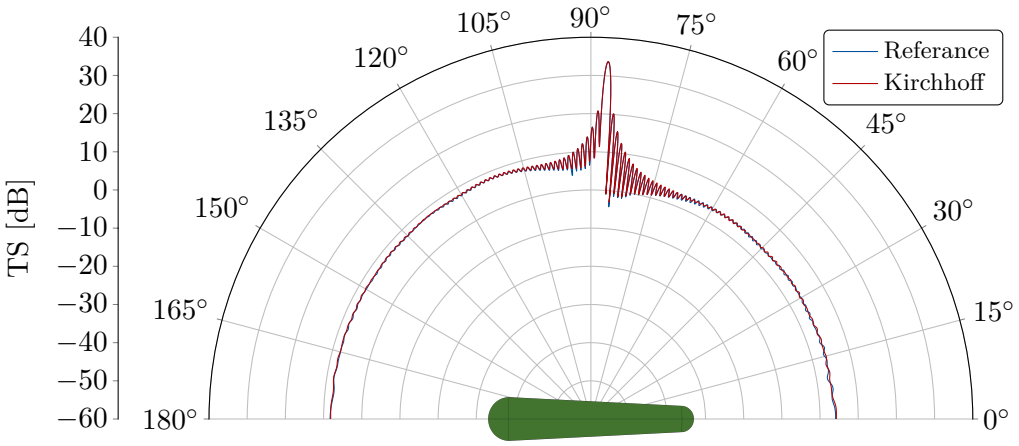

(a) The BeTSSi model 3

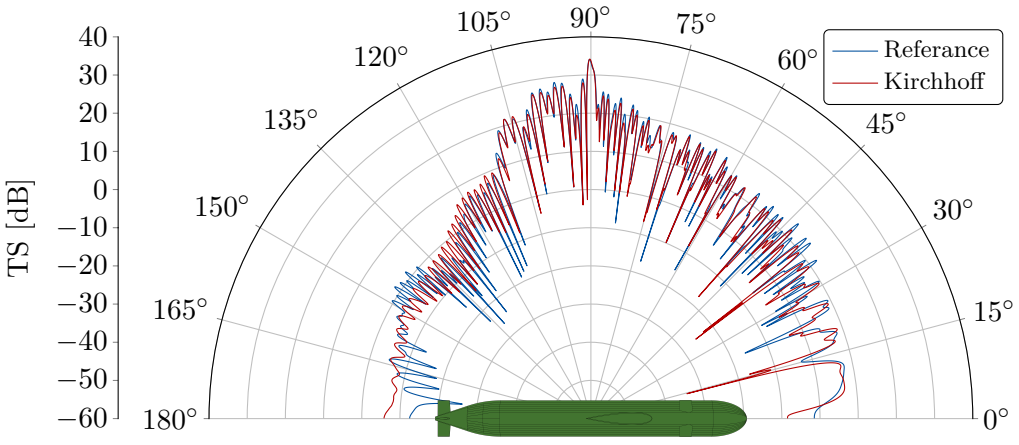

(b) The BeTSSi submarine

Figure 3: **Rigid scattering on BeTSSi models**: Comparison of the monostatic target strength (Eq. (15)) for the Kirchhoff approximation (Eq. (32)) and IGABEM reference solutions. The Kirchhoff approximation is obtained by classical Gauss-Legendre integration. This benchmark is one of the BeTSSi test cases with elevation angle $\beta_s = 0°$ and frequency $f = 1\,\mathrm{kHz}$.

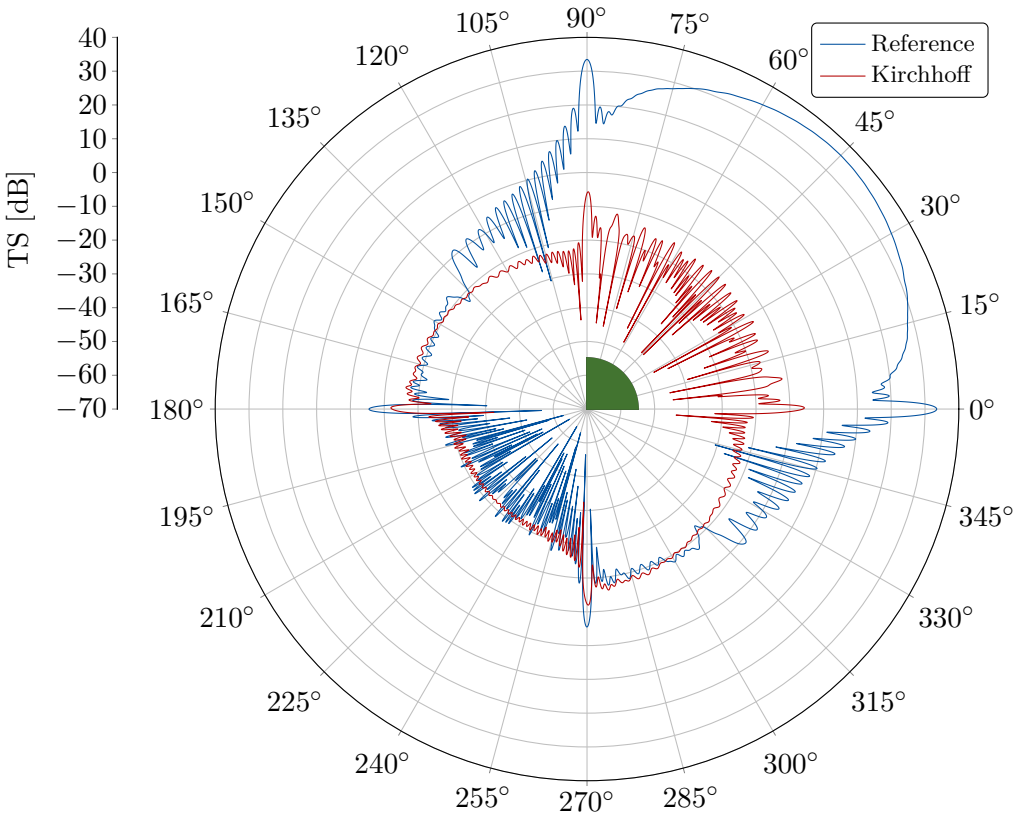

Figure 4: **Rigid scattering on BeTSSi model 4**: Comparison of the monostatic target strength (Eq. (15)) for the Kirchhoff approximation (Eq. (32)) and a IGABEM reference solution. The Kirchhoff approximation is obtained by classical Gauss-Legendre integration. This benchmark is one of the BeTSSi test cases with elevation angle $\beta_\mathrm{s} = 30°$ and frequency $f = 10\,\mathrm{kHz}$.

This model is a corner reflector which yields high TS for aspect angles that "sees" this corner (i.e. $\alpha, \beta \in (0, 90°)$). Since Kirchhoff approximation does not handle multiple reflections, this domain yields particularly large discrepancies.

If the domain Γ_i is polygonal and the boundary of Γ_i lies on polygonal edges, the integrals in Eqs. (17) and (18) can be exactly evaluated by subdividing each polygon into triangles and using barycentric coordinates. On each triangle $\Gamma_{\mathrm{i},n}$ the barycentric coordinates are given by

$$\boldsymbol{y} = \boldsymbol{y}(\xi_1, \xi_2) = (\boldsymbol{P}_{n,1} - \boldsymbol{P}_{n,3})\xi_1 + (\boldsymbol{P}_{n,2} - \boldsymbol{P}_{n,3})\xi_2 + \boldsymbol{P}_{n,3} \tag{19}$$

where $\boldsymbol{P}_i$ are the corners of the triangle. Then the integral in Eq. (18) may be

written as

$$
\begin{aligned}
p_0(\hat{\boldsymbol{x}}) &\approx -\frac{\mathrm{i}kP_{\mathrm{inc}}}{\pi}\sum_{n=1}^{N}|\Gamma_{\mathrm{i},n}|\int_0^1\int_0^{1-\xi_1}\hat{\boldsymbol{x}}\cdot\boldsymbol{n}_n\mathrm{e}^{-2\mathrm{i}k\hat{\boldsymbol{x}}\cdot\boldsymbol{y}}\,\mathrm{d}\xi_2\,\mathrm{d}\xi_1\\
&= -\frac{\mathrm{i}kP_{\mathrm{inc}}}{\pi}\sum_{n=1}^{N}|\Gamma_{\mathrm{i},n}|\hat{\boldsymbol{x}}\cdot\boldsymbol{n}_n\int_0^1\int_0^{1-\xi_1}\mathrm{e}^{D_{n,0}+D_{n,1}\xi_1+D_{n,2}\xi_2}\,\mathrm{d}\xi_2\,\mathrm{d}\xi_1\\
&= -\frac{\mathrm{i}kP_{\mathrm{inc}}}{\pi}\sum_{n=1}^{N}|\Gamma_{\mathrm{i},n}|\hat{\boldsymbol{x}}\cdot\boldsymbol{n}_n g(D_{n,1},D_{n,2})\mathrm{e}^{D_{n,0}} \qquad (20)
\end{aligned}
$$

with

$$
\begin{aligned}
g(D_{n,1},D_{n,2}) &= \int_0^1\int_0^{1-\xi_1}\mathrm{e}^{D_{n,1}\xi_1+D_{n,2}\xi_2}\,\mathrm{d}\xi_2\,\mathrm{d}\xi_1\\
&= \frac{D_{n,1}(1-\mathrm{e}^{D_{n,2}})+D_{n,2}(\mathrm{e}^{D_{n,1}}-1)}{D_{n,1}D_{n,2}(D_{n,1}-D_{n,2})}
\end{aligned}
$$

$$
\begin{aligned}
D_{n,0} &= -2\mathrm{i}k\hat{\boldsymbol{x}}\cdot\boldsymbol{P}_{n,3}\\
D_{n,1} &= -2\mathrm{i}k\hat{\boldsymbol{x}}\cdot(\boldsymbol{P}_{n,1}-\boldsymbol{P}_{n,3})\\
D_{n,2} &= -2\mathrm{i}k\hat{\boldsymbol{x}}\cdot(\boldsymbol{P}_{n,2}-\boldsymbol{P}_{n,3}).
\end{aligned}
$$

Note that

$$
\begin{aligned}
\lim_{D_{n,1}\to 0} g(D_{n,1},D_{n,2}) &= -\frac{1}{D_{n,2}^2}\Big(1+D_{n,2}-\mathrm{e}^{D_{n,2}}\Big),\\
\lim_{D_{n,2}\to 0} g(D_{n,1},D_{n,2}) &= -\frac{1}{D_{n,1}^2}\Big(1+D_{n,1}-\mathrm{e}^{D_{n,1}}\Big),\\
\lim_{D_{n,1},D_{n,2}\to 0} g(D_{n,1},D_{n,2}) &= \frac{1}{2},\\
\lim_{D_{n,1}\to D_{n,2}} g(D_{n,1},D_{n,2}) &= \frac{1}{D_{n,2}^2}\Big(1-\mathrm{e}^{D_{n,2}}+D_{n,2}\mathrm{e}^{D_{n,2}}\Big).
\end{aligned}
$$

If Γ_{i} does not lie on polygonal edges, some geometric errors are introduced which goes to zero when $h_{\max}\to 0$. Usually, Γ is not only represented by polygonal surfaces. However, using a tessellation of the model where this approach can be employed is the most common way of using Kirchhoff approximation.

3. Numerical steepest descent

Consider first the one-dimensional case of the oscillatory integral in Eq. (3). To illustrate the technique of numerical steepest descent we consider the integral

$$
I = \int_a^b f(x)\mathrm{e}^{\mathrm{i}\omega g(x)}\,\mathrm{d}x. \qquad (21)
$$

This integral is highly oscillatory for large values of ω and non-constant oscillator g due to the exponential factor $\mathrm{e}^{\mathrm{i}\omega g(x)}$. However, this factor is not oscillatory along paths $z = h_x(p)$ (parameterized with the parameter p) in the complex plane satisfying

$$g(h_x(p)) = \mathrm{i}p + g(x) \tag{22}$$

This is because, for a given x we have $\mathrm{e}^{\mathrm{i}\omega g(z)} = \mathrm{e}^{-\omega p}\mathrm{e}^{\mathrm{i}\omega g(x)}$, and the factor $\mathrm{e}^{-\omega p}$ is not oscillatory. In fact, it is exponentially decaying in the complex plane. The idea of numerical steepest descent is to evaluate the oscillatory integral along such paths in the complex plane. For the case of no stationary points where $g'(z) = 0$ Theorem 2.1 in [29] states that the integral in Eq. (21) may be decomposed as

$$I = F(a) - F(b) + \mathcal{O}(\mathrm{e}^{-\omega d_0})$$

where (with the substitution $p = q/\omega$)

$$F(\xi) = \int_0^\infty f(h_\xi(p))\mathrm{e}^{\mathrm{i}\omega(g(\xi)+\mathrm{i}p)}h'_\xi(p)\,\mathrm{d}p \tag{23}$$

$$= \frac{\mathrm{e}^{\mathrm{i}\omega g(\xi)}}{\omega}\int_0^\infty f(h_\xi(q/\omega))\mathrm{e}^{-q}h'_\xi(q/\omega)\,\mathrm{d}q. \tag{24}$$

Consider now stationary points $z = \xi$ of order r (that is, $g'(\xi) = g''(\xi) = \cdots = g^{(r)}(\xi) = 0$ and $g^{(r+1)}(\xi) \neq 0$). Since the inverse of g is multivalued around these points, several paths $h_{\xi,j}$, $j = 0, \ldots, r$, exists that all satisfy Eq. (22). Using a Taylor expansion of $g(z)$ around $z = \xi$ yields

$$h_{\xi,j}(p) \sim \xi + \sqrt[r+1]{\mathrm{i}\frac{(r+1)!p}{g^{(r+1)}(\xi)}}, \qquad h'_{\xi,j}(p) \sim \frac{1}{r+1}\sqrt[r+1]{\mathrm{i}\frac{(r+1)!}{g^{(r+1)}(\xi)}}p^{\frac{1}{r+1}-1}.$$

That is if we have a stationary point at $z = \xi$ of order r the substitution introduces weakly singular behavior near the real axis. This can be handled by a generalized Gauss Laguerre quadrature as explained in [29].

Alternatively, Freud-type Gaussian (GF) quadrature may be applied. With an additional substitution $q = u^{r+1}$ we get

$$h_{\xi,j}(p) \sim \xi + \sqrt[r+1]{\mathrm{i}\frac{(r+1)!}{\omega g^{(r+1)}(\xi)}}u, \qquad h'_{\xi,j}(p) \sim \frac{\omega}{r+1}\sqrt[r+1]{\mathrm{i}\frac{(r+1)!}{\omega g^{(r+1)}(\xi)}}u^{-r} \tag{25}$$

since $\mathrm{d}q = (r+1)u^r\mathrm{d}u$ the function $F_j(\xi)$ in Eq. (23) may be written as

$$F_j(\xi) = \frac{(r+1)\mathrm{e}^{\mathrm{i}\omega g(\xi)}}{\omega}\int_0^\infty f(h_{\xi,j}(u^{r+1}/\omega))\mathrm{e}^{-u^{r+1}}h'_{\xi,j}(u^{r+1}/\omega)u^r\,\mathrm{d}u.$$

The factor u^r effectively cancels the singular behavior of $h'_{\xi,j}(p)$ in Eq. (25).

For the case $f(x) = x^n$ and $g(x) = x^m$, the integral in Eq. (21) can be expressed in terms of the (upper) incomplete gamma function (for integer m)

$$\int_0^1 x^n \mathrm{e}^{\mathrm{i}\omega x^m}\,\mathrm{d}x = \frac{1}{m(-\mathrm{i}\omega)^{\frac{n+1}{m}}}\left[\Gamma\Big(\frac{n+1}{m},0\Big) - \Gamma\Big(\frac{n+1}{m},-\mathrm{i}\omega\Big)\right]$$

where

$$\Gamma(s,z) = \int_z^\infty t^{s-1}\mathrm{e}^{-t}\,\mathrm{d}t$$

is implemented in MATLAB as `igamma(s,z)`. For integer n and $m = 1$ we have

$$\Gamma(n+1,z) = \mathrm{e}^{-z}\sum_{m=0}^{n}\frac{n!}{m!}z^m$$

such that

$$\int_0^1 x^n \mathrm{e}^{\mathrm{i}\omega x}\,\mathrm{d}x = \frac{1}{(-\mathrm{i}\omega)^{n+1}}\left[n! - \mathrm{e}^{\mathrm{i}\omega}\sum_{m=0}^{n}\frac{n!}{m!}(-\mathrm{i}\omega)^m\right].$$

With $g(z) = z$ we have the two paths $h_0(p) = \mathrm{i}p$ and $h_1(p) = \mathrm{i}p + 1$ starting from $z = 0$ and $z = 1$, respectively. Along these paths we have $z = h_x(p)$ and $\mathrm{d}z = h_x'(p)\,\mathrm{d}p = \mathrm{i}\,\mathrm{d}p$. Such that the integral in Eq. (21) may be decomposed as

$$\begin{aligned}
I_1 &= \int_0^1 x^n \mathrm{e}^{\mathrm{i}\omega x}\,\mathrm{d}x \\
&= \mathrm{e}^{\mathrm{i}\omega g(0)}\int_0^\infty f(h_0(p))\mathrm{e}^{-\omega p}h_0'(p)\,\mathrm{d}p - \mathrm{e}^{\mathrm{i}\omega g(1)}\int_0^\infty f(h_1(p))\mathrm{e}^{-\omega p}h_1'(p)\,\mathrm{d}p \\
&= \int_0^\infty \mathrm{i}(\mathrm{i}p)^n\mathrm{e}^{-\omega p}\,\mathrm{d}p - \mathrm{e}^{\mathrm{i}\omega}\int_0^\infty \mathrm{i}(\mathrm{i}p+1)^n\mathrm{e}^{-\omega p}\,\mathrm{d}p \\
&= \frac{\mathrm{i}}{\omega}\left[\int_0^\infty (\mathrm{i}q/\omega)^n\mathrm{e}^{-q}\,\mathrm{d}q - \mathrm{e}^{\mathrm{i}\omega}\int_0^\infty (\mathrm{i}q/\omega+1)^n\mathrm{e}^{-q}\,\mathrm{d}q\right].
\end{aligned}$$

The generalized Gauss-Laguerre (GGL) quadrature rule integrates the integral

$$\int_0^\infty \tilde{f}(q)x^\alpha\mathrm{e}^{-q}\,\mathrm{d}q, \quad \alpha = -\frac{r}{r+1}$$

exactly for polynomials $\tilde{f}(q)$ of order up to $2n_{\mathrm{qp}} - 1$, and so we should expect exact results whenever $n \leqslant 2n_{\mathrm{qp}} - 1$. This is indeed observed in Figure 5.

Consider now the case $m = 2$. The paths are then given by $h_x(p) = \pm\sqrt{\mathrm{i}p + x^2}$. For the point $x = 1$ the sign must be chosen to satisfy $h_1(0) = 1$. Thus, the path starting from $z = 1$ is given by $h_1(p) = \sqrt{\mathrm{i}p + 1}$. For the point $x = 0$ each of the signs satisfy $h_0(0) = 0$, and must be chosen such that this paths share the same branch as the path from $x = 1$. Hence, the path starting from $z = 0$ is given by $h_0(p) = \sqrt{\mathrm{i}p}$. In Figure 6 these paths are visualized on top of a contour plot of $\mathrm{Im}(\mathrm{i}g(z)) = (\mathrm{Re}\,z)^2 - (\mathrm{Im}\,z)^2$. Along these two paths we have $z = h_x(p)$ and

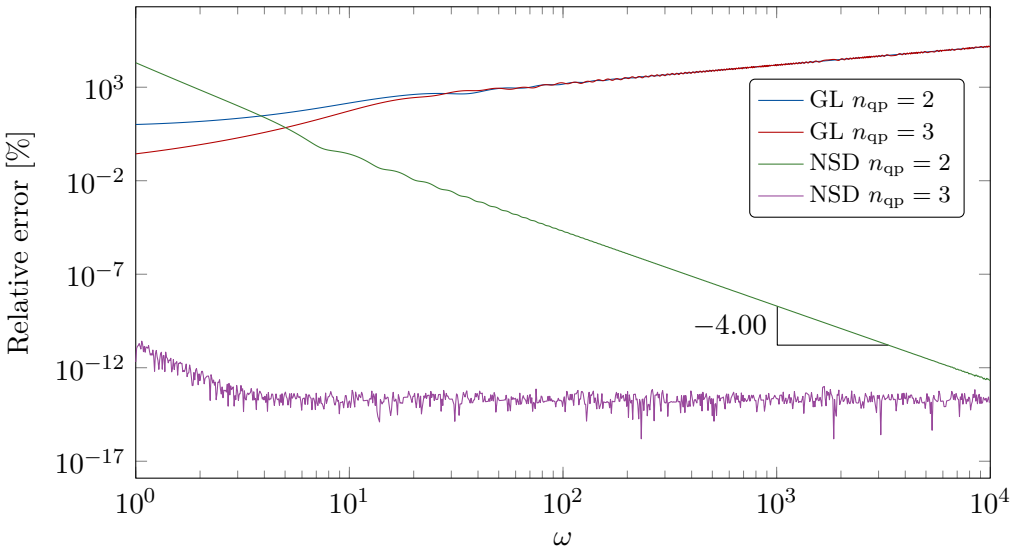

Figure 5: **Numerical steepest descent**: The relative numerical error of the NSD and Gauss Legendre quadrature applied to the integral I_1 with $n = 5$. Machine epsilon results is expected for the NSD when using $n_{\mathrm{qp}} = 3$. Correct convergence rate of $-2n_{\mathrm{qp}} - \alpha = -4$ is observed when using $n_{\mathrm{qp}} = 2$ (note that $\alpha = 0$ for I_1).

$\mathrm{d}z = h_x'(p)\,\mathrm{d}p = \mathrm{i}/2(\mathrm{i}p + x^2)^{-1/2}\,\mathrm{d}p$. Such that the integral in Eq. (21) may be decomposed as

$$
\begin{aligned}
I_2 &= \int_0^1 x^n \mathrm{e}^{\mathrm{i}\omega x^2}\,\mathrm{d}x \\
&= \mathrm{e}^{\mathrm{i}\omega g(0)} \int_0^\infty f(h_0(p))\mathrm{e}^{-\omega p} h_0'(p)\,\mathrm{d}p - \mathrm{e}^{\mathrm{i}\omega g(1)} \int_0^\infty f(h_1(p))\mathrm{e}^{-\omega p} h_1'(p)\,\mathrm{d}p \\
&= \int_0^\infty \frac{\mathrm{i}}{2}(\mathrm{i}p)^{n/2-1/2}\mathrm{e}^{-\omega p}\,\mathrm{d}p - \mathrm{e}^{\mathrm{i}\omega} \int_0^\infty \frac{\mathrm{i}}{2}(\mathrm{i}p+1)^{n/2-1/2}\mathrm{e}^{-\omega p}\,\mathrm{d}p \\
&= \frac{\mathrm{i}}{2\omega}\left[\int_0^\infty (\mathrm{i}q/\omega)^{n/2-1/2}\mathrm{e}^{-q}\,\mathrm{d}q - \mathrm{e}^{\mathrm{i}\omega} \int_0^\infty (\mathrm{i}q/\omega+1)^{n/2-1/2}\mathrm{e}^{-q}\,\mathrm{d}q\right] \\
&= \left[\int_0^\infty (\mathrm{i}u/\omega)^{n}\mathrm{e}^{-u^2}\,\mathrm{d}u - \frac{\mathrm{i}\mathrm{e}^{\mathrm{i}\omega}}{\omega} \int_0^\infty u(\mathrm{i}u^2/\omega+1)^{n/2-1/2}\mathrm{e}^{-u^2}\,\mathrm{d}u\right].
\end{aligned}
$$

In Figure 7 we can again observe convergence rates close to the expected values. The GGL quadrature and GF quadrature perform very similar here. A heuristic study was made on these two quadrature techniques and the performance depend on the oscillator function g. For the oscillators with stationary points of high order, the GF points seems to be desirable, but for low r the GLL points gave the best results. Further investigation into this is suggested as future work.

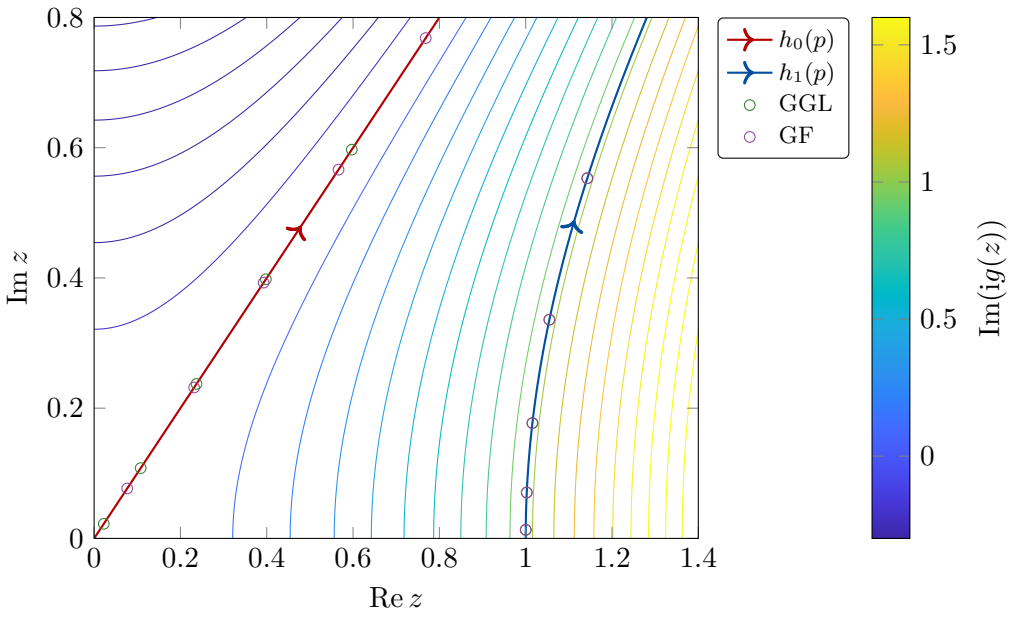

Figure 6: **Numerical steepest descent**: Paths in the complex plane at which the imaginary part of the oscillator $g(z)$ is constant. The paths from $z = 0$ and $z = 1$ are drawn as red dashed lines, with $n_{\text{qp}} = 5$ Gauss Laguerre quadrature points on top. Note that due to the scaling $q = \omega p$ the quadrature points will get closer to the real axis as ω gets smaller (here, $\omega = 10$).

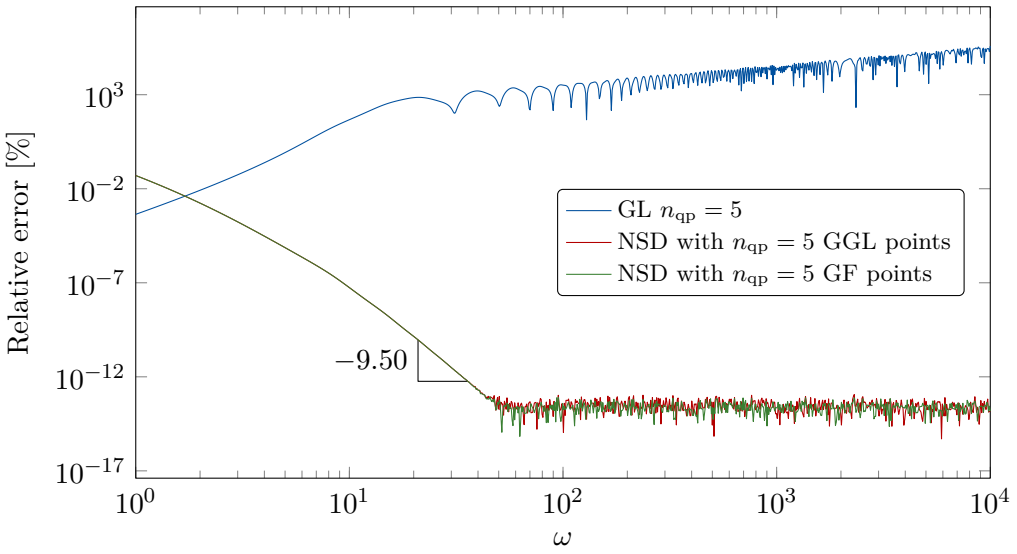

Figure 7: **Numerical steepest descent**: The relative numerical error of the NSD and Gauss Legendre quadrature applied to the integral I_2 with $n = 4$. Correct convergence rate of $-2n_{\mathrm{qp}} - \alpha = -9.5$ is observed when using $n_{\mathrm{qp}} = 5$ (note that $\alpha = -0.5$ for the path starting from $z = 0$ and that $\alpha = 0$ for the path starting from $z = 1$ such that GGL points and GF points are identical on this path).

3.1. Starting value for Newton iterations

We use Taylor expansion around ξ to find a starting value for Newton iterations to obtain the path $h_\xi(p)$

$$g(x) = g(\xi) + g'(\xi)(x - \xi) + \frac{1}{2}g''(\xi)(x - \xi)^2 + \dots$$

where $x = h_\xi(p)$. Since

$$g(h_\xi(p)) = g(\xi) + \mathrm{i}p \tag{26}$$

we get

$$\mathrm{i}p = g'(\xi)(h_\xi(p) - \xi) + \frac{1}{2}g''(\xi)(h_\xi(p) - \xi)^2 + \dots$$

So in case of a stationary point of order r we can use

$$\begin{aligned} h_\xi(p) &\approx \xi + \mathrm{e}^{\frac{2\pi j\mathrm{i}}{r+1}} \sqrt[r+1]{\frac{(r+1)!p}{g^{(r+1)}(\xi)}\mathrm{i}} \\ &= \xi + \exp\left[\frac{(4j+1)\pi - 2\arg g^{(r+1)}(\xi)}{2(r+1)}\mathrm{i}\right] \sqrt[r+1]{\frac{(r+1)!p}{|g^{(r+1)}(\xi)|}}. \end{aligned}$$

where $j = 0, 1, \cdots, r$ must be chosen such that the endpoints of to neighboring paths have the same sign of the imaginary part.

Whenever $g'(\xi) \neq 0$ and $g''(\xi) = 0$ we simply use the linear approximation

$$h_\xi(p) \approx \xi + \frac{\mathrm{i}p}{g'(\xi)}.$$

If $g'(\xi) \neq 0$ and $g''(\xi) \neq 0$, we use a quadratic approximation

$$h_\xi(p) \approx \xi + \frac{-g'(\xi) \pm \sqrt{g'(\xi)^2 + 2\mathrm{i}g''(\xi)p}}{g''(\xi)}$$

The sign can be determined (using Eq. (26)) by the following requirement

$$h'_\xi(p) = \frac{\mathrm{i}}{g'(h_\xi(p))} \qquad \Rightarrow \qquad h'_\xi(0) = \frac{\mathrm{i}}{g'(h_\xi(0))} = \frac{\mathrm{i}}{g'(\xi)} \tag{27}$$

such that (since $z = \operatorname{sgn}(\operatorname{Re} z)\sqrt{z^2}$)

$$h_\xi(p) \approx \xi - \frac{g'(\xi) - \operatorname{sgn}(\operatorname{Re} g'(\xi))\sqrt{g'(\xi)^2 + 2\mathrm{i}g''(\xi)p}}{g''(\xi)}.$$

Slightly more involved formulas can be obtained for the cubic approximation (requiring $g^{(3)}(\xi) \neq 0$)

$$h_\xi(p) \approx \xi + W - \frac{P}{3W} - \frac{g''(\xi)}{g^{(3)}(\xi)}, \quad W = \mathrm{e}^{2\pi\mathrm{i}j/3}\left(\frac{Q}{2} + \sqrt{\frac{Q^2}{4} + \frac{P^3}{27}}\right)^{1/3}, \quad j = 0, 1, 2$$

where

$$P = \frac{6g'(\xi)}{g^{(3)}(\xi)} - 3\left[\frac{g''(\xi)}{g^{(3)}(\xi)}\right]^2, \qquad Q = \frac{6g'(\xi)g''(\xi)}{\left[g^{(3)}(\xi)\right]^2} + \frac{6\mathrm{i}p}{g^{(3)}(\xi)} - 2\left[\frac{g''(\xi)}{g^{(3)}(\xi)}\right]^3.$$

The integer j must be determined from Eq. (27).

Alternatively, a Taylor expansion can be obtained by expanding $h_\xi(p)$ around $p = 0$

$$h_\xi(p) = \xi + h'_\xi(0)p + \frac{1}{2}h''_\xi(0)p^2 + \frac{1}{6}h^{(3)}_\xi(0)p^3 + \frac{1}{24}h^{(4)}_\xi(0)p^4 + \ldots$$

where one can compute

$$h'_\xi(0) = \frac{\mathrm{i}}{g'(\xi)}, \quad h''_\xi(0) = \frac{g''(\xi)}{[g'(\xi)]^3}, \quad h^{(3)}_\xi(0) = \frac{g^{(3)}(\xi)g'(\xi) - 3[g''(\xi)]^2}{[g'(\xi)]^5}\mathrm{i}$$
$$h^{(4)}_\xi(0) = -\frac{g^{(4)}(\xi)[g'(\xi)]^2 - 10g^{(3)}(\xi)g''(\xi)g'(\xi) + 15[g''(\xi)]^3}{[g'(\xi)]^7}$$

with the assumption that $g'(\xi) \neq 0$. Because of this assumption, this expansion cannot be used to approximate paths from stationary points.

3.2. The case of no critical points or resonance points in 2D

Assuming we first integrate in the η-direction, we define the path $v_\eta(\xi, q)$ in the complex plane defined by

$$g(\xi, v_{\eta_j}(\xi, q)) = g(\xi, \eta_j) + \mathrm{i}q$$

such that

$$\begin{aligned} I &= \int_{\xi_1}^{\xi_n} \int_{\eta_1}^{\eta_m} f(\xi, \eta) \mathrm{e}^{\mathrm{i}kg(\xi,\eta)} \,\mathrm{d}\eta \,\mathrm{d}\xi \\ &= \int_{\xi_1}^{\xi_n} \Bigg[\mathrm{e}^{\mathrm{i}kg(\xi,\eta_1)} \int_0^\infty f(\xi, v_{\eta_1}(\xi, q)) \mathrm{e}^{-kq} \frac{\partial v_{\eta_1}}{\partial q}(\xi, q) \,\mathrm{d}q \\ &\qquad - \mathrm{e}^{\mathrm{i}kg(\xi,\eta_m)} \int_0^\infty f(\xi, v_{\eta_m}(\xi, q)) \mathrm{e}^{-kq} \frac{\partial v_{\eta_m}}{\partial q}(\xi, q) \,\mathrm{d}q \Bigg] \,\mathrm{d}\xi \end{aligned}$$

We continue by defining

$$g(u_{\xi_i}(p), \eta_j) = g(\xi_i, \eta_j) + \mathrm{i}p$$

such that

$$I = F_{\mathrm{yx}}(\xi_1, \eta_1) - F_{\mathrm{yx}}(\xi_2, \eta_1) - [F_{\mathrm{yx}}(\xi_1, \eta_2) - F_{\mathrm{yx}}(\xi_2, \eta_2)]$$

where

$$\begin{aligned} F_{\mathrm{yx}}(\xi, \eta) = \mathrm{e}^{\mathrm{i}kg(\xi,\eta)} \int_0^\infty \int_0^\infty & f(u_\xi(p), v_\eta(u_\xi(p), q)) \mathrm{e}^{-k(q+p)} \\ & \cdot \frac{\partial v_\eta}{\partial q}(u_\xi(p), q) u'_\xi(p) \,\mathrm{d}q \,\mathrm{d}p. \end{aligned} \tag{28}$$

Similar expressions may be found by first integration over the ξ-direction

$$I = F_{\mathrm{xy}}(\xi_1, \eta_1) - F_{\mathrm{xy}}(\xi_2, \eta_1) - [F_{\mathrm{xy}}(\xi_1, \eta_2) - F_{\mathrm{xy}}(\xi_2, \eta_2)]$$

where

$$\begin{aligned} F_{\mathrm{yx}}(\xi, \eta) = \mathrm{e}^{\mathrm{i}kg(\xi,\eta)} \int_0^\infty \int_0^\infty & f(u_\xi(p, v_\eta(q)), v_\eta(q)) \mathrm{e}^{-k(q+p)} \\ & \cdot \frac{\partial u_\xi}{\partial p}(p, v_\eta(q)) v'_\eta(q) \,\mathrm{d}p \,\mathrm{d}q. \end{aligned} \tag{29}$$

Here, the paths $u_{\xi_i}(p, \eta)$ solve

$$g(u_{\xi_i}(p, \eta), \eta) = g(\xi_i, \eta) + \mathrm{i}p$$

and the paths $v_\eta(q)$ solve

$$g(\xi_i, v_\eta(q)) = g(\xi_i, \eta_j) + \mathrm{i}q.$$

3.3. Resonance points

On a rectangular domain $[\xi_1, \xi_n] \times [\eta_1, \eta_m]$ we have a resonance point (ξ, η_j) on the boundary $\xi = \xi_1$ or $\xi = \xi_n$ if

$$\frac{\partial g(\xi, \eta_j)}{\partial \eta}\Big|_{\xi=\xi_1} = 0 \quad \text{or} \quad \frac{\partial g(\xi, \eta_j)}{\partial \eta}\Big|_{\xi=\xi_n} = 0$$

respectively. Correspondingly we have a resonance point (ξ_i, η) on the boundary $\eta = \eta_1$ or $\eta = \eta_m$ if

$$\frac{\partial g(\xi_i, \eta)}{\partial \xi}\Big|_{\eta=\eta_1} = 0 \quad \text{or} \quad \frac{\partial g(\xi_i, \eta)}{\partial \xi}\Big|_{\eta=\eta_n} = 0,$$

respectively.

Assume that we have n_{η_1} critical points, $\xi_{\eta_1,i}$, $i = 1, \ldots, n_{\eta_1}$ in the ξ-direction where $\eta = \eta_1$, and n_{η_2} critical points, $\xi_{\eta_2,i}$, $i = 1, \ldots, n_{\eta_2}$ in the ξ-direction where $\eta = \eta_2$. Finally, assume that

$$\frac{\partial g(\xi, \eta)}{\partial \eta} \neq 0.$$

Then,

$$I = \int_{\xi_1}^{\xi_2} \left[\mathrm{e}^{\mathrm{i}kg(\xi,\eta_1)} \int_0^\infty f(\xi, v_{\eta_1}(\xi, q)) \mathrm{e}^{-kq} \frac{\partial v_{\eta_1}}{\partial q}(\xi, q)\, \mathrm{d}q \right.$$
$$\left. - \mathrm{e}^{\mathrm{i}kg(\xi,\eta_m)} \int_0^\infty f(\xi, v_{\eta_m}(\xi, q)) \mathrm{e}^{-kq} \frac{\partial v_{\eta_m}}{\partial q}(\xi, q)\, \mathrm{d}q \right] \mathrm{d}\xi$$

where the paths $v_{\eta_j}(\xi, q)$ solve

$$g(\xi, v_{\eta_j}(\xi, q)) = g(\xi, \eta_j) + \mathrm{i}q$$

We may then write

$$I = \sum_{i=1}^{n_{\eta_1}-1} [F_{\mathrm{yx}}(\xi_{\eta_1,i}, \eta_1) - F_{\mathrm{yx}}(\xi_{\eta_1,i+1}, \eta_1)] - \sum_{i=1}^{n_{\eta_2}-1} [F_{\mathrm{yx}}(\xi_{\eta_2,i}, \eta_2) - F_{\mathrm{yx}}(\xi_{\eta_2,i+1}, \eta_2)]$$

where

$$F_{\mathrm{yx}}(\xi, \eta) = \mathrm{e}^{\mathrm{i}kg(\xi,\eta)} \int_0^\infty \int_0^\infty f(u_\xi(p), v_\eta(u_\xi(p), q)) \mathrm{e}^{-k(p+q)} \frac{\partial v_\eta}{\partial q}(u_\xi(p), q) u'_\xi(p)\, \mathrm{d}q\, \mathrm{d}p$$

where the paths $u_{\xi_i}(p)$ solve

$$g(u_{\xi_i}(p), \eta_j) = g(\xi_i, \eta_j) + \mathrm{i}p.$$

Assume now that we have n_{ξ_1} critical points, $\eta_{\xi_1,j}$, $j = 1, \ldots, n_{\xi_1}$ in the η-direction where $\xi = \xi_1$, and n_{ξ_2} critical points, $\eta_{\xi_2,j}$, $j = 1, \ldots, n_{\xi_2}$ in the η-direction where $\xi = \xi_2$. Finally, assume that

$$\frac{\partial g(\xi, \eta)}{\partial \xi} \neq 0.$$

Then,

$$I = \int_{\eta_1}^{\eta_2} \Bigg[\mathrm{e}^{\mathrm{i}kg(\xi_1,\eta)} \int_0^\infty f(u_{\xi_1}(p,\eta),\eta) \mathrm{e}^{-kp} \frac{\partial u_{\xi_1}}{\partial p}(p,\eta)\,\mathrm{d}p - \mathrm{e}^{\mathrm{i}kg(\xi_2,\eta)} \int_0^\infty f(u_{\xi_2}(p,\eta),\eta) \mathrm{e}^{-kp} \frac{\partial u_{\xi_2}}{\partial p}(p,\eta)\,\mathrm{d}p \Bigg] \mathrm{d}\eta$$

where the paths $u_{\xi_i}(p,\eta)$ solve

$$g(u_{\xi_i}(p,\eta),\eta) = g(\xi_i,\eta) + \mathrm{i}p$$

We may then write

$$I = \sum_{i=1}^{n_{\xi_1}-1} [F_{\mathrm{xy}}(\xi_1, \eta_{\xi_1,i}) - F_{\mathrm{xy}}(\xi_1, \eta_{\xi_1,i+1})] - \sum_{i=1}^{n_{\xi_2}-1} [F_{\mathrm{xy}}(\xi_2, \eta_{\xi_2,i}) - F_{\mathrm{xy}}(\xi_2, \eta_{\xi_2,i+1})]$$

where

$$F_{\mathrm{xy}}(\xi,\eta) = \mathrm{e}^{\mathrm{i}kg(\xi,\eta)} \int_0^\infty \int_0^\infty f(u_\xi(p, v_\eta(q)), v_\eta(q)) \mathrm{e}^{-k(p+q)} \frac{\partial u_\xi}{\partial p}(p, v_\eta(q)) v'_\eta(q)\,\mathrm{d}p\,\mathrm{d}q$$

where the paths $v_\eta(q)$ solve

$$g(\xi_i, v_\eta(q)) = g(\xi_i, \eta_j) + \mathrm{i}q.$$

4. Numerical examples

Before evaluating the Kirchhoff-Helmholtz integral on a CAD model, we consider scattering on a rigid sphere which enables a simple parametrization with NSD paths in closed form. This enables control of the implemented path finding algorithm using Newtons method.

4.1. Scattering on a rigid sphere

Consider a plane wave (given by Eq. (16)) scattered by a rigid sphere of radius R_0. In the special case of $\boldsymbol{d}_{\mathrm{s}} = \boldsymbol{e}_z$ the analytic solution [30] to the problem is given by[3]

[3]Where $\mathrm{j}_n(x)$ is the n^{th} spherical Bessel function of the first kind and $\mathrm{h}_n(x)$ is the n^{th} spherical Hankel function of the first kind.

(expressed in spherical coordinates)

$$p(r,\theta) = -P_{\mathrm{inc}} \sum_{n=0}^{\infty} \mathrm{i}^n (2n+1) \frac{\mathrm{j}_n'(kR_0)}{\mathrm{h}_n'(kR_0)} \mathrm{P}_n(\cos\theta) \mathrm{h}_n(kr) \tag{30}$$

which can be generalized to arbitrary vectors $\boldsymbol{d}_{\mathrm{s}}$ using a orthogonal transformation. The backscattered (at $\vartheta = \pi$) far field pressure (Eq. (11)) is given by

$$p_0 = -\frac{P_{\mathrm{inc}}}{\mathrm{i}k} \sum_{n=0}^{\infty} (-1)^n (2n+1) \frac{\mathrm{j}_n'(kR_0)}{\mathrm{h}_n'(kR_0)}. \tag{31}$$

In the special case of monostatic scattering ($\boldsymbol{d}_{\mathrm{s}} = \hat{\boldsymbol{x}}$), the far field is independent of the incident direction $\boldsymbol{d}_{\mathrm{s}}$ due to spherical symmetry. For this reason, the integral in the far field approximation in Eq. (18) is evaluated to be (using $\boldsymbol{d}_{\mathrm{s}} = \boldsymbol{e}_{\mathrm{z}}$ and spherical coordinates)

$$p_0 \approx -\frac{\mathrm{i}kP_{\mathrm{inc}}}{2\pi} \int_{\Gamma_{\mathrm{i}}} \hat{\boldsymbol{x}} \cdot \frac{\boldsymbol{y}}{R_0} \mathrm{e}^{-2\mathrm{i}k\hat{\boldsymbol{x}}\cdot\boldsymbol{y}} \,\mathrm{d}\Gamma(\boldsymbol{y}) \tag{32}$$

$$= -\frac{\mathrm{i}kP_{\mathrm{inc}}R_0^2}{2\pi} \int_0^{2\pi} \int_0^{\frac{\pi}{2}} \cos\vartheta \mathrm{e}^{-2\mathrm{i}kR_0\cos\vartheta} \sin\vartheta \,\mathrm{d}\vartheta \,\mathrm{d}\varphi \tag{33}$$

$$= -\mathrm{i}kP_{\mathrm{inc}}R_0^2 \int_0^1 u\mathrm{e}^{-2\mathrm{i}kR_0 u} \,\mathrm{d}u = \frac{\mathrm{i}P_{\mathrm{inc}}}{4k} \left[1 - (1 + 2\mathrm{i}kR_0)\mathrm{e}^{-2\mathrm{i}kR_0}\right] \tag{34}$$

with the following asymptotic expansion for high frequencies

$$p_0 \sim \frac{P_{\mathrm{inc}}R_0}{2} \mathrm{e}^{-2\mathrm{i}kR_0}. \tag{35}$$

In the limit $k \to \infty$ the target strength in Eq. (15) is thus

$$\mathrm{TS} = 20 \log_{10}\left(\frac{R_0}{2}\right) \tag{36}$$

which is the asymptotic limit of the analytic solution in Eq. (31). These formulas are compared in Figures 8 and 9.

Consider a parametrization of the surface of a sphere given by

$$\boldsymbol{Y}(\xi,\eta) = R_0 \begin{bmatrix} \cos\eta\cos\xi \\ \cos\eta\sin\xi \\ \sin\eta \end{bmatrix}$$

where $\xi \in (-\pi, \pi]$ and $\eta \in [-\pi/2, \pi/2]$. The surface element is then computed as

$$\mathrm{d}\Gamma(\boldsymbol{Y}) = \left| \frac{\partial \boldsymbol{Y}}{\partial \xi} \times \frac{\partial \boldsymbol{Y}}{\partial \eta} \right| \mathrm{d}\eta \,\mathrm{d}\xi = R_0^2 \cos\eta \,\mathrm{d}\eta \,\mathrm{d}\xi$$

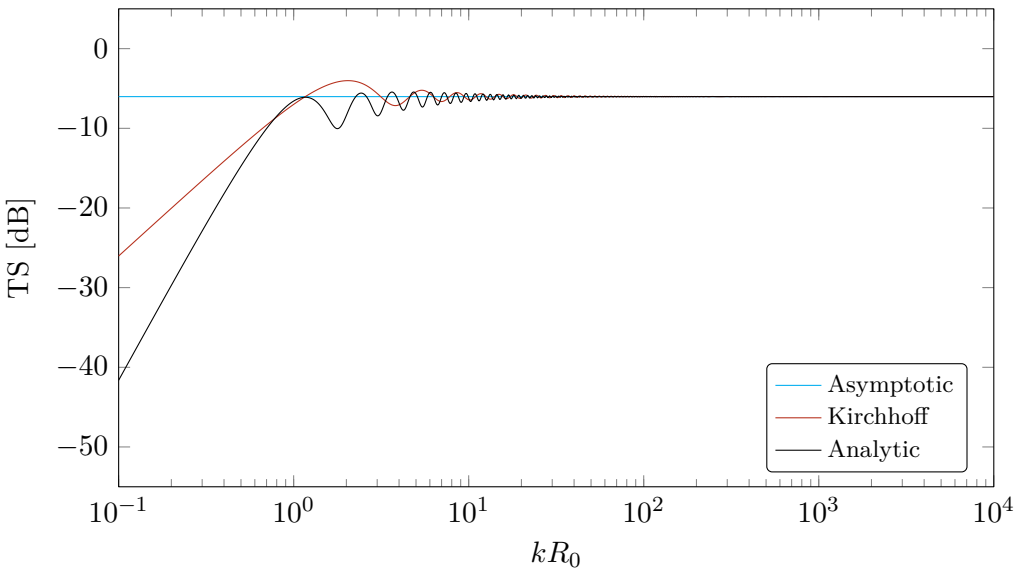

Figure 8: **Scattering on a rigid sphere**: Comparison of the target strength (Eq. (15)) for the Kirchhoff approximation (Eq. (32)), the asymptotic limit (Eq. (35)) and the analytic solution (Eq. (31)).

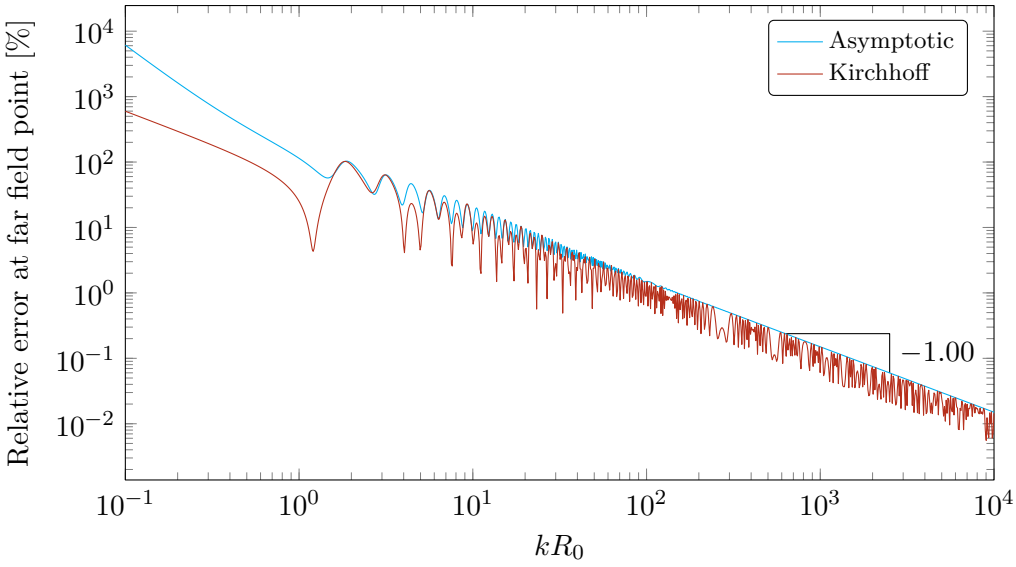

Figure 9: **Scattering on a rigid sphere**: Comparison of the relative error for the far field backscattered pressure for the Kirchhoff approximation (Eq. (32)) and the asymptotic limit (Eq. (35)) (compared to the analytic solution in Eq. (31)).

As the far field expression in Eq. (18) can be written as

$$p_0(\hat{\boldsymbol{x}}) \approx -\frac{\mathrm{i}kP_{\mathrm{inc}}}{2\pi}\int_{\Gamma_{\mathrm{i}}} \hat{\boldsymbol{x}}\cdot\boldsymbol{n}(\boldsymbol{y})\mathrm{e}^{-2\mathrm{i}k\hat{\boldsymbol{x}}\cdot\boldsymbol{y}}\,\mathrm{d}\Gamma(\boldsymbol{y}) \tag{37}$$

$$= -\frac{\mathrm{i}kP_{\mathrm{inc}}R_0^2}{2\pi}\int_{\Gamma_{\mathrm{i}}} \hat{\boldsymbol{x}}\cdot\boldsymbol{n}(\boldsymbol{y})\mathrm{e}^{-2\mathrm{i}k\hat{\boldsymbol{x}}\cdot\boldsymbol{y}}\cos\eta\,\mathrm{d}\eta\,\mathrm{d}\xi \tag{38}$$

we define the amplitude function f by

$$f(\xi,\eta) = -\frac{\mathrm{i}kP_{\mathrm{inc}}R_0}{2\pi}\hat{\boldsymbol{x}}\cdot\boldsymbol{Y}(\xi,\eta)\cos\eta$$

Moreover, let $g(\xi,\eta)$ be the oscillator function defined by

$$g(\xi,\eta) = \boldsymbol{d}\cdot\boldsymbol{Y}(\xi,\eta), \qquad \boldsymbol{d} = -2\hat{\boldsymbol{x}}.$$

The derivatives are found by

$$\frac{\partial^{i+j}g}{\partial^i\xi\partial^j\eta} = \boldsymbol{d}\cdot\frac{\partial^{i+j}\boldsymbol{Y}}{\partial^i\xi\partial^j\eta}$$

Along the boundaries where $\eta = \pm\frac{\pi}{2}$ we have $\frac{\partial g}{\partial\xi} = 0$. That is, there are no oscillations at all (any point is a resonance point), and the numerical steepest descent cannot be used for the integral along these boundaries. However, as there are no oscillations, the integral can be computed with regular Gaussian quadrature.

Solving $\frac{\partial g}{\partial\xi} = 0$ (for $\eta = \pm\frac{\pi}{2}$) yields solutions along $\tan\xi = \frac{d_2}{d_1}$ (for $d_1 \neq 0$). If $d_1 = 0$ then solutions are found at $\xi = \pm\frac{\pi}{2}$ (for $d_2 \neq 0$). For the case $d_1 = d_2 = 0$, $\frac{\partial g}{\partial\xi} = 0$ in the whole domain.

Solving $\frac{\partial g}{\partial\eta} = 0$ yields solutions along $\cot\eta = \frac{d_1\cos\xi + d_2\sin\xi}{d_3}$ (for $d_3 \neq 0$). If $d_3 = 0$ then solutions are found at $\eta = 0$ and $\tan\xi = -\frac{d_1}{d_2}$ (for $d_2 \neq 0$). For the case $d_2 = d_3 = 0$, solutions are found at $\xi = \pm\frac{\pi}{2}$ and $\eta = 0$.

Due to the periodicity, if $\nabla g(-\pi,\eta) = \boldsymbol{0}$ for some η, then $\nabla g(\pi,\eta) = \boldsymbol{0}$. Four boundary SPs ($\nabla g = 0$) are found at

$$(\xi,\eta) = \left(\arctan\left(-\frac{d_1}{d_2}\right), \pm\frac{\pi}{2}\right), \quad (\xi,\eta) = \left(\arctan\left(-\frac{d_1}{d_2}\right) - \operatorname{sgn}\left(-\frac{d_1}{d_2}\right)\pi, \pm\frac{\pi}{2}\right),$$

for $d_2 \neq 0$, and at $(\xi,\eta) = (\pm\pi/2, \pm\pi/2)$ when $d_2 = 0$. Internal SPs are found at

$$(\xi,\eta) = \left(\arctan\left(\frac{d_2}{d_1}\right), \operatorname{arccot}\left(\frac{\operatorname{sgn}(d_1)\sqrt{d_1^2+d_2^2}}{d_3}\right)\right)$$

and

$$(\xi,\eta) = \left(\arctan\left(\frac{d_2}{d_1}\right) - \operatorname{sgn}\left(\frac{d_2}{d_1}\right)\pi, \operatorname{arccot}\left(-\frac{\operatorname{sgn}(d_1)\sqrt{d_1^2+d_2^2}}{d_3}\right)\right)$$

when $d_1 \neq 0$ and $d_3 \neq 0$. If $d_3 = 0$ and $d_1 \neq 0$, SPs are found at

$$(\xi, \eta) = \left(\arctan\left(\frac{d_2}{d_1}\right), 0\right), \qquad (\xi, \eta) = \left(\arctan\left(\frac{d_2}{d_1}\right) - \operatorname{sgn}\left(\frac{d_2}{d_1}\right)\pi, 0\right).$$

If $d_1 = d_3 = 0$, SPs are found at $(\xi, \eta) = (\pm\pi/2, 0)$. If $d_1 = 0$ and $d_2 \neq 0$

$$(\xi, \eta) = \left(\pm\frac{\pi}{2}, \arctan\left(\pm\frac{d_3}{d_2}\right)\right).$$

There are no internal SPs for $d_1 = d_2 = 0$.

The paths are found by inversion. If $\zeta = g(\xi, \eta)$ then

$$\eta = -\mathrm{i}\operatorname{Log}\left(\frac{\frac{\zeta}{R} \pm \sqrt{\left(\frac{\zeta}{R}\right)^2 - d_3^2 - \gamma^2}}{\gamma - \mathrm{i}d_3}\right)$$

where $\gamma = d_1 \cos\xi + d_2 \sin\xi$. Correspondingly

$$\xi = -\mathrm{i}\operatorname{Log}\left(\frac{\frac{\zeta}{R} - d_3 \sin\eta \pm \sqrt{\left(\frac{\zeta}{R} - d_3 \sin\eta\right)^2 - (d_1^2 + d_2^2)\cos^2\eta}}{(d_1 - \mathrm{i}d_2)\cos\eta}\right)$$

where it is assumed that $\cos\eta \neq 0$ and $d_1 - \mathrm{i}d_2 \neq 0$ (in these cases there exist no inverse as $\frac{\partial g}{\partial \xi} = 0$). The function Log is the principal valued natural logarithm defined by

$$\operatorname{Log} z = \ln|z| + \mathrm{i}\operatorname{atan2}(y, x), \quad \operatorname{atan2}(y, x) = \begin{cases} \arctan(\frac{y}{x}) & \text{if } x > 0 \\ \arctan(\frac{y}{x}) + \pi & \text{if } x < 0 \text{ and } y \geq 0 \\ \arctan(\frac{y}{x}) - \pi & \text{if } x < 0 \text{ and } y < 0 \\ \frac{\pi}{2} & \text{if } x = 0 \text{ and } y > 0 \\ -\frac{\pi}{2} & \text{if } x = 0 \text{ and } y < 0 \\ \text{undefined} & \text{if } x = 0 \text{ and } y = 0 \end{cases}$$

for any non-zero complex number $z = x + \mathrm{i}y$.

Consider the case of monostatic scattering from a unit sphere with $d_2 = d_3 = 0$, $d_1 = -2$, $R_0 = 1\,\mathrm{m}$ and $P_{\mathrm{inc}} = 1\,\mathrm{Pa}$. Then the oscillatory function simplifies to

$$g(\xi, \eta) = -2\cos\eta\cos\xi, \tag{39}$$

and the amplitude function simplifies to

$$f(\xi, \eta) = -\frac{\mathrm{i}k}{2\pi}\cos\xi\cos^2\eta. \tag{40}$$

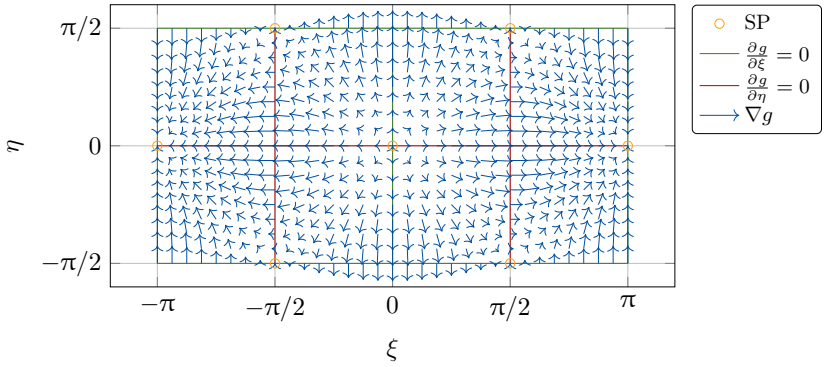

Figure 10: **Scattering on a rigid sphere**: Quiver plot of the gradient of $g(\xi, \eta)$ in Eq. (39). The stationary points (SPs) are marked by circles.

Moreover, the paths for the integration in the yx-integration order is given by

$$v_\eta(\xi, q) = \arccos\left(\cos\eta - \frac{\mathrm{i}q}{2\cos\xi}\right)$$

and

$$u_\xi(p) = \arccos\left(\cos\xi - \frac{\mathrm{i}p}{2\cos\eta_j}\right).$$

The paths for the integration in the xy-integration order is given by

$$u_\xi(p, \eta) = \arccos\left(\cos\xi - \frac{\mathrm{i}p}{2\cos\eta}\right)$$

and

$$v_\eta(q) = \arccos\left(\cos\eta - \frac{\mathrm{i}q}{2\cos\xi_i}\right).$$

A quiver plot of the oscillatory function g is given in Figure 10, and the integrand (of equation Eq. (37)) is visualized in the physical space and the parametric space in Figures 11 and 12, respectively.

Due to symmetry it suffices to consider the domain $[0, \pi/2]^2$ (and multiply the results by four). The integrand over this domain is visualized in Figure 13. In this domain we have stationary points in the origin and at the upper right corner $(\xi, \eta) = (\pi/2, \pi/2)$ (see Figure 10). Moreover, $\frac{\partial g}{\partial \xi} = 0$ at the left and upper boundaries and $\frac{\partial g}{\partial \eta} = 0$ at the right and lower boundaries. This yields an integrand around the top right corner which is significantly less oscillatory than the rest. The domain $\tilde{\Gamma}_1 = [\pi/2 - \delta, \pi/2 - \delta]^2$ is for this reason, integrated with classical Gauss-Legendre quadrature. For convenience, define $\xi_1 = 0$, $\xi_2 = \pi/2 - \delta$,

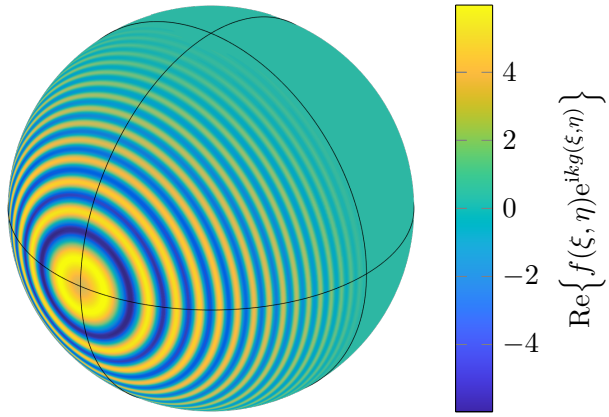

Figure 11: **Scattering on a rigid sphere**: The real part of the integrand (of equation Eq. (37)) is visualized on a CAD model of a sphere with $kR_0 = 50$.

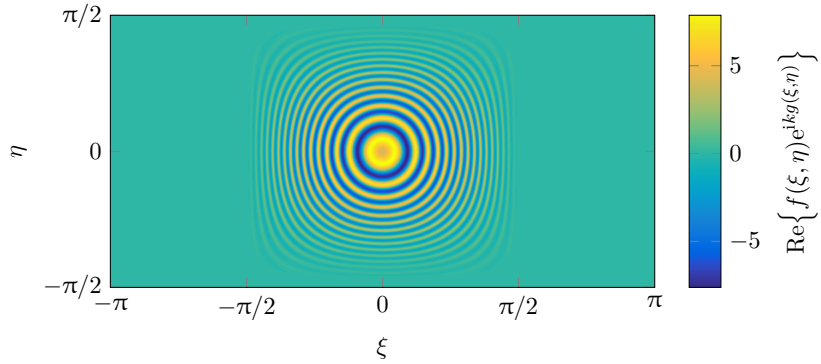

Figure 12: **Scattering on a rigid sphere**: The real part of the integrand (of equation Eq. (37)) is visualized in the parametric space with $kR_0 = 50$.

$\xi_3 = \pi/2$, $\eta_1 = 0$, $\eta_2 = \pi/2 - \delta$, and $\eta_3 = \pi/2$. The integral over $\tilde{\Gamma}_1$ may then be written as

$$I_{\mathrm{ne}} = \int_{\xi_2}^{\xi_3} \int_{\eta_2}^{\eta_3} f(\xi,\eta) \mathrm{e}^{\mathrm{i}kg(\xi,\eta)} \,\mathrm{d}\eta \,\mathrm{d}\xi$$

The size of this domain, governed by δ, should be frequency dependent such that the number of needed quadrature points can remain fixed for all frequencies.

Consider now the left domain $\tilde{\Gamma}_2 = [0, \pi/2 - \delta] \times [0, \pi/2]$. The integral over this domain may be decomposed as

$$\begin{aligned} I_{\mathrm{w}} &= \int_{\xi_1}^{\xi_2} \int_{\eta_1}^{\eta_3} f(\xi,\eta) \mathrm{e}^{\mathrm{i}kg(\xi,\eta)} \,\mathrm{d}\eta \,\mathrm{d}\xi \\ &= \int_{\xi_1}^{\xi_2} \Bigg[\mathrm{e}^{\mathrm{i}kg(\xi,\eta_1)} \int_0^\infty f(\xi, v_{\eta_1}(\xi,q)) \mathrm{e}^{-kq} \frac{\partial v_{\eta_1}}{\partial q}(\xi,q) \,\mathrm{d}q \\ &\qquad - \mathrm{e}^{\mathrm{i}kg(\xi,\eta_3)} \int_0^\infty f(\xi, v_{\eta_3}(\xi,q)) \mathrm{e}^{-kq} \frac{\partial v_{\eta_3}}{\partial q}(\xi,q) \,\mathrm{d}q \Bigg] \,\mathrm{d}\xi \end{aligned}$$

As $g(\xi, \eta_3) = 0$ the latter integral over ξ is not oscillatory and classical quadrature may be used to integrate over the variable ξ. On the other hand, the first integral over ξ is oscillatory and we may use another decomposition to obtain the following

$$I_{\mathrm{w}} = F_{\mathrm{yx}}(\xi_1, \eta_1) - F_{\mathrm{yx}}(\xi_2, \eta_1) - G_{\mathrm{yx}}(\eta_3)$$

with F_{yx} as defined in Eq. (28) and

$$G_{\mathrm{yx}}(\eta) = \int_{\xi_1}^{\xi_2} \int_0^\infty f(\xi, v_\eta(\xi,q)) \mathrm{e}^{-kq} \frac{\partial v_\eta}{\partial q}(\xi,q) \,\mathrm{d}q \,\mathrm{d}\xi.$$

For the final integral over the domain $\tilde{\Gamma}_3 = [\pi/2 - \delta, \pi/2] \times [0, \pi/2 - \delta]$ we integrate first over ξ

$$\begin{aligned} I_{\mathrm{w}} &= \int_{\eta_1}^{\eta_2} \int_{\xi_2}^{\xi_3} f(\xi,\eta) \mathrm{e}^{\mathrm{i}kg(\xi,\eta)} \,\mathrm{d}\xi \,\mathrm{d}\eta \\ &= \int_{\eta_1}^{\eta_2} \Bigg[\mathrm{e}^{\mathrm{i}kg(\xi_2,\eta)} \int_0^\infty f(u_{\xi_2}(p,\eta),\eta) \mathrm{e}^{-kq} \frac{\partial v_{\eta_1}}{\partial q}(\xi,q) \,\mathrm{d}q \\ &\qquad - \mathrm{e}^{\mathrm{i}kg(\xi_3,\eta)} \int_0^\infty f(u_{\xi_3}(p,\eta),\eta) \mathrm{e}^{-kq} \frac{\partial v_{\eta_m}}{\partial q}(\xi,q) \,\mathrm{d}q \Bigg] \,\mathrm{d}\eta. \end{aligned}$$

The latter integral over η is again not oscillatory since $g(\xi_3, \eta) = 0$ and classical quadrature may be used here. The first integral over η is oscillatory and we may use another decomposition to obtain the following

$$I_{\mathrm{se}} = F_{\mathrm{xy}}(\xi_2, \eta_1) - F_{\mathrm{xy}}(\xi_2, \eta_2) - G_{\mathrm{xy}}(\xi_3)$$

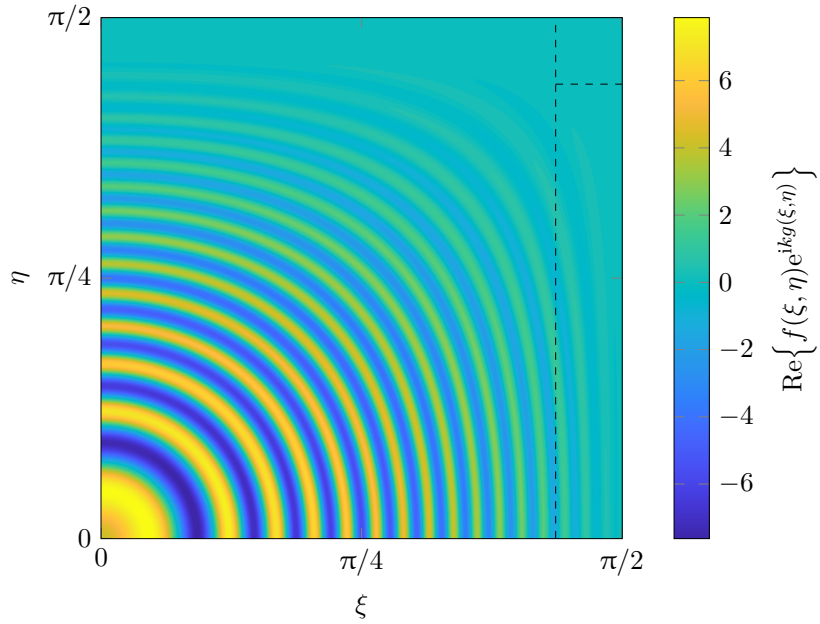

Figure 13: **Scattering on a rigid sphere**: The integration domain over $[0, \pi/2]^2$ is separated into three parts separated by the dashed lines.

with F_{xy} as defined in Eq. (29) and

$$G_{\mathrm{xy}}(\xi) = \int_{\eta_1}^{\eta_2} \int_0^{\infty} f(u_\xi(p,\eta),\eta) \mathrm{e}^{-kp} \frac{\partial u_\xi}{\partial p}(p,\eta)\, \mathrm{d}p\, \mathrm{d}\eta.$$

Summing up each contribution yields the far field monostatic pressure

$$p(\hat{\boldsymbol{x}}) = 4(I_{\mathrm{ne}} + I_{\mathrm{w}} + I_{\mathrm{se}})$$

In Figures 14 and 15 some results of Kirchhoff approximation using polygonal approximation of the geometry in Eq. (20) are presented. We here use the triangulation method based on the exact CAD model in Figure 1a described in the introduction. The key observation is that the error is not only depending on the geometrical approximation, but also the frequency resolution of the problem which is consistent with the results presented in [8] and discussed in [10]. From Figure 15, we can deduce experimentally that the relative error for the polygonal approximation of the Kirchhoff approximation goes as $E_{\mathrm{r}} \sim 14h^2kR_0$ for high frequencies. This contradicts the claim made in [7] and [9] that the size limitation of the triangle only depends on the approximation of the curvature of the object. However, the number of points is greatly reduced compared to using classical Gaussian quadrature on the exact geometry.

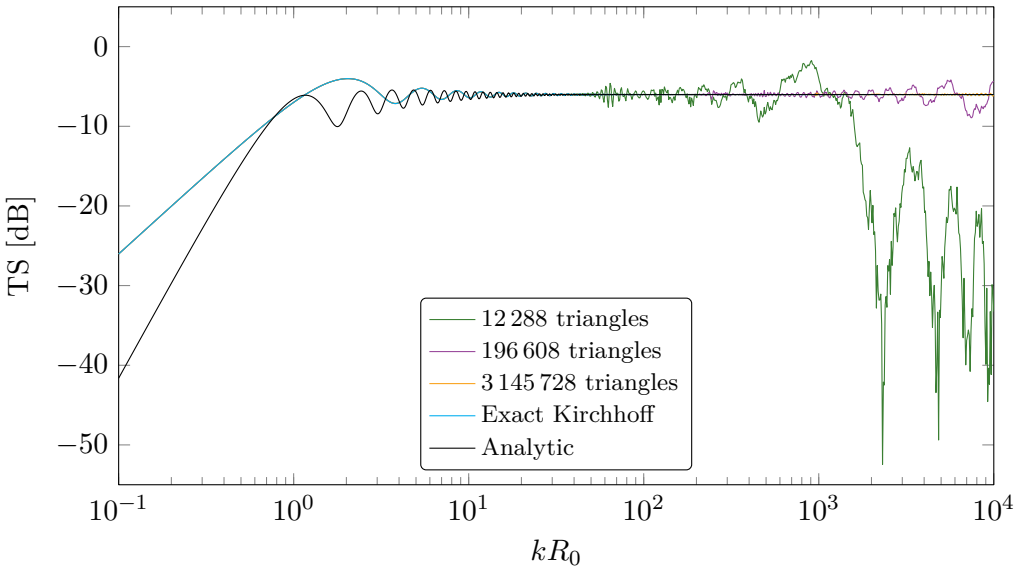

Figure 14: **Scattering on a rigid sphere**: Comparison of Kirchhoff approximation using a polygonal approximation of the geometry (Eq. (20)) instead of exact geometric representation by NURBS. The exact Kirchhoff approximation is given by Eq. (32).

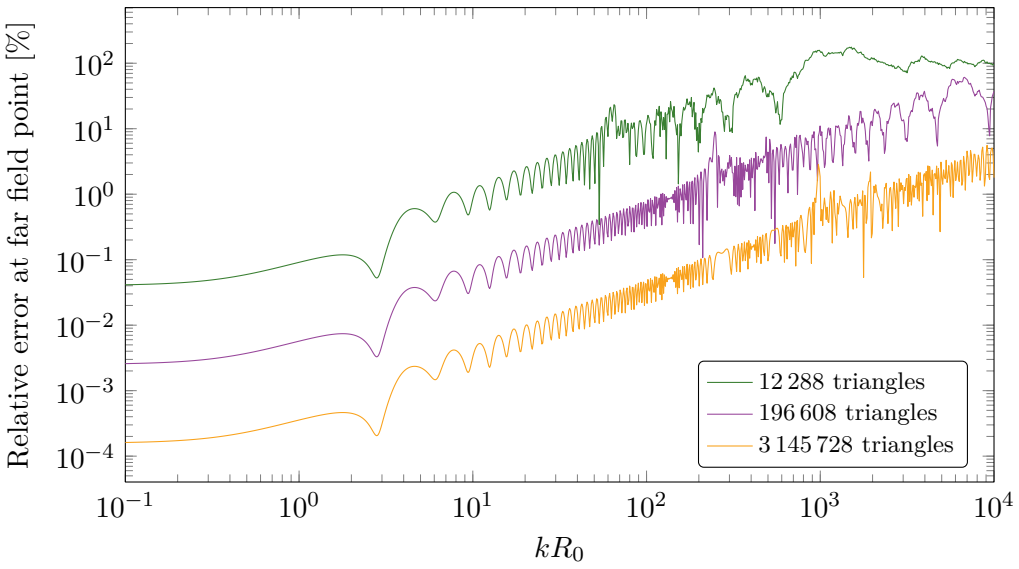

Figure 15: **Scattering on a rigid sphere**: Comparison of Kirchhoff approximation using a polygonal approximation of the geometry (Eq. (20)). The reference solution is the exact Kirchhoff approximation in Eq. (32).

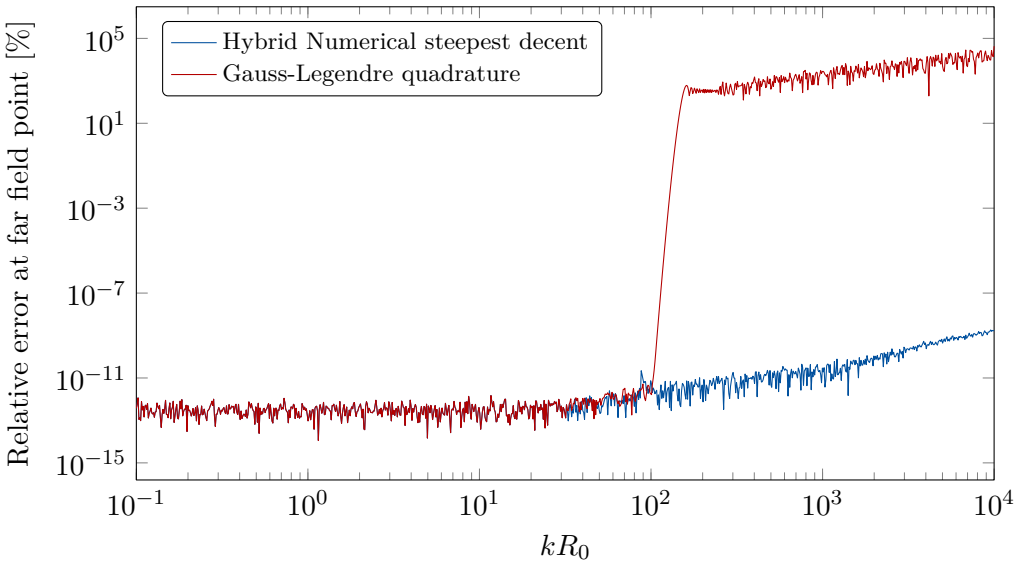

Figure 16: **Scattering on a rigid sphere**: Comparison of Kirchhoff approximation using standard Gauss-Legendre quadrature and using numerical steepest descent. The reference solution is the exact Kirchhoff approximation in Eq. (32).

For the hybrid NSD consider a rather large size of the domain $\tilde{\Gamma}_1$ (compared to the frequency) given by $\delta = \min\{\pi/2, 9/\sqrt{k}\}$ (heuristically obtained). The Gauss-Legendre integrals are evaluated by a (fixed) 100^{th} order quadrature scheme. The integrals for the numerical steepest descent are computed by a 5^{th} order Gauss-Laguerre quadrature scheme. Whenever the oscillatory integrals span less than 5 wavelengths Gauss-Legendre integration is used. For this reason, we call the method a hybrid numerical steepest descent.

As expected, and illustrated in Figure 16, using classical Gauss-Legendre quadrature to approximate the integrals in the Kirchhoff approximation yields poor results for higher frequencies. Combining Gauss-Legendre quadratures with the numerical steepest descent into the hybrid method resolves the problem for higher frequencies. This hybrid method will converge for all frequencies as opposed to the triangular approximation approach as illustrated in Figure 17.

The computational savings for the hybrid NSD method compared to the triangularized approach is significant. For example, to achieve engineering precision ($<1\%$) accuracy for $kR_0 = 10^3$ we can see from Figure 15 that the triangularized approach needs about $3 \cdot 10^6$ triangles. This single simulation is computed in roughly 160 second whereas the numerical steepest decent only need about 1 second (and obtaining machine epsilon precision). It is much easier to implement an efficient triangularized formulation than the NSD formulation, and so we would like to argue that the computational savings of using the NSD formulation could

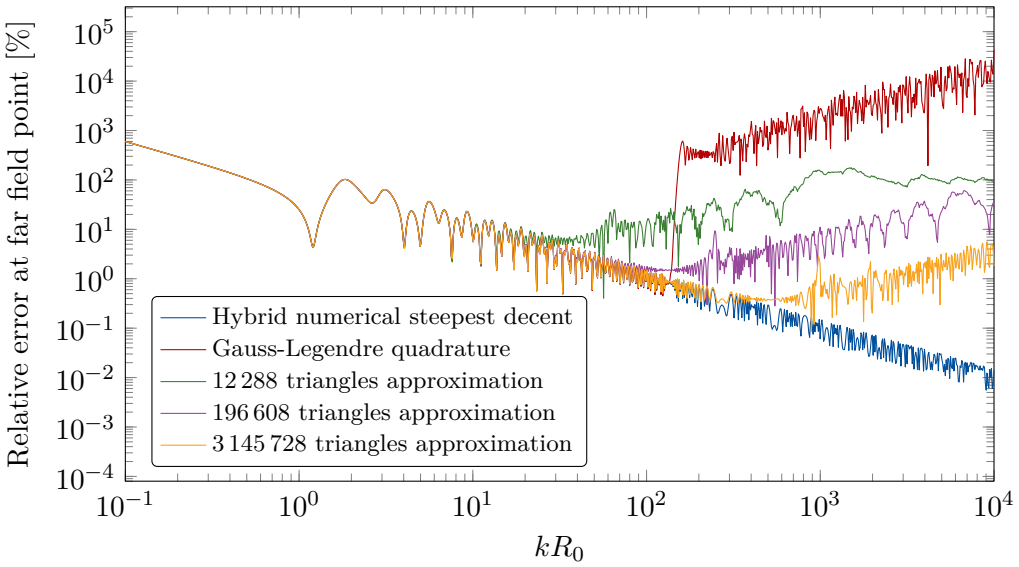

Figure 17: **Scattering on a rigid sphere**: Comparison of Kirchhoff approximation using standard Gauss-Legendre quadrature and using numerical steepest descent, in addition to the polygon approximation of the geometry. The reference solution is the analytic solution in Eq. (31).

potentially be even greater.

5. Conclusion

This article addresses acoustic scattering characterized by sound waves reflected by man-made elastic objects. The present approach is characterized by:

- The scattered pressure is approximated by Kirchhoff approximation.
- The computations are evaluated on the exact computer aided design model.
- The Helmholtz integrals are evaluated by the numerical steepest descent.

The main finding of the present study is that Kirchhoff approximation may be computed with a complexity independent of the frequency in the isogeometric analysis framework.

Furthermore, the following observations are made

- The accuracy of the method converges as a function of the frequency, as opposed to a triangular approximation method where the accuracy diverges.

- The computational complexity of the Kirchhoff approximation method is at least one order less than finite/boundary element methods resulting in computational savings in orders of magnitudes. The cost of these savings is reduced accuracy, and for some geometries the Kirchhoff approximation simply is not applicable.

- The NSD formulation outperforms the triangulation approximation approach when considering the computational time as a function of the error or frequency.

The Kirchhoff approximation method in an isogeometric framework has good potential, but many challenges remains to be resolved before the presented code is fully automated.

Some challenges remain to be resolved for this work to be applicable to general CAD geometries. First, for each incident wave and for each element in the CAD mesh, all resonance and stationary points must be found. This could be implemented as a preprocessing step. Second, if the shadow boundary does not coincide with element boundaries, this must be resolved in the NSD algorithm. The parent domain will in this case not be rectangular, but rather parametrized boundary which requires special treatment in the NSD algorithm. Moreover, this challenge will affect the first challenge as potential resonance points may lie on the shadow boundary. Third, interior stationary points have not been considered in this work but is discussed in [29]. Finally, rules must be established for the number of Gauss-Legendre points and Gauss-Laguerre points needed in the hybrid method.

To have an automated algorithm that tackles all of these challenges is a huge task. The integrals from the usage of curvilinear facets in [14] contains well behaved oscillatory functions (g is second order polynomial) and may for this reason be a simpler approach. Especially since it is easier to discretize the scatterer, Γ, with curvilinear triangles in such a way that the shadow boundary lies on element edges.

Acknowledgements

This work was supported by the Department of Mathematical Sciences at the Norwegian University of Science and Technology and by the Norwegian Defence Research Establishment.

We would like to thank Arieh Iserles for hosting us at our research stay at the Department of Applied Mathematics and Theoretical Physics at University of Cambridge (UK) during the fall of 2016. His guidance related to highly oscillatory integration is highly appreciated. We would also like to thank Daan Huybrechs at K.U. Leuven University (Belgium) for valuable comments about the numerical steepest descent method.

References

[1] S. G. Conti, P. Roux, C. Fauvel, B. D. Maurer, D. A. Demer, Acoustical monitoring of fish density, behavior, and growth rate in a tank, *Aquaculture*, 251:314–323 (2006).

[2] N. D. Manh, Isogeometric analysis and shape optimization in electromagnetism, Ph.D. thesis, Technical University of Denmark, Department of Informatics and Mathematical Modeling (2012).

[3] J. A. Fawcett, Modeling of high-frequency scattering from objects using a hybrid Kirchhoff/diffraction approach, *The Journal of the Acoustical Society of America*, 109:1312–1319 (2001).

[4] E. Pouliquen, O. Bergem, N. G. Pace, Time-evolution modeling of seafloor scatter. I. Concept, *The Journal of the Acoustical Society of America*, 105:3136–3141 (1999).

[5] H. Medwin, C. S. Clay, *Fundamentals of Acoustical Oceanography*, Applications of Modern Acoustics, Academic Press, 1997.

[6] B. Nolte, I. Schäfer, C. de Jong, L. Gilroy, BeTSSi II benchmark on target strength simulation, in *Proceedings of Forum Acusticum*, 2014.

[7] H. G. Schneider, R. Berg, L. Gilroy, I. Karasalo, I. MacGillivray, M. Morshuizen, A. Volker, Acoustic scattering by a submarine: Results from a benchmark target strength simulation workshop, *ICSV10*, pp. 2475–2482 (2003).

[8] L. Fillinger, M. Nijhof, C. de Jong, An efficient numerical target strength prediction model: Validation against analysis solutions, in *Papadakis, JS Bjorno, L., Proceedings 2nd International Conference and Exhibition on Underwater Acoustics, UA2014, 22-27 June, Rhodes, Greece, 487–493*, 2014.

[9] M. Östberg, Target echo strength modelling at FOI, including results from the BeTSSi II workshop, *arXiv preprint arXiv:1604.02257* (2016).

[10] L. Gilroy, Target echo strength software benchmarking, Tech. rep., DRDC-RDDC (2017).

[11] K. G. Foote, D. T. I. Francis, Comparing Kirchhoff-approximation and boundary-element models for computing gadoid target strengths, *The Journal of the Acoustical Society of America*, 111:1644–1654 (2002).

[12] A. T. Abawi, Kirchhoff scattering from non-penetrable targets modeled as an assembly of triangular facets, *The Journal of the Acoustical Society of America*, 140:1878–1886 (2016).

[13] N. J. Pignier, C. J. O'Reilly, S. Boij, A Kirchhoff approximation-based numerical method to compute multiple acoustic scattering of a moving source, *Applied Acoustics*, 96:108–117 (2015).

[14] E. Lavia, J. D. Gonzalez, S. Blanc, Modelling high-frequency backscattering from a mesh of curved surfaces using Kirchhoff approximation, *arXiv preprint arXiv:1805.06945* (2018).

[15] M. Peake, J. Trevelyan, G. Coates, Extended isogeometric boundary element method (XIBEM) for three-dimensional medium-wave acoustic scattering problems, *Computer Methods in Applied Mechanics and Engineering*, 284:762–780 (2015), Isogeometric Analysis Special Issue.

[16] V. Dominguez, I. G. Graham, V. P. Smyshlyaev, Stability and error estimates for Filon-Clenshaw-Curtis rules for highly oscillatory integrals, *IMA Journal of Numerical Analysis*, 31:1253–1280 (2011).

[17] A. Iserles, S. P. Nørsett, On quadrature methods for highly oscillatory integrals and their implementation, *BIT Numerical Mathematics*, 44:755–772 (2004).

[18] A. Iserles, S. P. Nørsett, Efficient quadrature of highly oscillatory integrals using derivatives, *Proceedings of the Royal Society A: Mathematical, Physical and Engineering Sciences*, 461:1383–1399 (2005).

[19] D. Levin, Fast integration of rapidly oscillatory functions, *Journal of Computational and Applied Mathematics*, 67:95–101 (1996).

[20] S. Olver, Moment-free numerical integration of highly oscillatory functions, *IMA Journal of Numerical Analysis*, 26:213–227 (2006).

[21] D. Huybrechs, S. Vandewalle, On the evaluation of highly oscillatory integrals by analytic continuation, *SIAM Journal on Numerical Analysis*, 44:1026–1048 (2006).

[22] A. Deaño, D. Huybrechs, A. Iserles, *Computing Highly Oscillatory Integrals*, Society for Industrial and Applied Mathematics, Philadelphia, PA, 2018.

[23] A. Asheim, D. Huybrechs, Complex Gaussian quadrature for oscillatory integral transforms, *IMA Journal of Numerical Analysis*, 33:1322–1341 (2013).

[24] A. Deaño, D. Huybrechs, A. Iserles, The kissing polynomials and their Hankel determinants, *arXiv e-prints*, p. arXiv:1504.07297 (2015).

[25] S. N. Chandler-Wilde, I. G. Graham, S. Langdon, E. A. Spence, Numerical-asymptotic boundary integral methods in high-frequency acoustic scattering, *Acta Numerica*, 21:89–305 (2012).

[26] F. Ihlenburg, *Finite Element Analysis of Acoustic Scattering*, vol. 132 of *Applied Mathematical Sciences*, Springer, New York, USA, 1998.

[27] J. V. Venås, Isogeometric analysis of acoustic scattering, Master's thesis, Norwegian University of Science and Technology, Trondheim, Norway (2015).

[28] J. V. Venås, T. Kvamsdal, Isogeometric boundary element method for acoustic scattering by a submarine, *Computer Methods in Applied Mechanics and Engineering* (2019).

[29] D. Huybrechs, S. Vandewalle, The construction of cubature rules for multivariate highly oscillatory integrals, *Mathematics of Computation*, 76:1955–1981 (2007).

[30] J. V. Venås, T. Jenserud, Exact 3D scattering solutions for spherical symmetric scatterers, *Journal of Sound and Vibration*, 440:439–479 (2019).

Addendum

Spectral Element Analysis of Acoustic Scattering using Infinite Elements

Jon Vegard Venås and Trond Kvamsdal

Spectral Element Analysis of Acoustic Scattering using Infinite Elements

Jon Vegard Venås[a,*], Trond Kvamsdal[a]

[a] *Department of Mathematical Sciences, Norwegian University of Science and Technology, Alfred Getz' vei 1, 7034 Trondheim, Norway*

Abstract

A spectral element method (SEM) solver is presented for acoustic scattering. The classical 3D scattering benchmark on a sphere impinged by a plane wave in an unbounded domain is investigated. The unbounded domain is handled by the infinite element method. In this example the geometry (a spherical shell between the scatterer and an artificial boundary) is approximated by 6 patches using Lagrange polynomial interpolation at the Gauss-Lobatto-Legendre nodes. The results are compared to spectral properties of isogeometric analysis (IGA) where the conditioning of the system is of particular interest in addition to the geometrical approximation differences. In particular, the exponential behavior of the condition number with respect to the polynomial order is observed for the IGA while an algebraic behavior is observed for the SEM.

1. Introduction

Acoustic scattering problems on unbounded domain has been tackled with a vast set of methods. For the finite element method in this context, several methods has been used to solve the problem of unboundedness of the domain, including the method of perfectly matched layer (PML) [1, 2], local differential absorbing boundary condition operators [3–6], Dirichlet to Neumann operators [7] and infinite elements [8–10]. The boundary element method has also been investigated thoroughly [11–14]. Moreover, high frequency approximation methods like the Kirchhoff approximation method [15, 16] and ray/beam tracing [17–19] has been of particular interest for the high frequency spectrum as the classical element methods becomes too computationally expensive in this realm. An attempt to solve this problem for element methods in acoustics has been suggested in [14, 20, 21] where the basis functions are enriched by oscillatory functions.

*Corresponding author.
Email addresses: Jon.Venas@ntnu.no (J.V. Venås), Trond.Kvamsdal@ntnu.no (T. Kvamsdal).

Away from non-smooth parts of the scatterer, the solution is smooth, and it would make sense to exploit this fact by using smooth basis functions in the analysis. As illustrated in [22], using IGA with $C^{\check{p}-1}$ continuity instead of the classical FEM C^0 continuity increases the accuracy. The natural question would then be if even higher continuity continues to improve the results. The method of fundamental solution [23] is such an attempt where the C^∞ basis functions are collocated at the boundary to satisfy the boundary condition. This method has spectral convergence for smooth geometries. However, as these basis functions do not incorporate the reduced continuity at the non-smooth parts of the scatterer, sub-optimal results would be obtained in these cases. A remedy for this would be to use the spectral element method where one naturally incorporates the G^0 continuity of the scatterer into the basis functions of C^0 continuity across the element boundaries and maintains the C^∞ continuity in the interior of each element. Surprisingly little work has been done using spectral element methods for solving acoustic scattering problems. Mehdizadeh et al. [24] investigated the 2D spectral element method using the PML method and Jørgensson et al. [25] used spectral element methods for 2D room acoustics. The lacking literature on the usage of spectral element analysis of 3D scattering problems using infinite elements is therefore a motivating factor of this work.

2. Lagrange basis functions and GLL nodes

The Lagrange polynomials are given by[1]

$$l_i(\xi) = \prod_{\substack{j=1 \\ j\neq i}}^{n} \frac{\xi - \xi_j}{\xi_i - \xi_j}$$

where $\boldsymbol{t}_\xi = \{\xi_i\}_{i=1}^n$ are the interpolation nodes. Note the important interpolatory property of the Lagrange basis functions

$$l_i(\xi_j) = \delta_{ij} \tag{1}$$

where δ_{ij} is the Kronecker delta

$$\delta_{ij} = \begin{cases} 1 & i = j \\ 0 & i \neq j. \end{cases}$$

Also note that the derivative of the Lagrange basis functions are given by

$$l_i'(\xi) = \sum_{\substack{l=1 \\ l\neq i}}^{n} \frac{1}{\xi_i - \xi_l} \prod_{\substack{j=1 \\ j\neq i,l}}^{n} \frac{\xi - \xi_j}{\xi_i - \xi_j}.$$

[1] Note that we do not use the conventional notation $l_i(x)$ for the Lagrange basis functions due to conflict with the index l.

In particular,

$$l_i'(\xi_i) = \sum_{\substack{l=1 \\ l\neq i}}^{n} \frac{1}{\xi_i - \xi_l} \tag{2}$$

and

$$l_i'(\xi_l) = \frac{1}{\xi_i - \xi_l} \prod_{\substack{j=1 \\ j\neq i,l}}^{n} \frac{\xi_l - \xi_j}{\xi_i - \xi_j} \qquad l \neq i. \tag{3}$$

Definition 1. *The Gauss-Lobatto-Legendre (GLL[2]) nodes, $\{\xi_i\}_{i=1}^n$, are the roots of the completed Lobatto polynomial of degree n. That is, they are the solutions to the following equation*

$$(1-\xi^2)\mathrm{P}'_{n-1}(\xi) = 0$$

where $\mathrm{P}_{\check{p}}(\xi)$ are the Legendre polynomial of degree $\check{p}$.

Note that $\xi_1 = -1$ and $\xi_n = 1$. Inspired by [26, p. 305-306] we present the following theorem[3].

Theorem 1. *Let $\{\xi_i\}_{i=1}^n$ be the GLL nodes. Then the Lagrange polynomials defined by these nodes have the property*

$$l_i'(\xi_i) = \begin{cases} -\frac{n(n-1)}{4} & i = 1 \\ \frac{n(n-1)}{4} & i = n \\ 0 & \textit{otherwise.} \end{cases}$$

Proof. Consider the *generating polynomial*

$$\Phi_n(\xi) = \prod_{j=1}^{n}(\xi - \xi_j) = (\xi - \xi_1)(\xi - \xi_2)\cdots(\xi - \xi_n)$$

and note that (using the product rule)

$$\Phi_n'(\xi) = \sum_{l=1}^{n}\prod_{\substack{j=1 \\ j\neq l}}^{n}(\xi - \xi_j) \qquad \Rightarrow \qquad \Phi_n'(\xi_i) = \prod_{\substack{j=1 \\ j\neq i}}^{n}(\xi_i - \xi_j) \tag{4}$$

and

$$\Phi_n''(\xi) = \sum_{l=1}^{n}\sum_{m=1}^{n}\prod_{\substack{j=1 \\ j\neq l,m}}^{n}(\xi - \xi_j) \qquad \Rightarrow \qquad \Phi_n''(\xi_i) = 2\sum_{\substack{l=1 \\ l\neq i}}^{n}\prod_{\substack{j=1 \\ j\neq i,l}}^{n}(\xi_i - \xi_j).$$

[2]These nodes also goes by the name Legendre-Gauss-Lobatto (LGL) nodes.

[3]The converse theorem was proved in [26, p. 305-306].

Then, by writing the sum of fractions in Eq. (2) as a single fraction (with a common denominator) we get

$$l_i'(\xi_i) = \sum_{\substack{j=1 \\ j\neq i}}^{n} \frac{1}{\xi_i - \xi_j} = \frac{\sum_{\substack{l=1 \\ l\neq i}}^{n} \prod_{\substack{j=1 \\ j\neq i,l}}^{n} (\xi_i - \xi_j)}{\prod_{\substack{j=1 \\ j\neq i}}^{n} (\xi_i - \xi_j)} = \frac{\frac{1}{2}\Phi_n''(\xi_i)}{\Phi_n'(\xi_i)}. \tag{5}$$

Since $\{\xi_i\}_{i=2}^{n-1}$ are the roots of $\mathrm{P}_{n-1}'(\xi)$ we may write

$$\mathrm{P}_{n-1}'(\xi) = C \prod_{j=2}^{n-1} (\xi - \xi_j) \tag{6}$$

for some non-zero constant C, and thus

$$\left(\xi^2 - 1\right)\mathrm{P}_{n-1}'(\xi) = C\Phi_n(\xi). \tag{7}$$

We know that the Legendre polynomials $\mathrm{P}_{n-1}(\xi)$ solves the Legendre differential equation

$$\frac{\mathrm{d}}{\mathrm{d}\xi}\left[\left(1 - \xi^2\right)\frac{\mathrm{d}}{\mathrm{d}\xi}\mathrm{P}_{n-1}(\xi)\right] + n(n-1)\mathrm{P}_{n-1}(\xi) = 0. \tag{8}$$

Combining Eq. (7) and Eq. (8) yields

$$-C\Phi_n'(\xi) = -2\xi\mathrm{P}_{n-1}'(\xi) + \left(1 - \xi^2\right)\mathrm{P}_{n-1}''(\xi) = -n(n-1)\mathrm{P}_{n-1}(\xi)$$

and then

$$C\Phi_n''(\xi) = n(n-1)\mathrm{P}_{n-1}'(\xi). \tag{9}$$

This means that $\Phi_n''(\xi_i) = 0$ for $i = 2, \ldots, n-1$, and thus, from Eq. (5) we see that $l_i'(\xi_i) = 0$ for $i = 2, \ldots, n-1$.

Using Eqs. (4), (6) and (9) we have

$$\begin{aligned} C\Phi_n''(\xi_1) &= n(n-1)\mathrm{P}_{n-1}'(\xi_1) = n(n-1)C\prod_{j=2}^{n-1}(\xi_1 - \xi_j) \\ &= C\frac{n(n-1)}{\xi_1 - \xi_n}\Phi_n'(\xi_1) = -C\frac{n(n-1)}{2}\Phi_n'(\xi_1) \end{aligned}$$

and correspondingly

$$C\Phi_n''(\xi_n) = C\frac{n(n-1)}{2}\Phi_n'(\xi_n)$$

which enables us to write $l_1'(\xi_1)$ and $l_n'(\xi_n)$ as (using Eq. (5))

$$l_1'(\xi_1) = -\frac{n(n-1)}{4} \quad \text{and} \quad l_n'(\xi_n) = \frac{n(n-1)}{4},$$

respectively. □

Remark 2.1. *Using Eq.* (4) *one can rewrite Eq.* (3) *as*

$$l_i'(\xi_l) = \frac{1}{\xi_i - \xi_l} \prod_{\substack{j=1 \\ j\neq i,l}}^{n} \frac{\xi_l - \xi_j}{\xi_i - \xi_j} = \frac{1}{\xi_l - \xi_i} \frac{\Phi_n'(\xi_l)}{\Phi_n'(\xi_i)} \qquad l \neq i.$$

Remark 2.2. *Using Eq.* (3) *one can evaluate the following special cases in closed form*

$$l_n'(\xi_1) = \frac{(-1)^n}{2} \quad \textit{and} \quad l_1'(\xi_n) = -\frac{(-1)^n}{2}.$$

3. Geometry approximation

Given a patch parameterized by the mapping

$$\boldsymbol{X} \colon [-1,1]^3 \to \mathbb{R}^3, \qquad (\xi,\eta,\zeta) \mapsto \boldsymbol{X}(\xi,\eta,\zeta).$$

Using least squares, we can approximate this mapping by Lagrange polynomials (of polynomial degrees $\check{p}_\xi = n_\xi - 1$, $\check{p}_\eta = n_\eta - 1$ and $\check{p}_\zeta = n_\zeta - 1$ in the three parametric directions) with the mapping

$$\boldsymbol{C}(\xi,\eta,\zeta) = \sum_{i=1}^{n_\xi} \sum_{j=1}^{n_\eta} \sum_{l=1}^{n_\zeta} \boldsymbol{c}_{i,j,l} l_{i,\boldsymbol{t}_\xi}(\xi) l_{j,\boldsymbol{t}_\eta}(\eta) l_{l,\boldsymbol{t}_\zeta}(\zeta)$$

where

$$l_{i,\boldsymbol{t}_\xi}(\xi) = \prod_{\substack{j=1 \\ j\neq i}}^{n_\xi} \frac{\xi - \xi_j}{\xi_i - \xi_j}$$

and $\boldsymbol{t}_\xi = \{\xi_i\}_{i=1}^{n_\xi}$ are the GLL nodes, and correspondingly for the other parametric directions. For the ease of notation, we use

$$l_{i,\boldsymbol{t}_\xi}(\xi) \to l_i(\xi), \qquad l_{j,\boldsymbol{t}_\eta}(\eta) \to l_j(\eta), \qquad l_{l,\boldsymbol{t}_\zeta}(\zeta) \to l_l(\zeta)$$

as the sets of basis functions are given by the index symbol (i, j or l).

Consider approximation of the geometry with least squares where the functional to be minimized is given by

$$\begin{aligned} f(\boldsymbol{c}) &= \frac{1}{2} \int_{-1}^{1} \int_{-1}^{1} \int_{-1}^{1} \|\boldsymbol{C}(\xi,\eta,\zeta) - \boldsymbol{X}(\xi,\eta,\zeta)\|^2 \,\mathrm{d}\xi \,\mathrm{d}\eta \,\mathrm{d}\zeta \\ &= \frac{1}{2} \int_{-1}^{1} \int_{-1}^{1} \int_{-1}^{1} \boldsymbol{C} \cdot \boldsymbol{C} - 2\boldsymbol{C} \cdot \boldsymbol{X} + \boldsymbol{X} \cdot \boldsymbol{X} \,\mathrm{d}\xi \,\mathrm{d}\eta \,\mathrm{d}\zeta \end{aligned}$$

where $\boldsymbol{c}$ is a multidimensional array containing the coefficients of $\boldsymbol{C}$. The least squares solution demands that the partial derivatives of f with respect to the coefficients $\boldsymbol{c}_{i,j,l}$ (of the mapping $\boldsymbol{C}$) to be zero

$$\nabla_{\boldsymbol{c}_{i,j,l}} f(\boldsymbol{c}) = \int_{-1}^{1}\int_{-1}^{1}\int_{-1}^{1} [\boldsymbol{C}(\xi,\eta,\zeta) l_i(\xi) l_j(\eta) l_l(\zeta) - \boldsymbol{X}(\xi,\eta,\zeta) l_i(\xi) l_j(\eta) l_l(\zeta)]\,\mathrm{d}\xi\,\mathrm{d}\eta\,\mathrm{d}\zeta = \boldsymbol{0}$$

for all i, j, l. We therefore have a linear system of equations as the following equation

$$\begin{aligned}\int_{-1}^{1}\int_{-1}^{1}\int_{-1}^{1} \boldsymbol{C}(\xi,\eta,\zeta) l_i(\xi) l_j(\eta) l_l(\zeta)\,\mathrm{d}\xi\,\mathrm{d}\eta\,\mathrm{d}\zeta \\ = \int_{-1}^{1}\int_{-1}^{1}\int_{-1}^{1} \boldsymbol{X}(\xi,\eta,\zeta) l_i(\xi) l_j(\eta) l_l(\zeta)\,\mathrm{d}\xi\,\mathrm{d}\eta\,\mathrm{d}\zeta\end{aligned} \tag{10}$$

must hold for all i, j, l. Note that, using Eq. (1), we have

$$\boldsymbol{C}(\xi_i, \eta_j, \zeta_l) = \boldsymbol{c}_{i,j,l}.$$

Approximating these integrals by the GLL quadrature approximation we find

$$\begin{aligned}&\int_{-1}^{1}\int_{-1}^{1}\int_{-1}^{1} \boldsymbol{C}(\xi,\eta,\zeta) l_i(\xi) l_j(\eta) l_l(\zeta) \\ &\approx \sum_{\alpha,\beta,\gamma} \rho_\alpha \rho_\beta \rho_\gamma \boldsymbol{C}(\xi_\alpha, \eta_\beta, \zeta_\gamma) l_i(\xi_\alpha) l_j(\eta_\beta) l_l(\zeta_\gamma) \\ &= \sum_{\alpha,\beta,\gamma} \rho_\alpha \rho_\beta \rho_\gamma \boldsymbol{c}_{\alpha,\beta,\gamma} \delta_{i\alpha} \delta_{j\beta} \delta_{l\gamma} \\ &= \rho_i \rho_j \rho_l \boldsymbol{c}_{i,j,l}.\end{aligned}$$

Correspondingly for the right side of Eq. (10) we have

$$\int_{-1}^{1}\int_{-1}^{1}\int_{-1}^{1} \boldsymbol{X}(\xi,\eta,\zeta) l_i(\xi) l_j(\eta) l_l(\zeta)\,\mathrm{d}\xi\,\mathrm{d}\eta\,\mathrm{d}\zeta \approx \rho_i \rho_j \rho_l \boldsymbol{X}(\xi_i, \eta_j, \zeta_l).$$

Thus, we can approximate the least squares solution by using the coefficients

$$\boldsymbol{c}_{i,j,l} = \boldsymbol{X}(\xi_i, \eta_j, \zeta_l)$$

which is equivalent to interpolation at the GLL nodes.

For smooth geometries this approach has spectral convergence to the exact geometry as illustrated in Figure 1.

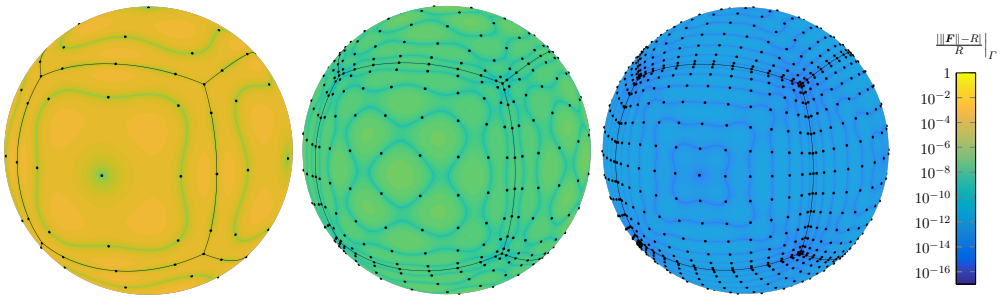

(a) $p_\xi = p_\eta = p_\zeta = 4$ (b) $p_\xi = p_\eta = p_\zeta = 9$ (c) $p_\xi = p_\eta = p_\zeta = 14$

Figure 1: Geometric error in the approximation of the sphere geometry using 6 patches. Machine epsilon precision is reached for polynomial degrees above 19. The approximation is based on the exact parametrization of a sphere using 6 NURBS patches.

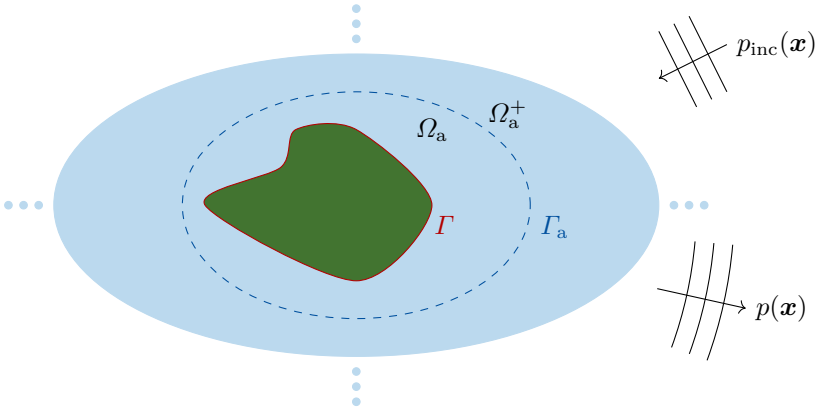

Figure 2: An artificial boundary Γ_{a} is introduced such that the exterior domain Ω^+ is decomposed by the two domains Ω_{a} (which is bounded by Γ and Γ_{a}) and Ω_{a}^+. Thus, $\Omega^+ = \Omega_{\text{a}} \cup \Omega_{\text{a}}^+$.

4. Exterior Helmholtz problems

The exterior Helmholtz problem is given by

$$\nabla^2 p + k^2 p = 0 \qquad \text{in} \quad \Omega^+, \tag{11}$$

$$\partial_n p = g \qquad \text{on} \quad \Gamma, \tag{12}$$

$$\frac{\partial p}{\partial r} - \mathrm{i}kp = o\left(r^{-1}\right) \quad \text{with} \quad r = |\boldsymbol{x}| \tag{13}$$

where the Sommerfeld condition [27] in Eq. (13) restricts the field in the limit $r \to \infty$ uniformly in $\hat{\boldsymbol{x}} = \frac{\boldsymbol{x}}{r}$, such that no waves originate from infinity. The Neumann condition given by the function g will in the case of rigid scattering be given by the incident wave p_{inc}. Zero displacement of the fluid normal on the scatterer (rigid scattering) implies that $\partial_n(p + p_{\mathrm{inc}}) = 0$ where ∂_n denotes the partial derivative in the normal direction on the surface Γ (pointing "out" from Ω^+), which implies that

$$g = -\frac{\partial p_{\mathrm{inc}}}{\partial n}. \tag{14}$$

Plane incident waves (with amplitude $\mathrm{P}_{\mathrm{inc}}$) traveling in the direction $\boldsymbol{d}_{\mathrm{s}}$ can be written as

$$p_{\mathrm{inc}}(\boldsymbol{x}) = \mathrm{P}_{\mathrm{inc}} \mathrm{e}^{\mathrm{i}k\boldsymbol{d}_{\mathrm{s}} \cdot \boldsymbol{x}}. \tag{15}$$

The normal derivative on the surface of any smooth geometry may then be computed by

$$\frac{\partial p_{\mathrm{inc}}}{\partial n} = \boldsymbol{n} \cdot \nabla p_{\mathrm{inc}} = \mathrm{i}k\boldsymbol{d}_{\mathrm{s}} \cdot \boldsymbol{n} p_{\mathrm{inc}}. \tag{16}$$

The weak formulation for the Helmholtz problem can be shown to be (for details regarding the involved spaces, cf. [22] and references therein)

$$\text{Find} \quad p \in H_w^{1+}(\Omega^+) \quad \text{such that} \quad B(q,p) = L(q), \qquad \forall q \in H_{w^*}^1(\Omega^+), \tag{17}$$

where the bilinear form is given by

$$B(q,p) = \int_{\Omega^+} \left[\nabla q \cdot \nabla p - k^2 qp\right] \mathrm{d}\Omega \tag{18}$$

and the corresponding linear form is given by

$$L(q) = \int_{\Gamma} qg \, \mathrm{d}\Gamma.$$

The numerical solution (trial function) is expressed by the same Lagrange basis functions used to approximate the geometry

$$\hat{p}(\xi,\eta,\zeta) = \sum_{i=1}^{n_\xi} \sum_{j=1}^{n_\eta} \sum_{l=1}^{n_\zeta} \hat{p}_{i,j,l} l_i(\xi) l_j(\eta) l_l(\zeta).$$

The parametric solution is related to the solution in the physical space by

$$\hat{p}(\xi,\eta,\zeta) = (p \circ \boldsymbol{C})(\xi,\eta,\zeta).$$

The derivatives are then given by the chain rule

$$\frac{\partial \hat{p}}{\partial \xi} = \frac{\partial p}{\partial x_1}\frac{\partial F_1}{\partial \xi} + \frac{\partial p}{\partial x_2}\frac{\partial F_2}{\partial \xi} + \frac{\partial p}{\partial x_3}\frac{\partial F_3}{\partial \xi} = \nabla p \cdot \frac{\partial \boldsymbol{C}}{\partial \xi}$$

and correspondingly for the other parametric derivatives such that

$$\hat{\nabla}\hat{p} = \boldsymbol{J}^\top \nabla p$$

where

$$\boldsymbol{J} = \begin{bmatrix} \frac{\partial \boldsymbol{C}}{\partial \xi} & \frac{\partial \boldsymbol{C}}{\partial \eta} & \frac{\partial \boldsymbol{C}}{\partial \zeta} \end{bmatrix} = \begin{bmatrix} \frac{\partial C_1}{\partial \xi} & \frac{\partial C_1}{\partial \eta} & \frac{\partial C_1}{\partial \zeta} \\ \frac{\partial C_2}{\partial \xi} & \frac{\partial C_2}{\partial \eta} & \frac{\partial C_2}{\partial \zeta} \\ \frac{\partial C_3}{\partial \xi} & \frac{\partial C_3}{\partial \eta} & \frac{\partial C_3}{\partial \zeta} \end{bmatrix}.$$

We therefore have

$$\nabla p = \boldsymbol{J}^{-\top}\hat{\nabla}\hat{p}.$$

Insertion of the trial function into the bilinear form (restricted to Ω_a) in Eq. (18) alongside test functions of the form

$$\hat{q}(\xi,\eta,\zeta) = l_{\tilde{i}}(\xi) l_{\tilde{j}}(\eta) l_{\tilde{l}}(\zeta), \quad 1 \leqslant \tilde{i} \leqslant n_\xi, \quad 1 \leqslant \tilde{j} \leqslant n_\eta, \quad 1 \leqslant \tilde{l} \leqslant n_\zeta$$

yields

$$\begin{aligned}
B(q,p) &= \int_{\Omega_\mathrm{a}} \Big(\nabla q \cdot \nabla p - k^2 q p\Big)\,\mathrm{d}\Omega = \int_{-1}^{1}\int_{-1}^{1}\int_{-1}^{1} \Big((\hat{\nabla}\hat{q})^\top \boldsymbol{J}^{-1}\boldsymbol{J}^{-\top}\hat{\nabla}\hat{p} - k^2\hat{q}\hat{p}\Big) J\,\mathrm{d}\xi\,\mathrm{d}\eta\,\mathrm{d}\zeta \\
&= \sum_{i,j,l}\int_{-1}^{1}\int_{-1}^{1}\int_{-1}^{1} \hat{p}_{i,j,l}\Big([l_{\tilde{i}}'(\xi) l_{\tilde{j}}(\eta) l_{\tilde{l}}(\zeta), l_{\tilde{i}}(\xi) l_{\tilde{j}}'(\eta) l_{\tilde{l}}(\zeta), l_{\tilde{i}}(\xi) l_{\tilde{j}}(\eta) l_{\tilde{l}}'(\zeta)] \\
&\qquad\qquad \tilde{\boldsymbol{G}}[l_i'(\xi) l_j(\eta) l_l(\zeta), l_i(\xi) l_j'(\eta) l_l(\zeta), l_i(\xi) l_j(\eta) l_l'(\zeta)]^\top \\
&\qquad\qquad -k^2 l_{\tilde{i}}(\xi) l_{\tilde{j}}(\eta) l_{\tilde{l}}(\zeta) l_i(\xi) l_j(\eta) l_l(\zeta) J\Big)\,\mathrm{d}\xi\,\mathrm{d}\eta\,\mathrm{d}\zeta \\
&\approx \sum_{i,j,l}\hat{p}_{i,j,l}\sum_{\alpha\beta\gamma}\Big([l_{\tilde{i}}'(\xi_\alpha) l_{\tilde{j}}(\eta_\beta) l_{\tilde{l}}(\zeta_\gamma), l_{\tilde{i}}(\xi_\alpha) l_{\tilde{j}}'(\eta_\beta) l_{\tilde{l}}(\zeta_\gamma), l_{\tilde{i}}(\xi_\alpha) l_{\tilde{j}}(\eta_\beta) l_{\tilde{l}}'(\zeta_\gamma)] \\
&\qquad\qquad \tilde{\boldsymbol{G}}_{\alpha\beta\gamma}[l_i'(\xi_\alpha) l_j(\eta_\beta) l_l(\zeta_\gamma), l_i(\xi_\alpha) l_j'(\eta_\beta) l_l(\zeta_\gamma), l_i(\xi_\alpha) l_j(\eta_\beta) l_l'(\zeta_\gamma)]^\top \\
&\qquad\qquad -k^2 l_{\tilde{i}}(\xi_\alpha) l_{\tilde{j}}(\eta_\beta) l_{\tilde{l}}(\zeta_\gamma) l_i(\xi_\alpha) l_j(\eta_\beta) l_l(\zeta_\gamma) J_{\alpha\beta\gamma}\Big) \\
&= \sum_{i,j,l}\hat{p}_{i,j,l}\sum_{\alpha\beta\gamma}\Big([D^{\boldsymbol{t}_\xi}_{\tilde{i}\alpha}\delta_{\tilde{j}\beta}\delta_{\tilde{l}\gamma}, \delta_{\tilde{i}\alpha}D^{\boldsymbol{t}_\eta}_{\tilde{j}\beta}\delta_{\tilde{l}\gamma}, \delta_{\tilde{i}\alpha}\delta_{\tilde{j}\beta}D^{\boldsymbol{t}_\zeta}_{\tilde{l}\gamma}]\tilde{\boldsymbol{G}}_{\alpha\beta\gamma}[D^{\boldsymbol{t}_\xi}_{i\alpha}\delta_{j\beta}\delta_{l\gamma}, \delta_{i\alpha}D^{\boldsymbol{t}_\eta}_{j\beta}\delta_{l\gamma}, \delta_{i\alpha}\delta_{j\beta}D^{\boldsymbol{t}_\zeta}_{l\gamma}]^\top \\
&\qquad\qquad -k^2\delta_{\tilde{i}\alpha}\delta_{\tilde{j}\beta}\delta_{\tilde{l}\gamma}\delta_{i\alpha}\delta_{j\beta}\delta_{l\gamma}J_{\tilde{i}\tilde{j}\tilde{l}}\Big) \\
&= -k^2\rho_{\tilde{i}}\rho_{\tilde{j}}\rho_{\tilde{l}}\hat{p}_{\tilde{i},\tilde{j},\tilde{l}}J_{\tilde{i}\tilde{j}\tilde{l}} + \sum_{i,j,l}\hat{p}_{i,j,l}\sum_{\alpha\beta\gamma} w_{ijl\alpha\beta\gamma\tilde{i}\tilde{j}\tilde{l}}
\end{aligned}$$

where

$$J_{\alpha\beta\gamma} = J(\xi_\alpha, \eta_\beta, \zeta_\gamma), \quad J = \det \boldsymbol{J}, \quad \tilde{\boldsymbol{G}}_{\alpha\beta\gamma} = \rho_\alpha \rho_\beta \rho_\gamma \tilde{\boldsymbol{G}}(\xi_\alpha, \eta_\beta, \zeta_\gamma),$$
$$\tilde{\boldsymbol{G}} = J\boldsymbol{G}, \quad \boldsymbol{G} = \boldsymbol{J}^{-1}\boldsymbol{J}^{-\top} \quad D_{i\alpha}^{\boldsymbol{t}_\xi} = l_i'(\xi_\alpha), \quad D_{j\beta}^{\boldsymbol{t}_\eta} = l_j'(\eta_\beta), \quad D_{l\gamma}^{\boldsymbol{t}_\zeta} = l_l'(\zeta_\gamma)$$
$$w_{ijl\alpha\beta\gamma\tilde{i}\tilde{j}\tilde{l}} = [D_{\tilde{i}\alpha}^{\boldsymbol{t}_\xi}\delta_{\tilde{j}\beta}\delta_{\tilde{l}\gamma}, \delta_{\tilde{i}\alpha}D_{\tilde{j}\beta}^{\boldsymbol{t}_\eta}\delta_{\tilde{l}\gamma}, \delta_{\tilde{i}\alpha}\delta_{\tilde{j}\beta}D_{\tilde{l}\gamma}^{\boldsymbol{t}_\zeta}]\tilde{\boldsymbol{G}}_{\alpha\beta\gamma}[D_{i\alpha}^{\boldsymbol{t}_\xi}\delta_{j\beta}\delta_{l\gamma}, \delta_{i\alpha}D_{j\beta}^{\boldsymbol{t}_\eta}\delta_{l\gamma}, \delta_{i\alpha}\delta_{j\beta}D_{l\gamma}^{\boldsymbol{t}_\zeta}]^\top.$$

For a set of indices $i, j, l, \tilde{i}, \tilde{j}, \tilde{l}$, we have

$$\begin{aligned}
\sum_{\alpha\beta\gamma} w_{ijl\alpha\beta\gamma\tilde{i}\tilde{j}\tilde{l}} &= \sum_{\alpha\beta\gamma}[D_{\tilde{i}\alpha}^{\boldsymbol{t}_\xi}\delta_{\tilde{j}\beta}\delta_{\tilde{l}\gamma}, \delta_{\tilde{i}\alpha}D_{\tilde{j}\beta}^{\boldsymbol{t}_\eta}\delta_{\tilde{l}\gamma}, \delta_{\tilde{i}\alpha}\delta_{\tilde{j}\beta}D_{\tilde{l}\gamma}^{\boldsymbol{t}_\zeta}]\tilde{\boldsymbol{G}}_{\alpha\beta\gamma}[D_{i\alpha}^{\boldsymbol{t}_\xi}\delta_{j\beta}\delta_{l\gamma}, \delta_{i\alpha}D_{j\beta}^{\boldsymbol{t}_\eta}\delta_{l\gamma}, \delta_{i\alpha}\delta_{j\beta}D_{l\gamma}^{\boldsymbol{t}_\zeta}]^\top \\
&= \sum_{\alpha\beta\gamma}\Big(\Big[(\tilde{G}_{11})_{\alpha\beta\gamma}D_{i\alpha}^{\boldsymbol{t}_\xi}\delta_{j\beta}\delta_{l\gamma} + (\tilde{G}_{12})_{\alpha\beta\gamma}\delta_{i\alpha}D_{j\beta}^{\boldsymbol{t}_\eta}\delta_{l\gamma} + (\tilde{G}_{13})_{\alpha\beta\gamma}\delta_{i\alpha}\delta_{j\beta}D_{l\gamma}^{\boldsymbol{t}_\zeta}\Big]D_{\tilde{i}\alpha}^{\boldsymbol{t}_\xi}\delta_{\tilde{j}\beta}\delta_{\tilde{l}\gamma} \\
&\qquad + \Big[(\tilde{G}_{21})_{\alpha\beta\gamma}D_{i\alpha}^{\boldsymbol{t}_\xi}\delta_{j\beta}\delta_{l\gamma} + (\tilde{G}_{22})_{\alpha\beta\gamma}\delta_{i\alpha}D_{j\beta}^{\boldsymbol{t}_\eta}\delta_{l\gamma} + (\tilde{G}_{23})_{\alpha\beta\gamma}\delta_{i\alpha}\delta_{j\beta}D_{l\gamma}^{\boldsymbol{t}_\zeta}\Big]\delta_{\tilde{i}\alpha}D_{\tilde{j}\beta}^{\boldsymbol{t}_\eta}\delta_{\tilde{l}\gamma} \\
&\qquad + \Big[(\tilde{G}_{31})_{\alpha\beta\gamma}D_{i\alpha}^{\boldsymbol{t}_\xi}\delta_{j\beta}\delta_{l\gamma} + (\tilde{G}_{32})_{\alpha\beta\gamma}\delta_{i\alpha}D_{j\beta}^{\boldsymbol{t}_\eta}\delta_{l\gamma} + (\tilde{G}_{33})_{\alpha\beta\gamma}\delta_{i\alpha}\delta_{j\beta}D_{l\gamma}^{\boldsymbol{t}_\zeta}\Big]\delta_{\tilde{i}\alpha}\delta_{\tilde{j}\beta}D_{\tilde{l}\gamma}^{\boldsymbol{t}_\zeta}\Big) \\
&= \delta_{\tilde{l}\tilde{l}}(\tilde{G}_{12})_{i\tilde{j}l}D_{\tilde{i}i}^{\boldsymbol{t}_\xi}D_{\tilde{j}\tilde{j}}^{\boldsymbol{t}_\eta} + \delta_{\tilde{j}\tilde{j}}(\tilde{G}_{13})_{ij\tilde{l}}D_{\tilde{i}i}^{\boldsymbol{t}_\xi}D_{\tilde{l}\tilde{l}}^{\boldsymbol{t}_\zeta} + \delta_{\tilde{j}\tilde{j}}\delta_{\tilde{l}\tilde{l}}\sum_{\alpha=1}^{n_\xi}(\tilde{G}_{11})_{\alpha jl}D_{i\alpha}^{\boldsymbol{t}_\xi}D_{\tilde{i}\alpha}^{\boldsymbol{t}_\xi} \\
&\quad + \delta_{\tilde{l}\tilde{l}}(\tilde{G}_{12})_{\tilde{i}jl}D_{i\tilde{i}}^{\boldsymbol{t}_\xi}D_{\tilde{j}j}^{\boldsymbol{t}_\eta} + \delta_{\tilde{i}\tilde{i}}(\tilde{G}_{23})_{ij\tilde{l}}D_{\tilde{j}j}^{\boldsymbol{t}_\eta}D_{l\tilde{l}}^{\boldsymbol{t}_\zeta} + \delta_{\tilde{i}\tilde{i}}\delta_{\tilde{l}\tilde{l}}\sum_{\beta=1}^{n_\eta}(\tilde{G}_{22})_{i\beta l}D_{j\beta}^{\boldsymbol{t}_\eta}D_{\tilde{j}\beta}^{\boldsymbol{t}_\eta} \\
&\quad + \delta_{\tilde{j}\tilde{j}}(\tilde{G}_{13})_{\tilde{i}jl}D_{i\tilde{i}}^{\boldsymbol{t}_\xi}D_{l\tilde{l}}^{\boldsymbol{t}_\zeta} + \delta_{\tilde{i}\tilde{i}}(\tilde{G}_{23})_{i\tilde{j}l}D_{j\tilde{j}}^{\boldsymbol{t}_\eta}D_{l\tilde{l}}^{\boldsymbol{t}_\zeta} + \delta_{\tilde{i}\tilde{i}}\delta_{\tilde{j}\tilde{j}}\sum_{\gamma=1}^{n_\zeta}(\tilde{G}_{33})_{ij\gamma}D_{l\gamma}^{\boldsymbol{t}_\zeta}D_{\tilde{l}\gamma}^{\boldsymbol{t}_\zeta}
\end{aligned}$$

where we have exploited the symmetry of $\tilde{\boldsymbol{G}}$. Although the 1D stiffness matrix for an element is fully dense, this is not the case for higher dimensional SEM stiffness matrices. This is again due to Eq. (1). An upper bound on the number of non-zero elements in the stiffness matrix can be shown to be $n_\xi n_\eta^2 n_\zeta^2 + n_\xi^2 n_\eta n_\zeta^2 + n_\xi n_\eta^2 n_\zeta$. Defining $n = \max\{n_\xi, n_\eta, n_\zeta\}$, then an lower bound on the sparsity of the stiffness matrix is $1 - d/n$ (with d being the dimension of the problem), meaning the sparsity is increased as a function of the number of degrees of freedom. This is in stark contrast to an IGA element matrix which will in general be fully dense (cf. [28]) when pure $\check{p}$-refinement is used.

For the linear form, we simply get (assuming the boundary Γ is parameterized by ξ and η at $\zeta = 0$)

$$L(q) = \int_\Gamma qg \,\mathrm{d}\Gamma = \rho_{\tilde{i}}\rho_{\tilde{j}}\hat{g}_{\tilde{i}\tilde{j}}H_{\tilde{i}\tilde{j}}\delta_{0\tilde{l}}.$$

where

$$\hat{g}_{\alpha,\beta} = (g \circ \boldsymbol{C})(\xi_\alpha, \eta_\beta, -1), \quad H_{\alpha\beta} = H(\xi_\alpha, \eta_\beta), \quad H(\xi, \eta) = \left\| \frac{\partial \boldsymbol{C}|_\Gamma}{\partial \xi} \times \frac{\partial \boldsymbol{C}|_\Gamma}{\partial \eta} \right\|.$$

In order to evaluate the derivatives of the mapping $\boldsymbol{C}$ at the GLL nodes we note that

$$\left.\frac{\partial \boldsymbol{C}}{\partial \xi}\right|_{(\xi_\alpha, \eta_\beta, \zeta_\gamma)} = \sum_{i,j,l} \boldsymbol{c}_{i,j,l} l_i'(\xi_\alpha) l_j(\eta_\beta) l_l(\zeta_\gamma) = \sum_{i=1}^{n_\xi} \boldsymbol{c}_{i,\beta,\gamma} l_i'(\xi_\alpha).$$

If we then store the derivatives $l_i'(\xi_\alpha)$ in the matrix $\boldsymbol{D}^{\boldsymbol{t}_\xi} \in \mathbb{R}^{n_\xi \times n_\xi}$ all evaluations may be done efficiently by the matrix-matrix products $\boldsymbol{D}^{\boldsymbol{t}_\xi}\boldsymbol{c}$ where the multidimensional array $\boldsymbol{c} \in \mathbb{R}^{3\times n_\xi \times n_\eta \times n_\zeta}$ is the collection of all coefficients of $\boldsymbol{C}$. Note that $\boldsymbol{c}$ must be rearranged in order to make sense of the product with $\boldsymbol{D}^{\boldsymbol{t}_\xi}$. Corresponding efficient evaluations of the other derivatives at the GLL points can be performed in a similar procedure.

The contributions from the infinite elements can be correspondingly efficiently evaluated using the following formulas

$$
\begin{aligned}
A^{(1)}_{ij\tilde{i}\tilde{j}} &= \int_{-1}^{1}\int_{-1}^{1} l_i(\xi)l_j(\eta)l_{\tilde{i}}(\xi)l_{\tilde{j}}(\eta)\sin[\vartheta(\xi,\eta)]J^{(3)}(\xi,\eta)\,\mathrm{d}\xi\,\mathrm{d}\eta \\
&\approx \delta_{i\tilde{i}}\delta_{j\tilde{j}}\rho_{\tilde{i}}\rho_{\tilde{j}}\sin\vartheta_{\tilde{i}\tilde{j}}J^{(3)}_{\tilde{i}\tilde{j}} \\
A^{(2)}_{ij\tilde{i}\tilde{j}} &= \int_{-1}^{1}\int_{-1}^{1} \Big[J^{(5)}_{11}l_i'l_{\tilde{i}}'l_jl_{\tilde{j}} + J^{(5)}_{12}\Big(l_i'l_{\tilde{i}}l_jl_{\tilde{j}}' + l_il_{\tilde{i}}'l_j'l_{\tilde{j}}\Big) + J^{(5)}_{13}l_il_{\tilde{i}}l_j'l_{\tilde{j}}'\Big]\sin\vartheta\,\mathrm{d}\xi\,\mathrm{d}\eta \\
&\approx \delta_{j\tilde{j}}\sum_{\alpha=1}^{n_\xi} J^{(5)}_{11,\alpha j}D^{\boldsymbol{t}_\xi}_{i\alpha}D^{\boldsymbol{t}_\xi}_{\tilde{i}\alpha} + J^{(5)}_{12,\tilde{i}j}D^{\boldsymbol{t}_\xi}_{i\tilde{i}}D^{\boldsymbol{t}_\eta}_{\tilde{j}j} + J^{(5)}_{12,i\tilde{j}}D^{\boldsymbol{t}_\xi}_{\tilde{i}i}D^{\boldsymbol{t}_\eta}_{j\tilde{j}} + \delta_{i\tilde{i}}\sum_{\beta=1}^{n_\eta} J^{(5)}_{13,i\beta}D^{\boldsymbol{t}_\eta}_{j\beta}D^{\boldsymbol{t}_\eta}_{\tilde{j}\beta} \\
A^{(3)}_{ij\tilde{i}\tilde{j}} &= \int_{-1}^{1}\int_{-1}^{1} l_i(\xi)l_j(\eta)l_{\tilde{i}}(\xi)l_{\tilde{j}}(\eta)\sin[\vartheta(\xi,\eta)]J_3(\xi,\eta)\,\mathrm{d}\xi\,\mathrm{d}\eta \\
&\approx \delta_{i\tilde{i}}\delta_{j\tilde{j}}\rho_{\tilde{i}}\rho_{\tilde{j}}\cos^2\vartheta_{\tilde{i}\tilde{j}}\sin\vartheta_{\tilde{i}\tilde{j}}J^{(3)}_{\tilde{i}\tilde{j}} \\
A^{(4)}_{ij\tilde{i}\tilde{j}} &= \int_{-1}^{1}\int_{-1}^{1} \Big[J^{(5)}_{21}l_i'l_{\tilde{i}}'l_jl_{\tilde{j}} + J^{(5)}_{22}\Big(l_i'l_{\tilde{i}}l_jl_{\tilde{j}}' + l_il_{\tilde{i}}'l_j'l_{\tilde{j}}\Big) + J^{(5)}_{23}l_il_{\tilde{i}}l_j'l_{\tilde{j}}'\Big]\frac{1}{\sin\vartheta}\,\mathrm{d}\xi\,\mathrm{d}\eta \\
&\approx \delta_{j\tilde{j}}\sum_{\alpha=1}^{n_\xi} J^{(5)}_{21,\alpha j}D^{\boldsymbol{t}_\xi}_{i\alpha}D^{\boldsymbol{t}_\xi}_{\tilde{i}\alpha} + J^{(5)}_{22,\tilde{i}j}D^{\boldsymbol{t}_\xi}_{i\tilde{i}}D^{\boldsymbol{t}_\eta}_{\tilde{j}j} + J^{(5)}_{22,i\tilde{j}}D^{\boldsymbol{t}_\xi}_{\tilde{i}i}D^{\boldsymbol{t}_\eta}_{j\tilde{j}} + \delta_{i\tilde{i}}\sum_{\beta=1}^{n_\eta} J^{(5)}_{23,i\beta}D^{\boldsymbol{t}_\eta}_{j\beta}D^{\boldsymbol{t}_\eta}_{\tilde{j}\beta} \\
A^{(5)}_{ij\tilde{i}\tilde{j}} &= \int_{-1}^{1}\int_{-1}^{1} \Big[J^{(5)}_{21}l_i'l_{\tilde{i}}'l_jl_{\tilde{j}} + J^{(5)}_{22}\Big(l_i'l_{\tilde{i}}l_jl_{\tilde{j}}' + l_il_{\tilde{i}}'l_j'l_{\tilde{j}}\Big) + J^{(5)}_{23}l_il_{\tilde{i}}l_j'l_{\tilde{j}}'\Big]\frac{\cos^2\theta}{\sin\vartheta}\,\mathrm{d}\xi\,\mathrm{d}\eta \\
&\approx \delta_{j\tilde{j}}\sum_{\alpha=1}^{n_\xi} J^{(5)}_{31,\alpha j}D^{\boldsymbol{t}_\xi}_{i\alpha}D^{\boldsymbol{t}_\xi}_{\tilde{i}\alpha} + J^{(5)}_{32,\tilde{i}j}D^{\boldsymbol{t}_\xi}_{i\tilde{i}}D^{\boldsymbol{t}_\eta}_{\tilde{j}j} + J^{(5)}_{32,i\tilde{j}}D^{\boldsymbol{t}_\xi}_{\tilde{i}i}D^{\boldsymbol{t}_\eta}_{j\tilde{j}} + \delta_{i\tilde{i}}\sum_{\beta=1}^{n_\eta} J^{(5)}_{33,i\beta}D^{\boldsymbol{t}_\eta}_{j\beta}D^{\boldsymbol{t}_\eta}_{\tilde{j}\beta}
\end{aligned}
$$

where

$$
\begin{aligned}
J^{(5)}_{1j,\alpha\beta} &= \rho_\alpha\rho_\beta\sin\theta_{\alpha\beta}J^{(5)}_{1j}(\xi_\alpha,\eta_\beta), \quad J^{(5)}_{2j,\alpha\beta} = \frac{\rho_\alpha\rho_\beta}{\sin\theta_{\alpha\beta}}J^{(5)}_{2j}(\xi_\alpha,\eta_\beta), \\
J^{(5)}_{3j,\alpha\beta} &= \rho_\alpha\rho_\beta\frac{\cos^2\theta_{\alpha\beta}}{\sin\theta_{\alpha\beta}}J^{(5)}_{2j}(\xi_\alpha,\eta_\beta), \quad \boldsymbol{J}^{(4)} = \begin{bmatrix} J^{(4)}_{11} & J^{(4)}_{12} \\ J^{(4)}_{21} & J^{(4)}_{22}\end{bmatrix} := \Big[\boldsymbol{J}^{(3)}\Big]^{-\top} \\
\boldsymbol{J}^{(5)} &= \begin{bmatrix} J^{(5)}_{11} & J^{(5)}_{12} & J^{(5)}_{13} \\ J^{(5)}_{21} & J^{(5)}_{22} & J^{(5)}_{23}\end{bmatrix} := J^{(3)}\begin{bmatrix} J^{(4)}_{11}J^{(4)}_{11} & J^{(4)}_{12}J^{(4)}_{11} & J^{(4)}_{12}J^{(4)}_{12} \\ J^{(4)}_{21}J^{(4)}_{21} & J^{(4)}_{22}J^{(4)}_{21} & J^{(4)}_{22}J^{(4)}_{22}\end{bmatrix}
\end{aligned}
$$

where $\theta_{\alpha\beta}$ is the polar angle (evaluated using [22, Equation (A.4)]) at the GLL point $\boldsymbol{X}(\xi_\alpha,\eta_\beta,1)$.

5. Numerical examples

5.1. Poisson 1D problem

As a motivational example, consider first the simplest 1D Poisson problem given by

$$\begin{aligned} \nabla^2 u &= -f, \quad \text{in} \quad \Omega = (-1,1) \\ u(-1) &= u(1) = 0 \end{aligned}$$

with $f(x) = (x^2+4x+1)\mathrm{e}^x$ and analytic solution given by $u(x) = (1-x^2)\mathrm{e}^x$. We solve this problem using the spectral element method with one element, and compare with IGA using one and five elements (where the former is equivalent to FEM using the Bernstein basis and the latter is refined with $\check{k}$-refinement). The relative error in the energy norm (H^1-seminorm for Poisson) is plotted in Figure 3. Note first the expected spectral convergence. Using IGA with $n_{\text{el}} = 1$ one should obtain identical results in the absence of round off errors and errors in the integral approximations as the Bernstein and Lagrange basis functions both span $P_{\check{p}}$ in this case. The integrals are computed by $n = \check{p}+1$ quadrature points such that both SEM and IGA obtains exact integration of the bilinear form. This is because the integrand in the bilinear form has polynomial degree $2\check{p}-2 = 2n-4$ and Lobatto (for SEM) and Legendre (for IGA) quadrature rules integrates exactly polynomials up to degree $2n-3$ and $2n-1$, respectively. The integral for the right-hand side, however, is not evaluated exactly (as the integrand is not a polynomial) and gives slightly different results for the two methods (in favor of IGA). Using more elements in IGA reduces the continuity of the basis functions to $C^{\check{p}-1}$ which reduces the quality of the solution, suggesting using maximum continuity wherever the solution is smooth (in this case in the whole domain). Finally, we observe instabilities for the IGA method for high polynomial orders which can be explained by the exponential increase of the condition number of the stiffness matrix illustrated in Figure 4 as opposed to the algebraic increase of the condition number for the SEM. Similar results are presented in [28]. In fact, they present the behavior of the condition number for the stiffness matrix as

$$\text{SEM:} \quad \text{Cond}(\boldsymbol{K}) \sim h^{-2}\check{p}^3 \tag{19}$$

$$C^0\text{-IGA:} \quad \text{Cond}(\boldsymbol{K}) \sim \begin{cases} h^{-2}\check{p}^2 & \text{if } h < \sqrt{\check{p}^{2+d/2}4^{-d\check{p}}} \\ \check{p}^{-d/2}4^{d\check{p}} & \text{otherwise} \end{cases} \tag{20}$$

$$C^{\check{p}-1}\text{-IGA:} \quad \text{Cond}(\boldsymbol{K}) \sim \begin{cases} h^{-2}\check{p} & \text{if } h < \mathrm{e}^{-d\check{p}/2} \\ \check{p}\mathrm{e}^{d\check{p}} & \text{if } \mathrm{e}^{-d\check{p}/2} < h < 1/\check{p} \\ \left(\frac{\mathrm{e}}{4}\right)^{d/h}\check{p}^{-d/2}h^{-d/2-1}4^{d\check{p}} & \text{otherwise.} \end{cases} \tag{21}$$

In other words, degree elevation are more restricted using IGA compared to SEM.

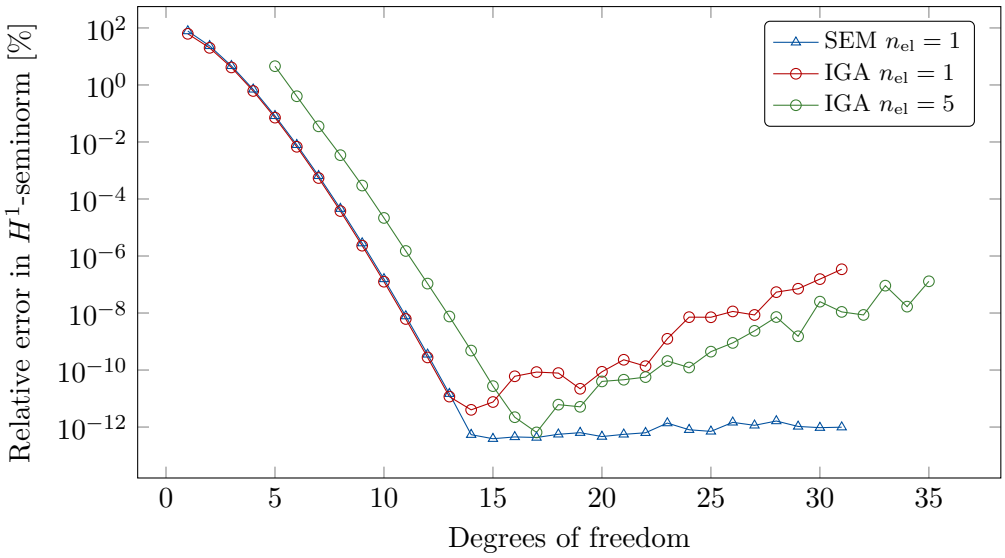

Figure 3: **Poisson 1D problem**: Illustration of the spectral convergence for SEM and IGA.

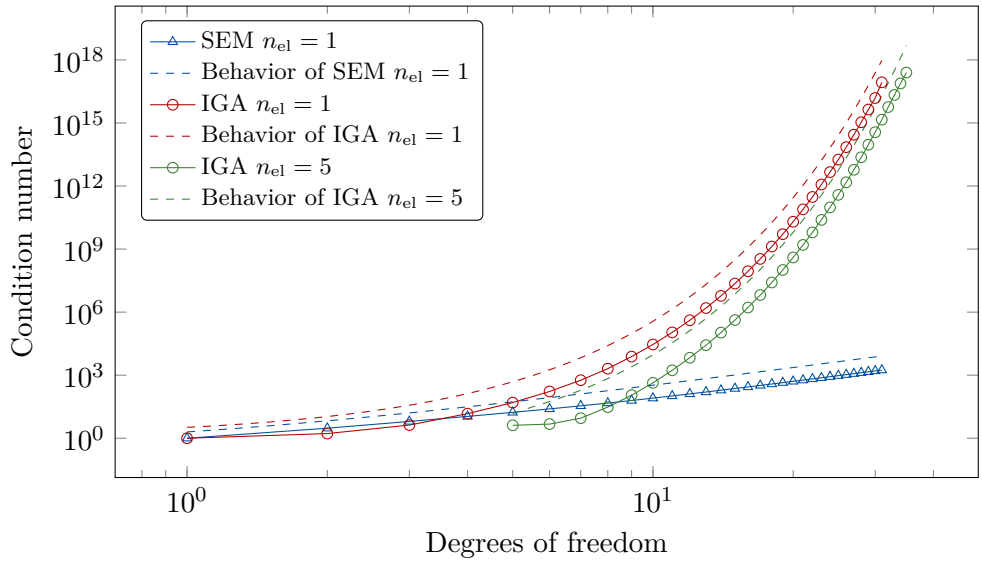

Figure 4: **Poisson 1D problem**: An exponential behavior of the condition number is obtained for IGA, but only algebraic order is obtained for SEM when considering $\check{p}$-refinement and $\check{k}$-refinement, respectively. The behavior estimates for the two methods (found in Eqs. (19) and (21), respectively) has been added

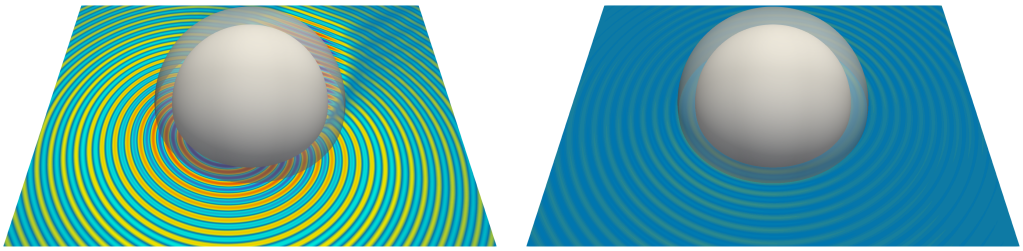

Figure 5: **Rigid scattering on a sphere**: Plots of the near field of the scattered pressure resulting from a plane wave incident on a sphere at $f = 10\,\mathrm{kHz}$. The plot to the left is the full solution, whereas the plot to the right is the solution resulting from the three first terms in the series expansion of the exact solution. The visualization was done in Paraview.

5.2. Rigid scattering on a sphere

Consider the S1 benchmark problem in [29] where a unit sphere ($R_0 = 1\,\mathrm{m}$) is impinged by the plane wave in Eq. (15). In the special case of $\boldsymbol{d}_\mathrm{s} = \boldsymbol{e}_\mathrm{z}$ the analytic solution to the problem is given by[4] (expressed using spherical coordinates)

$$p(r,\theta) = -\mathrm{P}_\mathrm{inc} \sum_{n=0}^{\infty} \mathrm{i}^n (2n+1) \frac{\mathrm{j}_n'(kR_0)}{\mathrm{h}_n'(kR_0)} \mathrm{P}_n(\cos\theta) \mathrm{h}_n(kr) \tag{22}$$

which can be generalized to arbitrary vectors $\boldsymbol{d}_\mathrm{s}$ using a orthogonal transformation. In the S1 benchmark problem the incident plane wave travels in the direction

$$\boldsymbol{d}_\mathrm{s} = -\begin{bmatrix} \cos\beta_\mathrm{s}\cos\alpha_\mathrm{s} \\ \cos\beta_\mathrm{s}\sin\alpha_\mathrm{s} \\ \sin\beta_\mathrm{s} \end{bmatrix}, \quad \text{where} \quad \alpha_\mathrm{s} = 240^\circ,\ \beta_\mathrm{s} = 30^\circ. \tag{23}$$

We shall use the same number of terms in the analytic series in Eq. (22) as the number of basis functions in the radial direction in the infinite elements to eliminate pollution from the infinite elements (cf. [30]). In the experiments we choose the Bubnov–Galerkin unconjugated (BGU) formulation and we only use $N = 3$ radial basis functions in the infinite elements to lower the conditioning of the system. The differences in the solutions are illustrated in Figure 5, where it is apparent that using only three terms in the series of the analytic solution is not even close to represent the full solution. But for the sake of convergence analysis it makes sense to consider this case to remove redundant noise from the infinite elements.

[4]Where $\mathrm{j}_n(x)$ is the n^th spherical Bessel function of the first kind and $\mathrm{h}_n(x)$ is the n^th spherical Hankel function of the first kind.

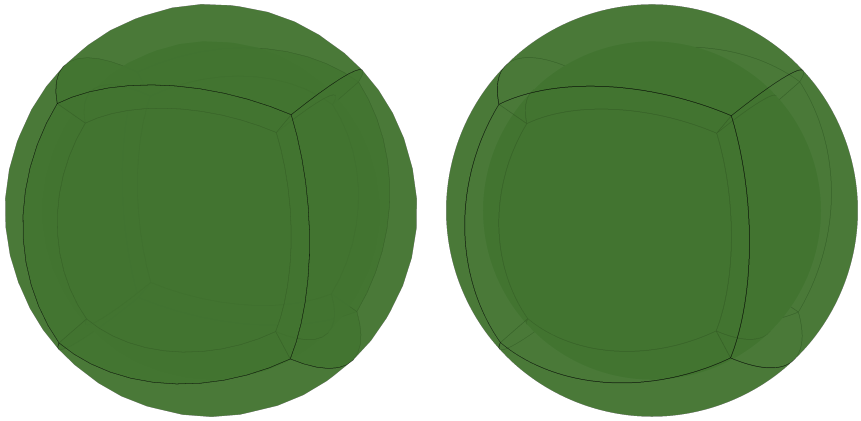

(a) IGA mesh (b) SEM mesh

Figure 6: **Rigid scattering on a sphere**: The exact IGA meshing of the spherical shell domain is visually identical to the SEM approximation of the same geometry using only $\check{p} = 4$.

We use the following definition of the energy norm (as in [22])

$$|||p|||_{\Omega_\mathrm{a}} = \sqrt{\int_{\Omega_\mathrm{a}} |\nabla p|^2 + k^2 |p|^2 \,\mathrm{d}\Omega} \tag{24}$$

and compute the integral by high order Gaussian quadrature (as the error should be more accurately computed than using the GLL nodes)

$$\begin{aligned}\int_{\Omega_\mathrm{a}} |\nabla p|^2 + k^2 |p|^2 \,\mathrm{d}\Omega &= \sum_{e=1}^{n_\mathrm{el}} \int_{\Omega_\mathrm{a}^e} |\nabla p|^2 + k^2 |p|^2 \,\mathrm{d}\Omega \\ &= \sum_{e=1}^{n_\mathrm{el}} \int_{-1}^{1}\int_{-1}^{1}\int_{-1}^{1} \left(|\nabla p|^2 + k^2 |p|^2\right) J \,\mathrm{d}\xi \,\mathrm{d}\eta \,\mathrm{d}\zeta.\end{aligned}$$

The meshes for both IGA and SEM are made based on 6 patches as illustrated in Figure 6. In Figure 7 we can again observe the expected spectral convergence for both IGA and SEM. Two simulations have been added for low and high frequencies[5], $f = 1\,\mathrm{kHz}$ and $f = 10\,\mathrm{kHz}$, respectively. For the high frequency case, it is apparent that the geometry approximation is of less importance compared to the low frequency case as the error from resolving the wavelength is dominating the error in the geometry approximation. We can again here observe the instabilities for IGA for high polynomial orders. This is again due to the large condition numbers in the stiffness and mass matrices for the IGA as illustrated in Figure 8.

[5]Given by $f = kc_\mathrm{f}/(2\pi)$ with $c_\mathrm{f} = 1500\,\mathrm{m/s}$.

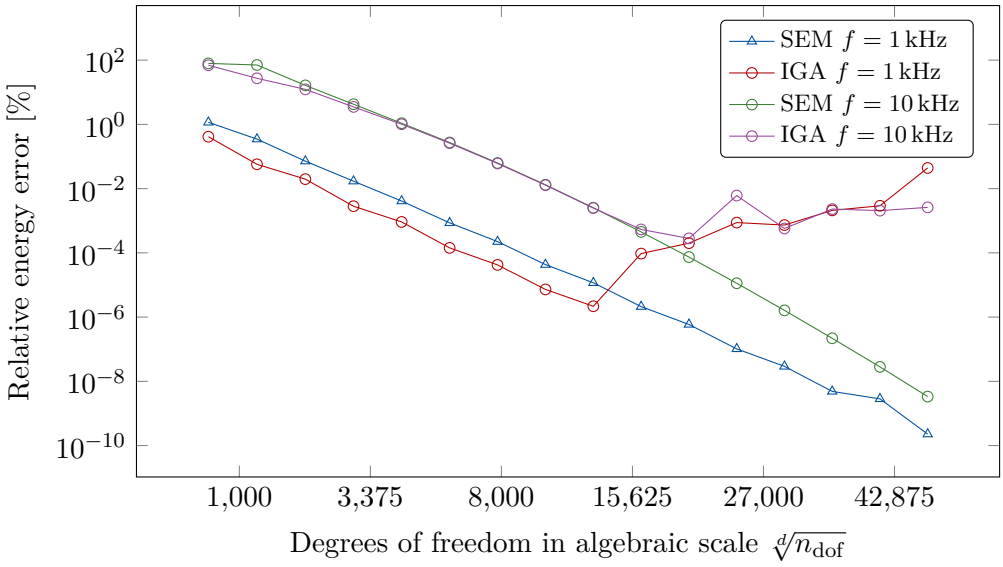

Figure 7: **Rigid scattering on a sphere**: Illustration of the spectral convergence for SEM and IGA.

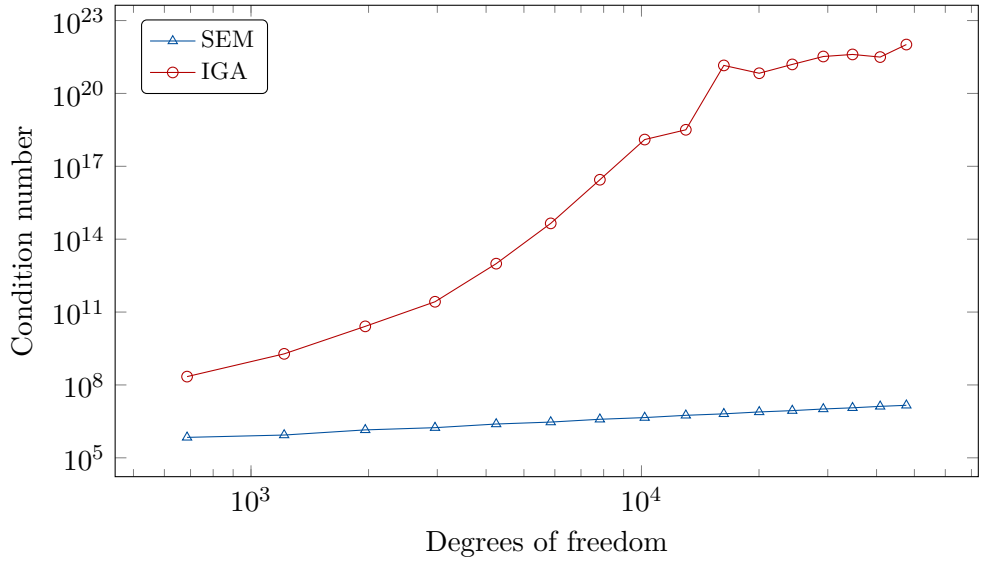

Figure 8: **Rigid scattering on a sphere**: An exponential behavior of the condition number is obtained for IGA, but only algebraic order is obtained for SEM when considering $\check{p}$-refinement.

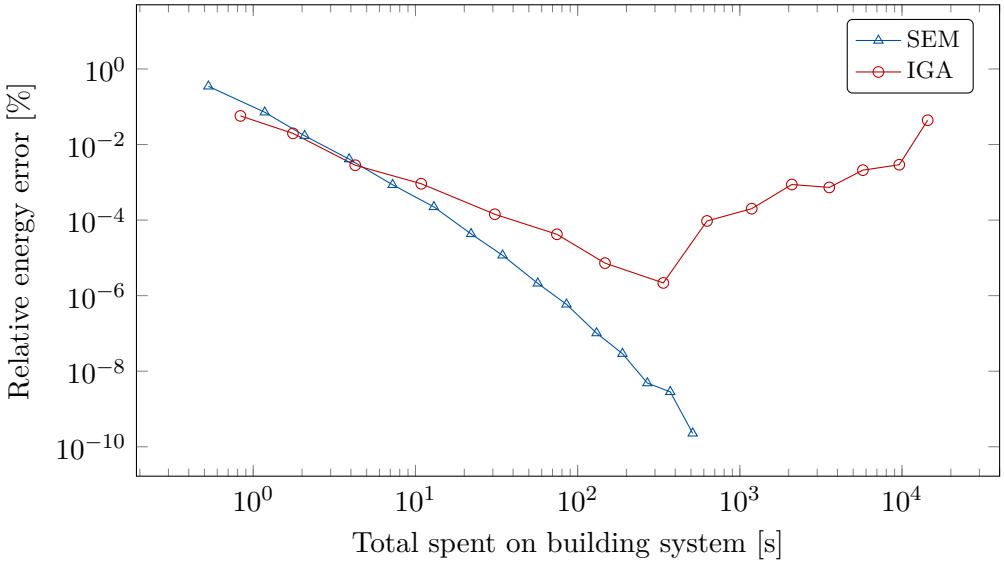

Figure 9: **Rigid scattering on a sphere**: The relative energy error is plotted against the total time spent on building the mass matrix, the stiffness matrix and the right-hand side vector.

The timings for building and solving the system for SEM and IGA are reported in Figure 9 and Figure 10, respectively. These figures are added to show the total timings in Figure 11. Here the key takeaway is the difference in convergence rate as a function of the time spent for both building and solving the system. The patch matrix construction is faster for SEM as the patch matrix sparsity goes as $\mathcal{O}(n^{-1})$, which is in contrast to the corresponding IGA matrices which are fully dense. This is also the reason for better timings for solving the system using SEM as the global matrices are much sparser compared to the global matrices for IGA.

It should be mentioned that many improvements are here possible for both SEM and IGA. An iterative method (GMRES, BiCGstab, etc.) would be preferable for the SEM to reduce memory requirement and increase the computational efficiency. The tensor product structure in the IGA method could be exploited better instead of looping through every quadrature points individually [31].

6. Conclusions

The usage of Lagrange polynomials yields a convenient method of obtaining a geometry approximation as interpolation and least squares (approximated with Lobatto quadrature) are equivalent. The geometry approximation is then obtained simply by evaluating the geometry parametrization in the GLL nodes in the

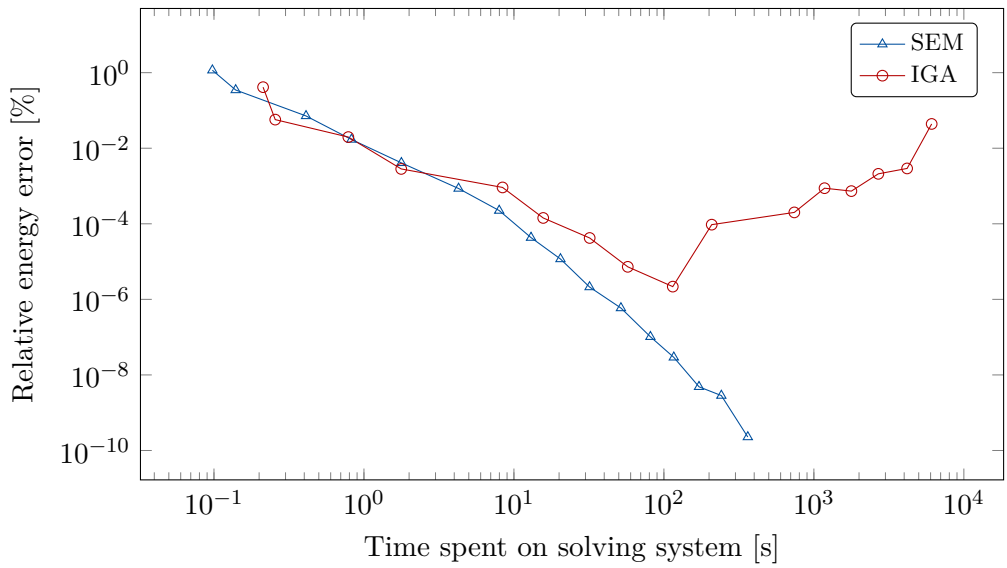

Figure 10: **Rigid scattering on a sphere**: The relative energy error is plotted against the computational time required to solve the system using a direct solver.

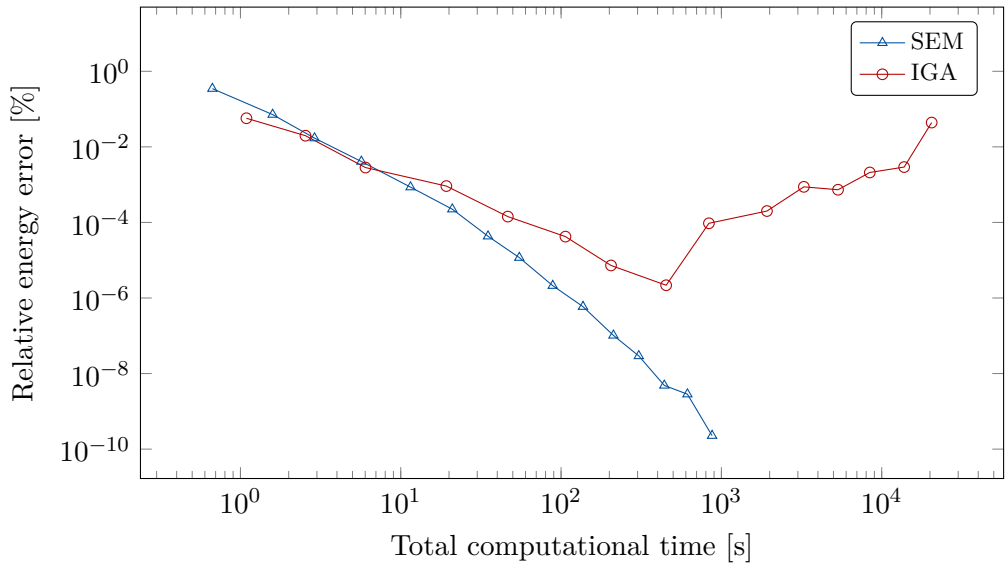

Figure 11: **Rigid scattering on a sphere**: The relative energy error is plotted against the total computational time (sum of the figures in Figure 9 and Figure 10).

parametric space. Thus, using this procedure, any tensor IGA mesh with exact geometry can easily be transformed to a SEM mesh with spectral convergence to the same exact geometry.

The spectral properties of IGA and SEM are similar, but IGA has instability with respect to high polynomial orders due to conditioning of the system. Moreover, due to the Kronecker delta property of the Lagrange basis functions, the computational times for both building and solving the system is favorable for SEM compared to IGA in the $\check{p}$-refinement case.

The usage of Lagrange polynomials as basis functions in the SEM increases the sparsity of the global matrices compared to any other set of basis functions for finite element analysis when pure $\check{p}$-refinement is used. Moreover, the choice of the GLL nodes as the nodes both for the Lagrange polynomials and integrational approximation increases the stability and computational efficiency, respectively.

Whenever there is a need to resolve the wavelength in acoustic scattering problems the geometry approximation becomes of less importance, as the error from the mesh resolution of the waves dominated the geometrical errors.

The examples illustrated in this work have C^∞-continuity which are ideal for SEM, as the basis functions are maximally smooth within each patch. Such problems would be optimally solved by spectral methods in the sense of convergence order. In the context of engineering, however, not only is an error of 0.1% (where IGA is competitive anyways) satisfactory results, we do not necessarily have smooth solutions. One must then turn to adaptive techniques, which is more suited for FEM than SEM.

A. A note on the infinite element method

The following problem occurs only in the very special scenario when quadrature points are placed at the poles (for the coordinate system used by the infinite elements) of the artificial boundary (refer to [22] for details and notations).

The integrand of the angular integrals [22, Eq. (A.18)] must be evaluated by limiting expressions at the poles ($\vartheta \to 0^+$ and $\vartheta \to \pi^-$). For the integrals

$$A_{IJ}^{(1)} = \int_{\varphi=0}^{2\pi} \int_{\vartheta=0}^{\pi} R_I R_J \sin\vartheta |J_3| \,\mathrm{d}\eta \,\mathrm{d}\xi$$

and

$$A_{IJ}^{(3)} = \int_{\varphi=0}^{2\pi} \int_{\vartheta=0}^{\pi} R_I R_J \cos^2\vartheta \sin\vartheta |J_3| \,\mathrm{d}\eta \,\mathrm{d}\xi$$

the problematic factors at the poles can be evaluated to be (using Maple)

$$\lim_{\vartheta\to 0^+} \sin\vartheta |J_3| = \frac{J_{1,1}J_{2,2} - J_{1,2}J_{2,1}}{r_\mathrm{a}^2 - \Upsilon^2} = -\lim_{\vartheta\to\pi^-} \sin\vartheta |J_3|.$$

where $J_{i,j}$ are the components of the matrix

$$\boldsymbol{J} = \begin{bmatrix} \frac{\partial x}{\partial \xi} & \frac{\partial x}{\partial \eta} \\ \frac{\partial y}{\partial \xi} & \frac{\partial y}{\partial \eta} \\ \frac{\partial z}{\partial \xi} & \frac{\partial z}{\partial \eta} \end{bmatrix}.$$

Note that

$$\lim_{\vartheta \to 0^+} J_{3,1} = 0, \qquad \lim_{\vartheta \to \pi^-} J_{3,1} = 0, \qquad \lim_{\vartheta \to 0^+} J_{3,2} = 0, \qquad \lim_{\vartheta \to \pi^-} J_{3,2} = 0.$$

The remaining angular integrals must be resolved by considering the limit of the sum of the integrals. Consider

$$\begin{aligned} &A_{IJ}^{(2)} l_{\tilde{n}+\tilde{m}+j}^{(1)} + A_{IJ}^{(4)} l_{\tilde{n}+\tilde{m}+j-1}^{(2)} - \varrho_1^2 A_{IJ}^{(5)} l_{\tilde{n}+\tilde{m}+j+1}^{(2)} \\ &= \int_1^\infty \frac{\mathrm{e}^{2\mathrm{i}\varrho_2 \rho}}{\rho^{\tilde{n}+\tilde{m}+j}} \int_{\varphi=0}^{2\pi} \int_{\vartheta=0}^{\pi} \Bigg(\frac{\partial R_I}{\partial \vartheta} \frac{\partial R_J}{\partial \vartheta} \\ &\qquad + \frac{\rho^2 - \varrho_1^2 \cos^2 \vartheta}{\rho^2 - \varrho_1^2} \frac{\partial R_I}{\partial \varphi} \frac{\partial R_J}{\partial \varphi} \frac{1}{\sin^2 \vartheta} \Bigg) \sin \vartheta |J_3| \, \mathrm{d}\eta \, \mathrm{d}\xi \, \mathrm{d}\rho \end{aligned}$$

where $j = 0$ for Bubnov Galerkin formulations and $j = 2$ for Petrov Galerkin formulations. The limit values at the poles for the integrand of this integral is given by (using Maple)

$$\begin{aligned} &\lim_{\vartheta \to 0^+} \left(\frac{\partial R_I}{\partial \vartheta} \frac{\partial R_J}{\partial \vartheta} + \frac{\rho^2 - \varrho_1^2 \cos^2 \vartheta}{\rho^2 - \varrho_1^2} \frac{\partial R_I}{\partial \varphi} \frac{\partial R_J}{\partial \varphi} \frac{1}{\sin^2 \vartheta} \right) \sin \vartheta |J_3| \\ &= \frac{\left(J_{1,1}^2 + J_{2,1}^2\right) \frac{\partial R_J}{\partial \eta} \frac{\partial R_I}{\partial \eta} - (J_{1,1} J_{1,2} + J_{2,1} J_{2,2}) \left(\frac{\partial R_J}{\partial \eta} \frac{\partial R_I}{\partial \xi} + \frac{\partial R_J}{\partial \xi} \frac{\partial R_I}{\partial \eta} \right) + \left(J_{1,2}^2 + J_{2,2}^2\right) \frac{\partial R_J}{\partial \xi} \frac{\partial R_I}{\partial \xi}}{J_{1,1} J_{2,2} - J_{1,2} J_{2,1}} \\ &= - \lim_{\vartheta \to \pi^-} \left(\frac{\partial R_I}{\partial \vartheta} \frac{\partial R_J}{\partial \vartheta} + \frac{\rho^2 - \varrho_1^2 \cos^2 \vartheta}{\rho^2 - \varrho_1^2} \frac{\partial R_I}{\partial \varphi} \frac{\partial R_J}{\partial \varphi} \frac{1}{\sin^2 \vartheta} \right) \sin \vartheta |J_3| \end{aligned}$$

Computationally, if a quadrature point is placed at one of the poles, this limiting value should be added to the computation of the integral $A_{IJ}^{(2)}$, while $A_{IJ}^{(4)}$ and $A_{IJ}^{(5)}$ gets no contribution from this quadrature point.

References

[1] A. Bermúdez, L. Hervella-Nieto, A. Prieto, R. Rodríguez, An optimal perfectly matched layer with unbounded absorbing function for time-harmonic acoustic scattering problems, *Journal of Computational Physics*, 223:469–488 (2007).

[2] C. Michler, L. Demkowicz, J. Kurtz, D. Pardo, Improving the performance of perfectly matched layers by means of *hp*-adaptivity, *Numerical Methods for Partial Differential Equations*, 23:832–858 (2007).

[3] J. J. Shirron, Solution of exterior Helmholtz problems using finite and infinite elements, Ph.D. thesis, University of Maryland College Park (1995).

[4] A. Bayliss, M. Gunzburger, E. Turkel, Boundary conditions for the numerical solution of elliptic equations in exterior regions, *SIAM Journal on Applied Mathematics*, 42:430–451 (1982).

[5] T. Hagstrom, S. Hariharan, A formulation of asymptotic and exact boundary conditions using local operators, *Applied Numerical Mathematics*, 27:403–416 (1998), Special Issue on Absorbing Boundary Conditions.

[6] R. Tezaur, A. Macedo, C. Farhat, R. Djellouli, Three-dimensional finite element calculations in acoustic scattering using arbitrarily shaped convex artificial boundaries, *International Journal for Numerical Methods in Engineering*, 53:1461–1476 (2001).

[7] D. Givoli, *Numerical methods for problems in infinite domains*, vol. 33, Elsevier, 2013.

[8] F. Ihlenburg, *Finite Element Analysis of Acoustic Scattering*, vol. 132 of *Applied Mathematical Sciences*, Springer, New York, USA, 1998.

[9] P. Bettess, Infinite elements, *International Journal for Numerical Methods in Engineering*, 11:53–64 (1977).

[10] P. Bettess, O. C. Zienkiewicz, Diffraction and refraction of surface waves using finite and infinite elements, *International Journal for Numerical Methods in Engineering*, 11:1271–1290 (1977).

[11] S. A. Sauter, C. Schwab, *Boundary Element Methods*, Springer Berlin Heidelberg, Berlin, Heidelberg, 2011, pp. 183–287.

[12] M. Schanz, O. Steinbach, *Boundary Element Analysis: Mathematical Aspects and Applications*, Lecture Notes in Applied and Computational Mechanics, Springer Berlin Heidelberg, 2007.

[13] S. Marburg, B. Nolte, *Computational Acoustics of Noise Propagation in Fluids-Finite and Boundary Element Methods*, vol. 578, Springer, 2008.

[14] S. N. Chandler-Wilde, I. G. Graham, S. Langdon, E. A. Spence, Numerical-asymptotic boundary integral methods in high-frequency acoustic scattering, *Acta Numerica*, 21:89–305 (2012).

[15] K. G. Foote, D. T. I. Francis, Comparing Kirchhoff-approximation and boundary-element models for computing gadoid target strengths, *The Journal of the Acoustical Society of America*, 111:1644–1654 (2002).

[16] L. Fillinger, M. Nijhof, C. de Jong, An efficient numerical target strength prediction model: Validation against analysis solutions, in *Papadakis, JS Bjorno, L., Proceedings 2nd International Conference and Exhibition on Underwater Acoustics, UA2014, 22-27 June, Rhodes, Greece, 487–493*, 2014.

[17] F. B. Jensen, W. A. Kuperman, M. B. Porter, H. Schmidt, *Computational Ocean Acoustics*, 2nd edition, Springer New York, 2011.

[18] R. Burgschweiger, I. Schafer, M. Ochmann, B. Nolte, Results of the ray-tracing based solver BEAM for the approximate determination of acoustic backscattering from thin-walled objects, in *INTER-NOISE and NOISE-CON Congress and Conference Proceedings*, vol. 249, Institute of Noise Control Engineering, 2014, pp. 1218–1227.

[19] P. S. Heckbert, P. Hanrahan, Beam tracing polygonal objects, *ACM SIGGRAPH Computer Graphics*, 18:119–127 (1984).

[20] M. Peake, J. Trevelyan, G. Coates, Extended isogeometric boundary element method (XIBEM) for two-dimensional Helmholtz problems, *Computer Methods in Applied Mechanics and Engineering*, 259:93–102 (2013).

[21] M. Peake, J. Trevelyan, G. Coates, Extended isogeometric boundary element method (XIBEM) for three-dimensional medium-wave acoustic scattering problems, *Computer Methods in Applied Mechanics and Engineering*, 284:762–780 (2015), Isogeometric Analysis Special Issue.

[22] J. V. Venås, T. Kvamsdal, T. Jenserud, Isogeometric analysis of acoustic scattering using infinite elements, *Computer Methods in Applied Mechanics and Engineering*, 335:152–193 (2018).

[23] G. Fairweather, A. Karageorghis, P. Martin, The method of fundamental solutions for scattering and radiation problems, *Engineering Analysis with Boundary Elements*, 27:759–769 (2003), Special issue on Acoustics.

[24] O. Z. Mehdizadeh, M. Paraschivoiu, Investigation of a two-dimensional spectral element method for Helmholtz's equation, *Journal of Computational Physics*, 189:111–129 (2003).

[25] F. K. P. Jörgensson, M. S. Mejling, A. P. Engsig-Karup, C.-H. Jeong, J. Strømann-Andersen, Room acoustic simulations using high-order spectral element methods, in *Euronoise 2018*, 2018.

[26] A. Fichtner, *Full seismic waveform modelling and inversion*, Springer Science & Business Media, 2010.

[27] A. Sommerfeld, *Partial differential equations in physics*, vol. 1, Academic press, 1949.

[28] P. Gervasio, L. Dede, O. Chanon, A. Quarteroni, Comparing isogeometric analysis and spectral element methods: accuracy and spectral properties, Tech. rep., Polytechnic University of Milan (2018).

[29] J. V. Venås, T. Jenserud, Exact 3D scattering solutions for spherical symmetric scatterers, *Journal of Sound and Vibration*, 440:439–479 (2019).

[30] K. Gerdes, F. Ihlenburg, On the pollution effect in FE solutions of the 3D-Helmholtz equation, *Computer Methods in Applied Mechanics and Engineering*, 170:155–172 (1999).

[31] P. Antolin, A. Buffa, F. Calabrò, M. Martinelli, G. Sangalli, Efficient matrix computation for tensor-product isogeometric analysis: The use of sum factorization, *Computer Methods in Applied Mechanics and Engineering*, 285:817–828 (2015).

Appendices

Appendices

A. Derivation of bilinear form for the infinite elements

In this appendix, a derivation of the bilinear form for the infinite elements for non-separable geometries (IENSG) after Shirron and Dey [1] is presented (as these formulas are left out in [1]). Continuing the notation from [2, Appendix A] the bilinear form (in the domain outside the artificial boundary) can in the Petrov–Galerkin formulations be simplified to (in the unconjugated case)

$$\begin{aligned} B_{\mathrm{PGU}}(R_I\psi_n, R_J\phi_m) &= \lim_{\gamma\to\infty} \int_{\Omega_{\mathrm{a}}^{\gamma}} \Big[\nabla(R_I\psi_n)\cdot\nabla(R_J\phi_m) - k^2 R_I\psi_n R_J\phi_m\Big]\,\mathrm{d}\Omega \\ &= \int_{\Omega_{\mathrm{a}}^{+}} \Big[\nabla(R_I\psi_n)\cdot\nabla(R_J\phi_m) - k^2 R_I\psi_n R_J\phi_m\Big]\,\mathrm{d}\Omega. \end{aligned} \tag{A.1}$$

As the artificial boundary is no longer given at a constant radius r_{a} in the prolate spheroidal coordinate system, it must be given as a function of the angular parameters, that is, $r_{\mathrm{a}} = r_{\mathrm{a}}(\vartheta,\varphi)$. This function is the radius in the prolate spheroidal coordinate system of the intersecting point of the boundary Γ and the prolate radial curve at the angles ϑ and ϕ. The boundary Γ is parametrized by $\boldsymbol{X} = \boldsymbol{X}(\xi,\eta)$ and the prolate spheroidal radius has the expression

$$r(x,y,z) = \frac{1}{2}(c_1 + c_2)$$

where

$$c_1 = \sqrt{T - 2z\Upsilon}, \qquad c_2 = \sqrt{T + 2z\Upsilon}, \quad \text{and} \quad T = x^2 + y^2 + z^2 + \Upsilon^2.$$

Then,

$$r_{\mathrm{a}}(\vartheta,\varphi) = r(\boldsymbol{X}[\xi(\vartheta,\varphi),\eta(\vartheta,\varphi)]).$$

By noting that

$$\frac{\partial r}{\partial x} = \frac{x}{2}\Big(\frac{1}{c_1} + \frac{1}{c_2}\Big), \qquad \frac{\partial r}{\partial y} = \frac{y}{2}\Big(\frac{1}{c_1} + \frac{1}{c_2}\Big), \quad \text{and} \quad \frac{\partial r}{\partial z} = \frac{1}{2}\Big(\frac{z-\Upsilon}{c_1} + \frac{z+\Upsilon}{c_2}\Big),$$

we can compute the partial derivatives of r_a w.r.t. ϑ and φ by

$$\begin{bmatrix} \frac{\partial r_\mathrm{a}}{\partial \vartheta} & \frac{\partial r_\mathrm{a}}{\partial \varphi} \end{bmatrix} = \begin{bmatrix} \frac{\partial r}{\partial x} & \frac{\partial r}{\partial y} & \frac{\partial r}{\partial z} \end{bmatrix} \begin{bmatrix} \frac{\partial x}{\partial \vartheta} & \frac{\partial x}{\partial \varphi} \\ \frac{\partial y}{\partial \vartheta} & \frac{\partial y}{\partial \varphi} \\ \frac{\partial z}{\partial \vartheta} & \frac{\partial z}{\partial \varphi} \end{bmatrix}$$

where

$$\begin{bmatrix} \frac{\partial x}{\partial \vartheta} & \frac{\partial x}{\partial \varphi} \\ \frac{\partial y}{\partial \vartheta} & \frac{\partial y}{\partial \varphi} \\ \frac{\partial z}{\partial \vartheta} & \frac{\partial z}{\partial \varphi} \end{bmatrix} = \begin{bmatrix} \frac{\partial x}{\partial \xi} & \frac{\partial x}{\partial \eta} \\ \frac{\partial y}{\partial \xi} & \frac{\partial y}{\partial \eta} \\ \frac{\partial z}{\partial \xi} & \frac{\partial z}{\partial \eta} \end{bmatrix} \begin{bmatrix} \frac{\partial \xi}{\partial \vartheta} & \frac{\partial \xi}{\partial \varphi} \\ \frac{\partial \eta}{\partial \vartheta} & \frac{\partial \eta}{\partial \varphi} \end{bmatrix}.$$

and

$$\begin{bmatrix} \frac{\partial \xi}{\partial \vartheta} & \frac{\partial \xi}{\partial \varphi} \\ \frac{\partial \eta}{\partial \vartheta} & \frac{\partial \eta}{\partial \varphi} \end{bmatrix} = \boldsymbol{J}_3^{-1}, \qquad \boldsymbol{J}_3 = \begin{bmatrix} \frac{\partial \vartheta}{\partial \xi} & \frac{\partial \vartheta}{\partial \eta} \\ \frac{\partial \varphi}{\partial \xi} & \frac{\partial \varphi}{\partial \eta} \end{bmatrix} = \begin{bmatrix} \frac{\partial \vartheta}{\partial x} & \frac{\partial \vartheta}{\partial y} & \frac{\partial \vartheta}{\partial z} \\ \frac{\partial \varphi}{\partial x} & \frac{\partial \varphi}{\partial y} & \frac{\partial \varphi}{\partial z} \end{bmatrix} \begin{bmatrix} \frac{\partial x}{\partial \xi} & \frac{\partial x}{\partial \eta} \\ \frac{\partial y}{\partial \xi} & \frac{\partial y}{\partial \eta} \\ \frac{\partial z}{\partial \xi} & \frac{\partial z}{\partial \eta} \end{bmatrix}.$$

The "radial shape" functions are given by

$$\phi_m(r,\vartheta,\varphi) = \mathrm{e}^{\mathrm{i}k(r-r_\mathrm{a}(\vartheta,\varphi))} Q_m\Big(\frac{r_\mathrm{a}(\vartheta,\varphi)}{r}\Big), \quad m = 1,\dots,N$$
$$\psi_n(r,\vartheta,\varphi) = \mathrm{e}^{\mathrm{i}k(r-r_\mathrm{a}(\vartheta,\varphi))} \tilde{Q}_n\Big(\frac{r_\mathrm{a}(\vartheta,\varphi)}{r}\Big), \quad n = 1,\dots,N$$

such that the partial derivative can be computed by

$$\frac{\partial \phi_m}{\partial r} = \Big[\mathrm{i}kQ_m\Big(\frac{r_\mathrm{a}(\vartheta,\varphi)}{r}\Big) - \frac{r_\mathrm{a}(\vartheta,\varphi)}{r^2} Q_m'\Big(\frac{r_\mathrm{a}(\vartheta,\varphi)}{r}\Big)\Big] \mathrm{e}^{\mathrm{i}k(r-r_\mathrm{a}(\vartheta,\varphi))}$$
$$\frac{\partial \phi_m}{\partial \vartheta} = \Big[-\mathrm{i}kQ_m\Big(\frac{r_\mathrm{a}(\vartheta,\varphi)}{r}\Big) + \frac{1}{r} Q_m'\Big(\frac{r_\mathrm{a}(\vartheta,\varphi)}{r}\Big)\Big] \frac{\partial r_\mathrm{a}(\vartheta,\varphi)}{\partial \vartheta} \mathrm{e}^{\mathrm{i}k(r-r_\mathrm{a}(\vartheta,\varphi))}$$
$$\frac{\partial \phi_m}{\partial \varphi} = \Big[-\mathrm{i}kQ_m\Big(\frac{r_\mathrm{a}(\vartheta,\varphi)}{r}\Big) + \frac{1}{r} Q_m'\Big(\frac{r_\mathrm{a}(\vartheta,\varphi)}{r}\Big)\Big] \frac{\partial r_\mathrm{a}(\vartheta,\varphi)}{\partial \varphi} \mathrm{e}^{\mathrm{i}k(r-r_\mathrm{a}(\vartheta,\varphi))}.$$

and corresponding expressions for ψ_n. The expressions for the test functions in the conjugated cases are

$$\bar{\psi}_n(r,\vartheta,\varphi) = \mathrm{e}^{-\mathrm{i}k(r-r_\mathrm{a}(\vartheta,\varphi))} \tilde{Q}_n\Big(\frac{r_\mathrm{a}(\vartheta,\varphi)}{r}\Big), \quad n = 1,\dots,N$$

such that the partial derivative can be computed by

$$\frac{\partial \bar{\psi}_m}{\partial r} = \Big[-\mathrm{i}kQ_m\Big(\frac{r_\mathrm{a}(\vartheta,\varphi)}{r}\Big) - \frac{r_\mathrm{a}(\vartheta,\varphi)}{r^2} Q_m'\Big(\frac{r_\mathrm{a}(\vartheta,\varphi)}{r}\Big)\Big] \mathrm{e}^{-\mathrm{i}k(r-r_\mathrm{a}(\vartheta,\varphi))}$$
$$\frac{\partial \bar{\psi}_m}{\partial \vartheta} = \Big[\mathrm{i}kQ_m\Big(\frac{r_\mathrm{a}(\vartheta,\varphi)}{r}\Big) + \frac{1}{r} Q_m'\Big(\frac{r_\mathrm{a}(\vartheta,\varphi)}{r}\Big)\Big] \frac{\partial r_\mathrm{a}(\vartheta,\varphi)}{\partial \vartheta} \mathrm{e}^{-\mathrm{i}k(r-r_\mathrm{a}(\vartheta,\varphi))}$$
$$\frac{\partial \bar{\psi}_m}{\partial \varphi} = \Big[\mathrm{i}kQ_m\Big(\frac{r_\mathrm{a}(\vartheta,\varphi)}{r}\Big) + \frac{1}{r} Q_m'\Big(\frac{r_\mathrm{a}(\vartheta,\varphi)}{r}\Big)\Big] \frac{\partial r_\mathrm{a}(\vartheta,\varphi)}{\partial \varphi} \mathrm{e}^{-\mathrm{i}k(r-r_\mathrm{a}(\vartheta,\varphi))}.$$

The dot product expression in the bilinear form in Eq. (A.1) can now be expressed as

$$\begin{aligned}\nabla(R_I\psi_n)\cdot\nabla(R_J\phi_m) &= \frac{1}{h_{\mathrm{r}}^2}\frac{\partial(R_I\psi_n)}{\partial r}\frac{\partial(R_J\phi_m)}{\partial r} + \frac{1}{h_{\vartheta}^2}\frac{\partial(R_I\psi_n)}{\partial \vartheta}\frac{\partial(R_J\phi_m)}{\partial \vartheta} + \frac{1}{h_{\varphi}^2}\frac{\partial(R_I\psi_n)}{\partial \varphi}\frac{\partial(R_J\phi_m)}{\partial \varphi}\\ &= \frac{1}{h_{\mathrm{r}}^2}\frac{\partial\psi_n}{\partial r}\frac{\partial\phi_m}{\partial r}R_IR_J + \frac{1}{h_{\vartheta}^2}\left(\frac{\partial R_I}{\partial\vartheta}\psi_n + R_I\frac{\partial\psi_n}{\partial\vartheta}\right)\left(\frac{\partial R_J}{\partial\vartheta}\phi_m + R_J\frac{\partial\phi_m}{\partial\vartheta}\right)\\ &\quad + \frac{1}{h_{\varphi}^2}\left(\frac{\partial R_I}{\partial\varphi}\psi_n + R_I\frac{\partial\psi_n}{\partial\varphi}\right)\left(\frac{\partial R_J}{\partial\varphi}\phi_m + R_J\frac{\partial\phi_m}{\partial\varphi}\right)\end{aligned}$$

which multiplied with the Jacobian J_1 yields

$$\begin{aligned}\nabla(R_I\psi_n)\cdot\nabla(R_J\phi_m)J_1 = \Bigg[&\left(r^2-\Upsilon^2\right)\frac{\partial\psi_n}{\partial r}\frac{\partial\phi_m}{\partial r}R_IR_J\\ &+\left(\frac{\partial R_I}{\partial\vartheta}\psi_n + R_I\frac{\partial\psi_n}{\partial\vartheta}\right)\left(\frac{\partial R_J}{\partial\vartheta}\phi_m + R_J\frac{\partial\phi_m}{\partial\vartheta}\right)\\ &+\frac{r^2-\Upsilon^2\cos^2\vartheta}{(r^2-\Upsilon^2)\sin^2\vartheta}\left(\frac{\partial R_I}{\partial\varphi}\psi_n + R_I\frac{\partial\psi_n}{\partial\varphi}\right)\left(\frac{\partial R_J}{\partial\varphi}\phi_m + R_J\frac{\partial\phi_m}{\partial\varphi}\right)\Bigg]\sin\vartheta.\end{aligned}$$

Combining all of this into Eq. (A.1) yields

$$B(R_I\psi_n, R_J\phi_m) = \int_0^{2\pi}\int_0^{\pi} K(\vartheta,\varphi)\sin\vartheta\,\mathrm{d}\vartheta\,\mathrm{d}\varphi \tag{A.2}$$

where

$$\begin{aligned}K(\vartheta,\varphi) &= \int_{r_{\mathrm{a}}(\vartheta,\varphi)}^{\infty}\Bigg\{\left(r^2-\Upsilon^2\right)\frac{\partial\psi_n}{\partial r}\frac{\partial\phi_m}{\partial r}R_IR_J + \left(\frac{\partial R_I}{\partial\vartheta}\psi_n + R_I\frac{\partial\psi_n}{\partial\vartheta}\right)\left(\frac{\partial R_J}{\partial\vartheta}\phi_m + R_J\frac{\partial\phi_m}{\partial\vartheta}\right)\\ &\quad+\frac{r^2-\Upsilon^2\cos^2\vartheta}{(r^2-\Upsilon^2)\sin^2\vartheta}\left(\frac{\partial R_I}{\partial\varphi}\psi_n + R_I\frac{\partial\psi_n}{\partial\varphi}\right)\left(\frac{\partial R_J}{\partial\varphi}\phi_m + R_J\frac{\partial\phi_m}{\partial\varphi}\right)\\ &\quad-k^2(r^2-\Upsilon^2\cos^2\vartheta)\psi_n\phi_m R_IR_J\Bigg\}\,\mathrm{d}r\\ &= \int_{r_{\mathrm{a}}(\vartheta,\varphi)}^{\infty}\Bigg\{R_IR_J\Bigg[\left(r^2-\Upsilon^2\right)\frac{\partial\psi_n}{\partial r}\frac{\partial\phi_m}{\partial r} - k^2(r^2-\Upsilon^2\cos^2\vartheta)\psi_n\phi_m + \frac{\partial\psi_n}{\partial\vartheta}\frac{\partial\phi_m}{\partial\vartheta}\\ &\qquad+\frac{r^2-\Upsilon^2\cos^2\vartheta}{(r^2-\Upsilon^2)\sin^2\vartheta}\frac{\partial\psi_n}{\partial\varphi}\frac{\partial\phi_m}{\partial\varphi}\Bigg]\\ &\quad+\frac{\partial R_I}{\partial\vartheta}\frac{\partial R_J}{\partial\vartheta}\psi_n\phi_m + \frac{\partial R_I}{\partial\vartheta}R_J\psi_n\frac{\partial\phi_m}{\partial\vartheta} + R_I\frac{\partial R_J}{\partial\vartheta}\frac{\partial\psi_n}{\partial\vartheta}\phi_m\\ &\quad+\frac{r^2-\Upsilon^2\cos^2\vartheta}{(r^2-\Upsilon^2)\sin^2\vartheta}\left(\frac{\partial R_I}{\partial\varphi}\frac{\partial R_J}{\partial\varphi}\psi_n\phi_m + \frac{\partial R_I}{\partial\varphi}R_J\psi_n\frac{\partial\phi_m}{\partial\varphi} + R_I\frac{\partial R_J}{\partial\varphi}\frac{\partial\psi_n}{\partial\varphi}\phi_m\right)\Bigg\}\,\mathrm{d}r.\end{aligned}$$

Insertion of the expressions for the "radial shape functions" ϕ and ψ yields some cancellation that removes some problematic terms for the Bubnov formulation. We here show the expressions for the PGU formulation. The procedure for the other three formulation is similar. Inserting the expressions for ϕ and ψ with their corresponding partial derivatives we obtain the following expression using

the substitution $\rho = \frac{r}{r_\mathrm{a}}$ and the notation $\varrho_1 = \Upsilon/r_\mathrm{a}$ (the eccentricity of the infinite-element spheroid), $\varrho_2 = kr_\mathrm{a}$ and $\varrho_3 = k\Upsilon$ where we take the liberty of omitting the angular dependence notation of the function r_a

$$
\begin{aligned}
K(\vartheta,\varphi) = r_\mathrm{a}\mathrm{e}^{-2\mathrm{i}kr_\mathrm{a}} \int_1^\infty \Bigg\{ R_I R_J \Bigg[\Big(\rho^2 - \varrho_1^2\Big) \Big[\mathrm{i}\varrho_2 \tilde{Q}_n\Big(\frac{1}{\rho}\Big) - \frac{1}{\rho^2}\tilde{Q}'_n\Big(\frac{1}{\rho}\Big)\Big] \Big[\mathrm{i}\varrho_2 Q_m\Big(\frac{1}{\rho}\Big) - \frac{1}{\rho^2}Q'_m\Big(\frac{1}{\rho}\Big)\Big] \\
&\quad -(\varrho_2^2\rho^2 - \varrho_3^2\cos^2\vartheta)\tilde{Q}_n\Big(\frac{1}{\rho}\Big)Q_m\Big(\frac{1}{\rho}\Big) \\
&\quad +\Big[-\mathrm{i}\varrho_2\tilde{Q}_n\Big(\frac{1}{\rho}\Big) + \frac{1}{\rho}\tilde{Q}'_n\Big(\frac{1}{\rho}\Big)\Big]\Big[-\mathrm{i}\varrho_2 Q_m\Big(\frac{1}{\rho}\Big) + \frac{1}{\rho}Q'_m\Big(\frac{1}{\rho}\Big)\Big] \\
&\quad \cdot\frac{1}{r_\mathrm{a}^2}\Bigg[\Big(\frac{\partial r_\mathrm{a}}{\partial\vartheta}\Big)^2 + \frac{\rho^2 - \varrho_1^2\cos^2\vartheta}{(\rho^2-\varrho_1^2)\sin^2\vartheta}\Big(\frac{\partial r_\mathrm{a}}{\partial\varphi}\Big)^2\Bigg]\Bigg] \\
&\quad +\Bigg[\frac{\partial R_I}{\partial\vartheta}\frac{\partial R_J}{\partial\vartheta} + \frac{\rho^2-\varrho_1^2\cos^2\vartheta}{(\rho^2-\varrho_1^2)\sin^2\vartheta}\frac{\partial R_I}{\partial\varphi}\frac{\partial R_J}{\partial\varphi}\Bigg]\tilde{Q}_n\Big(\frac{1}{\rho}\Big)Q_m\Big(\frac{1}{\rho}\Big) \\
&\quad +\Bigg[\frac{\partial r_\mathrm{a}}{\partial\vartheta}\frac{\partial R_I}{\partial\vartheta}R_J + \frac{\rho^2-\varrho_1^2\cos^2\vartheta}{(\rho^2-\varrho_1^2)\sin^2\vartheta}\frac{\partial r_\mathrm{a}}{\partial\varphi}\frac{\partial R_I}{\partial\varphi}R_J\Bigg] \\
&\quad \cdot\frac{1}{r_\mathrm{a}}\Big[-\mathrm{i}\varrho_2 Q_m\Big(\frac{1}{\rho}\Big) + \frac{1}{\rho}Q'_m\Big(\frac{1}{\rho}\Big)\Big]\tilde{Q}_n\Big(\frac{1}{\rho}\Big) \\
&\quad +\Bigg[\frac{\partial r_\mathrm{a}}{\partial\vartheta}R_I\frac{\partial R_J}{\partial\vartheta} + \frac{\rho^2-\varrho_1^2\cos^2\vartheta}{(\rho^2-\varrho_1^2)\sin^2\vartheta}\frac{\partial r_\mathrm{a}}{\partial\varphi}R_I\frac{\partial R_J}{\partial\varphi}\Bigg] \\
&\quad \cdot\frac{1}{r_\mathrm{a}}\Big[-\mathrm{i}\varrho_2\tilde{Q}_n\Big(\frac{1}{\rho}\Big) + \frac{1}{\rho}\tilde{Q}'_n\Big(\frac{1}{\rho}\Big)\Big]Q_m\Big(\frac{1}{\rho}\Big)\Bigg\}\mathrm{e}^{2\mathrm{i}kr_\mathrm{a}\rho}\,\mathrm{d}\rho
\end{aligned}
$$

Inserting the expressions for $\tilde{Q}_n$ and Q_m (found in [2, pp. 158-159]) yields

$$
\begin{aligned}
K(\vartheta,\varphi) = r_\mathrm{a}\mathrm{e}^{-2\mathrm{i}kr_\mathrm{a}} D_{m\tilde{m}}\tilde{D}_{n\tilde{n}} \int_1^\infty \Bigg\{ R_I R_J \Bigg[\Big(\rho^2 - \varrho_1^2\Big) \Big[\frac{\mathrm{i}\varrho_2}{\rho^{\tilde{n}+2}} - \frac{1}{\rho^2}\frac{\tilde{n}+2}{\rho^{\tilde{n}+1}}\Big] \Big[\frac{\mathrm{i}\varrho_2}{\rho^{\tilde{m}}} - \frac{1}{\rho^2}\frac{\tilde{m}}{\rho^{\tilde{m}-1}}\Big] \\
&\quad -(\varrho_2^2\rho^2 - \varrho_3^2\cos^2\vartheta)\frac{1}{\rho^{\tilde{n}+2}}\frac{1}{\rho^{\tilde{m}}} \\
&\quad +\Big[-\frac{\mathrm{i}\varrho_2}{\rho^{\tilde{n}+2}} + \frac{1}{\rho}\frac{\tilde{n}+2}{\rho^{\tilde{n}+1}}\Big]\Big[-\frac{\mathrm{i}\varrho_2}{\rho^{\tilde{m}}} + \frac{1}{\rho}\frac{\tilde{m}}{\rho^{\tilde{m}-1}}\Big] \\
&\quad \cdot\frac{1}{r_\mathrm{a}^2}\Bigg[\Big(\frac{\partial r_\mathrm{a}}{\partial\vartheta}\Big)^2 + \frac{\rho^2 - \varrho_1^2\cos^2\vartheta}{(\rho^2-\varrho_1^2)\sin^2\vartheta}\Big(\frac{\partial r_\mathrm{a}}{\partial\varphi}\Big)^2\Bigg]\Bigg] \\
&\quad +\Bigg[\frac{\partial R_I}{\partial\vartheta}\frac{\partial R_J}{\partial\vartheta} + \frac{\rho^2-\varrho_1^2\cos^2\vartheta}{(\rho^2-\varrho_1^2)\sin^2\vartheta}\frac{\partial R_I}{\partial\varphi}\frac{\partial R_J}{\partial\varphi}\Bigg]\frac{1}{\rho^{\tilde{n}+2}}\frac{1}{\rho^{\tilde{m}}} \\
&\quad +\Bigg[\frac{\partial r_\mathrm{a}}{\partial\vartheta}\frac{\partial R_I}{\partial\vartheta}R_J + \frac{\rho^2-\varrho_1^2\cos^2\vartheta}{(\rho^2-\varrho_1^2)\sin^2\vartheta}\frac{\partial r_\mathrm{a}}{\partial\varphi}\frac{\partial R_I}{\partial\varphi}R_J\Bigg] \\
&\quad \cdot\frac{1}{r_\mathrm{a}}\Big[-\frac{\mathrm{i}\varrho_2}{\rho^{\tilde{m}}} + \frac{1}{\rho}\frac{\tilde{m}}{\rho^{\tilde{m}-1}}\Big]\frac{1}{\rho^{\tilde{n}+2}} \\
&\quad +\Bigg[\frac{\partial r_\mathrm{a}}{\partial\vartheta}R_I\frac{\partial R_J}{\partial\vartheta} + \frac{\rho^2-\varrho_1^2\cos^2\vartheta}{(\rho^2-\varrho_1^2)\sin^2\vartheta}\frac{\partial r_\mathrm{a}}{\partial\varphi}R_I\frac{\partial R_J}{\partial\varphi}\Bigg] \\
&\quad \cdot\frac{1}{r_\mathrm{a}}\Big[-\frac{\mathrm{i}\varrho_2}{\rho^{\tilde{n}+2}} + \frac{1}{\rho}\frac{\tilde{n}+2}{\rho^{\tilde{n}+1}}\Big]\frac{1}{\rho^{\tilde{m}}}\Bigg\}\mathrm{e}^{2\mathrm{i}kr_\mathrm{a}\rho}\,\mathrm{d}\rho.
\end{aligned}
$$

Some algebraic manipulations give the final expression

$$
\begin{aligned}
K(\vartheta,\varphi) = \Bigg\{ R_I R_J \Bigg[& -2\varrho_2^2 B^{(1)}_{\tilde{n}+\tilde{m}} - \mathrm{i}\varrho_2(\tilde{n}+\tilde{m}+2) B^{(1)}_{\tilde{n}+\tilde{m}+1} + \Big[(\tilde{n}+2)\tilde{m} + \varrho_3^2\Big(1+\cos^2\vartheta\Big)\Big] B^{(1)}_{\tilde{n}+\tilde{m}+2} \\
& + \mathrm{i}\varrho_1\varrho_3(\tilde{n}+\tilde{m}+2) B^{(1)}_{\tilde{n}+\tilde{m}+3} - \varrho_1^2(\tilde{n}+2)\tilde{m} B^{(1)}_{\tilde{n}+\tilde{m}+4} \\
& + \Big[-\varrho_2^2 - \mathrm{i}\varrho_2(\tilde{n}+\tilde{m}+2) + (\tilde{n}+2)\tilde{m}\Big] \\
& \qquad \cdot \frac{1}{r_\mathrm{a}^2}\left[\left(\frac{\partial r_\mathrm{a}}{\partial\vartheta}\right)^2 B^{(1)}_{\tilde{n}+\tilde{m}+2} + \frac{\left(\frac{\partial r_\mathrm{a}}{\partial\varphi}\right)^2}{\sin^2\vartheta}\Big(B^{(2)}_{\tilde{n}+\tilde{m}+1} - \varrho_1^2\cos^2\theta B^{(2)}_{\tilde{n}+\tilde{m}+3}\Big)\right]\Bigg] \\
& + \left[\frac{\partial R_I}{\partial\vartheta}\frac{\partial R_J}{\partial\vartheta} + \frac{\tilde{m}-\mathrm{i}\varrho_2}{r_\mathrm{a}}\frac{\partial r_\mathrm{a}}{\partial\vartheta}\frac{\partial R_I}{\partial\vartheta} R_J + \frac{\tilde{n}+2-\mathrm{i}\varrho_2}{r_\mathrm{a}}\frac{\partial r_\mathrm{a}}{\partial\vartheta} R_I \frac{\partial R_J}{\partial\vartheta}\right] B^{(1)}_{\tilde{n}+\tilde{m}+2} \\
& + \left[\frac{\partial R_I}{\partial\varphi}\frac{\partial R_J}{\partial\varphi} + \frac{\tilde{m}-\mathrm{i}\varrho_2}{r_\mathrm{a}}\frac{\partial r_\mathrm{a}}{\partial\varphi}\frac{\partial R_I}{\partial\varphi} R_J + \frac{\tilde{n}+2-\mathrm{i}\varrho_2}{r_\mathrm{a}}\frac{\partial r_\mathrm{a}}{\partial\varphi} R_I \frac{\partial R_J}{\partial\varphi}\right] \\
& \cdot \frac{1}{\sin^2\theta}\Big(B^{(2)}_{\tilde{n}+\tilde{m}+1} - \varrho_1^2\cos^2\theta B^{(2)}_{\tilde{n}+\tilde{m}+3}\Big)\Bigg\} r_\mathrm{a}\mathrm{e}^{-2\mathrm{i}kr_\mathrm{a}} D_{m\tilde{m}}\tilde{D}_{n\tilde{n}}
\end{aligned}
$$

where

$$
B_n^{(1)}(r_\mathrm{a}(\vartheta,\varphi)) = \int_1^\infty \frac{\mathrm{e}^{2\mathrm{i}kr_\mathrm{a}\rho}}{\rho^n}\,\mathrm{d}\rho, \quad B_n^{(2)}(r_\mathrm{a}(\vartheta,\varphi)) = \int_1^\infty \frac{\mathrm{e}^{2\mathrm{i}kr_\mathrm{a}\rho}}{(\rho^2-\varrho_1^2)\rho^{n-1}}\,\mathrm{d}\rho
$$

for $n \geqslant 1$. In [1] a Chebyshev approximation is made of $B_n^{(i)}$ (as a function of r_a), on the interval $[r_\mathrm{min}, r_\mathrm{mex}]$. These bounds must be precomputed.

Similar derivations for the other formulations can be obtained. The PGC formulation has the expression

$$
\begin{aligned}
K(\vartheta,\varphi) = \Bigg\{ R_I R_J \Bigg[& -\mathrm{i}\varrho_2(\tilde{n}-\tilde{m}+2) B^{(1)}_{\tilde{n}+\tilde{m}+1} + \Big[(\tilde{n}+2)\tilde{m} + \varrho_3^2\Big(-1+\cos^2\vartheta\Big)\Big] B^{(1)}_{\tilde{n}+\tilde{m}+2} \\
& + \mathrm{i}\varrho_1\varrho_3(\tilde{n}-\tilde{m}+2) B^{(1)}_{\tilde{n}+\tilde{m}+3} - \varrho_1^2(\tilde{n}+2)\tilde{m} B^{(1)}_{\tilde{n}+\tilde{m}+4} \\
& + \Big[\varrho_2^2 - \mathrm{i}\varrho_2(\tilde{n}-\tilde{m}+2) + (\tilde{n}+2)\tilde{m}\Big] \\
& \qquad \cdot \frac{1}{r_\mathrm{a}^2}\left[\left(\frac{\partial r_\mathrm{a}}{\partial\vartheta}\right)^2 B^{(1)}_{\tilde{n}+\tilde{m}+2} + \frac{\left(\frac{\partial r_\mathrm{a}}{\partial\varphi}\right)^2}{\sin^2\vartheta}\Big(B^{(2)}_{\tilde{n}+\tilde{m}+1} - \varrho_1^2\cos^2\theta B^{(2)}_{\tilde{n}+\tilde{m}+3}\Big)\right]\Bigg] \\
& + \left[\frac{\partial R_I}{\partial\vartheta}\frac{\partial R_J}{\partial\vartheta} + \frac{\tilde{m}-\mathrm{i}\varrho_2}{r_\mathrm{a}}\frac{\partial r_\mathrm{a}}{\partial\vartheta}\frac{\partial R_I}{\partial\vartheta} R_J + \frac{\tilde{n}+2+\mathrm{i}\varrho_2}{r_\mathrm{a}}\frac{\partial r_\mathrm{a}}{\partial\vartheta} R_I \frac{\partial R_J}{\partial\vartheta}\right] B^{(1)}_{\tilde{n}+\tilde{m}+2} \\
& + \left[\frac{\partial R_I}{\partial\varphi}\frac{\partial R_J}{\partial\varphi} + \frac{\tilde{m}-\mathrm{i}\varrho_2}{r_\mathrm{a}}\frac{\partial r_\mathrm{a}}{\partial\varphi}\frac{\partial R_I}{\partial\varphi} R_J + \frac{\tilde{n}+2+\mathrm{i}\varrho_2}{r_\mathrm{a}}\frac{\partial r_\mathrm{a}}{\partial\varphi} R_I \frac{\partial R_J}{\partial\varphi}\right] \\
& \cdot \frac{1}{\sin^2\theta}\Big(B^{(2)}_{\tilde{n}+\tilde{m}+1} - \varrho_1^2\cos^2\theta B^{(2)}_{\tilde{n}+\tilde{m}+3}\Big)\Bigg\} r_\mathrm{a} D_{m\tilde{m}}\tilde{D}_{n\tilde{n}}
\end{aligned}
$$

the BGC formulation has the expression

$$
\begin{aligned}
K(\vartheta,\varphi) = \Bigg\{ R_I R_J \Bigg[& -\mathrm{i}\varrho_2(\tilde{n}-\tilde{m}) B^{(1)}_{\tilde{n}+\tilde{m}-1} + \Big[\tilde{n}\tilde{m} + \varrho_3^2\Big(-1+\cos^2\vartheta\Big)\Big] B^{(1)}_{\tilde{n}+\tilde{m}} \\
& + \mathrm{i}\varrho_1\varrho_3(\tilde{n}-\tilde{m}) B^{(1)}_{\tilde{n}+\tilde{m}+1} - \varrho_1^2 \tilde{n}\tilde{m} B^{(1)}_{\tilde{n}+\tilde{m}+2} \\
& + \Big[\varrho_2^2 - \mathrm{i}\varrho_2(\tilde{n}-\tilde{m}) + \tilde{n}\tilde{m}\Big] \\
& \qquad \cdot \frac{1}{r_\mathrm{a}^2}\left[\left(\frac{\partial r_\mathrm{a}}{\partial\vartheta}\right)^2 B^{(1)}_{\tilde{n}+\tilde{m}} + \frac{\left(\frac{\partial r_\mathrm{a}}{\partial\varphi}\right)^2}{\sin^2\vartheta}\Big(B^{(2)}_{\tilde{n}+\tilde{m}-1} - \varrho_1^2\cos^2\theta B^{(2)}_{\tilde{n}+\tilde{m}+1}\Big)\right]\Bigg] \\
& + \left[\frac{\partial R_I}{\partial\vartheta}\frac{\partial R_J}{\partial\vartheta} + \frac{\tilde{m}-\mathrm{i}\varrho_2}{r_\mathrm{a}}\frac{\partial r_\mathrm{a}}{\partial\vartheta}\frac{\partial R_I}{\partial\vartheta}R_J + \frac{\tilde{n}+\mathrm{i}\varrho_2}{r_\mathrm{a}}\frac{\partial r_\mathrm{a}}{\partial\vartheta}R_I\frac{\partial R_J}{\partial\vartheta}\right] B^{(1)}_{\tilde{n}+\tilde{m}} \\
& + \left[\frac{\partial R_I}{\partial\varphi}\frac{\partial R_J}{\partial\varphi} + \frac{\tilde{m}-\mathrm{i}\varrho_2}{r_\mathrm{a}}\frac{\partial r_\mathrm{a}}{\partial\varphi}\frac{\partial R_I}{\partial\varphi}R_J + \frac{\tilde{n}+\mathrm{i}\varrho_2}{r_\mathrm{a}}\frac{\partial r_\mathrm{a}}{\partial\varphi}R_I\frac{\partial R_J}{\partial\varphi}\right] \\
& \cdot \frac{1}{\sin^2\theta}\Big(B^{(2)}_{\tilde{n}+\tilde{m}-1} - \varrho_1^2\cos^2\theta B^{(2)}_{\tilde{n}+\tilde{m}+1}\Big)\Bigg\} r_\mathrm{a} D_{m\tilde{m}}\tilde{D}_{n\tilde{n}} \\
& - \mathrm{i} r_\mathrm{a}\varrho_2 D_{m1}\tilde{D}_{n1} R_I R_J
\end{aligned}
$$

and the BGU formulation has the expression

$$
\begin{aligned}
K(\vartheta,\varphi) = \Bigg\{ R_I R_J \Bigg[& -2\varrho_2^2 B^{(1)}_{\tilde{n}+\tilde{m}-2}(1-\delta_{\tilde{n}1}\delta_{\tilde{m}1}) - \mathrm{i}\varrho_2(\tilde{n}+\tilde{m}) B^{(1)}_{\tilde{n}+\tilde{m}-1} \\
& + \Big[\tilde{n}\tilde{m} + \varrho_3^2\Big(1+\cos^2\vartheta\Big)\Big] B^{(1)}_{\tilde{n}+\tilde{m}} \\
& + \mathrm{i}\varrho_1\varrho_3(\tilde{n}+\tilde{m}) B^{(1)}_{\tilde{n}+\tilde{m}+1} - \varrho_1^2 \tilde{n}\tilde{m} B^{(1)}_{\tilde{n}+\tilde{m}+2} \\
& + \Big[-\varrho_2^2 - \mathrm{i}\varrho_2(\tilde{n}+\tilde{m}) + \tilde{n}\tilde{m}\Big] \\
& \qquad \cdot \frac{1}{r_\mathrm{a}^2}\left[\left(\frac{\partial r_\mathrm{a}}{\partial\vartheta}\right)^2 B^{(1)}_{\tilde{n}+\tilde{m}} + \frac{\left(\frac{\partial r_\mathrm{a}}{\partial\varphi}\right)^2}{\sin^2\vartheta}\Big(B^{(2)}_{\tilde{n}+\tilde{m}-1} - \varrho_1^2\cos^2\theta B^{(2)}_{\tilde{n}+\tilde{m}+1}\Big)\right]\Bigg] \\
& + \left[\frac{\partial R_I}{\partial\vartheta}\frac{\partial R_J}{\partial\vartheta} + \frac{\tilde{m}-\mathrm{i}\varrho_2}{r_\mathrm{a}}\frac{\partial r_\mathrm{a}}{\partial\vartheta}\frac{\partial R_I}{\partial\vartheta}R_J + \frac{\tilde{n}-\mathrm{i}\varrho_2}{r_\mathrm{a}}\frac{\partial r_\mathrm{a}}{\partial\vartheta}R_I\frac{\partial R_J}{\partial\vartheta}\right] B^{(1)}_{\tilde{n}+\tilde{m}} \\
& + \left[\frac{\partial R_I}{\partial\varphi}\frac{\partial R_J}{\partial\varphi} + \frac{\tilde{m}-\mathrm{i}\varrho_2}{r_\mathrm{a}}\frac{\partial r_\mathrm{a}}{\partial\varphi}\frac{\partial R_I}{\partial\varphi}R_J + \frac{\tilde{n}-\mathrm{i}\varrho_2}{r_\mathrm{a}}\frac{\partial r_\mathrm{a}}{\partial\varphi}R_I\frac{\partial R_J}{\partial\varphi}\right] \\
& \cdot \frac{1}{\sin^2\theta}\Big(B^{(2)}_{\tilde{n}+\tilde{m}-1} - \varrho_1^2\cos^2\theta B^{(2)}_{\tilde{n}+\tilde{m}+1}\Big)\Bigg\} r_\mathrm{a}\mathrm{e}^{-2\mathrm{i}\varrho_2} D_{m\tilde{m}}\tilde{D}_{n\tilde{n}} \\
& - \mathrm{i}\varrho_2 r_\mathrm{a} D_{m1}\tilde{D}_{n1} R_I R_J.
\end{aligned}
$$

A.1. Numerical examples

Some numerical examples are here given, comparing the target strength simulations using IGABEM (with the GBM formulation) as reference solution and IENSG

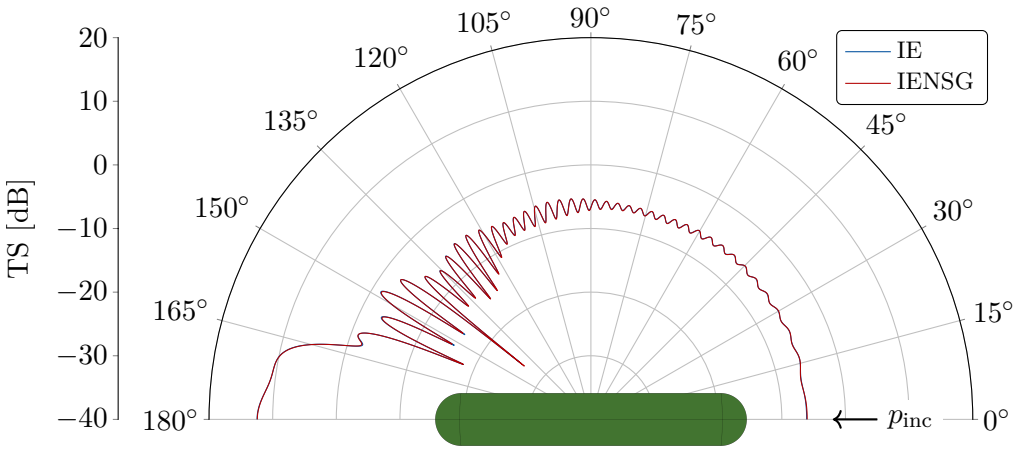

Figure A.1: **Shirron's mock shell**: Bistatic scattering on the mock shell with $\alpha_s = 0°$ and $\beta_s = 0°$ at $ka = 10$ (where $a = 1\,\text{m}$ is the radius of the hemispherical endcaps).

(with the BGU formulation). Both methods are using the same mesh on the scatterer, Γ.

Results for the hemispherically-capped cylinder (mock shell model) considered in [1, Fig. 10] is produced using IGA in Figure A.1 (with Γ represented by 9578 dofs), illustrating very good results for the infinite elements attached directly onto the scatterer using only $N = 3$ basis functions in the radial direction. Results for the BeTSSi model 1 is produced in a similar fashion in Figure A.2 (with Γ represented by 38 414 dofs), illustrating very good results even if the infinite elements are attached directly onto the non-smooth scatterer using only $N = 3$ basis functions in the radial direction. However, the results diverge at $f = 1\,\text{kHz}$ as illustrated in Figure A.3.

B. Ray/beam tracing in the isogeometric framework

Beam tracing builds upon ray tracing and was introduced by Heckbert and Hanrahan [3]. It offers a high frequency approximation of scattering problems and has been frequently used in the BeTSSi community. In the following we investigate ray/beam tracing in the isogeoemtric framework. Again, the meshing procedure is avoided, and the ray tracing algorithm may operate directly on the CAD model.

Ray tracing approximates the solution of the Helmholtz equation [4]

$$\nabla^2 p(\boldsymbol{x}) + k^2 p(\boldsymbol{x}) = 0$$

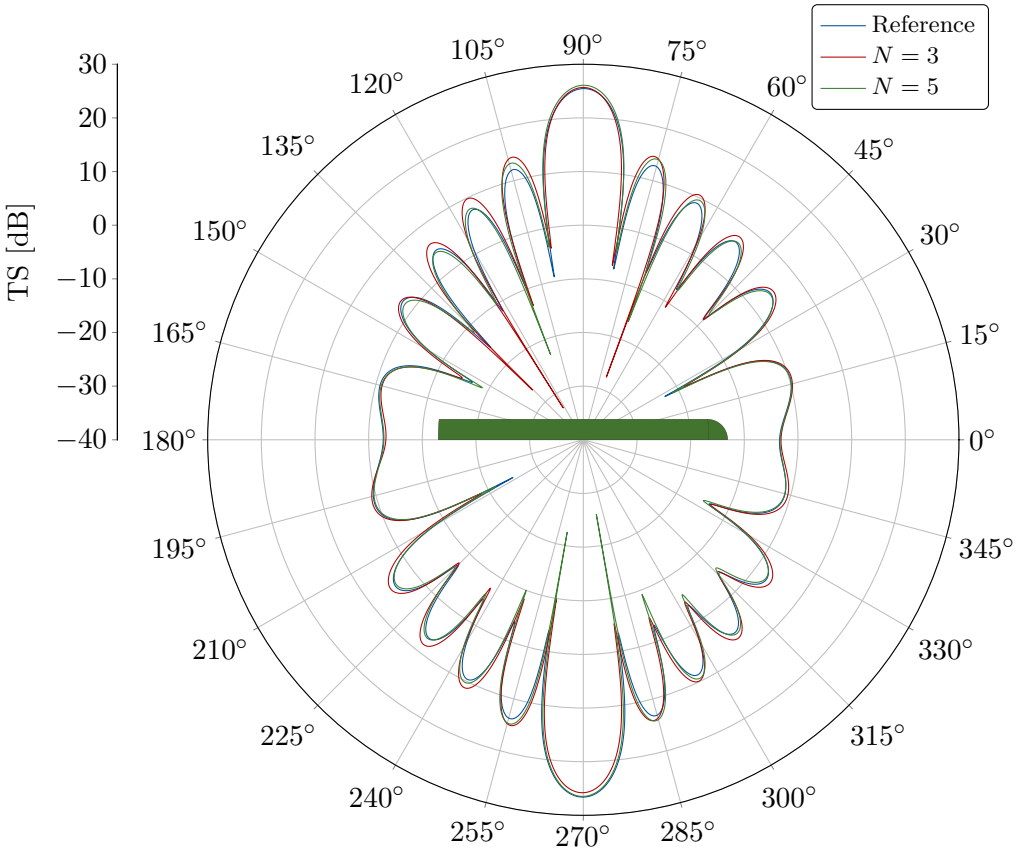

Figure A.2: **BeTSSi model 1**: Monostatic scattering at $f = 100\,\mathrm{Hz}$ and $c_\mathrm{f} = 1500\,\mathrm{m/s}$.

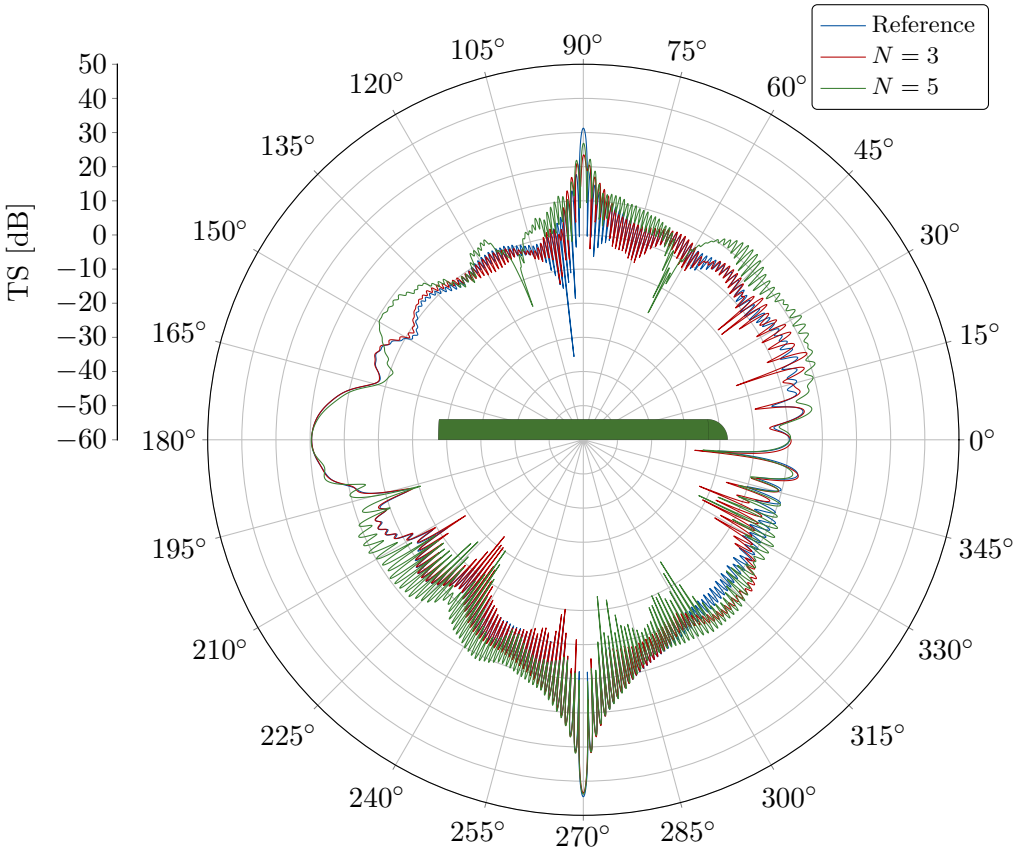

Figure A.3: **BeTSSi model 1**: Monostatic scattering at $f = 1000\,\mathrm{Hz}$ and $c_\mathrm{f} = 1500\,\mathrm{m/s}$.

as a ray series

$$p(\boldsymbol{x}) = \mathrm{e}^{\mathrm{i}\omega\tau(\boldsymbol{x})} \sum_{j=0}^{\infty} \frac{A_j(\boldsymbol{x}_j)}{(\mathrm{i}\omega)^j}$$

which yields the eikonal and transport equations

$$\begin{aligned}
\mathcal{O}(\omega^2): &\quad |\nabla\tau|^2 = c^{-2}(\boldsymbol{x}) \\
\mathcal{O}(\omega): &\quad 2\nabla\tau\cdot\nabla A_0 + (\nabla^2\tau)A_0 = 0, \\
\mathcal{O}(\omega^{1-j}): &\quad 2\nabla\tau\cdot\nabla A_j + (\nabla^2\tau)A_j = -\nabla^2 A_{j-1}, \quad j = 1, 2, \ldots.
\end{aligned}$$

Beam tracing forms an alternative to finding eigenrays. As opposed to finding eigenrays, beam tracing does not require solving the non-linear problem of finding eigenrays. In case of constant sound speed, c_f, the ray trajectories are linear curves, and the pressure along ray j is given by

$$p_j(s) = \frac{A_{0,j}}{s}\mathrm{e}^{\mathrm{i}ks}.$$

Ray/Beam tracing then reduces to finding intersection between straight lines and surfaces. The amplitude of a ray is constructed in such a way that we have energy conservation

$$\int_{\partial V_0} |p_j|^2 \,\mathrm{d}S = \int_{\partial V_1} |p_j|^2 \,\mathrm{d}S = \text{const},$$

where ∂V_0 and ∂V_1 are two reference cross sections along the beam. A beam can be constructed using linear shape functions with s being the parameter along the center ray, and n the normal distance from the observation point to the central ray

$$p_\mathrm{beam}(s,n) = A_\mathrm{beam}(s)\phi(s,n)\mathrm{e}^{\mathrm{i}ks}, \quad \phi(s,n) = \begin{cases} \frac{W(s)-n}{W(s)} & n \leqslant W(s) \\ 0 & \text{else.} \end{cases}$$

B.1. Beam tracing using linear shape functions

Assuming the object under consideration is parametrized by NURBS, the control polygon bounds the domain (Figure B.4a). Projecting the control points onto a plane with normal vector given by $\boldsymbol{d}_\mathrm{inc}$ (direction of incidence of the plane wave), we find a polygon bounding a domain where rays can originate. The rays originate from vertices of equilateral triangles structured as a FEM 2D mesh of the projected polygon. To compute the scattered field at a given point, $\boldsymbol{x}$, first find the beams having support at this point (Figure B.4b). Let the center ray of a given beam be given by

$$\boldsymbol{r}_1(s) = \boldsymbol{x}_1 + s\boldsymbol{d}_1.$$

Minimization of the distance from $\boldsymbol{x}$ to center ray, $\|\boldsymbol{r}_1(s) - \boldsymbol{x}\|$, yields

$$s = (\boldsymbol{x} - \boldsymbol{x}_1)\cdot\boldsymbol{d}_1 \quad \Rightarrow \quad \boldsymbol{P}_1 = \boldsymbol{x}_1 + [(\boldsymbol{x} - \boldsymbol{x}_1)\cdot\boldsymbol{d}_1]\boldsymbol{d}_1.$$

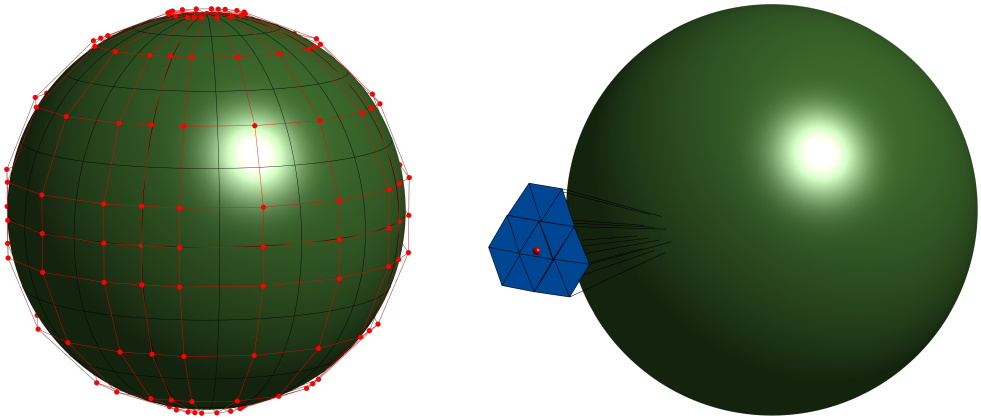

(a) The control polygon bounds the scatterer. (b) Three beams having support at $\boldsymbol{x}$.

Figure B.4: Preprocessing and postprocessing in beam tracing.

The boundary of the beam around $\boldsymbol{x}$ is determined by the vertices $\boldsymbol{P}_i$. These vertices are found by solving $(\boldsymbol{r}_i(s) - \boldsymbol{P}_1) \cdot \boldsymbol{d}_1 = 0$ where $\boldsymbol{r}_i(s) = \boldsymbol{x}_i + s\boldsymbol{d}_i$

$$s = \frac{(\boldsymbol{P}_1 - \boldsymbol{x}_i) \cdot \boldsymbol{d}_1}{\boldsymbol{d}_i \cdot \boldsymbol{d}_1} \quad \Rightarrow \quad \boldsymbol{P}_i = \boldsymbol{x}_i + \frac{(\boldsymbol{P}_1 - \boldsymbol{x}_i) \cdot \boldsymbol{d}_1}{\boldsymbol{d}_i \cdot \boldsymbol{d}_1} \boldsymbol{d}_i.$$

Write $\boldsymbol{x}$ in terms of barycentric coordinates

$$\boldsymbol{x} = \boldsymbol{P}_1 + \xi_2(\boldsymbol{P}_2 - \boldsymbol{P}_1) + \xi_3(\boldsymbol{P}_3 - \boldsymbol{P}_1)$$

then

$$\boldsymbol{x} \in \Delta(\boldsymbol{P}_1, \boldsymbol{P}_2, \boldsymbol{P}_3) \quad \text{if} \quad \xi_2, \xi_3 \geqslant 0 \quad \wedge \quad \xi_2 + \xi_3 \leqslant 1.$$

Solving for ξ_2 and ξ_3 yields (with $\boldsymbol{v}_1 = \boldsymbol{P}_2 - \boldsymbol{P}_1$ and $\boldsymbol{v}_2 = \boldsymbol{P}_3 - \boldsymbol{P}_1$)

$$\xi_2 = \frac{(\boldsymbol{v}_2 \cdot \boldsymbol{v}_2)(\boldsymbol{x} - \boldsymbol{P}_1) \cdot \boldsymbol{v}_1 - (\boldsymbol{v}_1 \cdot \boldsymbol{v}_2)(\boldsymbol{x} - \boldsymbol{P}_1) \cdot \boldsymbol{v}_2}{(\boldsymbol{v}_1 \cdot \boldsymbol{v}_1)(\boldsymbol{v}_2 \cdot \boldsymbol{v}_2) - (\boldsymbol{v}_1 \cdot \boldsymbol{v}_2)^2}$$
$$\xi_3 = \frac{(\boldsymbol{v}_1 \cdot \boldsymbol{v}_1)(\boldsymbol{x} - \boldsymbol{P}_1) \cdot \boldsymbol{v}_2 - (\boldsymbol{v}_1 \cdot \boldsymbol{v}_2)(\boldsymbol{x} - \boldsymbol{P}_1) \cdot \boldsymbol{v}_1}{(\boldsymbol{v}_1 \cdot \boldsymbol{v}_1)(\boldsymbol{v}_2 \cdot \boldsymbol{v}_2) - (\boldsymbol{v}_1 \cdot \boldsymbol{v}_2)^2}$$

which is well defined because of Cauchy-Schwarz inequality.

For the far field evaluations, note that the center ray goes asymptotically as

$$\boldsymbol{r}_1(s) \sim s\boldsymbol{d}_1.$$

Minimization of the distance from $\boldsymbol{x}$ to center ray, $\|\boldsymbol{r}_1(s) - \boldsymbol{x}\|$, yields

$$s \sim \boldsymbol{x} \cdot \boldsymbol{d}_1 \quad \Rightarrow \quad \boldsymbol{P}_1 \sim (\boldsymbol{x} \cdot \boldsymbol{d}_1)\boldsymbol{d}_1.$$

The boundary of the beam around $\boldsymbol{x}$ is determined by the vertices $\boldsymbol{P}_i$. These vertices are found by solving $(\boldsymbol{r}_i(s) - \boldsymbol{P}_1) \cdot \boldsymbol{d}_1 = 0$

$$s \sim \frac{\boldsymbol{P}_1 \cdot \boldsymbol{d}_1}{\boldsymbol{d}_i \cdot \boldsymbol{d}_1} \quad \Rightarrow \quad \boldsymbol{P}_i \sim \frac{\boldsymbol{x} \cdot \boldsymbol{d}_1}{\boldsymbol{d}_i \cdot \boldsymbol{d}_1} \boldsymbol{d}_i.$$

With

$$\boldsymbol{v}_1 = \boldsymbol{P}_2 - \boldsymbol{P}_1 \sim (\boldsymbol{x} \cdot \boldsymbol{d}_1)\left(\frac{\boldsymbol{d}_2}{\boldsymbol{d}_1 \cdot \boldsymbol{d}_2} - \boldsymbol{d}_1 \right)$$

and

$$\boldsymbol{v}_2 = \boldsymbol{P}_3 - \boldsymbol{P}_1 \sim (\boldsymbol{x} \cdot \boldsymbol{d}_1)\left(\frac{\boldsymbol{d}_3}{\boldsymbol{d}_1 \cdot \boldsymbol{d}_3} - \boldsymbol{d}_1 \right)$$

we find

$$\begin{aligned}
\boldsymbol{v}_1 \cdot \boldsymbol{v}_2 &\sim (\boldsymbol{x} \cdot \boldsymbol{d}_1)^2 \left(\frac{\boldsymbol{d}_2 \cdot \boldsymbol{d}_3}{(\boldsymbol{d}_1 \cdot \boldsymbol{d}_2)(\boldsymbol{d}_1 \cdot \boldsymbol{d}_3)} - 1 \right) \\
\boldsymbol{v}_1 \cdot \boldsymbol{v}_1 &\sim (\boldsymbol{x} \cdot \boldsymbol{d}_1)^2 \left(\frac{1}{(\boldsymbol{d}_1 \cdot \boldsymbol{d}_2)^2} - 1 \right) \\
\boldsymbol{v}_2 \cdot \boldsymbol{v}_2 &\sim (\boldsymbol{x} \cdot \boldsymbol{d}_1)^2 \left(\frac{1}{(\boldsymbol{d}_1 \cdot \boldsymbol{d}_3)^2} - 1 \right).
\end{aligned}$$

Write $\boldsymbol{x}$ in terms of barycentric coordinates

$$\boldsymbol{x} = \boldsymbol{P}_1 + \xi_2(\boldsymbol{P}_2 - \boldsymbol{P}_1) + \xi_3(\boldsymbol{P}_3 - \boldsymbol{P}_1)$$

then

$$\boldsymbol{x} \in \Delta(\boldsymbol{P}_1, \boldsymbol{P}_2, \boldsymbol{P}_3) \quad \text{if} \quad \xi_2, \xi_3 \geqslant 0 \quad \wedge \quad \xi_2 + \xi_3 \leqslant 1.$$

Solving for ξ_2 and ξ_3 yields

$$\begin{aligned}
\xi_2 &= \frac{\left(\frac{1}{(\boldsymbol{d}_1 \cdot \boldsymbol{d}_3)^2} - 1 \right)\left(\frac{\hat{\boldsymbol{x}} \cdot \boldsymbol{d}_2}{(\hat{\boldsymbol{x}} \cdot \boldsymbol{d}_1)(\boldsymbol{d}_1 \cdot \boldsymbol{d}_2)} - 1 \right) - \left(\frac{\boldsymbol{d}_2 \cdot \boldsymbol{d}_3}{(\boldsymbol{d}_1 \cdot \boldsymbol{d}_2)(\boldsymbol{d}_1 \cdot \boldsymbol{d}_3)} - 1 \right)\left(\frac{\hat{\boldsymbol{x}} \cdot \boldsymbol{d}_3}{(\hat{\boldsymbol{x}} \cdot \boldsymbol{d}_1)(\boldsymbol{d}_1 \cdot \boldsymbol{d}_3)} - 1 \right)}{\left(\frac{1}{(\boldsymbol{d}_1 \cdot \boldsymbol{d}_2)^2} - 1 \right)\left(\frac{1}{(\boldsymbol{d}_1 \cdot \boldsymbol{d}_3)^2} - 1 \right) - \left(\frac{\boldsymbol{d}_2 \cdot \boldsymbol{d}_3}{(\boldsymbol{d}_1 \cdot \boldsymbol{d}_2)(\boldsymbol{d}_1 \cdot \boldsymbol{d}_3)} - 1 \right)^2} \\
\xi_3 &= \frac{\left(\frac{1}{(\boldsymbol{d}_1 \cdot \boldsymbol{d}_2)^2} - 1 \right)\left(\frac{\hat{\boldsymbol{x}} \cdot \boldsymbol{d}_3}{(\hat{\boldsymbol{x}} \cdot \boldsymbol{d}_1)(\boldsymbol{d}_1 \cdot \boldsymbol{d}_3)} - 1 \right) - \left(\frac{\boldsymbol{d}_2 \cdot \boldsymbol{d}_3}{(\boldsymbol{d}_1 \cdot \boldsymbol{d}_2)(\boldsymbol{d}_1 \cdot \boldsymbol{d}_3)} - 1 \right)\left(\frac{\hat{\boldsymbol{x}} \cdot \boldsymbol{d}_2}{(\hat{\boldsymbol{x}} \cdot \boldsymbol{d}_1)(\boldsymbol{d}_1 \cdot \boldsymbol{d}_2)} - 1 \right)}{\left(\frac{1}{(\boldsymbol{d}_1 \cdot \boldsymbol{d}_2)^2} - 1 \right)\left(\frac{1}{(\boldsymbol{d}_1 \cdot \boldsymbol{d}_3)^2} - 1 \right) - \left(\frac{\boldsymbol{d}_2 \cdot \boldsymbol{d}_3}{(\boldsymbol{d}_1 \cdot \boldsymbol{d}_2)(\boldsymbol{d}_1 \cdot \boldsymbol{d}_3)} - 1 \right)^2}.
\end{aligned}$$

The area of $\Delta(\boldsymbol{P}_1, \boldsymbol{P}_2, \boldsymbol{P}_3)$ is given by

$$S = \frac{1}{2} \| \boldsymbol{v}_1 \times \boldsymbol{v}_2 \|$$

which in the far field has the expression

$$S \sim \frac{1}{2} (\boldsymbol{x} \cdot \boldsymbol{d}_1)^2 \left\| \frac{\boldsymbol{d}_2}{\boldsymbol{d}_1 \cdot \boldsymbol{d}_2} \times \frac{\boldsymbol{d}_3}{\boldsymbol{d}_1 \cdot \boldsymbol{d}_3} + \boldsymbol{d}_1 \times \left(\frac{\boldsymbol{d}_2}{\boldsymbol{d}_1 \cdot \boldsymbol{d}_2} - \frac{\boldsymbol{d}_3}{\boldsymbol{d}_1 \cdot \boldsymbol{d}_3} \right) \right\|.$$

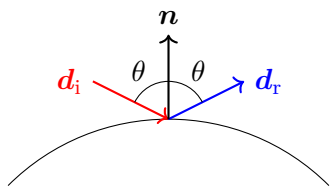

Figure B.5: **Ray tracing**: *The law of reflection* states that the angle of incidence is equal to the angle of reflection.

The scattered field is then computed by

$$p(\boldsymbol{x}) = \sum_{j \in \{i \,:\, \boldsymbol{x} \in B_i\}} \sqrt{\frac{E_j}{S_j}} \xi_1 \mathrm{e}^{\mathrm{i}k(s-s_0)}$$

where

$$s = \|\boldsymbol{x} - \boldsymbol{x}_1\|$$

and

$$E_j = \int_{\partial V_0} |p_j|^2 \, \mathrm{d}S$$

corresponds to the energy of the beam B_j, S_j is the cross-sectional area of beam B_j at $\boldsymbol{x}$, s_0 is the phase shift and ξ_1 is the first barycentric coordinate at $\boldsymbol{x}$.

Exact ray reflections on a rigid sphere (radius R_0) from straight lines on the form

$$\boldsymbol{x}(s) = \boldsymbol{o} + \boldsymbol{d}s$$

can be found at (by solving $\|\boldsymbol{x}(s)\| = R_0$)

$$s = -\boldsymbol{o} \cdot \boldsymbol{d} - \sqrt{D}, \quad D = (\boldsymbol{o} \cdot \boldsymbol{d})^2 + R_0^2 - \|\boldsymbol{o}\|^2,$$

where we have reflection iff $D \geqslant 0$. A ray reflecting at a surface point with normal vector $\boldsymbol{n}$ has incident direction ($\boldsymbol{d}_\mathrm{i}$) and reflected direction ($\boldsymbol{d}_\mathrm{r}$) related by

$$\boldsymbol{d}_\mathrm{r} = \boldsymbol{d}_\mathrm{i} - 2(\boldsymbol{d}_\mathrm{i} \cdot \boldsymbol{n})\boldsymbol{n}$$

with $\|\boldsymbol{d}_\mathrm{r}\| = \|\boldsymbol{d}_\mathrm{i}\| = \|\boldsymbol{n}\| = 1$.

Let the incident wave $p_\mathrm{inc}(\boldsymbol{x}) = P_\mathrm{inc} \mathrm{e}^{\mathrm{i}k\boldsymbol{d}_\mathrm{inc} \cdot \boldsymbol{x}}$ at $\boldsymbol{x}_1 = R_0 \boldsymbol{e}_\mathrm{x}$ be represented by a beam with circular cross section with radius δ (where $\boldsymbol{d}_\mathrm{inc} = -\boldsymbol{e}_\mathrm{x}$). Then, $E = \int_{\partial V_0} |p_\mathrm{inc}|^2 \, \mathrm{d}S = |P_\mathrm{inc}|^2 \pi \delta^2$. Based on the previous formulas, we find (see Figure B.6)

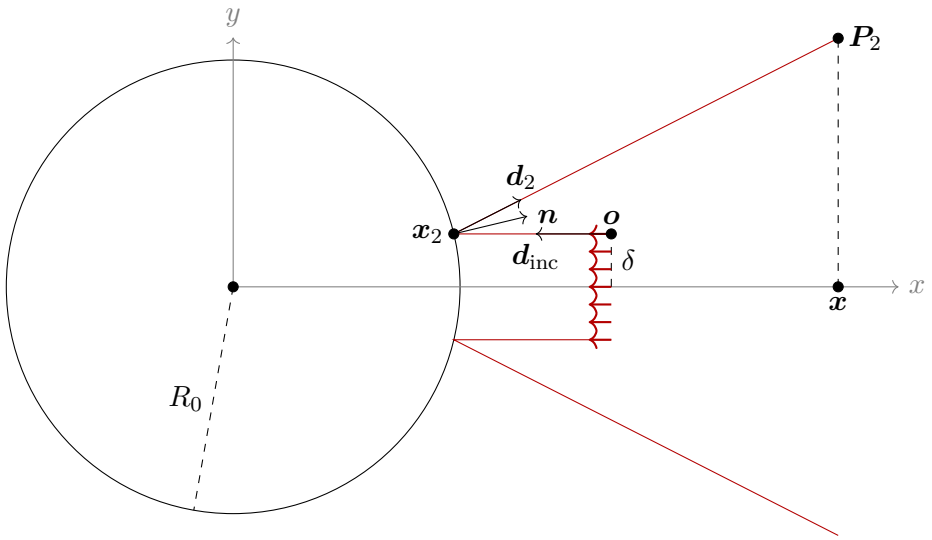

Figure B.6: Computation of exact beam scattering solution.

$$\boldsymbol{x}_2 = \sqrt{R_0^2 - \delta^2}\boldsymbol{e}_{\text{x}} + \delta \boldsymbol{e}_{\text{y}}$$
$$\boldsymbol{d}_2 = \left(1 - 2\left(\frac{\delta}{R_0}\right)^2\right)\boldsymbol{e}_{\text{x}} + 2\frac{\delta}{R_0}\sqrt{1 - \left(\frac{\delta}{R_0}\right)^2}\boldsymbol{e}_{\text{y}}$$
$$\boldsymbol{P}_2 = \boldsymbol{x} + \frac{\delta R_0^2 - 2\|\boldsymbol{x}\|\delta\sqrt{R_0^2 - \delta^2}}{2\delta^2 - R_0^2}\boldsymbol{e}_{\text{y}}.$$

The cross-section area of the beam at $\boldsymbol{x}$ is then

$$S_j = \pi\|\boldsymbol{P}_2 - \boldsymbol{x}\|^2 = \pi\left(\frac{\delta R_0^2 - 2\|\boldsymbol{x}\|\delta\sqrt{R_0^2 - \delta^2}}{2\delta^2 - R_0^2}\right)^2.$$

The far field backscattered pressure is found by considering the limit $\|\boldsymbol{x}\| \to \infty$

$$p_0(\hat{\boldsymbol{x}}) = \frac{|P_{\text{inc}}|}{2\sqrt{R_0^2 - \delta^2}}(R_0^2 - 2\delta^2)\text{e}^{-2ikR_0}.$$

If we finally consider the limit $\delta \to 0$ we find

$$p_0(\hat{\boldsymbol{x}}) = \frac{|P_{\text{inc}}|R_0}{2}\text{e}^{-2ikR_0}$$

which is the exact expression for rigid scattering on a sphere using the Kirchhoff approximation (investigated in Paper IV). This gives the target strength

$$\text{TS} = 20\log_{10}\left(\frac{R_0}{2}\right)$$

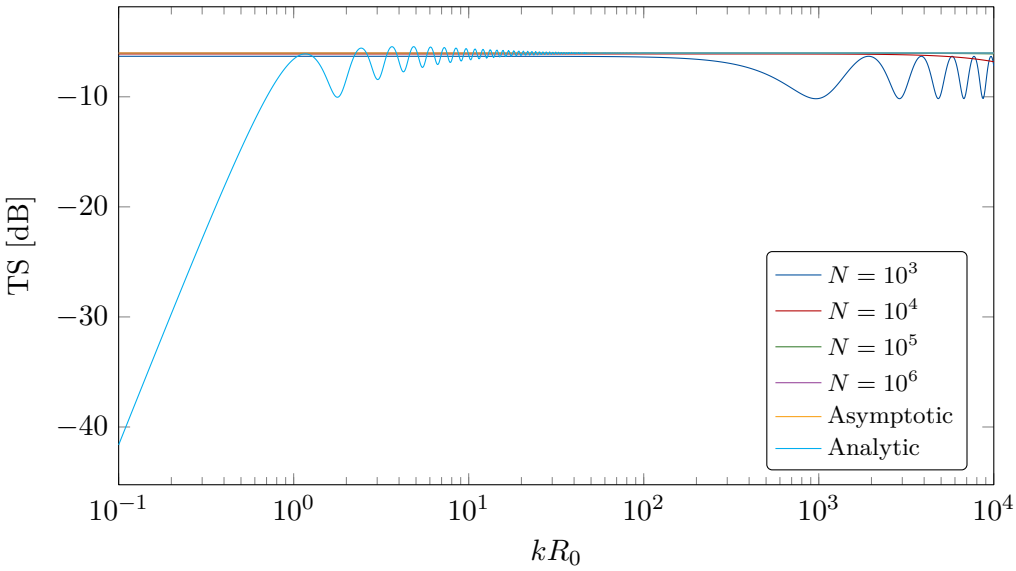

Figure B.7: **Frequency sweep of rigid sphere**: The target strength is plotted against the dimensionless wave number.

which is the asymptotic limit of the analytic solution as $k \to \infty$ [5].

As can be seen from Figures B.7 to B.9, beam approximation increase in accuracy as a function of the number of initial beams (geometry approximation), N, and increase in accuracy as a function of frequency (for sufficiently high N), but loses accuracy from the plane wave approximation for high frequencies at a fixed N. This is very similar to corresponding simulations using Kirchhoff approximation investigated in paper IV. The geometric approximation can be improved by adapting the beams for the incident wave and splitting beams at edge reflections. As the raytracing part is independent of frequency, frequency sweep calculations are very efficient using ray/beam tracing. In Figures B.10 to B.12 it can clearly be seen that the ability to model forward scattering using ray/beam tracing is lacking.

B.2. Ray tracing in the isogeometric framework

Usually the scatterer is tessellated with plane facets at which ray reflection can be trivially computed. The problem with this procedure is identical to the same approach using Kirchhoff approximation. Namely frequency dependent memory consumption and accuracy. The isogeometric framework resolves both of these issues by computing the reflections directly on the CAD-model, which in most cases can be assumed to be represented by NURBS. Additionally, IGA avoids the tesselation step entirely. However, widespread use of ray tracing using NURBS is

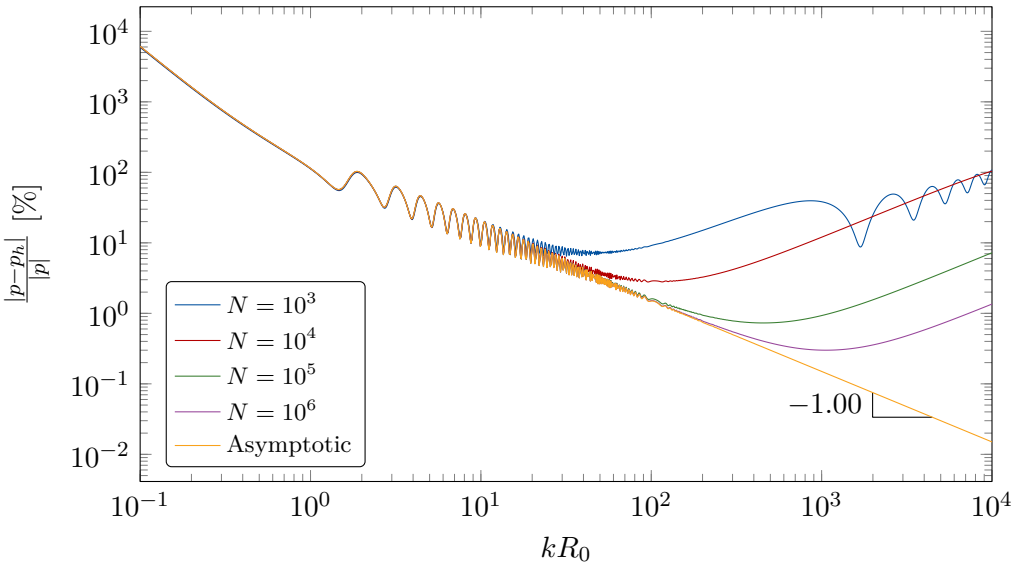

Figure B.8: **Frequency sweep of rigid sphere**: The relative error (of the far field) is plotted against the dimensionless wave number.

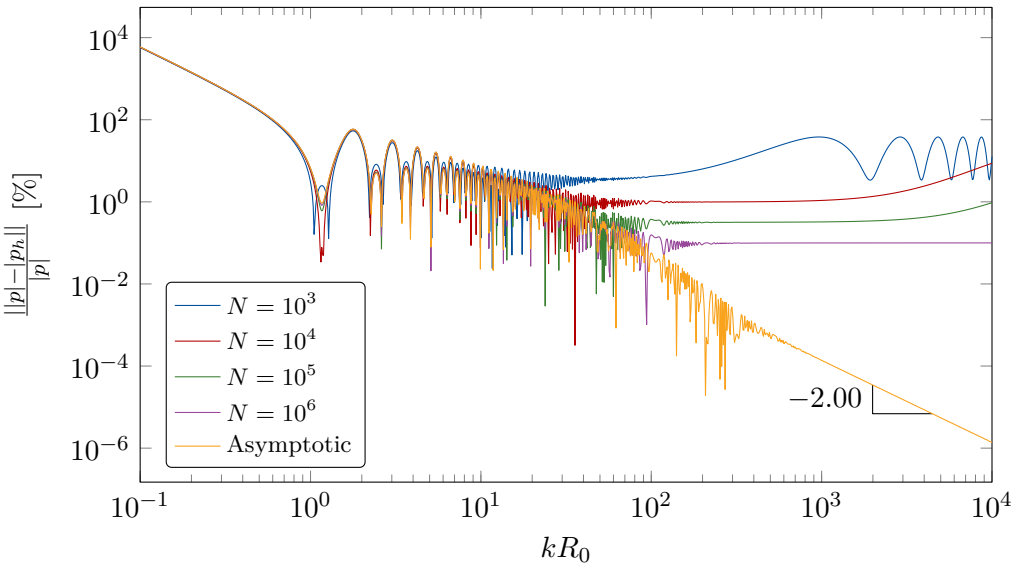

Figure B.9: **Frequency sweep of rigid sphere**: The relative absolute error (of the far field) is plotted against the dimensionless wave number.

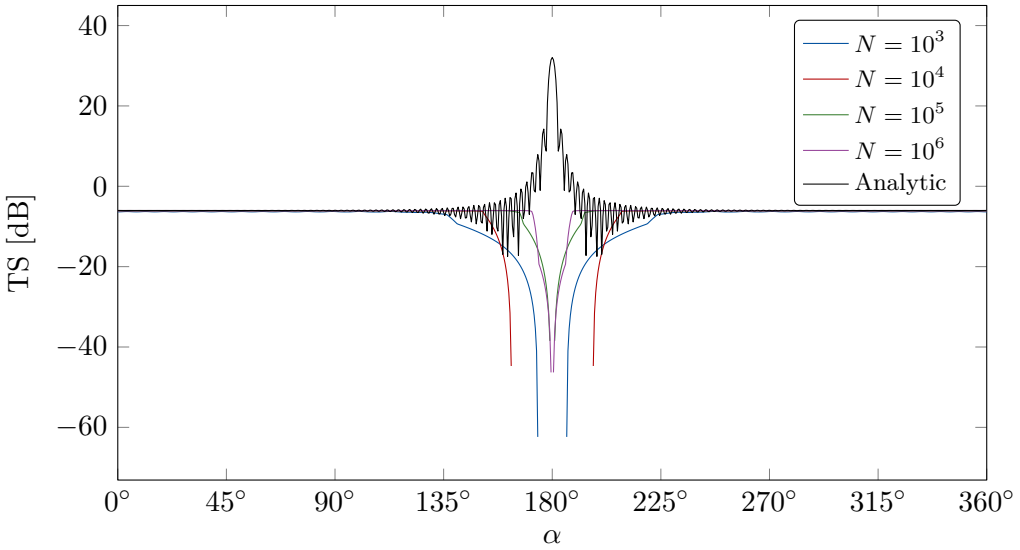

Figure B.10: **Bistatic scattering of rigid sphere**: The target strength is plotted against the aspect angle at $f = 20\,\mathrm{kHz}$.

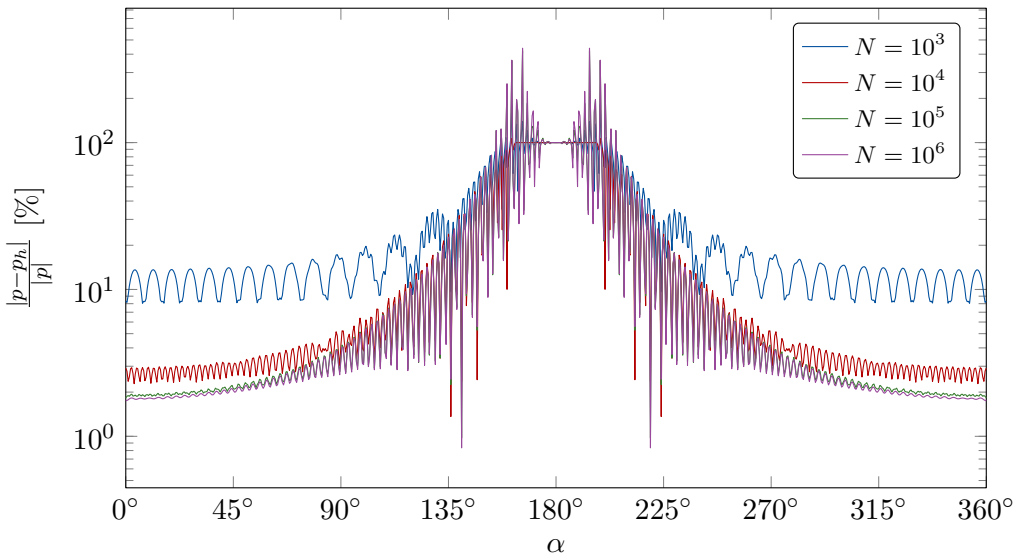

Figure B.11: **Bistatic scattering of rigid sphere**: The relative error (of the far field) is plotted against the aspect angle at $f = 20\,\mathrm{kHz}$.

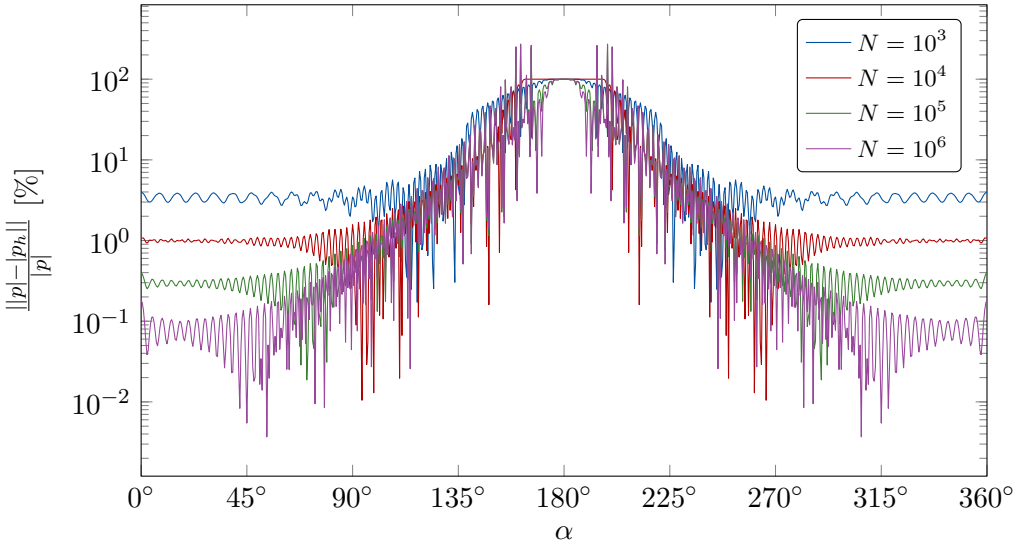

Figure B.12: **Bistatic scattering of rigid sphere**: The relative absolute error (of the far field) is plotted against the aspect angle at $f = 20\,\text{kHz}$.

lacking due to algebraic complexity [6].

A ray tracing algorithm is presented by Martin et al. [6]. The algorithm first finds the intersections of the rays and a set of axis-aligned bounding boxes (see Figure B.13). Then for each box hit, root finding is iteratively applied (using Newton iteration) until a convergence or a divergence criterion is met. As a preprocessing step the control mesh is flattened using refinement. This step is important to obtain a good initial guess for the Newton iterations. Moreover, it reduces the chance of multiple roots in a sub-patch. This new refinement forms a basis for the bounding volume hierarchy. Note that the refined mesh data is only needed in this initial step. Flattening means refining the mesh such that each element satisfies some flatness criteria. More advanced adaptive method could be

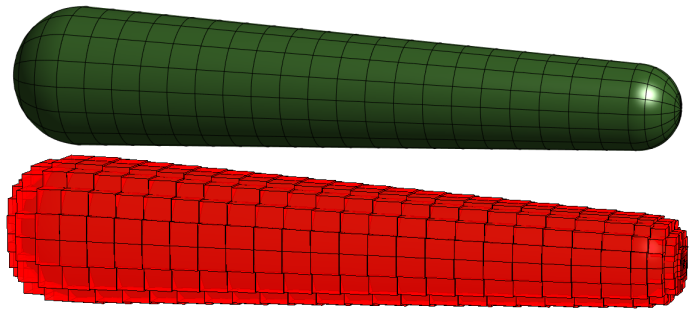

Figure B.13: Uniform refinements gives a basis for the bounding boxes.

utilized. Especially local refinement methods. Martin et al. [6] consider a heuristic tensor product refinement strategy based on the curvature and the arclength. For each knot span, consider the number of new knots to be added is given by

$$n = C \cdot \max_{\xi \in [\xi_i, \xi_{i+1})} \{\text{curvature}(\boldsymbol{X}(\xi))\} \cdot \underset{\xi \in [\xi_i, \xi_{i+1})}{\text{arclength}}(\boldsymbol{X}(\xi))^{3/2}$$

where C is a user defined parameter to control fineness. Several estimates are involved in calculating these quantities, including polynomial estimation of rational curves (NURBS-curves). In the ξ-direction, the number n is computed for each non-empty knot span $[\eta_{j+1}, \eta_j)$, such that the final number of knots to be added in $[\xi_{i+1}, \xi_i)$ is the maximum of these numbers. This procedure is repeated in the η-direction of the tensor product mesh. The inserted knots are spaced uniformly in each sub interval. The final step of the flattening procedure is to duplicate the knots in the knot vector such that each knot is repeated p times. The control points for each element then forms a basis for its bounding box.

The empirical parameter C must be carefully chosen by the user. To small, and it can result in failure in the root finding process. To large, and the bounding volume hierarchy becomes large and computationally expensive. The hierarchy is built based upon the created bounding boxes: the leaves. These leaves are used to provide initial guess for the Newton iteration (midpoint in the element). The root and internal nodes of the tree will contain larger volumes which bounds portions of the underlying surface. The tree is formed by sorting the volumes according to the axis direction which has greatest extent across the bounding volumes, splitting the data in half, and repeating the process.

To ensure that the resulting root, $\boldsymbol{P}$, obtained by Newton iterations lie on the line, $\boldsymbol{r}(s) = \boldsymbol{o} + s\boldsymbol{d}$, the following projection is made

$$s = (\boldsymbol{P} - \boldsymbol{o}) \cdot \boldsymbol{d}$$

Self-intersection can be avoided by a requirement that the new ray has traveled a minimum distance.

As for the sphere, the exact beams may be computed for the BeTSSi model 3. The monostatic target strength in the xy-plane as a function of the azimuth angle φ is

$$\text{TS} = \begin{cases} 20\log_{10}\left(\frac{R_{\text{o}2}}{2}\right) & 0 \leqslant \varphi < \varphi_{\max} \\ \infty & \varphi = \phi_{\max} \\ 20\log_{10}\left(\frac{R_{\text{o}1}}{2}\right) & \varphi_{\max} < \varphi \leqslant \pi \end{cases}$$

where [7, p. 108]

$$\varphi_{\max} = \frac{\pi}{2} - \tan^{-1}\left(\frac{R_{\text{o}1} - R_{\text{o}2}}{L - R_{\text{o}1} - R_{\text{o}2}}\right) = 1.522054475 = 87.20729763^{\circ}.$$

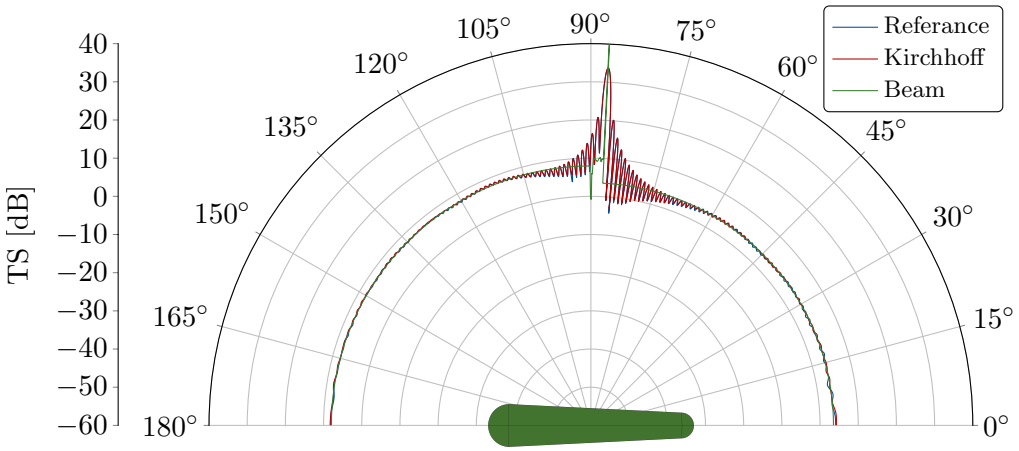

Figure B.14: Scattering on BeTSSi model 3 at 1 kHz.

In Figure B.14 a comparison is made with the beam tray tracing algorithm, the Kirchhoff algorithm (paper IV) and a reference solution created by IGABEM (paper III). The ray tracing procedure fails to obtain accurate results for the far field from the straight sections of the geometry as opposed to the Kirchhoff approximation. On the other hand, the Kirchhoff approximation (based on a simple physical optics approximation) does not model multiple reflections. A remedy for this is to use the Kirchhoff approximation based on the rays leaving the scatterer.

B.3. Computation of reflection and transmission coefficients

For thin elastic layers, rigid boundary conditions perform poorly even for the high frequency spectrum ($f \sim 10\,\text{kHz}$). A ray hitting a surface should be divided into a reflected ray and a transmitted ray. Computation of the transmission and reflection coefficients are then necessary. The steps are presented in the following based on the work of Brekhovskikh [8].

In the solid layer we not only have longitudinal waves, but also transverse waves. For any smooth surface where reflection can be defined, the scatterer can locally be approximated by a plane surface. The transmission and reflection coefficients are then computed on an infinite elastic plate. Without loss of generality the (plane) wave fronts are assumed to lie in the xz-plane and the layers are normal to the z-axis. At each interface we require continuity of displacement and pressure (details in paper I)

$$\rho_\text{f}\omega^2 u_i n_i - \frac{\partial p_\text{tot}}{\partial n} = 0, \quad \sigma_{ij} n_i n_j + p_\text{tot} = 0$$

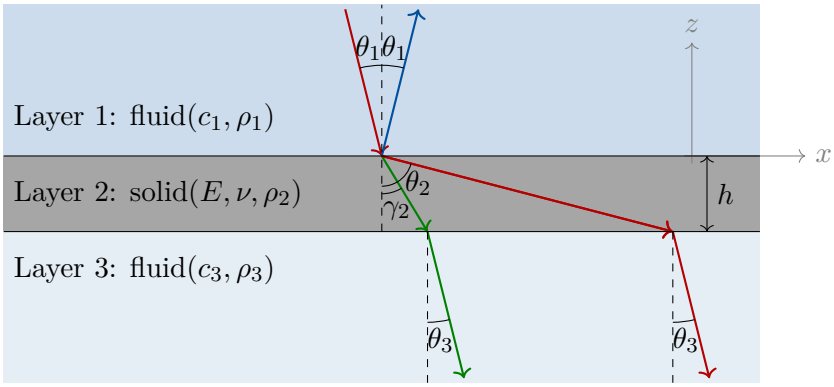

Figure B.15: The incident wave is both reflected and transmitted (into longitudinal and transverse waves) through a solid infinitely large plate.

which in our case is equivalent with

$$\rho_{\mathrm{f}}\omega^2 u_z - \frac{\partial p_{\mathrm{tot}}}{\partial z} = 0, \quad \left(K - \frac{2G}{3}\right)\frac{\partial u_{\mathrm{x}}}{\partial x} + \left(K + \frac{4G}{3}\right)\frac{\partial u_{\mathrm{z}}}{\partial z} + p_{\mathrm{tot}} = 0. \tag{B.1}$$

Here, $p_{\mathrm{tot}} = p_1 + p_{\mathrm{inc}}$ for $z > h$ (layer 1) and $p_{\mathrm{tot}} = p_2$ for $z < 0$ (layer 3) where $p_{\mathrm{inc}} = P_{\mathrm{inc}}\mathrm{e}^{\mathrm{i}k_1(x\sin\theta_1 - z\cos\theta_1)}$. The exterior traction vector, $\boldsymbol{T}$, has components

$$T_i = \sigma_{ij} n_j$$

That is, $\boldsymbol{T} = \sigma_{13}\boldsymbol{e}_{\mathrm{x}} + \sigma_{23}\boldsymbol{e}_{\mathrm{y}} + \sigma_{33}\boldsymbol{e}_{\mathrm{z}}$. For our case the tangential traction free boundary conditions are given by

$$\sigma_{13} = 0 \quad \text{and} \quad \sigma_{23} = 0,$$

which is equivalent with

$$\frac{\partial u_{\mathrm{x}}}{\partial z} + \frac{\partial u_{\mathrm{z}}}{\partial x} = 0 \quad \text{and} \quad \frac{\partial u_{\mathrm{z}}}{\partial y} + \frac{\partial u_{\mathrm{y}}}{\partial z} = 0. \tag{B.2}$$

The solution of the general Navier equation

$$G\nabla^2\boldsymbol{u} + \left(K + \frac{G}{3}\right)\nabla(\nabla\cdot\boldsymbol{u}) + \rho_{\mathrm{s}}\omega^2\boldsymbol{u} = \boldsymbol{0}$$

can be written on the form

$$\boldsymbol{u} = \nabla\phi + \nabla\times\boldsymbol{\psi}.$$

In our special case we have (setting $\boldsymbol{\psi} = \psi\boldsymbol{e}_{\mathrm{y}}$)

$$u_{\mathrm{x}} = \frac{\partial\phi}{\partial x} - \frac{\partial\psi}{\partial z}, \quad u_{\mathrm{y}} = 0, \quad u_{\mathrm{z}} = \frac{\partial\phi}{\partial z} + \frac{\partial\psi}{\partial x}$$

ϕ and ψ are called the potentials for the longitudinal and transverse waves, respectively. These potentials satisfy the Helmholtz equation

$$\nabla^2\phi + a^2\phi = 0 \quad \text{and} \quad \nabla^2\psi + b^2\psi = 0$$

where

$$a = \frac{\omega}{c_{\mathrm{s},1}}, \quad b = \frac{\omega}{c_{\mathrm{s},2}}, \quad c_{\mathrm{s},1} = \sqrt{\frac{3K+4G}{3\rho_{\mathrm{s}}}}, \quad c_{\mathrm{s},2} = \sqrt{\frac{G}{\rho_{\mathrm{s}}}}.$$

The pressure in the fluids also solve the Helmholtz equation

$$\nabla^2 p_1 + k_1^2 p_1 = 0 \quad \text{and} \quad \nabla^2 p_2 + k_2^2 p_2 = 0$$

where

$$k_1 = \frac{\omega}{c_{\mathrm{f},1}} \quad \text{and} \quad k_2 = \frac{\omega}{c_{\mathrm{f},2}}.$$

We look for solutions on the form

$$\begin{aligned}
\phi &= A_\phi \mathrm{e}^{\mathrm{i}(a_{\mathrm{x}}x + a_{\mathrm{z}}z)} \\
\psi &= A_\psi \mathrm{e}^{\mathrm{i}(b_{\mathrm{x}}x + b_{\mathrm{z}}z)} \\
p_1 &= A_1 \mathrm{e}^{\mathrm{i}(k_{1\mathrm{x}}x + k_{1\mathrm{z}}z)} \\
p_2 &= A_2 \mathrm{e}^{\mathrm{i}(k_{2\mathrm{x}}x + k_{2\mathrm{z}}z)}
\end{aligned}$$

where

$$\begin{aligned}
a^2 &= a_{\mathrm{x}}^2 + a_{\mathrm{z}}^2 \\
b^2 &= b_{\mathrm{x}}^2 + b_{\mathrm{z}}^2 \\
k_1^2 &= k_{1\mathrm{x}}^2 + k_{1\mathrm{z}}^2 \\
k_2^2 &= k_{2\mathrm{x}}^2 + k_{2\mathrm{z}}^2.
\end{aligned}$$

The traction free boundary conditions applied to the potentials ϕ and ψ are

$$\frac{\partial^2\phi}{\partial z \partial x} - \frac{\partial^2\psi}{\partial z^2} + \frac{\partial^2\phi}{\partial x \partial z} + \frac{\partial^2\psi}{\partial x^2} = 0.$$

Insertion yields

$$-2a_{\mathrm{x}}a_{\mathrm{z}}\phi - \left(b_{\mathrm{x}}^2 - b_{\mathrm{z}}^2\right)\psi = 0$$

which evaluated at $z = 0$ (upper boundary of solid) gives

$$b_{\mathrm{x}} = a_{\mathrm{x}}$$

Evaluation of the other boundary conditions in a similar fashion yield

$$a_{\mathrm{x}} = k_{1\mathrm{x}} = k_{2\mathrm{x}} = k_1 \sin\theta_1.$$

By writing

$$a_{\mathrm{x}} = a\sin\theta_2, \quad b_{\mathrm{x}} = b\sin\gamma_2, \quad k_{1\mathrm{x}} = k_1\sin\theta_1, \quad k_{2\mathrm{x}} = k_2\sin\theta_3$$

we obtain Snell's law

$$a\sin\theta_2 = b\sin\gamma_2 = k_1\sin\theta_1 = k_2\sin\theta_3.$$

We have

$$\begin{aligned} a_{\mathrm{z}} &= \pm\sqrt{a^2 - a_{\mathrm{x}}^2} \qquad & b_{\mathrm{z}} &= \pm\sqrt{b^2 - b_{\mathrm{x}}^2} \\ k_{1\mathrm{z}} &= \pm\sqrt{k_1^2 - k_{1\mathrm{x}}^2} \qquad & k_{2\mathrm{z}} &= \pm\sqrt{k_2^2 - k_{2\mathrm{x}}^2} \end{aligned}$$

so since we require no waves to originate from infinity for p_1 and p_2, then $k_{1\mathrm{x}} > 0$ and $k_{2\mathrm{x}} < 0$. The solution may thus be written as

$$\begin{aligned} \phi &= A_\phi^{(1)} \mathrm{e}^{\mathrm{i}a(x\sin\theta_2 + z\cos\theta_2)} + A_\phi^{(2)} \mathrm{e}^{\mathrm{i}a(x\sin\theta_2 - z\cos\theta_2)} \\ \psi &= A_\psi^{(1)} \mathrm{e}^{\mathrm{i}b(x\sin\gamma_2 + z\cos\gamma_2)} + A_\psi^{(2)} \mathrm{e}^{\mathrm{i}b(x\sin\gamma_2 - z\cos\gamma_2)} \\ p_1 &= A_1 \mathrm{e}^{\mathrm{i}k_1(x\sin\theta_1 + z\cos\theta_1)} \\ p_2 &= A_2 \mathrm{e}^{\mathrm{i}k_2(x\sin\theta_3 - z\cos\theta_3)}. \end{aligned}$$

Insertion of these expressions into the boundary conditions (Eqs. (B.1) and (B.2)) evaluated at $z = 0$ and $z = -h$ yields a linear system of equations

$$\boldsymbol{H}\boldsymbol{C} = \boldsymbol{D}$$

where

$$\boldsymbol{H} = \begin{bmatrix} -\frac{k_1\cos\theta_1}{\rho_{\mathrm{f},1}\omega^2} & a\cos\theta_2 & -a\cos\theta_2 & b\sin\gamma_2 & b\sin\gamma_2 & 0 \\ 1 & a^2\left(-K - G\left(\frac{1}{3} + \cos 2\theta_2\right)\right) & a^2\left(-K - G\left(\frac{1}{3} + \cos 2\theta_2\right)\right) & -Gb^2\sin 2\gamma_2 & Gb^2\sin 2\gamma_2 & 0 \\ 0 & -a^2\sin 2\theta_2 & a^2\sin 2\theta_2 & b^2\cos 2\gamma_2 & b^2\cos 2\gamma_2 & 0 \\ 0 & -a^2\mathrm{e}^{-\mathrm{i}ah\cos\theta_2}\sin 2\theta_2 & a^2\mathrm{e}^{\mathrm{i}ah\cos\theta_2}\sin 2\theta_2 & b^2\mathrm{e}^{-\mathrm{i}bh\cos\gamma_2}\cos 2\gamma_2 & b^2\mathrm{e}^{\mathrm{i}bh\cos\gamma_2}\cos 2\gamma_2 & 0 \\ 0 & a\mathrm{e}^{-\mathrm{i}ah\cos\theta_2}\cos\theta_2 & -a\mathrm{e}^{\mathrm{i}ah\cos\theta_2}\cos\theta_2 & b\mathrm{e}^{-\mathrm{i}bh\cos\gamma_2}\sin\gamma_2 & b\mathrm{e}^{\mathrm{i}bh\cos\gamma_2}\sin\gamma_2 & \frac{k_2\mathrm{e}^{\mathrm{i}k_2h\cos\theta_3}\cos\theta_3}{\rho_{\mathrm{f},2}\omega^2} \\ 0 & a^2\left(-K - G\left(\frac{1}{3} + \cos 2\theta_2\right)\right)\mathrm{e}^{-\mathrm{i}ah\cos\theta_2} & a^2\left(-K - G\left(\frac{1}{3} + \cos 2\theta_2\right)\right)\mathrm{e}^{\mathrm{i}ah\cos\theta_2} & -Gb^2\mathrm{e}^{-\mathrm{i}bh\cos\gamma_2}\sin 2\gamma_2 & Gb^2\mathrm{e}^{\mathrm{i}bh\cos\gamma_2}\sin 2\gamma_2 & \mathrm{e}^{\mathrm{i}k_2h\cos\theta_3} \end{bmatrix}$$

and

$$\boldsymbol{C} = \begin{bmatrix} A_1 \\ A_\phi^{(1)} \\ A_\phi^{(2)} \\ A_\psi^{(1)} \\ A_\psi^{(2)} \\ A_2 \end{bmatrix}, \qquad \boldsymbol{D} = \begin{bmatrix} -\frac{P_{\mathrm{inc}}k_1\cos\theta_1}{\rho_{\mathrm{f},1}\omega^2} \\ -P_{\mathrm{inc}} \\ 0 \\ 0 \\ 0 \\ 0 \end{bmatrix}.$$

Table 1: Transmission and reflection coefficients for a steel shell of thickness $h = 20\,\text{mm}$ with water in layer 1 and air in layer 3 at $\theta_1 = 0$.

f [kHz]	$\operatorname{Re} T$	$\operatorname{Im} T$	$\operatorname{Re} R$	$\operatorname{Im} R$
1	0.000 379 767	0.000 249 719	−0.395 896 148	−0.917 881 662
3	0.000 111 197	0.000 219 612	0.591 993 753	−0.805 804 333
10	0.000 012 214	0.000 081 497	0.956 075 958	−0.293 076 432
30	0.000 001 290	0.000 029 418	0.996 162 573	−0.087 503 949

Solving this system, we obtain the following expressions for the reflection coefficient R and transmission coefficient T

$$R = \frac{p_1|_{x=0,z=0}}{P_{\text{inc}}} = \frac{A_1}{P_{\text{inc}}} = \frac{M(Z_{\text{f},2} - Z_{\text{f},1}) + \text{i}\big[(M^2 - N^2)Z_{\text{f},2} + Z_{\text{f},1}\big]}{M(Z_{\text{f},2} + Z_{\text{f},1}) + \text{i}[(M^2 - N^2)Z_{\text{f},2} - Z_{\text{f},1}]}$$

$$T = \frac{p_2|_{x=0,z=-h}}{P_{\text{inc}}} = \frac{A_2 \text{e}^{\text{i}k_2 h\cos\theta_3}}{P_{\text{inc}}} = \frac{2NZ_{\text{f},2}}{M(Z_{\text{f},2} + Z_{\text{f},1}) + \text{i}[(M^2 - N^2)Z_{\text{f},2} - Z_{\text{f},1}]}$$

where

$$N = \frac{Z_{\text{s},1}\cos^2(2\gamma_2)}{Z_{\text{f},2}\sin P} + \frac{Z_{\text{s},2}\sin^2(2\gamma_2)}{Z_{\text{f},2}\sin Q}$$

$$M = \frac{Z_{\text{s},1}}{Z_{\text{f},2}}\cos^2(2\gamma_2)\cot P + \frac{Z_{\text{s},2}}{Z_{\text{f},2}}\sin^2(2\gamma_2)\cot Q$$

and

$$P = ah\cos\theta_2, \quad Q = bh\cos\gamma_2$$

$$Z_{\text{f},1} = \frac{\rho_{f,1}c_{\text{f},1}}{\cos\theta_1}, \quad Z_{\text{s},1} = \frac{\rho_{\text{s}}c_{\text{s},1}}{\cos\theta_2}, \quad Z_{\text{s},2} = \frac{\rho_{\text{s}}c_{\text{s},2}}{\cos\gamma_2}, \quad Z_{\text{f},2} = \frac{\rho_{f,2}c_{\text{f},2}}{\cos\theta_3}.$$

For the BeTSSi model 3 a thickness of $h = 8\,\text{mm}$ is used (water on both sides of shell) and for BeTSSi model 1 and 2 a thickness of $h = 20\,\text{mm}$ is used (water in layer 1 and air in layer 3). As can be seen from Figure B.16, the elastic shell has reduced transparency for higher frequencies. Figure B.17 illustrates how well air is approximated with vacuum. The coefficients in Tables 1 and 2 can be used as an approximation (for all θ_1) if the above formulas become too cumbersome to evaluate when simulating the BeTSSi models.

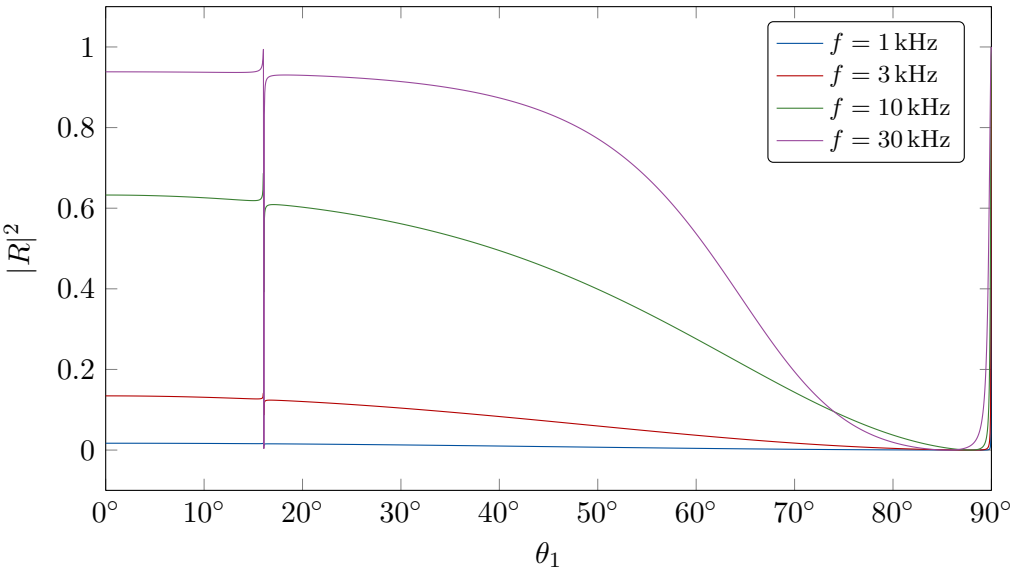

Figure B.16: Reflection coefficient for steel plate ($h = 8\,\mathrm{mm}$) in water

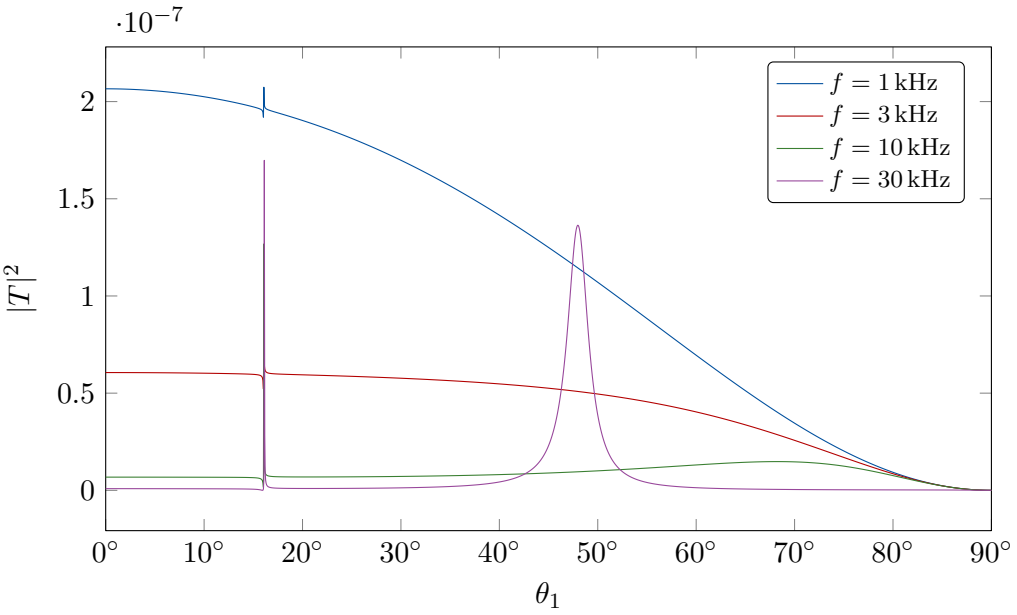

Figure B.17: Transmission coefficient for steel plate ($h = 20\,\mathrm{mm}$) between water and air

Table 2: Transmission and reflection coefficients for a steel shell of thickness $h = 8\,\mathrm{mm}$ with water on both sides of shell at $\theta_1 = 0$.

f [kHz]	$\mathrm{Re}\,T$	$\mathrm{Im}\,T$	$\mathrm{Re}\,R$	$\mathrm{Im}\,R$
1	0.982 994 356	0.129 425 410	0.017 005 608	−0.129 158 694
3	0.865 266 600	0.341 838 512	0.134 733 079	−0.341 038 325
10	0.366 032 206	0.483 053 261	0.633 964 233	−0.480 384 557
30	0.059 738 860	0.241 054 269	0.940 228 789	−0.233 010 583

References

[1] J. J. Shirron, S. Dey, Acoustic infinite elements for non-separable geometries, *Computer Methods in Applied Mechanics and Engineering*, 191:4123–4139 (2002).

[2] J. V. Venås, T. Kvamsdal, T. Jenserud, Isogeometric analysis of acoustic scattering using infinite elements, *Computer Methods in Applied Mechanics and Engineering*, 335:152–193 (2018).

[3] P. S. Heckbert, P. Hanrahan, Beam tracing polygonal objects, *ACM SIGGRAPH Computer Graphics*, 18:119–127 (1984).

[4] F. B. Jensen, W. A. Kuperman, M. B. Porter, H. Schmidt, *Computational Ocean Acoustics*, 2nd edition, Springer New York, 2011.

[5] L. Fillinger, M. Nijhof, C. de Jong, An efficient numerical target strength prediction model: Validation against analysis solutions, in *Papadakis, JS Bjorno, L., Proceedings 2nd International Conference and Exhibition on Underwater Acoustics, UA2014, 22-27 June, Rhodes, Greece, 487–493*, 2014.

[6] W. Martin, E. Cohen, R. Fish, P. Shirley, Practical ray tracing of trimmed NURBS surfaces, *Journal of Graphics Tools*, 5:27–52 (2000).

[7] J. V. Venås, Isogeometric analysis of acoustic scattering, Master's thesis, Norwegian University of Science and Technology, Trondheim, Norway (2015).

[8] L. Brekhovskikh, *Waves in layered media*, vol. 16, Elsevier, 2012.

ISBN 978-82-326-4306-6 (printed version)
ISBN 978-82-326-4307-3 (electronic version)
ISSN 1503-8181

NTNU
Norwegian University of
Science and Technology

Jon Vegard Venås
Doctoral Thesis

Doctoral theses at NTNU, 2019:355

Jon Vegard Venås

Acoustic Scattering in an Isogeometric Framework

Doctoral theses at NTNU, 2019:355
NTNU

NTNU
Norwegian University of
Science and Technology
Faculty of Information Technology
and Electrical Engineering
Department of Mathematical Sciences

NTNU
Norwegian University of
Science and Technology